Behaviour and Analysis of Steel Fibre-Reinforced Concrete under Reversed Cyclic Loading

by

Jun Wei Luo

A thesis submitted in conformity with the requirements
for the degree of Master of Applied Science

Graduate Department of Civil Engineering
University of Toronto

Behaviour and Analysis of Steel Fibre-Reinforced Concrete Subjected to Reversed Cyclic Loading

Jun Wei Luo

Master of Applied Science

Graduate Department of Civil Engineering
University of Toronto

2014

Abstract

It is well known that the monotonic behaviour of reinforced concrete can be improved with the addition of steel fibres. However, test data on the influence of steel fibres on reinforced concrete's cyclic behaviour are scarce.

Ten large-scale panels were tested with the objective of obtaining data useful for developing constitutive relationships for the reversed cyclic behaviour of steel fibre-reinforced concrete (SFRC). The parameters of study included the fibre volume fraction, fibre diameter, and loading protocol. Mechanical properties of the concrete used were also determined through uniaxial tension tests and bending tests. Test results showed that SFRC was effective in resisting damage from the cycling of load, and the panels' reversed cyclic envelope curves closely matched their monotonic backbone curves.

Analyses of the panels and other member-level specimens using VecTor2, a nonlinear finite element program, showed that the reversed cyclic behaviour of SFRC can be adequately represented with currently available constitutive models.

Acknowledgements

Table of Contents

vii

List of Tables

List of Figures

List of Notations

Latin Upper Case Symbols

AR_f	Aspect ratio of fibre
A_b	Area of steel reinforcement bar [mm^2]
A_c	Cross-sectional area of the failure crack, bh [mm^2]
A_f	Cross-sectional area of the fibres [mm^2]
$A_{j,comp}$	Area of the compression jacks of the panel tester [mm^2]
$A_{j,tens}$	Area of the tension jacks of the panel tester [mm^2]
A_{panel}	Cross-sectional area of the panel [mm^2]
A_s	Cross-sectional area of steel reinforcing bar [mm^2]
A_v	Cross-sectional area of stirrups (both legs) [mm^2]
CV	Coefficient of variation [%]
E_{cs}	Secant modulus of elasticity for concrete in compression [MPa]
E_{ct}	Tangent modulus of elasticity for concrete in tension [MPa]
E_f	Young's Modulus of fibre [MPa]
E_s	Young's Modulus of steel reinforcing bar [MPa]
G_{abs}	Absorbed energy for reversed cyclic tests [kN.mm]
P_{max}	Maximum Load [kN]
P_p	Peak load of concrete bending for MOR tests [kN]
P_u	Load at ultimate [kN]
V_u	Ultimate shear force attained (coupling beam analysis) [kN]
V_f	Fibre volume fraction (ratio of the volume of fibres to the volume of concrete) [%]
$V_{f,measure}$	Measured fibre volume fraction [%]

Latin Lower Case Symbols

a	Shear span for beams [mm]
a/d	Shear span-to-depth ratio for beams

a_{max}	Maximum aggregate diameter (VecTor2) [mm]
b	Width of concrete specimen, beam, or failure crack [mm]
d	Depth of reinforcement [mm]
d_b	Diameter of steel reinforcing bar [mm]
d_f	Diameter of fibre [mm]
d_v	Effective shear depth for beams [mm]
f_{cr}	First-cracking stress of concrete in bending for MOR tests [MPa]
f_{xxx}^D	Residual stress at a midspan displacement of L/xxx for MOR tests [MPa]
$f_{c,test}$	Peak compressive stress in the concrete on panel test day [MPa]
f_c'	28-day compressive strength of concrete [MPa]
$f_{c1,cr}$	Principal tesile stress of concrete at cracking [MPa]
$f_{c1,max}$	Maximum principal tensile stress of concrete attained [MPa]
$f_{c1,fail}$	Principal tensile stress of concrete at failure [MPa]
f_{c1}	Principal tensile stress of concrete [MPa]
$f_{c2,max}$	Maximum principal compressive stress of concrete attained [MPa]
$f_{c2,fail}$	Principal compressive stress of concrete at failure [MPa]
f_{c2}	Principal compressive stress of concrete [MPa]
f_{ct}	Residual tensile stress in concrete [MPa]
f_{cx}	Stress in the concrete in the x-direction for concrete panel [MPa]
f_{cy}	Stress in the concrete in the y-direction for concrete panel [MPa]
f_p	Peak stress of concrete in bending for MOR tests [MPa]
f_r	Modulus of rupture of concrete [MPa]
$f_{sx,max}$	Maximum stress in the reinforcement in the x-direction for concrete panel [MPa]
f_{sx}	Stress in the reinforcement in the x-direction for concrete panel [MPa]
$f_{sy,max}$	Maximum stress in the reinforcement in the y-direction for concrete panel [MPa]
f_{sy}	Stress in the reinforcement in the y-direction for concrete panel [MPa]
f_{tu}	Ultimate tensile stress attained after first cracking (dogbone) [MPa]
f_t'	First-cracking strength of concrete [MPa]
f_{tu}	Ultimate tensile stress attained by dogbone specimen after first-cracking [MPa]

f_u	Ultimate strength of steel reinforcing bar [MPa]
f_{uf}	Ultimate tensile strength of fibre [MPa]
f_y	Yield strength of steel reinforcing bar [MPa]
h	Height of concrete specimen [mm]
l	Length of concrete specimen [mm]
l_f	Length of fibre [mm]
s_m	Mean/average crack spacing (panel tests) [mm]
t	Thickness of concrete specimen [mm]
v_{cr}	Cracking shear stress (panel tests) [MPa]
v_u	Ultimate shear stress [MPa] (the maximum shear stress attained during the test)
v_{xy}	Shear stress [MPa]
$w_{cr,avg}$	Average crack width [mm]
$w_{cr,max}$	Maximum crack width [mm]
w_{cr}	Crack width [mm]
w_m	Mean/average crack width (panel tests) [mm]

Greek Symbols

Δ_{pos}	Maximum drift in the positive loading direction [%]
Δ_{neg}	Maximum drift in the negative loading direction [%]
Δ_{sum}	Maximum total drift from both the positive and the negative direction [%]
α_f	Fibre orientation factor
γ_{cr}	Cracking shear strain (panel tests) [x10^{-3}]
γ_u	Shear strain correspond to maximum shear stress (panel tests) [x10^{-3}]
γ_{max}	Maximum shear strain (panel tests) [x10^{-3}]
γ_{xy}	Shear strain [x10^{-3}]
δ_{max}	Deflection at maximum applied load [mm]
δ_u	Deflection at failure [mm]
δ_1	Deflection at initial cracking [mm]
δ_p	Deflection at peak load [mm]

ε_1	Principal tensile strain [x10^{-3}]
ε_2	Principal compressive strain [x10^{-3}]
ε_h	Horizontal direction strain for concrete panel [x10^{-3}]
ε_c'	Concrete strain at peak compressive stress [x10^{-3}]
ε_{c1}	Principal tensile strain of concrete [x10^{-3}]
$\varepsilon_{c1,fail}$	Principal tensile strain of concrete at failure [x10^{-3}]
ε_{c2}	Principal compressive strain of concrete [x10^{-3}]
$\varepsilon_{c2,fail}$	Principal compressive strain of concrete at failure [x10^{-3}]
ε_{sx}	x- direction reinforcement strain for concrete panel
ε_{sy}	y- direction reinforcement strain for concrete panel
ε_t'	Concrete strain at cracking stress
ε_u	Ultimate strain of steel reinforcing bar
ε_v	Vertical direction strain for concrete panel
ε_x	X-direction strain for concrete panel
ε_y	Y-direction strain for concrete panel
ε_y	Yield strain of steel reinforcing bar
θ_ε	Angle of inclination of the principal tensile strain (counter clockwise to the x-axis) [deg]
θ_σ	Angle of inclination of the principal tensile strain (counter clockwise to the x-axis) [deg]
μ_δ	Ductility of flexure critical beams subjected to reversed cyclic loading (Daniel and Loukili, 2002)
ρ_l	Longitudinal reinforcement ratio in concrete beams [%]
ρ_w	Web shear reinforcement ratio ($A_v/(b_w \cdot S)$)[%]
ρ_x	Reinforcement ratio in the longitudinal (or x-) direction [%]
ρ_y	Reinforcement ratio in the transverse (or y-) direction [%]

<div align="center">

Chapter 1
Introduction

</div>

1. Introduction

1.1   Fibre Reinforced Concrete

For thousands of years, small and discrete fibres have been used to reinforce brittle materials. In ancient times, for example, the Egyptians used straws to improve the cracking resistance of sun-dried mud bricks used for constructing huts (Mansour et al., 2007). The feasibility of using fibres to improve the ductility and tensile strength of concrete, however, was not fully realized until the publication of classic reports from Romualdi and Baston in 1963 followed by Romualdi and Mandel in 1964. Soon after, the modern era of research and development of fibre reinforcement technologies began (Zollo, 1997).

Brittle materials, such as concrete, are considered to have no significant post-cracking strength and ductility. When the principal tensile stress for plain concrete exceeds the tensile strength, cracks will develop. The addition of discrete fibres into the concrete matrix can help to reduce microcracking, decrease localized macrocracking and provide improved post-cracking strength and ductility (Shah and Rangan, 1971; Thomas and Ramaswamy, 2007; Grzybowski and Shah, 1990). However, the addition of fibres has little effect on the behaviour of concrete before cracking (ACI Committee 544, 2008).

Flexural and shear reinforcement bars are normally added to concrete to create what is commonly known as reinforced concrete (RC). The introduction of mild steel reinforcement bars in concrete can prevent failure after cracking and dramatically increase the strength and ductility of the concrete material. Various studies have shown that the addition of fibres, steel fibres in particular, to reinforced concrete can reduce or potentially eliminate these conventional primary reinforcement requirements in some cases (Susetyo et al., 2011; Daniel and Loukili, 2002; Lequesne et al., 2010).

Fibre reinforced concrete (FRC) also provides advantages over the use of conventional reinforced concrete for non-structural applications. Studies have shown that FRC will result in smaller crack widths and better abrasion resistance relative to their non-fibrous counterpart

(Johnston, 2001). As a result, secondary reinforcements, such as shrinkage and temperature reinforcement, may also be eliminated with the addition of fibres (Susetyo et al., 2011).

FRC is defined as "concrete made primarily of hydraulic cements, aggregates, and discrete reinforcing fibres" by the American Concrete Institute (ACI) Committee 544 (2008). The fibres can be made from a variety of materials such as steel, carbon, glass, plastic, polypropylene, nylon, and cotton. ACI committee 544 (2008) categorized FRC into four major groups: Steel Fibre Reinforced Concrete (SFRC), Glass Fibre Reinforced Concrete (GFRC), Synthetic Fibre Reinforced Concrete (SNFRC), and Natural Fibre Reinforced Concrete (NFRC). Not all fibres are ideal for the concrete matrix; the following properties are important for fibres in order to obtain satisfactory performance as reinforcement for the concrete matrix (Johnston, 2001):

1. The fibres should have a higher tensile strength than the matrix in order to carry the tensile stresses after cracking.
2. The fibres should be able to withstand high tensile strains in order to have significant deformation before fracturing; this helps to provide significant toughness to the FRC matrix.
3. The fibres should have a higher elastic modulus than concrete to reduce the post-cracking composite strain.
4. The fibres' Poisson's ratio should be low to avoid fibre debonding.
5. The fibres should be elastic and not prone to creep to avoid stress relaxation.
6. The fibres should be physically and chemically compatible with the concrete matrix.

Steel fibre is one of the few fibre types that can satisfy all the above requirements reasonably well. As a result, SFRC technology has grown into a mature industry over the last three decades (ACI Committee 544, 2008), and steel fibres have become the most commonly used fibre in both research and industry. The focus of this work is on SFRC.

SFRC has been utilized for various non-structural applications such as end uses in construction. For example, steel fibres have been used for tunnel lining, rock slope stabilization, lagging for the support of excavation and slabs on ground (ACI Committee 544, 2008). The placement of reinforcing bars or mesh in these applications may be eliminated with the addition of steel fibres. However, SFRC has seen limited structural usage and had some early acceptance as primary reinforcement only in flexural-critical structural members (Meda et al., 2005); these early examples include the elevated slabs of the Heathrow Airport car park in London (ACI

Committee 544, 1988) and the foundation slabs of Postdamer Platz in Berlin (Falkner et al., 1997). Recently, SFRC has gained acceptance in design codes for shear-critical members (ACI Committee 318, 2008) but usage in this type of member, especially for seismic applications, is uncommon. This is likely attributable to the limited research and design recommendations on SFRC for these applications (Wight and MacGregor, 2009). The experimental investigations performed in this work will study the effectiveness of SFRC for cyclically loaded elements and contribute to expanding the limited database. More detailed discussions on the behaviour of SFRC are provided in Chapter 2.

1.2   Objective and Scope of the Thesis

There are three primary objectives in this research program:

1. To investigate the compressive, tensile, flexural, and shear behaviour of SFRC.
2. To study the effects of monotonic and reversed cyclic shear loading conditions on the behaviour of SFRC, addressing the feasibility of steel fibres as reinforcement for cyclically loaded shear-critical elements.
3. To investigate the accuracy of currently available constitutive models in capturing the monotonic and cyclic behaviour of shear-critical SFRC members using finite element analysis procedures.

An experimental test program was undertaken and completed in the structural laboratories at the University of Toronto in order to fulfill the above objectives. A series of large-scale in-plane panel specimens (890 x 890 x 70 mm) were tested using the University of Toronto's Panel Element Tester, a facility capable of isolating shear-related mechanisms. The panels had conventional reinforcement with varying steel fibre volume fractions and fibre diameters. The panel loading conditions included in-plane monotonic shear and reversed cyclic shear. Data from the panel tests allowed a comprehensive investigation into the effects of the presence of steel fibres and conventional reinforcements on cracking characteristics, post-cracking rotation of principal stresses and principal strains, slip along the crack surface, tension stiffening, and tension softening. To supplement the panel tests, three types of material tests were conducted to understand the mechanical properties of SFRC: cylinder compression tests, uniaxial direct tension tests, and modulus of rupture tests.

VecTor2, a nonlinear finite element analysis (NLFEA) software for reinforced concrete structures, was used to investigate the adequacy of currently available constitutive models in predicting the monotonic and cyclic behaviour of SFRC. From this study, deficiencies in the program with respect to the modelling of SFRC and areas for future work were addressed.

1.3   Organization of the Thesis

This thesis provides a detailed description of the experimental and analytical work undertaken to investigate the behaviour of SFRC subjected to in-plane reversed cyclic shear loading condition. The goal of this work is to better understand the behaviour of the material under such loading condition and to expand the limited database of experimental tests. The thesis has seven chapters. The background for fibre reinforced concrete was provided in Chapter 1.

Chapter 2 presents a summary of the available research on the behaviour of SFRC. The properties of SFRC will be presented, followed by a discussion of the shear behaviour of SFRC under monotonic and reversed cyclic loading.

Chapter 3 provides a description of the experimental program, which includes the cylinder compression tests, uniaxial tension tests, bending tests and panel tests. Details of the test specimens, testing methodologies and instrumentation techniques are presented.

Chapter 4 discusses the results from the material tests: the cylinder compression, uniaxial tension, and bending tests. The panel test results are presented in Chapter 5. For all tests, the data analysis procedures, results of the data analysis, and comparative studies performed to investigate the influence of the parameters of study are discussed in their respective chapters.

Chapter 6 presents the finite element analyses using VecTor2 (Vecchio, 1990). The specimens modelled include the panels tested in this work and other structural-level specimens tested by previous researchers. The results of the finite element analyses are discussed and deficiencies encountered are addressed.

Lastly, Chapter 7 presents the conclusions drawn from the experimental and analytical studies. Recommendations for future investigations are provided.

<div align="center">

Chapter 2
Literature Review

</div>

2. Literature Review

2.1 Introduction

This chapter presents a literature review of topics related to this research study. The goal is to provide a description of the currently available knowledge and highlight areas where understanding is lacking. A comprehensive review of SFRC properties will be presented, followed by a summary of experimental investigations into the monotonic and reversed cyclic behaviour of SFRC.

2.2 Steel Fibre Reinforced Concrete Properties

2.2.1 Background

ACI Committee 544 (2008) defines SFRC as "concrete made of hydraulic cements containing fine or fine and coarse aggregate and discontinuous discrete steel fibres". The idea of adding steel fibres in concrete can be dated back to the 1800s when metallic waste was added in concrete (Minelli, 2005). However, like the other types of fibre reinforced concrete, the modern era and research on SFRC did not begin until the 1960s (Zollo, 1997).

The use of steel fibres in reinforced concrete has been known to improve primarily the post-cracking tensile response and crack control characteristics (Shah and Rangan, 1971). The fundamental concept of SFRC is simple. Concrete is weak in tension and reinforcement steel bars are continuous at some specified locations only; hence, the tensile response of conventionally reinforced concrete is improved only in the direction of the reinforcement. Steel fibres, on the other hand, are randomly distributed and discontinuous. These characteristics allow cracks in any direction to be bridged by the fibres and permit improved stress transfer across all cracks, improving post-cracking shear and flexural resistance (Susetyo et al., 2011). Further, fibre bridging allows crack openings to be controlled, enabling the development of additional cracks. In turn, this reduces the crack width and crack spacing, increasing post-cracked ductility and energy absorption capacity (Johnston, 2001; Grzybowski and Shah, 1990;

Deluce and Vecchio, 2013; Susetyo et al., 2011). In tension, SFRC fails only after the fibres fracture or are pulled out from the matrix (ACI Committee 544, 2008). In compression, similar to the tensile response, the addition of steel fibres primarily improves the post-peak ductility and toughness (Thomas and Ramaswamy, 2007).

2.2.2 Fibre Volume Content

One of the key variables influencing the behaviour of SFRC is the fibre volume fraction, V_f. Many tension-critical tests, such as the uniaxial direct tension test, flexural test and direct shear test, have shown that increases in fibre volume fraction will lead to improved toughness, ductility and strength (Shah and Rangan, 1971; Khaloo and Kim, 1997). As the fibre content increases, more fibres are likely to intersect cracks, improving the matrix's ability to bridge cracks and enhance post-cracked behaviour. Research by Shah and Rangan (1971) showed that toughness, defined as the area under the load-deflection diagram, is significantly improved with increases in fibre content; this results in a significant increase in ductility. Strength, however, is only marginally improved. As shown in Figure 2-1, doubling the fibre content from 0.5% to 1.0% increased the concrete uniaxial tensile toughness from 1.8 times to 2.7 times that of the plain concrete, but the concrete uniaxial tensile strength was only increased from 1.1 times to 1.3 times that of plain concrete. These improved behaviours were more pronounced in flexural tests.
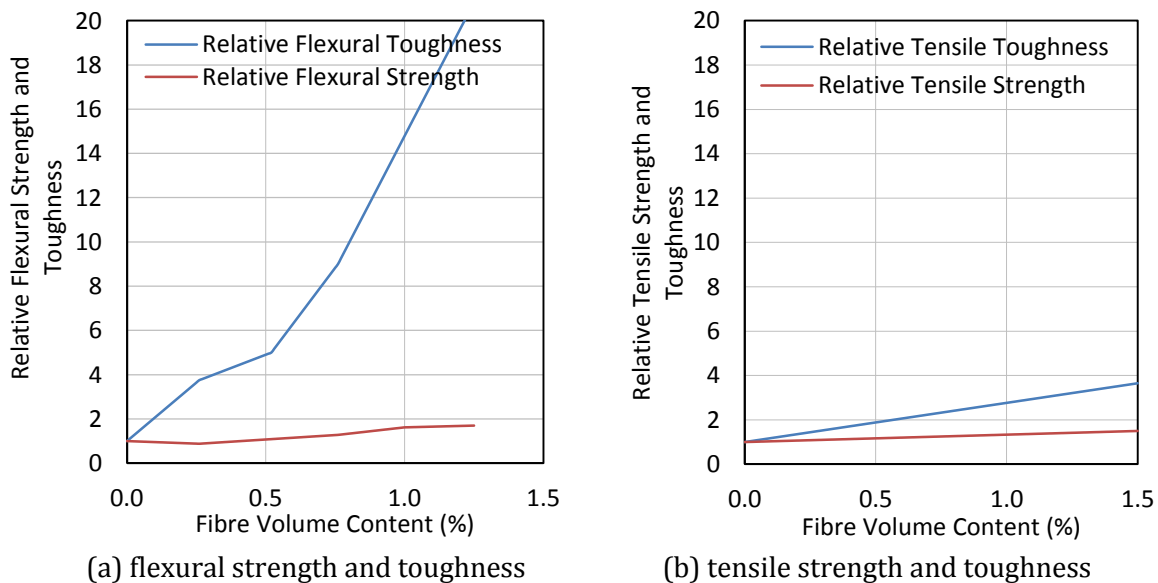
(a) flexural strength and toughness   (b) tensile strength and toughness
Figure 2-1: Influence of fibre volume content on the behaviour of SFRC (Shah and Rangan, 1971)

In direct shear tests, increases in fibre volume fraction also increase the normalized peak shear stress. Some tests had shown that specimens with a medium concrete strength and 0.5%, 1.0% and 1.5% fibre content showed an increase of 33.6%, 58.8% and 73.2%, respectively, in the normalized peak shear stress relative to plain concrete (Khaloo and Kim, 1997). A high fibre volume can cause strain-hardening behaviour, a desirable response where the concrete's maximum tensile stress is higher than the first-cracking stress (Naaman, 1987). Although the exact fibre amount required for strain-hardening depends on other properties of the fibre, some studies have shown that 1.5% fibre volume may be sufficient to cause strain-hardening (Susetyo, 2009; Setkit, 2012).

Similar to the tensile response, increasing the fibre volume fraction improves the compressive post-peak response of concrete (Fanella and Naaman, 1985; Thomas and Ramaswamy, 2007). With increasing fibre content, the pre-peak ascending branch of the compressive stress-strain relationship is marginally improved resulting in a slightly higher elastic modulus (Susetyo, 2009); this improvement results chiefly from the higher modulus of elasticity of steel fibres. However, SFRC typically has a lower modulus of elasticity than non-fibrous concrete (see Figure 2-2). This is because SFRC requires a smaller amount of coarse aggregates than non-fibrous concrete (Susetyo, 2009). The addition of steel fibres only marginally improves the compressive strength, in the range of 0% to 15% (Fanella and Naaman, 1985; Thomas and Ramaswamy, 2007). Further, the strain corresponding to the maximum compressive strength will increase with increasing amounts of steel fibres, leading to greater energy absorption capacity. The toughness and strain at peak stress varies approximately linearly with $V_f * l_f/d_f$, where l_f/d_f (fibre length divided by the fibre diameter) is the fibre aspect ratio (Fanella and Naaman, 1985). The descending branch of the compressive stress-strain relationship, however, is substantially improved with the addition of steel fibres. Increasing the fibre volume fraction will lead to a flatter descending branch, resulting in a significantly enhanced toughness and ductility.

Despite the advantages associated with increases in the fibre content, limits should be placed on the maximum fibre volume fraction due to workability issues and fibre saturation. An increase in fibre content will reduce workability because the fibres reduce the paste volume fraction available for the free movement of coarse aggregates and fibres. As a result, producing SFRC with high fibre contents often requires special mixing and placing methods (Zollo, 1997). Although the maximum fibre content for sufficient workability depends on many variables,

including placement conditions, conventional reinforcement ratios, composition of the concrete mix and fibre properties, ACI Committee 544 (1993) recommends a maximum fibre volume fraction of 2.0% for conventional SFRC. If small steel microfibres were used, the fibre content can be between 5.0 - 9.0% and the product becomes what is commonly known as ultra-high performance fibre reinforced concrete (UHPFRC) (Chao et al., 2009). It is important to note that there may exist a point, the fibre saturation point, for conventional SFRC at which any increase in fibre content will lead to negligible improved behaviour; some studies have shown that this saturation point could be near 1.0% to 1.5% (Susetyo, 2009; Parra-Montesinos, 2006).
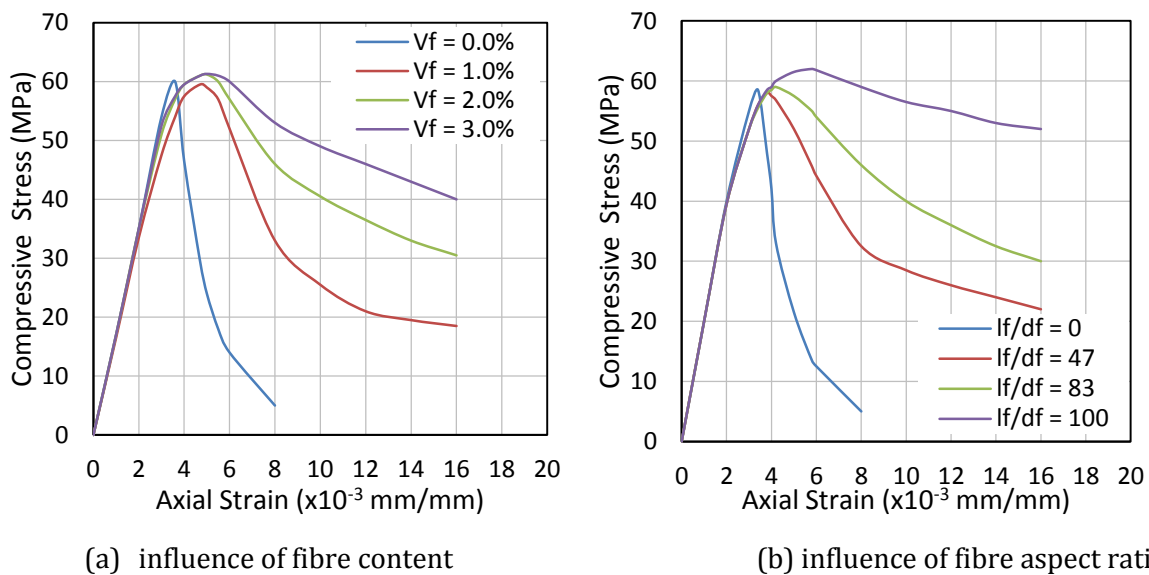
(a) influence of fibre content   (b) influence of fibre aspect ratio

Figure 2-2: SFRC compressive stress-strain curve (Fanella and Naaman, 1985)

2.2.3 Fibre Aspect Ratio

The fibre aspect ratio, defined as the ratio of the fibre length to fibre diameter ($AR_f = l_f/d_f$), has important influence over the effectiveness of fibre reinforcement. Under the same fibre volume, a higher aspect ratio will lead to higher fibre surface area which, in turn, creates an improved bond between the fibres and the matrix; this has the effect of creating a stiffer matrix and improving composite actions (Johnston, 2001).

Flexural tests and uniaxial tension tests conducted by Shah and Rangan (1971) showed that fibres with higher aspect ratio (same diameter but varying length) produced SFRC with marginally a higher strength, but significantly higher toughness. Interestingly, Shah and Rangan (1971) studied fibre aspect ratios in the range of 25 to 100, and found that the

improved tensile response from higher aspect ratios is only true up to an aspect ratio of 75; thereafter, the tensile response worsened for any further increase in the aspect ratio. Direct shear tests performed by Khaloo and Kim (1997) showed increases in the normalized shear strength and the maximum displacement with increases in the aspect ratio. Further, as shown in Figure 2-2, cylinder compression tests with higher aspect ratio fibres showed improved post-peak responses, resulting in a significant increase in toughness and ductility (Fanella and Naaman, 1985).

2.2.4 Fibre Geometry

The fibre length, l_f, may also be an influential factor in the structural behaviour of SFRC. Various studies have shown improvements in overall response when shorter fibres were used (Susetyo, 2009; Deluce, 2011). With the same fibre aspect ratio, shorter fibres will result in a significantly larger number of fibres required to achieve the same fibre volume fraction; this larger number of fibres would lead to improved crack bridging and better stress transfer across the cracks.

The shape of the fibre is another important variable. Steel fibres may be straight, end-hooked, crimpled, flattened-end, etc. (see Figure 2-3). Many studies have shown that at the onset of failure, steel fibres tends to be pulled out from the matrix instead of rupturing (Susetyo, 2009; Carnovale, 2013); as a result, the mechanical anchorage from deformed fibres are critical in the overall response of SFRC. Recent experimental investigations and constitutive model developments have been based upon straight fibres with end-hooks (Lee et al., 2012; Voo and Foster, 2003; Carnovale, 2013; Chalioris, 2013; Setkit, 2012).

(a) straight   (b) end-hooked   (c) crimped   (d) flattened-end
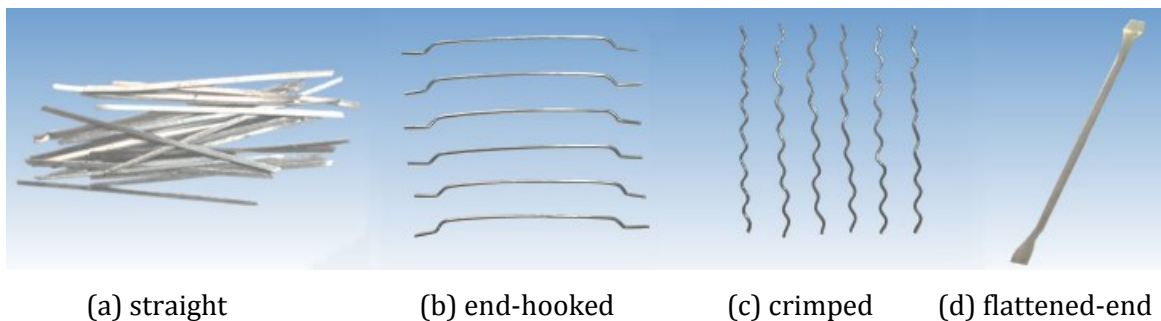
Figure 2-3: Various steel fibre profile (adapted from Susetyo, 2009)

2.2.5 Fibre Orientation

Fibre orientation is a difficult yet important factor to measure. As with conventional reinforcement, fibres are most efficient when they are aligned parallel to the direction of the tensile stress, and are least efficient when they are perpendicular to the tensile stress direction (Shah and Rangan, 1971). This is because the embedment length of the fibres and the number of fibres crossing a crack will decrease as the fibre angle becomes more oblique to the direction of the tensile stress. The efficiency of random fibre orientation is between the above two limiting conditions.

In the modelling of SFRC, many account for the effects of fibre orientation and its impact on the efficiency of fibres through a so-called fibre orientation factor, α_f (Lee et al., 2011; Lee et al., 2012; Voo and Foster, 2003). This fibre orientation factor typically accounts for the fibre orientation angle, fibre dimensions, and member dimensions (Soroushian and Lee, 1990). In short, this factor is the average ratio of the projected fibre length in the direction of the tensile stress to the fibre length itself for all possible fibre orientations. Shown below in Figure 2-4, the fibre orientation factor increases as the SFRC member becomes thinner. This is due to the increased probabilities of fibres aligning themselves in the direction of the tensile stress in a thin member, allowing a more efficient use of steel fibres.
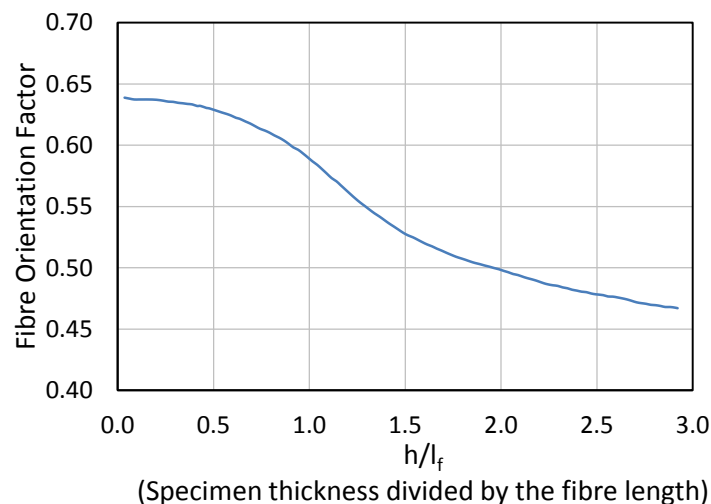
Figure 2-4: Influence of member thickness on the orientation factor (Soroushian and Lee, 1990)

2.2.6 Material Strength

The compressive strength of the matrix can affect the behaviour of SFRC, albeit to a lesser extent. It is well known that a higher compressive strength will produce a higher first-crack tensile strength; however, the post-cracking behaviour of concrete is insignificantly influenced by the matrix's compressive strength (Susetyo, 2009; Thomas and Ramaswamy, 2007). Although a higher concrete strength can increase the bond strength, which is the interfacial shear strength between the fibres and the concrete, the fibres will also experience a higher interfacial shear stress at the onset of cracking due to the higher first-cracking strength. Consequently, more bond slip may occur before fibres can be fully debonded, resulting in a similar post-cracked behaviour relative to lower strength SFRC (Susetyo, 2009). On the contrary, Khaloo and Kim (1997) found that the shear strength enhancement from direct shear test was more pronounced for higher strength concrete.

As with the compressive strength of the matrix, the ultimate tensile strength of the fibres has limited influence over the behaviour of SFRC. Although a higher ultimate strength can increase the fibre's resistance against fracture, many experiments showed that fibre pull-out is the predominant mode of failure (Susetyo, 2009; Carnovale, 2013; Chalioris, 2013; Setkit, 2012). This is in part due to the fibres' relatively high tensile strength, which typically ranges from 1000 MPa to 2300 MPa.

2.3   Shear Behaviour under Monotonic Loading

2.3.1 Background

Unlike flexure failures, shear failures in reinforced concrete are much more brittle, can occur without warning and are more difficult to predict; hence, means for improving the shear response and ductility of reinforced concrete are highly desirable. As aforementioned, the addition of steel fibres can significantly enhance the matrix's tensile response and cracking characteristics. One of the primary structural benefits as a result of these improvements is in enhancing the matrix's shear strength and shear response. Similar to the effects of transverse reinforcement, the addition of steel fibres allows a more uniform distribution of diagonal shear cracks and reduced crack widths (Parra-Montesinos, 2006; Adebar et al., 1997); this, in turn, improves the concrete matrix's shear resistance mechanism, aggregate interlock. This enhanced behaviour is particularly important in large members, where the so-called "size

effect" is predominant and the member becomes more dependent on aggregate interlock to resist shear (Ghannoum, 1998).

In past decades, a significant amount of research into the shear behaviour of SFRC under monotonic loading was conducted. The results of these studies led to the permitted structural use of SFRC in the ACI building code. ACI Committee 318 (2008) now permits SFRC beams to be exempt from minimum conventional shear reinforcement. Most studies related to SFRC under monotonic loading were based upon beam tests. A summary of some of these researches are presented below.

2.3.2 Beam Tests

Steel fibres can generally prevent localization of tensile cracking and produce multiple diagonal cracks (Choi et al., 2007; Aoude et al., 2012; Parra-Montesinos, 2006). As a result, after initial diagonal cracking, SFRC beams will have a higher stiffness and can decrease the beam deflection. Greater ductility can also be achieved with the addition of steel fibres (Aoude et al., 2012). Further, the presence of fibres generally increases the beam's first diagonal cracking load and ultimate shear strength (Mansur et al., 1986).

Numerous studies have shown that the effectiveness of steel fibre depends on the geometry of the beams. Swamy and Bahia (1985) found that the shear strength enhancement varies for different types of beams under monotonic loading; with 0.8% fibre content, T-beams exhibited an 80% increase in shear strength while rectangular beams showed a 30% shear strength improvement. As well, the increase in the cracking load and the ultimate load was more pronounced for beams with smaller shear span-depth ratios (Mansur et al., 1986; Ashou el at., 1992).

Parra-Montesinos (2006) compiled a database of 147 monotonically loaded SFRC beams without stirrups to evaluate the feasibility of using steel fibers as minimum shear reinforcement in lieu of stirrups. ACI suggests the value for concrete's contribution to a beam's shear strength to be $0.17\sqrt{f'_c}$ (MPa) (ACI Committee 318; 2008). However, to be conservative, ACI requires the use of minimum shear reinforcement if the ultimate shear stress exceeds half of plain concrete's contribution, $0.085\sqrt{f'_c}$ (MPa). Parra-Montesinos's (2006) database showed that all SFRC beams with at least 0.75% fibre volume fraction exhibited a normalized shear stress at failure larger than $0.3\sqrt{f'_c}$ (MPa); this value is significantly higher than plain

concrete's contribution. Hence, the data support the use of deformed steel fibres as an alternative to conventional shear reinforcement for shear demands up to $0.17\sqrt{f'_c}$ (MPa).

Aoude et al. (2012) performed a series of full-scale SFRC beam tests with and without minimum conventional shear reinforcement. The beams tested had a depth of 250 mm to 500 mm. The concrete matrix consisted of low strength concrete with hooked-end fibres that had an aspect ratio of 55. Overall, the test results were consistent with findings from Parra-Montesinos (2006). As shown in Table 2-1, beams without shear reinforcement benefited significantly from the addition of steel fibres; a 1.0% fibre addition increased the peak load by more than 50% and considerably improved the ductility. In some cases, 1.0% fibre content was sufficient in altering the failure mode from shear to flexure; however, the load carrying capacity of these fibrous beams was only 81% of the capacity reached by the beams with minimum stirrups. That is, the fibres used in these beam tests were not sufficient in replacing the minimum stirrups. For beams reinforced with minimum shear reinforcement, flexural failures occurred as expected. The addition of fibres in these flexural-critical beams introduced significantly less benefits and did not lead to increases in the load-carrying capacity. This is due to the fact that significant tensile straining would have occurred when the longitudinal reinforcement yielded, and the limited tensile straining capacity of fibres restricts the fibres contribution to the post-yielding capacity. Nevertheless, the post-peak behaviour of these transversely reinforced beams was improved with steel fibres; a 90% increase in the peak deflection was observed with a fibre content of 1.0%.

Table 2-1: Results of full-scale SFRC beam tests (Aoude et al., 2012)

Test ID	V_f [%]	Section [mm x mm]	a /d	d [mm]	Transverse Steel (ρ_w)	f'_c [MPa]	v_u [kN]	v_u [MPa]	v_u /$\sqrt{f'_c}$
A0.0%	-					23.3	36.5	1.20	0.25
A0.5%	0.5	150 x 250	3.0	202	-	21.3	47.5	1.57	0.34
A1.0%	1.0					19.6	56.5	1.86	0.42
B0.0%	-					23.3	125.1	0.95	0.20
B0.5%	0.5	300 x 500	3.1	437	-	21.3	154.3	1.18	0.26
B1.0%	1.0					19.6	198.0	1.51	0.34
BF0.0%	-				10M at	23.3	245.0	1.87	0.39
BF0.5%	0.5	300 x 500	3.1	437	275mm	21.3	244.0	1.86	0.40
BF1.0%	1.0				(0.24%)	19.6	244.3	1.86	0.42

Note: all of the fibres used had a length of 30 mm, an aspect ratio of 55, and a strength of 1100MPa

2.3.3 Panel Tests

Although the above SFRC beam tests can demonstrate the effectiveness of steel fibres as a means to improving the shear behaviour of concrete, the experimental data are not sufficient for developing general constitutive models for SFRC due to the obscuring effects of flexure. To overcome this problem, Susetyo et al. (2011) conducted a series of panel tests using the Panel Element Tester, a facility capable of isolating shear-related mechanisms, located at the structural laboratories of University of Toronto (Vecchio, 1979). The panels were subjected to in-plane monotonic pure shear. Since the panel tester can impose a constant and uniform shear stress over the large specimen (890 x 890 x 70 mm), a thorough investigation on the various behaviours of SFRC under pure shear was possible. Namely, the post-cracking rotation of principal stresses and principal strains, slip along the crack surface, tension stiffening, tension softening, and compression softening (Vecchio and Collins, 1993). These insights will help in the development of constitutive models such that the behaviour of SFRC in shear could be accurately represented by the Modified Compression Field Theory (MCFT; Vecchio and Collins, 1986) or the Disturbed Stress Field Model (DSFM; Vecchio, 2000).

Susetyo et al.'s (2011) test matrix and experimental results are summarized below in Table 2-2. All panels had 3.31% primary reinforcement. However, the SFRC panels had no transverse reinforcement while the control panels had 0.42% transverse reinforcement. Susetyo et al. (2011) found that good shear behaviour can be obtained with sufficient amounts of fibre contents. Panels with at least 1.0% fibre content withstood at least 87% of the maximum shear stress sustained by the control panels; the panel with 0.5% fibre content, however, only sustained 61% of the control panel's peak shear stress. The improvement in ductility as a result of steel fibre additions was less pronounced but significant. Panels with at least 1.0% fibre content exhibited at least 62% of the control panel's peak shear strain, while the panel with 0.5% fibre content would only sustain 46% of the control panel's peak shear strain.

The benefits of fibre addition to the post-cracking tensile behaviour can be further demonstrated by examining the panel's principal tensile stress-strain relationship. Shown in Figure 2-5, the control panel exhibited strain-softening behaviour as expected. On the other hand, SFRC panels with at least 1.0% fibre content displayed strain-hardening response enabling significant transfer of stresses across cracks. Although 0.5% fibre content was not sufficient in developing strain-hardening response, panel C1F1V1 still demonstrated an

improved tensile response relative to the control panel. Figure 2-5 also shows the influence of fibre types; short fibres with a high aspect ratio (i.e. RC80/30BP) had the best response and achieved slight strain-hardening with a 1.5% volume fraction. The impact of fibre length appears to be more significant than fibre aspect ratio as the shorter fibre (i.e. RC65/35BN) performed better than the longer fibre with a higher aspect ratio (i.e. RC80/50BN).

Table 2-2: Results of monotonically loaded shear panel tests (Susetyo, 2009)

Test ID	V_f [%]	l_f [mm]	AR_f	f'_c [MPa]	v_u [MPa]	γ_u [x10^{-3}]	$f_{c1,max}$ [MPa]	$f_{c1,f}$ [MPa]	$w_{cr,max}$ [mm]	s_m [MPa]
C1C	-	-	-	65.7	5.77	6.01	2.87	1.43	0.55	57
C1F1V1	0.5	50	81	51.4	3.53	2.77	2.83	1.85	0.55	114
C1F1V2	1.0	50	81	53.4	5.17	5.27	3.04	2.82	0.45	55
C1F1V3	1.5	50	81	49.7	5.37	5.10	3.13	2.97	0.45	57
C1F2V3	1.5	30	79	59.7	6.68	6.20	3.89	3.69	0.45	38
C1F3V3	1.5	35	64	45.5	5.59	4.27	3.85	3.08	0.50	57
C2C	-	-	-	90.5	6.40	7.00	2.55	1.23	0.50	66
C2F1V3	1.5	50	81	79.0	6.90	5.25	3.66	3.44	0.70	36
C2F2V3	1.5	30	79	76.5	6.31	4.35	3.75	3.62	0.65	47
C2F3V3	1.5	35	64	62.0	5.57	4.97	2.93	2.89	0.60	41
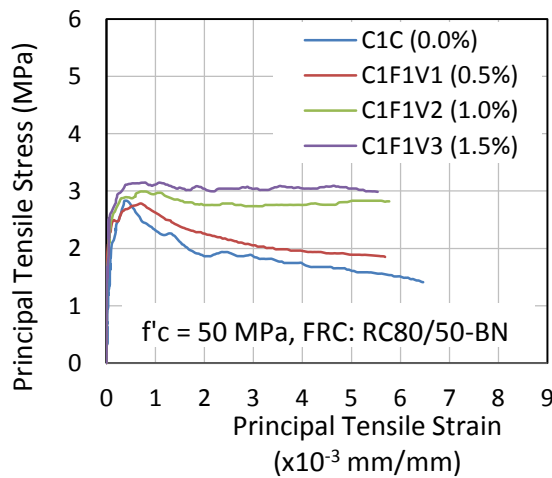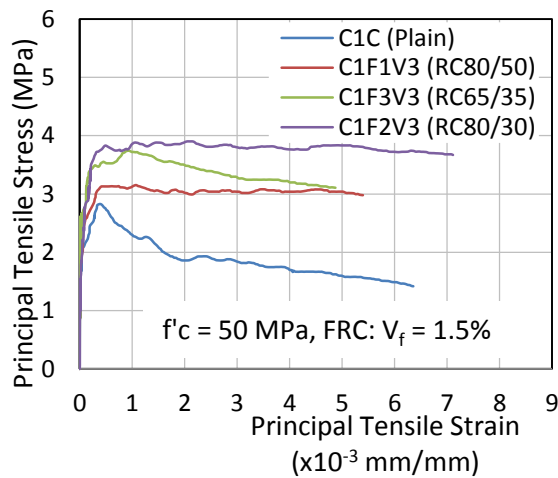
(a) influence of fibre content   (b) influence of fibre type

Figure 2-5: Principal tensile stress-strain response of concrete panels (Susetyo, 2009)

2.4   Shear Behaviour under Reversed Cyclic Loading

2.4.1 Background

Cyclic loading is one of the most challenging cases of loading, as each layer of the structural member is subjected to alternating tension and compression. Under these alternating stresses, the load-deflection envelope curve for shear-critical members will typically exhibit a lower maximum load capacity and a softer post-peak envelope relative to the monotonically loaded backbone curve (Daniel and Loukili, 2002; Chalioris, 2013). Various mechanisms are involved in producing the lower ultimate load, such as the bond deterioration between the concrete and the steel reinforcement, the cyclic softening of materials, the time lag of the force redistribution in the compressive zone due to crack closure, etc. (Popov, 1984; Daniel and Loukili, 2002). Progressive stiffness degradation upon reloading and unloading in inelastic deformation cycles and pinching of hysteretic loops are also characteristic features of shear-critical reinforced concrete elements (Ozcebe and Saatcioglu, 1989; Saatcioglu, 1991; Carnovale, 2013). Limited research has been done to investigate the shear behaviour of SFRC under reversed cyclic loading; however, many of these studies conclude positive effects are attained from the addition of steel fibres in reinforced concrete. These effects include improved energy dissipation, shear strength, and crack control (Chalioris, 2013; Daniel and Loukili, 2002; Setkit, 2012; Carnovale, 2013; Filiatrault et al., 1995). A brief summary of some of these investigations are presented in this section.

2.4.2 Beam-Column Joint Tests

Numerous studies for shear-critical beam-column joint indicated that the use of SFRC near the joint region can improve joint confinement, shear resistance, load at first diagonal crack, stiffness degradation, energy absorption and ductility in joint regions (Jiuru et al., 1992; Filiatrault et al., 1994; Filiatrault et al., 1995). Jiuru et al. (1992) noted that joints using SFRC showed a significant increase in the first diagonal crack shear strength and ultimate shear capacity; these values were increased by about 30% with 1.5% fibre volume. Better bond and reinforcement anchorage was also noted with the use of SFRC.

Compared to plain concrete joints with full seismic reinforcement details, Filiatrault et al. (1994 and 1995) noted that SFRC joints with significantly reduced stirrups generally showed a similar level of stiffness and energy absorption. However, the stiffness and strength

degradation was more rapid in the partially reinforced SFRC joint than the conventionally reinforced joint. Filiatrault et al.'s (1994 and 1995) experiment concluded that the use of 1.6% by volume of end-hooked steel fibres could potentially replace the special seismic requirements for closely spaced stirrups near and at the joint; however, a complete replacement of stirrups was deemed not feasible.

2.4.3 Coupling Beam Tests

Setkit (2012) conducted a series of slender coupling beam tests to evaluate the seismic behaviour of SFRC coupling beams with simplified reinforcement detailing. The SFRC beams had strain-hardening behaviour under direct tension as a result of the high fibre volume fraction, 1.5%. Dramix RC80/30BP fibres, short end-hooked steel fibres with an aspect ratio of 80, were used. The experiment concluded that SFRC beams subjected to large shear reversals ($0.7\sqrt{f'_c}$ (MPa) to $0.9\sqrt{f'_c}$ (MPa)) can exhibit a stable behaviour despite the reduced diagonal and confinement reinforcements. A direct comparison between the SFRC beam with the non-fibrous RC beam (both had identical reinforcement layouts, concrete dimensions, and concrete compressive strengths) showed that the use of a high fibre volume fraction led to a significantly improved response; the peak normalized shear stress increased by 15% (from $0.63\sqrt{f'_c}$ (MPa) to $0.72\sqrt{f'_c}$ (MPa)), and the average drift capacity increased by 64% (from 5.6% drift to 9.2% drift) (Setkit, 2012). The experiment concluded that for design purposes, the shear stress contribution from SFRC material with 1.5% fibre volume can be estimated to be $0.42\sqrt{f'_c}$ (MPa).

2.4.4 Shear Wall Tests

Athanasopoulou and Parra-Montesinos (2013) experimentally investigated the seismic behaviour of low-rise SFRC shear walls with simplified reinforcement detailing. The shear walls had a shear span-to-length ratio of 1.2 or 1.5. The conventionally reinforced concrete walls were detailed according to the seismic provisions of ACI 318-05. The SFRC walls had simplified reinforcement details primarily through reducing or eliminating confinement reinforcement in the boundary regions. Some distributed reinforcement in the web regions was also reduced in the SFRC walls. Strain-hardening behaviour under direction tension was achieved in the SFRC material as a result of the high fibre volume fractions, 1.5% - 2.0%. The results of the experiment are shown in Table 2-3. The experiment showed that SFRC walls with

simplified reinforcement layout exhibited a stable seismic behaviour with significantly improved damage tolerance and narrower cracks. Other than specimen FRC (RS)-M-1.2, all the SFRC walls showed comparable or improved behaviour compared to the companion code-compliant reinforced concrete wall. Specimen FRC (RS)-M-1.2 experienced a low peak load due to the premature sliding shear failure at the wall-foundation interface, which demonstrated the need for dowel reinforcement at that cold joint. All other SFRC walls were strengthen with dowel bars at the wall-foundation interface.

Table 2-3: Results of shear wall tests (Athanasopoulou and Parra-Montesinos, 2013)

Test ID	ρ_{trans}	a/d	V_f [%]	l_f [MPa]	AR_f [MPa]	f_{uf} [MPa]	f'_c [MPa]	v_u [kN]	Drift at max load [%]	Drift capacity [%]
RC-M-1.2	Ø4 at 25	1.2	-	-	-	-	45.8	345	2.1	2.3
FRC(RS)-M-1.2*	-	1.2	2.0	30	55	1100	48.2	265	1.6	3.0
RC-M-1.5	Ø4 at 25	1.5	-	-	-	-	46.5	350	1.5	2.1
FRC(RS)-M-1.5	-	1.5	2.0	30	55	1100	46.7	395	1.6	2.0
RC-H-1.2	Ø4 at 25	1.2	-	-	-	-	45.8	465	0.75	1.5
FRC(HS)-H-1.2	Ø4 at 100	1.2	1.5	30	79	2300	39.5	350	0.85	1.5
RC-H-1.5	Ø4 at 25	1.5	-	-	-	-	42.4	530	0.9	1.5
FRC(HS)-H-1.5	Ø4 at 100	1.5	1.5	30	79	2300	37.9	455	1.1	2.2

* This specimen's response was characterised by large sliding displacement at wall-foundation interface, and was the only SFRC specimen without dowel reinforcement at the wall-foundation interface.
Notes: ρ_{trans} is transverse confinemnt reinforcement at the boundary region; Ø4 smooth wire had an area of 12.6 mm²; a/d is wall shear span-to-length ratio; drift capacity is defined as the maximum drift attained prior to a strength loss greater than 20%.

2.4.5 Beam Tests

As shown in Table 2-4, Daniel and Loukili (2002) found that the addition of steel fibres improved cracking characteristics and post-cracking secant stiffness in flexure-critical beams subjected to reversed cyclic loadings. High strength end-hooked steel fibres with an aspect ratio of 80 were used. Daniel and Loukili (2002) found that the improved responses as result of fibre addition were less pronounced in beams with higher flexural reinforcement ratios; this was believed to be the result of wider crack openings for higher reinforcement ratios which hinder the ability of fibres to bridge cracks. Moreover, steel fibres reduced the ductility

(μ_δ, ratio of deflection corresponding to a load drop of 15% to deflection at maximum load) of these flexural-critical beams; this demonstrated the inefficiency of fibres in the post peak stage due to both the more severe bond deterioration between the reinforcement bars and concrete as a result of the higher maximum load attained by fibre usage, and the repetitive stretching and buckling of the fibres (Daniel and Loukili, 2002). Interestingly, the longer fibres produced better results, especially with regards to energy dissipation, contrary to previous panel test findings on shorter fibres being better (Susetyo, 2009). The improved response for longer fibres relative to shorter fibres was more pronounced in beams with higher reinforcement ratios. This can be due to the fact that longer fibres, instead of having random orientations, are more likely to align in the direction of the primary reinforcements (Susetyo, 2009). Unlike panel tests, in the case of beam tests such alignment turns out to be perpendicular to the main cracks; hence, the post-cracking tensile response would be further improved. As the flexural reinforcement ratios in the beams increase, the likelihood of the longer fibres aligning in the direction of the reinforcement increases.

Table 2-4: Results of flexure-critical cyclic beam tests (Daniel and Loukili, 2002)

Test ID	V_f [%]	l_f [MPa]	AR_f [MPa]	ρ_l [%]	f'_c [MPa]	P_{max} [kN]	δ_{max} [mm]	μ_δ [mm]
L-ref	-	-	-	0.55	97	58.5	9.2	1.52
L-30	1.0	30	79	0.55	110	85.8	9.9	1.31
L-60	1.0	60	80	0.55	116	93.1	9.9	1.28
M-ref	-	-	-	0.97	95	89.0	10.3	1.40
M-30	1.0	30	79	0.97	112	115.6	11.0	1.22
M-60	1.0	60	80	0.97	117	124.2	12.1	1.20
H-ref	-	-	-	1.52	94	151.1	15.1	1.20
H-30	1.0	30	79	1.52	114	159.2	13.7	1.20
H-60	1.0	60	80	1.52	117	178.5	15.0	1.18

Note: all of the beams had a depth (d) of 270 mm and a shear span-to-depth ratio (a/d) of 4.1

As part of the experimental work mentioned above, Daniel and Loukili (2002) also studied the influence of reverse cyclic loading conditions on structural properties for conventionally reinforced concrete beams. Two companion beams for M-ref and H-ref were made and tested under monotonic loading conditions. As shown in Table 2-5, the pre-peak secant stiffness was largely unchanged regardless of the loading condition while the peak load was reduced by approximately 10%. Beyond the peak-load, cyclically loaded beams experienced a significant

decrease in ductility. This reduced ductility and steeper post-peak branch was due to the cyclic softening of materials and crack closure which led to a lag in the force redistribution in the compression zone.

Table 2-5: Results of conventional reinforced concrete beams subjected to different loading conditions (Daniel and Loukili, 2002)

Test ID	Loading Protocol	ρ_l [%]	f'_c [MPa]	P_{max} [kN]	δ_{max} [mm]	μ_δ [mm]
M-ref	Monotonic	0.97	91	102.0	18.0	2.38
	Cyclic	0.97	95	89.0	10.3	1.40
H-ref	Monotonic	1.52	97	166.8	17.6	N/A*
	Cyclic	1.52	94	151.1	15.1	1.20

*data acquisition was stopped shortly after the peak load

Similar to flexure-critical beams, the addition of long end-hooked steel fibres to cyclically loaded shear-critical beams was found to increase the load for first flexural crack, load for first diagonal shear crack, ultimate load, ultimate drift and energy dissipation with respect to the plain concrete (Chalioris, 2013). However, the addition of steel fibres not only inhibited crack growth and crack propagation but also limited crack closing during load reversal; this effect led to greater residual deformation upon unloading. Pinching of the hysteretic loops, reflected by a change in slope during reloading, was also greater in the SFRC beam than the corresponding non-fibrous reinforced concrete beam. Shown in Table 2-6, the addition of a low fibre volume, 0.5%, to plain concrete marginally improved the strength degradation between the monotonic loading and the cyclic loading from 20% (for plain concrete) to 14% (for SFRC). Relative to the plain concrete beam with no stirrups, the addition of 0.75% by volume of fibres can alter the failure mode of the beam from a shear failure to a shear-flexure failure while increasing the shear strength by 85%. However, a fibre volume of 0.75% is not sufficient in replacing conventional stirrups; a beam with this fibre volume can only match the shear strength of a beam with 0.50% conventional shear reinforcement but cannot attain the same failure mode as the conventionally shear reinforced beam, a flexure failure mode (Chalioris, 2013).

Table 2-6: Results of shear-critical cyclic beam tests (Chalioris, 2013)

Test ID	V_f [%]	l_f [MPa]	AR_f [MPa]	ρ_l [%]	ρ_w [%]	f'_c [MPa]	Loading Protocol	v_u [MPa]	$v_u / \sqrt{f'_c}$	Failure Mode
MP	-	-	-	0.55	-	27	Monotonic	0.98	0.19	Shear
MF50	0.50	60	75	0.55	-	27	Monotonic	1.56	0.30	Shear
CP	-	-	-	0.55	-	27	Cyclic	0.78	0.15	Shear
CF50	0.50	60	75	0.55	-	27	Cyclic	1.34	0.26	Shear
CF75	0.75	60	75	0.55	-	27	Cyclic	1.44	0.28	Shear-flexure
CP-S	-	-	-	0.55	0.50	27	Cyclic	1.48	0.28	Flexure
CF50-S	0.50	60	75	0.55	0.50	27	Cyclic	1.63	0.31	Flexure

Note: all of the beams had a depth (d) of 275 mm and a shear span-to-depth ratio (a/d) of 2.0

2.4.6 Panel Tests

The success of Susetyo's (2011) experimental program (SFRC panels subjected to monotonic in-plane shear) in developing general constitutive models gave rise to an experimental program for testing SFRC panels under reversed cyclic in-plane shear. Carnovale's (2013) work included a pilot investigation for this experimental program and one SFRC panel (panel DC-P4) under reversed cyclic in-plane shear was included in his test matrix (see Table 2-7). Similar to Susetyo's (2009) panels, Carnovale (2013) used a primary reinforcement ratio of 3.31% for all panels, and a transverse reinforcement ratio of 0.42% for the conventional RC panel while the SFRC panels had no transverse reinforcement.

Shown in Table 2-7, the loading conditions had a significant impact on the in-plane shear response of the SFRC; under cyclic loading, the peak shear stress and shear strain were severely reduced by 25% and 52% respectively compared to the monotonic loading. Moreover, under reversed cyclic loading, the addition of 1.0% steel fibres could not replace the transverse reinforcement; the cyclically loaded SFRC panel showed a 23% decrease in shear strength and a 64% decrease in peak shear strain compared to the RC control panel. Carnovale's (2013) pilot investigation, however, could not provide a comprehensive overview on the cyclic behaviour of SFRC because only one such panel was tested. Further, the testing for the cyclically loaded SFRC panel was interrupted due to a hydraulic failure. Although the test was resumed after a one week long repair, the response of the panel may have been compromised as a result of the

incident. The work of this thesis aims to expand on Carnovale's (2013) groundwork and produce a more expansive database of SFRC elements under reversed cyclic in-plane shear.

Table 2-7: Results of reversed cyclically loaded SFRC panel tests (Carnovale, 2013)

Test ID	V_f [%]	l_f [mm]	AR_f	f'_c [MPa]	Loading Protocol	v_u [MPa]	γ_u [x10^{-3}]	$f_{c1,max}$ [MPa]	$f_{c1,u}$ [MPa]	w_m [mm]	s_m [MPa]
DC-P1	-	-	-	71.7	Cyclic	5.79	7.98	2.82	0.65	0.57	55.6
DC-P2	1.0	30	79	62.1	Mono.	5.97	5.94	3.37	2.95	0.21	43.0
DC-P4	1.0	30	79	66.0	Cyclic	4.47	2.87	3.54	2.59	0.22	71.0

Note: Carnovale's (2013) macro-synthetic fibre reinforced concrete panel tests are excluded in the above table.

The aforementioned literature review demonstrates that the addition of steel fibres is an attractive option in partially replacing conventional shear reinforcement and the special confinement reinforcement needed for seismic detailing. However, the research available for cyclically loaded SFRC elements is limited and the majority of the studies performed focused on the cyclic response of structural members, limiting the usefulness of these experimental results in the development of constitutive models for SFRC under cyclic loading.

In this work, the influence of steel fibres on the shear behaviour of panel elements under monotonic and reversed cyclic loadings will be examined. To accomplish this and build on the work of Carnovale (2013), a more comprehensive series of SFRC panel tests were conducted. The panel tests eliminated the obscuring effects of flexure and provide needed data for developing rational constitutive models for cyclically loaded SFRC elements. These constitutive models together with a rational governing behavioural model such as the Modified Compression Field Theory (Vecchio and Collins, 1986) or the Disturbed Stress Field Model (Vecchio, 2000) can accurately represent the behaviour of SFRC members in shear.

<div align="center">

Chapter 3
Experimental Program

</div>

3. Experimental Program

3.1   Introduction

This chapter provides a detailed description of the experimental program performed. A total of four types of experiments were completed, with the panel tests providing the primary data for the investigation of the reversed cyclic behaviour of SFRC elements. The three material tests were supplementary tests performed to study the mechanical properties of the SFRC used for the panels. A brief description of each experiment is provided in Table 3-1. All experiments were conducted in the structural laboratories at the University of Toronto over a span of 12 months, from January 2013 to January 2014.

Section 3.2 outlines the test matrix and the parameters studied. Section 3.3 provides the properties of the various materials: concrete, reinforcement bars, and fibres. A description of the concrete mix procedures is provided in Section 3.4. Lastly, Sections 3.5 to 3.8 provide details on the specimen, specimen preparation, test instrumentation, and test procedures for the four tests.

<div align="center">

Table 3-1: Types of experiments conducted and their purposes

</div>

Type of Test	Purpose of Test
Cylinder Compression Test	to evaluate the compressive strength and compressive behaviour of SFRC
Uniaxial Tension Test	to study the direct tensile strength and direct tensile behaviour of SFRC
Bending Test	to evaluate the bending strength and residual flexural behaviour of SFRC
Panel Test	to investigate the shear behaviour of SFRC panels under monotonic and reversed cyclic in-plane pure shear

3.2 Experiment Outline

In order to provide a comprehensive database of SFRC elements subjected to reversed cyclic loading, ten series of test specimens were constructed; a panel test was performed for each series. As outlined in Table 3-2, eight of the ten series used SFRC, while the other two series consisted of plain concrete and were the control series. Since every two series had the same concrete mix, the test matrix can be partitioned into five pairs. The two series of the same pair were cast simultaneously with the same batch of concrete; a total of five casts were needed. Each cast consisted of nine cylinders, three dogbones, two modulus of rupture (MOR) prisms, and two panels.

Three parameters deemed important to the behaviour of shear-critical SFRC elements were studied in this work: the fibre volume fraction (V_f), the fibre aspect ratio (AR_f) and the loading condition. The codified names of the SFRC test series comprised of the following three groupings of alphanumeric characters. The first part indicated the fibre type: "F1" for RC80/30BP and "F2" for ZP305. The second part represented the fibre volume fraction: "V1" for 0.5%, "V2" for 1.0%, and "V3" for 1.5%. The last part indicated the loading condition: "MS" for monotonic shear and "RC" for reversed cyclic shear. The codified names of the control series began with a "C" to indicate that it was a control series, while the last part represented the loading condition similar to the SFRC series' codified names.

Table 3-2: Test series and parameters studied

Test ID	Fibre Type	V_f[%]	AR_f	Loading Protocol
CMS	-	-	-	Monotonic
CRC	-	-	-	Reversed Cyclic
F1V1MS	RC80/30BP	0.5	79	Monotonic
F1V1RC	RC80/30BP	0.5	79	Reversed Cyclic
F1V2MS	RC80/30BP	1.0	79	Monotonic
F1V2RC	RC80/30BP	1.0	79	Reversed Cyclic
F1V3MS	RC80/30BP	1.5	79	Monotonic
F1V3RC	RC80/30BP	1.5	79	Reversed Cyclic
F2V2MS	ZP305	1.0	55	Monotonic
F2V2RC	ZP305	1.0	55	Reversed Cyclic

Note: all series had a target compressive strength (f'_c) of 50 MPa and used fibres with a fibre length (l_f) of 30mm

The loading condition was either in-plane monotonic or in-plane reversed cyclic. Five of the panels were subjected to monotonic loading, while their twins were subjected to reversed cyclic loading. It was the objective of this experiment to investigate the reversed cyclic behaviour of SFRC elements; hence, it was desirable to also investigate the monotonic behaviour of SFRC elements so as to better understand the relationship between the two.

As discussed in the literature review, the fibre volume fraction is one of the most important parameters influencing the behaviour of SFRC elements and thus a necessary parameter for this work. The chosen fibre contents were 0.5%, 1.0%, and 1.5%. A fibre volume fraction lower than 0.5% would have negligible influence over the behaviour of the concrete matrix, while a fibre addition larger than 1.5% would lead to significant workability issues and marginally improved behaviour due to fibre saturation (Johnston, 2001; ACI Committee 544, 2008; Susetyo, 2009).

Many previous studies had emphasized the importance of fibre aspect ratio (AR_f) and this work will expand the database on the impact of varying fibre aspect ratios. The majority of the SFRC series used end-hooked Dramix® RC80/30BP fibres which had a fibre aspect ratio of 79 (l_f=30 mm, d_f = 0.38 mm) (Bekaert, 2013). These fibres were chosen due to the relatively high aspect ratio and short fibre length; previous studies have generally concluded that these fibre properties were desirable (Susetyo et al., 2011; Johnston, 2001; Deluce and Vecchio, 2013). The thinness of the panel also required short fibres in order to achieve reasonably realistic fibre orientations. This work intends to compare the shear behaviour of SFRC with different aspect ratios (same length); hence, specimens from Pair #5 used Dramix® end-hooked ZP305 fibres which had a fibre aspect ratio of 55 (l_f=30 mm, d_f = 0.55 mm) (Bekaert, 2013).

All test series had a target concrete compressive strength of 50 MPa. Although a different compressive strength will lead to a different tensile strength of the concrete matrix, the overall behaviour of the shear-critical panels would be insignificantly influenced by the matrix's compressive strength (Susetyo et al., 2011). Hence, the compressive strength was not a variable in this work. The target compressive strength of 50 MPa was selected as this concrete strength is practical and common in industry.

It is of interest to note that Carnovale (2013) tested two reversed cyclically loaded panels (DCP1, DCP4) and one monotonically loaded panel (DCP2) identical to the ones in this test matrix (CRC as DCP1, F1V2MS as DCP2, F1V2RC as DCP4), while one monotonically loaded

panels from Susetyo's (2009) experiment (C1C) was similar to the one in this work (CMS as C1C). Some of these previously tested panels were included in the discussion in later chapters.

3.3   Material Properties

3.3.1 Concrete

Two types of concrete were used in this program, one for SFRC and one for non-fibrous plain concrete. Both types had a target 28-day compressive strength of 50 MPa. The mix designs for both mixes were based on the ones used by Susetyo (2009) and Carnovale (2013); adjustments were necessary due to differences in available material, target compressive strength and workability requirement. The SFRC mix design from Susetyo (2009) and Carnovale (2013) were based on the work of Naaman et al. (2006) at the University of Michigan. Multiple trial batches were made to determine the appropriate mix design adjustments. The dry composition per cubic metre of concrete for both mixes are shown in Table 3-3.

Table 3-3: Concrete mix design (m³ of concrete)

Type of Test	Unit	Plain Concrete	SFRC
Type 10 Cement	kg	360	480
Water	kg	144	206
Sand	kg	847	1114
10 mm Limestone	kg	1080	792
HRWR: Glenium® 7700	mL	2800	3750
Steel Fibres	kg	-	39.3/78.5/117.8*

* corresponds to 0.5%, 1.0%, and 1.5% fibre content respectively

The SFRC mix had a water to cement ratio of 0.43, while the plain concrete mix had a water to cement ratio of 0.40. The addition of steel fibres results in a larger surface area of solids required to be coated by cement paste (Naaman et al., 2006). To compensate, the SFRC mix had less coarse aggregates and a higher paste volume. In addition, a larger amount of high-range water-reducer (HRWR) was added to the SFRC mix to achieve reasonable concrete workability. The amount of fibres required for the various volume fractions was calculated based on assuming the fibres had a density of 7850 kg/m³.

The cement used was Type 10 Portland Cement produced in the Holcim Canada Mississauga Cement Plant. Both the sand and the limestone aggregate were obtained from Dufferin Construction. The aggregates were sieved down to a maximum size of 10 mm using a sieve machine. The HRWR used was Glenium® 7700 from BASF.

3.3.2 Reinforcing Steel

Two types of reinforcing steel were used for the panels: D8 and D4 deformed wires. The SFRC panels used D8 wires only and had no transverse reinforcement. The control panels used D8 as primary reinforcement and D4 as transverse reinforcement.

The mechanical properties of the reinforcing steel were determined by performing steel coupon tests. The steel coupon specimens were 250 mm long, with a free length of 150 mm. An MTS clip gauge with a gauge length of 50 mm was used to record the strain. Due to the short gauge length relative to the free length, many of the coupon specimens fractured outside of the gauge length; this may had marginally reduced the ultimate strain, ε_u.

The coupon test results are shown in Table 3-4. All deformed wires used were cold-formed and exhibited no defined yield plateau. As a result, the yield strength and strain were taken as the proportionality limit. The complete stress-strain relationships for the deformed wires are shown in Appendix A.4.

Table 3-4: Mechanical properties of the reinforcing steel

Wire Type	d_b [mm]	A_s [mm²]	E_s [GPa]	f_y [MPa]	ε_y [x10^{-3}]	f_u [MPa]	ε_u [x10^{-3}]
D4	5.70	25.5	190.5	490.6	2.60	639.2	21.8
D8	8.10	51.5	184.7	457.8	2.48	591.9	33.7

3.3.3 Steel Fibres

As previously mentioned, two types of end-hooked fibres were used in this experiment: Dramix® RC80/30BP fibres, and Dramix® ZP305 fibres. All fibres were obtained from Bekaert. Images of the fibres are shown below in Figure 3-1. The mechanical properties of these fibres were obtained directly from Bekaert (2013) and are summarized below in Table 3-5. Note that the lower aspect ratio for the ZP305 fibre meant fewer fibres would exist in a unit volume of

concrete compared to concrete with the RC80/30BP fibre. The number of fibres in a unit volume of concrete with 1.0% ZP305 is approximately the same as the number of fibres in a unit volume of concrete with 0.5% RC80/30BP.
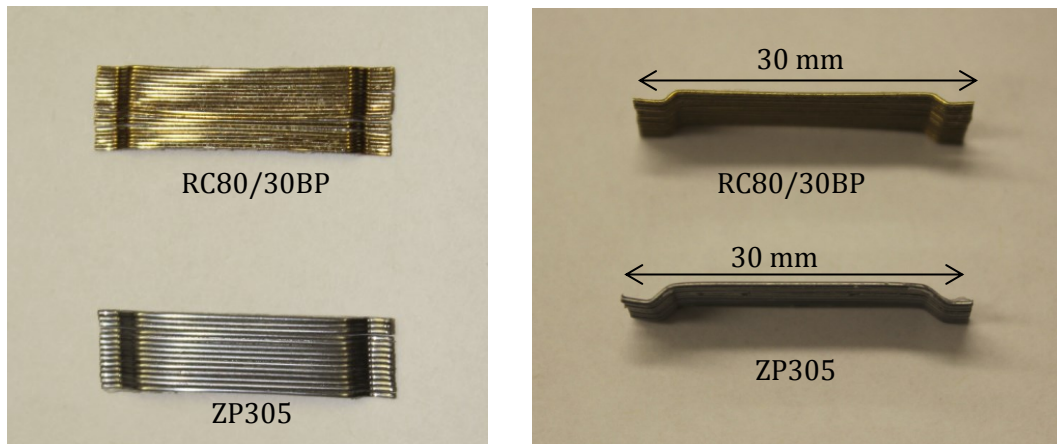
Figure 3-1: Dramix® end-hooked fibres

Table 3-5: Mechanical properties of fibres (Bekaert, 2013)

Fibre Type	l_f [mm]	d_f [mm]	AR_f [mm/mm]	f_{uf} [MPa]
RC80/30BP	30	0.38	79	2300
ZP305	30	0.55	55	1300

3.4 Concrete Casting

3.4.1 Concrete Mixing Procedure

All of the concrete used in this experimental program was mixed using a 150 litre capacity pan-mixer in the structural laboratory at the University of Toronto (see Figure 3-2). Such a large pan-mixer was necessary because one cast, which included two panels, two MORS, three dogbones, and nine cylinders, required approximately 150 litres of concrete. Two types of concrete were mixed in this experimental program: SFRC and non-fibrous plain concrete. The mixing procedure, adopted and modified from Susetyo (2009) and Carnovale (2013), was identical for both types of concrete and is summarized below:

1. The concrete mixer drum, rotor and chute were cleaned and rinsed with water.

2. The coarse aggregate was added to the mixer and then dry-mixed for 30 seconds.

3. The cement was added, followed by the sand. The mix was then dry-mixed for 3 minutes.

4. As the drum rotated, one-half of the water quantity and one-half of the HRWR was mixed in a bucket and was gradually added to the mix. At this point, the mix inside the drum became very stiff and could potentially have led to overheating of the mixer. To prevent this, the next step was completed in a timely manner.

5. As the drum rotated, the remaining one-half of the water and one-half of the HRWR were mixed in a bucket and gradually added to the mix. The mixing process continued for another 3 minutes.

6. The mixing process was stopped for 30 seconds and the quality of the mix was checked. The mix at this stage should have been very workable (slump should be above 200 mm); otherwise, a small amount of water (1.5 L) and HRWR (70 ml) was added. Regardless of the adjustment, the concrete was mixed for another 2 minutes.

7. For SFRC mixes, all of the fibres were sprinkled into the drum while the drum rotated. The sprinkling process took approximately 1 minute per 20 kg of fibres (i.e. 0.25% volume fraction). Afterwards, the mixing process continued for another 3 minutes. For the plain concrete mix, this step was omitted.

8. The concrete mixing was completed. A slump cone test was performed at this stage to ensure the concrete was workable. The target slump was 150 mm.

9. The concrete was then loaded into a buggy and the specimens were cast.

Figure 3-2: Eirich Concrete Mixer (150 litre capacity)

3.4.2 Workability Assessment

The workability of concrete was assessed using the conventional slump cone test. The slump for each test series is shown in Table 3-6. Images of the completed mixes are also shown below in Figure 3-3.

Table 3-6: Slump cone test results

ID	V_f [%]	AR_f	Slump [mm]
CMS	-	-	
CRC	-	-	190
F1V1MS	0.5	79	
F1V1RC	0.5	79	130
F1V2MS	1.0	79	
F1V2RC	1.0	79	90
F1V3MS	1.5	79	
F1V3RC	1.5	79	170
F2V2MS	1.0	55	
F2V2RC	1.0	55	160

Control
190 mm slump – Plain

F1V1
130 mm slump – 0.50% RC80/30BP

F1V2	F1V3
90 mm slump – 1.0% RC80/30BP	170 mm slump – 1.5% RC80/30BP
F2V2	
160 mm slump – 1.0% ZP305	

Figure 3-3: Completed Mixes

3.4.3 Curing Procedure

The casting and curing process followed procedures outlined by ASTM Standard C192/C192M (2002). Details of the casting procedure for each specimen type are discussed in their respective section. Once the concrete was cast, the surface was screeded and hand floated with trowels and attempts were made to remove any fibres sticking out of the surface. The concrete was left uncovered in open air after casting for approximately three hours to allow time for

initial setting. Afterwards, one final round of surface finishing was performed and all concrete specimens were covered with wet burlap and polytarp plastic.

One day after casting, the cylinders, dogbones, and MOR prisms were demoulded and continued to be cured with wet burlap and polytarp for the next six days; the panels, on the other hand, were cured with plastic-covered wet burlap for the next six days and removed from the casting table afterwards. Seven days after casting, all specimens would had been moist-cured for one week and were then left in open air and cured in ambient conditions.

3.4.4 Fibre Distribution

The fibre distribution within the specimens and the apparent fibre volume fraction are another measure of the success of the casting procedure. To assess these factors, the number of fibres crossing the failure plane were counted after the specimens were tested. Equation 3.1 (Lee et al., 2011) was used to determine the theoretical fibre orientation factor which was then used to calculate the theoretical fibre volume fraction using Equation 3.2 (Soroushian and Lee, 1990).

$$a_f = \frac{0.13}{(b \cdot t / l_f^2)^{1.12}} + 0.087 \left(\left(\frac{l_f}{b} \right)^{1.12} + \left(\frac{l_f}{t} \right)^{1.12} \right) + 0.5 \tag{3.1}$$

$$V_f = \frac{N_f \cdot A_f}{A_c \cdot a_f} \tag{3.2}$$

where,

A_c = cross-sectional area of the failure crack [mm²]

A_f = cross-sectional area of the fibres [mm²]

N_f = number of fibres crossing the failure plane

V_f = fibre volume fraction [%]

b = length of failure plane [mm]

t = width of failure plane [mm]

l_f = length of fibre [mm]

a_f = fibre orientation factor

The above relationship for the fibre orientation factor was calibrated to the values employed in the Diverse Embedment Model for three-dimensional members (Lee et al., 2011). Carnovale (2013) had success obtaining the measured fibre volume fraction using the above equations.

The equation yielded a fibre orientation factor of 0.5693, 0.5317, and 0.5489 for the dogbones, MORs, and panels, respectively. Since the cross-sectional area of the failure plane varied marginally between different specimens, a constant fibre orientation factor was used for specimens of the same type. To account for the reinforcements crossing the panel failure plane, the thickness used for panel's orientation factor was reduced to 53.6 mm. The relationship between the fibre volume fraction and the number of fibres bridging the crack surface was from the work of Soroushian and Lee (1990). The corresponding calculated fibre volume fraction for all test series and all specimen types are shown in Table 3-7.

Table 3-7: Measured fibre volume fraction

Series	V_f [%]	Dogbone	MOR	Panel
F1V1MS	0.5	0.48 (5.88)	0.44 (1.50)	0.31 [75% back]
F1V1RC	0.5			0.31 [68% back]
F1V2MS	1.0	0.98 (7.33)	0.84 (5.41)	0.60 [68% back]
F1V2RC	1.0			0.59 [72% back]
F1V3MS	1.5	1.07 (9.34)	0.67 (7.75)	0.62 [68% back]
F1V3RC	1.5			0.74 [75% back]
F2V2MS	1.0	0.83 (17.1)	0.70 (9.60)	0.58 [73% back]
F2V2RC	1.0			0.61 [66% back]

* values given are $V_{f,measure}$ in % (coefficient of variation in %) [% fibres at back face]

Overall, the measured fibre volume fractions were lower than the design values for all specimens. This was partly due to the fact that failure occurs at the weakest section along the specimen, and this weaker section likely has fewer fibres bridging the crack.

It is important to note that for the F1V3 series, a large variation in fibre concentration was observed during casting. It is believed that some regions of the F1V3 specimens had significantly larger concentrations of fibres while some regions had significantly less; as a result, the failure plane had a notably lower number of fibres.

Except for the F1V3 series, the dogbone and MOR specimens achieved a measured fibre volume fraction comparable to the design value; for the panels, however, the measured fibre volume fraction was approximately 60% of the design value for all series (and less than half for the F1V3 series). Since all failure planes were aligned with and next to the primary reinforcement, the discrepancy in the fibre volume fractions may be attributed to the difficulty in achieving

good fibre distribution near these heavily reinforced zones (see Figure 3-4). As well, nearly 70% of all fibres were concentrated in the top half (near the finished face) of the panels due to difficulty in moving fibres down the tightly reinforced cage. This was apparent upon examining the failure plane of all panels (see Figure 3-4). The implications of the above non-ideal fibre distributions will be discussed in later chapters.
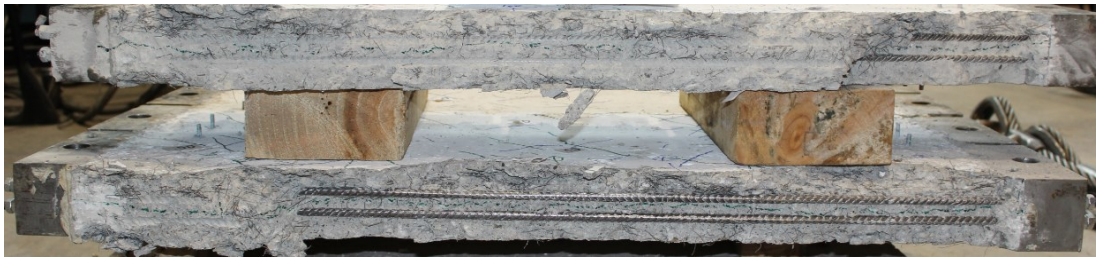
(a) full size

(b) scaled up

(Note: the top side is the finished face)

Figure 3-4: Representative panel failure plane (F1V3RC)

3.5   Cylinder Compression Test

3.5.1 Cylinder Size Effect

The purpose of the cylinder compression test was to evaluate the uniaxial compressive response of SFRC. Small cylinders with a height of 200 mm and a diameter of 100 mm were used in this work. However, large cylinders with a height of 300 mm and a diameter of 150 mm were used with panel tests previously performed at the University of Toronto (Susetyo, 2009; Carnovale, 2013). Large cylinders were expected to achieve a more representative behaviour

because they allow a better fibre distribution and random fibre orientation. Nevertheless, the cylinder size was reduced in this work to allow easier handling of cylinders and, more importantly, to retain enough concrete so two panels could be made in one cast; making two panels with large cylinders in one cast was not possible with the 150 litre capacity pan-mixer.

The use of small cylinders was believed to be justified for this experiment for the following reasons. First, since random fibre orientation would be reasonably achieved if the thickness of the member was more than three times the fibre length (i.e. 90 mm), the 100 mm diameter small cylinder was able to achieve a sufficient degree of random fibre orientation. Second, the thickness of the panels was only 70 mm; hence, the smaller cylinder was able to better represent the compressive behaviour of the panels. Third, the main purpose of the cylinder tests was to determine the compressive strength of the material which was insignificantly affected by the presence of fibres. Lastly, the use of small cylinders is common in SFRC research today (Dinh, 2009; Setkit, 2012).

In order to experimentally verify the insignificance of cylinder size, a small trial batch using 1.5% RC80/30BP fibres (same mix as the F1V3 series) was made to study the compressive behaviour between large and small cylinders; a total of three larger and three small cylinders were made and tested on 21st day. As shown in Figure 3-5, the compressive behaviour between the large and small cylinders was nearly identical. The average compressive strength between the two sizes had a 2.3% difference.
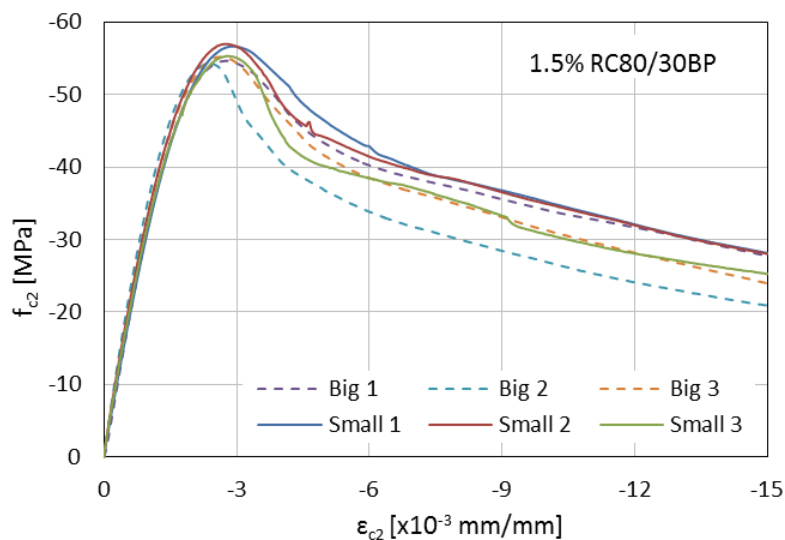

Figure 3-5: Compressive behaviour between large and small cylinders

3.5.2 Test Preparation and Procedure

All cylinders were cast in three layers, and a tamping rod was used to manually consolidate the concrete at each layer. All cylinders were moist-cured with plastic-covered wet-burlap for one week. The cylinders' ends needed to be ground in order to remove the ends' weak paste and to ensure that both ends were parallel to each other. All cylinders were ground flat using a cylinder grinding machine. Due to the sharp fibres, a special steel fibre grinding disk was used to grind all SFRC cylinders. Note that many of the SFRC cylinders previously tested at the University of Toronto were sawn with a target saw and then capped with a sulfur component instead (Carnovale, 2013). This process was time consuming and likely led to a marginally lower compressive strength due to pre-cracking of the sulfur cap. Further, the compressive strength of the sulfur capping material was approximately 60 MPa – less than the strength of some cylinders.

A total of nine cylinders were made from each cast; two were tested on 7th day, three were tested on 28th day, and the last four were tested on the day of the corresponding panel tests (two per each panel test). Using a Forney testing machine, the 7-day test was performed to determine the peak strength and was used as a means to predict the 28-day strength; no strain data were recorded for the 7-day test. The 28-day tests were performed using a MTS Stiff Frame Machine and the full stress-strain relationship was determined. The four cylinder tests performed on the day of the corresponding panel test was tested using the MTS Stiff Frame Machine as well; however, only the peak strength was needed and no displacement data were recorded.

The MTS Stiff Frame Machine used had a capacity of 4,500 kN and was a closed-loop control system controlled by displacement transducers. Linear Variable Differential Transducers (LVDTs) were used to measure the linear displacement throughout the test. As shown below in Figure 3-6, a specially designed LVDT rig was clamped onto the two ends of the cylinders. Two LVDTs were affixed to the two opposing sides of the rig (see Figure 3-7). The LVDTs had a stroke of ± 2.5 mm; hence, the initial position of the LVDTs was set back to 2 mm to allow a maximum displacement of 4.5 mm. The loading rate of the test was set to 0.0044 mm/s. As the two halves of the rig moved with the cylinder, the LVDTs retracted and provided a continuous measure of displacement. The test stopped when the maximum stroke of the LVDTs was reached.

Figure 3-6: Cylinder compression test
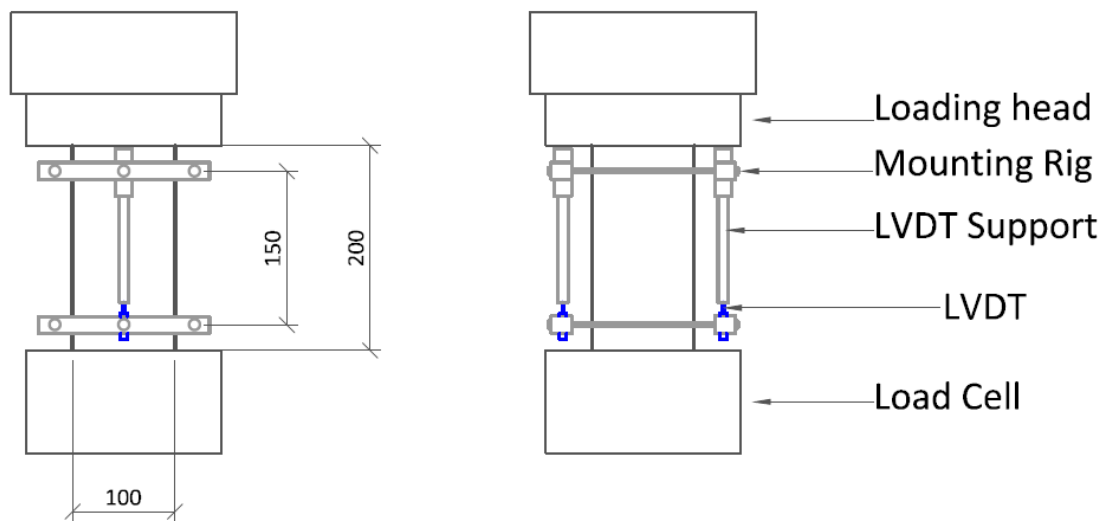
Note: all dimensions in mm

Figure 3-7: Instrumentation setup for the cylinder test

3.6   Uniaxial Tension Test

The purpose of the uniaxial tension test was to assess the tensile behaviour of the SFRC. As discussed in Chapter 2, the addition of steel fibres will significantly enhance the post-cracking behaviour of the concrete matrix; hence, it is necessary to examine the tensile load-displacement relationship. Although the tensile behaviour of concrete can be studied with other standardized tests such as the modulus of rupture bending test (ASTM C1609/C1609M, 2010), the obscuring effect of flexure is undesirable. The uniaxial tension test, informally known as the dogbone test, can provide data for a direct evaluation of the contribution of fibres

in post-cracking behaviour. The uniaxial tension test also provides useful data for determining the tensile constitutive model for SFRC.

Although the dogbone test method is not standardized and is difficult to perform due to uncertainty with the failure crack location, the procedures employed at the University of Toronto have shown good results in the past. The dogbone test procedures in this work were based on methods developed by Carnovale (2013) and Susetyo (2009).

3.6.1 Specimen Description

The dimensions of the dogbone specimens are shown in Figure 3-8. The specimen was designed to fail at the narrow mid-section which had a dimension of 100x70 mm. This dimension was chosen to allow some degree of random fibre orientation, to resemble the thickness of the panel (70 mm), and to permit portability. Although the recommended member thickness for achieving random fibre orientation should be three times the fibre length (ASTM C1019, 1997) – 90 mm for fibres used in this work, a compromise was made to produce resemblance to the panel specimens.

Note: all dimensions in mm
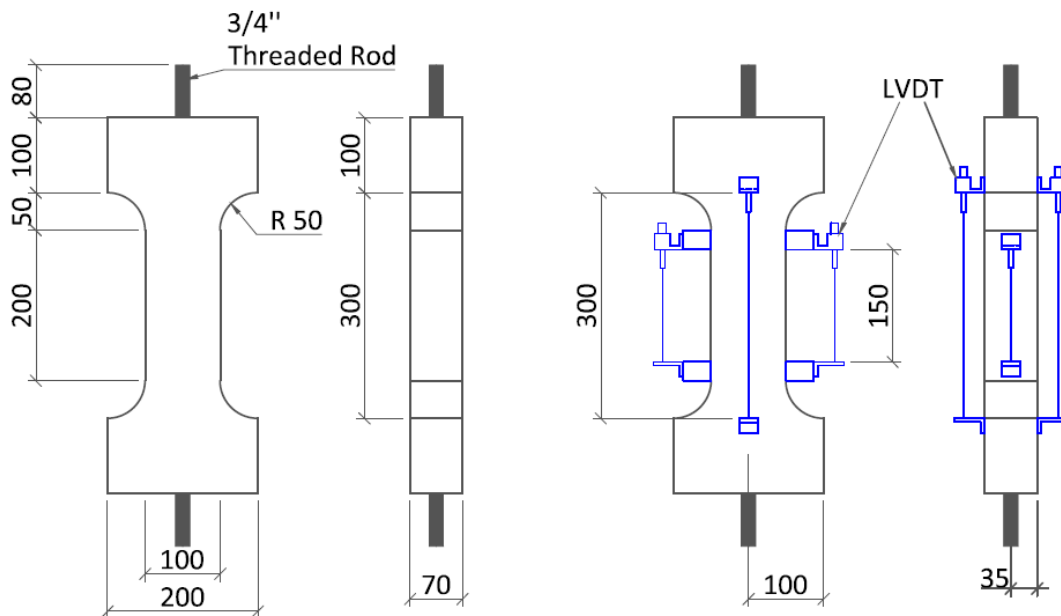
(a) specimen dimension   (b) LVDT configuration

Figure 3-8: Uniaxial tension test

In order to attach the dogbones to the testing machine, ¾''-10 threaded rods were attached to steel form end plates before casting. As shown in Figure 3-9, one nut was placed on the outside

face to secure the threaded rod, another nut was placed at the ends of the threaded rod on the inside face to provide some mechanical anchorage and to faciltitate better stress transfer. The threaded rod was later directly attached to the testing machine. The threaded rod extended 70 mm into the specimen. Carnovale's (2013) work indicated a longer inside length for the threaded rod may lead to propagation of the failure crack due to stress concentration at the ends of the rod.

Figure 3-9: Dogbone forms with ¾'' threaded rods locked in

Before Carnovale's (2013) use of threaded rods to directly connect the dogbone specimen with the testing machine, many of the dogbone specimens tested at the University of Toronto were connected to the testing machine through bonded steel end plates (Susetyo, 2009; Hrynyk, 2013). For this method, the ends of the dogbones were smoothened using a miller machine, then a diamond blade was used to make inclined cuts at the ends; lastly, the steel end plates were bonded to the ends of dogbones using structural epoxy. This method was very labour intensive and the threaded rod method was used in this work instead. However, one problem associated with the use of threaded rods inside the specimen was the stress concentration around the rod which may potentially lead to splitting cracks at the edge of the specimen. To overcome this, the V-shaped clamping rig shown in Figure 3-10 was used to supply a compressive stress at the ends of the dogbone to prevent splitting cracks.

Three specimens were made from each cast. During casting, concrete was poured into the form in two layers and an external form vibrator was used to consolidate the concrete at each layer. The dogbone specimens were moist-cured with plastic-covered wet-burlap for one week.
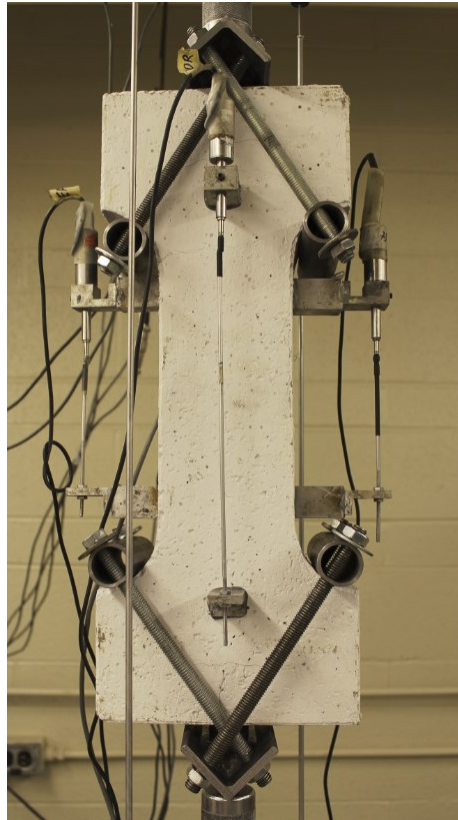
Figure 3-10: Dogbone test setup with clamping rig

3.6.2 Test Instrumentation

As shown in Figure 3-8, four LVDTs with two different gauge lengths were used for each dogbone to better capture the displacement at the failure crack. One pair of LVDTs had a gauge length of 300 mm, while the other pair had a gauge length of 150 mm. As mentioned earlier, the failure crack location was uncertain and not always at the mid-section of the dogbone. Occasionally, failure cracks occured near the transition zone between the mid-section and the end-section. Although it is ideal to only monitor displacements within the mid-section (i.e. within the 150 mm gauge length) where the strain distribution was uniform, a longer gauge length was necessary to capture cracks occuring outside of the mid-section. Susetyo (2009) found that the two guage length configuration depicted above was most practical in capturing the displacement at the failure crack.

3.6.3 Test Preparation and Procedure

To prepare the specimen for testing, the specimen was first painted using a mixture of one part white latex paint and one part water. Using Fastweld 10 epoxy, four pairs of LVDT mounts and reaction plates were then epoxied onto the specimen at the appropriate locations to allow for a gauge length of 150 mm and 300 mm. The actual gauge length was checked and recorded before commencing the test.

The test was performed using an MTS Universal Testing Machine at the University of Toronto (Figure 3-11). The machine was a closed loop machine controlled by displacement transducers and had a capacity of 245 kN. The displacement rate was controlled using LVDTs mounted to the test frame; these LVDTs measured the displacement between the upper and lower machine head. The MTS machine came equipped with two sets of universal joints. The free ends of the joints had a mechanical coupler with ¾'' – 10 threads, which allowed a simple connection between the threaded rod of the specimen and the machine. The data acquisition rate was set to 10 hertz. A loading rate of 0.001 mm/s was initially utilized. When a significant degradation in the post-peak load carrying capacity was observed, the loading rate was gradually increased to 0.01 mm/s.

The LVDTs had a stroke of ±5 mm and were set to -3 mm before commencing the test, so a total stroke of 8 mm was achievable. The test was stopped when approximately 10% of the maximum load was reached in order to produce a complete load-displacement response. If the LVDTs' strokes approached saturation before the end of the test, they were reset to -3 mm and were later accounted for in the data analysis. When the test stopped, the instrumentations were removed and the machine head was retracted to help split the dogbone into two pieces. The fibres intersecting the failure plane for both halves were counted and the failure plane's cross-sectional dimension was recorded.
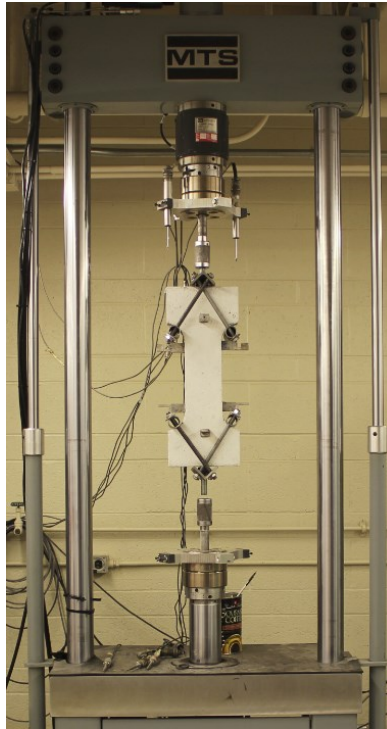
Figure 3-11: Universal testing machine (245 kN capacity)

3.7   Bending Test

The bending test, also known as the modulus of rupture test, was performed to study the tensile behaviour of SFRC subjected to flexure. More specifically, the flexural strength, toughness and ductility were investigated. The test used a non-slotted beam subjected to four-point loading and followed test procedures outlined by ASTM Standard C1609/C1609M (2012).

Another common standardized bending test is the notched beam test under three-point loading (RILEM TC 162). Although the notched beam forces the crack location and simplifies the measurement of the crack mouth opening displacement, the notch introduces weakness in the beam and the results may not reflect the actual flexural response of the concrete.

3.7.1 Specimen Description

The dimensions and the loading arrangement for the specimen are shown in Figure 3-12. The specimen had a cross-sectional dimension of 152x152 mm with a span of 533 mm. The clear span between the supports was 456 mm, and the two loading points were 152 mm away from the support.

Two MOR bending specimens were made for each cast. The number of bending specimens was largely controlled by the capacity of the pan-mixer. The beam was cast in two layers; an external form vibrator was used to consolidate the concrete at each layer. The specimens were then moist-cured with plastic-covered wet-burlap for one week.
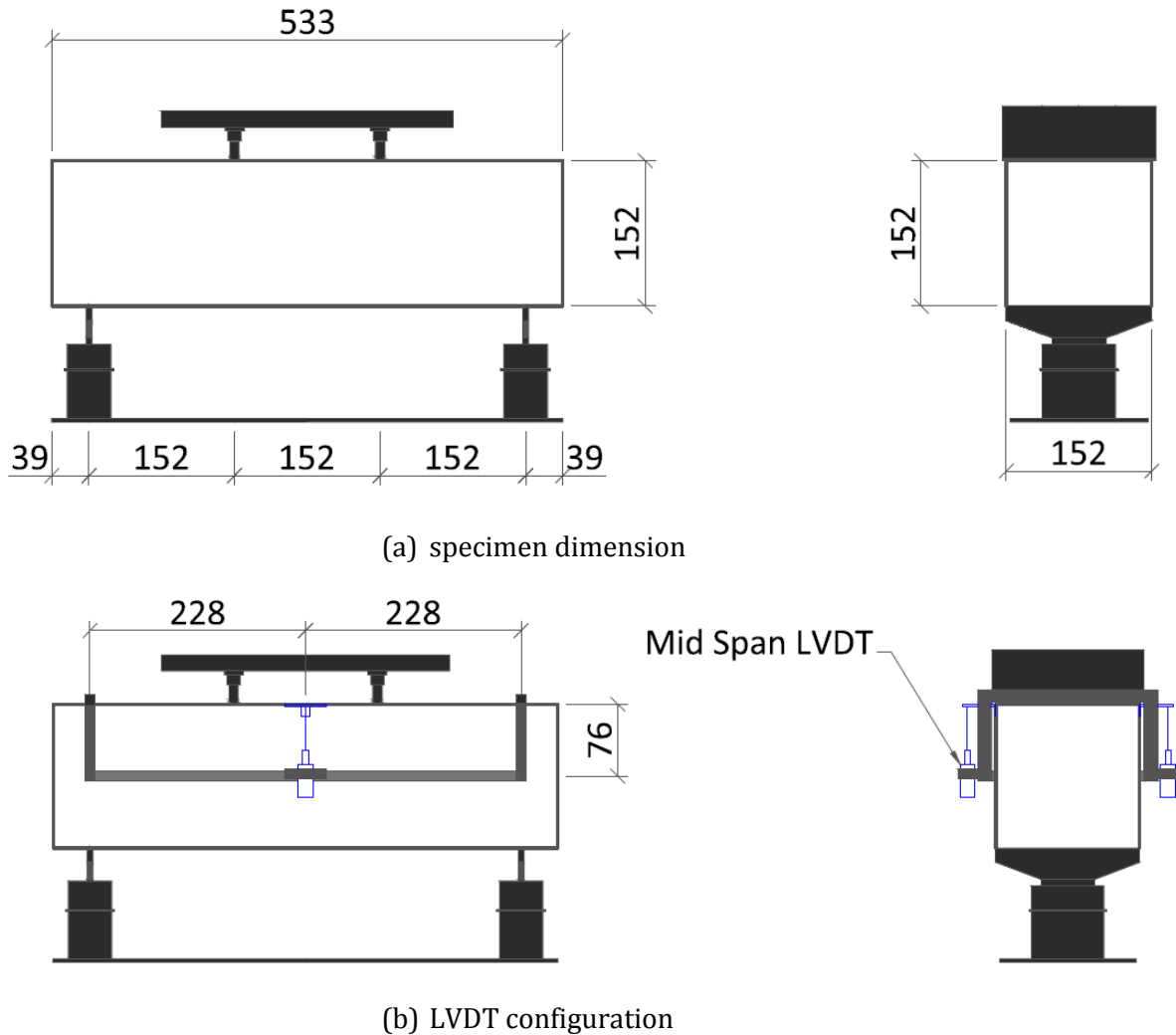

(a) specimen dimension

(b) LVDT configuration

Note: all dimensions in mm

Figure 3-12: Bending test

3.7.2 Test Instrumentation

As depicted in Figure 3-13, the MOR beam was simply supported at the ends with a dual-point loading apparatus at the top of the beam. The two point loads were at the third-points, creating a constant moment with zero shear at the mid-section. A LVDT mounting rig, fabricated at the University of Toronto following specifications set forth by ASTM Standard C1609 (2012), was used to measure the mid-depth displacement at mid-span. The mounting rig was mounted onto

the specimen and allowed the mid-span net deflection to be directly obtained without the need to measure support displacements. Two LVDTs, one for each vertical face, were held by the mounting rig. The LVDTs acted against the reactions plate epoxied onto the top of the beam.
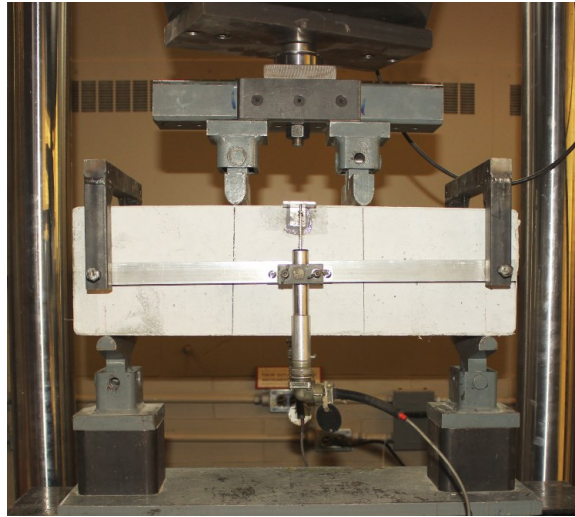

Figure 3-13: Bending test setup

3.7.3 Test Preparation and Procedure

Before testing, the specimens were painted white using a mixture of one part latex paint and one part water. One LVDT reaction plate was epoxied to each vertical face of the beam using Fastweld 10 epoxy; the finished face was the back vertical face. To ease the placement of the LVDT rig, locations of the point loadings and supports were marked. The actual gauge length for the LVDT was measured and recorded before the test.

The test was performed using a MTS Four Post Test Machine which had a capacity of 1000 kN (Figure 3-14). Before commencing the test, the rig was accurately placed on the specimen at the marked locations. Then, the LVDTs were mounted to the rig and the cross-head with the dual-point loading apparatus was carefully placed on top of the marked locations.

Since the LVDTs for the beam test had a stroke of ± 8 mm, they were set back to a value of -4 mm so a total stroke of 12 mm was attainable. The data sample rate was set to 5 hertz. The test began with a loading rate of 0.006 mm/s. After reaching the peak load, the loading rate was gradually increased to 0.02 mm/s. As specified by ASTM Standard C1609 (2010), the test stopped when the specimen no longer displayed load-carrying capacities or the mid-span

deflection had reached 7.5 mm (i.e. L/60). Once the test was completed, the number of fibres intersecting the failure plane for both halves were counted.

Figure 3-14: MTS Four Post Test Machine

3.8   Panel Test

Panel tests were performed to investigate the behaviour of SFRC co-reinforced with conventional deformed reinforcing bar (R/SFRC) under in-plane pure shear and to compare the structural response against conventionally reinforced concrete elements. One of the key benefits from the addition of steel fibres to reinforced concrete is in improving the tensile behaviour of the structural element (Shah and Rangan, 1971). Panel tests were deemed necessary in understanding the key benefits of SFRC because they are much larger in scale when compared to the uniaxial tension test and can better replicate the behaviour of full-sized SFRC members. Unlike the bending test, the panel test can eliminate the obscuring effects of flexure. Further, the addition of conventional reinforcement in the panels allowed for an investigation on the effectiveness of steel fibres under conditions more typical of actual usage in construction. The panel tester machine underwent a major repair during this experimental program before commencing any panel test. A summary of the repair is also presented in this section.

Section 3.8.1 provides a description of the panel tester, the hydraulic jacks together with their repair work, and the hydraulic system used in this work. A description of the specimen is provided in Section 3.8.2, while the instrumentation set up is shown in Section 3.8.3. Lastly, the test preparation and procedure are explained in Section 3.8.4.

3.8.1 Apparatus Description

3.8.1.1 Panel Tester Description

The panel tests were conducted at the University of Toronto using the Panel Tester Machine developed by Vecchio (1979). The machine was the first facility in the world capable of testing large concrete elements in a state of pure shear. The development of the machine was triggered by the need to develop a rational theory for reinforced concrete members under shear. The experimental results for the first major project from the Panel Tester Machine led to the development of the original form of MCFT (Vecchio and Collins, 1986); the theory later became the basis for the current shear design provisions in CSA A23.3-04 (2004).

The machine was designed to allow various in-plane loadings by adjusting the level of thrust or pull from each set of hydraulic jacks acting on the panel. Axial tension, axial compression, pure shear, or combined states of all three loading conditions can be applied to the concrete panel. As depicted in Figure 3-15, the panel has twenty shear keys located around its perimeter through which load is applied. The shear keys have several important functions: they serve as anchorage point for the reinforcement cage, they become part of the form during casting, and they serve as a means of connecting the panel to the testing machine. Each shear key is connected to two links, one vertical and one horizontal. Except for the three rigid links, each link is connected to a hydraulic jack where the load is applied; a total of 40 links and 37 hydraulic jacks are connected to the tester machine.

To prevent the panel from moving in the out-of-plane direction, a lateral support frame is provided on the back of the tester machine as shown in Figure 3-15. The lateral support frame's protruding legs are fixed to the blue reaction frame, and tie-rods are used to connect the lateral support frame to the shear keys. The tie-rods permit translational movement of the shear keys within the plane of the specimen, but resist any out-of-plane movement.
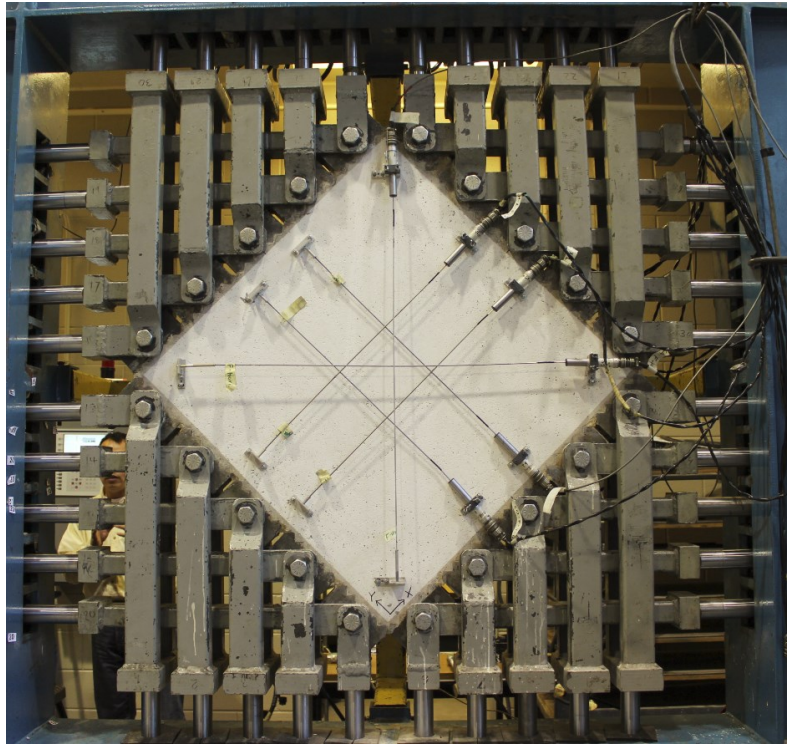
(a) front face
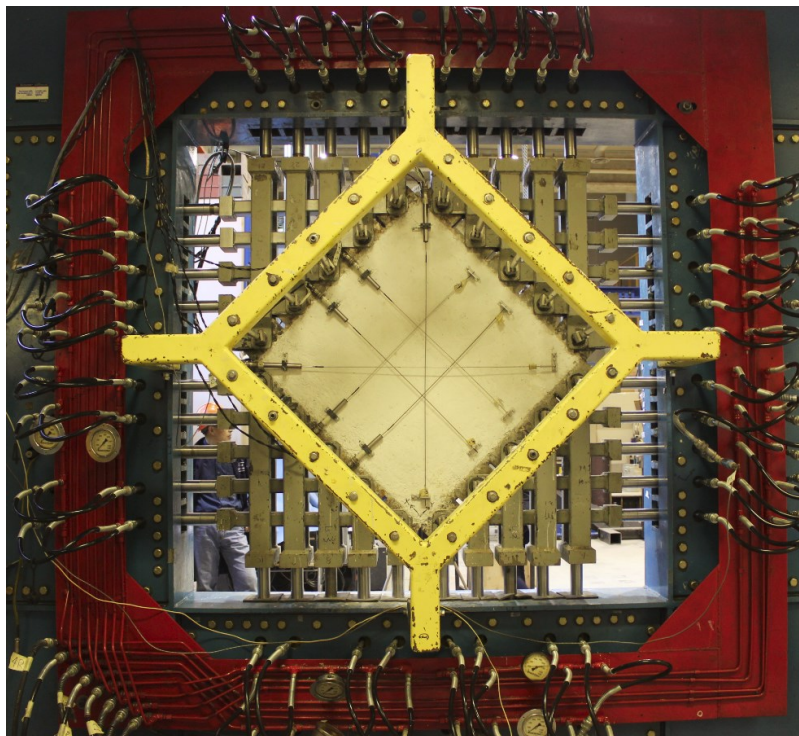
(b) back face

Figure 3-15: Panel Tester Machine

3.8.1.2   Hydraulic Jacks

The 37 jacks used in the testing machine are the Enerpac RD-2510 high precision double-acting hydraulic cylinders. As shown in Figure 3-16, one end of each jack is connected to a link which transfers the load to the shear keys, while the other end is connected to an eye mount serving to fix the jacks to the reaction frame through a pin connection. As each jack has a measured effective area of 3167 mm² in compression (advancing) and 1387 mm² in tension (retracting), a higher pressure is needed for the retracting jacks if all jacks were to exert forces equal in magnitude; the pressure ratio between the advancing jacks and the retracting jacks should be 0.438 (1387 mm²/3167mm²). The hydraulic jacks used have a rated hydraulic pressure capacity of 68.9 MPa (10,000 psi), which translate to a force capacity of 218 kN in push and 95.6 kN in pull. The maximum stroke of the shaft is 10 inches (Vecchio, 1979).

Figure 3-16: Dissembled hydraulic jack

During this experimental program, the Panel Tester Machine underwent a major repair before commencing any panel tests. The objective of the repair was to replace the mechanical seals around the shafts for all of the jacks to prevent oil leakage. This required the disassembling of the entire panel tester and all of the jacks as shown in Figure 3-16. The repair was deemed necessary as the old seals experienced significant wear and tear over the years and oil leakage was observed before the repair. Typical damage in the old seals, and the new seals, are shown in Figure 3-17.
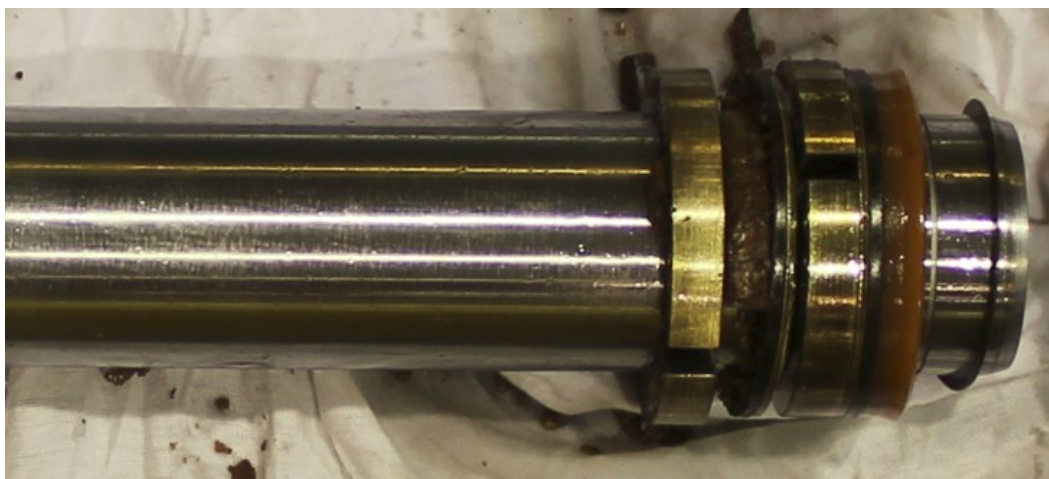
(a) old seal

(b) new seal

Figure 3-17: Mechanical seal for the shafts

After the jacks were upgraded with the new seals, a friction test was performed on five randomly selected jacks. Shown in Figure 3-18, the friction test applied a pressure through either the advancing port or the retracting port of the jack while a load cell connected to the jack measured the corresponding reaction load. The applied pressure was obtained through the pressure transducer connected to the pressure maintainer. The purpose of the friction test was to provide a pressure vs. load relationship for the jacks in both tension and compression. Results from the test allowed the examination of possible static and dynamic friction within the jacks and the determination of an equivalent effective area for converting jack pressure to load.

Figure 3-18: Friction test for the hydraulic jacks

As shown below in Figure 3-19, the five randomly selected jacks gave identical responses indicating that the repair was successful. The pressure vs. load relationship was stable (i.e. had a near constant slope) after approximately 200 psi; this showed that a negligible amount of static friction existed within the jacks. It is important to note that the panel specimens in this work typically experience first-cracking near a jack pressure of 2000 psi and failure near a jack pressure of 4000 - 6000 psi.

The equivalent effective area was obtained by dividing the force readings from the load cell by the pressure readings from the pressure transducer. The average equivalent effective area for the five selected jacks was 3057 mm² for advancing and 1330 mm² for retracting. These values were approximately 4% smaller than the measured effective areas (i.e. 3167 mm² and 1387 mm²) reported by Vecchio (1979) and were likely due to dynamic frictions and measurement errors.

As shown in Figure 3-20, the equivalent effective area was also calculated for the various levels of jack pressures. For the advancing jacks, the equivalent effective area slightly increased as the pressure increased indicating a reduction in dynamic friction under higher pressure. The retracting jacks' equivalent effective area was, on the other hand, nearly constant for all levels of pressure. This can be attributed to the lower loads experienced by the retracting jacks due to the smaller effective area. The equivalent effective area obtained from the friction test will be used to convert pressure to load for the analysis of the panel test results.
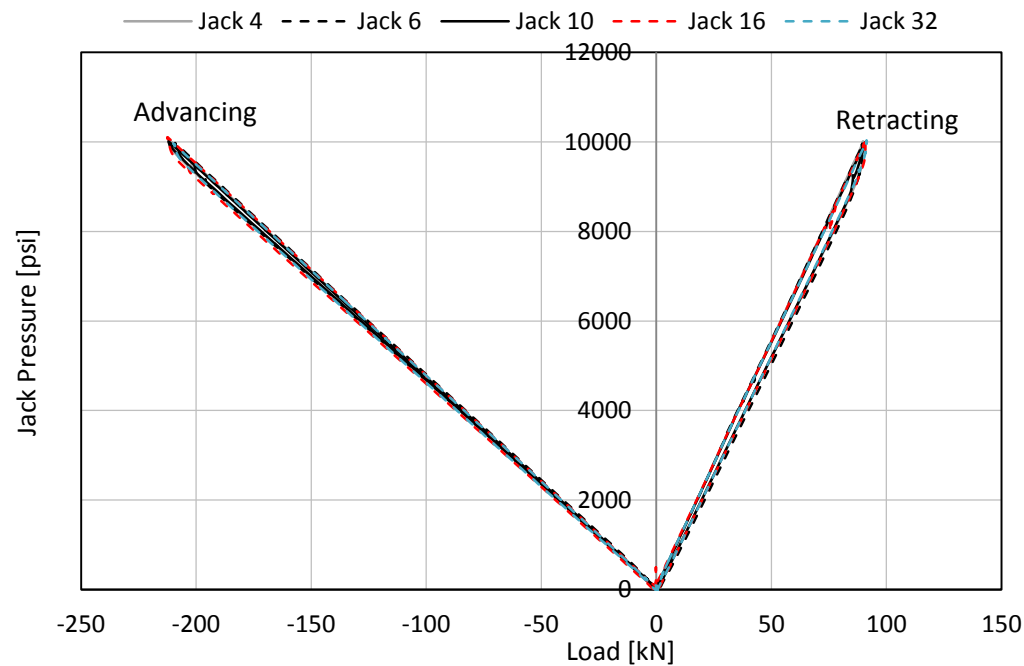
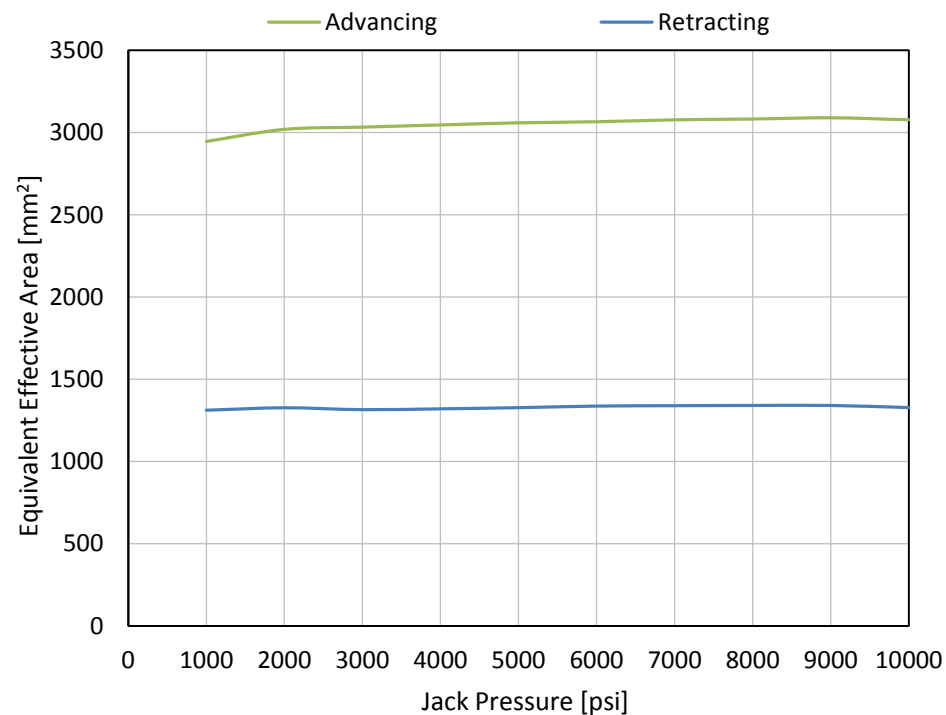Figure 3-19: Friction test results for the five repaired jacks

Figure 3-20: Average equivalent effective area for the five repaired jacks

3.8.1.3   Hydraulic System

The installed panel is inclined 45° such that each shear key will experience a horizontal and a vertical force. The five parallel jacks on each side of the panel exert the same force, resulting in eight separate groups of jacks; two groups per panel edge (shown in Figure 3-21 as Group 1-8). For each panel edge, as one of the two groups applies a compressive force and the other applies an equal tensile force, the normal force components would be cancelled resulting in a pure shear loading condition.
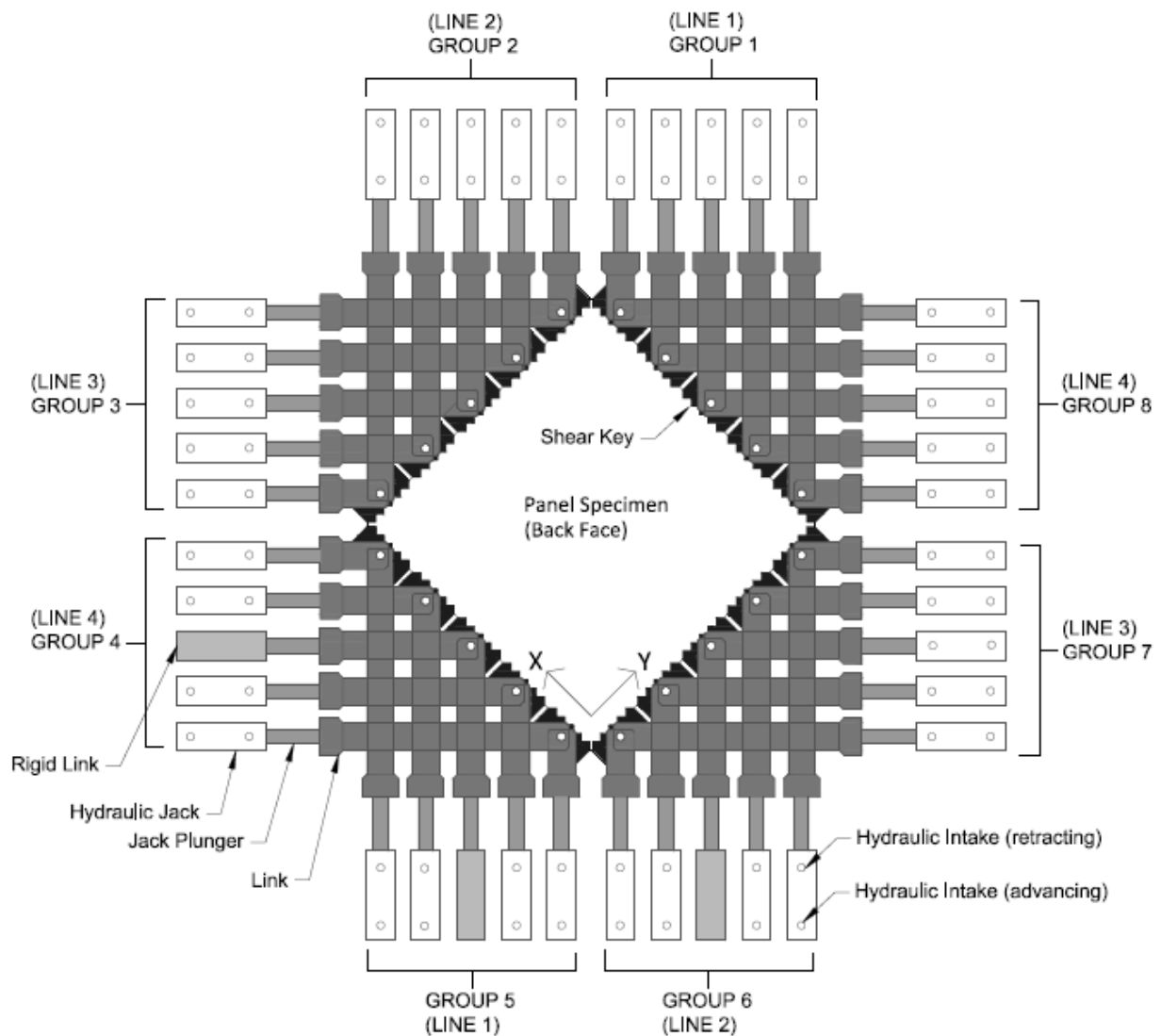
Figure 3-21: Jack arrangement of panel tester machine (back face)

To maintain equilibrium, the two groups of jacks that are diametrically opposite always exert the same force in the same direction, creating the need for only four separate intake pressure lines at

any one time for any load condition; one intake pressure line per pair of diametrically opposed set of jacks (shown in Figure 3-21 as Line 1-4). It is important to note that four more separate return pressures lines are necessary to return the oil back into the pump. In other words, if one of the four intake pressure lines is connected to the retracting ports of the two groups of diametrically opposed jacks, then the advancing ports of these two groups of jacks need to be connected to a return pressure line.

To create a pure shear loading condition, two intake pressure lines need to apply the same tensile force while the other two intake pressure lines apply an equal but opposite compressive force. Hence, only two different intake pressures are necessary; one intake pressure for all retracting jacks and one for all advancing jacks. Since each jack has a larger effective area in advancing than retracting, a higher pressure is needed for the retracting jacks to ensure all jacks are exerting forces equal in magnitude. The pressure ratio between the retracting line and the advancing line should be 0.438 (1387 mm^2/3167 mm^2), and a load maintainer is used to maintain this pressure ratio throughout the test.

To supply pressure to the hydraulic jacks in the manner described above, a feeder-frame bolted onto the back of the reaction frame is used (see Figure 3-15). The feeder-frame is used to hold the feeder lines that form the core of the hydraulic system. A diagram displaying the feeder line system for positive shear is shown in Figure 3-22.

As mentioned earlier, two different intake pressures are required to be fed into this feeder line system. As depicted in Figure 3-23, the hydraulic system for supplying pressure employed by Calvi (2014) was used in this experiment. The advantage of this pressure supply system is that the direction of the load can be reversed by simply switching the direction of the two four-way valves.
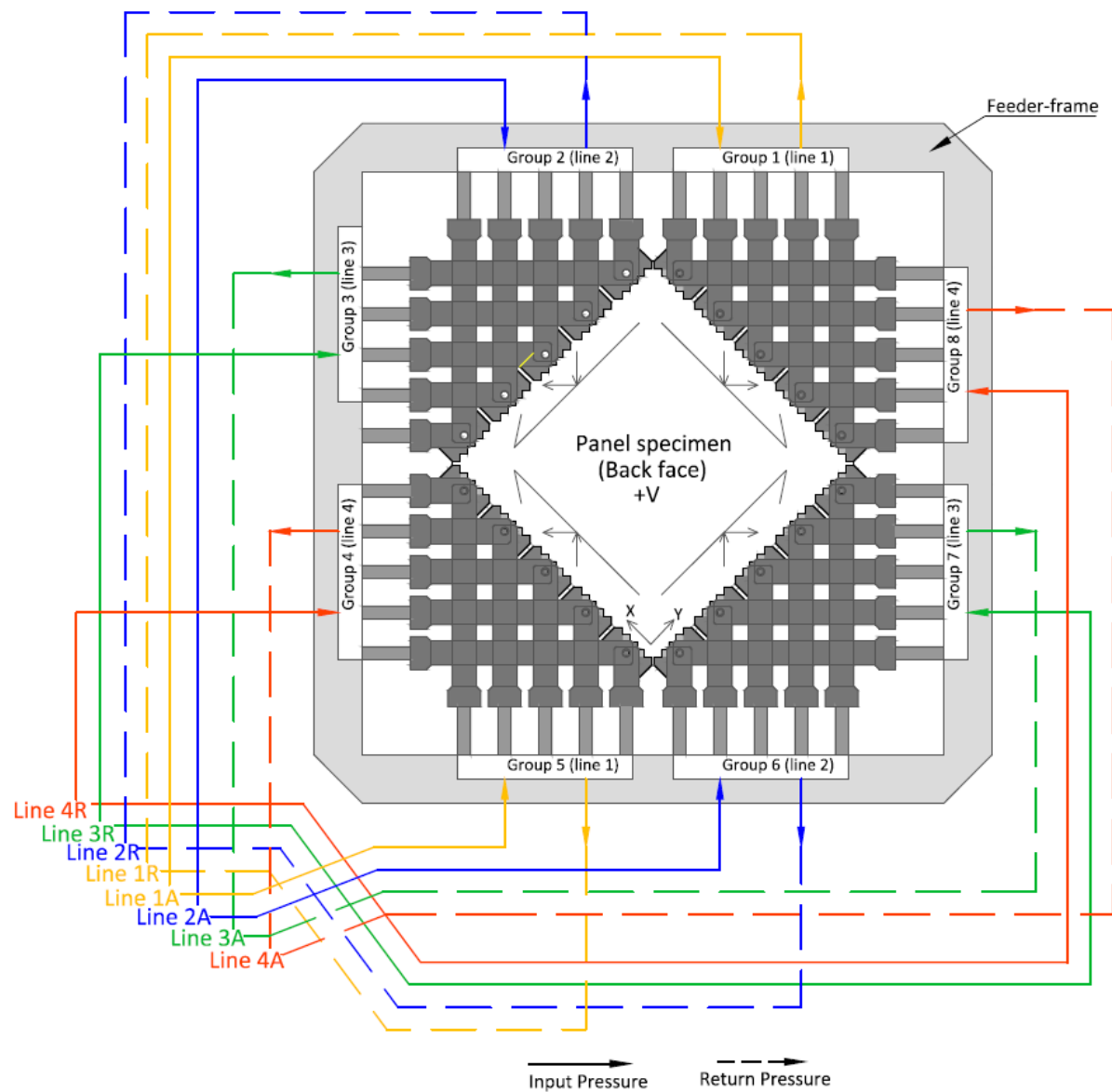
Figure 3-22: Feeder line diagram for the feeder-frame (for positive shear)
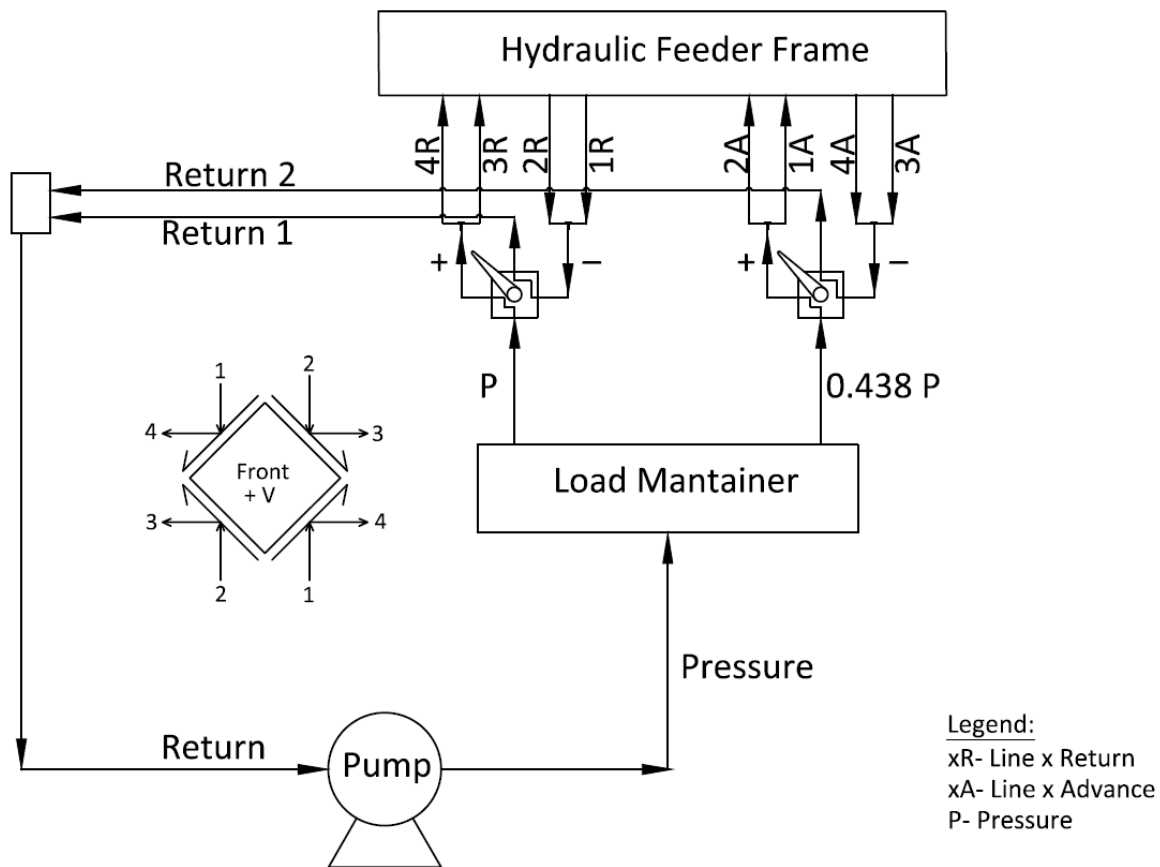
Figure 3-23: Hydraulic System (for positive shear)

3.8.2 Specimen Description

Two different reinforcement configurations were used for the 890x890x70 mm panel specimens. As shown in Figure 3-24, the control panels consisted of regular concrete and had conventional reinforcement in both the x- and y-directions. On the other hand, the SFRC panels incorporated steel fibres but had conventional reinforcement in the x-direction only. The design of the panels was identical to the ones used by Carnovale (2013) and Susetyo (2009).

For the control panels, 40-D8 (8.1 mm) deformed bars were used in the x-direction as primary reinforcement, which translated to a reinforcement ratio of 3.31%. The secondary reinforcement in the y-direction consisted of 10-D4 (5.7 mm) wires, which gave a reinforcement ratio of 0.42%. Deformed wires in both directions were placed through the holes in the shear keys. The ends of the bars were threaded and two nuts were applied to the ends of the bars on the outside face of the shear keys in order to secure the reinforcement cage. In the y-direction, 20-5/16" (5.7 mm) short threaded rods were provided in addition to the 20-D4

wires to improve the stress transfer between the concrete panel and the shear keys. Nuts were applied to both ends of the threaded rods.

As shown in Figure 3-25, the design of the SFRC panels was similar to the control panels. The SFRC panel had the same reinforcement layout in the x-direction, but had no continuous bars in the y-direction. In order to provide sufficient stress transfer to the shear keys in the absence of continuous wires, 40-5/16'' threaded rods were used in the y-direction. These 40 threaded rods were staggered to prevent a plane of stress concentrations.

The x-direction reinforcement ratio were chosen to prevent these primary reinforcement from yielding during the test and to allow sufficient post-cracking behaviour to be observed; the reinforcement ratio of 3.31% was successful in accomplishing this in the past (Carnovale, 2013; Susetyo, 2009). The y-direction reinforcement was meant to represent the minimum reinforcement requirements. The Canadian Highway Bridge Design Code (CHBDC) states that the "minimum area of shrinkage and temperature reinforcement in each face and in each direction shall be 500 mm²/m and the spacing of the bars shall not exceed 300 mm" (CAN/CSA Standard S6-06, 2006). Assuming the typical concrete deck thickness to be 250 mm, the CHBDC (2006) would require the minimum temperature and shrinkage reinforcement ratio to be 0.40%. Hence, the chosen secondary reinforcement ratio was 0.42%. It is important to note that the 0.42% transverse reinforcement ratio is larger than several design standards' prescribed minimum reinforcement ratio. For example, CAN/CSA Standard A23.3-04 (2004) stated that the minimum temperature and shrinkage reinforcement for a slab is 0.20% of the gross cross section (in the longitudinal and transverse direction).

In the context of shear reinforcement, the secondary reinforcement used for the panels can somewhat represent minimum shear reinforcements. CAN/CSA Standard A23.3-04 (2004) states that the shear reinforcement ratio (ρ_w) for concrete based on the minimum shear reinforcement area requirement (i.e. $\rho_w = 0.06\sqrt{f'_c}/f_y$) is approximately 0.10% with 50 MPa concrete. However, when the minimum shear reinforcement is controlled by the code's maximum stirrup spacing requirement (i.e. $S_{max} = \min(0.7d_v, 600)$), the shear reinforcement ratio may be increased to 0.20–0.40% or more depending on the member's geometry. Nevertheless, the chosen 0.42% transverse reinforcement ratio can be a good estimate of the shear strength of conventional reinforced concrete with minimum transverse reinforcement.

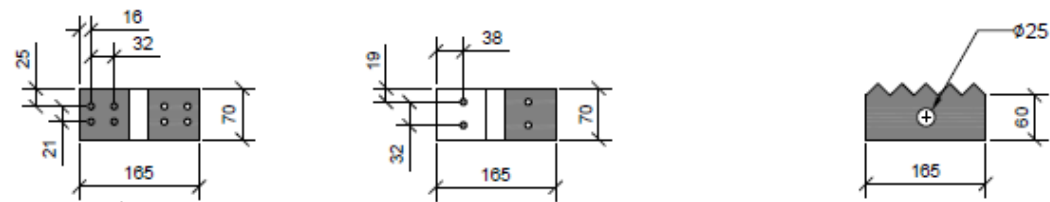(a) reinforcement layout
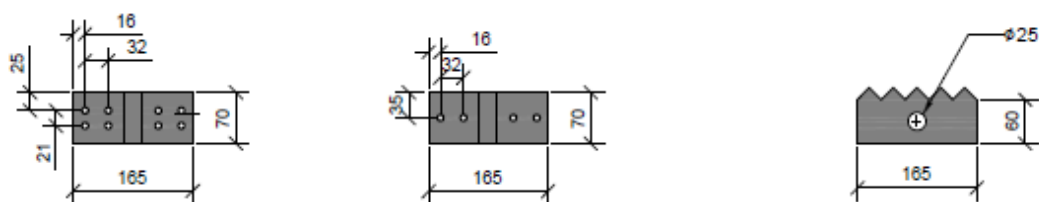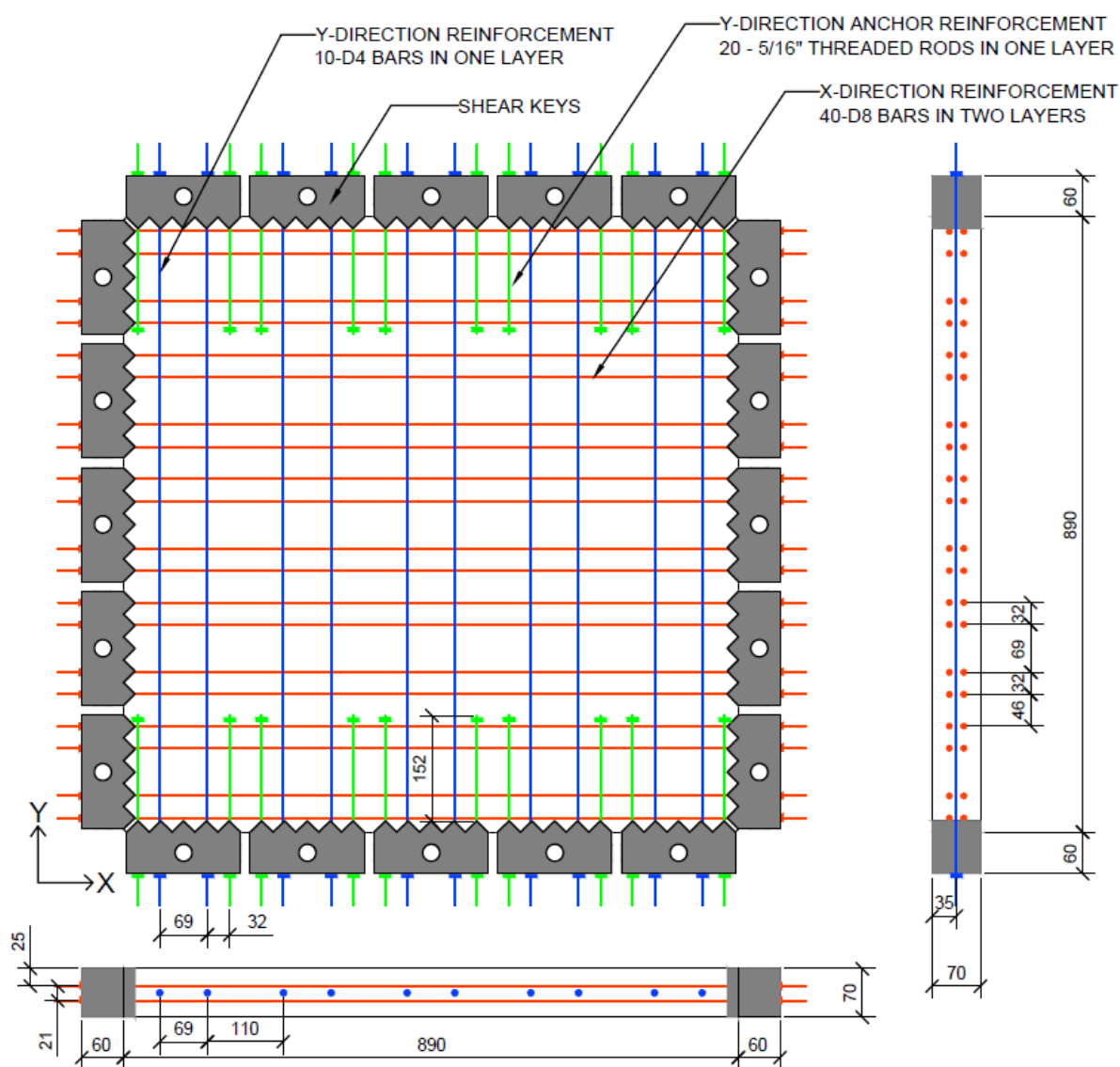
(b) shear key details

Note: all dimensions in mm

Figure 3-24: RC control panel specifications
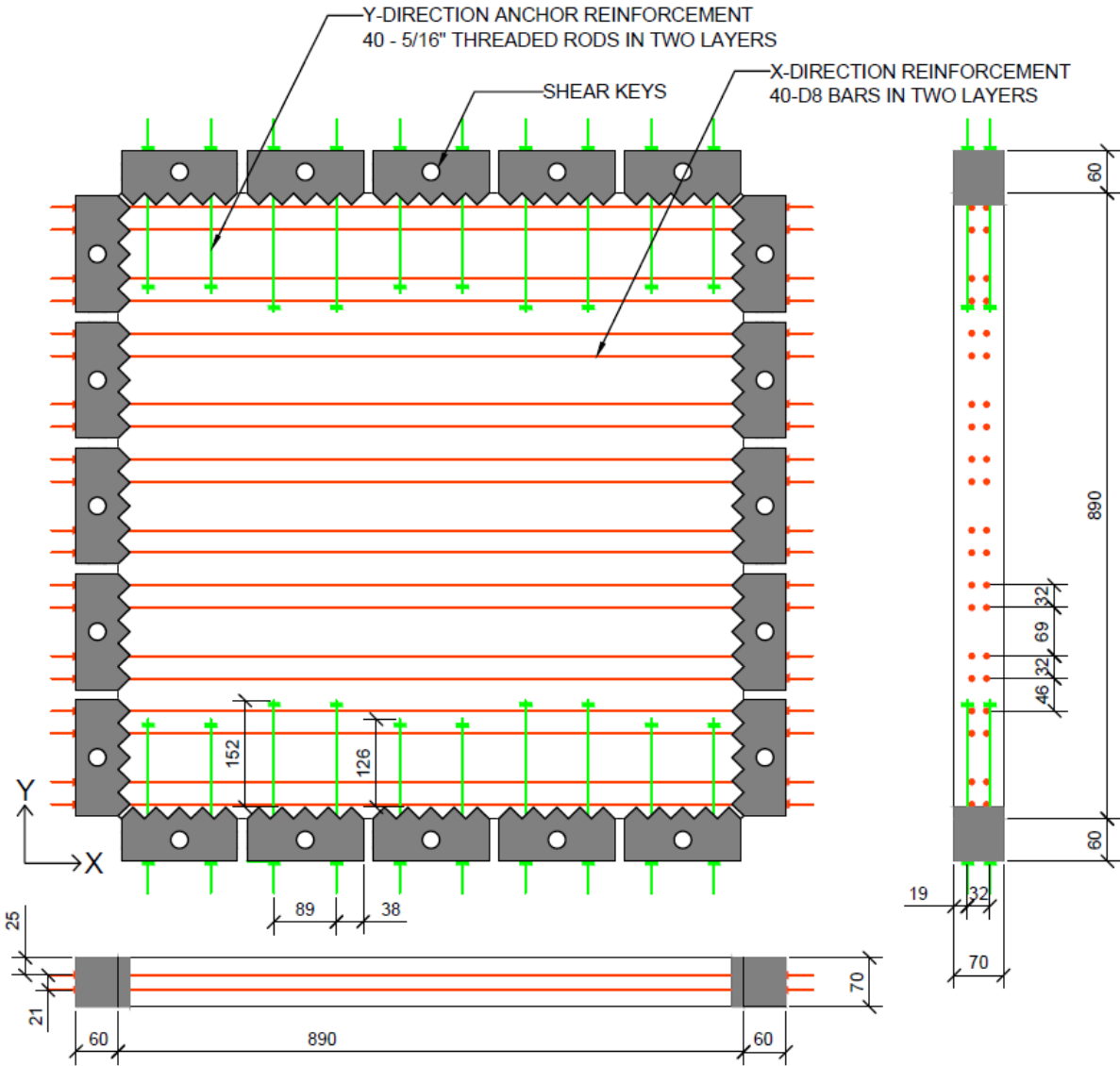
(a) reinforcement layout

(b) shear key details

Note: all dimensions in mm

Figure 3-25: SFRC panel specifications

Before constructing the specimen, reinforcing bars and threaded rods were cut to the appropriate length with the ends ground and polished. Then, approximately 50 mm of the reinforcing bar ends were threaded using a lathe machine. To begin cage construction, all twenty shear keys were aligned and bolted on the casting table (see Figure 3-26). Hydraulic oil was applied to the surface of the casting table to ease the removal of the panel after curing. The reinforcements were placed one layer at a time. To secure the reinforcing cage, the ends of all reinforcements and threaded rods were fastened with two nuts on the outside face of the shear keys. The threaded rods had a nut at the inside end as well to facilitate better stress transfer. Once the cage was completed, all unused holes within the shear keys and gaps between the shear keys were filled with plasticine.

The panel was cast in two layers; an external form vibrator attached to the bottom of the casting table was used to consolidate the concrete after each layer. After being allowed to set for three hours after casting, the specimens were then moist-cured with plastic-covered wet-burlap for seven days. To prevent restrained shrinkage from the bolted connection to the casting table, the bolts were removed from the table three to four days after casting.
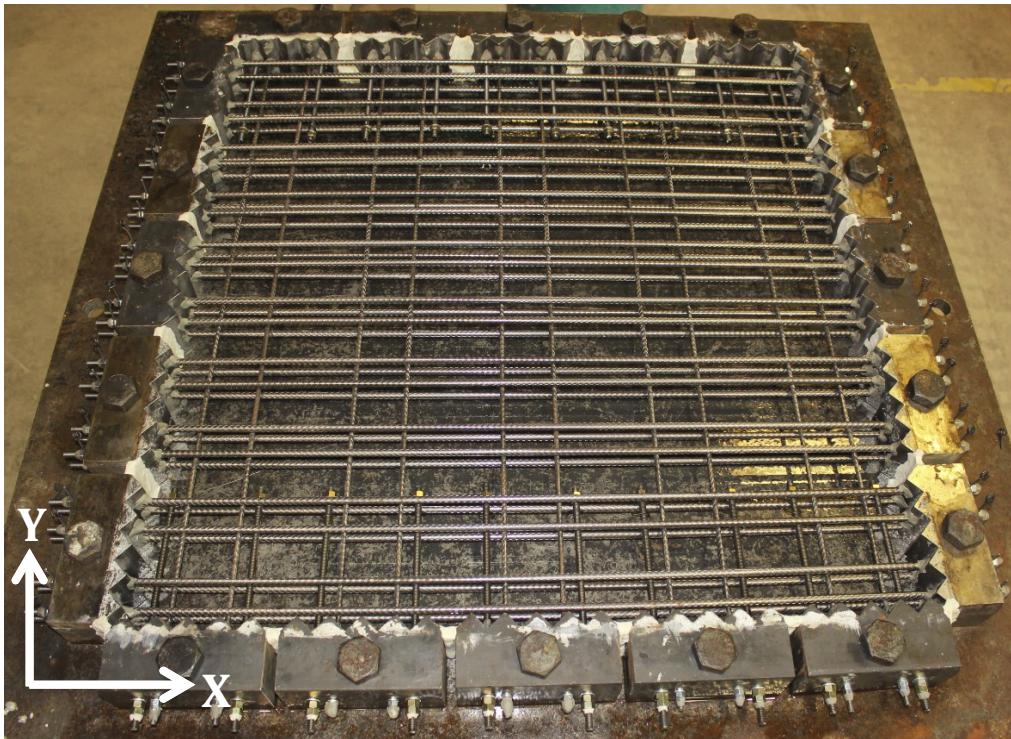
(a) RC control panel
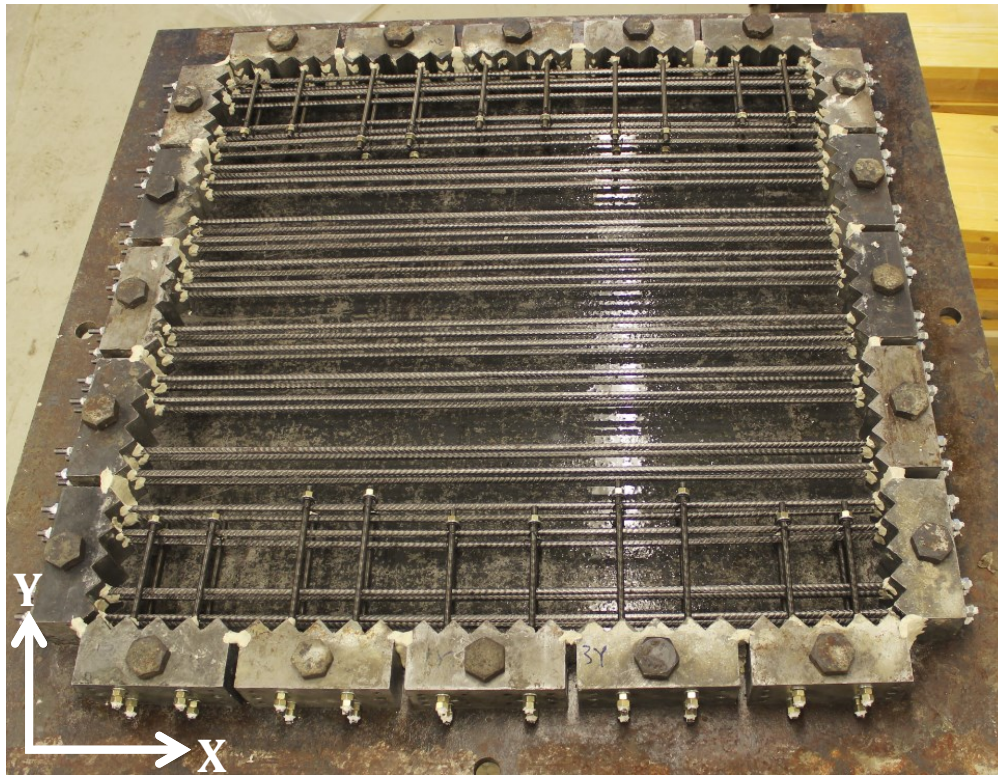
(b) SFRC panel

Figure 3-26: Panel reinforcement cage

3.8.3 Test Instrumentation

3.8.3.1   Linear Variable Differential Transducers (LVDT)

As previously mentioned, LVDTs can provide continuous measurement of the strain throughout the test by monitoring the length change within the LVDT gauge length. As a result, the LVDTs only record the average strain in the panel over multiple cracks. Localized strain due to widening of cracks was not captured and this was desirable in this experiment. The LVDTs used had a maximum stroke of ±14 mm.

Six LVDTs were used for both the front face and the back face of the panel; this was deemed necessary due to possible out-of-plane bending. As shown in Figure 3-27, for each face, two LVDTs were placed in the x-direction, two in the y-direction, one in the vertical direction, and one in the horizontal direction. The vertical and horizontal LVDTs were angled at 45° with respect to the x- or y-direction. Having LVDTs in the x, y, horizontal, and vertical directions allow all strain parameters to be obtained using the Mohr's Circle diagram.

Previous panel tests performed at the University of Toronto also utilized Zurich gauge targets or LED targets to measure localized strain behaviour (Carnovale, 2013; Susetyo, 2009). These targets were placed at the back of the panel specimen forming nine 200x200 mm subgrids. The use of these targets was excluded in this work because only the average strain data were necessary. Another function of the target readings was to verify the LVDT readings. Since only three strain conditions were necessary to construct the Mohr's Circle but a total of twelve LVDTs were used, no additional strain measurement verification was deemed necessary. Previous panel tests showed that the average strain data from these targets were consistent with the LVDT readings.
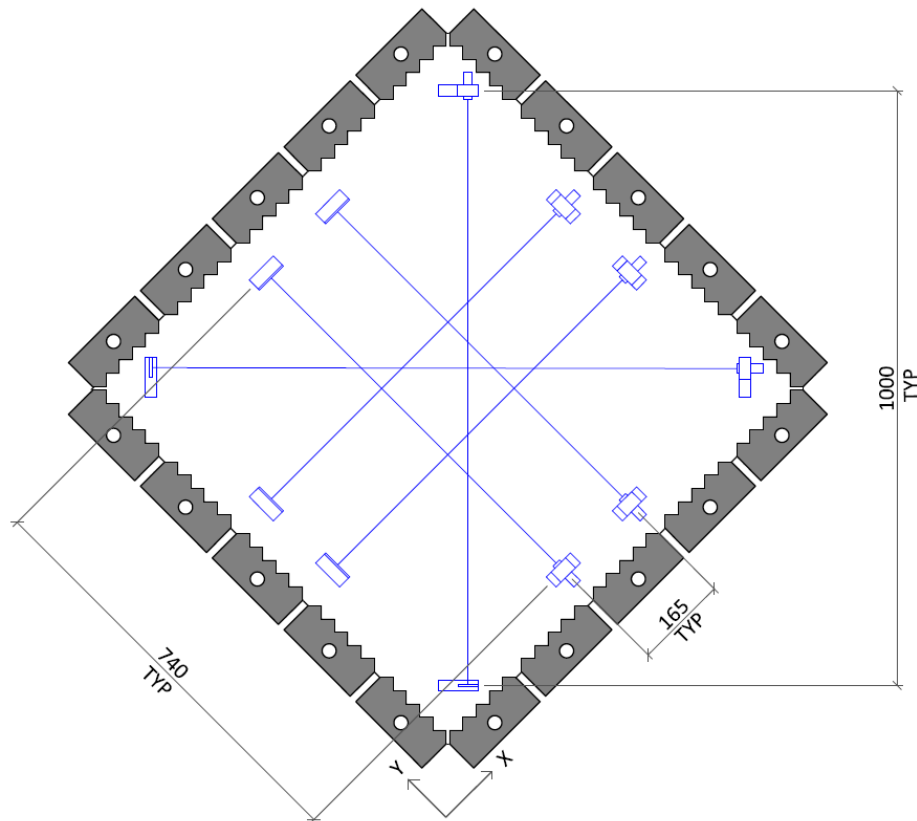
Figure 3-27: LVDT configuration (front view)

3.8.3.2   Load Cells and Pressure Transducers

The three rigid links mentioned above were directly connected to load cells. The readings from the load cells were recorded throughout the test to ensure the reaction forces at these rigid links were in equilibrium with the forces applied through the hydraulic jacks. Under pure shear, the magnitude of the forces should be the same for every hydraulic jack and load cell.

Four pressure transducers were used to record the pressure at four points within the hydraulic system to ensure that the correct pressure was applied. As previously mentioned, only two different pressure lines (i.e. two different input pressures) were needed for a pure shear loading condition. One pressure transducer was used for each of the two input pressures to ensure that the correct pressure ratio was maintained by the load maintainer. The other two pressure transducers were periodically moved around the various hydraulic jack intakes to verify that the pressure diverted from the load maintainer through the hydraulic system was correct.

An acquisition system recorded the data from the LVDTs, load cells, and the pressure transducers simultaneously. The system was set to acquire data every time the shear stress changed by 0.033 MPa (i.e. if the pressure changed by 31 psi), or the horizontal/vertical LVDT readings changed by 0.1 mm.

3.8.4 Test Preparation and Procedure

3.8.4.1   Test Preparation

Preparation of the panel specimen began after the panel had been moist-cured for one week. The steps necessary to prepare the panel before connecting it to the testing machine are summarized below:

1. Holes for the rods that hold the LVDT mounts and reaction plates were pilot drilled with a masonry drill bit.
2. The panel was painted using a mixture of one part white paint and one part water.
3. Short 10-32" threaded rods were affixed into the drilled holes using Fastweld 10 epoxy.
4. The panel was then turned over and was prepared following the same procedure.

Once the panel had been prepared on the ground, the following procedures were implemented to install the panel into the testing machine and prepare it for testing:

1. The panel was hoisted and mounted onto the Panel Tester using a crane.
2. The three rigid links were then connected to the shear keys to hold the panel in place. The crane was removed from the specimen after this point.
3. One by one, the hydraulic jacks were connected to the shear keys using a hydraulic pump.

4. Once the panel was fully connected to the machine, LVDT mounts and reaction plates were attached to the panel by fastening them against the threaded rods previously epoxied.

5. The 12 LVDTs for both faces of the panel were affixed to the mounts. The LVDTs were connected to the extension rods using shrink tubing before being zeroed manually.

6. To remove any out-of-straightness, a 0.50 MPa biaxial tension was applied to the panel specimen before attaching the tie-rods.

7. All of the tie-rods were then connected to the lateral support frame. The tie-rods were tightened by alternately shortening or elongating the tie-rods; this ensures half of the tie-rods were pulling while the other half were pushing to keep the panel in-plane.

8. Once completed, the pressure for the biaxial tension was removed from the specimen.

3.8.4.2   Test Procedure

Before the test began, all of the LVDTs were digitally zeroed. The load maintainer was manually operated to change the pressure. When the target shear stress was reached, a load stage was taken. At each load stage, the cracks were marked and the crack widths were measured when necessary. As well, the pressure was reduced by 10% during load stages as a safety precaution. At the end of the test, the number of fibres crossing the failure plane was counted and the failure plane's cross-sectional dimensions were measured.

For the monotonically loaded tests, the first load stage was taken when the initial crack formed. After cracking, a load stage was taken at approximately every 0.50 MPa shear stress increment until the panel was displaying significant strain increases, then the increment was decreased to 0.25 MPa. Cracks were marked and crack widths were measured at every load stage. A sample of the monotonic loading protocol is shown in Figure 3-28. Note that all monotonically loaded panels were subjected to positive shear only (i.e. the cracks were vertical)

For the reversed cyclically loaded tests, the test was ran on a double cycle basis; that is, the load was only increased after every two cycles. Every load cycle consisted of two load stages, so every double cycle had four load stages (see Figure 3-29). Before cracking, the load increment was 1.0 MPa shear stress at every double cycle. This continued until the specimen experienced its first crack. After initial cracking, the double cycle load increment was set to 0.50 MPa. Toward the end of the test when the specimen showed significant strain increases, the load increment was reduced such that the peak shear strain increment was approximately 1.0×10^{-3}

mm/mm; this typically resulted in a 0.25 MPa shear stress increment. After reaching the target shear stress for a load stage, the load was reduced to zero and the four-way valves were switched in order to reverse the load. Cracks were marked at every load stage, but the crack widths were only measured at the third and fourth load stage of the double cycle in the interest of time. Note that panels were first loaded in the positive direction.
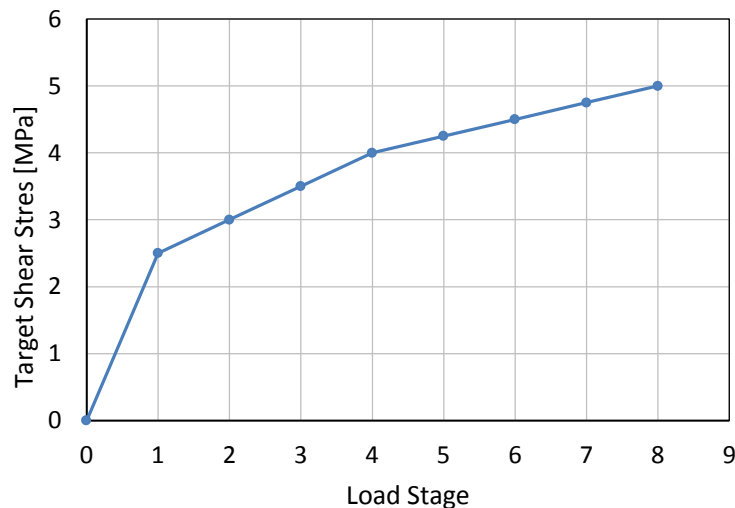
Note: this sample loading protocol assumes the first crack occurs at a shear stress of 2.5 MPa

Figure 3-28: Sample monotonic loading protocol
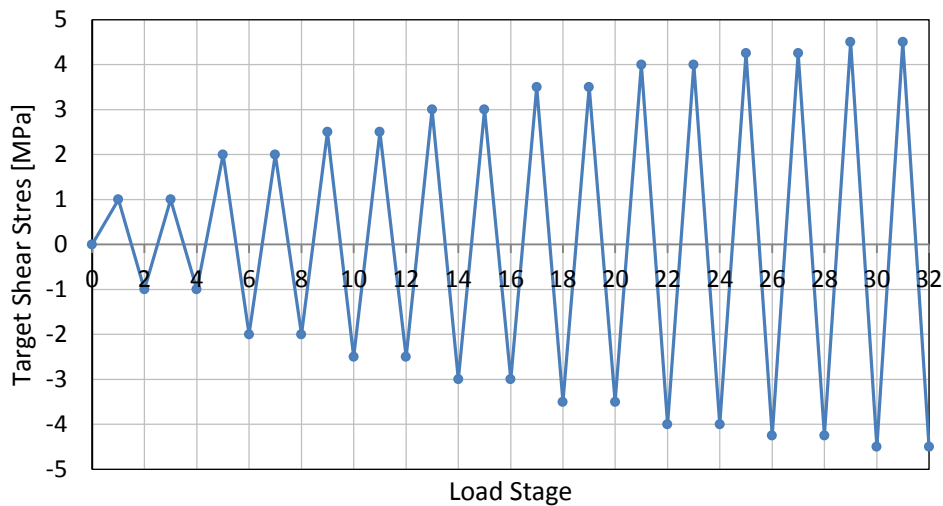
Note: this sample loading protocol assumes cracking occurs at a shear stress of 2.5 MPa

Figure 3-29: Sample reversed cyclic loading protocol

<div style="text-align:center">

Chapter 4
Material Test Results

</div>

4. Material Test Results

4.1   Introduction

Results from the three material tests are presented in this chapter. The experimental observations, calculation procedures, and experimental results will be discussed. This chapter begins by discussing the cylinder compression test, then the uniaxial tension test, and, lastly, the modulus of rupture test. For each test, emphasis will be placed on the influence of fibre volume fraction and fibre aspect ratio. Only summaries of each test series are provided below, the detailed results of each specimen are presented in Appendix A.

4.2   Cylinder Compression Test

This section discusses the results of the cylinder compression tests. As previously mentioned, for each cast, nine cylinders were made; two cylinders were tested on the seventh day, three cylinders were tested on the 28th day, and the remaining four were tested on the day of the panel test. The full stress-strain curve was only obtained for the cylinders tested on the 28th day. The full set of 28-day cylinder test data is presented in Appendix A.1. Only a summary of the 28-day test results for each test set is provided in this section.

4.2.1 Data Analysis

Analysis of the cylinder data was in accordance with ASTM C469 (2002) as outlined below. The strain data were obtained by dividing the LVDT displacements by the LVDT gauge length, 152 mm. The stress data were obtained by dividing the load cell readings by the cylinders' cross – sectional area. The diameter used was the measured diameter for each cylinder, which was approximately 101.5 mm. The secant modulus of elasticity in compression was determined as:

$$E_{cs} = \frac{S_2 - S_1}{\varepsilon_2 - \varepsilon_1} \qquad\qquad (4.1)$$

where,

S_1 = stress corresponding to a longitudinal strain of 50×10^{-6} [MPa]

S_2 = stress corresponding to 40% of the ultimate load [MPa]

ε_2 = 50×10^{-6}

ε_1 = the longitudinal strain at stress S_2

4.2.2 Test Results

Overall, the compressive behaviour of the cylinders was consistent with previous research (Susetyo, 2009). A summary of the 28-day cylinder test results together with the coefficient of variation (CV in %) for each set of cylinders is shown in Table 4-1. The table shows the peak compressive strength (f'_c), the strain at peak stress (ε'_c), and the compressive secant modulus of elasticity (E_{cs}). The crack pattern for representative cylinders of each test set is shown in Figure 4-1. Figure 4-2 shows the concrete stress-strain curve for all test series. Note that the average stress-strain curve for each test set was based on the most representative specimen, as opposed to the average of all specimens of the set.

Table 4-1: Summary of the 28-day cylinder test results

ID	V_f	AR_f	f'_c (CV) [MPa]	ε'_c (CV) [x10^{-3}]	E_{cs} (CV) [MPa]	$E_{cs}/\sqrt{f'_c}$
CMS CRC	-	-	43.0 (3.8)	2.60 (3.1)	32037 (4.1)	4883
F1V1MS F1V1RC	0.5%	79	53.2 (1.4)	2.89 (6.7)	33177 (6.4)	4550
F1V2MS F1V2RC	1.0%	79	57.5 (3.8)	3.00 (9.5)	32166 (3.6)	4243
F1V3MS F1V3RC	1.5%	79	48.9 (0.6)	3.06 (1.2)	32045 (4.9)	4581
F2V2MS F2V2RC	1.0%	55	50.1 (0.6)	3.18 (4.5)	29806 (3.6)	4212

Control
43.0 MPa – Plain

F1V1
53.2 MPa – 0.5% RC80/30BP

F1V2
57.5 MPa – 1.0% RC80/30BP

F1V3
48.9 MPa – 1.5% RC80/30BP

F2V2
50.1 MPa – 1.0% ZP305
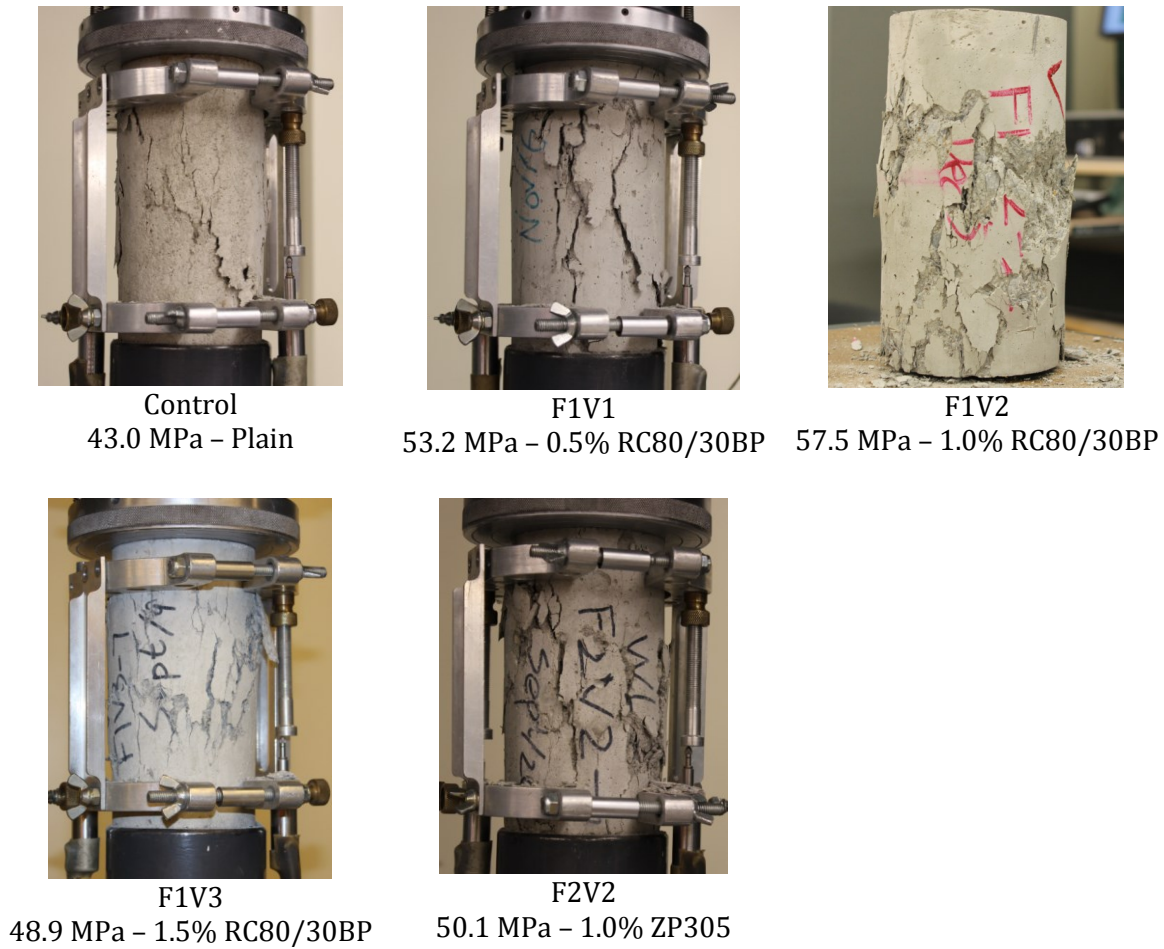
Figure 4-1: Representative cylinder crack patterns (with f'_c displayed)

As shown above in Table 4-1, the mix design used in this work yielded a compressive strength close to the target value of 50 MPa. Since the five batches of concrete were made separately, the variation in the peak strength was reasonable due to small differences in the moisture content of the raw material, mixing process, casting procedure, final adjustment for workability, etc. As anticipated, the fibre volume fraction and fibre aspect ratio did not show influence on the compressive peak strength.

As shown in Figure 4-2, the pre-peak behaviour of all concrete had little systematic difference. Overall, the secant modulus was close to the suggested value of $E_{cs} = 4500\sqrt{f'_c}$ (CAN/CSA Standard A23.3-04, 2004). The difference between the average secant modulus of plain concrete and fibrous concrete was less than 1.0%. Although a slightly higher secant modulus was expected for SFRC with higher volume fractions, this was not observed in this experiment due to insufficient data points. The fibre aspect ratio had no influence on the secant modulus

either. The data showed an indication of an increase in the peak compressive strain with the addition of fibres, and the increase was more pronounced for higher volume fractions; however, this may be attributed to the lower compressive strength of the plain concrete.

The benefits of fibre addition were primarily in improving the post-peak behaviour. Evident in the normalized stress-strain curves shown in Figure 4-2, the fibrous concrete indicated a more gradual stress decay compared to the plain concrete. However, this stress decay difference was much less pronounced than anticipated, and was largely due to the unexpectedly ductile behaviour of the plain concrete. As shown in Figure 4-3, the unexpected ductility from the plain concrete was evident when comparing it against the standard Popovics base curve for concrete with the same strength (Collins and Mitchell, 1997).

For the fibrous concrete, a higher fibre volume fraction led to a higher residual stress and a more gradual stress decay. For the same fibre volume fraction, the test series with the lower aspect ratio (same fibre length) displayed a lower residual stress. As previously mentioned, due to the smaller aspect ratio, the series with 1.0 % ZP305 fibres (F2V2) had the same number of fibres as the one with 0.5% RC80/30BP (F1V1). Since the number of fibres in the mix tends to control the behaviour more so than the fibre volume fraction, the response from the F2V2 cylinders was very similar to the F1V1 cylinders (Johnston, 2001). The fibres did not rupture during the cylinder test; hence, the tensile strength of the fibres did not influence the response of the specimens.

(a) non-normalized   (b) normalized
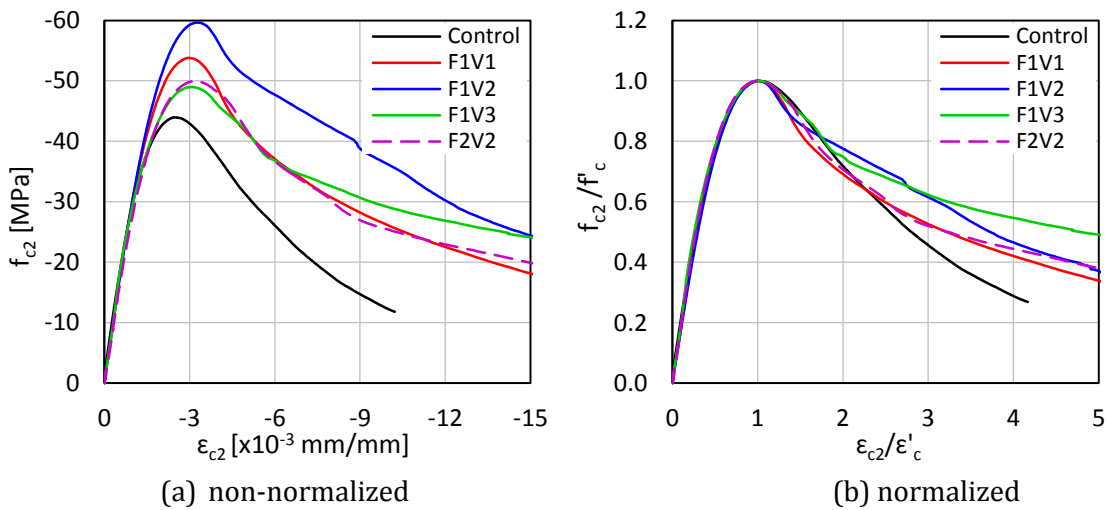
Figure 4-2: Comparison of the stress-strain curves from cylinder tests

(a) non-normalized   (b) normalized
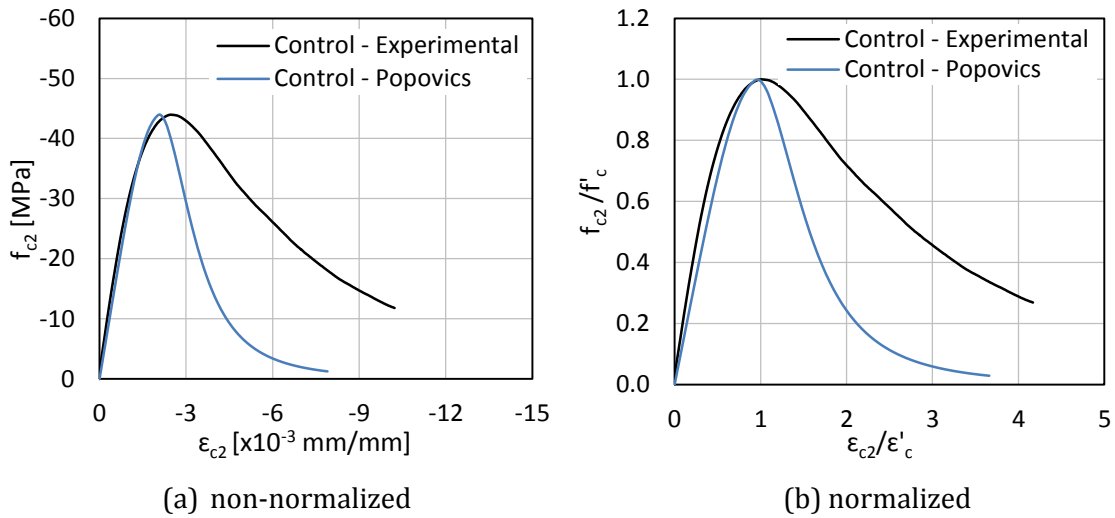
Figure 4-3: Comparison of the stress-strain curves for plain concrete

4.3   Uniaxial Tension Test

This section provides a detailed discussion of the uniaxial tension test results. Three dogbones were made for each batch of concrete. Depending on the lab staff availability, the dogbones were tested between the 28th to 35th day. Full sets of the dogbone test data and crack pattern photographs are presented in Appendix A.2.

4.3.1 Data Analysis

The pre-cracked and post-cracked analyses were performed separately for each dogbone specimen. For the pre-cracked analyses, the objective was to obtain the stress versus strain response. For the post-cracked analyses, however, it was desirable to obtain the residual strength versus crack width opening relationship. This is because the average tensile strain should be represented by multiple cracks, but only one dominant crack exists in the post-peak region. The following key assumptions were made in the dogbone analysis:

1. The tensile strain was distributed inversely proportional to the cross-sectional area.
2. The effect of stress concentrations was negligible and not accounted for in the analyses.
3. Beyond the maximum stress, the uncrack regions of the specimen were assumed to undergo elastic unloading.
4. Beyond the maximum stress, the elastic deformation around the crack was assumed to be negligible.

To convert the LVDT displacements to strain, the recorded displacements for each LVDT were divided by its gauge length. For the long LVDTs that covered the mid-section and the flared end regions of the dogbone, the gauge length was 300 mm but an effective gauge length of 285 mm was used. This was because the changing cross section within the LVDT gauges length led to a non-uniform strain distribution. Since the concrete strain was assumed to be proportional to the inverse of the cross section, an effective gauge length of 285 mm was obtained by numerically integrating the cross section over the length of the flared region and normalizing it to the mid-section cross-sectional area, 7000 mm² (Deluce, 2011). For the short LVDTs at the mid-section, the gauge length of 150 mm was used and was not modified. For the pre-cracked response, the average tensile strain was obtained by averaging all of the LVDTs' measured strain. The applied stress was obtained by dividing the machine load by the cross-sectional area of the specimen. Since the gauge length has been normalized to 285 mm, the area of the specimen was taken as 7000 mm² for all specimens regardless of the crack location. Using the above pre-peak stress versus strain values, the tensile tangent modulus of elasticity in MPa, E_{ct}, was calculated as follows:

$$E_{ct} = \frac{S_{t2} - S_{t1}}{\varepsilon_{t2} - \varepsilon_{t1}} \tag{4.2}$$

where,

S_{t1} = stress corresponding to a longitudinal strain of 1.0×10^{-6} [MPa]

S_{t2} = stress corresponding to 50% of the cracking load [MPa]

ε_{t2} = 1.0×10^{-6}

ε_{t1} = the longitudinal strain at stress S_{t2}

Once the peak load was exceeded, deformation localized to a single crack and stress versus crack width relationship was needed. The crack width in mm, w_{cr}, was calculated using the following equation:

$$w_{cr} = \Delta_t - \Delta_{el} - \Delta_p \tag{4.3}$$

where,

Δ_t = axial deformation measured by the LVDTs[mm]

Δ_{el} = elastic deformation correspond to the given stress [mm]

Δ_p = plastic deformation developed prior to obtaining the peak tensile stress [mm]

The three deformation components showed in Equation 4.3 was the average of the active LVDTs. That is, if the crack location was in the mid-section region, all LVDTs were used; otherwise, only the long LVDTs were used. The elastic deformation in mm, Δ_{el}, was calculated as follows:

$$\Delta_{el} = \frac{P \cdot L_g}{A_c \cdot E_{ct}}$$ (4.4)

where,

P = current applied force [N]

L_g = average effective gauge length [mm]

A_c = cross-sectional area of the specimen (7000 mm^2)

E_{ct} = tensile tangent modulus of elasticity [MPa]

Pre-peak plastic deformations were exhibited by some specimens due to the nonlinear pre-peak stress versus strain responses. The plastic deformation in mm, Δ_p, was a constant for each specimen and was calculated using the following equation:

$$\Delta_p = \Delta_{peak} - \Delta_{el,peak}$$ (4.5)

where,

Δ_{peak} = measured axial deformation at peak load [mm]

$\Delta_{el,peak}$ = calculated elastic deformation corresponding to the peak load from Equation
                4.4 [mm]

4.3.2 Test Observations

Overall, the dogbone test results had some scattering due to the sensitive nature of the test but were reasonably consistent. Problems related to stress concentration in the specimen, alignment of the specimen in the machine, and concrete consistency within the batch were the primary causes for the variability in the test results. The implications and consequences of these problems are discussed in this section.

| Control
Plain | F1V1
0.5% RC80/30BP | F1V2
1.0% RC80/30BP | F1V3
1.5% RC80/30BP | F2V2
1.0% ZP305 |
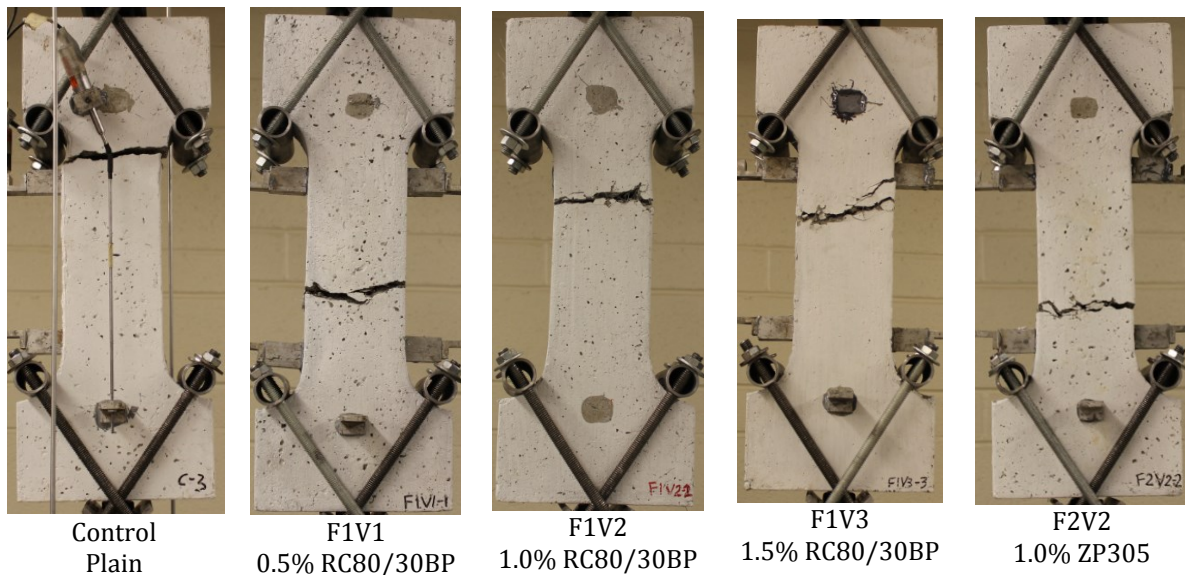
Figure 4-4: Representative dogbone crack patterns

As shown in Figure 4-4 and Appendix A.2's dogbone crack photographs, approximately 60% of the specimens tested had the failure crack located outside of the mid-section. For these cases, the non-uniform strain distribution and specimen geometry was accounted for in the analysis using the effecitve gauge length as mentioned earlier. In all cases, the load-carrying capacity of the specimen dropped after formation of the initial crack. The location and width of the initial crack was often not uniform across the full cross section of the specimen. As well, after cracking, out-of-plane bending was exhibited in majority of the specimens; the direction of bending was always toward the specimen's finished face (i.e. the finished face had a large crack). It is believed that the bending was primarily caused by the larger fraction of fibres concentrating near the form face of the specimen due to the forced vibration and downward movement of fibres during casting. This non-uniform fibre distribution led to a smaller number of fibres crossing the crack at the finished face. Due to the pinned end conditions used to restrain the dogbones, the specimens eventually realigned themselves to better carry tensile loads across the crack and evened out the crack width in all faces of the specimen.

The scattering in the dogbone results can also be attributed to the concrete consistency within the same batch of concrete. At the end of each dogbone test, the number of fibres crossing the failure crack was counted. Together with the fibre orientation factor calculated using the method described in the Fibre Distribution section (Section 3.4.4), the measured fibre volume fraction was obtained. Since the cross-sectional area of the failure plane was marginally larger

when the failure crack was located outside of the mid-section, a constant fibre orientation factor was used for all dogbones. As shown in Table 4-2, the number of fibres crossing the failure crack (N_f) was different for specimens of the same batch. As mentioned in Section 3.4.4 , for test series F1V3, the large variation in fibre concentration during casting led to a relatively small measured fibre volume fraction ($V_{f,meas}$) at the failure crack.

Table 4-2: Measured fibre volume fraction

ID	V_f	N_f	a_f	$V_{f,meas}$	$C.V.\,[\%]$
F1V1MS					
F1V1RC	0.5%	170	0.569	0.48%	5.88
F1V2MS					
F1V2RC	1.0%	343	0.569	0.98%	7.33
F1V3MS					
F1V3RC	1.5%	383	0.569	1.07%	9.34
F2V2MS					
F2V2RC	1.0%	140	0.569	0.83%	17.1

4.3.3 Test Results

A summary of the dogbone test results is shown in Table 4-3. The table shows the first-cracking strength (f'_t), the strain at first crack (ε'_t), the tensile tangnt modulus of elasticity (E_{ct}), the ultimate tensile stress attained after first-cracking (f_{tu}), and the stress correspond to different crack widths (f_{c1}). The coefficient of variation (%) is also displayed. Note that the average tensile stress-train curve for each test set presented in this section was based on the most representative specimen of the set.

Table 4-3: Summary of the dogbone results

ID	V_f	AR_f	f'_c [MPa]	f'_t (CV) [MPa]	ε'_t (CV) [x10^{-3}]	E_{ct} (CV) [MPa]	$f'_t/\sqrt{f'_c}$	$E_{ct}/\sqrt{f'_c}$	f_{tu} (CV) [MPa]	f_{c1} [MPa](CV) at a w_{cr} of	
										0.5 mm	1.5 mm
CMS CRC	-	-	43.0	3.91 (6.4)	0.131 (10.6)	32037 (4.4)	0.596	4886	-	-	-
F1V1MS F1V1RC	0.5%	79	53.2	3.66 (15.4)	0.094 (6.1)	41140 (9.3)	0.502	5640	2.75 (28.9)	2.35 (30.6)	2.19 (12.1)
F1V2MS F1V2RC	1.0%	79	57.5	4.13 (4.4)	0.146 (10.5)	35373 (2.0)	0.545	4665	3.12 (8.7)	3.03 (8.7)	2.31 (14.3)
F1V3MS F1V3RC	1.5%	79	48.9	3.89 (2.3)	0.138 (11.1)	37387 (9.5)	0.556	5347	3.28 (9.3)	3.18 (10.1)	2.67 (12.7)
F2V2MS F2V2RC	1.0%	55	50.1	3.32 (4.0)	0.114 (17.6)	34700 (15.1)	0.469	4902	2.34 (36.2)	1.96 (31.1)	1.60 (29.5)

The pre-cracked response for all specimens were similar with little discernible trends (see Figure 4-5). The initial tensile tangent stiffness (E_{ct}) for all fibrous concrete was higher than their corresponding compressive secant stiffness (E_{cs}); the average difference was 14% between compression and tension. This was caused by the fact that the compressive secant modulus was based on the stress corresponding to 40% of the peak compressive load, which is a region that tends to be more nonlinear than the region up to 50% of the peak tensile load. The tensile secant modulus was approximately $5100\sqrt{f'_c}$ for the fibrous concrete.

Similar to the tensile modulus of elasticity, no correlations between the tensile strength and the fibre volume fration or fibre aspect ratio was established. The direct tensile strength was approximately $0.52\sqrt{f'_c}$ for the fibrous concrete, and $0.60\sqrt{f'_c}$ for the plain concrete. In all cases, the tensile capacity was the initial cracking load. The variation in the tensile capacity was expected due to the high variance associated with concrete's cracking load.

(a) No plot offset   (b) plot offset
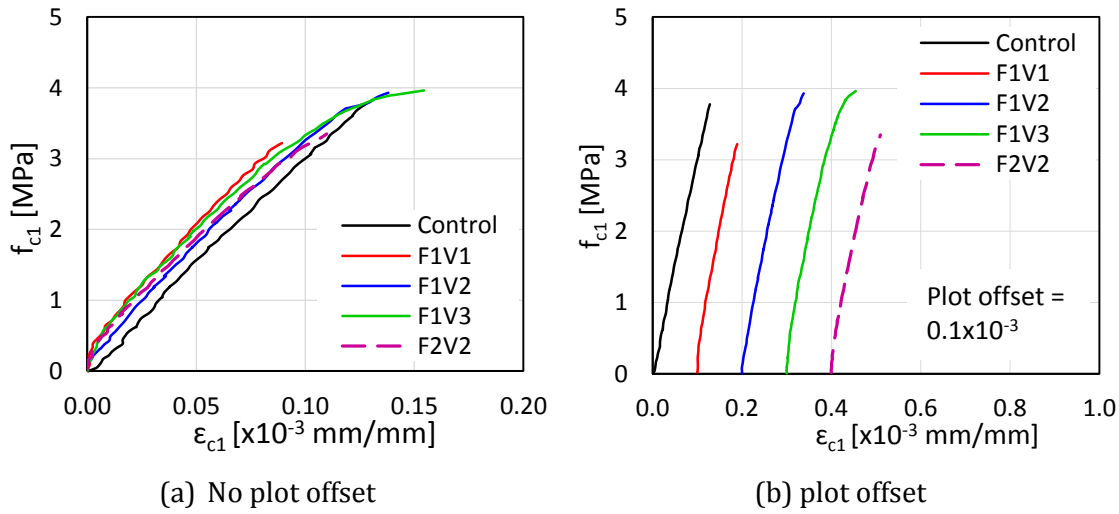
Figure 4-5: Uniaxial tension test pre-cracked response

(a) full response   (b) initial response
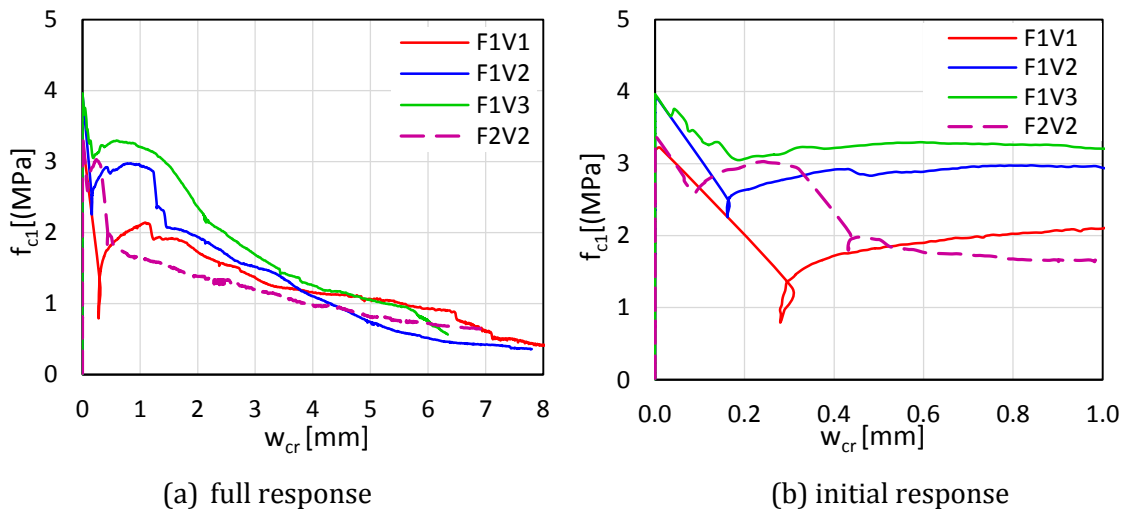
Figure 4-6: Uniaxial tension test post-cracked response

After cracking, the benefits of fibre addition became evident. As shown in Figure 4-6, while the plain concrete failed immediately after cracking and split into two halves, the SFRC dogbones continued to sustain significant stresses after cracking. As the fibre volume fraction increased, the concrete's tensile stress carrying capacity increased. To illustrate, immediately after initial cracking, dogbones with 0.5% fibre content exhibited an initial crack width opening of 0.28 mm while the tensile stress dropped 78% to 0.8 MPa; on the other hand, dogbones with 1.5% fibre content showed an initial crack width of 0.19 mm while the load carrying capacity dropped only 24% to 2.94 MPa. As shown in Table 4-3, as the fibre content increased, the load carrying capacities corresponding to crack width openings of 0.5 mm and 1.5 mm increased. The

improved post-cracking response was more pronounced when increasing the fibre content from 0.5% to 1.0% than 1.0% to 1.5%. This is in part due to the fibre saturation point, which may be near 1.5% (Susetyo, 2009). As well, the uneven distribution of fibres for the batch containing 1.5% fibre content also attributed to the less pronounced benefits, which was evident by the relatively fewer number of fibres counted at the failure plane (see Table 4-2).

The fibre aspect ratio also had a significant impact to the post-cracked behaviour of dogbones. As previously mentioned, the lower aspect ratio of the F2V2 series (1.0% ZP305 fibres) led to its dogbones having the same number of fibres as the F1V1 specimens (0.5% RC80/30BP). As a result, the F2V2 specimens' post-cracked behaviour was much closer to the F1V1 specimens than to the F1V2 specimens which had the same fibre content but a higher aspect ratio. For the F2V2 specimens, the load carrying capacity and the initial crack width opening immediately after initial cracking were similar to those in the F1V2 specimens; however, the load carrying capacity rapidly dropped afterwards, to levels below what the F1V1 specimen sustained. The above further justifies the notion that the impact of fibre count to the behaviour of SFRC is more important than the impact of fibre volume fraction. Since the failure mode of the specimens was fibre pull-out, the tensile strength of the fibres did not influence the response of the specimens.

At large crack widths, larger than 4 mm, the response for all dogbones specimens began to converge. This is because at small crack widths, the response is heavily influenced by the amount of fibres crossing the crack. As the crack width becomes larger, the embedded fibre length decreases and the specimen becomes more prone to fibre pull-out; as a result, the response at significantly large crack widths becomes more dependent on the fibre length (Susetyo, 2009). In this work, all fibres used had the same length. It is important to note that the response of SFRC structural elements is typically dependent on the response under small crack widths only; the response at significantly large crack widths is rarely of interest.

4.4   Bending Test

Modulus of rupture (MOR) prisms were tested to evaluate the concrete's flexural tensile strength. MOR tests are often performed for structural concrete experiments due to the simplicity of the test. The results of the MOR test will be discussed in this section. For each batch of concrete, two MOR beams were made. These beams were tested between the 28th and

35th day after casting, depending on the lab staff availability. Full sets of beam test data and crack pattern photographs are presented in Appendix A.3.

4.4.1 Data Analysis

The MOR tests and analyses were performed in accordance with the procedures outlined by ASTM Standard C1609/C1609M (2012). The mid-span deflections were obtained by averaging the values of the two mid-span LVDTs, and the load data were obtained directly from the machine readings.

The cracking stress in MPa, f_{cr}, was calculated using Equation 4.6 as given below. The formula is based on Navier's equation for the bending stress of a beam (i.e. $\sigma = M \cdot y/I$) and assumes that the neutral axis is located at mid-depth of the specimen. The equation is only applicable for linear elastic homogeneous materials and is frequently used for concrete prior to cracking. After cracking, the formula is no longer applicable but was still used in accordance to the governing standard. Thus, calculations for the residual stresses, f_{600}^D and f_{150}^D, corresponding to a net deflection of $L/600$ and $L/150$ were performed using Equation 4.6 as well.

$$f_{cr} = \frac{P_{cr} \cdot L}{b \cdot d^2} \tag{4.6}$$

where,

P_{cr} = corresponding load (cracking load in this case) [N]

L = specimen's span length (457 mm for all cases) [mm]

b = specimen's width (152 mm for all cases) [mm]

d = specimen's depth (152 mm for all cases) [mm]

The toughness of the specimen up to a net deflection of $L/150$ in Joules, T_{150}^D, was obtained by taking the area under the load versus deflection curve   from $\delta = 0$ to $\delta = L/150$ using the trapezoidal rule.

$$T_{150}^D = \sum_{i=1}^{n} \frac{1}{2} \cdot (\delta_{i+1} - \delta_i) \cdot (P_{i+1} + P_i) \tag{4.7}$$

where,

δ_i = mid-span deflection [mm]

P_i = load [kN]

Last, the equivalent flexural strength ratio, $R^D_{T,150}$, was found using the following equation:

$$R^D_{T,150} = \frac{150 \cdot T^D_{150}}{f_1 \cdot b \cdot d^2} \cdot 100\% \qquad (4.8)$$

4.4.2 Test Observations

Overall, the MOR beams exhibited some variability in their responses; the level of scattering in the test results was consistent with previous MOR tests performed (Susetyo, 2009; Carnovale, 2013). As shown in Appendix A.3, the load vs. deflection response for beams of the same set was reasonably consistent. The LVDT recordings between the front and back side of the specimen were almost identical. All of the specimens had the failure crack located in the centre region within the two loading points, the zone of constant moment and zero shear. The crack pattern for a representative MOR beam of each test set is shown in Figure 4-7.

Similar to the uniaxial tension test, the plain concrete specimens failed immediately after initial cracking while the SFRC beams exhibited significant post-cracking load carrying capacity. All SFRC specimens showed strain hardening response, a condition where the peak load was higher than the initial cracking load. Some specimens with a high volume fraction of 1.5% developed multiple cracks prior to reaching the peak load. Subsequently, all specimens' deformations were localized at one crack and the load carrying capacity dropped rapidly in a controlled manner.

As discussed in the Fibre Distribution section (Section 3.4.2), the fibre distribution within the MOR specimens was reasonable except for the F1V3 specimens. The average measured fibre volume fraction for the F1V3 prisms was only 0.67%, significantly smaller than the design volume fraction of 1.5%. The poor fibre distribution in the F1V3 specimens likely led to its poor post-cracking behaviour.

Control

F1V1

Plain

F1V2
1.0% RC80/30BP

0.5% RC80/30BP

F1V3
1.5% RC80/30BP

F2V2
1.0% ZP305
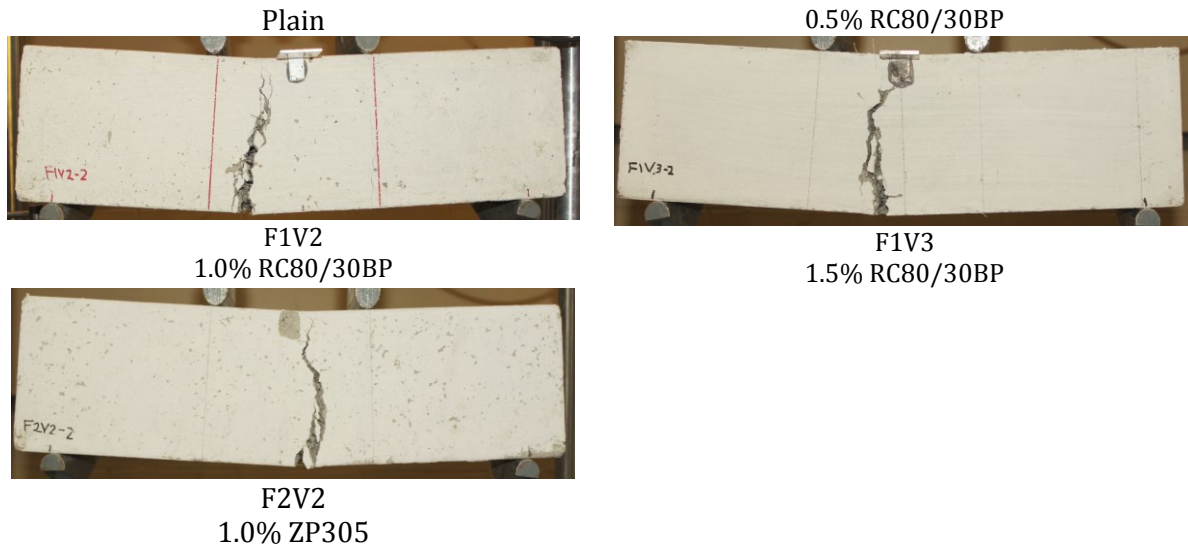
Figure 4-7: Representative MOR crack patterns

Table 4-4: Summary of the MOR test results

ID	V_f	AR_f	f'_c [MPa]	f'_t [MPa]	f_{cr} (CV) [MPa]	f_p (CV) [MPa]	f_{600}^D (CV) [MPa]	f_{150}^D (CV) [MPa]	T_{150}^D (CV) [MPa]	$R_{T,150}^D$ (CV) [MPa]	$f_{cr}/\sqrt{f'_c}$
CMS CRC	-	-	43.0	3.91	4.40 (0.8)	4.40 (0.8)	-	-	1.30 (21.7)	1.26 (22.9)	0.671
F1V1MS F1V1RC	0.5%	79	53.2	3.66	4.21 (4.6)	6.32 (0.10)	5.39 (11.7)	5.18 (0.80)	132.0 (0.90)	134.0 (5.50)	0.578
F1V2MS F1V2RC	1.0%	79	57.5	4.13	4.26 (1.3)	7.10 (7.5)	6.93 (8.1)	4.42 (7.1)	140.9 (7.1)	141.4 (8.4)	0.562
F1V3MS F1V3RC	1.5%	79	48.9	3.89	4.61 (10.0)	7.25 (8.6)	6.77 (2.50)	2.91 (9.2)	117.7 (0.30)	109.6 (9.70)	0.659
F2V2MS F2V2RC	1.0%	55	50.1	3.32	3.70 (2.5)	4.42 (6.2)	3.97 (3.7)	1.88 (32.6)	71.9 (8.8)	83.1 (11.2)	0.523

4.4.3 Test Results

Table 4-5 summarizes the MOR test results. The table displays the beam's first-cracking stress (f_1), the peak stress (f_p), the residual stresses (f_{600}^D and f_{150}^D), the toughness (T_{150}^D), and the equivalent flexural strength ratio ($R_{T,150}^D$). As shown in Figure 4-8, the average load vs. deflection response for each test set was based on the most representative specimen of the set.

Similar to the uniaxial tension test results, the pre-cracked response was similar for all specimens. Except for the F2V2 specimens, the flexural cracking stress for all specimens was alike; the F2V2 specimens had a cracking stress 15% lower than the average of the other fibrous specimens. The average flexural cracking stress for all SFRC specimens was $0.58\sqrt{f'_c}$.

All of the specimens displayed strain hardening behaviours. As the fibre volume fraction increased, the difference between the cracking load and the peak load increased, albeit to a lesser extent for concrete with the high volume fraction of 1.5%. Concrete with the low aspect ratio fibre (F2V2) exhibited the least gain in peak load after cracking; F2V2 had a 20% increase in the peak load, whereas the specimens with the high aspect ratio fibre had a peak load increase of approximately 60%. The small gain in the peak load for concrete with low aspect ratio fibres was primarily due to the fewer number of fibres crossing the crack. More specifically, concrete containing fibres with a lower aspect ratio had a smaller total fibre surface area for the same fibre volume; this led to poorer bond slip characteristics between the concrete and the fibres.

As shown in Figure 4-8, the mid-span deflection was the lowest for F2V2 as well. For concrete with the high aspect ratio fibre, increasing the fibre volume fraction decreased the deflection at peak load which triggered earlier strength decay; this is contrary to previous SFRC prism tests (Susetyo, 2009). It is believed that the poor fibre distribution for the F1V3 series, which resulted in a low measured fibre volume fraction, caused the early strength decay. F1V2 and F1V1 prisms had comparable mid-span deflection at peak load.

After reaching the peak load, all specimens experienced rapid strength decay. The slope of the decay branch was similar for all specimens; hence, the toughness value was primary affected by the peak load and the deflection at peak load. The toughness for the control specimens was negligible due to its lack of post-cracking load carrying capacity. As expected, F2V2 had the lowest toughness value. For specimens with the high aspect ratio fibre, the toughness value increased with increasing fibre volume fractions; the only exception was the F1V3 prisms due to their poor fibre distribution.
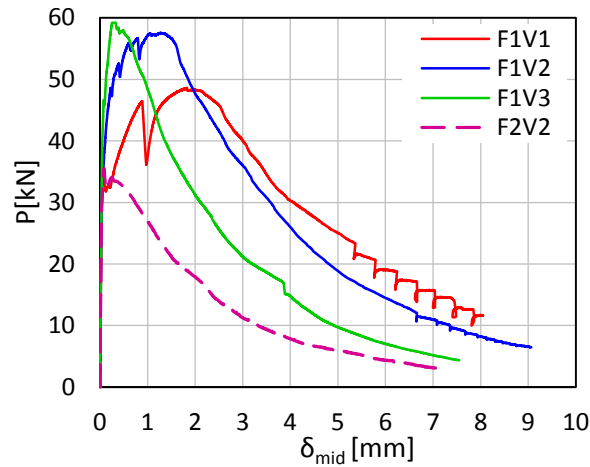
Figure 4-8: Bending test load vs. deflection response

4.5 Summary of the Material Test Results

The effects of fibre addition on the mechanical properties of SFRC were thoroughly examined through the three material tests performed in this work. The results for these material tests have been summarized in Table 4-5. The material tests primarily studied two parameters: fibre volume fraction and fibre aspect ratio. Although the fibre tensile strength varied between the two types of fibres used, it is believed that the fibre tensile strength has insignificant influence on the response of SFRC; the predominant mode of failure for SFRC members is fibre pull-out while the fracturing of fibres rarely occur (Chalioris, 2013; Setkit, 2012). The matrix strength varied between the different specimens as well, but this parameter is believed to have negligible influence due to the relatively small difference in the peak compressive stress. The following summary was drawn based on the results of the material tests:

1. Overall, the results for all three material tests were consistent and corroborate one another. Trends established for the parameters studied were observed in all three tests.
2. The pre-cracked response of concrete was in general not affected by fibre additions.
3. The cracking stress was higher for specimens under flexure than direct tension. The average direct cracking stress was $0.52\sqrt{f'_c}$, while the average flexural cracking stress was $0.58\sqrt{f'_c}$. This is because only the bottom fibres are under the maximum tensile stress in flexural tests (as oppose to every fibre in the direct tension case), and the probability of having a weak zone at the bottom layer to trigger cracking will be lower than having a weak zone in the entire cross section.

4. Increasing the fibre content led to improved post-cracked behaviour for all three material tests; the improvement was primarily in the form of higher residual stress and toughness, which was attributed to the higher number of fibres crossing the crack. The improved response was less pronounced for concrete with higher fibre contents.

5. Concrete with the high aspect ratio fibre (RC80/30BP) performed better than concrete with the low aspect ratio fibre (ZP305). This is because concrete with lower aspect ratio fibres has fewer fibres in the matrix for the same fibre volume fraction. In this work, the 1.0% ZP305 achieved marginally better post-cracking behaviour compared to the 0.5% RC80/30BP for the compression and direct tension test. For the flexural test, however, even the 0.5% RC80/30BP outperformed the 1.0% ZP305. Overall, the performance of 1.0% ZP305 was in between 0.5% RC80/30BP and 1.0% RC80/30BP.

6. Strain hardening was achieved only in the flexural tests; however, the tension test did exhibit hardening-type characteristics for concrete with higher fibre contents.

7. Specimens from the F1V3 set (1.5% RC80/30BP) achieved lower residual stresses than expected due to the poor fibre distribution during mixing. The underperformance was especially evident in the flexural test.

Table 4-5: Summary of the material test results

ID	V_f	AR_f	f'_c [MPa]	f'_t [MPa]	f_{tu} [MPa]	f_{cr} [MPa]	f_p [MPa]	E_{cs} [MPa]	E_{ct} [MPa]	$f'_t/\sqrt{f'_c}$	$f_{cr}/\sqrt{f'_c}$
CMS CRC	-	-	43.0	3.91	-	4.40	4.40	32037	32037	0.596	0.671
F1V1MS F1V1RC	0.5%	79	53.2	3.66	2.75	4.21	6.32	33177	41140	0.502	0.578
F1V2MS F1V2RC	1.0%	79	57.5	4.13	3.12	4.26	7.10	32166	35373	0.545	0.562
F1V3MS F1V3RC	1.5%	79	48.9	3.89	3.28	4.61	7.37	32045	37387	0.556	0.659
F2V2MS F2V2RC	1.0%	55	50.1	3.32	2.34	3.70	4.42	29806	34700	0.469	0.523

<div align="center">

Chapter 5
Panel Test Results

</div>

5. Panel Test Results

5.1   Introduction

In this section, the results of the panel tests will be discussed. Similar to the material test results, the panel test data analysis will be presented first, followed by the panel test observations, and, lastly, the analysis of the test results. Five different panels were subjected to reversed cyclic loading, while five more identical panels were subjected to monotonic loading. A total of five pairs of panels were constructed and tested. The two panels from each pair were cast with the same batch of concrete. The complete set of panel test data and test observations are presented in Appendix B. Only a summary of each panel test is provided in this chapter.

<div align="center">

Table 5-1: Summary of the panel test results

</div>

Test ID	V_f [%]	AR_f	$f_{c,test}$ [MPa]	v_{cr} [MPa]	v_u [MPa]	γ_u [x10^{-3}]	γ_{max} [x10^{-3}]	s_m [mm]	w_m [mm]	$w_{cr,max}$ [mm]
CMS	-	-	45.2	2.06	5.99	8.58	8.58	72.1	0.20	0.50
CRC	-	-	45.5	1.37	5.63	9.77	9.87	70.0	0.39	1.40
F1V1MS	0.5	79	55.9	2.18	3.34	4.07	4.07	148.8	0.19	0.35
F1V1RC	0.5	79	56.1	1.27	3.13	4.51	4.51	126.0	0.34	1.30
F1V2MS	1.0	79	58.1	1.81	4.65	4.96	4.96	54.8	0.18	0.65
F1V2RC	1.0	79	58.1	3.10	4.41	4.60	4.60	81.4	0.21	0.75
F1V3MS	1.5	79	50.9	2.34	4.93	3.40	3.40	96.9	0.12	0.50
F1V3RC	1.5	79	53.1	2.00	4.72	3.72	4.35	90.0	0.25	0.70
F2V2MS	1.0	55	52.1	1.79	3.96	4.16	4.16	74.0	0.25	0.80
F2V2RC	1.0	55	52.9	1.82	3.47	2.75	4.53	115.0	0.33	1.20

* Crack width and crack spacing values were based on manual measurements made in the final load stage (actual crack widths immediately before failure were likely larger)

A summary of the panel test results is shown in Table 5-1. The table gives the test day compressive strength ($f_{c,test}$), the cracking shear stress (v_{cr}), the ultimate shear stress attained (v_u), the corresponding ultimate shear strain (γ_u), the maximum shear strain attained (γ_{max}), the average

crack spacing (s_m), the average crack width (w_m), and the maximum crack width ($w_{cr,max}$). The test age of the panels is presented in Table 5-2. All of the SFRC panels experienced aggregate interlock failure. The test data showed that the SFRC panels' primary reinforcement did not yield and the concrete had not reached its compressive strength. The two control panels, however, failed due to yielding of the transverse reinforcement.

Table 5-2: Panel test age and strength

Test ID	V_f [%]	AR_f	Loading Protocol	Age at Testing [days]	f'_c [MPa]	$f_{c,test}$ [MPa]
CMS	-	-	Monotonic	44	43.0	45.2
CRC	-	-	Cyclic	52	43.0	45.5
F1V1MS	0.5	79	Monotonic	34	53.2	55.9
F1V1RC	0.5	79	Cyclic	42	53.2	56.1
F1V2MS	1.0	79	Monotonic	39	57.5	58.1
F1V2RC	1.0	79	Cyclic	42	57.5	58.1
F1V3MS	1.5	79	Monotonic	36	48.9	50.9
F1V3RC	1.5	79	Cyclic	50	48.9	53.1
F2V2MS	1.0	55	Monotonic	54	50.1	52.1
F2V2RC	1.0	55	Cyclic	61	50.1	52.9

Note that before the ten panels shown above were made, two pilot panels for the F1V2 pair were tested. Although these two pilot panels consisted of the same concrete (1.0% RC80/30BP), they were made separately with different batches of concrete and had their own cylinder, dogbone, and MOR specimens. These two pilot panels, F1V2MS-P and F1V2RC-P, were not included in the analyses below due to the many differences in testing and casting procedures. For example, because the two pilot panels were made separately, the strength and mechanical properties of the concrete were different, making the comparison between the monotonic and reversed cyclic response more obscure. The monotonically loaded pilot panel, F1V2MS-P, had a relatively low compressive strength (28% lower than F1V2RC-P) which produced a relatively weak shear response. The reversed cyclically loaded pilot panel, F1V2RC-P, had a very coarse loading protocol (the double cycle increments were 1.0 MPa shear stress) and did not result in sufficient number of loading cycles. Through these two pilot tests, much was learned on how to improve the testing and casting

procedures which resulted in the procedures outlined in Chapter 3. A full description of the results and analyses for these two pilot tests is shown in Appendix B.

5.2 Panel Data Analysis

The displacement data for the panel tests were obtained using LVDTs. The LVDTs provided continuous measures of the displacement in the x, y, horizontal (135° with respect to the x-axis), and vertical (45° with respect to the x-axis) directions for both faces of the specimen. The LVDT acquisition system was active during load stages when the crack widths were marked. The load cell data and pressure transducer readings were acquired continuously during the entire test. The load data and LVDT displacement data were automatically synchronized such that the stress versus strain relationship was directly obtained.

5.2.1 Data Analysis Procedure

This section summarizes the calculation procedures used to construct the various stress versus strain curves. Basic Mohr's Circle relationships were used in formulating the equations in this section. Although strain readings from only three directions are needed to represent any strain state in a Mohr's Circle diagram, the LVDTs measured strain in four different directions; the extra strain state can be used to verify the strain data. The strain parameters obtained from the Mohr's Circle were then used to obtain the stress parameters. The procedures used are shown below:

1. The average strain readings in the x-, y-, horizontal, and vertical directions were calculated.

$$\varepsilon_x = \frac{1}{n}\sum_{i=1}^{n}\varepsilon_{x,i} \; ; \; \varepsilon_y = \frac{1}{n}\sum_{i=1}^{n}\varepsilon_{y,i} \; ; \; \varepsilon_h = \frac{1}{n}\sum_{i=1}^{n}\varepsilon_{h,i} \; ; \; \varepsilon_v = \frac{1}{n}\sum_{i=1}^{n}\varepsilon_{v,i} \; ; \qquad (5.1)$$

2. Using the four strain state, three sets of engineering shear strains were calculated and averaged.

$$\gamma_{xy(x,y,v)} = 2\varepsilon_v - \varepsilon_x - \varepsilon_y \qquad (5.2a)$$

$$\gamma_{xy(x,v,h)} = \varepsilon_v - \varepsilon_h \qquad (5.2b)$$

$$\gamma_{xy(y,v,h)} = \varepsilon_v - \varepsilon_h \qquad (5.2c)$$

$$\gamma_{xy} = \frac{\gamma_{xy\,(x,y,v)} + \gamma_{xy\,(x,v,h)} + \gamma_{xy\,(y,v,h)}}{3} = \frac{4\varepsilon_v - 2\varepsilon_h - \varepsilon_x - \varepsilon_y}{3} \qquad (5.2d)$$

3. The principal tensile and compressive strains were then calculated.

$$\varepsilon_{1,2} = \left(\frac{\varepsilon_x + \varepsilon_y}{2}\right) \pm \sqrt{\left(\frac{\varepsilon_x - \varepsilon_y}{2}\right)^2 + \left(\frac{\gamma_{xy}}{2}\right)^2}$$ (5.3)

4. The orientation of the principal tensile strain was also calculated.

$$\theta_\varepsilon = \frac{1}{2}\tan^{-1}\left(\frac{\gamma_{xy}}{\varepsilon_x - \varepsilon_y}\right)$$ (5.4)

5. Together with the average strain previously calculated, the average reinforcement stresses were found using the stress-strain relationships obtained from the coupon tests (see Appendix A.4). If the reinforcement underwent post-yielding cycles, the post-yielding plastic offset was accounted for using the elastic-plastic model shown in Appendix B.2.2.

$$\varepsilon_{sx} = \varepsilon_x \; ; \; f_{sx} = f(\varepsilon_{sx})$$ (5.5a)

$$\varepsilon_{sy} = \varepsilon_y \; ; \; f_{sy} = f(\varepsilon_{sy})$$ (5.5b)

6. The concrete stresses in the x- and y- direction were calculated using the reinforcement stresses.

$$f_{cx} = -\rho_x f_{sx}$$ (5.6a)

$$f_{cy} = -\rho_y f_{sy}$$ (5.6a)

7. The applied shear stress was calculated.

$$v_{xy} = \frac{(P_{j,comp} \cdot A_{j,comp} + P_{j,tens} \cdot A_{j,tens}) \cdot \sin(45°) \cdot 5}{A_{panel}}$$ (5.7)

where,

$P_{j,comp}$ = recorded pressure in the compression jacks [MPa]

$P_{j,tens}$ = recorded pressure in the tension jacks [MPa]

$A_{j,comp}$ = area of the compression jacks [mm²]

$A_{j,tens}$ = area of the tension jacks [mm²]

A_{panel} = cross-sectional area of the panel [mm²]

8. The concrete principal compressive and principal tensile stresses were calculated.

$$f_{c1,2} = \left(\frac{f_{cx} + f_{cy}}{2}\right) \pm \sqrt{\left(\frac{f_{cx} - f_{cy}}{2}\right)^2 + (v_{xy})^2} \qquad (5.8)$$

9. Using the above, the orientation of the principal tensile stress was calculated.

$$\theta_\sigma = \frac{1}{2}\tan^{-1}\left(\frac{2v_{xy}}{f_{cx} - f_{cy}}\right) \qquad (5.9)$$

Using the above formulas, various stress versus strain relationships were obtained: shear stress versus shear strain, principal tensile stress versus principal tensile strain, principal compressive stress versus principal compressive strain, etc. A comprehensive set of these graphs for each panel test is presented in Appendix B.

5.2.2 Data Verification

Data for each panel test were verified by comparing the values measured from the four pressure transducers, the applied load against the load obtained from the load cells, and the LVDT response between the back face and front face.

For the four pressure transducers, one pair was located on the pressure maintainer to monitor the two sets of hydraulic pressure applied and to ensure that the pressure ratio was as required for a pure shear loading condition; the other pair of pressure transducers was directly connected to two random hydraulic jacks to ensure that the pressure applied through the load maintainer was the same as the pressure received by the jacks. Overall, the values recorded by all pressure transducers were consistent with expectation, and the pressure ratio was correct, at approximately 0.44, throughout the test.

The three load cells connected to the three rigid links measured the reaction forces throughout the test. Since a pure shear loading condition was used, the magnitude of the forces for each jack and rigid link should be the same. The load cells did not display ideal results throughout the test. In the negative shear direction, the forces measured by the three load cells after initial cracking were consistent with the load applied. In the positive shear direction, however, the horizontal load cell did not display any significant force until failure was near; at the same time, the load cell for the vertical rigid link that forms the roller connection with the horizontal rigid link registered forces that were sometimes one half of the expected values. The exact source of these unexpected load cell

values from the positive shear direction is unknown. The problem may be due to the slack around the reaction pin that connected the horizontal load cell to the reaction frame, as no forces would have been registered until the reaction pin is in contact with the load cell. Despite the positive direction load cell problem highlighted above, the response between the positive and negative direction were very consistent for all panels; hence, it is believed that the erroneous load cell measurements were not indicators of a non-pure shear loading condition in the positive direction.

Table 5-3: Comments on the response between the front and back face

Test ID	Loading Protocol	Comments on the out-of-plane bending
CMS	Monotonic	- identical between the front and back
CRC	Cyclic	- small amount of out-of-plane bending in the positive direction only, response near convergence at 3.0 MPa
F1V1MS	Monotonic	- identical between the front and back
F1V1RC	Cyclic	- moderate amount of out-of-plane bending in the positive direction only, response near convergence at 3.0 MPa
F1V2MS	Monotonic	- slight amount of out-of-plane bending, response converged at 3.0 MPa
F1V2RC	Cyclic	- small amount of out-of-plane bending in the negative direction only, response near convergence at 3.0 MPa
F1V3MS	Monotonic	- identical between the front and back
F1V3RC	Cyclic	- small amount of out-of-plane bending in both directions, response near convergence at 3.0 MPa
F2V2MS	Monotonic	- small amount of out-of-plane bending, response near convergence at 3.0 MPa
F2V2RC	Cyclic	- small amount of out-of-plane bending in both directions, response near convergence at 3.0 MPa

* small amount of out-of-plane bending suggests a shear strain difference of less than 0.5×10^{-3}, a moderate amount indicates a shear strain difference of approximately 1.0×10^{-3}

The comparison of the LVDT data between the front and back face of the panels revealed some discrepancies which indicated the presence of out-of-plane bending in the panels. A summary of the comments made regarding the out-of-plane bending for each panel is shown in Table 5-3; these comments were based on the shear stress-shear strain response of each panel. Overall, the amounts of out-of-plane bending exhibited by the panels were small; the peak shear strain difference between the front and back face was approximately less than 0.5×10^{-3} for majority of the panels. Only panel F1V1RC exhibited a moderate peak shear strain difference of approximately 1.0×10^{-3}. All panels' front and back face response were near convergence at a shear stress of 3.0 MPa. For all panels, the front face (the form face) displayed larger strains and experienced earlier initial cracking than the back face (the finished face). The majority of the monotonically loaded panels

exhibited a small to negligible amount of out-of-plane bending. The reversed cyclically loaded panels often displayed out-of-plane bending in one direction only, either in the positive shear direction or in the negative shear direction.

The source of this out-of-plane bending is difficult to pinpoint but the following sources are the most probable causes. First, the out-of-plane alignment of the panel may be non-ideal. The out-of-plane alignment was controlled and adjusted by altering the length of the tie-rods that connected the lateral support frame to the concrete panel when the specimen was under 0.50 MPa biaxial tension. Since the manual adjustment of the tie-rods can be somewhat subjective, improper adjustment was possible and can impose out-of-plane bending on the panel specimen.

Another possible cause of the out-of-plane bending was related to the finishing of the panel during casting. During casting, the form face of the panel, which is the front face, was flush with the shear keys. However, the concrete level for the finished face may be higher than the shear keys due to difficulties in levelling the surface; this may have led to the back face being slightly thicker.

Lastly, the non-uniform distribution of the fibres and aggregates may have led to the observed out-of-plane bending. Unlike the dogbone specimens, the dense reinforcement cage made it difficult for fibres to travel down to the form face and led to a concentration of fibres near the finished face. This was evident from the fibre count taken at the failure plane, where approximately 70% of the fibres were concentrated at the finished face (see Section 3.4.4). Further, the fibres concentrated at the finished face created a sieving effect for the aggregates, leading to a larger concentration of coarse aggregates near the top face. The concentration of fibres and coarse aggregates near the back face would create a stiffer response from that face.

Despite the stiffer response from the back face due to the various factors mentioned above, the degree of the out-of-plane bending for the different panels was overall less than previous panel tests conducted and the out-of-plane bending diminished earlier than previous panel tests performed (Carnovale, 2013; Susetyo, 2011). Thus, only the average LVDT response was used for the discussion and analysis below.

5.3   Panel Test Observations

A summary of each panel's test observations and test results is presented in this section. For each panel test, a more detailed description of the test observations, photos of the specimen during each load stage, a comprehensive set of stress versus strain relationships, and detailed analyses of the results are presented in Appendix B.

5.3.1 Panel CMS

Panel CMS was the monotonically loaded control panel consisting of normal concrete. The panel contained 3.31% reinforcement in the primary direction (x-direction), and 0.42% reinforcement in the transverse direction (y-direction). The reinforcement layout, concrete mix, and loading protocol for this panel were identical to Susetyo's (2011) control panel, C1C; the primary difference was the concrete compressive strength and the reinforcement yield strength. Determined from the cylinder compression test and the uniaxial tension test, this panel had a 28-day compressive strength of 43.0 MPa and a uniaxial tensile strength of 3.91 MPa; the test day compressive strength was 45.2 MPa.

Panel CMS's shear stress-shear strain response is shown in Figure 5-1. The panel first cracked at a shear stress, v_{cr}, of 2.06 MPa with a shear strain of 0.18×10^{-3}. The cracking shear stress was significantly lower than the uniaxial tensile strength obtained from the dogbone test. For the panels tested in this work, the cracking shear stress was approximately 50% of the uniaxial tensile strength; this was consistent with the results from previous panel tests (Carnovale, 2013; Susetyo, 2009). The relatively low cracking shear stress was attributed to the non-uniform stress applied to the panel specimens during the early stages of the test. The pressure applied to the shear keys were likely non-uniform due to friction within the hydraulic jacks, friction due to the bolted connections, self-weight of the links, etc. The out-of-plane effects were also most dominant during the early load stages; the resulting out-of-plane bending caused the earlier cracking of the front face and an overall lower cracking shear stress. Lastly, the tensile strengths determined from material tests were based on the plain concrete which are not necessarily indicative of actual tensile strengths of reinforced concrete.

Yielding of transverse reinforcement occurred at shear stress of 5.03 MPa and a shear strain of 4.30×10^{-3}. At failure, the ultimate shear stress, v_u, and the corresponding ultimate shear strain, γ_u, were 5.99 MPa and 8.58×10^{-3}, respectively. The failure of the panel was initiated by yielding of the transverse reinforcement which later led to the aggregate interlock failure. The peak average strain

for the transverse reinforcement was 8.75×10^{-3}, well below the rupturing strain of 21.8×10^{-3}. The peak strain for the primary reinforcement was 1.46×10^{-3}, below its yield strain of 2.48×10^{-3}.
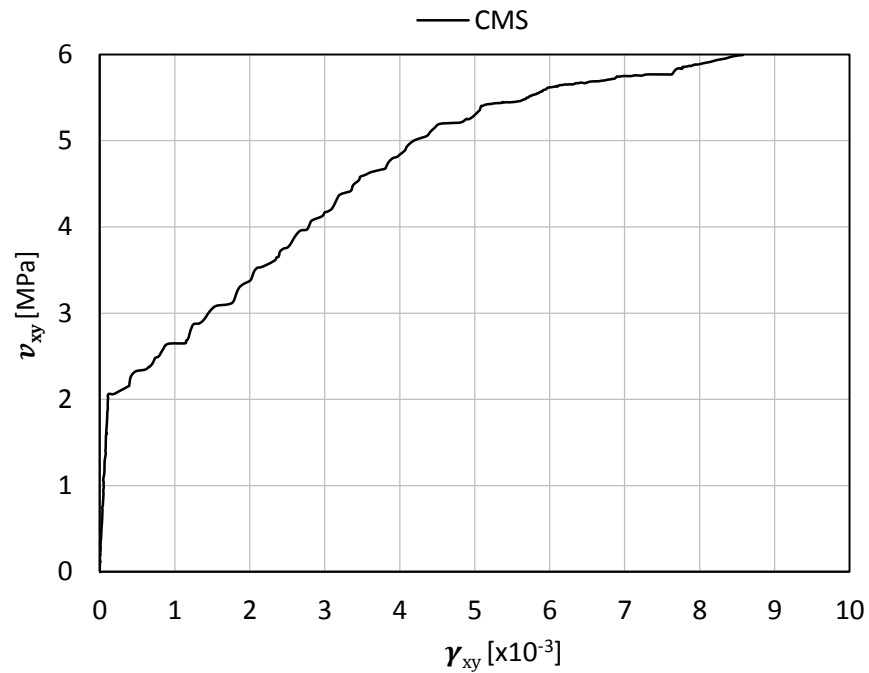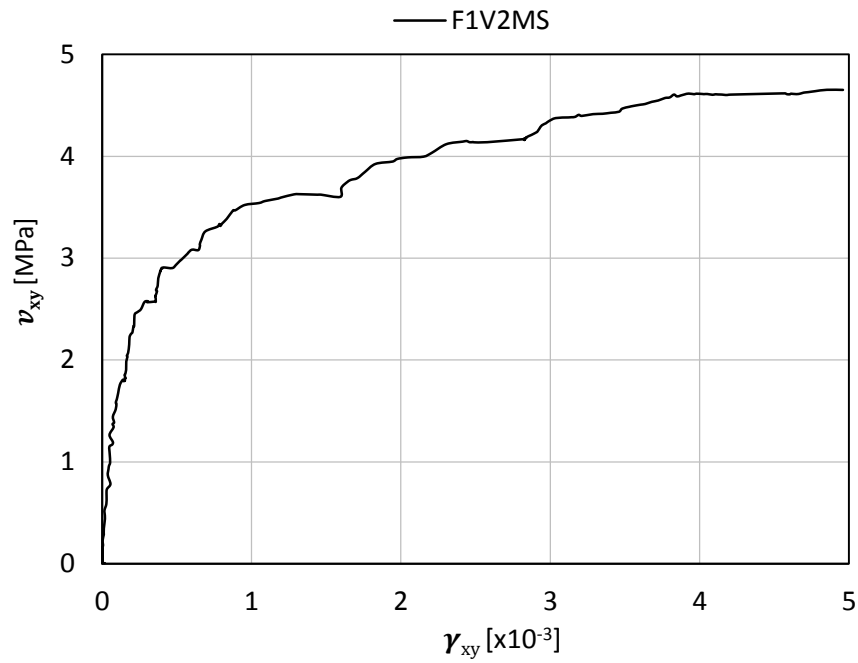

Figure 5-1: CMS shear stress vs. shear strain response
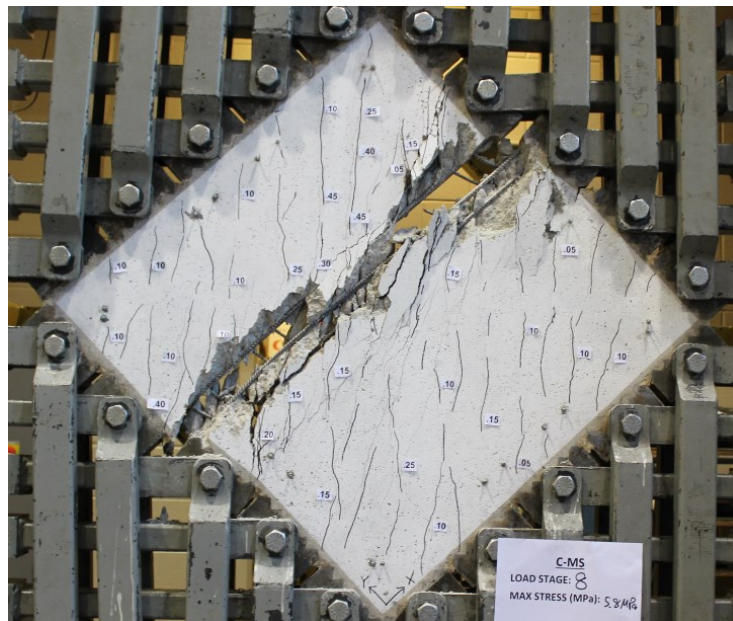
Figure 5-2: CMS failure crack pattern

As shown in Figure 5-2, the failure crack of panel CMS was parallel and right next to the primary reinforcement. Immediately before failure, the surface cracks were well distributed across the

panel, inclined approximately at an angle of 30° with respect to the x-axis. At the last load stage before failure, which was taken at a shear stress of 5.21 MPa, the maximum crack width, the average crack width, and the average crack spacing were 0.50 mm, 0.20 mm, and 72.1 mm, respectively.

5.3.2 Panel CRC

Panel CRC was the reversed cyclically loaded control panel and was the companion panel for panel CMS. Panel CRC also contained 3.31% reinforcement in the primary direction and 0.42% reinforcement in the transverse direction. The reinforcement layout and concrete mix for this panel was identical to Carnovale's (2013) reversed cyclically loaded control panel, DC-P1; the primary difference between these two panels was the concrete compressive strength. This panel had a 28-day compressive strength of 43.0 MPa and a uniaxial tensile strength of 3.91 MPa; the test day compressive strength was 45.5 MPa.

Figure 5-3 shows a schematic of the loading protocol used in this test. The first two double cycles had a stress increment of 1.0 MPa. After cracks were observed during the 2nd double cycle, the double cycle increment decreased to approximately 0.5 MPa until failure. The double cycle peak shear stresses were 1.00 MPa, 2.10 MPa, 2.65 MPa, 3.13 MPa, 3.65 MPa, 4.20 MPa, 4.80 MPa, 5.30 MPa, and 5.60 MPa. This loading protocol was successful in capturing the hysteretic response.
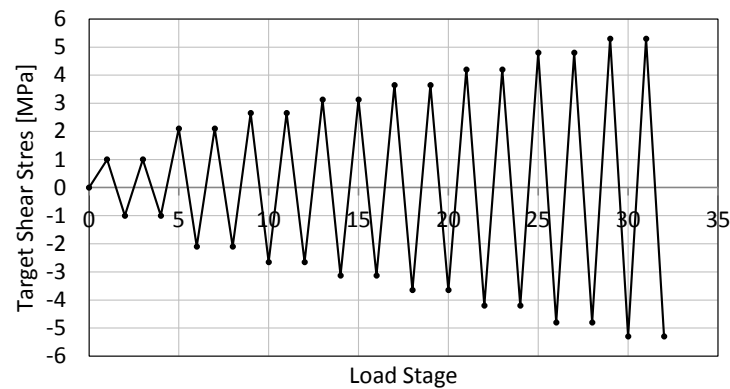
Figure 5-3: CRC loading protocol

Although visible cracks were not noticed until the 2nd double cycle, at a shear stress of 2.1 MPa, it is believed that the first crack formed at a shear stress, v_{cr}, of 1.37 MPa with a shear strain of $0.16×10^{-3}$ based on the recorded test results. Yielding of the transverse reinforcement occurred during the second load stage of the 7th double cycle (stage 26), at a shear stress of -4.75 MPa and a shear strain of $-4.23×10^{-3}$. Finally, failure of the specimen occurred during the excursion to the second load stage of the 9th double cycle (stage 34) at a shear stress and shear strain of -5.25 MPa

and -9.87×10^{-3}, respectively. The previously attained ultimate shear stress, v_u, was 5.62 MPa with a corresponding ultimate shear strain, γ_u, of 9.77×10^{-3}.

The full shear stress-shear strain response is shown in Figure 5-4, the monotonic response from panel CMS is also plotted (in both positive and negative direction) for comparison. As a result of the cyclic loading protocol, the degradation on the ultimate shear stress was 6.0%, while the ultimate shear strain was increased by 13.9%. Overall, the cyclic envelope curve closely matched the monotonic backbone curve until yielding of the transverse reinforcement; a small amount of strength degradation occurred thereafter.

The peak strain for the transverse reinforcement was 12.87×10^{-3}, within 60% of the rupturing strain. The peak strain for the primary reinforcement was 1.79×10^{-3}, below its yield strain. Hence, the brittle failure was initiated by the yielding of the transverse reinforcement followed by an aggregate interlock failure.

As shown in Figure 5-5, the location and angle of the failure crack for panel CRC was similar to panel CMS, parallel to the primary reinforcement and between the shear keys. The surface cracks before failure inclined approximately at an angle of 30° and 120° with respect to the x-axis. At the last load stage before failure, which was taken at a shear stress of 5.28 MPa, the maximum crack width, the average crack width, and the average crack spacing were 1.40 mm, 0.39 mm, and 70.0 mm, respectively.
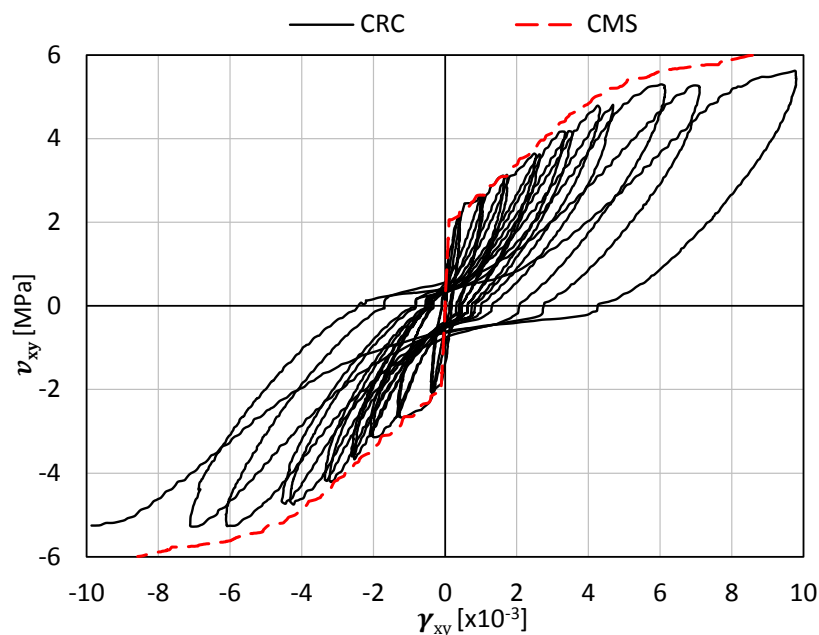
Figure 5-4: CRC shear stress vs. shear strain response (CMS included)
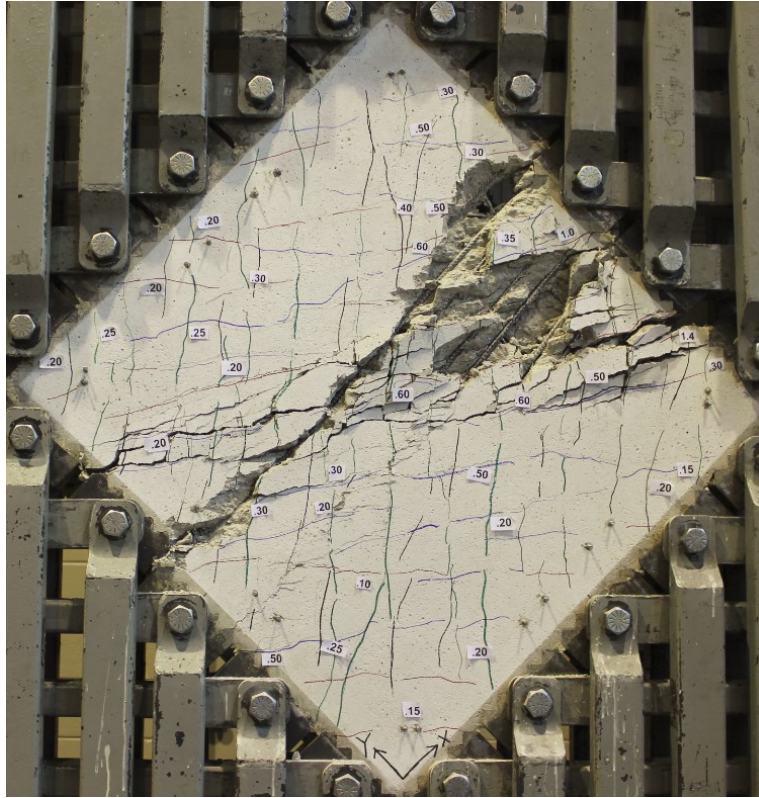
Figure 5-5: CRC failure crack pattern

5.3.3 Panel F1V1MS

Panel F1V1MS was monotonically loaded and constructed with steel fibre reinforced concrete containing 0.5% by volume of RC80/30BP fibres (l_f = 30 mm, d_f = 0.38 mm, f_{uf} = 2300 MPa). The longitudinal reinforcement ratio was 3.31% with no transverse reinforcement. This panel had a 28-day compressive strength of 53.2 MPa and a uniaxial tensile strength of 3.66 MPa; the test day compressive strength was 55.9 MPa.

The full shear stress-shear strain response of F1V1MS is shown in Figure 5-7. The panel exhibited a linear behaviour until the first crack appeared at a shear stress and shear strain of 2.18 MPa and 0.147×10^{-3}, respectively. After initial cracking, the panel exhibited significant softening until a plateau was reached at a shear stress and shear strain of 3.30 MPa and 1.99×10^{-3}, respectively. Similar to all SFRC panels, as the cracks widened, the load could no longer be transmitted through the aggregate interlock mechanism which led to a brittle failure. Both the primary reinforcement stress and the principal compressive stress were well below their ultimate strength. At failure, the ultimate shear stress was 3.34 MPa and the ultimate shear strain was 4.07×10^{-3}.
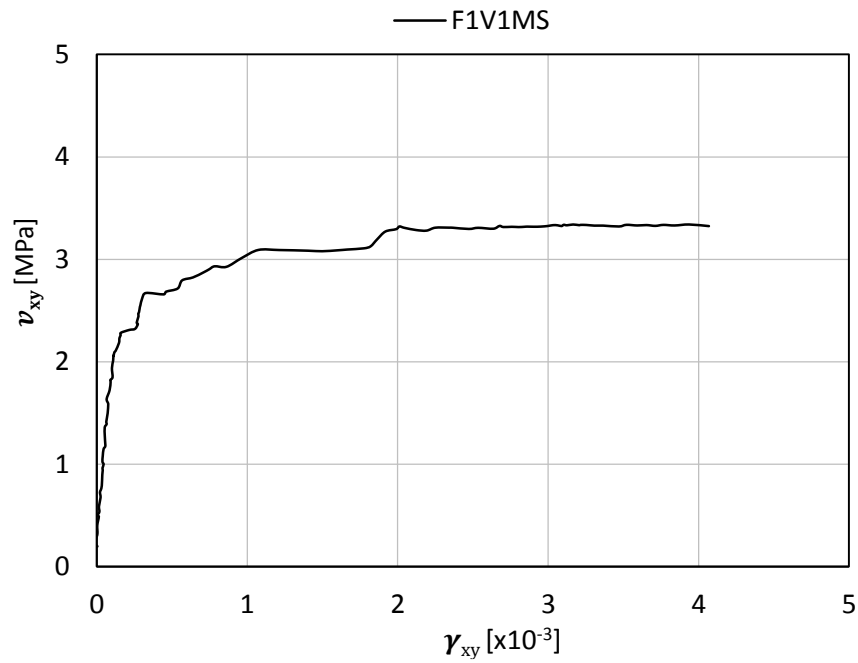
Figure 5-6: F1V1MS shear stress vs. shear strain response
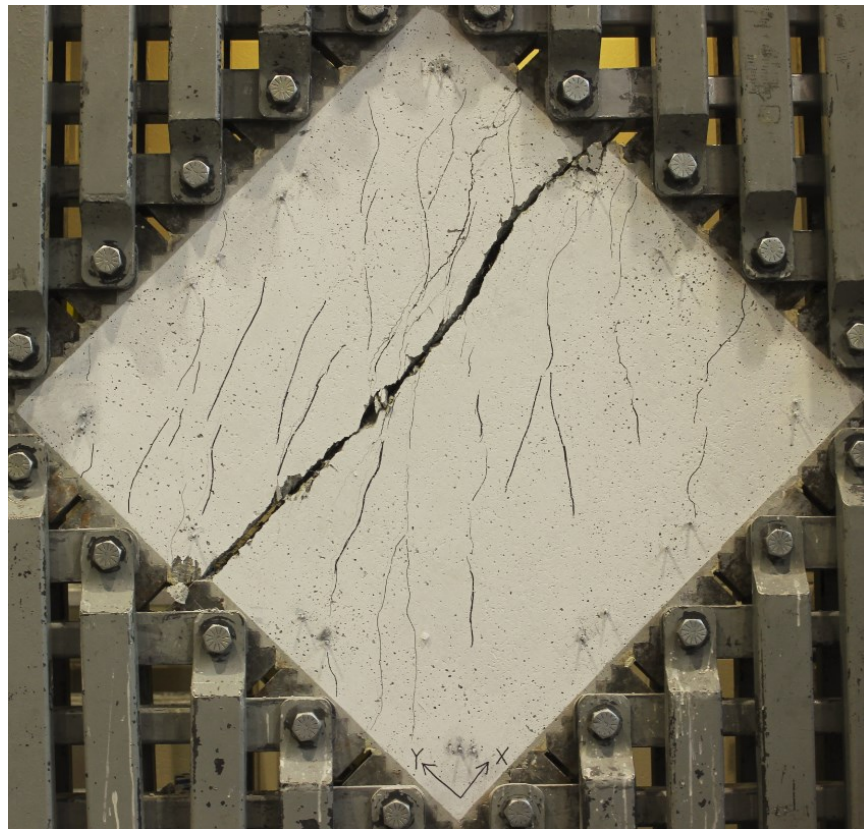
Figure 5-7: F1V1MS failure crack pattern

As shown in Figure 5-7, the failure crack of F1V1MS was parallel and adjacent to the primary reinforcement. Immediately before failure, cracks had small widths and large spacings but were adequately uniform across the panel. At the last load stage, which was taken at a shear stress of 3.11 MPa, the maximum crack width, the average crack width, and the average crack spacing were 0.35 mm, 0.19 mm, and 148.8 mm, respectively.

5.3.4 Panel F1V1RC

F1V1RC was constructed to be identical to F1V1MS. F1V1RC was reversed cyclically loaded and was constructed using steel fibre reinforced concrete containing 0.5% by volume of RC80/30BP fibres (l_f = 30 mm, d_f = 0.38 mm, f_{uf} = 2300 MPa). The longitudinal reinforcement ratio was 3.31% with no transverse reinforcement. This panel had a 28-day compressive strength of 53.2 MPa and a uniaxial tensile strength of 3.66 MPa; the test day compressive strength was 56.1 MPa.

Figure 5-8 shows a schematic of the loading protocol used for F1V1RC. The double cycle stress increment was gradually decreased in order to somewhat represent a strain-controlled regime. The double cycle peak shear stresses were 1.0 MPa, 1.6 MPa, 2.1 MPa, 2.6 MPa, 2.9 MPa, and 3.1 MPa.
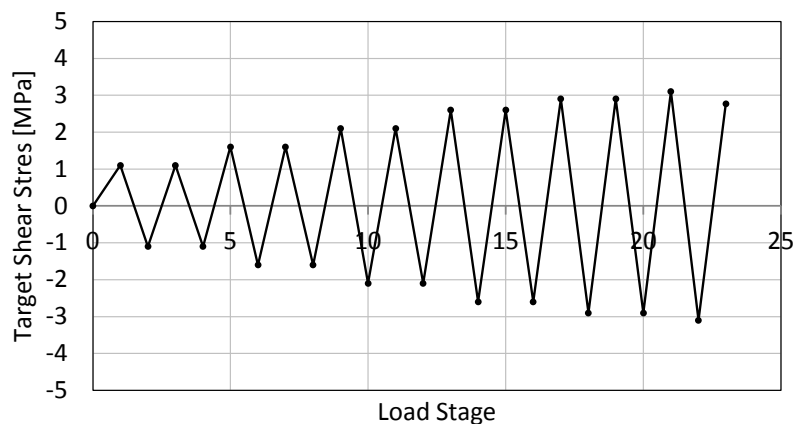
Figure 5-8: F1V1RC loading protocol

The first crack appeared during the second double cycle at a shear stress and a shear strain of 1.27 MPa and 0.16×10⁻³, respectively. As previously mentioned, F1V1RC experienced the largest out-of-plane bending for panels tested in this work; the peak shear strain difference between the two faces was approximately 1.0×10⁻³. The response between the two faces converged near the end of the test; as a result, cracks were only uniformly distributed near the maximum shear stress. For majority of the test, only a few horizontal cracks were developed and were concentrated at the bottom half of the panel. The vertical cracks, however, were overall sufficiently well distributed.

The panel experienced significant softening during the last negative cycle and failure occurred during the following positive cycle at a shear stress and shear strain of 2.77 MPa and 4.01×10^{-3}, respectively. The ultimate shear stress was 3.13 MPa with a corresponding ultimate shear strain of 4.51×10^{-3}. The failure of the panel was due to aggregate interlock failure, as both the primary reinforcement stress and the principal compressive stress were well below their ultimate strength.

The full shear stress-shear strain responses of F1V1RC and F1V1MS are shown in Figure 5-9. The cycling of load led to a strength degradation of 6.3% and a 10.8% increase in the ultimate shear strain. The cyclic envelope curve somewhat matched the monotonic backbone curve, but stress degradation began shortly after initial cracking.

As shown in Figure 5-10, the failure crack was parallel and right next to the primary reinforcement, similar to panel F1V1MS. At the last load stage, the maximum crack width, the average crack width, and the average crack spacing were 1.30 mm, 0.34 mm, and 126 mm, respectively. The crack widths for this panel were larger than the crack widths for the monotonically loaded companion panel.
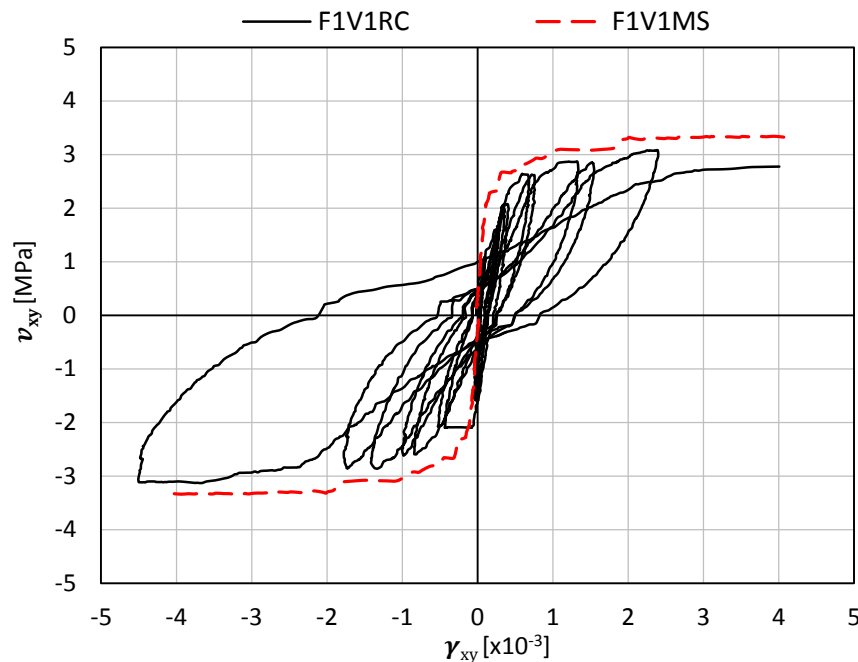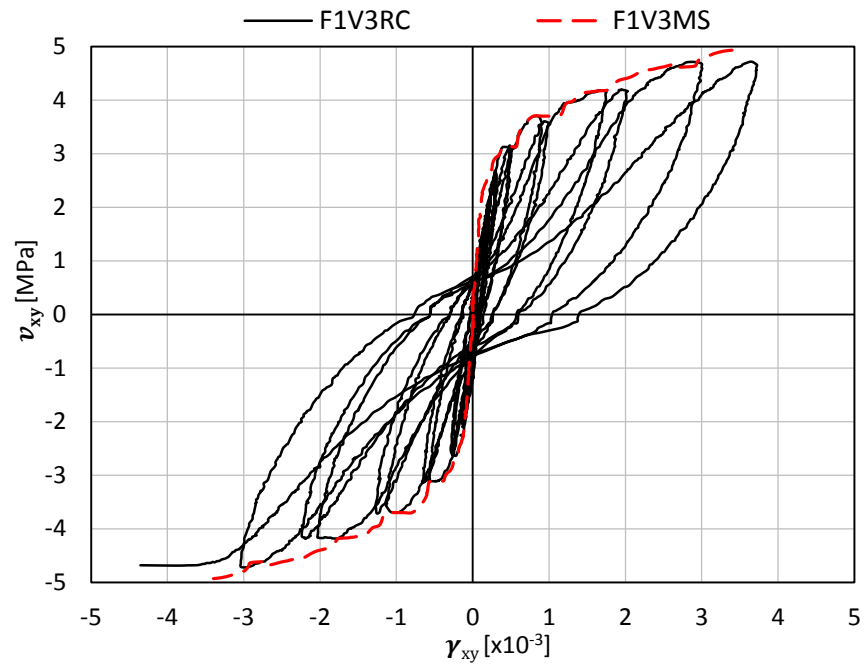

Figure 5-9: F1V1RC shear stress vs. shear strain response (F1V1MS included)
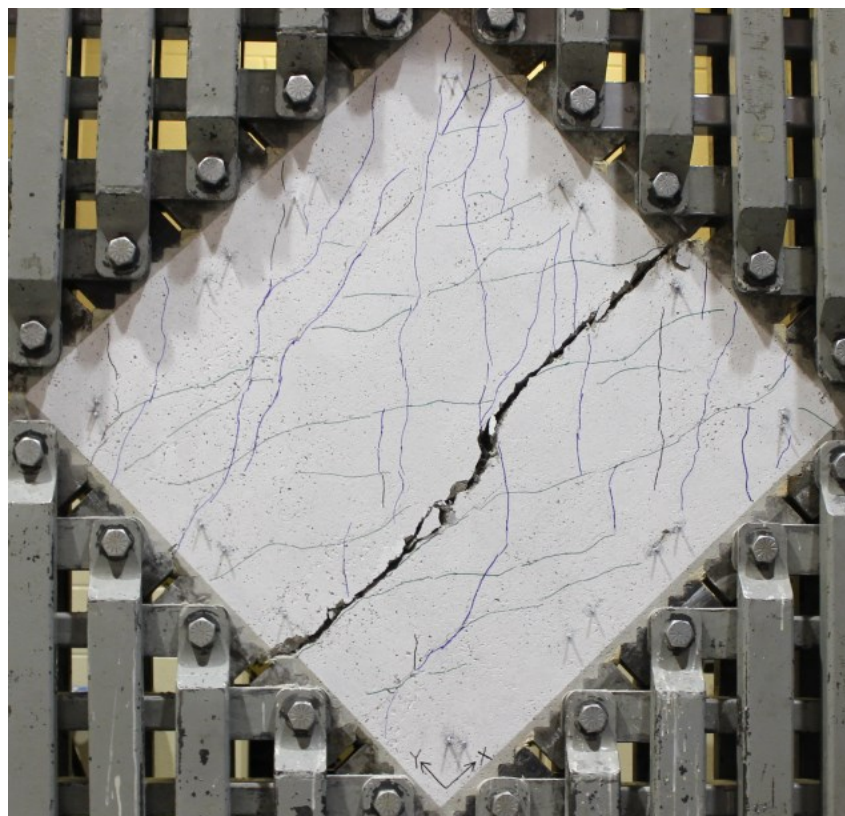
Figure 5-10: F1V1RC failure crack pattern

5.3.5 Panel F1V2MS

Panel F1V2MS was the monotonically loaded companion panel of the F1V2 pair. The panel was constructed using SFRC with 1.0% by volume of RC80/30BP fibres (l_f = 30 mm, d_f = 0.38 mm, f_{uf} = 2300 MPa). Identical to all SFRC panels, the longitudinal reinforcement ratio was 3.31% with no transverse reinforcement provided. The reinforcement layout, concrete mix, and loading protocol for this panel were identical to one of Carnovale's (2013) panels, DC-P2. This panel had a 28-day compressive strength of 57.5 MPa and a uniaxial tensile strength of 4.13 MPa; the test day compressive strength was 58.1 MPa.

The full shear stress-shear strain response of F1V2MS is shown in Figure 5-11. The panel response was linear up to first-cracking, which occurred at a shear stress of 1.81 MPa with a shear strain of 0.138×10^{-3}. Subsequently, the panel experienced gradual softening until failure occurred at a shear stress and shear strain of 4.65 MPa and 4.96×10^{-3}, respectively. The failure was initiated by fibre pull-out followed by the breakdown of the aggregate interlock mechanism. Both the primary reinforcement stress and the principal compressive stress were well below their ultimate strength.

Figure 5-11: F1V2MS shear stress vs. shear strain response
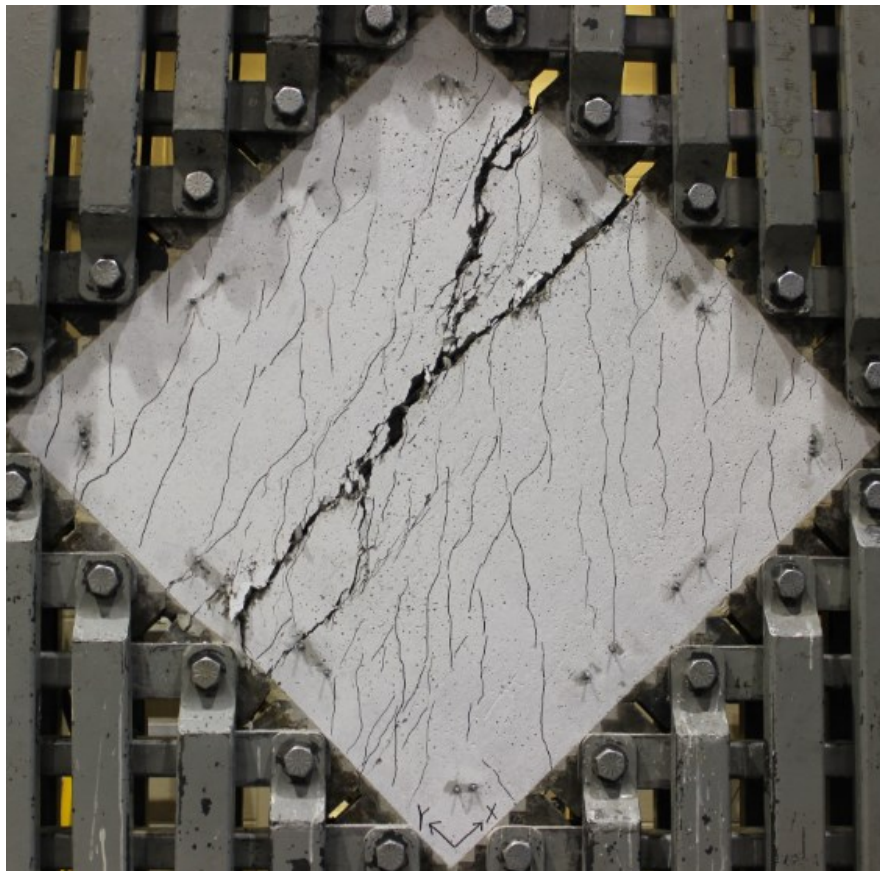
Figure 5-12: F1V2MS failure crack pattern

A shown in Figure 5-12, F1V2MS was the only panel in this work where the failure crack was not parallel to the primary reinforcement; instead, the crack crossed the primary reinforcement at an angle of approximately 30° with respect to the x-axis, consistent with the angle of the surface cracks before failure. Immediately before failure, many small cracks with small crack spacing were uniformly distributed across the panel. At the last load stage, taken at a shear stress of 4.61 MPa, the maximum crack width, the average crack width, and the average crack spacing were 0.65 mm, 0.18 mm, and 54.8 mm, respectively. Hence, this panel exhibited significantly improved crack control over F1V1MS.

5.3.6 Panel F1V2RC

Panel F1V2RC was the reversed cyclically loaded companion panel of the F1V2 pair. The panel was constructed using SFRC with 1.0% by volume of RC80/30BP fibres (l_f = 30 mm, d_f = 0.38 mm, f_{uf} = 2300 MPa). The longitudinal reinforcement ratio was 3.31% and no transverse reinforcement was provided. The reinforcement layout, concrete mix, and loading protocol for this panel were similar to one of Carnovale's (2013) panels, DC-P4. Results from compressive cylinder and uniaxial tensile tests indicated that the 28-day compressive strength was 57.5 MPa and the uniaxial tensile strength was 4.13 MPa; the test day compressive strength was 58.1 MPa. A schematic of the loading protocol used is shown in Figure 5-13. The double cycle peak shear stresses were 1.0 MPa, 2.1 MPa, 3.1 MPa, 3.6 MPa, 4.15 MPa, and 4.4 MPa.
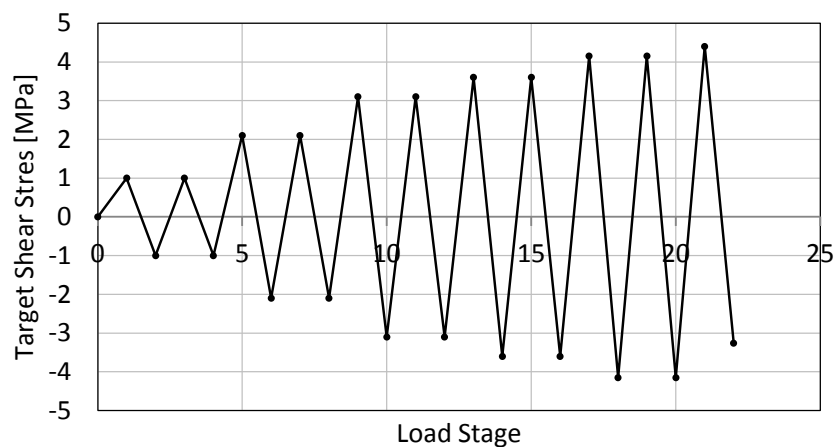
Figure 5-13: F1V2RC loading protocol

The response of the panel was linear until first-cracking, which occurred at a shear stress and shear strain of 3.10 MPa and 0.26×10^{-3}, respectively. Thereafter, the response was softened until failure occurred on the negative cycle at a shear stress of 3.26 MPa with a shear strain of 4.3×10^{-3}. The

previously attained ultimate shear stress was 4.41 MPa with a corresponding ultimate shear strain of 4.60×10^{-3}. The brittle failure of the panel was initiated by fibre pull-out which led to the breakdown of the aggregate interlock mechanism.

The full shear stress-shear strain responses of F1V2RC and F1V2MS are shown in Figure 5-14. The cycling of load led to a strength degradation of 5.2%, with a 7.3% decrease in the ultimate shear strain. Overall, the cyclic envelope curve matched the monotonic backbone curve and stress degradation occurred only on the last cycle. During the early cycles in the positive shear direction, the cyclic envelope curve unexpectedly reached a higher shear stress than the backbone curve.

The failure crack was a straight crack oriented parallel to the primary reinforcement (see Figure 5-15). Immediately before failure, the surface cracks were uniformly distributed. At the last load stage, the maximum crack width, the average crack width, and the average crack spacing were 0.75 mm, 0.21 mm, and 81.4 mm, respectively; the crack widths for this panel were larger than the crack widths for the monotonically loaded companion panel.
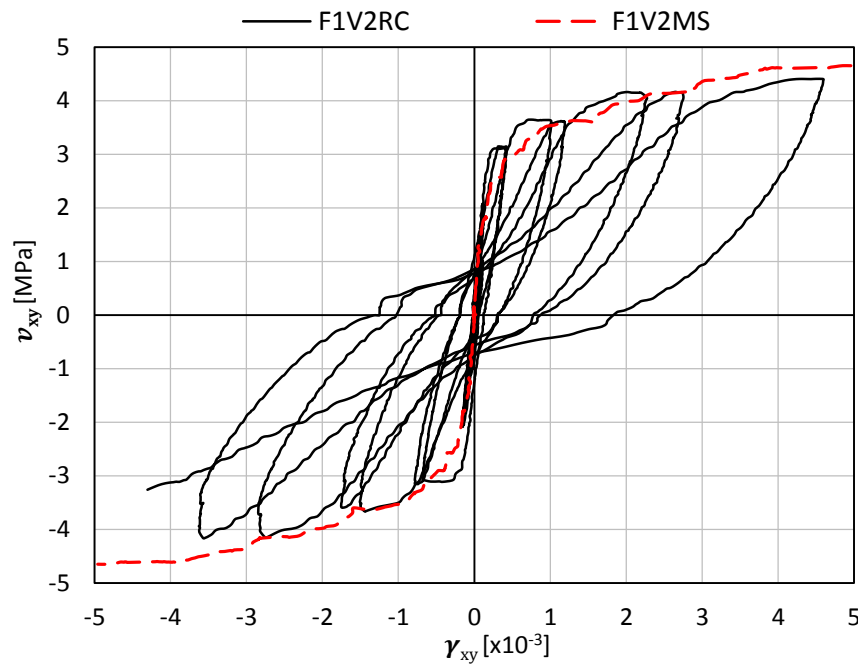
Figure 5-14: F1V2RC shear stress vs. shear strain response (F1V2MS included)
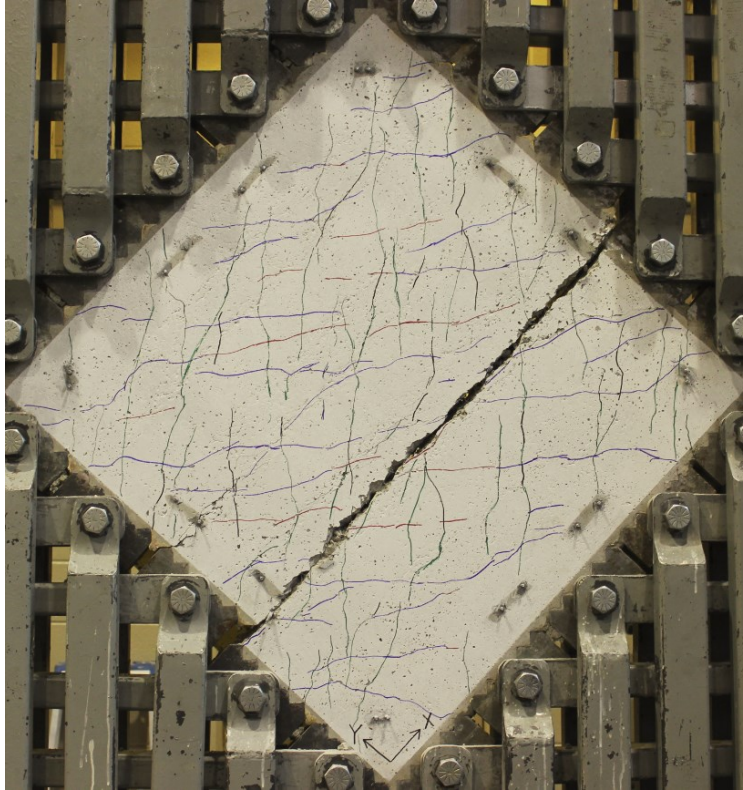
Figure 5-15: F1V2RC failure crack pattern

5.3.7 Panel F1V3MS

Panel F1V3MS was monotonically loaded and constructed with steel fibre reinforced concrete containing 1.5% by volume of RC80/30BP fibres (l_f = 30 mm, d_f = 0.38 mm, f_{uf} = 2300 MPa). The panel had a longitudinal reinforcement ratio of 3.31% with no transverse reinforcement provided. Results from compressive cylinder tests and uniaxial tensile tests indicated that the 28-day compressive strength was 48.9 MPa and the uniaxial tensile strength was 3.89 MPa; the test day compressive strength was 50.9 MPa.

As shown in Figure 5-16, the panel response was linear up to first-cracking, which occurred at a shear stress of 2.34 MPa with a shear strain of 0.141×10^{-3}. Gradual softening occurred thereafter and failure occurred at a shear stress and shear strain of 4.93 MPa and 3.40×10^{-3}, respectively. Similar to the other SFRC panels, the failure was initiated by fibre pull-out followed by breakdown of the aggregate interlock mechanism. However, the failure was more abrupt and unexpectedly early for this test; the maximum shear strain achieved was 31% less than the maximum shear strain of F1V2MS. As well, unlike the other monotonically loaded panels, F1V3MS had a relatively high tangent stiffness at failure and did not exhibit a well-defined plateau.

As discussed in Chapter 3's Fibre Distribution section (Section 3.4.2), the poor fibre distribution during casting for the F1V3 series led to some areas of the specimens having fewer fibres than other areas. The measured fibre volume fraction for F1V3MS, which was based on the number of fibres intersecting the failure plane, was 0.62%, only 42% of the design value (the measured fibre volume fraction for F1V3RC was 0.74%, 49% of the design value). It is important to note that the low measured fibre volume fraction for panels of the F1V3 pair is not as severe as it seems, because the measured fibre volume fraction for the other SFRC panels was, on average, 60% of the design value. Although it is evident that the weak zone created by the poor fibre distribution led to a shorter post-cracking response for F1V3MS, the pre-peak response was believed to be not affected as the average fibre volume fraction across the panel was approximately 1.5% and the surface cracks developed prior to failure were uniform.

As shown in Figure 5-17, the failure crack of F1V3MS was parallel and adjacent to the primary reinforcement. The large crack below the failure crack was formed after the failure of the panel. At the last load stage, the maximum crack width, the average crack width, and the average crack spacing were 0.50 mm, 0.12 mm, and 96.9 mm. The average crack spacing was unexpectedly larger than the 54.8 mm crack spacing from panel F1V2MS and is believed to be caused by the non-ideal fibre distribution.
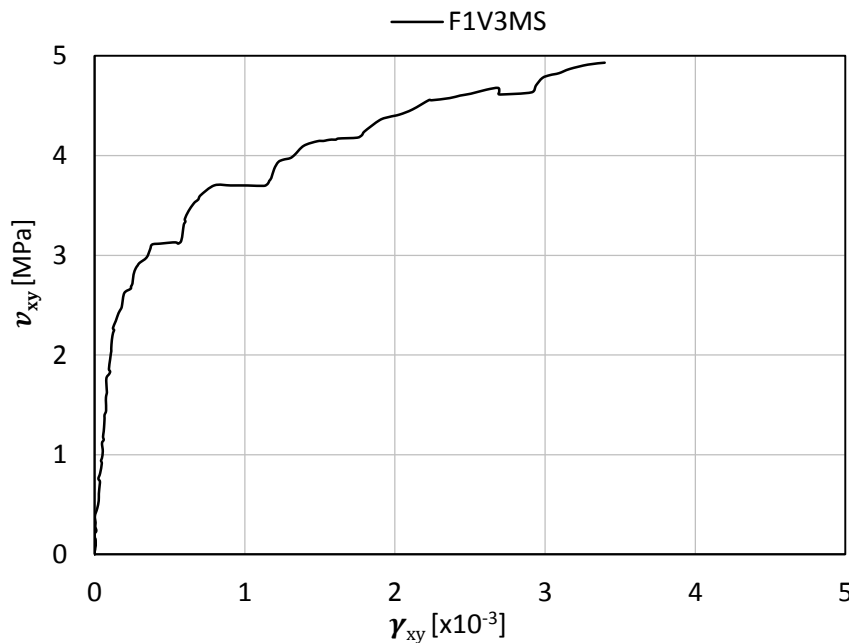
Figure 5-16: F1V3MS shear stress vs. shear strain response
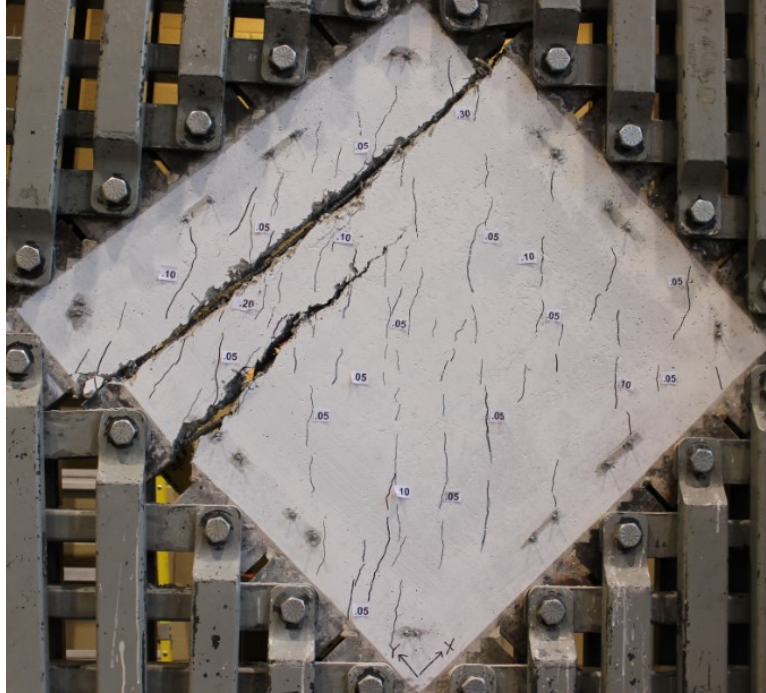
Figure 5-17: F1V3MS failure crack pattern

5.3.8 Panel F1V3RC

Panel F1V3RC was constructed of steel fibre reinforced concrete with 1.5% by volume of RC80/30BP fibres (l_f = 30 mm, d_f = 0.38 mm, f_{uf} = 2300 MPa). The panel was the reversed cyclically loaded companion panel of the F1V3 pair. The longitudinal reinforcement ratio was 3.31% with no transverse reinforcement provided. The 28-day compressive strength was 48.9 MPa and the uniaxial tensile strength was 3.89 MPa; the test day compressive strength was 50.9 MPa. The double cycle peak shear stresses were 1.1 MPa, 2.1 MPa, 2.6 MPa, 3.1 MPa, 3.7 MPa, 4.2 MPa, and 4.7 MPa.
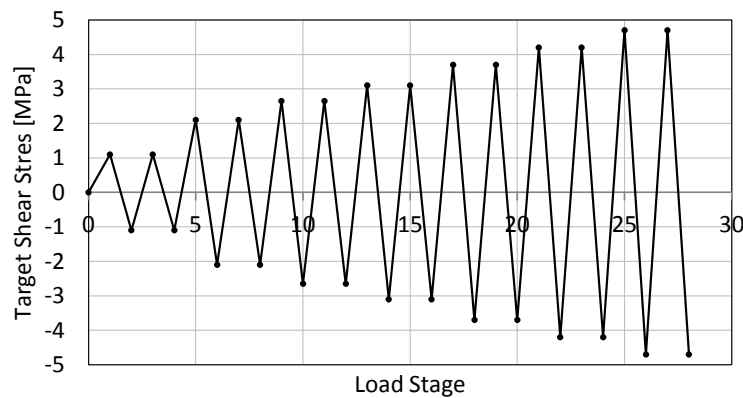
Figure 5-18: F1V3RC loading protocol

Similar to panel F1V3MS, the first crack occurred at a shear stress and shear strain of 2.00 MPa and 0.19×10^{-3}, respectively. The panel experienced gradual softening thereafter and failed at a shear stress of 4.68 MPa with a shear strain of 4.35×10^{-3}. The previously attained ultimate shear stress for F1V3RC was 4.72 MPa with a corresponding shear strain of 3.72×10^{-3}. The failure was initiated by fibre pull-out followed by the breakdown of the aggregate interlock mechanism. Relative to the monotonically loaded companion panel, F1V3MS, the failure for F1V3RC was less brittle and the shear strain at failure, the maximum shear strain, was considerable higher. The non-ideal fibre distribution for the F1V3 specimens noted earlier seemed to have a significantly lower impact on the reversed cyclically loaded panel. This can be attributed to the higher fibre count for the F1V3RC panel (fibre count for F1V3RC was 18% higher than F1V3MS).

Figure 5-19 shows the full shear stress-shear strain responses of F1V3RC and F1V3MS. Relative to the other reversed cyclically loaded panel, F1V3RC experienced the lowest strength degradation, 4.3%. The shear strain corresponding to the maximum shear stress, the ultimate shear strain, was 9.4% higher than the monotonically loaded companion panel. Overall, the cyclic envelope curve was nearly identical to the monotonic backbone curve, with no stress degradation until the final loading cycle.

As shown in Figure 5-20, the failure crack was oriented parallel to the primary reinforcement. Immediately before failure, the surface cracks were reasonably well distributed in terms of the crack spacing. Except for cracks near the critical crack, the crack widths were generally small across the panel with a width of approximately 0.1 to 0.2 mm; the crack widths near the critical crack were approximately 0.4 to 0.6 mm wide immediately before failure. At the last load stage, the maximum crack width, the average crack width, and the average crack spacing were 0.70 mm, 0.25 mm, and 90.0 mm, respectively; the crack widths for this panel were larger than the crack widths for the monotonically loaded companion panel.

Figure 5-19: F1V3RC shear stress vs. shear strain response (F1V3MS included)
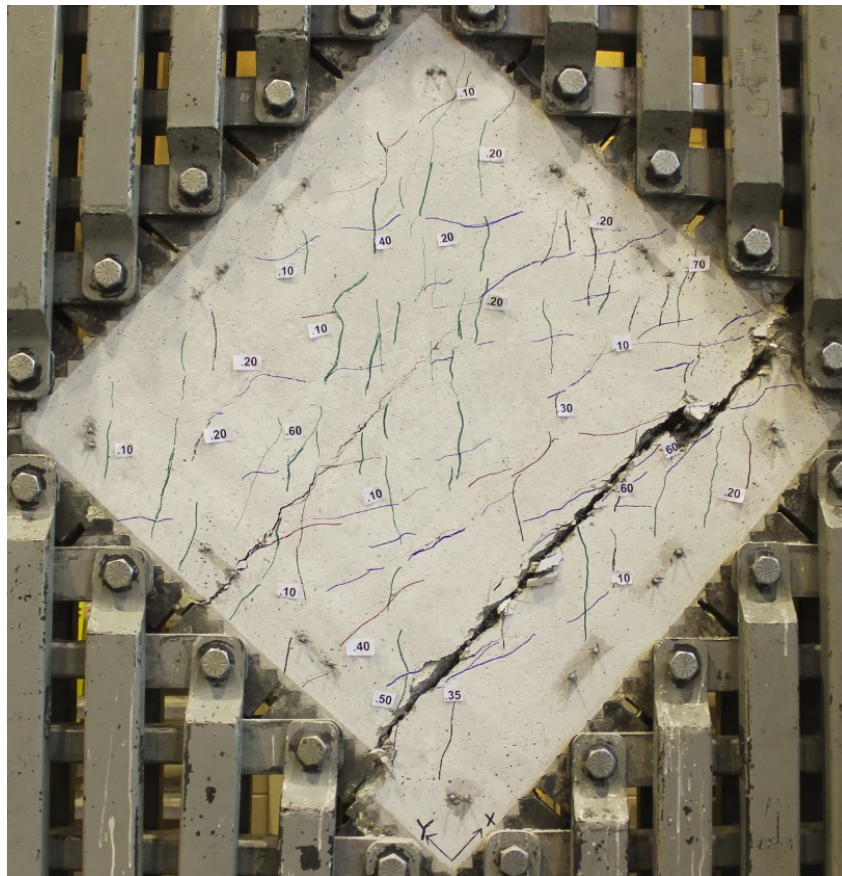
Figure 5-20: F1V3RC failure crack pattern

5.3.9 Panel F2V2MS

Panel F2V2MS was monotonically loaded and constructed of steel fibre reinforced concrete containing 1.0% by volume of ZP305 fibres (l_f = 30 mm, d_f = 0.55 mm, f_{uf} = 1300 MPa). As was the case with previously discussed SFRC panels, F2V2MS contained 3.31% longitudinal reinforcement with no transverse reinforcement provided. The 28-day compressive strength was 50.1 MPa and the uniaxial tensile strength was 3.32 MPa; the test day compressive strength was 52.1 MPa.

This panel was the first of those tested at the University of Toronto using low aspect ratio fibres (AR_f = 55). The panel with the lowest fibre aspect ratio previously tested was Susetyo et al.'s (2011) C1F3V3 panel, which used Dramix RC65/35BN fibres (l_f = 35 mm, d_f = 0.55 mm, f_{uf} = 1100 MPa) and had a fibre aspect ratio of 64. The purpose of the F2V2 pair of panels was to assess the influence of fibre aspect ratio on the behaviour of SFRC members; the impact of low aspect ratio fibres was of particular interest. The F2V2 pair contained the same volume of fibre as pair F1V2. Although the ZP305 fibres had a lower fibre tensile strength than the RC30/80BP fibres previously used, the failure of the panels was initiated by fibre pull-out and the behaviour was deemed not affected by the relatively high fibre tensile strength.

Figure 5-21 shows the panel's full shear stress-shear strain response. The first crack occurred at a shear stress of 1.79 MPa with a shear strain of 0.211×10^{-3}. At failure, the ultimate shear stress was 3.96 MPa and the corresponding shear strain was 4.16×10^{-3}. The failure was caused by the breakdown of the aggregate interlock mechanism. Both the primary reinforcement stress and principal compressive stress were well below their ultimate strength.

As shown in Figure 5-22, the cracks at failure were well distributed across the face of the panel. The failure crack was parallel to the primary reinforcement. At the last load stage, which was taken at a shear stress of 3.80 MPa, the maximum crack width, the average crack width, and the average crack spacing were 0.80 mm, 0.25 mm, and 74 mm, respectively. Consistent with the material test findings, this panel did not achieve the same level of crack control as F1V2MS (1.0% RC80/30BP), but was better than F1V1MS (0.5% RC80/30BP).
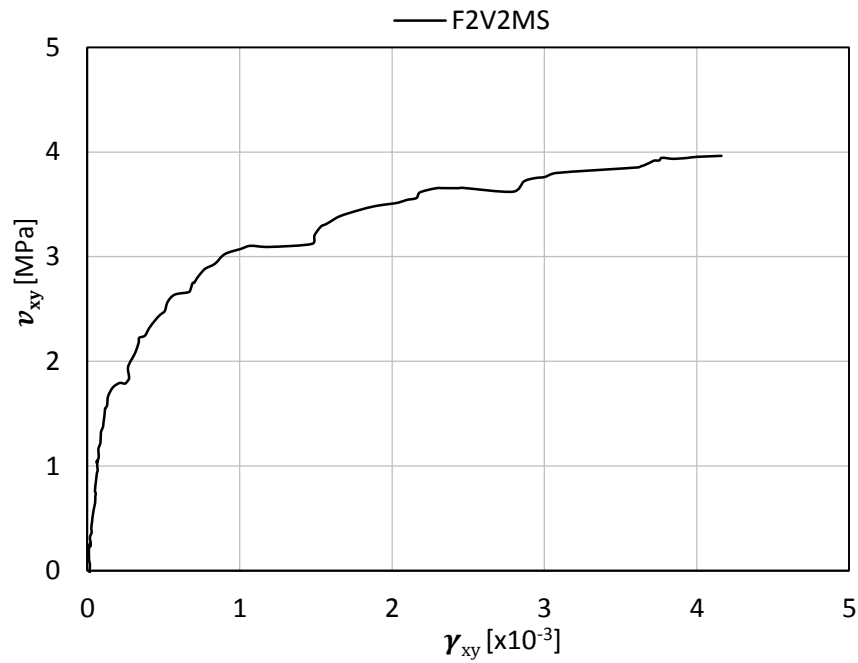
Figure 5-21: F2V2MS shear stress vs. shear strain response
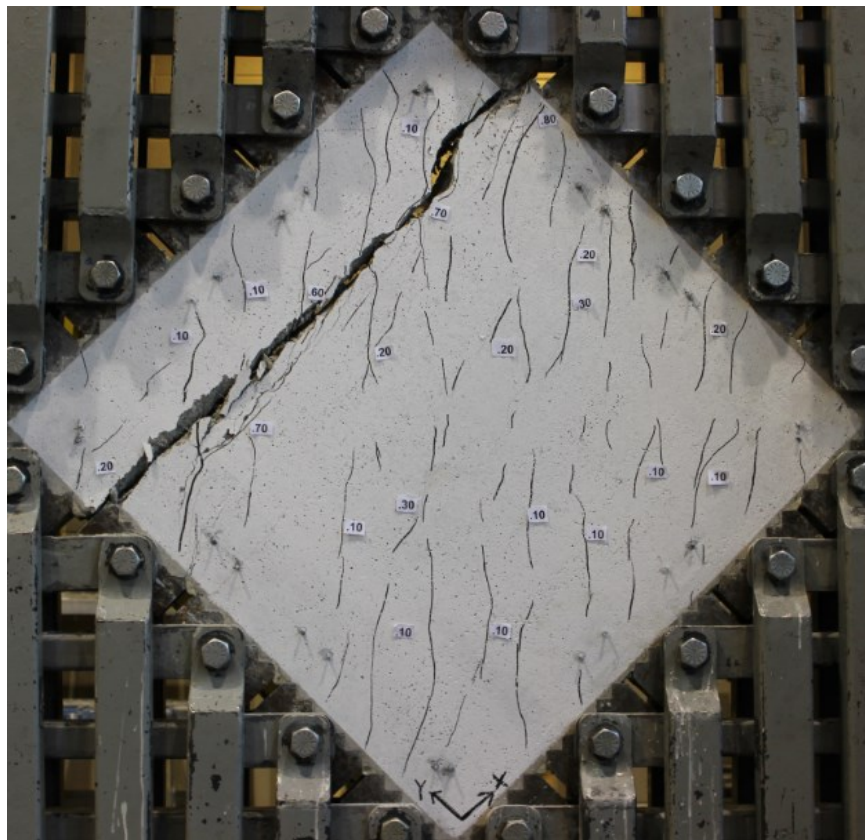
Figure 5-22: F2V2MS failure crack pattern

5.3.10 Panel F2V2RC

Panel F2V2RC was constructed of steel fibre reinforced concrete with 1.0% by volume of ZP305 fibres (l_f = 30 mm, d_f = 0.55 mm, f_{uf} = 1300 MPa). The panel was the reversed cyclically loaded companion panel of the F2V2 pair. As was the case with previously discussed SFRC panels, F2V2RC contained 3.31% longitudinal reinforcement with no transverse reinforcement. The 28-day compressive strength was 50.1 MPa and the uniaxial tensile strength was 3.32 MPa; the test day compressive strength was 52.9 MPa. As shown in Figure 5-23, the double cycle peak shear stresses were 1.1 MPa, 2.1 MPa, 2.6 MPa, 3.1 MPa, and 3.5 MPa.
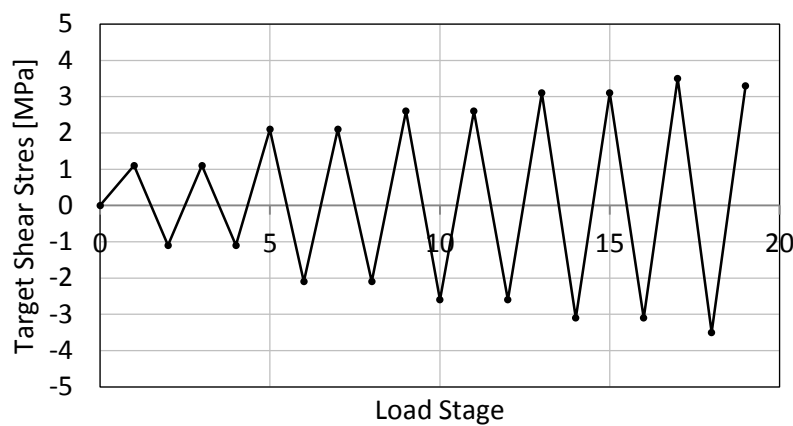
Figure 5-23: F2V2RC loading protocol

Similar to panel F2V2MS, F2V2RC experienced its first crack at a shear stress and shear strain of 1.82 MPa and 0.15×10^{-3}, respectively. Gradual softening appeared thereafter and failure occurred at a shear stress and shear strain of 3.30 MPa and 4.53×10^{-3}, respectively. The previously attained ultimate shear stress was 3.47 MPa and the corresponding shear strain was 2.75×10^{-3}. The failure was caused by the breakdown of the aggregate interlock mechanism.

The full shear stress-shear strain responses of F2V2RC and F2V2MS are shown in Figure 5-24. F2V2RC experienced a strength degradation of 12.4%, the largest of any panels. As well, the ultimate shear strain reduced by 34% relative to the monotonically loaded companion panel. The cyclic envelope curve was similar to the monotonic backbone curve with strength degradation occurring after a shear stress of 3.10 MPa. Prior to the strength degradation, the cyclic response achieved higher shear stresses than the monotonic response. This unexpected behaviour was presumably attributed to the out-of-plane bending for the two panels; the bending diminished near a shear stress of 3.0 MPa for both panels.
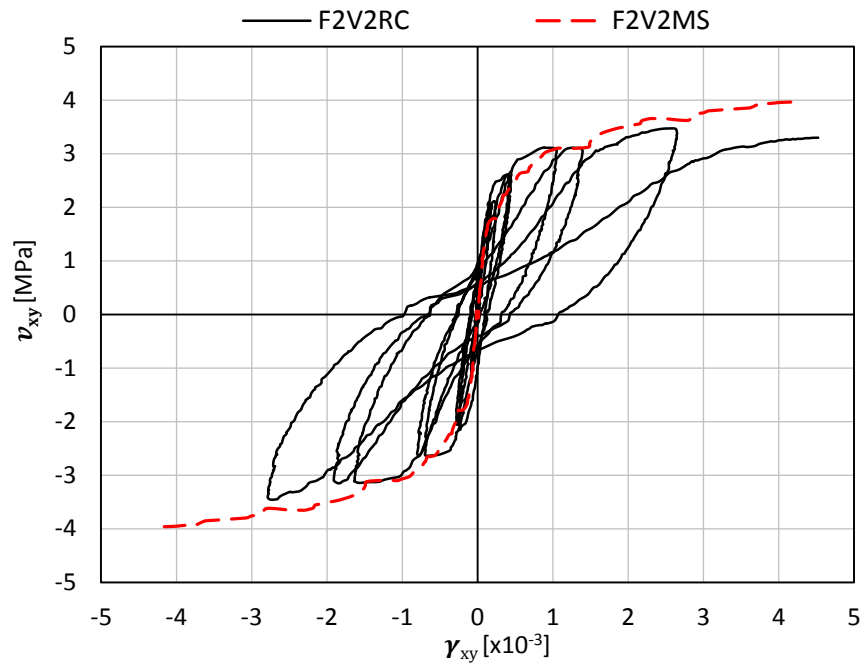
Figure 5-24: F2V2RC shear stress vs. shear strain response (F2V2MS included)
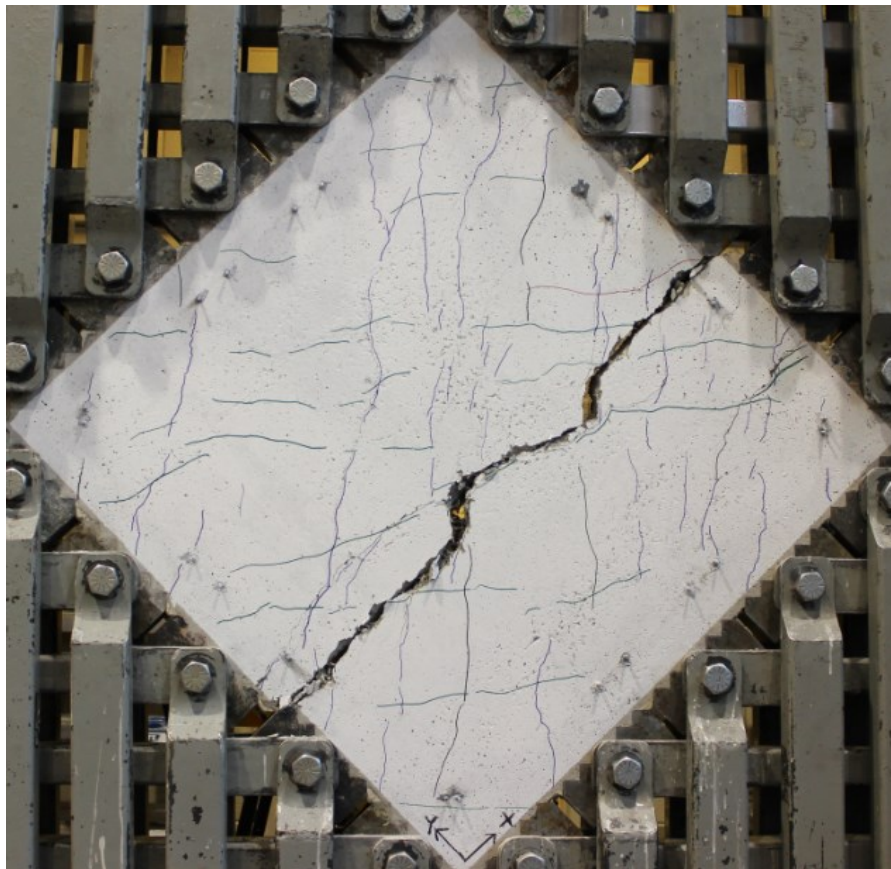
Figure 5-25: F2V2RC failure crack pattern

As shown in Figure 5-25, the cracks at failure were well distributed across the face of the panel. Like the majority of the panels, the failure crack was parallel to the primary reinforcement. At the last load stage, the maximum crack width, the average crack width, and the average crack spacing were 1.20 mm, 0.33 mm, and 115 mm, respectively. The crack widths for this panel were larger than those of the monotonic companion panel, consistent with the other pairs of panels.

5.4   Comparisons of Panel Response

This section discusses the structural response of the panels. The influence of fibre volume fraction, fibre aspect ratio, and loading protocol will be the emphasis of the discussions. The analyses and conclusions are based on the shear stress-shear strain response, principal tensile stress-principal tensile strain response, principal compressive stress-principal compressive strain response, inclination of the crack angles, crack control characteristics, and failure modes. A brief comparison against similar panels that were previously tested is also provided to confirm that the panels in this work produced consistent results.

5.4.1 Comparison with Previous Panel Tests

This section provides a comparison between panels in this work and similar panels that were previously tested at the University of Toronto. The purpose of this comparison was to ensure that the panels in this work have reasonable results and to identify any potential errors. Due to the differences in the materials used, testing procedure, and installation procedure, only panel tests performed in this work are included in the discussions following this section.

Table 5-4: Summary of results from previously performed panel tests (Carnovale, 2013; Susetyo, 2009)

Test ID	V_f [%]	AR_f	$f_{c,test}$ [MPa]	v_{cr} [MPa]	v_u [MPa]	γ_u [x10^{-3}]	γ_{max} [x10^{-3}]	s_m [mm]	w_m [mm]	$w_{cr,max}$ [mm]
CMS	-	-	45.2	2.06	5.99	8.58	8.58	72.1	0.20	0.50
C1C	-	-	65.7	2.01	5.77	6.01	6.01	57.2	0.34	0.55
CRC	-	-	45.5	1.37	5.63	9.77	9.87	70.0	0.39	1.40
DCP1	-	-	71.7	1.43	5.79	7.20	7.98	55.6	0.57	1.10
F1V2MS	1.0	79	58.1	1.81	4.65	4.96	4.96	54.8	0.18	0.65
DCP2	1.0	79	62.1	2.60	5.97	5.94	5.94	43.0	0.21	0.65
F1V2RC	1.0	79	58.1	3.10	4.41	4.60	4.60	81.4	0.21	0.75
DCP4	1.0	79	66.0	2.60	4.47	2.87	2.87	71.0	0.22	0.65

Carnovale (2013) tested two reversed cyclically loaded panels, DCP1 and DCP4, and one monotonically loaded panel, DCP2, identical to the ones in this work (CRC as DCP1, F1V2MS as DCP2, and F1V2RC as DCP4). As well, one monotonically loaded panel from Susetyo's (2009) experiment, C1C, was similar to the one in this work (CMS as C1C). A summary of these four pairs of panel tests are shown in Table 5-4. All panels were subjected to pure shear.

Both CMS and C1C were the monotonically loaded control panels and exhibited similar responses (see Figure 5-26). Both panels had 3.31% reinforcement in the x-direction and 0.42% reinforcement in the y-direction. The primary differences between the two panels were the transverse reinforcement's ultimate strength (639 MPa for CMS and 549 MPa for C1C) and the compressive strength (45.2 MPa for CMS and 65.7 MPa for C1C). Since the concrete's post-cracked residual strength, tension stiffening, is a function of the concrete's compressive strength, C1C's higher post-cracked shear stresses were expected. CMS, however, reached a higher ultimate shear strength because the failure was controlled by rupturing of the transverse reinforcement. The higher ultimate strength of C1C's transverse reinforcement delayed the bar rupturing failure.

CRC and DCP1 were the reversed cyclically loaded control panels. As shown in Figure 5-27, the overall response between these two panels was largely similar. Both panels had the same reinforcement layout in the x- and y-direction and similar reinforcement properties. The primary difference was the concrete compressive strength; DCP1's compressive strength was 71.7 MPa while CRC's compressive strength was 45.5 MPa. The higher compressive strength of DCP1 would result in greater tension stiffening effects for the panel and higher post-cracked shear stresses; this was evident in the higher cyclic envelope curve for DCP1. The failure mode was controlled by the rupturing of the transverse reinforcement. Since the ultimate strengths of the transverse reinforcement were similar between the two panels (639 MPa for CMS and 624 MPa for C1C), the ultimate shear strength was similar as well. Note that the panel analyses performed in this work used the new effective hydraulic jack cross-sectional area discussed in Section 3.8.1.2; the new effective area was approximately 4.0% smaller than the values previously used (Susetyo, 2009; Carnovale, 2013) which would result in shear stresses that were approximately 4.0% smaller. Relative to CRC, the ultimate shear strain corresponding to the ultimate shear stress was 26% smaller for DCP1. This is largely attributed to the premature failure of DCP1; the failure of DCP1 was caused by the separation of one of the shear keys from the panel with no distinct failure plane developing through the panel.
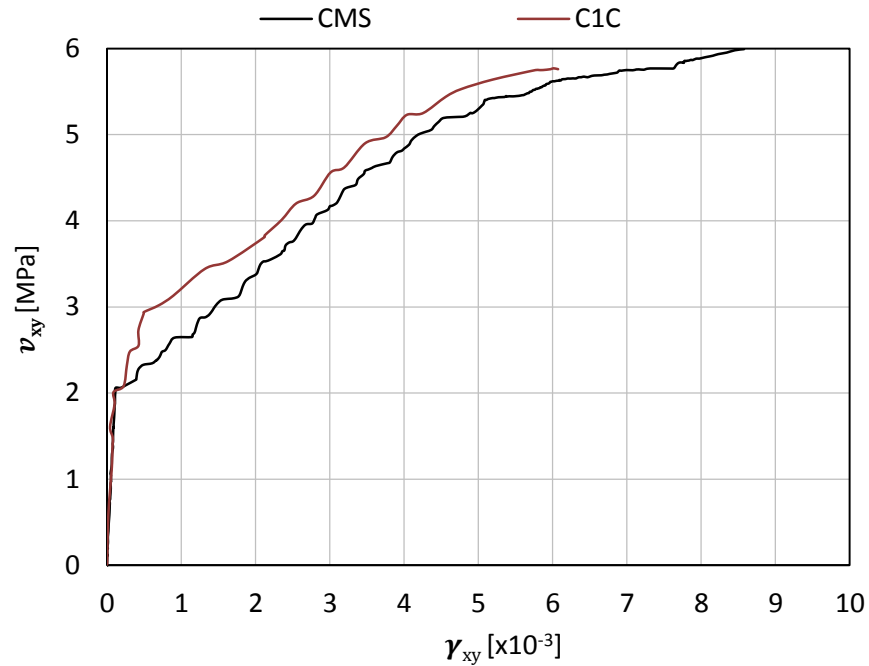
Figure 5-26: CMS vs. C1C shear stress-shear strain response
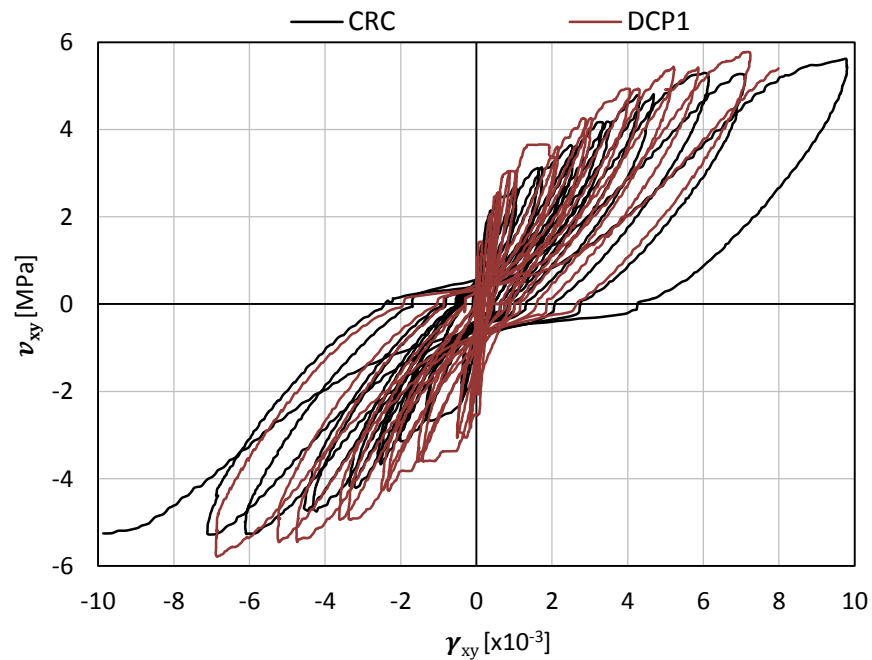
Figure 5-27: CRC vs. DCP1 shear stress-shear strain response

F1V2MS and DCP2 were two panels largely identical. Both panels had 3.31% reinforcement in the primary direction and used SFRC containing 1.0% RC80/30BP fibres (l_f = 30 mm, d_f = 0.38 mm, f_{uf} = 2300 MPa). The reinforcement properties and the compressive strength were similar as well; the compressive strength for F1V2MS was 6.4% lower and the modulus of elasticity for the primary

reinforcement was 4.1% lower than DCP2. Although similar responses between the two panels were expected, DCP2's ultimate shear stress was 28% higher (see Figure 5-28). This is believed to be attributed to the different mechanical properties of the concrete as a result of the separately made panels. For example, the ultimate uniaxial tensile stress attained after first-cracking (f_{tu}) was 3.12 MPa for F1V2MS, but was 3.52 MPa for DCP2. Since the behaviour of the panel was largely controlled by the complex mechanism of aggregate interlock and the bridging of cracks from randomly oriented fibres, the discrepancy in the behaviour as a result of the separately made concrete was deemed reasonable.

F1V2RC and DCP4 were the reversed cyclically loaded companion panels for the F1V2MS and DCP2 panel discussed earlier. Like their monotonic counterpart, F1V2RC and DCP4 had 3.31% reinforcement in the primary direction and were constructed with SFRC containing 1.0% RC80/30BP fibres. As shown in Figure 5-29, up to a shear strain of 2.3×10^{-3}, the response between these two panels was much more identical than their monotonic counterparts. The peak cycle stress, loading branch, unloading branch, and plastic offset were similar between the two panels. However, DCP4 failed much earlier and reached an ultimate shear strain that was 38% smaller than that of F1V2RC. The testing of DCP4 was interrupted due to a hydraulic cylinder failure which temporary applied a non-pure-shear loading condition to the specimen. The test was immediately stopped and was resumed after a one week long repair. It is believed that the response of DCP4 was compromised as a result of the incident which led to its early failure.
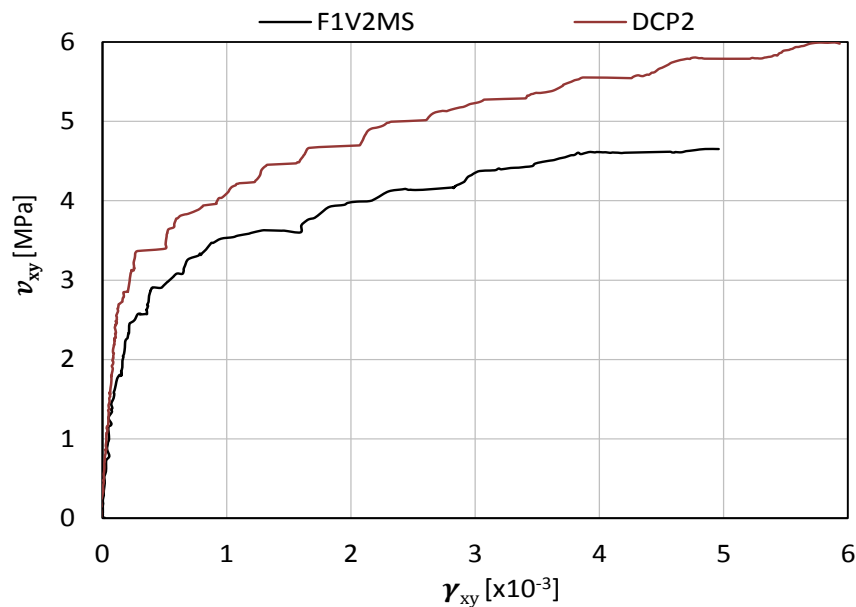
Figure 5-28: F1V2MS vs. DCP2 shear stress-shear strain response
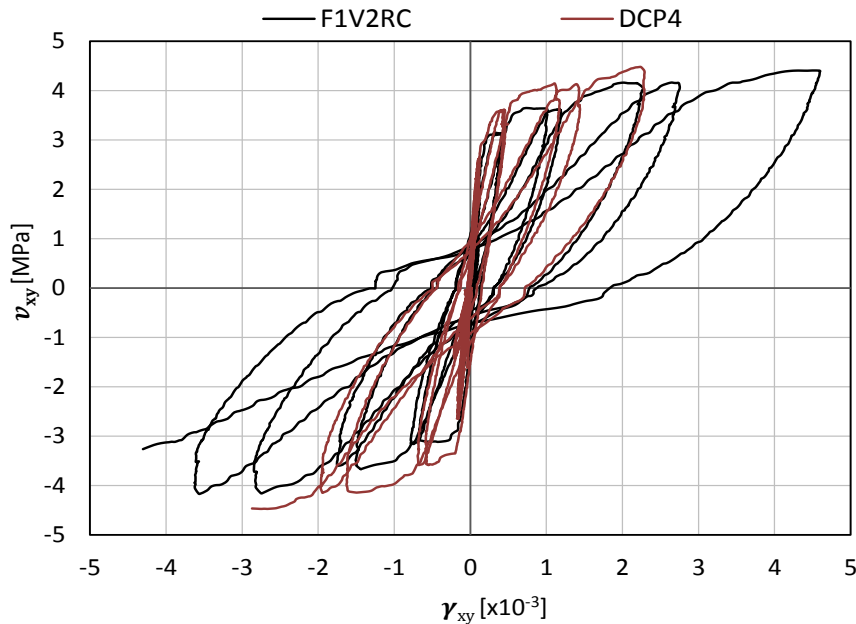
Figure 5-29: F1V2RC vs. DCP4 shear stress-shear strain response

5.4.2 Shear Resistance and Ductility

5.4.2.1   Influence of Fibre Type and Fibre Content

A summary of the detailed results for panels tested in this work is given in Table 5-5. The first table shows the test day compressive strength ($f_{c,test}$), the ultimate shear stress attained (v_u), the corresponding ultimate shear strain (γ_u), the maximum shear strain attained (γ_{max}), the average crack spacing (s_m), the average crack width (w_m), and the maximum crack spacing ($w_{cr,max}$). The second table presents the cracking shear stress (v_{cr}), the corresponding cracking shear strain (γ_{cr}), the cracking principal tensile stress ($f_{c1,cr}$), the maximum principal tensile stress attained during the test ($f_{c1,max}$), the principal tensile stress at failure ($f_{c1,fail}$), the maximum principal compressive stress attained during the test ($f_{c2,max}$), the maximum primary reinforcement stress ($f_{sx,max}$), and the maximum transverse reinforcement stress ($f_{sy,max}$).

All SFRC panels performed reasonably well in terms of the maximum shear stress. They managed to withstand at least 56% of the maximum shear stresses that were sustained by the control panels. Panel F1V3MS and F1V3RC withstood 82% and 84% of their respective control panel's maximum shear stresses. As indicated by the monotonic backbone curves and the cyclic envelope curves in Figure 5-30, it was evident that concrete with higher fibre volume fractions sustained higher shear stresses. The two panels from the F2V2 series contained low aspect ratio fibres which resulted in fewer numbers of fibres for the same fibre volume fraction; concrete with 1.0% ZP305 yielded

approximately the same number of fibres as concrete with 0.5% RC80/30BP. Since the performance of SFRC members is strongly linked to the number of fibres bridging the crack, the F2V2 panels (1.0% ZP305) expectedly reached shear stresses lower than that of the F1V2 panels (1.0% RC80/30BP), but higher than that of the F1V1 panels (0.5% RC80/30BP). The trend in terms of the maximum shear stress attained for the reversed cyclically loaded panels was consistent with that of the monotonically loaded panels.

Table 5-5: Panel test detailed results

Test ID	V_f [%]	AR_f	Loading	$f_{c,test}$ [MPa]	v_u [MPa]	γ_u [x10⁻³]	γ_{max} [x10⁻³]	s_m [mm]	w_m [mm]	$w_{cr,max}$ [mm]
CMS	-	-	Mono.	45.2	5.99	8.58	8.58	72.1	0.20	0.50
CRC	-	-	Cyclic	45.5	5.63	9.77	9.87	70.0	0.39	1.40
F1V1MS	0.5	79	Mono.	55.9	3.34	4.07	4.07	148.8	0.19	0.35
F1V1RC	0.5	79	Cyclic	56.1	3.13	4.51	4.51	126.0	0.34	1.30
F1V2MS	1.0	79	Mono.	58.1	4.65	4.96	4.96	54.8	0.18	0.65
F1V2RC	1.0	79	Cyclic	58.1	4.41	4.60	4.60	81.4	0.21	0.75
F1V3MS	1.5	79	Mono.	50.9	4.93	3.40	3.40	96.9	0.12	0.50
F1V3RC	1.5	79	Cyclic	53.1	4.72	3.72	4.35	90.0	0.25	0.70
F2V2MS	1.0	55	Mono.	52.1	3.96	4.16	4.16	74.0	0.25	0.80
F2V2RC	1.0	55	Cyclic	52.9	3.47	2.75	4.53	115.0	0.33	1.20

Test ID	v_{cr} [MPa]	γ_{cr} [x10⁻³]	$f_{c1,cr}$ [MPa]	$f_{c1,max}$ [MPa]	$f_{c1,fail}$ [MPa]	$f_{c2,max}$ [MPa]	$f_{sx,max}$ [MPa]	$f_{sy,max}$ [MPa]	Failure
CMS	2.06	0.183	1.99	1.99	1.04	-12.54	270	622	y-reinf. yield
CRC	1.37	0.158	1.38	2.04	-0.11	-13.48	330	633	y-reinf. yield
F1V1MS	2.18	0.147	2.16	2.52	1.54	-7.16	170	-	interlock fail
F1V1RC	1.27	0.160	1.29	2.65	1.03	-7.48	195	-	interlock fail
F1V2MS	1.81	0.138	1.80	3.16	2.29	-9.55	220	-	interlock fail
F1V2RC	3.10	0.256	3.12	3.18	1.67	-8.50	188	-	interlock fail
F1V3MS	2.34	0.141	2.33	3.37	3.15	-7.71	138	-	interlock fail
F1V3RC	2.00	0.190	1.97	3.06	2.59	-8.47	178	-	interlock fail
F2V2MS	1.79	0.211	1.80	2.77	2.20	-7.14	149	-	interlock fail
F2V2RC	1.82	0.146	1.80	2.41	1.59	-7.03	163	-	interlock fail

(a) Monotonic backbone curve (b) Cyclic envelope curve
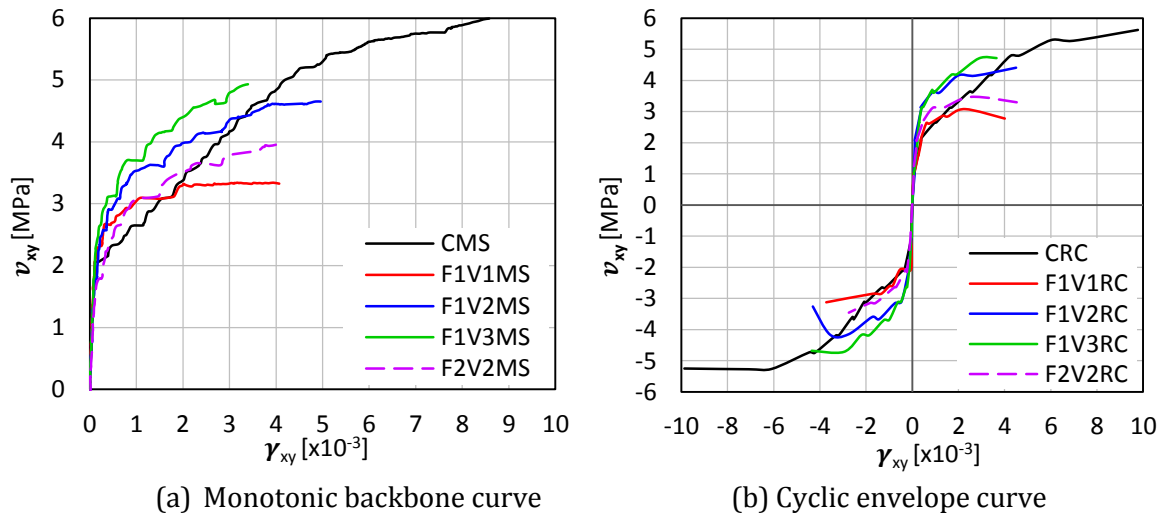
Figure 5-30: Comparison of shear stress-shear strain backbone response

All SFRC panels, except for panel F1V3MS, sustained a maximum shear deformation of at least 44% of that of the control panels. Due to the non-ideal fibre distribution of the F1V3 series noted earlier, panel F1V3MS only sustained 40% of the maximum shear deformation withstood by that of the control panel. The shear deformation capacity of all SFRC panels was similar with little discernible trends; for the SFRC panels, the average ultimate shear strain was 4.02×10^{-3} and the average maximum shear strain was 4.32×10^{-3}. However, if one accounted for the likely reduced deformation capacity of the F1V3 series due to its non-ideal fibre distribution, then it appeared that concrete with lower fibre volume fraction or lower aspect ratio fibre had lower shear deformation capacity. The control panels exhibited exceptionally high shear strains due to the transverse reinforcement's significant post-yielding deformation capacity.

As described above, in regard to the maximum shear stress or shear deformation capacity, it was clear that the fibres used in this work cannot replace 0.42% transverse reinforcement. However, the performance of the SFRC panels was still remarkable considering the absence of transverse reinforcement. It was also noted that 0.5% fibre content without transverse reinforcement cannot provide adequate shear resistance.

5.4.2.2 Influence of Loading Protocol

The complete shear stress-shear strain responses for the five pairs of panel tests performed are shown in Figure 5-31. The normal concrete panel, CRC, experienced minor stress degradation; the ultimate shear stress attained was reduced by 6.0% compared to its monotonic counterpart. However, the ultimate shear strain for CRC increased by 13.9% while the maximum shear strain

increased by 15.0%. The strength degradation was expected due to the cycling of load. The primary causes of the strength degradation were the deterioration of the concrete at the crack which led to the breakdown of the aggregate interlock mechanism and the bond deterioration between the concrete and the steel reinforcement. As discussed in the later sections, it is believed that the larger crack widths as a result of the cycling of load led to the larger ultimate shear strains. Note that the panel tests were load controlled which caused rapid changes in the shear deformations near failure.

The SFRC panels exhibited minor strength degradations relative to the control panels. Evident by the comparison between the monotonic backbone curve and the cyclic envelope curve (see Figure 5-31), concrete with lower fibre contents experienced higher strength degradation. Concrete containing 0.5%, 1.0%, and 1.5% of RC80/30BP fibres exhibited 6.3%, 5.2%, and 4.3% strength degradation, respectively. More importantly, for the panel with 0.5% fibre content, stress degradation occurred shortly after cracking and the cyclic envelope curve constantly lagged behind the monotonic backbone curve. On the other hand, the panel with 1.5% fibre content experienced nearly zero stress degradation until failure and the monotonic backbone curve was almost identical to the cyclic envelope curve. The panel with low aspect ratio fibres, F2V2RC, experienced the largest strength degradation, 12.4%; however, the stress degradation occurred only near failure and improved resistance to cyclic damages compared to F1V1RC was demonstrated.

No strong discernible trends were observed for the ultimate shear strain as a result of the cycling of load. For example, compared to its monotonic counterpart, panel F2V2RC experienced a large 34% decrease in the ultimate shear strain but exhibited an 8.9% increase in its maximum shear strain. This indistinct trend regarding ultimate shear strain was expected as the failure of SFRC panels was initiated by fibre pull-out followed by the breakdown of the aggregate interlock mechanism. As a result, the failures were largely strain controlled and all panels failed under a similar level of shear deformation.

The above examination of the shear resistance and ductility indicated the ability of SFRC members to resist cyclic deterioration; all cyclically loaded SFRC members achieved similar force and deformation capacity compared to their monotonic counterparts. Further, SFRC members with higher fibre volume fractions demonstrated improved resistance to cyclic deterioration.
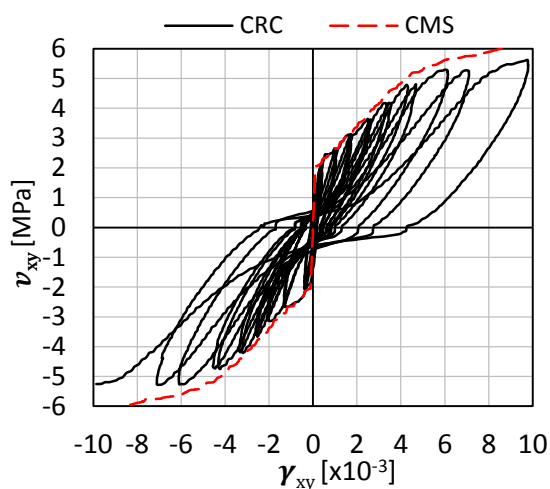
(a) Plain
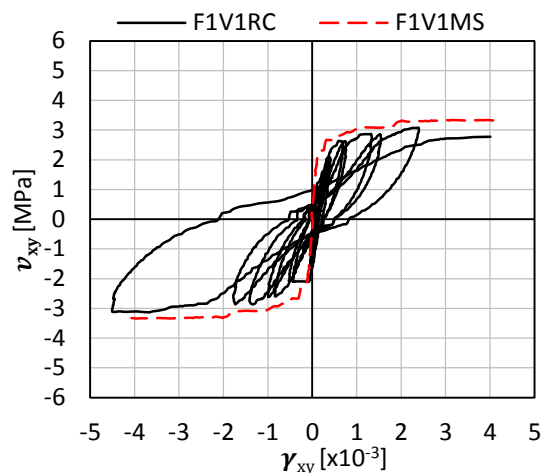
(b) 0.5% RC80/30BP
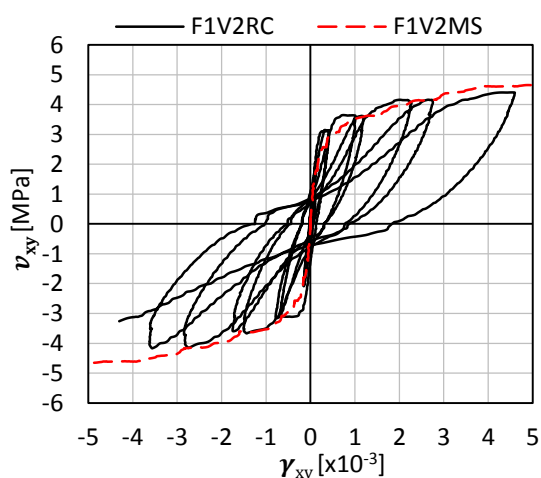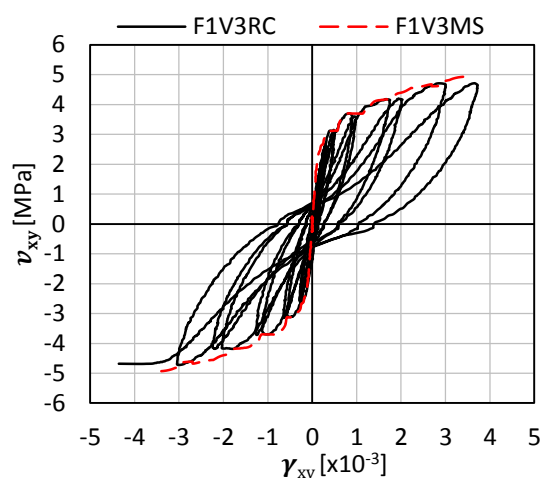
(c) 1.0% RC80/30BP

(d) 1.5% RC80/30BP
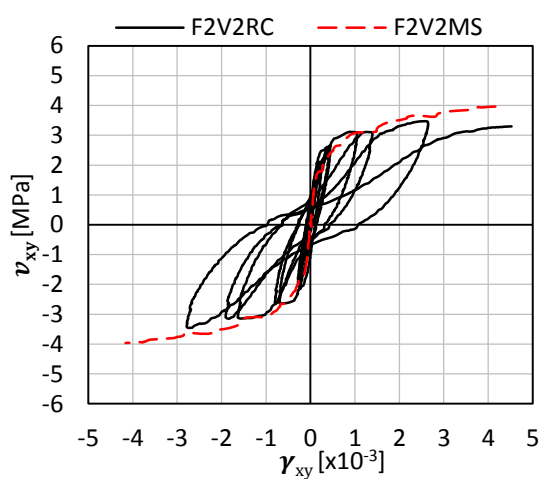
(e) 1.0% ZP305

Figure 5-31: Influence of loading protocol on shear stress-shear strain response

5.4.3 Principal Stress and Strain Response

5.4.3.1   *Influence of Fibre Type and Fibre Content*

The influence of fibre type and fibre content was further clarified by examining the principal tensile stress-principal tensile strain response of the panels. The principal tensile response of the monotonically loaded panels is shown in Figure 5-32 (a), while the envelope principal tensile response of the cyclically loaded panels is shown in Figure 5-32 (b). Note that for panel F1V1RC, the cyclic envelope response shown was based on the positive shear cycles only. This is because the principal tensile stresses for the negative shear cycles were erroneously high for F1V1RC (see Figure 5-34 (b)). During the test for F1V1RC, the horizontal cracks induced by negative shear were concentrated at the bottom half of the panel, below the two x-direction LVDTs. As a result, under negative shear, the x-direction LVDTs did not capture the opening of these horizontal cracks which erroneously caused a shift of the Mohr circle to the tension side, creating larger principal tensile stresses. In the positive shear direction, the vertical cracks were sufficiently well distributed and crossed the x-direction LVDTs; hence, the appropriate principal stresses were calculated and were used to construct the cyclic envelope curve.

For all panels, the principal tensile stress at first-cracking was consistent with the shear stress at first-cracking. The control panels exhibited strain softening immediately after cracking. Although the maximum principal tensile stress for CRC was 2.04 MPa while the principal tensile stress was 1.38 MPa when the first crack appeared, it is believed that this initial crack was premature and was caused by the out-of-plane bending. The panel response was linear until the maximum principal tensile stress was reached and therefore, it was assumed that no strain hardening behaviour was exhibited for CRC. For all SFRC panels, strain hardening behaviour after cracking and significantly post-cracking residual stresses were observed.

By increasing the fibre volume fraction, higher maximum principal tensile stress was usually attained and substantial improvements in the concrete tensile behaviour were observed. Although F1V3RC did not reach a maximum tensile stress higher than that of F1V2RC, the post-cracking residual stresses were significantly higher for F1V3RC. For the monotonically loaded panels, the post-cracking residual stress plateaued at a principal tensile strain of approximately 6.0×10^{-3}; due to the previously mentioned fibre distribution issues during mixing, F1V3MS only reached a maximum principal tensile strain of 3.63×10^{-3}. For the monotonically loaded panels with RC80/30BP fibres, the principal tensile stress plateau was approximately 1.5 MPa, 2.3 MPa, and 3.2

MPa with 0.5%, 1.0%, and 1.5% fibre addition, respectively. Relative to the 1.0 MPa stress plateau exhibited by the control panel, this represented a remarkable residual strength increase of 50%, 130%, and 220% for a fibre content of 0.5%, 1.0%, and 1.5%, respectively.

Consistent with the material test results, concrete with the low aspect ratio fibre did not perform as well as concrete with the high aspect ratio fibre. The residual tensile stress exhibited by concrete with 1.0% ZP305 (F2V2) was between that of concrete with 0.5% RC80/30BP (F1V1) and concrete with 1.0% RC80/30BP (F1V2).

The comparison of the principal compressive stress-principal compressive strain response of the monotonically loaded panels is shown in Figure 5-33. The compressive stress experienced by the panels was relatively small, well below the ultimate strength; hence, the degree of scattering was higher for the principal compressive response. However, the benefits of increased fibre addition were still observed. All of the panels experienced gradual shifts of the principal compressive strain toward the positive strain region at high compressive stresses, suggesting that significant crack slip and crack opening had occurred at the onset of failure. The control panel experienced a largely linear response in the principal compressive direction and the least strain shifting to the positive region. F1V1MS experienced the earliest strain shifting; further indicating that concrete with a fibre content of 0.5% will likely suffer significant fibre bond slip and cannot resist sufficient stresses at the crack.

5.4.3.2   Influence of Loading Protocol

The principal tensile response for the five pairs of panels is shown in Figure 5-34; the responses from the positive shear cycles and the negative shear cycles were separately displayed for the cyclically loaded panels. Overall, the response from the positive cycles was similar to that from the negative cycles, except for F1V1RC due to the non-uniform crack distribution mentioned earlier. All cyclically loaded panels reached a maximum principal tensile stress similar to that of their monotonic counterpart, and cyclic degradation in the principal response occurred thereafter. Consistent with the shear stress-shear strain response, the monotonic principal tensile curve was similar to the cyclic envelope principal tensile curve for each pair of panels. No discernible trends on the influence of fibre type and fibre content on the cyclic damage were observed.

The principal compressive response for all five pairs of panels is shown in Figure 5-35. During unloading of the cyclically loaded panels, the principal compressive strain gradually became positive due to crack slips and cracks remaining open. Since the concrete was insignificantly

stressed in the principal compressive direction, the influence of fibre addition on the cyclic damages was not apparent.

(a) Monotonic backbone curve

(b) Cyclic envelope curve
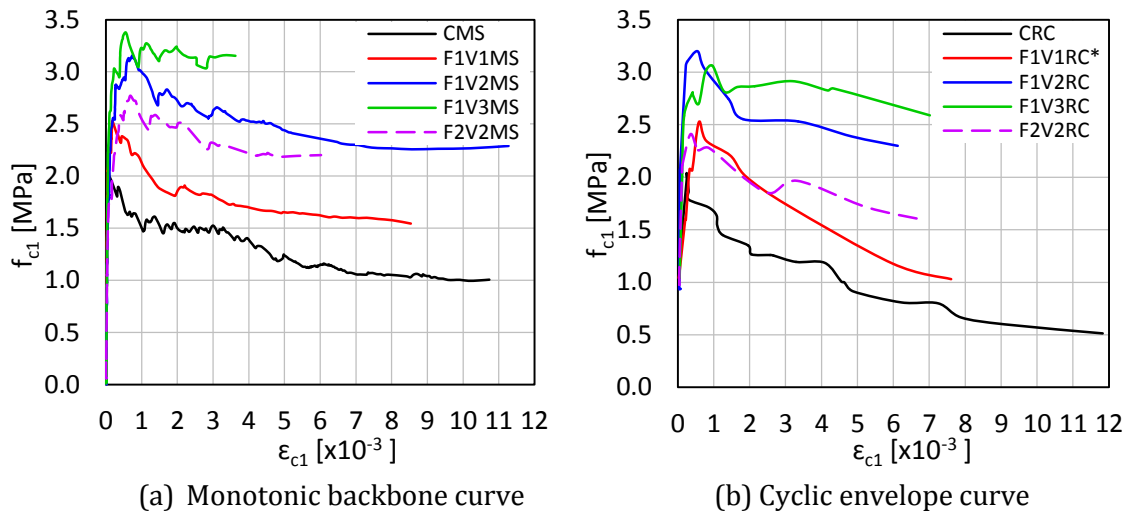
* F1V1RC envelope curve was based on positive shear cycles only

Figure 5-32: Comparison of principal tensile stress-principal tensile strain backbone response
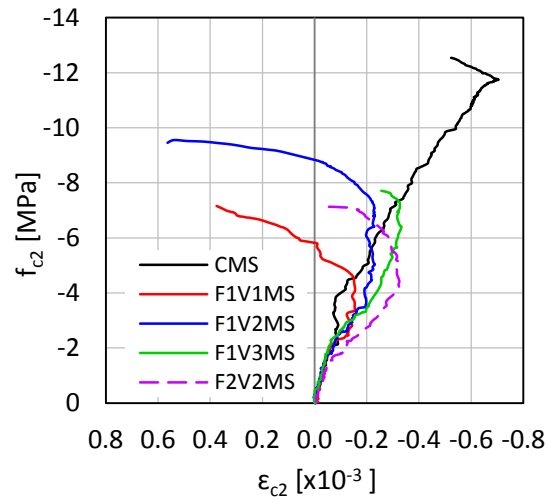
Figure 5-33: Comparison of principal compressive stress-principal compressive strain response for the monotonically loaded panels
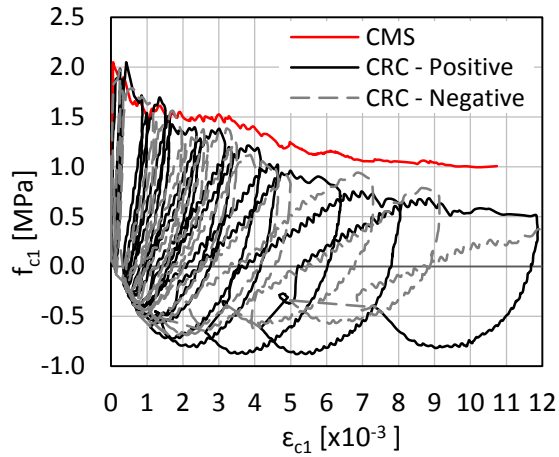
(a) Plain
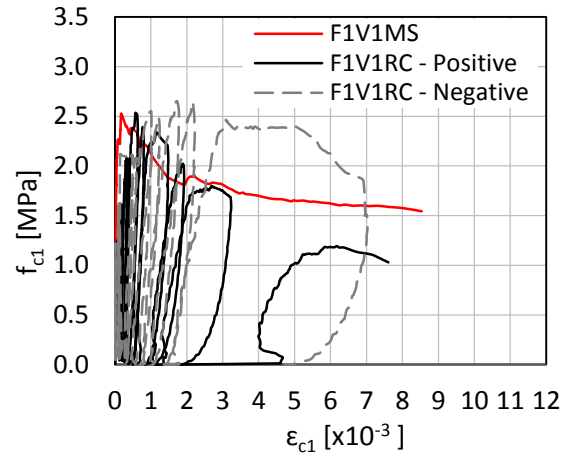
(b) 0.5% RC80/30BP
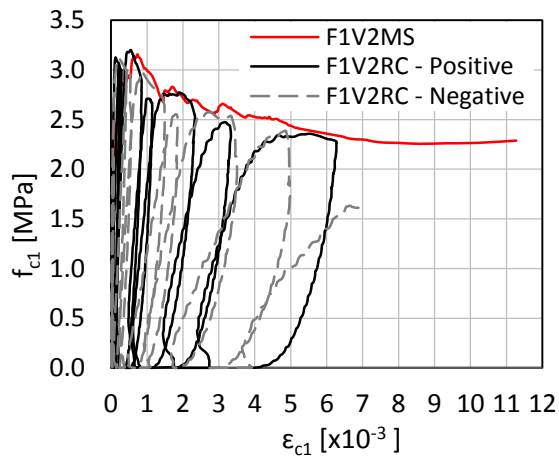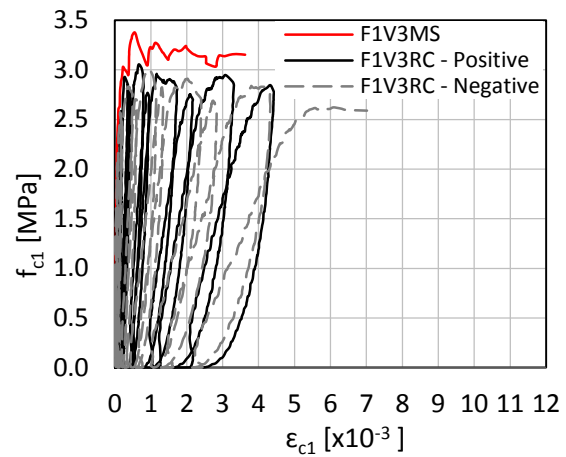
(c) 1.0% RC80/30BP
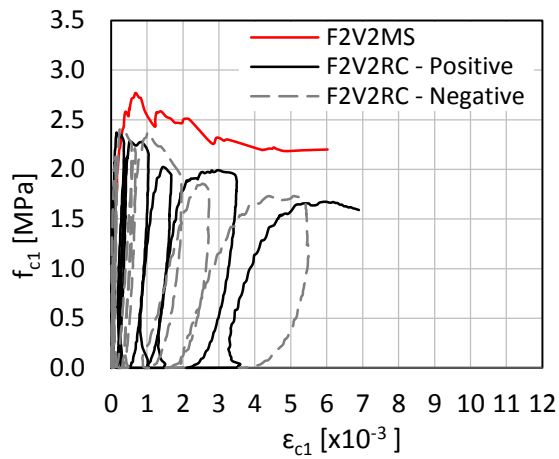
(d) 1.5% RC80/30BP

(e) 1.0% ZP305

Figure 5-34: Influence of loading protocol on principal tensile response
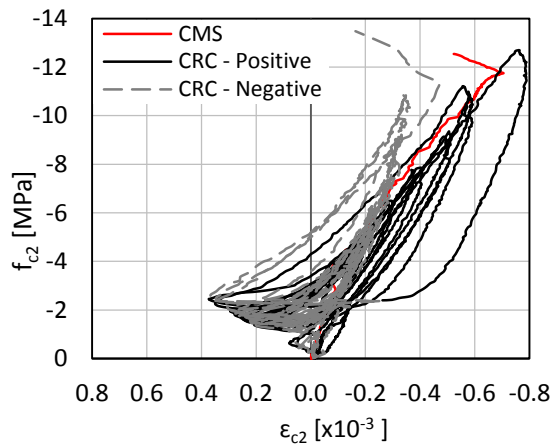
(a) Plain
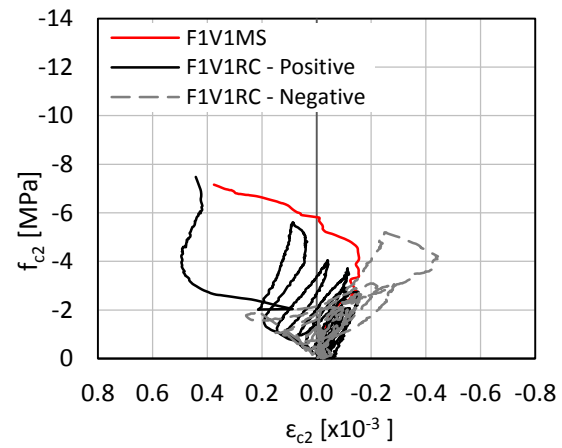
(b) 0.5% RC80/30BP
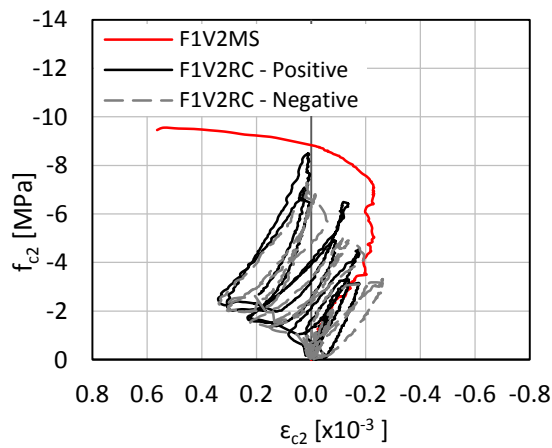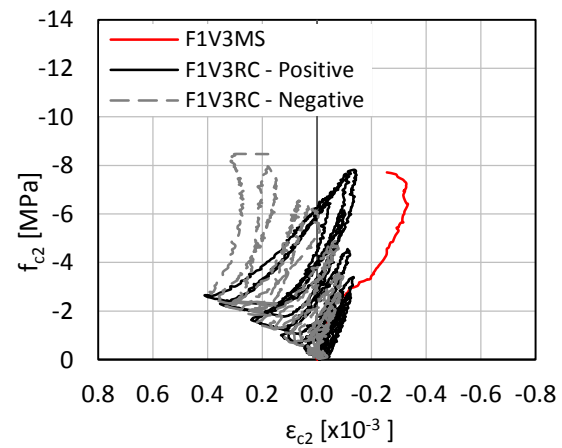
(c) 1.0% RC80/30BP

(d) 1.5% RC80/30BP
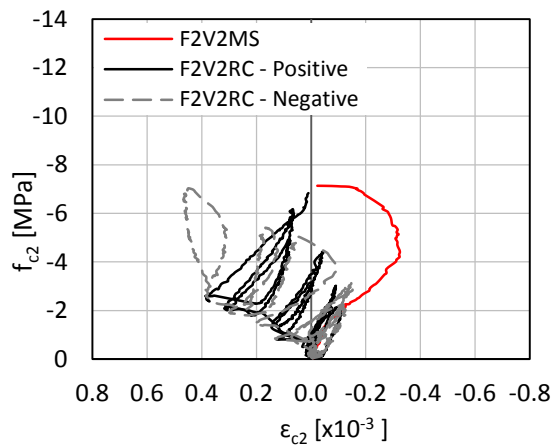
(e) 1.0% ZP305

Figure 5-35: Influence of loading protocol on principal compressive response

5.4.4 Crack Control Characteristics

5.4.4.1 *Influence of Fibre Type and Fibre Content*

One of the key benefits of SFRC is its ability to control crack propagation. Concrete by itself has no significant post-cracking strength and ductility. Discrete fibres from SFRC bridge the crack and reduce cracking and therefore, the post-cracking behaviour of the concrete is significantly improved.

The average crack width, maximum crack width, and the average crack spacing for the monotonically loaded panels and the reversed cyclically loaded panels are shown in Figure 5-36 (a) and Figure 5-36 (b), respectively. For simplicity, only the crack control parameters under positive shear are shown for the reversed cyclically loaded panels; the cyclic crack control characteristics were comparable between positive shear and negative shear (see Figure 5-37). Overall, the influence of fibre type and fibre content on the crack control characteristics of SFRC was similar between the monotonically loaded panels and the reversed cyclically loaded panels. Under higher fibre contents, smaller crack widths were developed and hence, the integrity of the cracked panel was maintained and higher shear stresses were reached. A comparison between panels from the F2V2 series (1.0% ZP305) and the F1V2 series (1.0% F1V2RC) revealed that fibres with lower aspect ratios developed larger crack widths under the same shear stress. Consistent with the findings from the material test results and the shear resistance analysis, the crack control ability of 1.0% ZP305 was between 1.0% RC80/30BP and 0.5% RC80/30BP.

For the RC80/30BP fibres, a fibre addition of 1.0% allowed the concrete to exhibit comparable or slightly improved crack control capabilities under the same shear stress compared to the control panels. With a fibre content of 1.5%, the concrete exhibited noticeably smaller crack widths compared to the control panel. This was remarkable considering the absence of transverse reinforcement in the SFRC panels. The smaller crack widths allowed greater stress to be transmitted across the crack and therefore, a higher shear stress was reached under the same shear strain.

(a) Monotonically loaded

(b) Reversed cyclically loaded
(positive shear only)
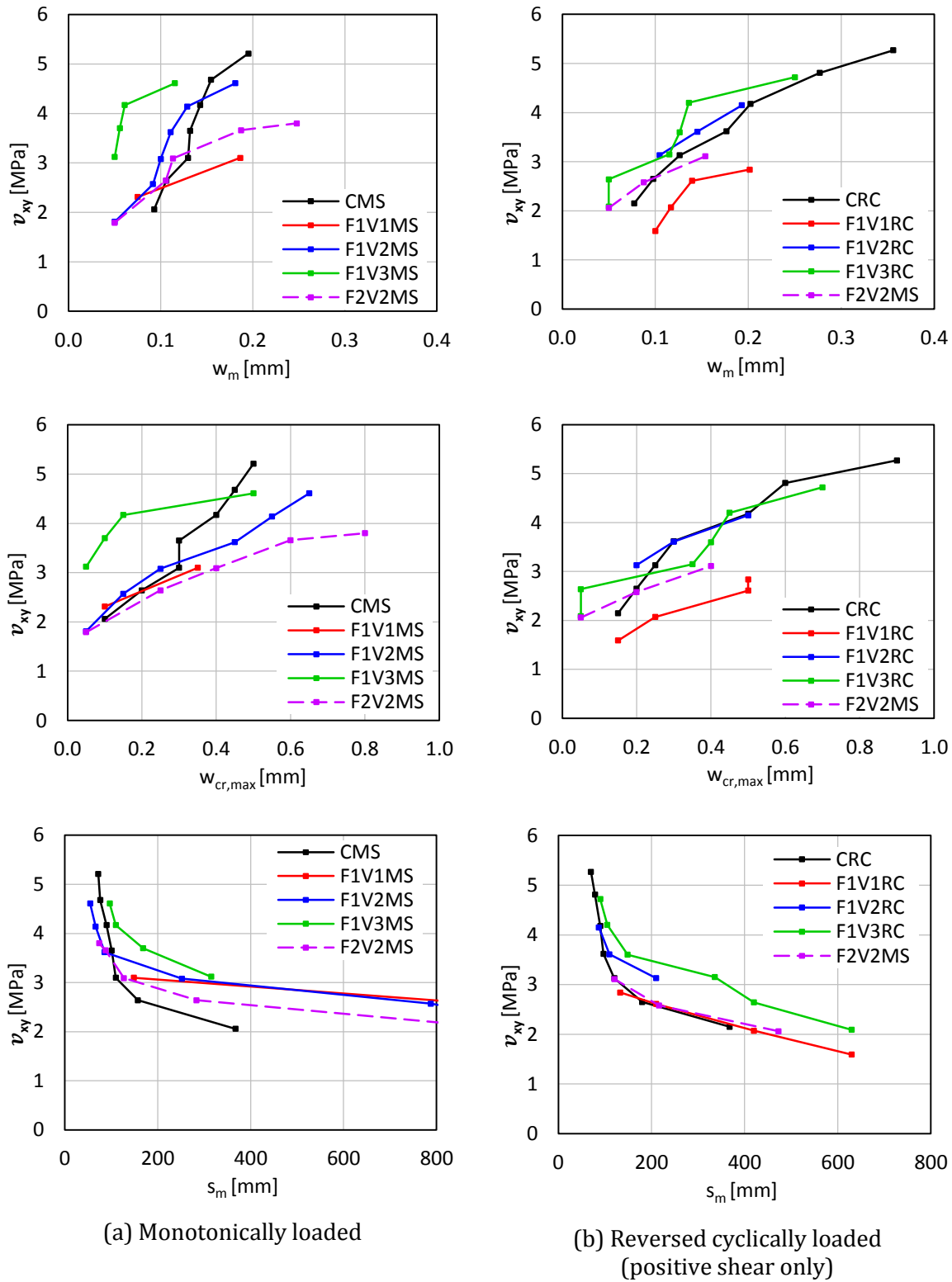
Figure 5-36: Comparison of average crack widths, maximum crack widths, and crack spacing
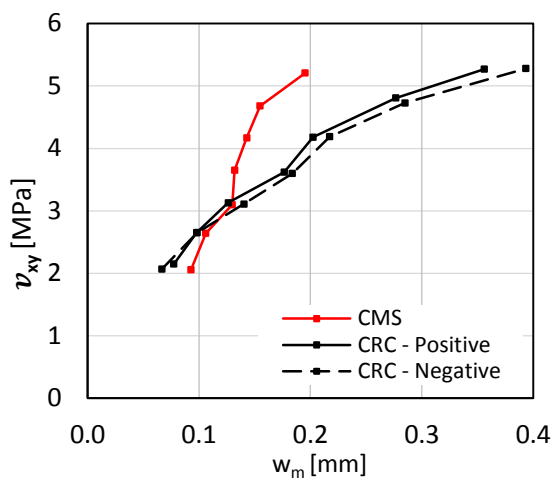
(a) Plain
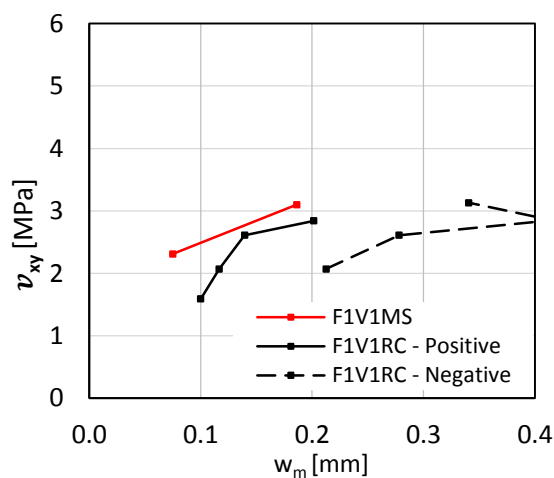
(b) 0.5% RC80/30BP
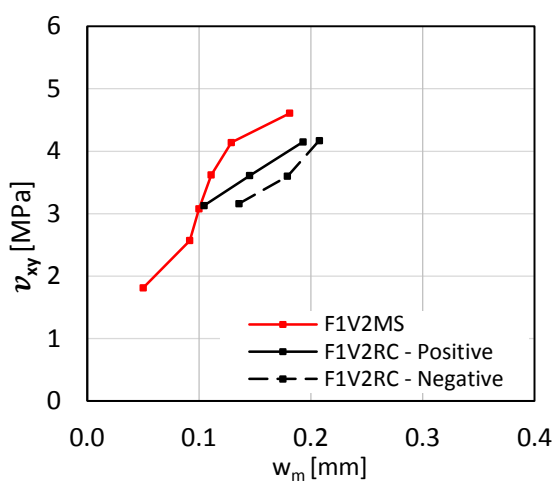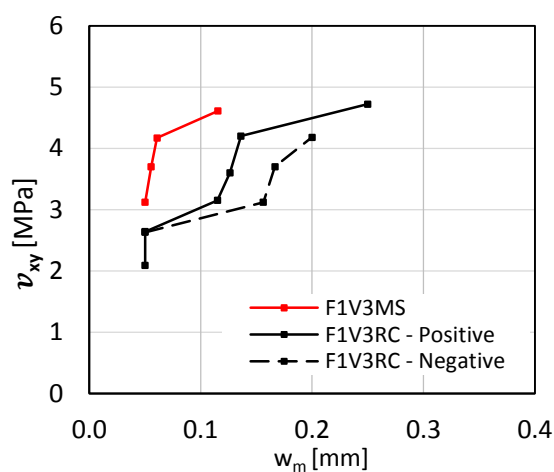
(c) 1.0% RC80/30BP

(d) 1.5% RC80/30BP
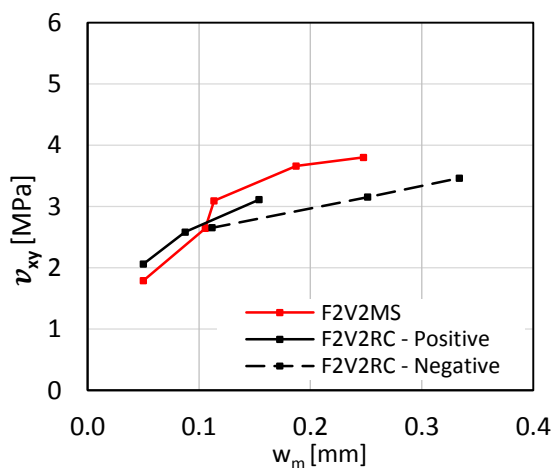
(e) 1.0% ZP305

Figure 5-37: Influence of loading protocol on average crack widths

5.4.4.2   Influence of Loading Protocol

The average crack widths for all five pairs of panels are shown in Figure 5-37. The crack widths of all cyclically loaded panels were larger than their monotonic counterpart's, demonstrating detrimental effects as a result of the cycling of load. The larger crack widths of the cyclically loaded panel inhibited the ability of fibres to transmit stress across the cracks, which in turn reduced the specimen's ability to generate further cracking. The crack widths under negative shear were similar but consistently larger than that of positive shear. This is expected because the reversed cyclic loading protocol always begins in the positive shear direction, resulting in the panel being more damaged by the time it reached the same load in the negative direction.

In terms of the crack width, no discernible trend is apparent with regards to the influence of fibre type or fibre content on the detrimental effects of the cycling of load. The panel with 0.5% fibre addition, F1V1RC, experienced the largest negative shear average crack widths. This is because under negative shear, only a few relatively wide cracks were developed and were concentrated at the bottom half of that panel. F1V1RC's negative average crack width experienced a rapid decrease near failure due to the sudden opening of many small cracks. The above signified the inability of SFRC with low fibre contents to produce uniform cracks, especially under reversed cyclic loadings.

5.4.5 Inclination of Stress and Strain Fields

5.4.5.1   Comparisons of θ_σ and θ_ε

The comparison of the angle of inclination of the principal tensile stress direction and the angle of inclination of the principal tensile strain direction for each panel is shown in Figure 5-38; both angles were measured as the counter-clockwise angle from the positive x-axis. Before cracking, both angles were approximately 45^0 (or 135^0 for negative shear) as expected. Thereafter, the angles became more inclined; this was consistent with the rotation of cracks observed during the test.

For the cyclically loaded panels, the principal strain angle was more steeply inclined than the principal stress angle for the same shear stress; this observation was more pronounced at negative shear stresses. For the monotonically loaded panels, however, the change in the principal strain angle was very similar to but generally lagged behind the principal stress angle. The discrepancy between the principal stress angle and the principal strain angle indicated shear slip along the crack (Vecchio, 2000). Overall, the direction of the principal tensile strain had larger fluctuations.

The above observations were consistent with previous panel experiments (Susetyo et al., 2011; Carnovale, 2013).

5.4.5.2   *Influence of Fibre Type and Fibre Content*

A comparison of the inclinations of the principal tensile stress and strain angles for the monotonically loaded panels is plotted in Figure 5-39. As shown by the analyses of the crack control characteristics and the principal stresses, the influence of fibre type and fibre content on the monotonic response was similar to that of the cyclic response; hence, only a comparison of the monotonic response was necessary in this section.

As shown in Figure 5-39 (a), the control panel experienced a rapid increase in the rotation of the principal stress direction immediately after cracking; this increase eventually plateaued at an angle of 56^0 until failure occurred. The SFRC panels, on the other hand, experienced a significantly slower initial increase in the principal stress angle after initial cracking. A lower principal angle suggested principal tensile stresses were oriented more parallel to the primary x-direction reinforcement and therefore, more stresses would be carried by the primary reinforcement. The positive influence of higher fibre content and fibre aspect ratio were evident by the resulting slower increase of the principal stress angle. There were no discernible trends on the principal stress angle at failure; the average principal stress angle at failure was 61.2^0.

The trends in the principal strain angle were overall consistent with the principal stress angle trends discussed. The principal strain direction, however, did showed a steeper inclination at failure which was consistent with the directions of the surface cracks at the onset of failure.
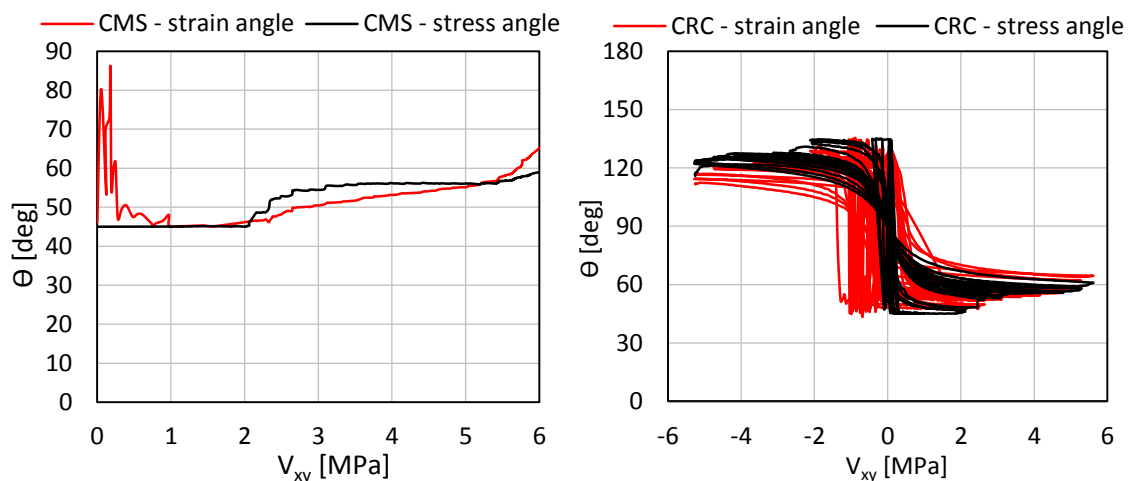
(a) Plain
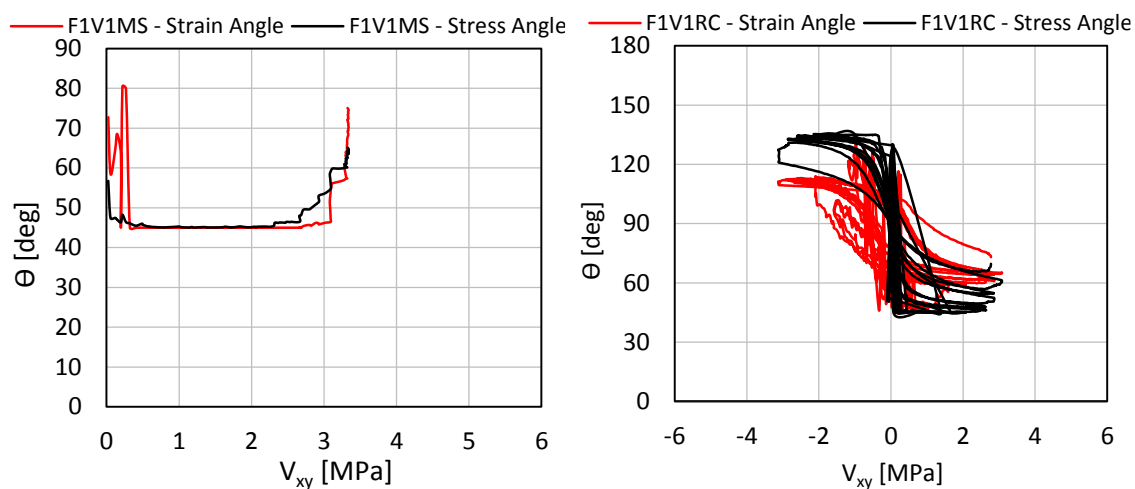
(b) 0.5% RC80/30BP
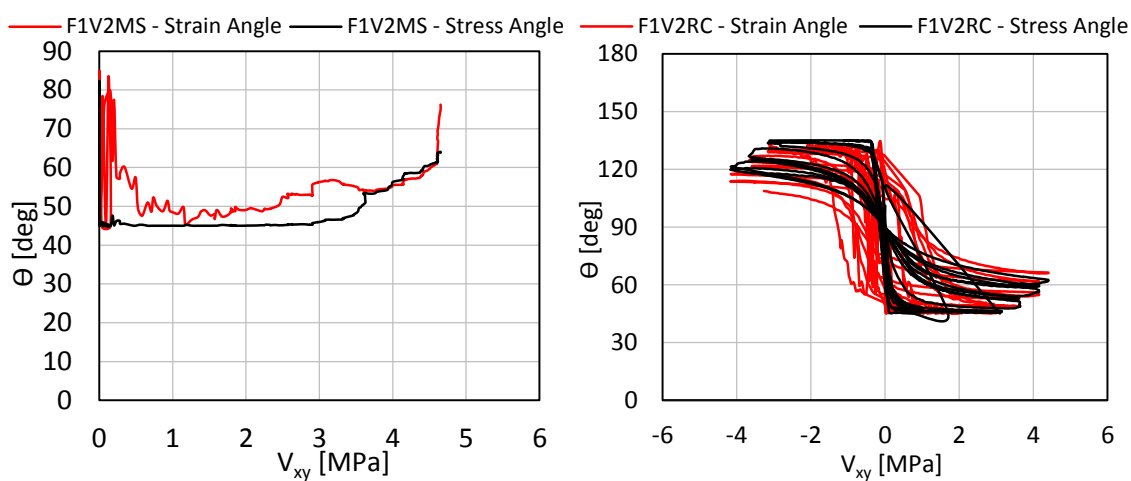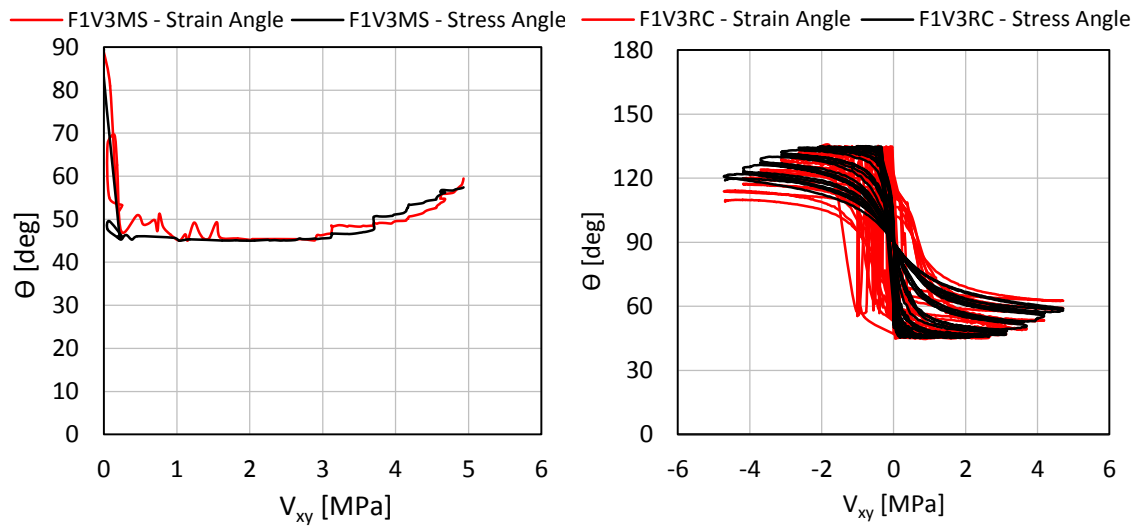
(c) 1.0% RC80/30BP

(d) 1.5% RC80/30BP
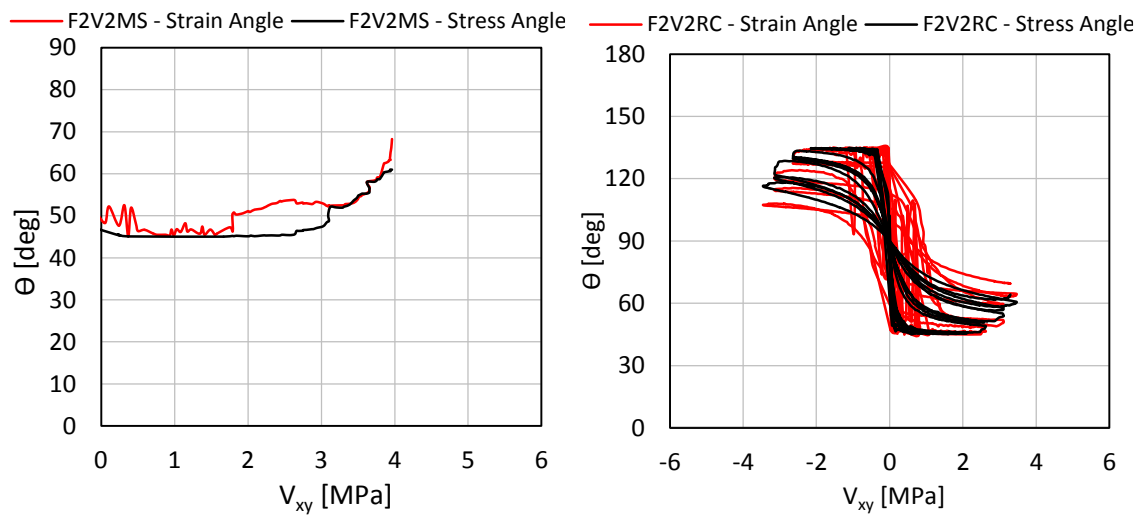
(e) 1.0% ZP305

Figure 5-38: Comparison of the principal stress angle and the principal strain angle for all panels

(a) Principal tensile stress angle   (b) Principal tensile strain angle
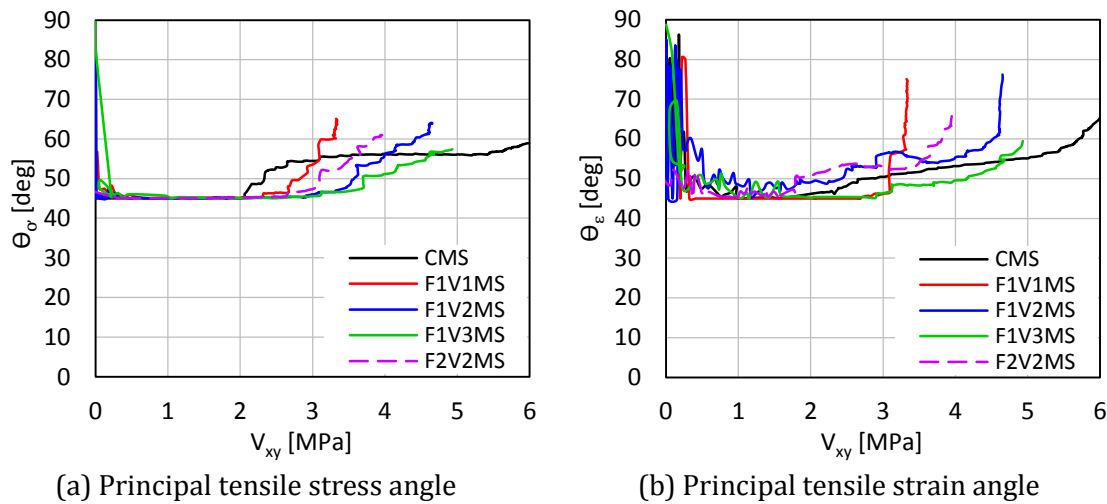
Figure 5-39: Comparison of principal angles for monotonically loaded panels

5.4.5.3   Influence of Loading Protocol

A comparison of the inclinations of the principal tensile stress and strain angles for cyclically loaded panels against their monotonically loaded companion panel is shown in Figure 5-40. The envelope principal stress angle for the cyclically loaded panels was nearly identical to that of the monotonically loaded panels; a small discrepancy did exist for the F2V2 series near failure.

The influence of loading protocol was more apparent when examining the principal strain angles. The larger discrepancy in these angles was especially pronounced under negative shear loading. This is because the monotonically loaded panels were only loaded in the positive direction, and the negative direction response of the cyclically loaded panels was expected to be weaker, with greater crack widths and larger principal angle rotations, due to the sequence of the loading protocol. With the exception of F1V1RC, the undesirable crack rotations occurred slightly earlier for the cyclically loaded panels. Panel F1V1RC exhibited a large change in the inclination of the principal tensile strain immediately after crack rotation began; this large discrepancy relative to its principal stress angle indicated large shear slip along crack surfaces and further suggested that SFRC with 0.5% fibre content were more susceptible to cyclic damages.

(a) Plain

(b) 0.5% RC80/30BP

(c) 1.0% RC80/30BP

(d) 1.5% RC80/30BP

(e) 1.0% ZP305
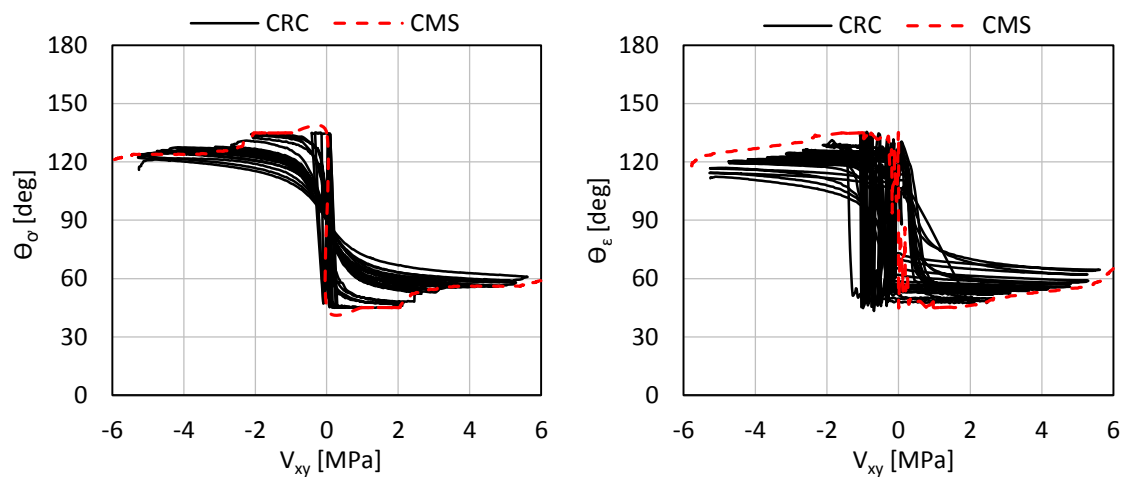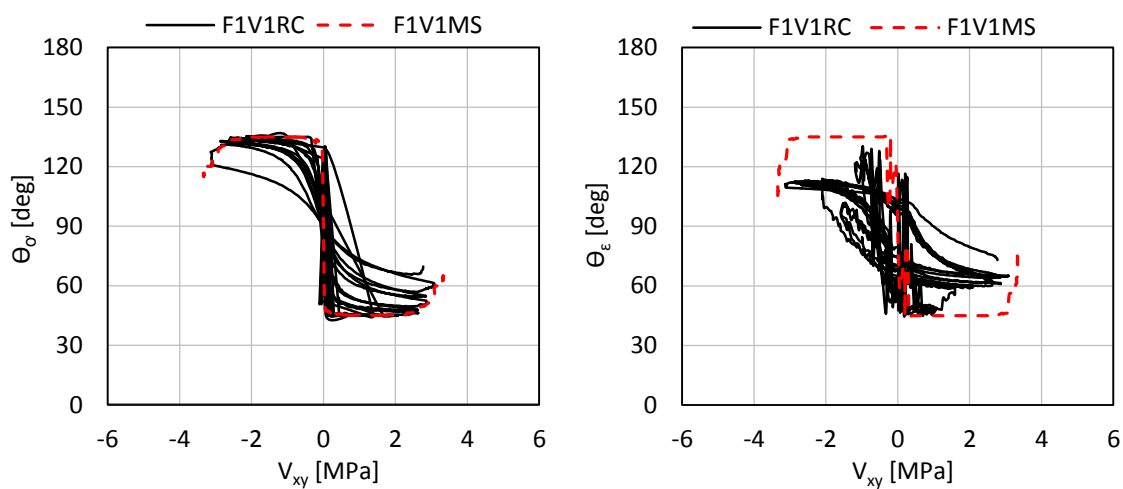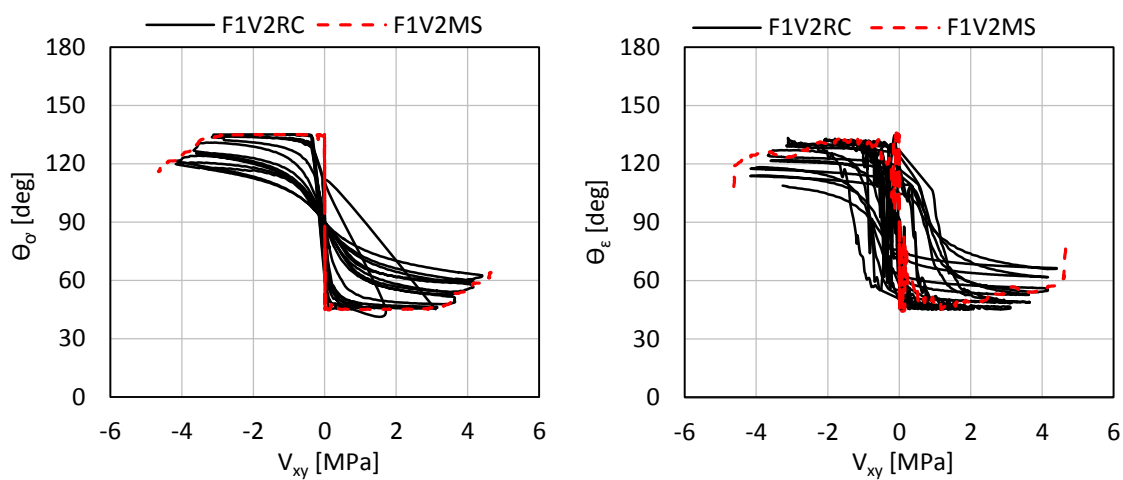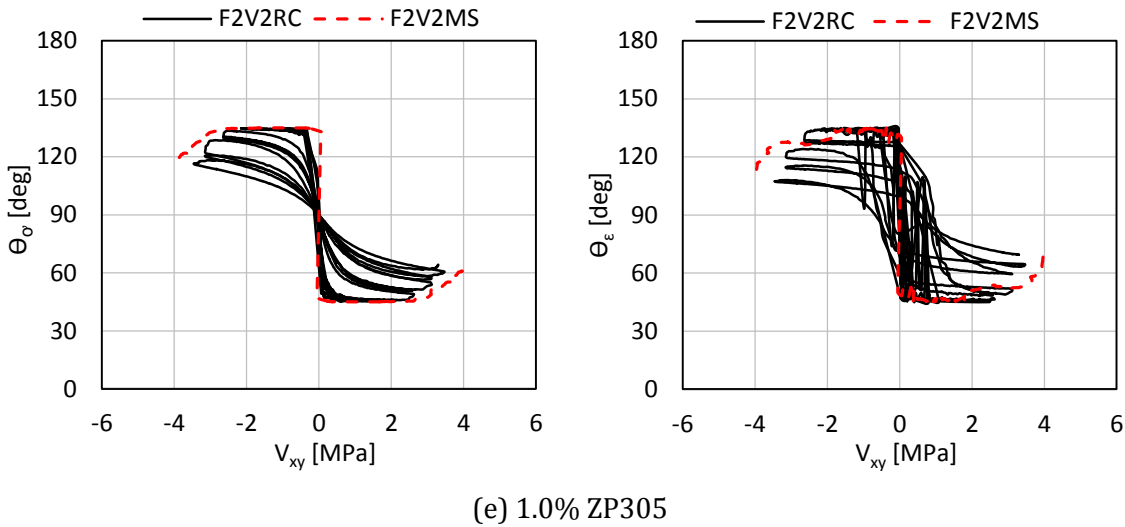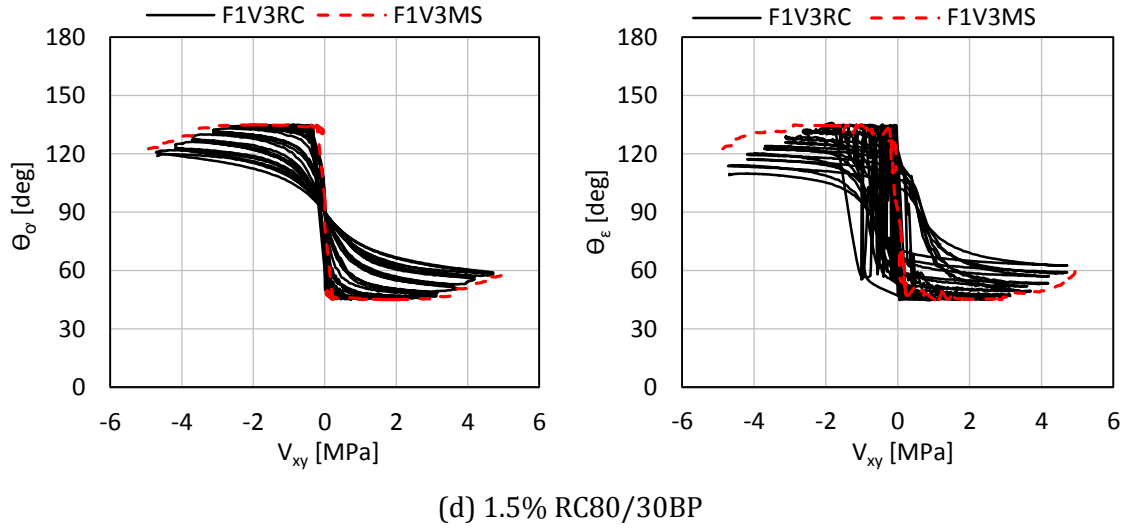
Figure 5-40: Influence of loading protocol on principal angles

5.5   Summary of Panel Test Results

The influence of fibre volume fraction, fibre aspect ratio, and loading protocol was studied through a series of ten panel tests. The results and analyses are summarized below:

1   Overall, the results of the ten panel tests were consistent and corroborated with the material test results.

2   SFRC with higher fibre contents exhibited higher maximum shear stress, better crack control characteristics, and reduced cyclic deterioration.

3   SFRC with lower fibre aspect ratio fibre (by using thicker fibres) showed poorer performance in terms of shear resistance and crack control.

4   Under reversed cyclic loading, SFRC panels exhibited stable hysteretic response with insignificant strength degradation and no noticeable changes in ductility. With the exception for panels with a fibre content of 0.5%, all panels' monotonic backbone curve closely matched the reversed cyclic envelope curve.

5   SFRC Panels with a fibre content of 0.5% were much more susceptible to damages from the cycling of load.

6   SFRC panels exhibited higher shear stiffness than the control panels until significant strains were reached; this effect was more pronounced for panels with 1.0% and 1.5% fibre content.

7   SFRC panels containing a fibre content of 1.5% managed to withstand at least 82% of the maximum shear stress that was sustained by the conventionally reinforced panels.

8   SFRC panels reached at most 58% of the maximum shear strain sustained by that of the conventionally reinforced panels.

<div align="center">

Chapter 6
Finite Element Modelling
</div>

6. Finite Element Modelling

6.1 Introduction

This chapter discusses the nonlinear finite element modelling (NLFEM) of SFRC members using VecTor2, a nonlinear finite element analysis program developed at the University of Toronto (Vecchio, 1990). This program employs a total load algorithm, secant stiffness formulation, with rotating crack models. The governing behavioural models of VecTor2 are the Modified Compression Field Theory (MCFT) (Vecchio and Collins, 1986) and the Disturbed Stress Field Model (DSFM) (Vecchio, 2000). These models characterize cracked concrete as an orthotropic material with smeared rotating cracks. The purpose of the finite element analyses was to investigate the adequacy of currently available constitutive models in predicting the monotonic and reversed cyclic behaviour of SFRC.

The panels tested in this work and the series of SFRC slender coupling beams tested at the University of Michigan by Setkit (2012) will be modelled using the current version of VecTor2 (April, 2014). All of the models were constructed using VecTor2's pre-processor software, FormWorks (Wong et al., 2012). VecTor2's post-processor, Augustus, was used to process and analyze the results (Bentz, 2010).

6.2 Panel Specimens

6.2.1 Modelling of the Panels

In VecTor2, the panels were modelled as a single four-node plane stress rectangular element with a dimension of 890x890x70 mm. The lower left corner of the element was restrained in the x- and y-direction, while the lower right corner was restrained in the y-direction only. As shown in Figure 6-1, the load was applied at the nodes to create a pure shear loading condition. To be consistent with the experiment, the numerical model was load-controlled.

For the monotonic panels, the numerical loading was monotonically increased by 0.5 kN (0.016 MPa shear stress) at each analysis step until failure. For the cyclic panels, a coarser load step of 2.5 kN was used (0.08 MPa shear stress) to reduce the computational cost; although five times larger than that used for the monotonic panels, this load step did produce the same results. The numerical cyclic loading protocol consisted of double cycles with a cycle shear stress increment of 0.5 MPa, consistent with the experimental program.

(a) Idealized panel sketch   (b) FormWorks model
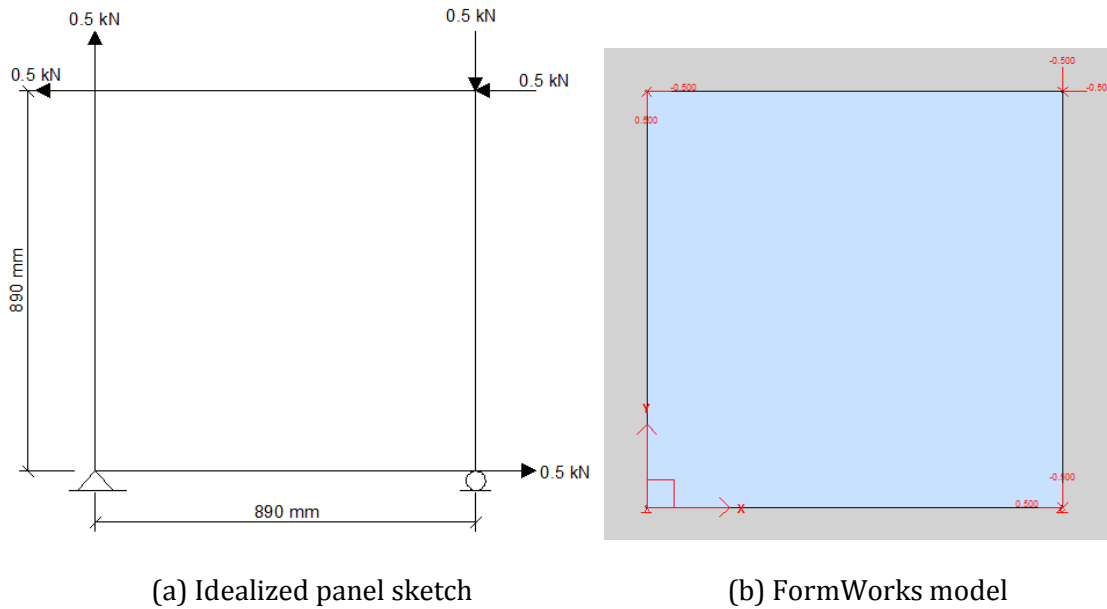
Figure 6-1: Finite element modelling of the panels

In order to verify the adequacy of the constitutive models for the concrete matrix, the majority of the mechanical properties determined through the material tests were not input into the program. Only the concrete compressive strength, maximum aggregate size, fibre properties, and reinforcement properties were entered. The fibre reinforcement was modelled as smeared reinforcement by selecting end-hooked steel fibre as the reference type. The conventional reinforcement was modelled as smeared reinforcement as well by using the ductile steel reinforcement reference type. The concrete and fibre properties used are shown in Table 6-1, and the reinforcement properties used are presented in Table 6-2. Since the deformed wires used were cold-formed and exhibited no defined yield plateau, the yield strain was used as the strain hardening point.

Table 6-1: Concrete and fibre properties for panel models

Test ID	f'_c [MPa]	a_{max} [mm]	V_f [%]	l_f [mm]	d_f [mm]	f_{uf} [MPa]
CMS	45.2	10	-	-	-	-
CRC	45.5	10	-	-	-	-
F1V1MS	55.9	10	0.5	30	0.38	2300
F1V1RC	56.1	10	0.5	30	0.38	2300
F1V2MS	58.1	10	1.0	30	0.38	2300
F1V2RC	58.1	10	1.0	30	0.38	2300
F1V3MS	50.9	10	1.5	30	0.38	2300
F1V3RC	53.1	10	1.5	30	0.38	2300
F2V2MS	52.1	10	1.0	30	0.55	1300
F2V2RC	52.9	10	1.0	30	0.55	1300

Table 6-2: Reinforcement properties for panel models

Direction	ρ [%]	d_b [mm]	f_y [MPa]	f_u [MPa]	E_s [GPa]	ε_{sh} [x10^{-3}]	ε_u [x10^{-3}]
x (0°)	3.31	8.10	457.8	591.9	184.7	2.48	33.7
y (90°)	0.42	5.72	490.6	639.2	190.5	2.60	21.8

Using the appropriate constitutive models is critical to the accuracy of the finite element (FE) analysis. Although VecTor2 provided a comprehensive selection of the most commonly used models for each behavioral mechanism, only the default models were used in most cases; this was to prevent any subjective tweaking on the choice of the constitutive models. As shown in Table 6-3, only two of the models used were not the default option. First, the chosen pre-peak compression model for concrete was the Popovics High Strength Model which was recommended for concrete with a compressive strength above 40 MPa. Second, the exponential tension softening model was used. This is because the formulation for the Simplified Diverse Embedment Model (SDEM), which was developed to account for the contribution of steel fibre reinforcement to concrete tensile stress, assumes the tension softening stress derived from the concrete matrix to be as calculated by the exponential model (Lee et al., 2012).

Table 6-3: Constitutive models used for panel FE analysis

Concrete Constitutive Models			
Compression Pre-Peak*	Popovics (HSC)	**Dilation**	Variable – Kupfer
Compression Post-Peak	Modified Park-Kent	**Cracking Criterion**	Mohr-Coulomb (Stress)
Compression Softening	Vecchio 1992-A	**Crack Stress Calc**	Basic (DSFM/MCFT)
Tension Stiffening	Modified Bentz 2003	**Crack Width Check**	Agg/5.0 Max Crack Width
Tension Softening*	Exponential	**Crack Slip Calc**	Walravan (Monotonic)
FRC Tension	SDEM - Monotonic	**Hysteretic Response**	Nonlinear w/ Plastic offset
Confined Strength	Kupfer/Richart		
Reinforcement Constitutive Models			
Hysteretic Response	Bauschinger Effect (Seckin)	**Buckling**	Refined Dhakal-Maekawa
Dowel Action	Tassios (Crack Slip)	**Concrete Bond**	Eligehausen

* only these models are not the default option

6.2.2 Conventionally Reinforced Concrete Panels

The FE analysis results for panel CMS and CRC are shown in Figure 6-2 and Figure 6-3, respectively. The numerical results were sufficiently accurate and predictions for the key parameters were generally well within 20% of the experimental results (see Table 6-4). The failure mode in the numerical models was due to yielding of the transverse reinforcement, consistent with the experimental findings. The only parameter that was not well captured was the average crack width. This was in part due to the subjective nature of the crack width measurements and averaging techniques. By examining the product of the principal tensile strain and the average crack spacing obtained from the experiment, which is a measure of the average crack width, it was evident that the crack widths obtained from VecTor2 were much more reasonable.

For the monotonically loaded control panel, the shear stress-shear strain, principal stress-principal strain, and orientation of the principal direction response were accurately represented by the FE model. Since a bilinear reinforcement stress-strain relationship was

employed for the FE model, the curvilinear stress-strain response of the reinforcement used was not captured (see Figure 6-2 (f)). As a result, the numerical model underestimated the shear stiffness after yielding of the transverse reinforcement, but the bilinear reinforcement relationship was not responsible for the underestimation of the ultimate shear stress because the peak transverse reinforcement stress was correctly captured in the numerical model.

For panel CRC, the cyclic behaviour overall was well predicted. The stiffness degradation, pinching of the hysteretic loop, and softness of the unloading branch were adequately captured. The rotation of the principal tensile stress and tensile strain directions was very well represented. Although the reinforcement stress-strain backbone curve was underestimated due to the chosen bilinear relationship, the reinforcement hysteretic response was correctly captured. The above allowed the overall response of CRC under medium to high stresses to be well represented; under low stresses, however, the FE model displayed deficiencies. The experimental results showed residual shear strains during load reversals, the shear strain for the numerical model always returned to zero when the shear stress was zero. The negative principal tensile stress as a result of cracks remaining open was also not shown in the numerical results. Hence, the plastic offset as a result of crack slips and cracks remaining open was not captured; some plastic offsets were displayed after yielding of the transverse reinforcement due to the hysteretic response of the reinforcement. Lastly, the numerical model did not display any stress degradation due to the cycling of load; the cyclic envelope curve was nearly identical to the monotonic backbone curve.
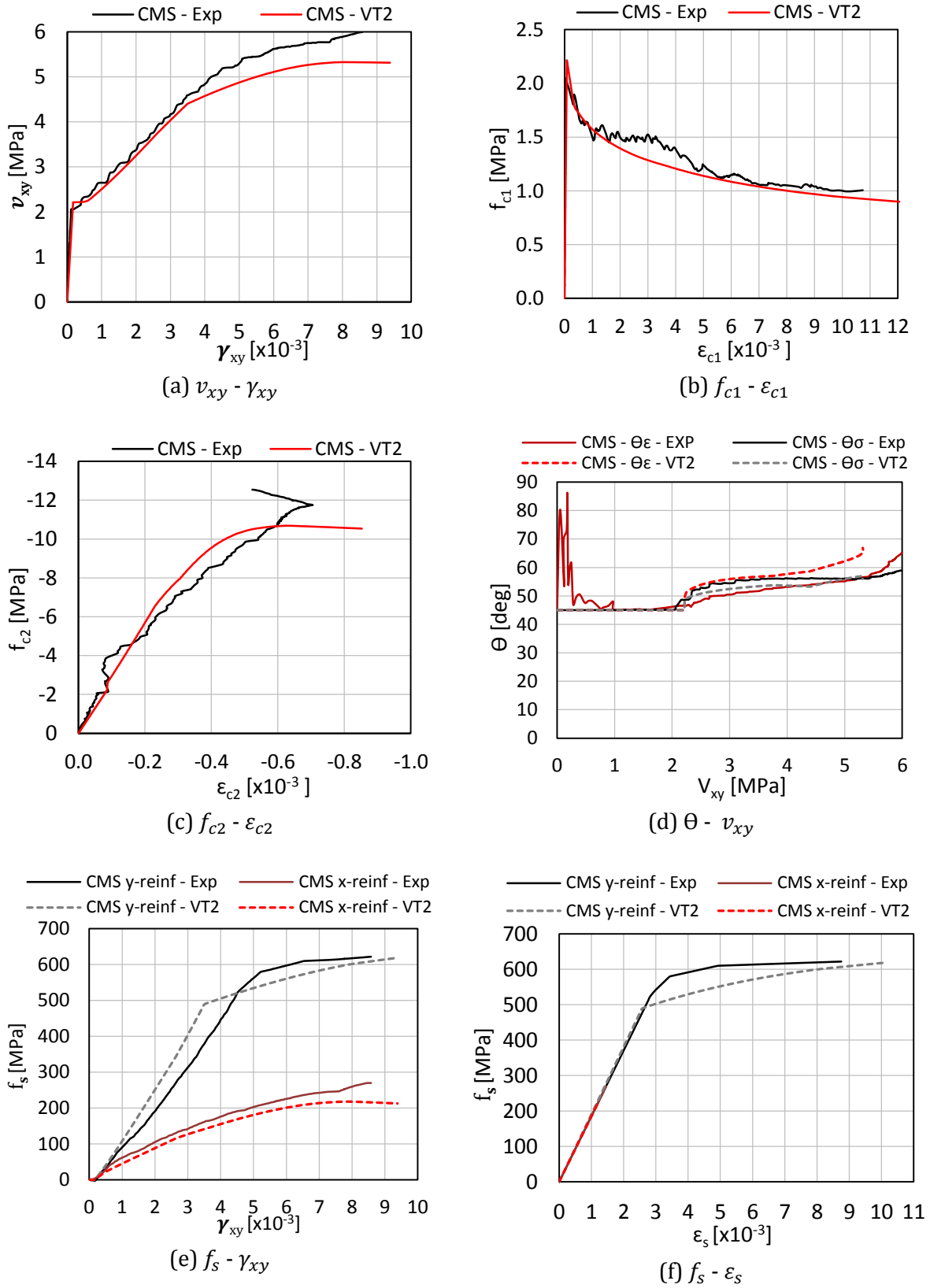
Figure 6-2: Comparison of numerical and experimental response for CMS

(a) v_{xy} - γ_{xy}

(b) f_{c1} - ε_{c1}

(c) f_{c2} - ε_{c2}

(d) $\theta\sigma$ - v_{xy}

(e) $\theta\varepsilon$ - v_{xy}

(f) f_s - γ_{xy}

(g) f_s - ε_s
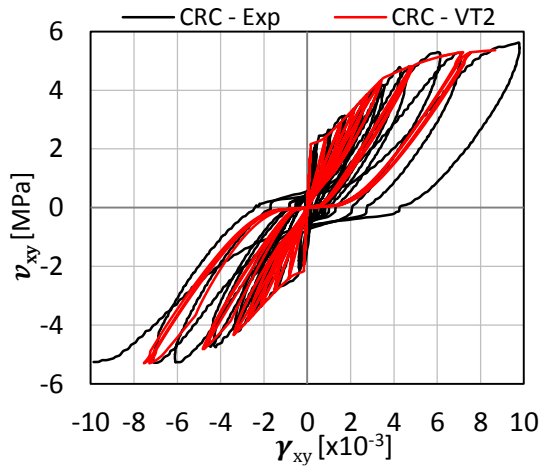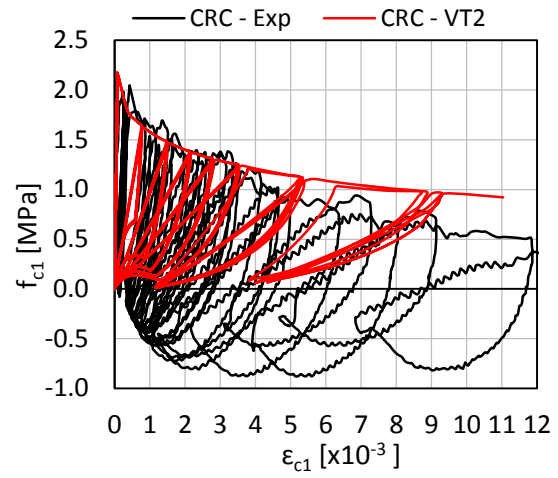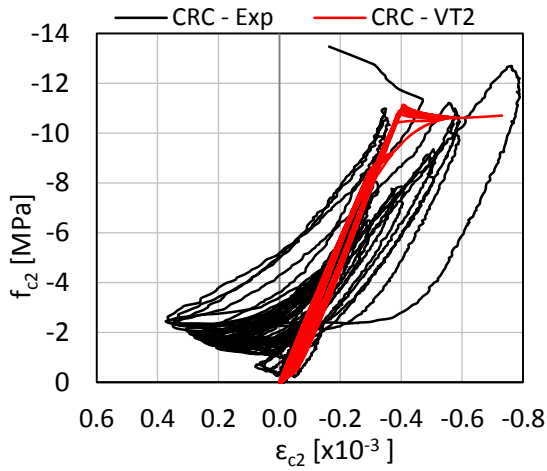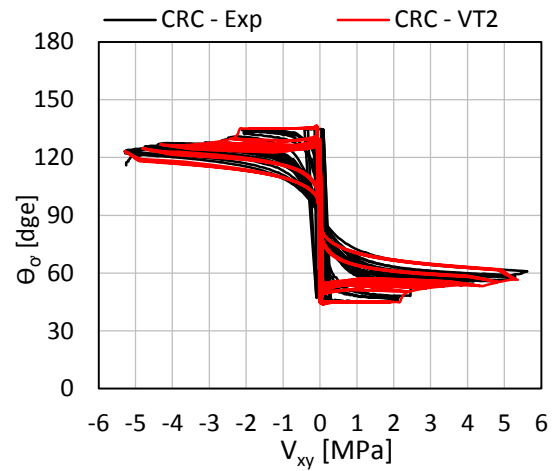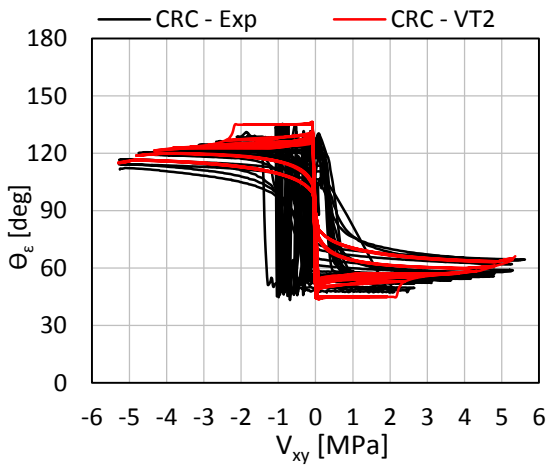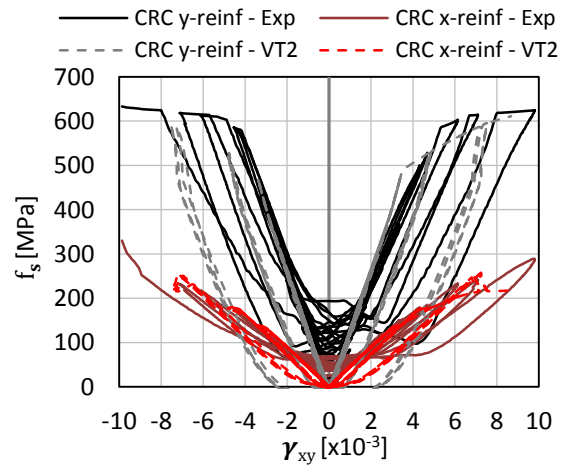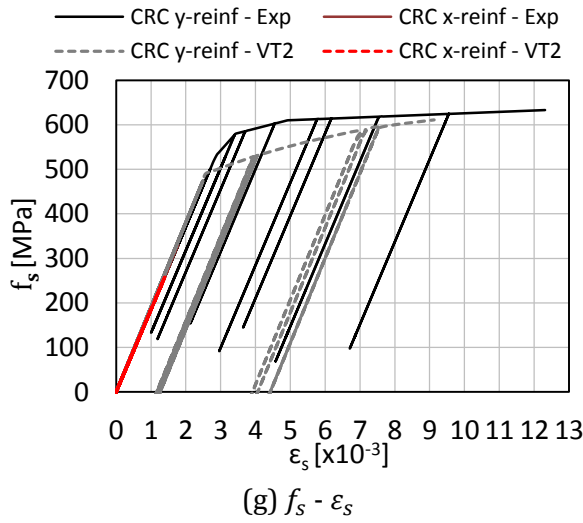
Figure 6-3: Comparison of numerical and experimental response for CRC

Table 6-4: Summary of numerical and experimental results for control panels

Panel	v_u [MPa]	$f_{c1,max}$ [MPa]	$f_{c1,fail}$ [MPa]	$f_{c2,max}$ [MPa]	$f_{sx,max}$ [MPa]	$f_{sy,max}$ [MPa]	$\frac{v_{u,VT2}}{v_{u,exp}}$
CMS	5.33 (5.99)	2.22 (1.99)	0.90 (1.04)	10.68 (-12.54)	218 (270)	619 (622)	0.89
CRC	5.36 (5.63)	2.17 (2.04)	0.92 (-0.11)	-11.14 (-13.48)	258 (330)	611 (633)	0.95

Panel	γ_u [x10^{-3}]	$\varepsilon_{c1,fail}$ [x10^{-3}]	$\varepsilon_{c2,fail}$ [x10^{-3}]	$\theta_{\sigma,fail}$ [deg]	$\theta_{\varepsilon,fail}$ [deg]	s_m [mm]	w_m [mm]	$\frac{\gamma_{u,VT2}}{\gamma_{u,exp}}$
CMS	9.38 (8.58)	12.13 (10.74)	-0.85 (-0.523)	56.0 (115.9)	66.9 (111.6)	97 (72.1)	1.13 (0.20)	1.09
CRC	8.68 (9.77)	11.04 (14.26)	-0.73 (-0.160)	56.5 (58.9)	66.3 (65.2)	98 (70.0)	1.05 (0.39)	0.89

Note: values in brackets are experimental results

6.2.3 Steel Fibre-Reinforced Concrete Panels

Comparisons of the numerical and experimental results for the four monotonically loaded SFRC panels are shown in Figure 6-4 to Figure 6-7; Figure 6-8 to Figure 6-11 shows the results for the four cyclically loaded SFRC panels. The behaviour models (MCFT/DSFM) and the fibre model for considering the contribution of steel fibre to concrete tensile strength (SDEM) were critical to the FE analysis of SFRC. Overall, the constitutive models in VecTor2 provided good results for the monotonically loaded SFRC panels while the predictions for the cyclically loaded

SFRC panels were adequate in terms of the force and deformation capacity, but were poor with regards to the cyclic behaviour.

In all panels, neither the concrete compressive strength nor the x-direction reinforcement yield strength were exceeded, indicating that the aggregate interlock failure mode was correctly predicted. Each of the SFRC numerical models exhibited some slip stresses and displacements as noted from the experiment. The load carrying capacity of the panels was very well predicted; the mean predicted-to-experimental shear strength was 1.03 with a coefficient of variation (CoV) of 12.6% (see Table 6-5). Due to the complex mechanism of aggregate interlock and random fibres bridging the crack, the shear deformation capacity of the panels was difficult to predict, but reasonable deformation predictions were achieved; the mean predicted-to-experimental ultimate shear strain was 1.41 with a CoV of 19.5%.

The mean crack spacing and crack width near failure for both normal concrete and SFRC are plotted in Figure 6-15 for comparison. The crack spacing predictions were sufficiently accurate for normal concrete panels, but significantly smaller for most of the SFRC panels. This underestimation was in part due to the relatively large measured crack spacing for the F1V3 series as a result of the non-ideal fibre distribution. As previously mentioned, the mean crack width at failure was significantly overestimated for normal concrete, but was reasonably well represented for SFRC. Since the crack measurement techniques were subjective in nature, VecTor2 provided overall reasonable predictions for these cracking characteristics.

The response of the monotonically loaded panels was well predicted. The post-cracking shear stiffness was consistently lower for the numerical models, indicating that the SDEM was underpredicting the contribution of steel fibre to concrete tensile stress; this was also evident in the principal tensile stress-strain response. The overall shear stress-shear strain response for all panels was, nevertheless, well predicted. The rotation of the principal tensile stress and strain directions was well represented. The mean predicted-to-experimental stress angle at failure was 1.04 with a COV of 3.6%, while the mean predicted-to-experimental strain angle at failure was 0.94 with a COV of 9.1%. Panel F1V3MS experienced the largest overestimation of ductility; this was primarily attributed to the non-ideal fibre distribution during mixing for this panel. By examining the principal tensile stresses, it was evident that the contribution of the thicker fibre (ZP305) to concrete tensile stress was most underpredicted, suggesting that the effect of fibre diameter was not effectively represented in the chosen constitutive models.
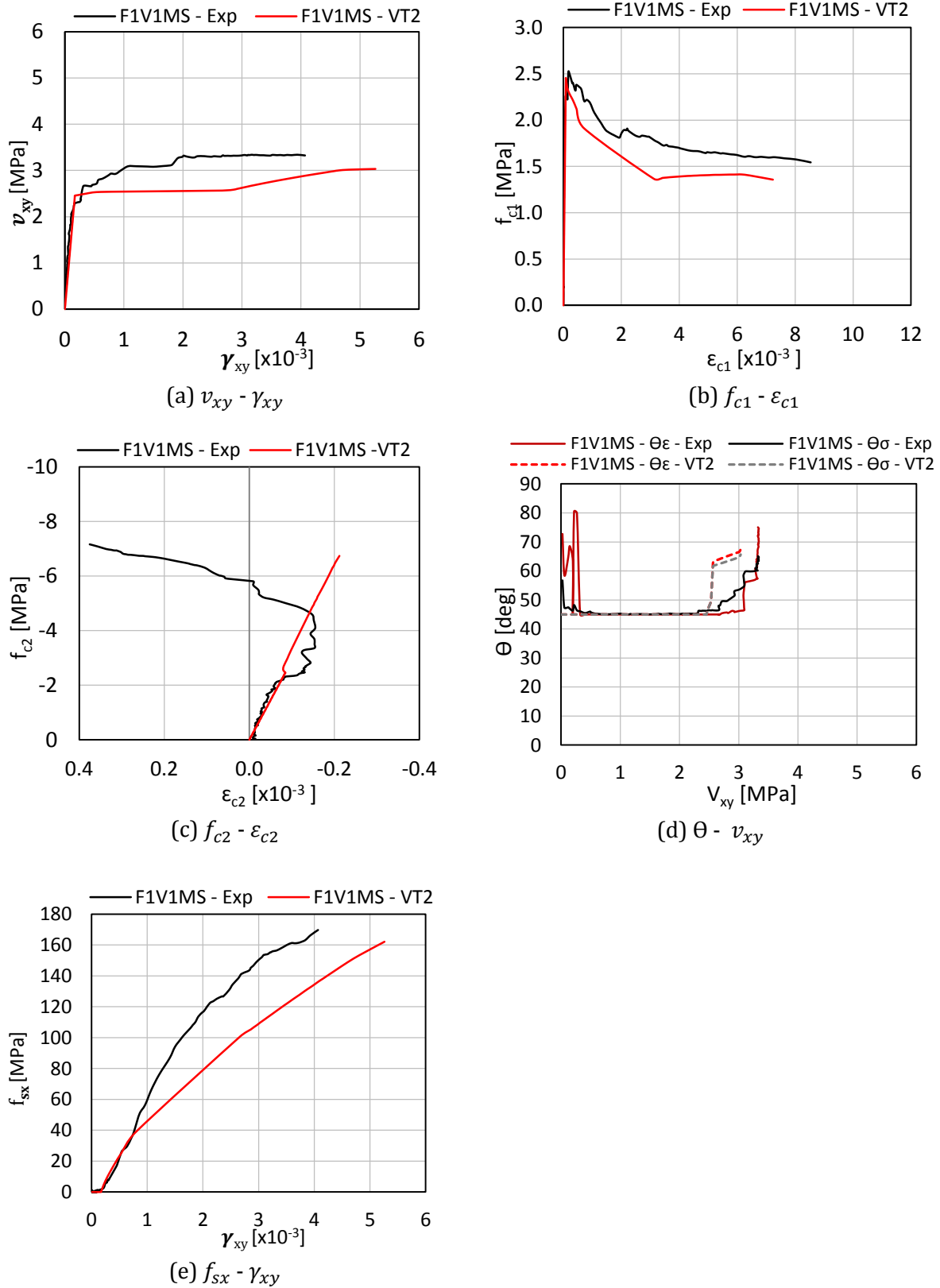
Figure 6-4: Comparison of numerical and experimental response for F1V1MS
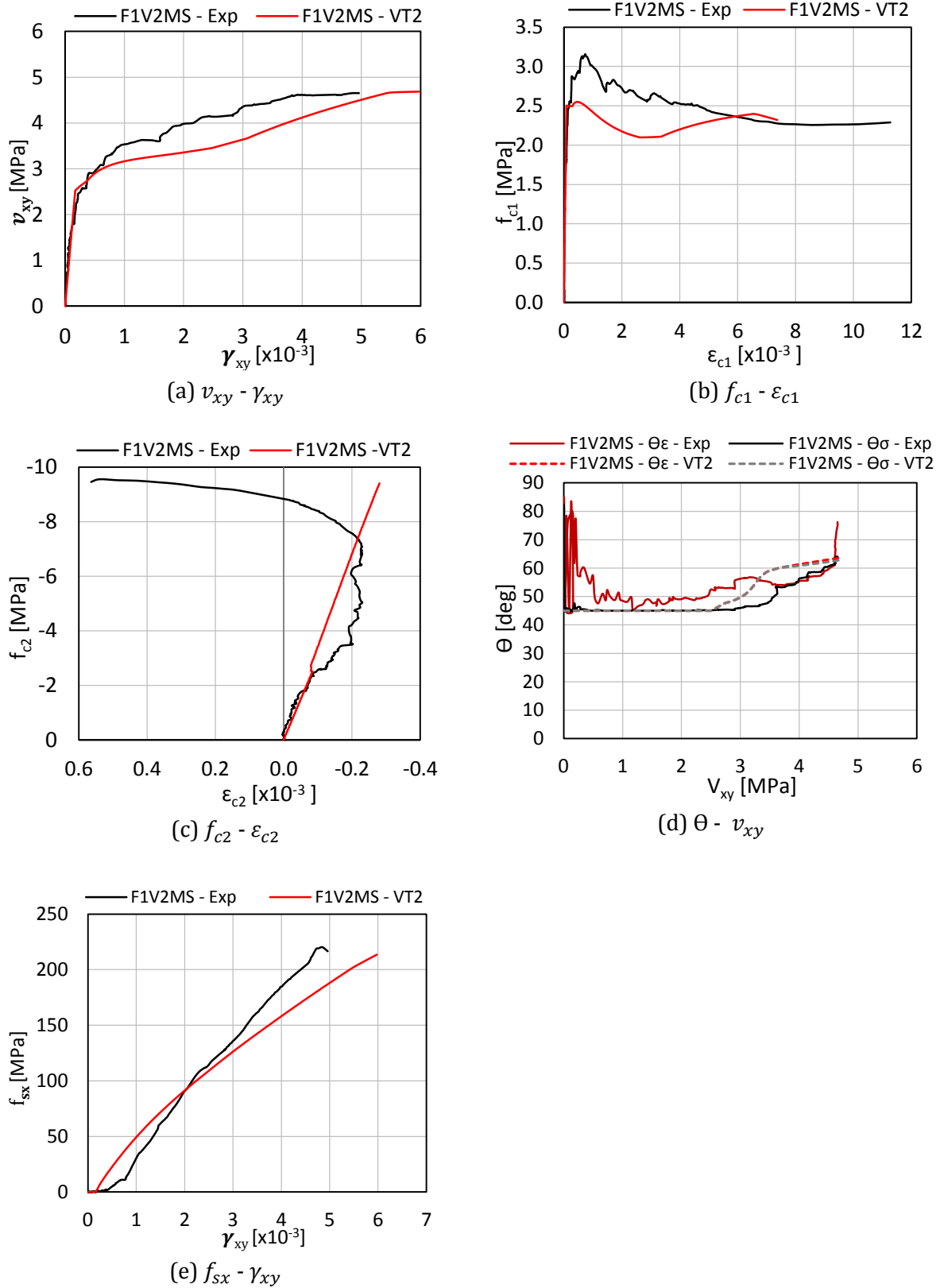
Figure 6-5: Comparison of numerical and experimental response for F1V2MS

(a) v_{xy} - γ_{xy}

(b) f_{c1} - ε_{c1}

(c) f_{c2} - ε_{c2}

(d) θ - v_{xy}

(e) f_{sx} - γ_{xy}
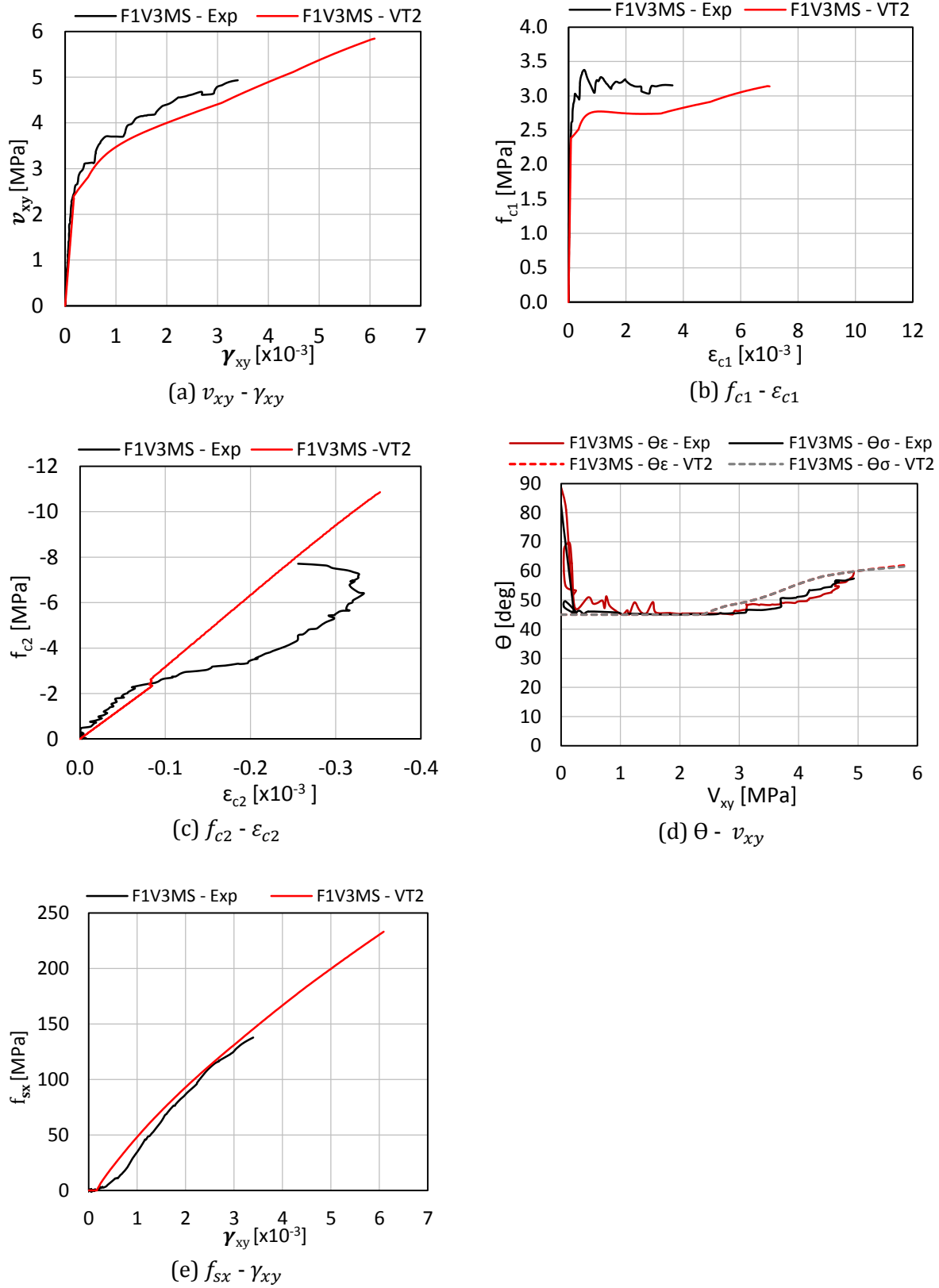
Figure 6-6: Comparison of numerical and experimental response for F1V3MS
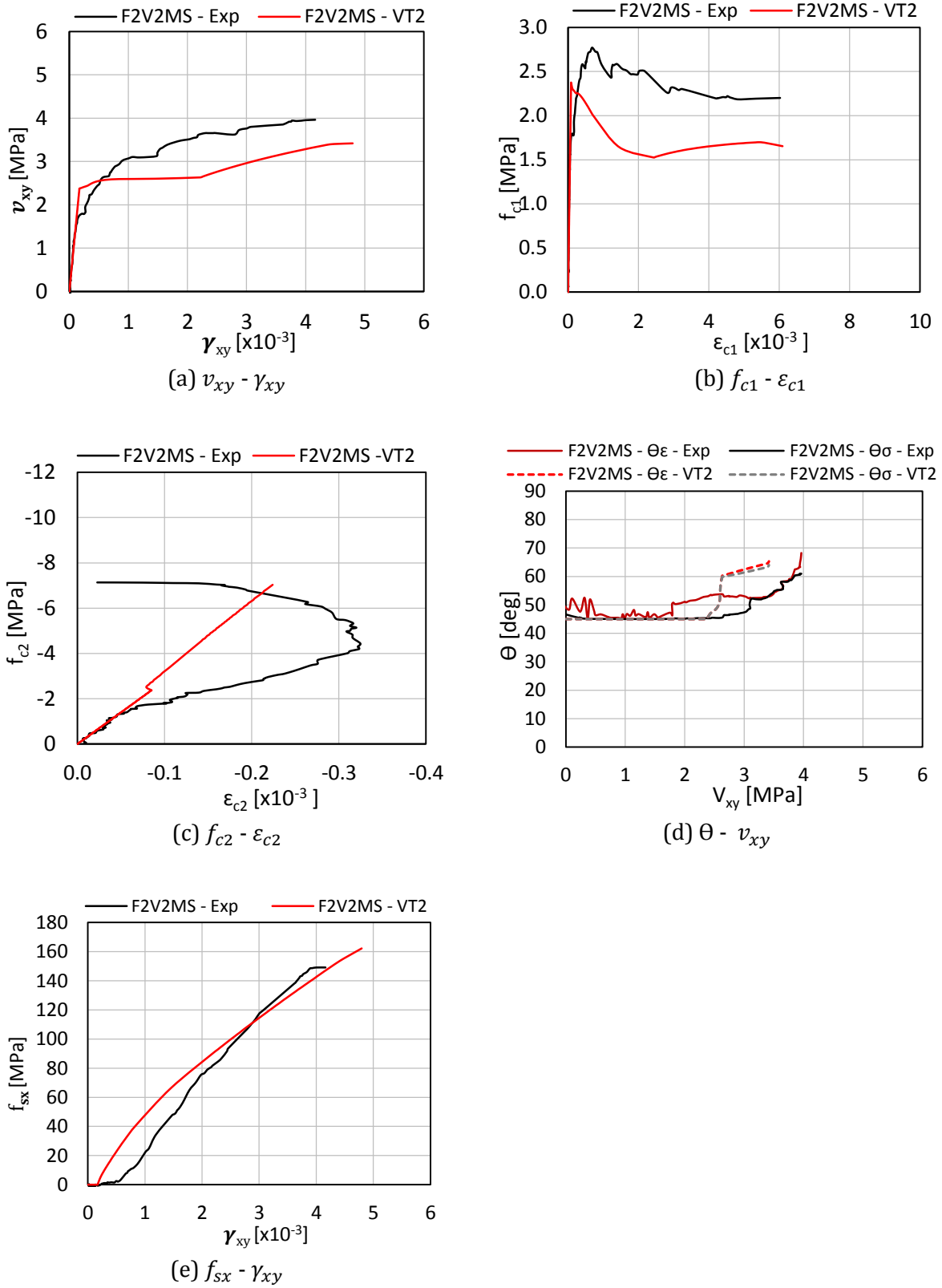
Figure 6-7: Comparison of numerical and experimental response for F2V2MS
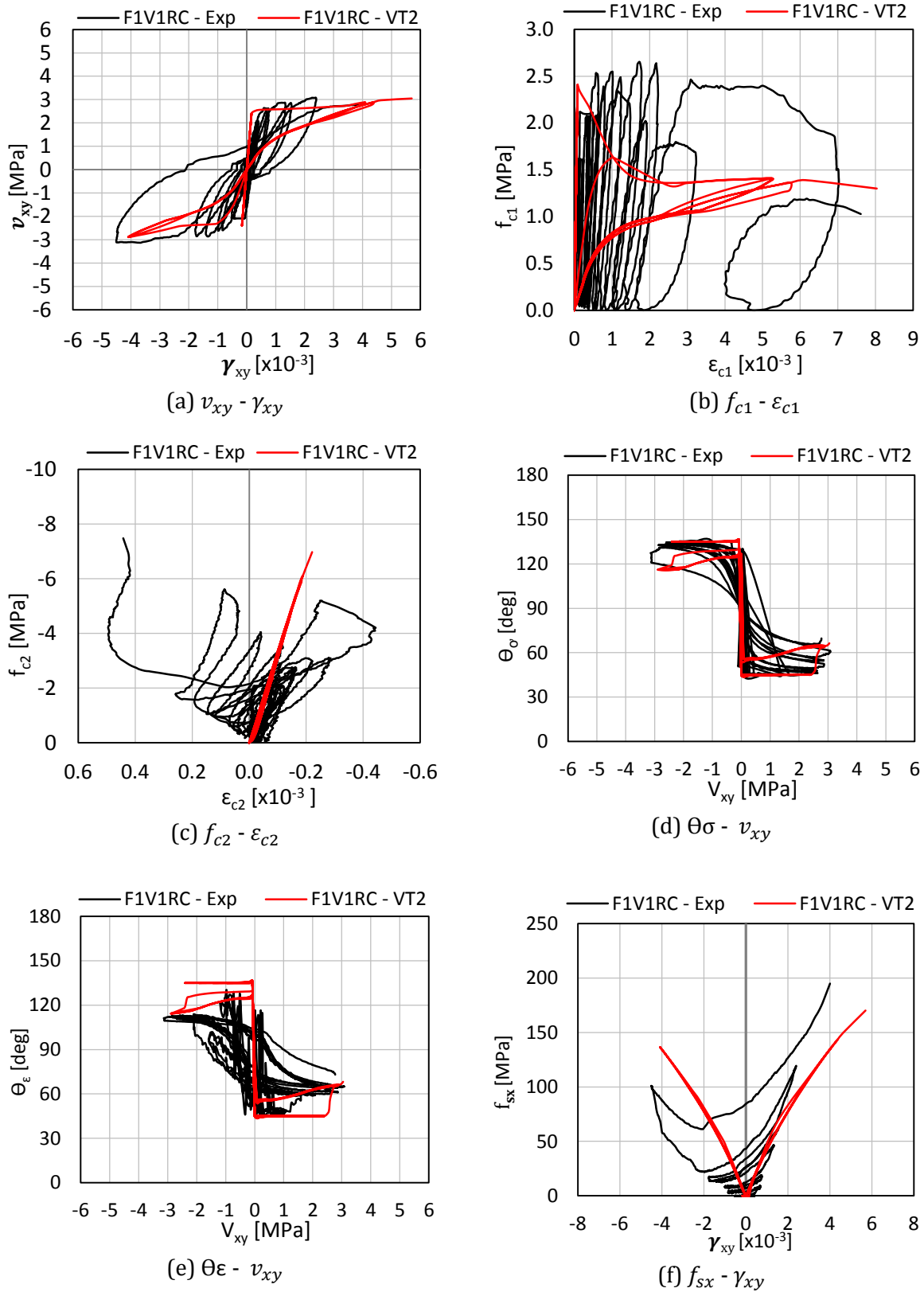
Figure 6-8: Comparison of numerical and experimental response for F1V1RC
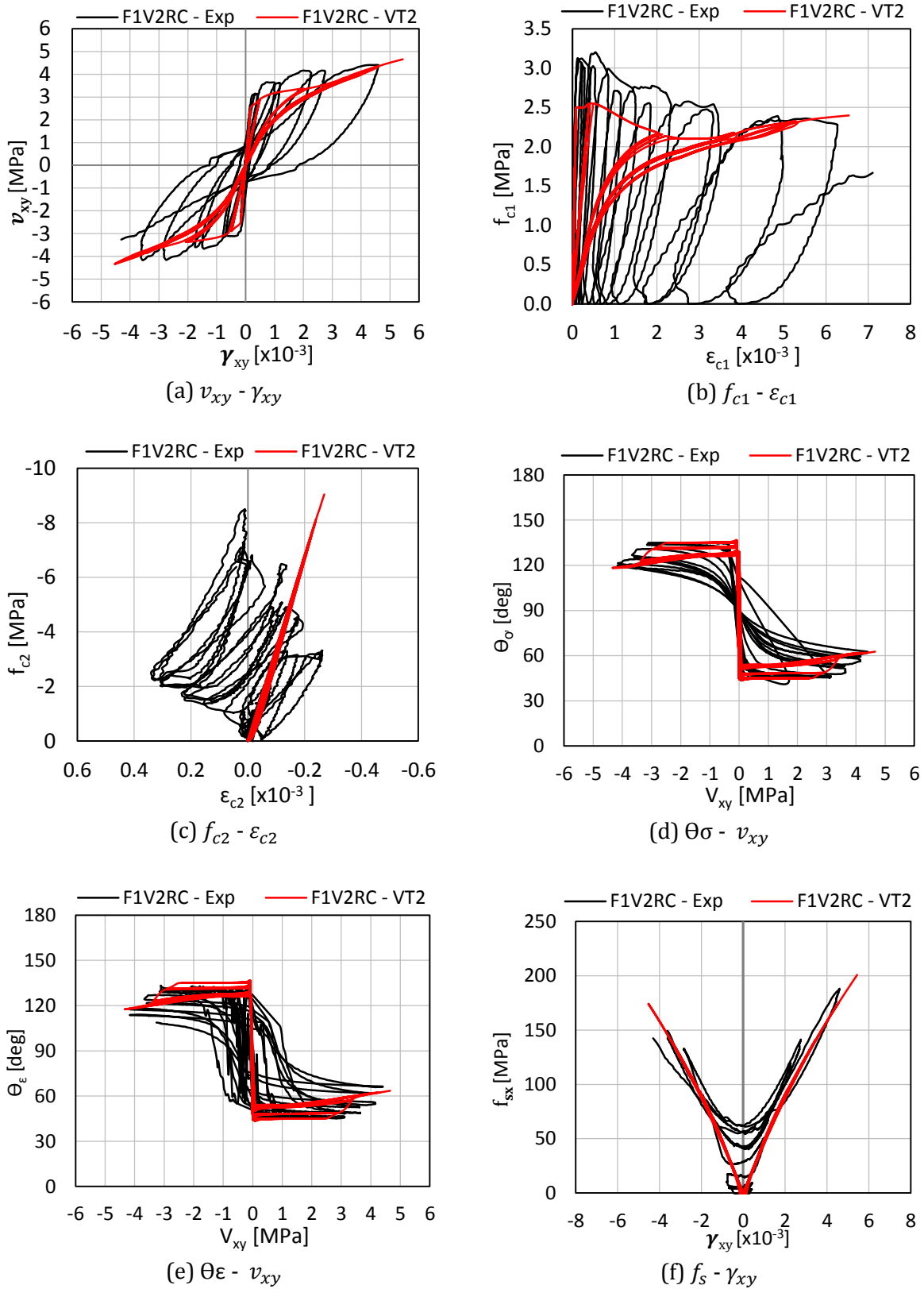
Figure 6-9: Comparison of numerical and experimental response for F1V2RC
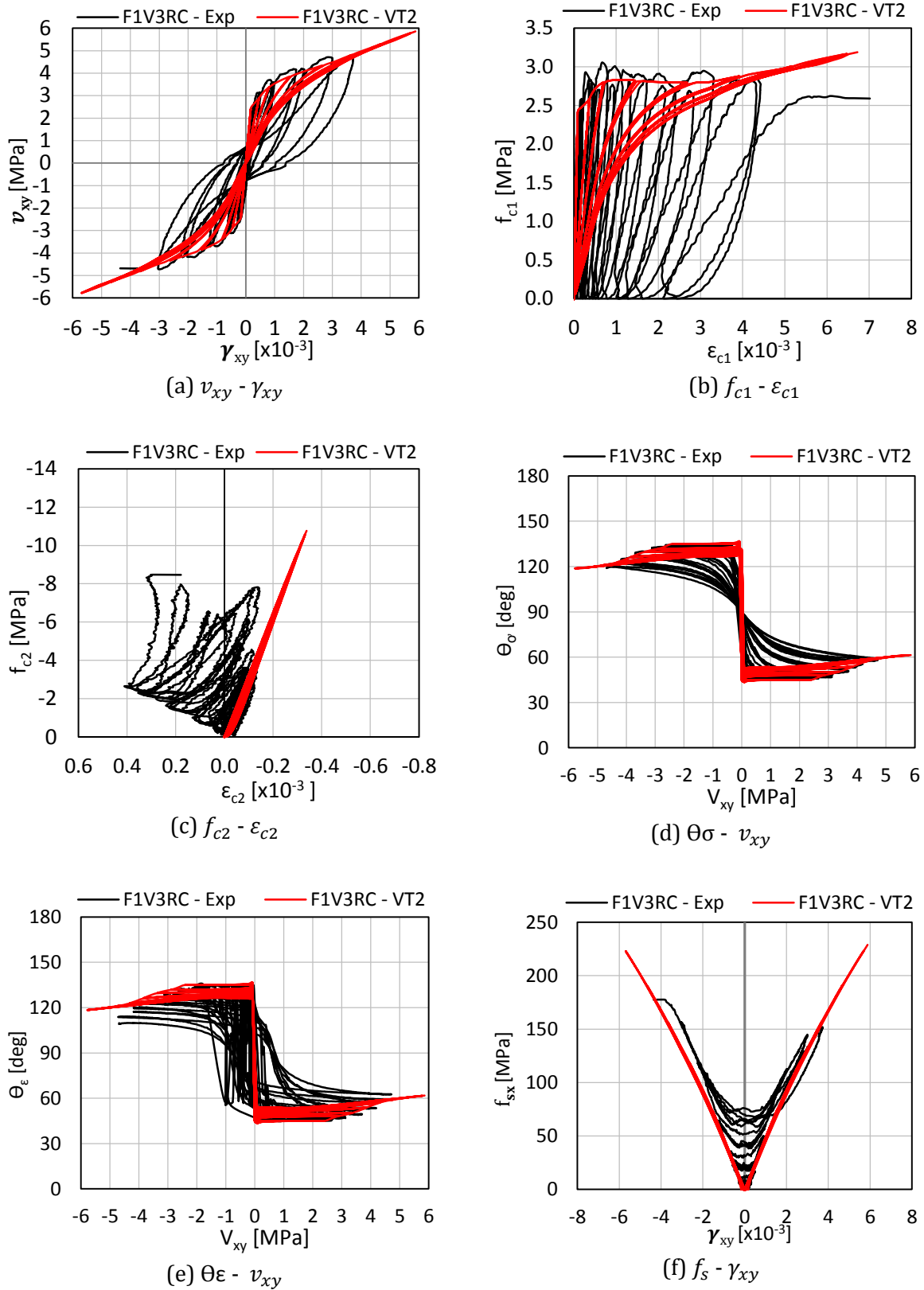
Figure 6-10: Comparison of numerical and experimental response for F1V3RC
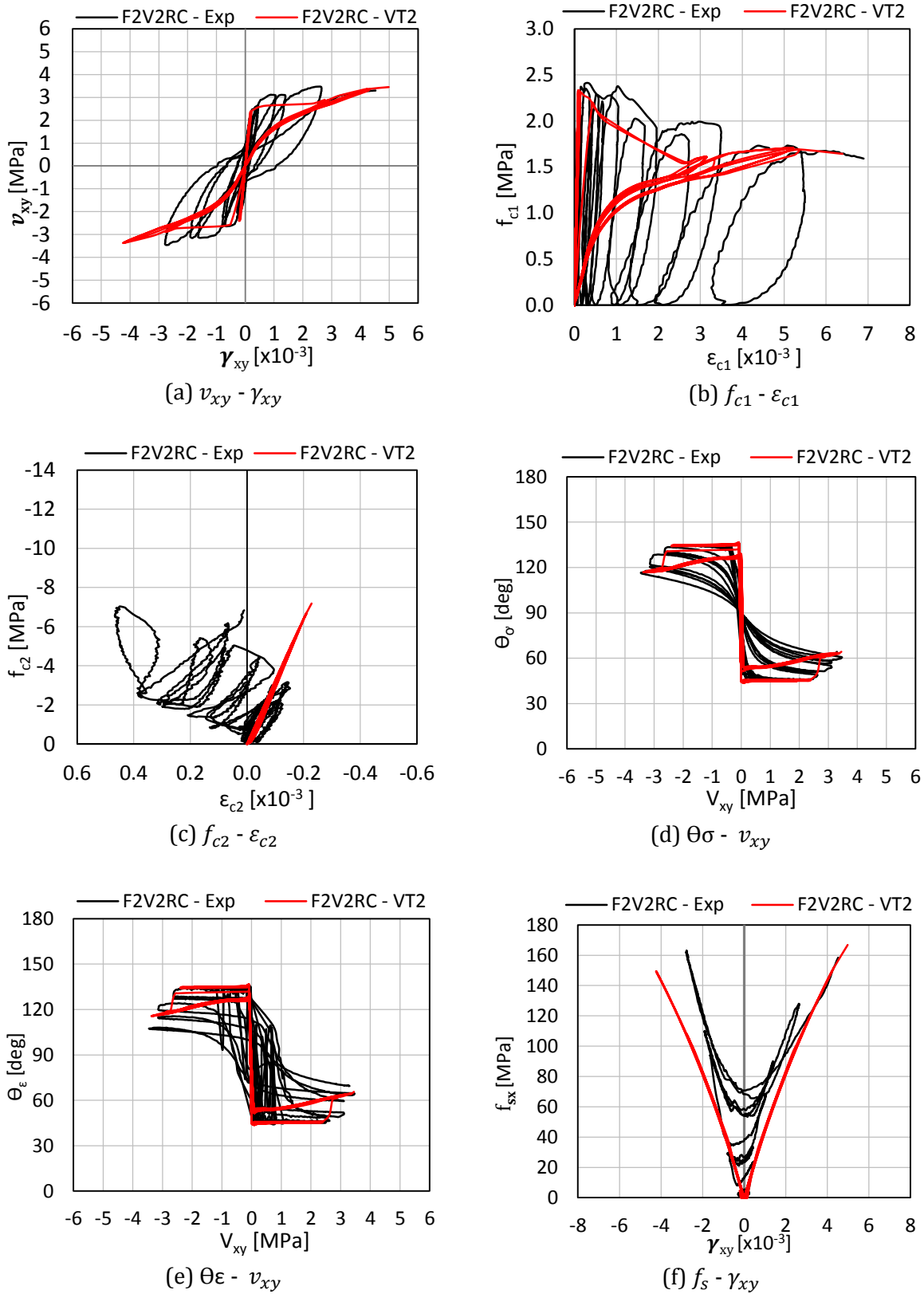
Figure 6-11: Comparison of numerical and experimental response for F2V2RC

Table 6-5: Summary of numerical and experimental results for SFRC panels

Panel	v_u [MPa]	$f_{c1,max}$ [MPa]	$f_{c1,fail}$ [MPa]	$f_{c2,max}$ [MPa]	$f_{sx,max}$ [MPa]	$\dfrac{v_{u,VT2}}{v_{u,exp}}$
F1V1MS	3.03 (3.34)	2.46 (2.52)	1.36 (1.54)	-6.74 (-7.16)	162 (170)	0.91
F1V1RC	3.05 (3.13)	2.41 (2.65)	1.30 (1.03)	-6.97 (-7.48)	170 (195)	0.97
F1V2MS	4.69 (4.65)	2.55 (3.16)	2.32 (2.29)	-9.40 (-9.55)	214 (220)	1.01
F1V2RC	4.66 (4.41)	2.55 (3.18)	2.40 (1.67)	-9.04 (-8.50)	201 (188)	1.06
F1V3MS	5.84 (4.93)	3.14 (3.37)	3.14 (3.15)	-10.86 (-7.71)	233 (138)	1.18
F1V3RC	5.86 (4.72)	3.19 (3.06)	3.19 (2.59)	-10.76 (-8.47)	229 (178)	1.24
F2V2MS	3.42 (3.96)	2.38 (2.77)	1.65 (2.20)	-7.03 (-7.14)	162.2 (149)	0.86
F2V2RC	3.45 (3.47)	2.33 (2.41)	1.64 (1.59)	-7.18 (-7.03)	167 (163)	0.99

Panel	γ_u [x10^{-3}]	$\varepsilon_{c1,fail}$ [x10^{-3}]	$\varepsilon_{c2,fail}$ [x10^{-3}]	$\theta_{\sigma,fail}$ [deg]	$\theta_{\varepsilon,fail}$ [deg]	s_m [mm]	w_m [mm]	$\dfrac{\gamma_{u,VT2}}{\gamma_{u,exp}}$
F1V1MS	5.26 (4.07)	7.23 (8.54)	-0.21 (0.38)	65.7 (65.1)	67.5 (75.1)	52.0 (148.8)	0.37 (0.19)	1.29
F1V1RC	5.70 (4.51)	8.03 (7.61)	0.22 (0.44)	66.3 (69.6)	68.2 (73.0)	52.0 (126.0)	0.42 (0.34)	1.26
F1V2MS	5.98 (4.96)	7.37 (11.27)	-0.28 (0.56)	63.4 (63.8)	64.3 (76.2)	40.0 (54.8)	0.30 (0.18)	1.21
F1V2RC	5.44 (4.60)	6.54 (7.11)	-0.27 (0.04)	62.7 (117.1)	63.5 (108.8)	40.0 (81.4)	0.26 (0.21)	1.18
F1V3MS	6.09 (3.40)	7.01 (3.63)	-0.35 (-0.26)	61.7 (57.4)	62.1 (59.5)	32.0 (96.9)	0.23 (0.12)	1.79
F1V3RC	5.88 (3.72)	6.72 (7.02)	-0.34 (0.18)	61.4 (118.9)	61.8 (109.8)	32.0 (90.0)	0.22 (0.25)	1.58
F2V2MS	4.80 (4.16)	6.09 (6.02)	-0.22 (-0.02)	64.0 (61.0)	65.3 (68.3)	54.0 (74.0)	0.33 (0.25)	1.15
F2V2RC	4.98 (2.75)	6.39 (6.90)	-0.23 (0.01)	64.3 (64.2)	65.6 (69.5)	54.0 (115.0)	0.35 (0.33)	1.81

Note: values in brackets are experimental results
Mean $v_{u,VT2}/v_{u,exp}$ = 1.03 with a CoV of 12.6%; Mean $\gamma_{u,VT2}/\gamma_{u,exp}$ = 1.41 with a CoV of 19.5%

(a) $s_{m,VT2}$ - $s_{m,exp}$
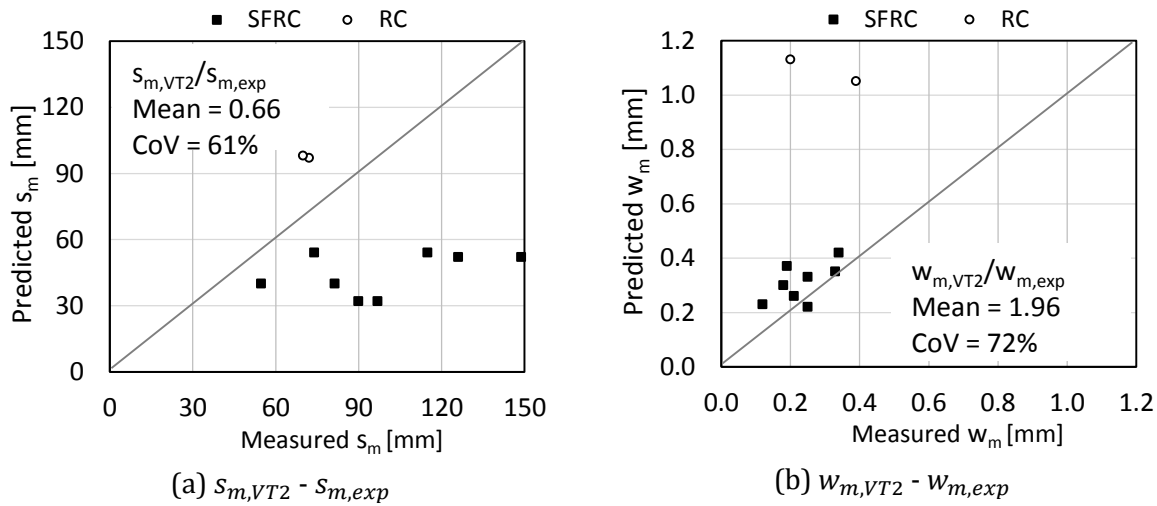
(b) $w_{m,VT2}$ - $w_{m,exp}$

Based on SFRC only: mean $s_{m,VT2}/s_{m,exp}$ = 0.48 with a CoV of 33.6%; mean $w_{m,VT2}/w_{m,exp}$ = 1.41 with a CoV of 27.9%

Figure 6-12: Comparison of numerical and experimental crack spacing and crack widths

Since the monotonic backbone curves for the SFRC panels were well simulated, the numerical models provided good results for the cyclically loaded SFRC panels with regards to the load carrying and deformation capacity; however, the cyclic behaviour was poorly represented. Although the loading branch for the numerical models correctly displayed some stiffness degradation, the unloading branch was peculiar and followed the loading branch. As a result, the energy dissipation capability of SFRC elements was not properly captured. Similar to the plain concrete panels, the influence of crack slips and cracks remaining open during load reversals was not represented; no plastic offsets were exhibited by the SFRC numerical models. Stress degradation as a result of the cycling of load was also not exhibited. Overall, the deficiencies exhibited by the plain concrete cyclic models were also displayed in the SFRC models. However, the poor predictions for the cyclic behaviour of SFRC panels were primarily attributed to the peculiar unloading branch.

6.2.4 Comparison against the previous version of VecTor2

The FE panel analysis results discussed above were based on the most recent version of VecTor2 (April, 2014). A number of changes had been made in the program over the past year for both plain concrete and SFRC. In order to provide a better understanding of the current version, a few of the critical changes are highlighted in this section. A comparison between the panel FE results of the current version and the previous version will be provided as well.

Previously, the calculation of slip at the crack was related to the maximum crack width which was a function of the element size for SFRC. As shown in Figure 6-13, the previous version of VecTor2 increased the maximum crack width as the element size increased; the ratio between the maximum crack width and the average crack width was 1.0 if the element size was less than the average crack spacing, and this ratio linearly increased to the maximum value ($1.7 + 3.4\frac{V_f l_f}{d_f}$) for element sizes up to 1000 mm. This maximum crack width relationship was employed because it produced better numerical results for a number of cases; however, element size effects became inherent in the FE computation and this is contrary to the basic principles of FE modelling.
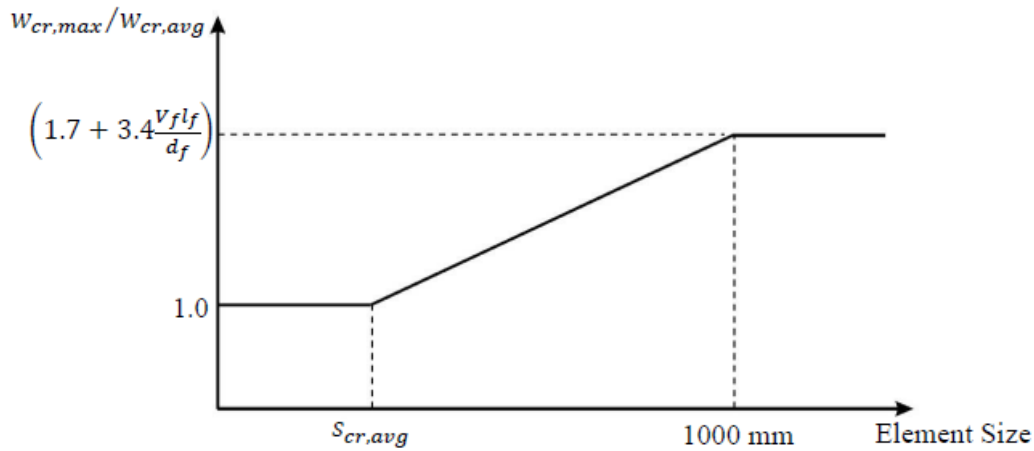
Figure 6-13: Effect of element size on maximum crack width of SFRC in VecTor2 (adapted from Carnovale, 2013)

To illustrate this element size effect, the 890x890 mm panel was modelled using 100 elements (each element was 89x89 mm) (see Figure 6-14 (a)). Note that the average crack spacing near failure was approximately 40 mm and hence, this element size resulted in a maximum crack width between that of the maximum and minimum value. The FE model for panel F1V2MS using 1 element and 100 elements were analyzed using the previous version of VecTor2. As shown in Figure 6-14 (b), the 100 element model produced an ultimate shear strength that was 23.5% higher and an ultimate shear strain that was 210% higher than the 1 element model. To correct this element size effect, the current version of VecTor2 assumed the maximum crack width to be the same as the maximum value ($1.7 + 3.4\frac{V_f l_f}{d_f}$), regardless of the element size, for the slip calculations. With the current version, a 1 element will give the same result as the 100 element model; the effect of element size is thus eliminated.
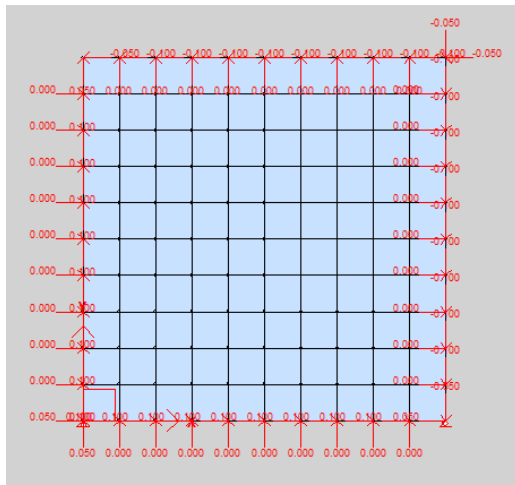
(a) FormWorks model
(100 element panel)
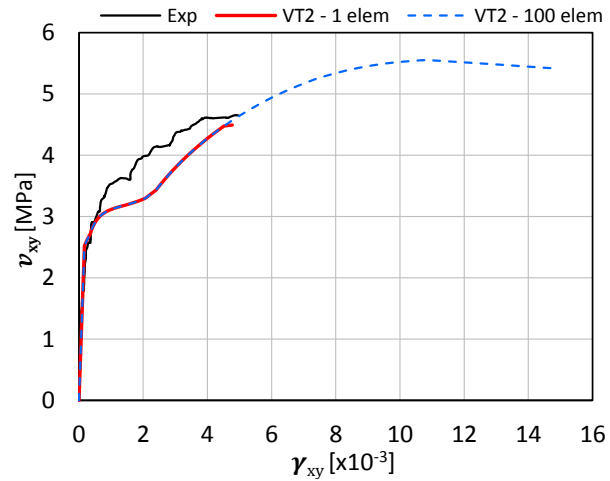
(b) Effect of element size on F1V2MS
(using previous version of VecTor2)

Figure 6-14: Comparison of FE results between different element sizes for F1V2MS (using previous version of VecTor2)

Some changes related to the computation for the average crack spacing were made as well. One of the crack spacing models available in VecTor2 was the CEB-FIP 1978 crack spacing model (CEB/FIP, 1978). The CEB-FIP formulation was also the basis for the SFRC crack spacing model used in VecTor2 (Deluce et al., 2014). In the CEB-FIP formulation, a parameter was used to represent the effective longitudinal bar spacing. In the previous version of VecTor2, this bar spacing parameter was a function of the fourth power of cosine of the reinforcement angle. This was believed to be irrational and the current version replaced the fourth power of cosine with the second power of cosine.

The panels tested in this work were analyzed using both the current version and the previous version of VecTor2. A summary of the results are provided in Table 6-6. Overall, both versions produced good and similar results. The predicted behaviours were nearly identical between the two versions with small differences in the load and deformation capacity; the current version achieved slightly better strength predictions but poorer ductility results.

Table 6-6: Comparison of panel results between the two versions of VecTor2

Panel	Experiment		VT2 – Current		VT2 - Previous		VT2-current/ experiment		VT2-previous/ experiment	
	v_u [MPa]	γ_u [x10^{-3}]	v_u [MPa]	γ_u [x10^{-3}]	v_u [MPa]	γ_u [x10^{-3}]	$\frac{v_{u,VT2}}{v_{u,exp}}$	$\frac{\gamma_{u,VT2}}{\gamma_{u,exp}}$	$\frac{v_{u,VT2}}{v_{u,exp}}$	$\frac{\gamma_{u,VT2}}{\gamma_{u,exp}}$
CMS	5.99	8.58	5.33	9.38	5.26	9.05	0.89	1.09	0.88	1.05
CRC	5.63	9.77	5.36	8.68	5.29	8.19	0.95	0.89	0.93	0.83
F1V1MS	3.34	4.07	3.03	5.26	2.92	4.38	0.91	1.29	0.87	1.08
F1V1RC	3.13	4.51	3.05	5.70	2.89	4.36	0.97	1.26	0.92	0.97
F1V2MS	4.65	4.96	4.69	5.98	4.49	4.78	1.01	1.21	0.97	0.96
F1V2RC	4.41	4.60	4.66	5.44	4.49	4.72	1.06	1.18	1.02	1.03
F1V3MS	4.93	3.40	5.84	6.09	5.63	5.14	1.18	1.79	1.14	1.51
F1V3RC	4.72	3.72	5.86	5.88	5.70	5.04	1.24	1.58	1.21	1.35
F2V2MS	3.96	4.16	3.42	4.80	3.29	3.96	0.86	1.15	0.83	0.95
F2V2RC	3.47	2.75	3.45	4.98	3.29	3.66	0.99	1.81	0.95	1.33
						Mean	1.01	1.33	0.97	1.11
						CoV	12.3%	22.9%	12.4%	19.6%

Since the changes made to VecTor2 were primarily related to the crack spacing and crack width, it is of interest to examine the average crack spacing and average crack width at failure. Values for these two parameters based on the experiment, current version of VecTor2, and previous version of VecTor2 are shown in Table 6-7 and plotted in Figure 6-15. With regards to the crack spacing, the current version predictions were slightly better for normal concrete, but significantly worse for SFRC. For the average crack width, both versions produced nearly identical results. Although the current version of VecTor2 did not produce better predictions for all cases, it represented a step toward a more rational FE approach and was used for the following coupling beam analysis.

Table 6-7: Comparison of crack spacing and crack width between the two versions of VecTor2

Panel	Experiment		VT2 – Current		VT2 - Previous		VT2-current/ experiment		VT2-previous/ experiment	
	s_m [mm]	w_m [mm]	s_m [mm]	w_m [mm]	s_m [mm]	w_m [mm]	$\frac{s_{m,VT2}}{s_{m,exp}}$	$\frac{w_{m,VT2}}{w_{m,exp}}$	$\frac{s_{m,VT2}}{s_{m,exp}}$	$\frac{w_{m,VT2}}{w_{m,exp}}$
CMS	72	0.20	97	1.13	102	1.14	1.35	5.65	1.41	5.70
CRC	70	0.39	98	1.05	104	1.03	1.40	2.69	1.49	2.64
F1V1MS	149	0.19	52	0.37	72	0.41	0.35	1.95	0.48	2.16
F1V1RC	126	0.34	52	0.42	72	0.41	0.41	1.24	0.57	1.21
F1V2MS	55	0.18	40	0.30	54	0.30	0.73	1.67	0.99	1.67
F1V2RC	81	0.21	40	0.26	54	0.29	0.49	1.24	0.66	1.38
F1V3MS	97	0.12	32	0.23	43	0.24	0.33	1.92	0.44	2.00
F1V3RC	90	0.25	32	0.22	42	0.23	0.36	0.88	0.47	0.92
F2V2MS	74	0.25	54	0.33	72	0.35	0.73	1.32	0.97	1.40
F2V2RC	115	0.33	54	0.35	71	0.31	0.47	1.06	0.62	0.94
						Mean	0.66	1.96	0.81	2.00
						CoV	60.7%	71.5%	47.8%	70.5%

(a) $s_{m,VT2}$ - $s_{m,exp}$

(b) $w_{m,VT2}$ - $w_{m,exp}$
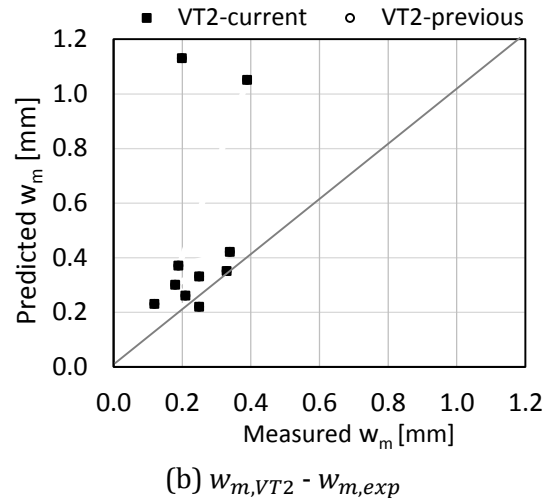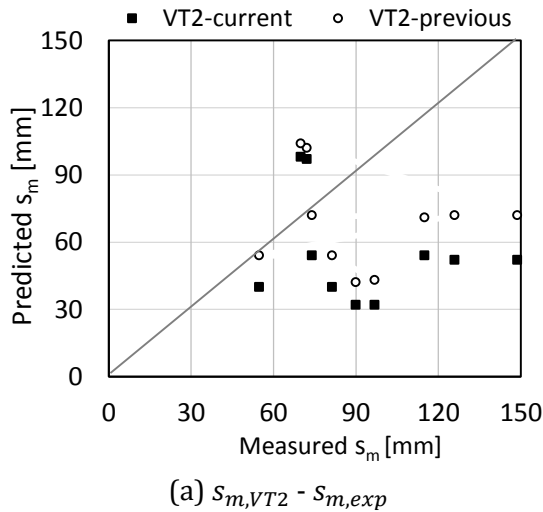
Figure 6-15: Comparison of crack spacing and crack width between the two versions of VecTor2

6.3 Modelling of Coupling Beams

6.3.1 Description of the Experiment

To investigate the adequacy of the available constitutive models modelling the cyclic response of SFRC structures, a series of large-scale slender SFRC coupling beams were also modelled with VecTor2. These coupling beams were tested at the University of Michigan by Setkit (2012). As mentioned in the literature review in Chapter 2, these tests were undertaken to evaluate the seismic behaviour of SFRC coupling beams with simplified reinforcement detailing. High performance fibre-reinforced concrete (HPFRC), a subclass of SFRC with the ability to achieve strain hardening response under direct tension, was used as a means to reduce the need for diagonal bars and confinement reinforcement. Given that SFRC members subjected to reversed cyclic loading are likely used as a ductile structural element, such as coupling beams or shear walls in a seismic force-resisting system, this test series serves as a practical verification study.

The experiment concluded that SFRC coupling beams subjected to large shear reversals $(0.7 \sqrt{f'_c}$ (MPa) to $0.9 \sqrt{f'_c}$ (MPa)) exhibited stable hysteretic behaviour despite the significantly simplified reinforcement detailing. The use of SFRC material provided sufficient confinement to the diagonal reinforcement which allowed noticeable relaxation in confinement reinforcement. Test results also suggested that elimination of diagonal bars while maintaining large drift capacity was possible by using SFRC. The experiment demonstrated that for design purposes, the shear stress contribution from HPFRC material can be conservatively estimated to be $0.42\sqrt{f'_c}$ (MPa).

Six large-scale coupling beams were constructed and tested for this experiment. As shown in Table 6-8, the experimental variables included beam aspect ratio (2.75 and 3.30), reinforcement layout (with and without diagonal reinforcement), and material type (SFRC and normal concrete). Five of the coupling beams were constructed of SFRC with varying simplified reinforcement layout compared to that of code-compliant reinforced concrete coupling beams. One additional normal concrete coupling beam (CB-4) with the same reinforcement detailing as one of the SFRC coupling beams (CB-2) was made to better evaluate the influence of the concrete material on coupling beam behaviour. A dosage of 1.5% RC80/30BP fibres (l_f = 30

mm, d_f = 0.38 mm, f_{uf} = 2300 MPa), the same fibre types as used for the panels, was used to produce the HPFRC.

Table 6-8: Overview of Setkit coupling beams

Test ID	Aspect ratio	Diagonal reinforcement	Target Shear Stress [MPa]	Concrete Material
CB-1	2.75	Yes	$0.83\sqrt{f'_c}$	SFRC
CB-2	2.75	Yes	$0.67\sqrt{f'_c}$	SFRC
CB-3	3.30	Yes	$0.67\sqrt{f'_c}$	SFRC
CB-4	2.75	Yes	$0.67\sqrt{f'_c}$	Concrete
CB-5	3.30	No	$0.67\sqrt{f'_c}$	SFRC
CB-6	2.75	No	$0.67\sqrt{f'_c}$	SFRC

Table 6-9: Reinforcement layout of Setkit Coupling Beams

Test ID	Diag. bars (per group)	Stirrups (at mid-span)	Transverse reinf. (at end)	Dowel bars (per face)	Long. bars (per side)	Intermediate long. Bars
CB-1	2 #6	#3 @ 203	#3 @ 70	4 #4	4 #5	4 #3
CB-2	2 #6	#3 @ 165	#4 @ 83	4 #4	2 #5	4 #3
CB-3	2 #6	#3 @ 152	#4 @ 76	4 #4	2 #6	4 #3
CB-4	2 #6	#3 @ 165	#4 @ 83	4 #4	2 #5	4 #3
CB-5	-	#4 @ 146	#4 @ 76	4 #4	4 #6	4 #4
CB-6	-	#4 @ 146	#4 @ 76	4 #4	2 #6 & 2 #5	4 #4

Note: the transverse reinforcement spacing is in mm

The reinforcement used for the coupling beams were categorized into six groups: diagonal bars (to provide shear resistance and to prevent sliding shear failure), stirrups at mid-span (to provide shear resistance), transverse reinforcement at the beam ends (to provide column-type confinement and to ensure sufficient plastic rotation), dowel bars at the beam-wall interface (to force plastic rotation away from the wall), top and bottom longitudinal reinforcement (to provide primary flexure resistance), and intermediate longitudinal reinforcement (to control cracks). Typically, confinement reinforcement around the diagonal bars was needed to prevent buckling of the diagonal reinforcement; these were eliminated due to the confinement effect from the SFRC material. The reinforcement details of each group for each specimen are

summarized in Table 6-9. The reinforcement layout of each specimen is shown in Figure 6-18 to Figure 6-23 of the next section.

All of the coupling beams were precast and then embedded into the concrete base blocks. The top and bottom concrete blocks, simulating the adjacent structural walls, were heavily reinforced and cast-in-place with normal concrete after insertion of the precast beam. The bottom block was anchored to the strong floor, while the top block was connected to the actuator. The dimensions of the top block and the bottom block were 2074 x 610 mm with a depth of 457 mm and 1829 x 610 mm with a depth of 457 mm, respectively. The dimension of the coupling beams were 1676 x 610 mm or 1676 x 508 mm with a depth of 152 mm. Two vertical rigid links were used to connect the top block to the ground in order to limit the rotation of the top block and to force a double curvature for the coupling beam.
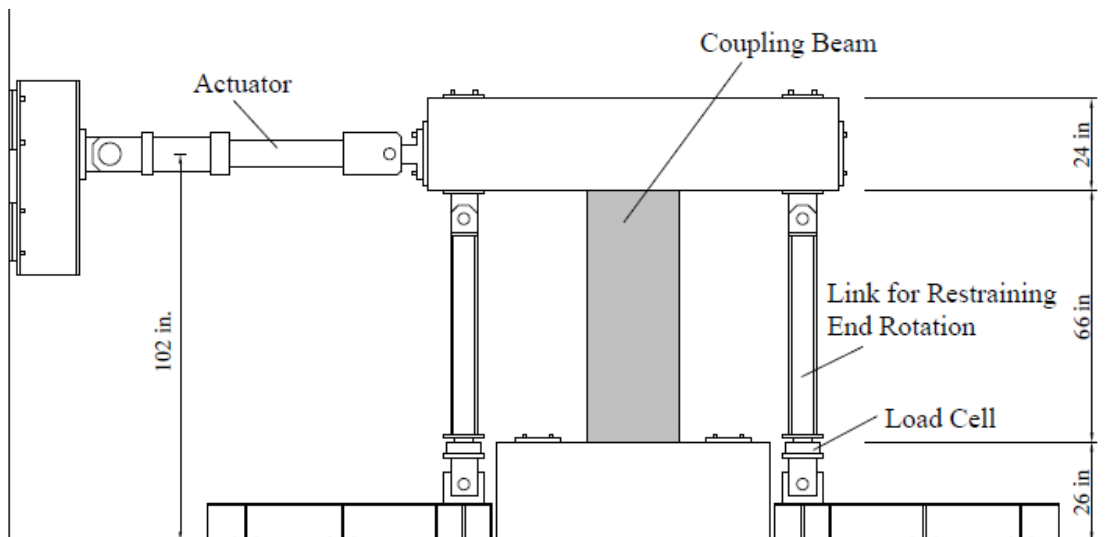
Figure 6-16: Coupling beam test setup (adapted from Setkit, 2012)

6.3.2 Modelling of the Coupling Beams

Guidelines for modelling the SFRC coupling beams using VecTor2 will be provided in this section. Consistent with the philosophy behind VecTor2, the general approach was to create models that can produce accurate results with minimal modelling complexity and computational cost. This involved producing FE models that were geometrically consistent with the experiment and included minimal manual inputs regarding the material properties and behaviour models.

The most challenging aspect of constructing the numerical models was the modelling of the beam reinforcements. As shown in Figure 6-17, the transverse reinforcement was uniformly distributed over their region and hence was modelled as smeared reinforcement. All of the other beam reinforcement was modelled as discrete reinforcement using truss elements. The vertical (y-direction) beam reinforcement was created using FormWorks' automatic meshing method; a method that can conveniently create the concrete elements and the reinforcement truss elements simultaneously. In order to produce uniformly rectangular concrete elements, the diagonal reinforcement had to be manually created by connecting the nodes with truss elements after the mesh was structured. All of the discrete reinforcement had a perfect bond between the bar and the adjacent concrete element. For the concrete blocks, the x- and y-direction reinforcement was smeared. All of the reinforcement' yield stress and ultimate stress were based on the reported reinforcement coupon test results. Although the reinforcement' strain parameters were not reported, a value of 10×10^{-3} mm/mm for the strain hardening point, 125×10^{-3} mm/mm for the ultimate strain, and 200,000 MPa for the Young's Modulus were recommended by Setkit (2014) and used for all of the reinforcement of the numerical models. As always, the steel fibres were modelled as smeared reinforcement.

To accommodate the different smeared reinforcement in the different regions, three types of concrete were generated. Concrete type 1 (coloured yellow in Figure 6-17) represented concrete in the middle portion of the coupling beam; the smeared reinforcement in this zone included steel fibres and stirrups. Concrete type 2 (coloured green) represented the end regions of the beam; the smeared reinforcement in this zone included steel fibres and transverse column-type confinement reinforcement. Lastly, the top and bottoms blocks were represented by concrete type 3 (coloured purple); the smeared reinforcement in this concrete comprised of x- and y-direction reinforcement. Since the actual reinforcement layout for these heavily reinforced blocks were not reported, a reinforcement ratio of 3.0% was assumed for both the x- and y-direction. The compressive strength of all concrete types was based on the reported cylinder test results. All concrete had a maximum aggregate size of 13 mm. Details of the concrete types, including their smeared components, and discrete reinforcement for each specimen are shown in Table 6-11 to Table 6-15.

(a) CB-2	(b) CB-5
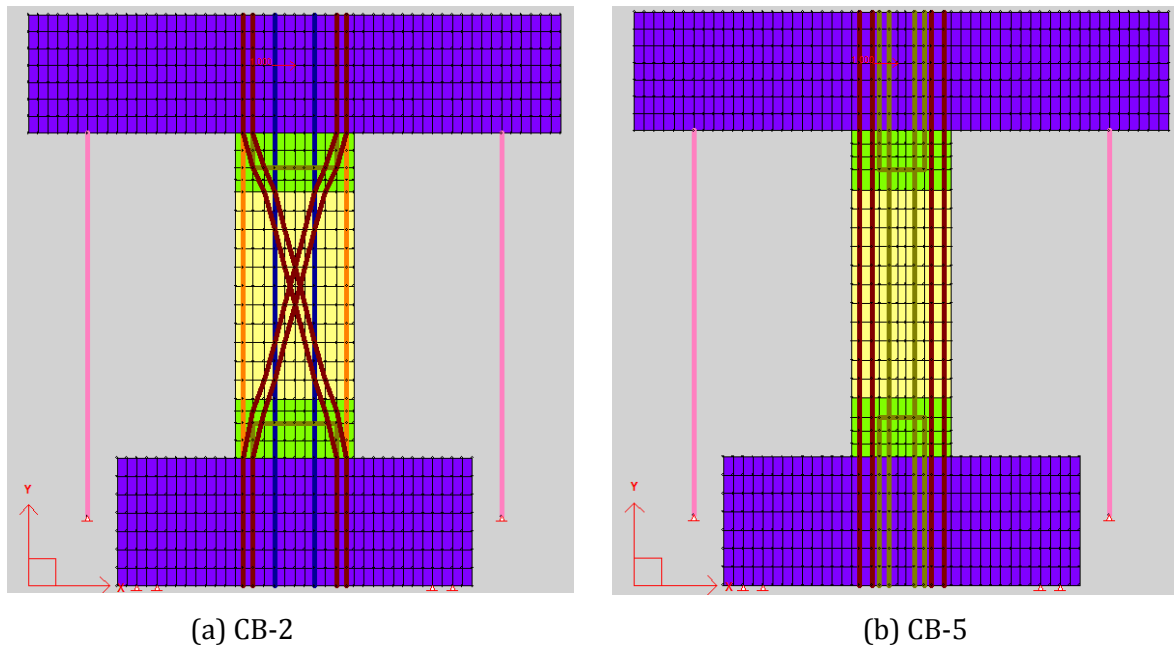
Figure 6-17: FormWorks model of the coupling beams

The rigid steel links used to restrict the rotation of the top block were modelled as truss elements. Details regarding these rigid links were not provided and their stiffness was difficult to estimate. An area of 1500 mm², yield strength of 250 MPa, and ultimate strength of 690 MPa were assigned to each link. These values were chosen because they led to levels of axial loads in the coupling beam that were consistent with the experimental values (i.e. 150 – 400 kN) without any noticeable yielding of the rigid links. Setkit (2012) recommended these values for FE modelling as well.

The mesh structure consisted of rectangular elements with an average size of 50x75 mm (x -, y-direction). This element size allowed an uniformly rectangular mesh to be structured and was deemed to be the most efficient; reducing the mesh size by half achieved similar predictions but increased the computational time considerably.

The boundary conditions consisted of hinge supports. Four nodes at the bottom of the concrete block were restrained in their translational degree of freedom through the use of hinge supports; the location of these four hinges correspond to the location of the threaded rods used to anchor the bottom block to the strong floor. The lower ends of the two rigid links were also hinge supported.
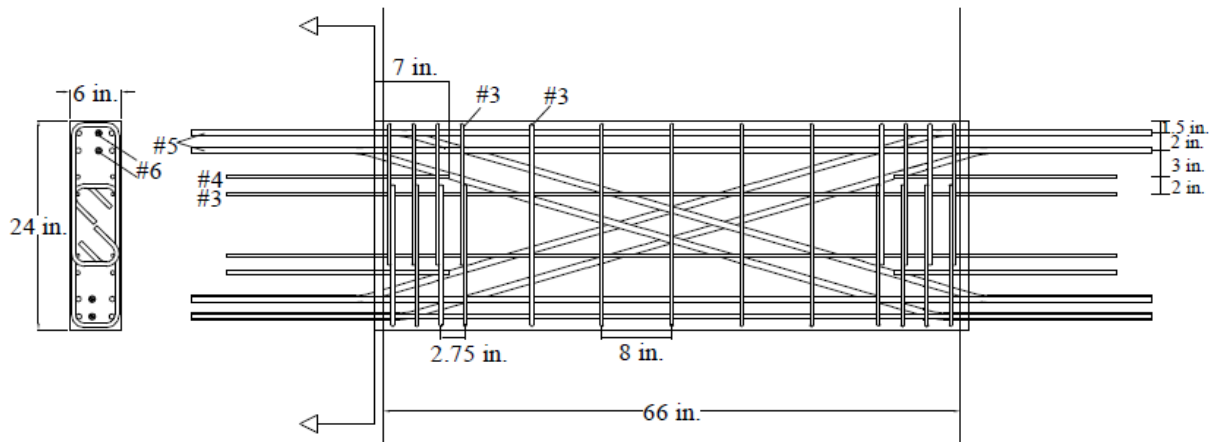
Figure 6-18: Reinforcement detailing for CB-1 (adapted from Setkit, 2012)

Table 6-10: Concrete and discrete reinforcement details for the FE model of CB-1

Concrete type	Region	Thickness [mm]	f'_c [MPa]	Smeared Reinforcement Components			
				Representation	Size	Direction (from x-axis)	Ratio (%)
1	Coupling Beam (mid)	152.4	49.6	Stirrup	#3	0	0.46
				Fibre	V_f = 1.5%, Dramix RC80/30BP		
2	Coupling Beam (end)	152.4	49.6	Stirrup	#3	0	1.33
				Fibre	V_f = 1.5%, Dramix RC80/30BP		
3	Blocks	457	37.9	Flexural reinf.	#5	0	3.0
				Stirrup	#5	90	3.0

Reinforcement Type	Steel area* [mm²]	Diameter [mm]	f_y [MPa]	f_u [MPa]	Representation
1	142	9.5	414	634	2 #3 intermediate long. bars
2	258	12.7	421	696	2 #4 dowel bars
3	400	15.9	421	683	2 #5 long. Bars
4	284	19.1	510	655	1 #6 diagonal bar
5	1500	19.1	250	690	Rigid link

* the cross-sectional area may represent multiple layers of reinforcement
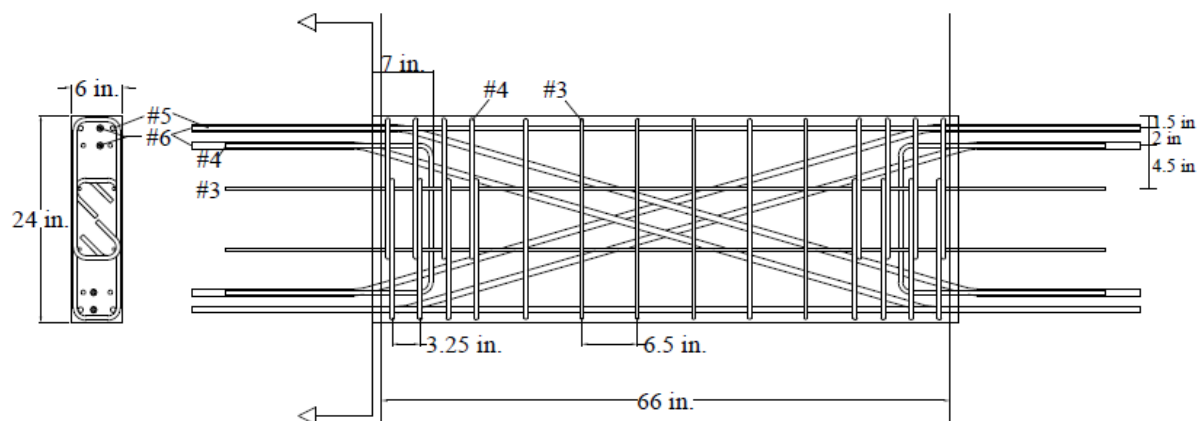
Figure 6-19: Reinforcement detailing for CB-2 (adapted from Setkit, 2012)

Table 6-11: Concrete and discrete reinforcement details for the FE model of CB-2

Concrete type	Region	Thickness [mm]	f'_c [MPa]	Smeared Reinforcement Components			
				Representation	Size	Direction (from x-axis)	Ratio (%)
1	Coupling Beam (mid)	152.4	59.3	Stirrup	#3	0	0.57
				Fibre	V_f = 1.5%, Dramix RC80/30BP		
2	Coupling Beam (end)	152.4	59.3	Stirrup	#4	0	2.0
				Fibre	V_f = 1.5%, Dramix RC80/30BP		
3	Blocks	457	32.0	Flexural reinf.	#5	0	3.0
				Stirrup	#5	90	3.0

Reinforcement Type	Steel area* [mm²]	Diameter [mm]	f_y [MPa]	f_u [MPa]	Representation
1	142	9.5	414	634	2 #3 intermediate long. bars
2	258	12.7	414	683	2 #4 dowel bars
3	400	15.9	421	689	2 #5 long. Bars
4	284	19.1	572	703	1 #6 diagonal bar
5	1500	19.1	250	690	Rigid link

* the cross-sectional area may represent multiple layers of reinforcement
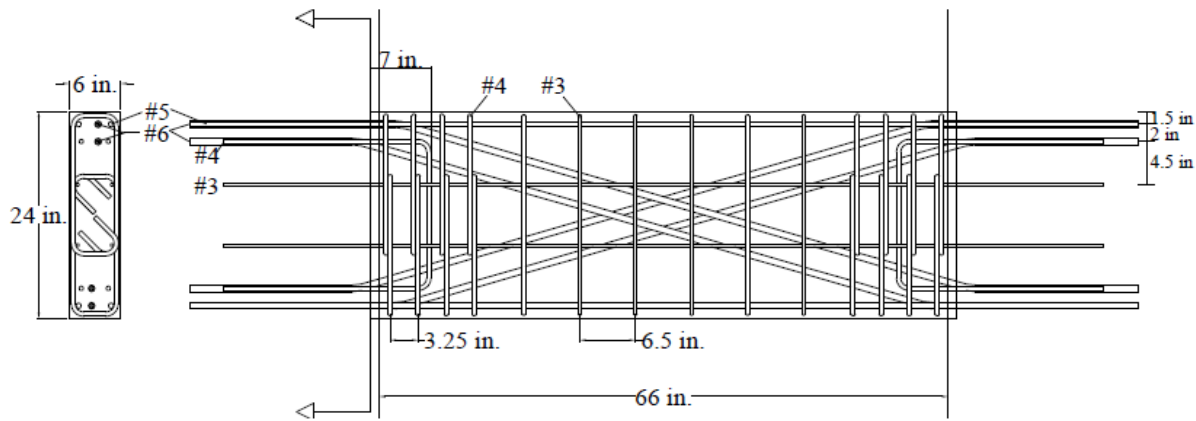
Figure 6-20: Reinforcement detailing for CB-3 (adapted from Setkit, 2012)

Table 6-12: Concrete and discrete reinforcement details for the FE model of CB-3

Concrete type	Region	Thickness [mm]	f'_c [MPa]	Smeared Reinforcement Components			
				Representation	Size	Direction (from x-axis)	Ratio (%)
1	Coupling Beam (mid)	152.4	61.4	Stirrup	#3	0	0.61
				Fibre	V_f = 1.5%, Dramix RC80/30BP		
2	Coupling Beam (end)	152.4	61.4	Stirrup	#4	0	2.2
				Fibre	V_f = 1.5%, Dramix RC80/30BP		
3	Blocks	457	40.0	Flexural reinf.	#5	0	3.0
				Stirrup	#5	90	3.0

Reinforcement Type	Steel area* [mm²]	Diameter [mm]	f_y [MPa]	f_u [MPa]	Representation
1	142	9.5	448	745	2 #3 intermediate long. bars
2	258	12.7	531	662	2 #4 dowel bars
3	400	15.9	545	689	2 #5 long. Bars
4	284	19.1	545	689	1 #6 diagonal bar
5	1500	19.1	250	690	Rigid link

* the cross-sectional area may represent multiple layers of reinforcement
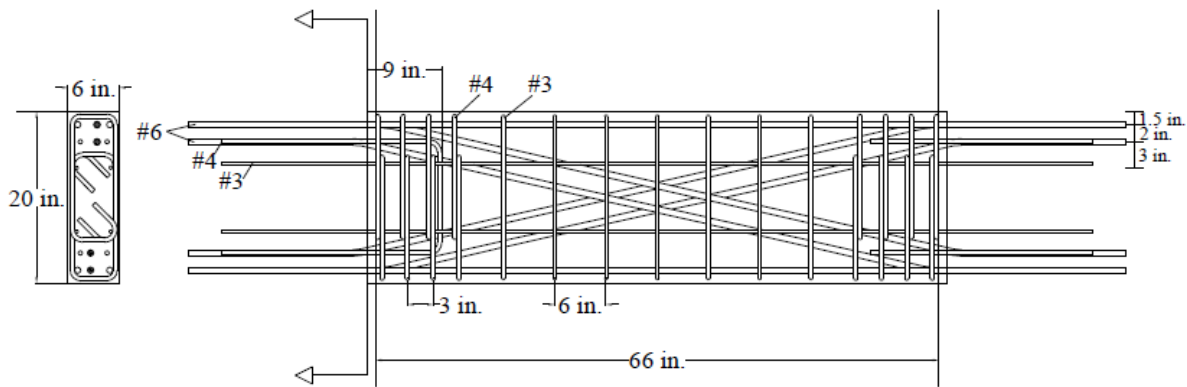
Figure 6-21: Reinforcement detailing for CB-4 (adapted from Setkit, 2012)

Table 6-13: Concrete and discrete reinforcement details for the FE model of CB-4

Concrete type	Region	Thickness [mm]	f'_c [MPa]	Smeared Reinforcement Components			
				Representation	Size	Direction (from x-axis)	Ratio (%)
1	Coupling Beam (mid)	152.4	62.1	Stirrup	#3	0	0.57
				Fibre	V_f = 1.5%, Dramix RC80/30BP		
2	Coupling Beam (end)	152.4	62.1	Stirrup	#4	0	2.0
				Fibre	V_f = 1.5%, Dramix RC80/30BP		
3	Blocks	457	42.7	Flexural reinf.	#5	0	3.0
				Stirrup	#5	90	3.0

Reinforcement Type	Steel area* [mm²]	Diameter [mm]	f_y [MPa]	f_u [MPa]	Representation
1	142	9.5	427	676	2 #3 intermediate long. bars
2	258	12.7	441	689	2 #4 dowel bars
3	400	15.9	476	738	2 #5 long. Bars
4	284	19.1	448	689	1 #6 diagonal bar
5	1500	19.1	250	690	Rigid link

* the cross-sectional area may represent multiple layers of reinforcement
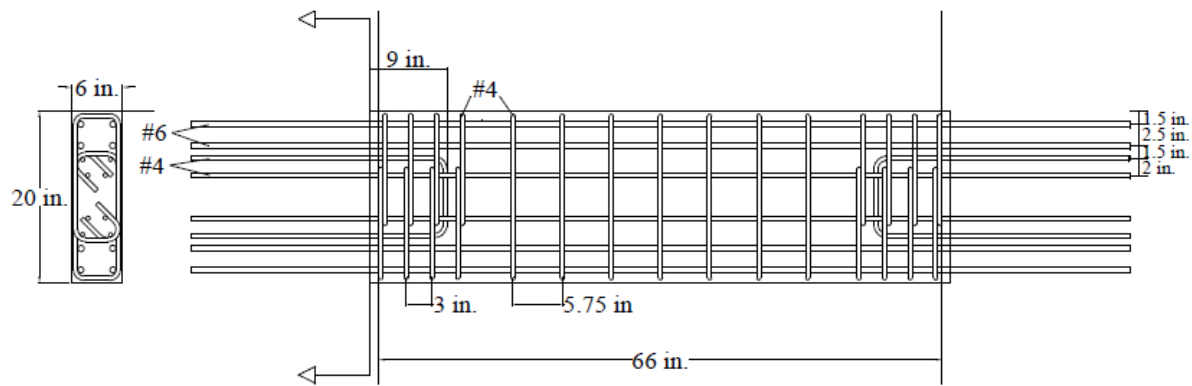
Figure 6-22: Reinforcement detailing for CB-5 (adapted from Setkit, 2012)

Table 6-14: Concrete and discrete reinforcement details for the FE model of CB-5

Concrete type	Region	Thickness [mm]	f'_c [MPa]	Smeared Reinforcement Components			
				Representation	Size	Direction (from x-axis)	Ratio (%)
1	Coupling Beam (mid)	152.4	68.3	Stirrup	#4	0	1.15
				Fibre	V_f = 1.5%, Dramix RC80/30BP		
2	Coupling Beam (end)	152.4	68.3	Stirrup	#4	0	2.2
				Fibre	V_f = 1.5%, Dramix RC80/30BP		
3	Blocks	457	42.7	Flexural reinf.	#5	0	3.0
				Stirrup	#5	90	3.0

Reinforcement Type	Steel area* [mm²]	Diameter [mm]	f_y [MPa]	f_u [MPa]	Representation
2	258	12.7	531	662	2 #4 dowel bars or 2 #4 intermediate long. bars
4	568	19.1	545	689	2 #6 long. bars
5	1500	19.1	250	690	Rigid link

* the cross-sectional area may represent multiple layers of reinforcement
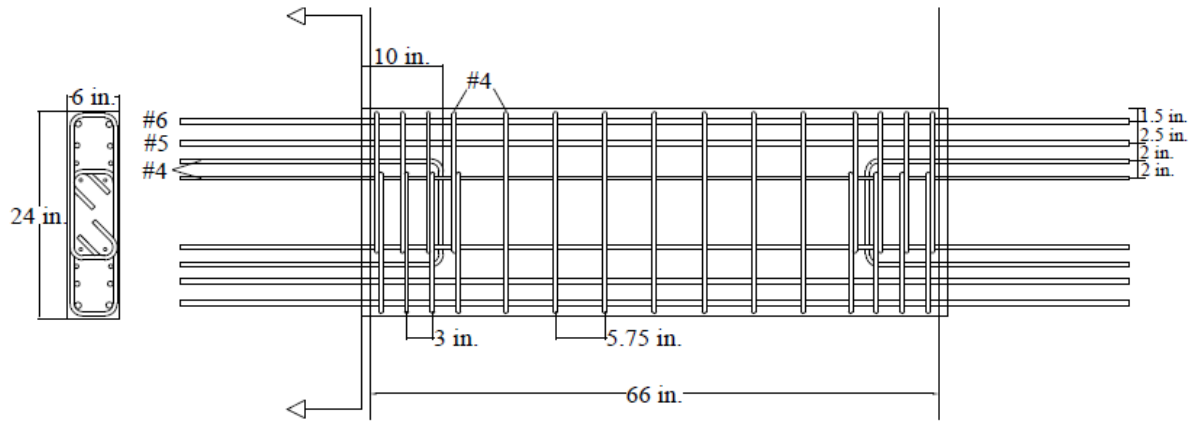
Figure 6-23: Reinforcement detailing for CB-6 (adapted from Setkit, 2012)

Table 6-15: Concrete and discrete reinforcement details for the FE model of CB-6

Concrete type	Region	Thickness [mm]	f'_c [MPa]	Smeared Reinforcement Components			
				Representation	Size	Direction (from x-axis)	Ratio (%)
1	Coupling Beam (mid)	152.4	67.6	Stirrup	#4	0	1.15
				Fibre	V_f = 1.5%, Dramix RC80/30BP		
2	Coupling Beam (end)	152.4	67.6	Stirrup	#4	0	2.2
				Fibre	V_f = 1.5%, Dramix RC80/30BP		
3	Blocks	457	37.9	Flexural reinf.	#5	0	3.0
				Stirrup	#5	90	3.0

Reinforcement Type	Steel area* [mm²]	Diameter [mm]	f_y [MPa]	f_u [MPa]	Representation
2	258	12.7	586	696	2 #4 dowel bars or 2 #4 intermediate long. bars
3	400	15.9	441	669	2 #5 long. bars
4	568	19.1	524	648	2 #6 long. bars
5	1500	19.1	250	690	Rigid link

* the cross-sectional area may represent multiple layers of reinforcement

The load was applied as a horizontal displacement at the mid-height of the top block. As shown in Figure 6-24, the experimental loading protocol consisted of approximately two sets of load increments: before 1.0% drift, the drift increment was approximately 0.25% with double cycles, after 1.0% drift, 0.5% drift increments were performed with single cycles. For simplicity, the FE model employed a loading protocol consisting of single cycles with a cycle drift increment of 0.5%. Applying a non-uniform loading protocol to the numerical model would add significant unjustified complications. A load step of 8 mm (0.5% drift) was used in order to minimize the computational cost; reducing the load step by half would double the computation time with similar to identical results.

To prevent any subjective tweaking, the behaviour models used for all of the numerical models were the same as the ones used for the panel FE analyses. In other words, the default models were used except for the pre-peak compression model (Popovics High Strength Model was used) and the tension softening model (exponential model was used).
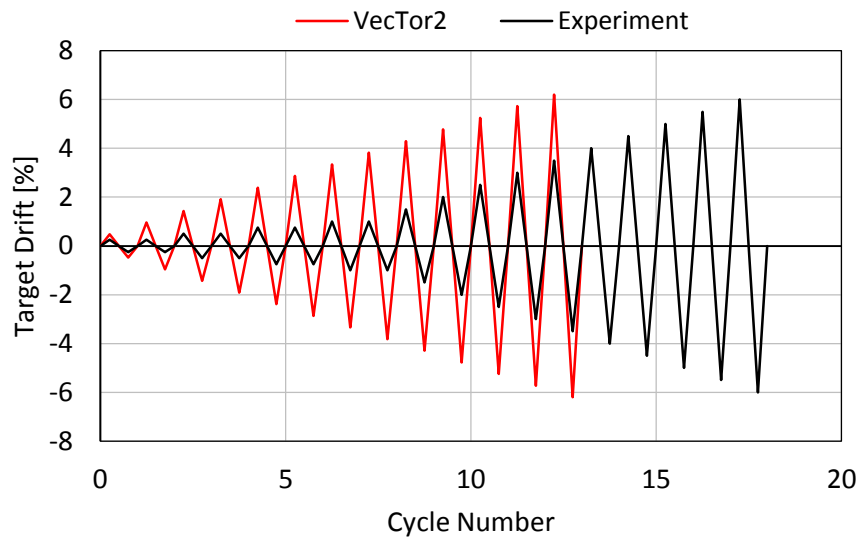
Figure 6-24: Comparison between the numerical and experimental loading protocol

6.3.3 Analysis Results

The FE models were numerically stable until the peak load decreased by approximately 10 – 30%. The time required for the computation of each model was approximately 30 minutes on a standard Windows 7 32-bit desktop computer. The experimental and numerical shear force versus drift responses are shown in Figure 6-24, while Table 6-16 shows a comparison of the

ultimate shear force (V_u), maximum drift for the positive and negative direction (Δ_{pos} and Δ_{neg}), and the total maximum drift from both directions (Δ_{sum}).

Overall, the behaviour of the coupling beams was well predicted using VecTor2. The force capacity prediction was reasonably accurate and within 15% for all specimens; the mean predicted-to-experimental shear force was 1.08 with a CoV of 2.8%. The drift capacity was defined as the largest drift level attained before a strength loss of 20% or more (i.e. when $V \leq 0.8V_u$). Similar to the panel FE analysis, the deformation capacity prediction for the beams was less accurate than the force prediction due to the complex interaction between crack opening and reinforcement yielding or rupturing near peak loads. Nevertheless, the drift capacity predictions were reasonably good; the mean predicted-to-experimental total drift capacity was 0.93 with a CoV of 21%.

For specimens CB-1 through CB-5, the predicted drift capacity was within the acceptable limit of 20%. The model for specimen CB-6, however, underpredicted the drift capacity by 36%. The reason for this underestimation was the significant shear sliding along the SFRC beam-RC wall interface during the experiment which was most pronounced for beams without diagonal reinforcements, CB-5 and CB-6. Setkit noted that the shear sliding was initiated by concentrated deformations due to bond slip and shear slip at the beam-wall interface and this behaviour was not properly captured in the numerical model. The experimental data suggested the shear sliding was most noticeable in CB-6 and resulted in a drift increase of approximately 2 to 3% in both directions.

The cyclic behaviour, including the stiffness degradation, pinching of the hysteretic loop, softness of the unloading branch, and plastic offset, was overall well captured. For all specimens, the numerical models' unloading branch was slightly less stiff; the loading branch, on the other hand, was stiffer. This led to an overall underestimation of the pinching of the hysteresis and is believed to be caused by VecTor2's inability to fully capture the sliding shear displacement at the bottom beam-wall interface. Since this shear sliding was most pronounced for CB-6, the pinching of hysteresis from the experiment was most noticeable and the underestimation of this effect from the numerical model was also most significant for this specimen. It is important to note that the coupling beams were precast, not monolithically constructed with the wall, and hence, a cold joint was created at the beam-wall interface and

this weaker plane would lead to greater shear sliding. The effect of cold joints was not considered in the numerical model.

One of the most noticeable differences between the numerical and experimental results was the over-predicted stiffness in the early loading cycles. This was believed to be primarily caused by the stiffness of the rigid steel links used to restrict the rotation of the top block (Setkit, 2012). Setkit noted the stiffness of these links was much lower during the early loading cycles and this reduced stiffness may be due to slack within the rigid link connections. Since these links were modelled as truss elements with a constant stiffness that led to levels of axial loads consistent with that of the experiment during the later loading cycles (i.e. 150-400 kN), the initial flexibility of the rigid links was not represented in the numerical model. As expected, numerical models with more flexible links (i.e. a smaller link cross-sectional area) yielded lower initial stiffness and lower cyclic envelope curve, but this envelope curve generally converged with that of the stiff link model near the maximum drift.

Comparisons between the crack patterns near the maximum drift from the numerical model and the experiment are shown in Figure 6-26. The crack patterns and overall damage were well captured with the use of VecTor2. Except for CB-4, all of the specimens exhibited large flexural cracks with minor shear damage at the middle third of the beam, consistent with the experiment. CB-4 was the only specimen made using normal concrete. As a result, significant shear cracks were developed in the middle area of the beam and large flexural cracks were exhibited at the beam ends, similar to the experiment. The location of the failure plane for majority of the specimens was near the beam ends, whereas the test indicated the failure plane was near the termination of the dowel bars. For specimens CB-2 and CB-4, VecTor2 correctly predicted the location of the failure plane.

The failure modes of the coupling beams were reasonably well predicted by VecTor2. Except for specimen CB-4, the numerical model indicated that all of the beams experienced rupturing of the main longitudinal bars and diagonal bars (if applicable) at the beam ends with some concrete crushing at the corners of the beam. For specimen CB-4, large diagonal cracks were developed at the middle area of the beam which led to significant shear slips at failure. Note that during the experiment, the test was stopped after significant loss of strength was observed and hence, the test results did not indicate a clear mode of failure for some specimens. Nevertheless, the overall condition and vital signs of the coupling beams at the maximum drift

was similar to the numerical predictions. For example, the test indicated CB-1 and CB-6 experienced rupturing of the main longitudinal reinforcement, while CB-3 exhibited fracturing of the diagonal reinforcement.

The above demonstrated that VecTor2 can provide adequate predictions for the behaviour of both plain concrete coupling beams and SFRC coupling beams. The comparison between CB-2 and CB-4 is of particular interest. These two coupling beams had identical reinforcement layout and material properties, but CB-4 was made of normal concrete while CB-2 was made using SFRC; the benefits and influences of SFRC on beam behaviour can be effectively demonstrated through these two beams. The test showed that the addition of 1.5% fibre content (RC80/30BP fibres) in the concrete matrix improved the peak shear force by 13% and increased the total maximum drift by 64%. This improved behaviour was very well captured by VecTor2, further verifying the adequacy of the SFRC constitutive model employed.

Table 6-16: Summary of numerical and experimental results for Setkit coupling beams

Key attributes				Experimental			Numerical			Comparison	
Test ID	Aspect ratio	Diagonal bars	Concrete Material	V_u [kN]	Δ_{pos} [%]	Δ_{neg} [%]	V_u [kN]	Δ_{pos} [%]	Δ_{neg} [%]	$\dfrac{V_{u,VT2}}{V_{u,exp}}$	$\dfrac{\Delta_{sum,VT2}}{\Delta_{sum,exp}}$
CB-1	2.75	Yes	SFRC	583	5.6	-5.2	645	6.2	-6.2	1.11	1.15
CB-2	2.75	Yes	SFRC	516	5.3	-3.9	578	4.3	-3.8	1.12	0.88
CB-3	3.30	Yes	SFRC	512	5.5	-4.5	534	5.7	-5.7	1.04	1.15
CB-4	2.75	Yes	Concrete	458	3.0	-2.6	491	2.9	-2.4	1.07	0.94
CB-5	3.30	No	SFRC	516	6.9	-6.8	541	5.7	-5.7	1.05	0.84
CB-6	2.75	No	SFRC	560	6.5	-5.7	598	4.0	-3.8	1.07	0.64

Mean $V_{u,VT2}/V_{u,exp}$ = 1.08 with a CoV of 2.8%; Mean $\Delta_{sum,VT2}/\Delta_{sum,exp}$ = 0.93 with a CoV of 21%
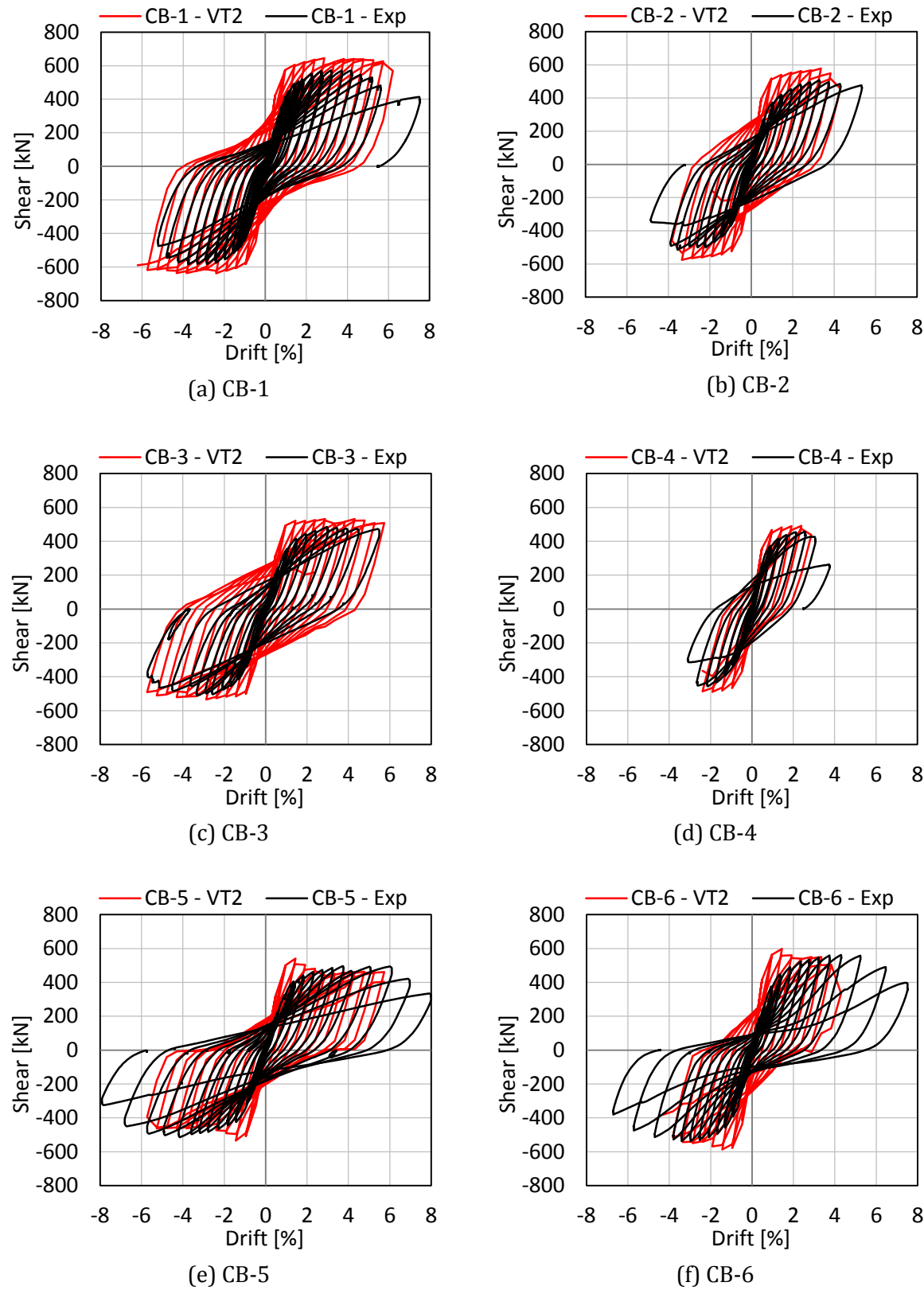
Figure 6-25: Comparison of numerical and experimental response for Setkit coupling beams
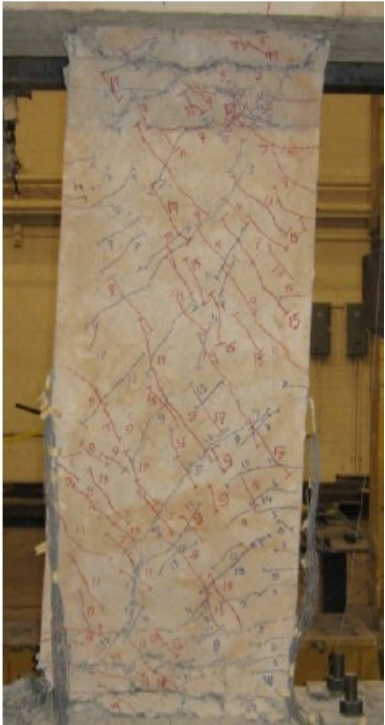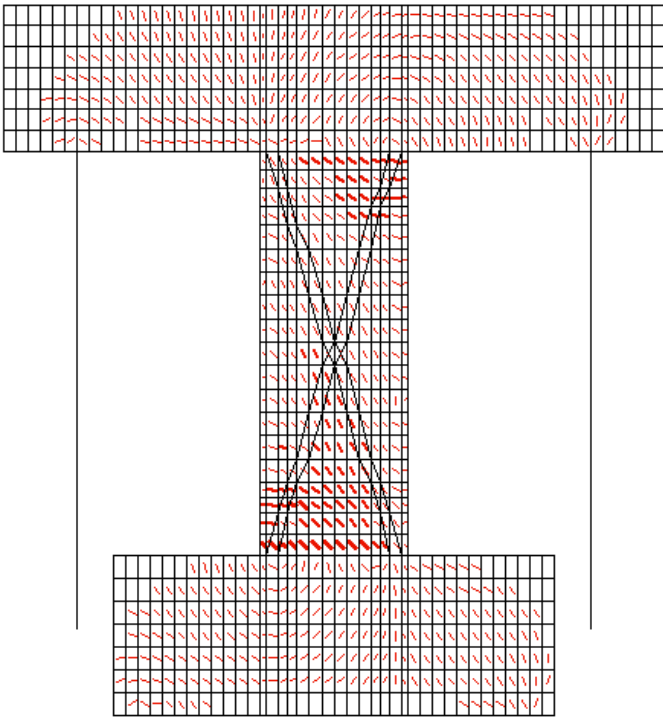
(a) CB-1
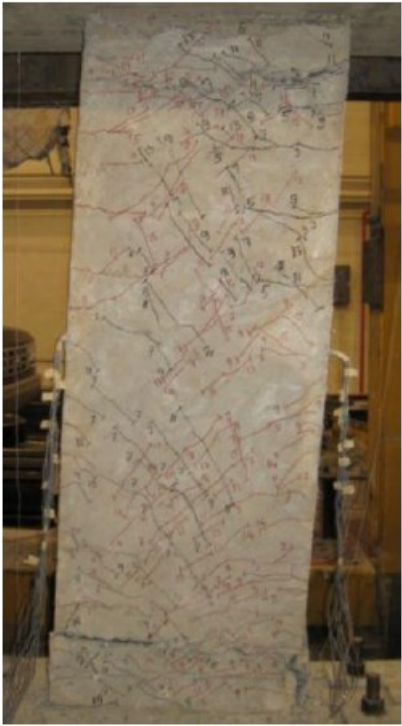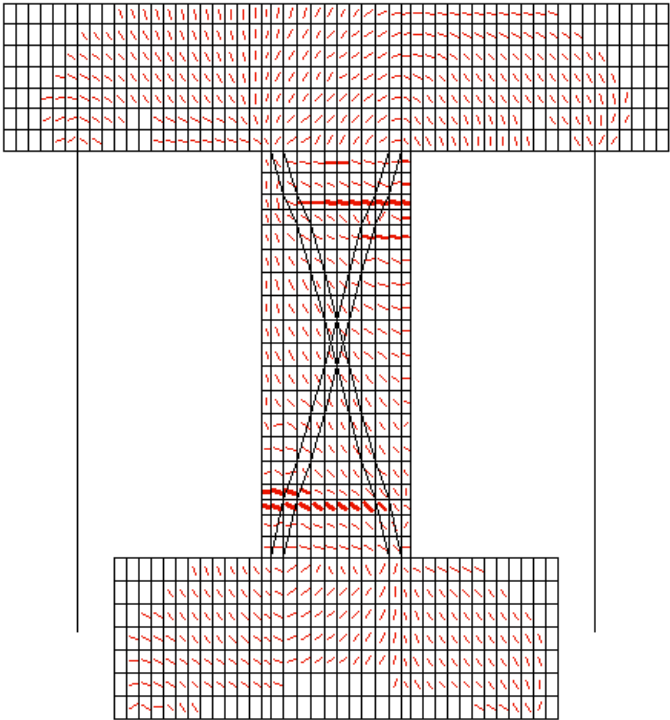
(a) CB-2
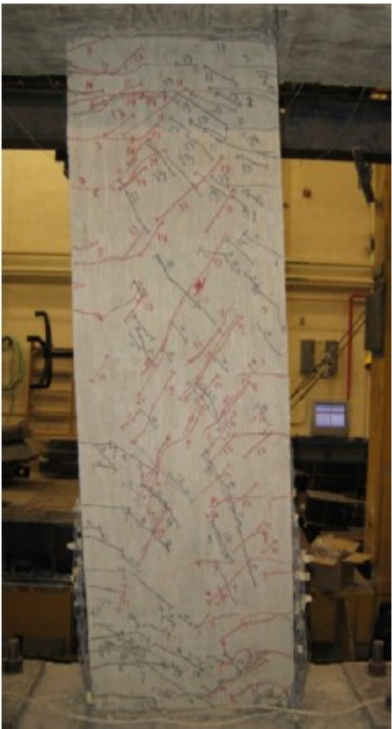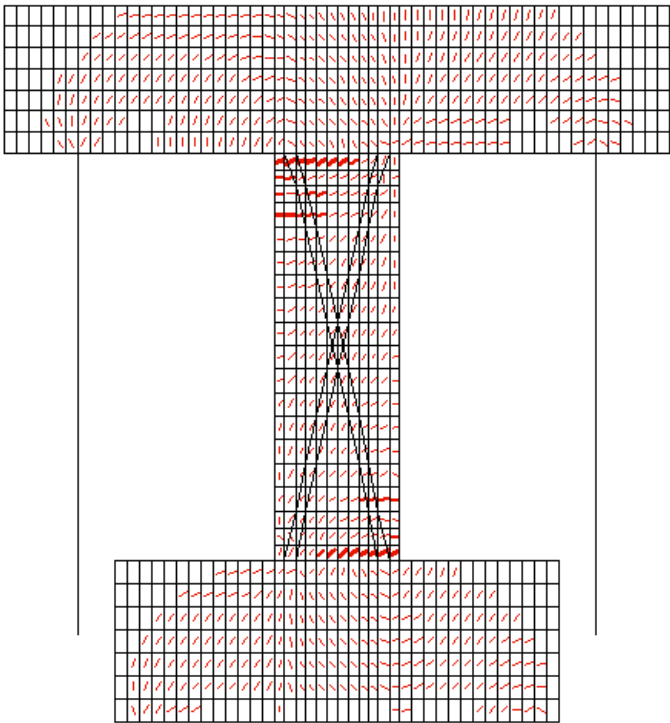
(a) CB-3
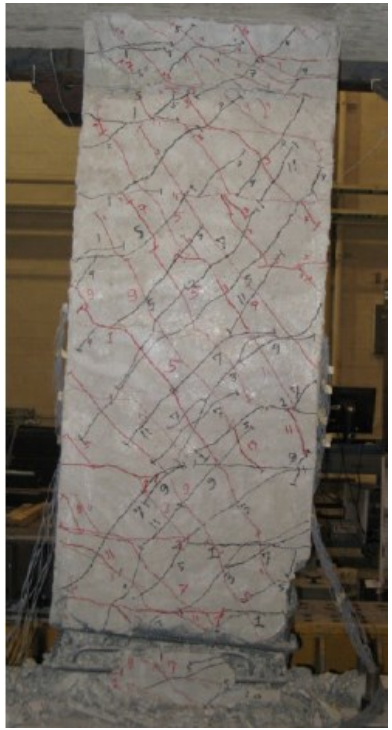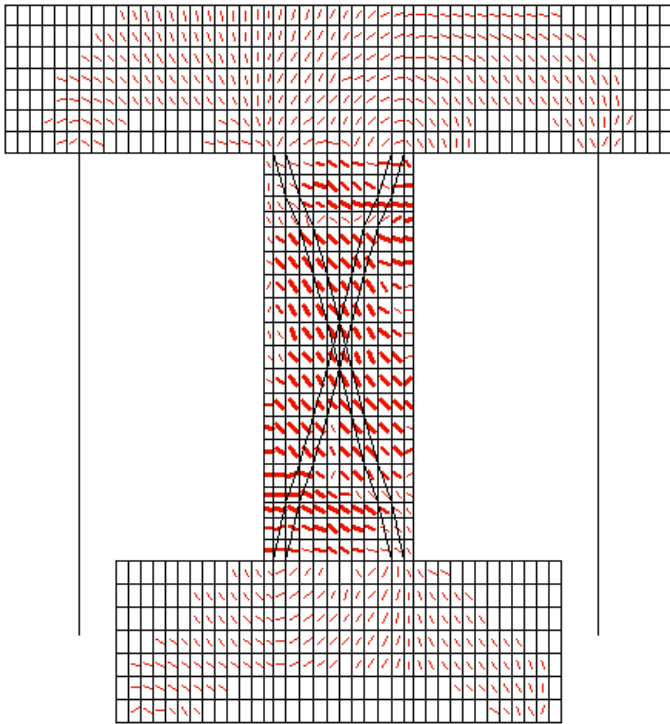
(a) CB-4
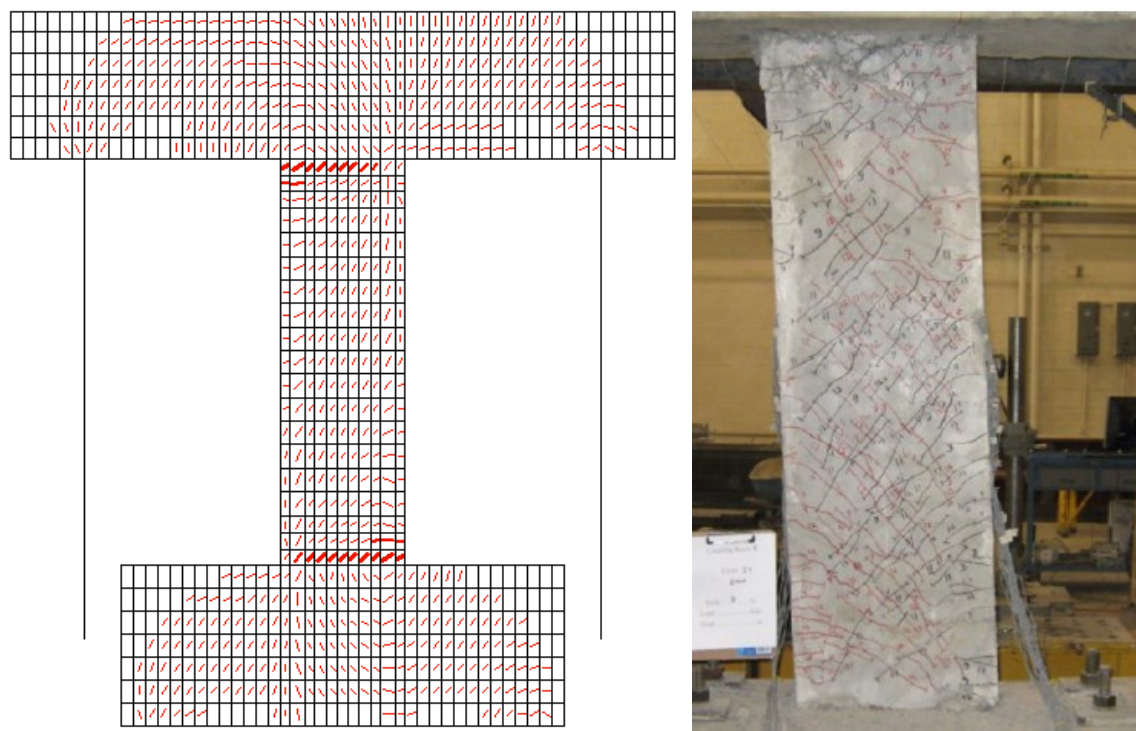
(a) CB-5
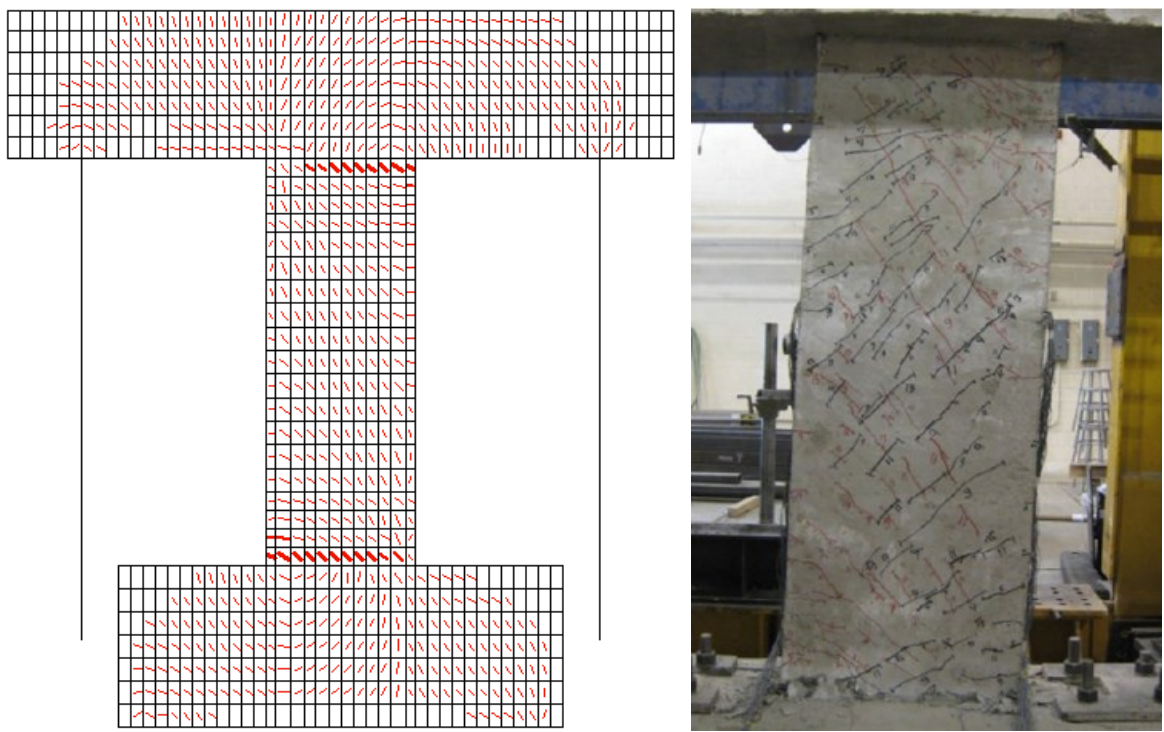
(a) CB-6

Figure 6-26: Comparison of numerical and experimental crack patterns near failure

6.3.4 Comparison against the previous version of VecTor2

The FE analyses of the coupling beams were performed using the current version of VecTor2 (April, 2014). As mentioned in Section 6.2.4, some changes were made for the current version and it was of interest to compare the results between the two versions of VecTor2.

The shear force versus drift response between the two VecTor2 versions and the experiment are shown in Figure 6-27 and are summarized in Table 6-17. For the FE panel analysis, the previous version of VecTor2 produced a lower force and deformation capacity. For the member level analysis, on the other hand, the previous version produced a higher force and lower deformation capacity. This discrepancy was reasonable as the behaviour at the macroscopic level is largely influenced by reinforcement yielding, and the impact of localized damage predictions is more apparent at the element level. For the coupling beams, the current version of VecTor2 produced better predictions for both the force and deformation capacity, the resulting cyclic envelope curve was also closer to that of the experiment. These improved results further highlight the importance of using rational relationships for development FE programs, as opposed to empirical relationships.

Table 6-17: Summary of coupling beam results between the two versions of VecTor2

Test ID	Experiment			VT2 - Current			VT2 - Previous			VT2-current/ experiment		VT2-previous/ experiment	
	V_u [kN]	Δ_{pos} [%]	Δ_{neg} [%]	V_u [kN]	Δ_{pos} [%]	Δ_{neg} [%]	V_u [kN]	Δ_{pos} [%]	Δ_{neg} [%]	$\frac{V_{u,VT2}}{V_{u,exp}}$	$\frac{\Delta_{sum,VT2}}{\Delta_{sum,exp}}$	$\frac{V_{u,VT2}}{V_{u,exp}}$	$\frac{\Delta_{sum,VT2}}{\Delta_{sum,exp}}$
CB-1	583	5.6	-5.2	645	6.2	-6.2	695	5.7	-5.3	1.11	1.15	1.19	1.02
CB-2	516	5.3	-3.9	578	4.3	-3.8	640	3.8	-3.8	1.12	0.88	1.24	0.83
CB-3	512	5.5	-4.5	534	5.7	-5.7	555	4.8	-4.8	1.04	1.15	1.09	0.96
CB-4	458	3.0	-2.6	491	2.9	-2.4	492	3.3	-2.4	1.07	0.94	1.07	1.03
CB-5	516	6.9	-6.8	541	5.7	-5.7	547	5.3	-5.3	1.05	0.84	1.06	0.77
CB-6	560	6.5	-5.7	598	4.0	-3.8	626	4.3	-4.3	1.07	0.64	1.12	0.70
									Mean	1.08	0.93	1.13	0.88
									CoV	2.8%	21%	6.4%	15.4%
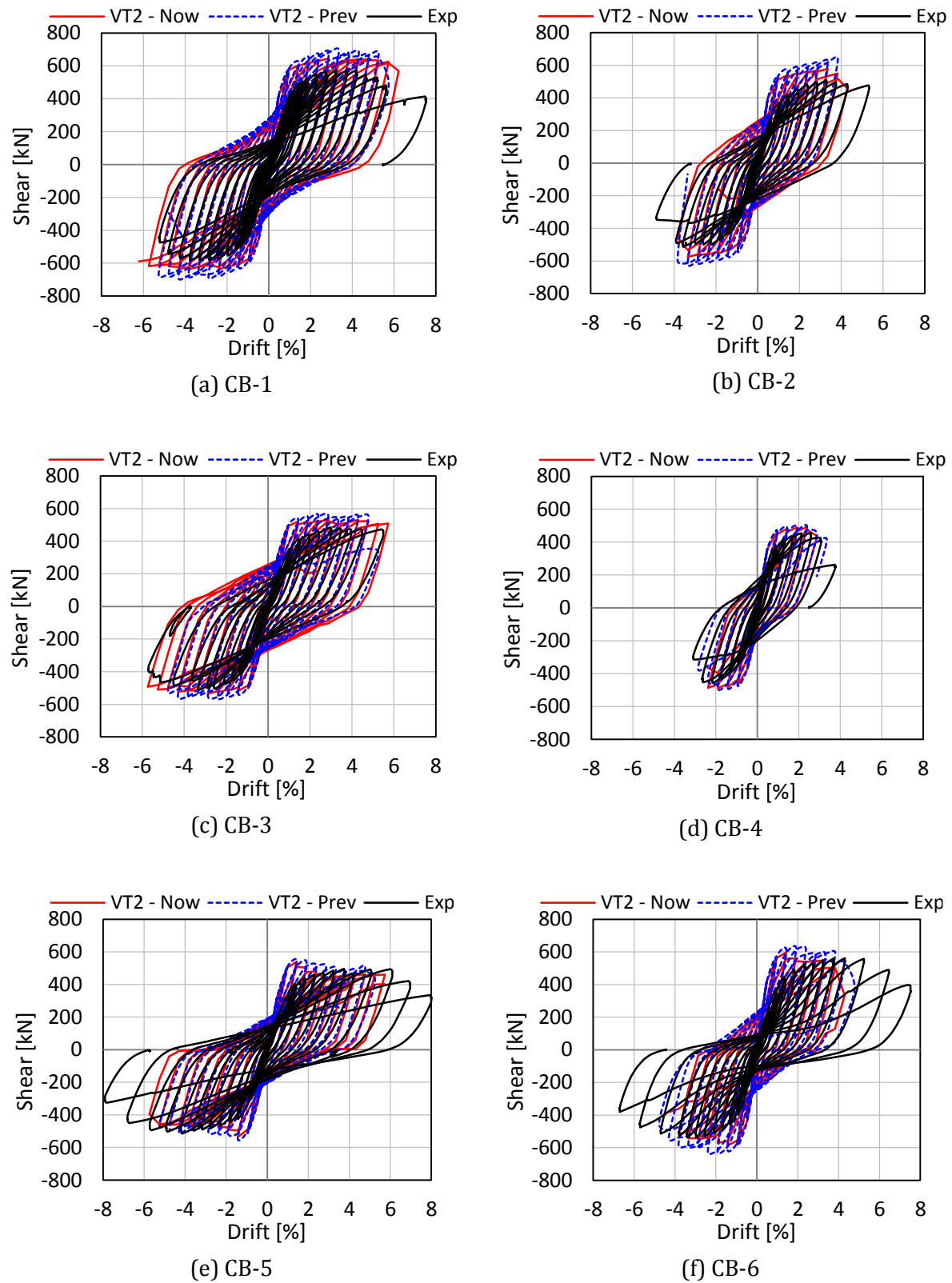
Figure 6-27: Comparison of coupling beam results between the two versions of VecTor2

6.4   Summary of Finite Element Modelling

The adequacy of the currently available constitutive models in VecTor2 was examined through the FE modeling of the panels tested in this work and the coupling beams tested by Setkit. Overall, the default behavioural model in VecTor2 provided adequate predictions for the specimens. The force capacity of all specimens was well predicted, while the accuracy of the deformation capacity predictions was more scattered but adequate.

Despite the good capacity predictions, significant more research is required for modelling the cyclic behaviour of concrete. Through the modeling of panels, it was revealed that VecTor2 was not able to capture the crack slips and cracks remaining open during load reversals and hence, plastic offsets were not exhibited for both plain concrete and SFRC. Further, the stress degradation as a result of the cycling of load was not accounted for in VecTor2. The unloading branch of SFRC panels followed the loading branch and was peculiar; investigations are required to correct this.

The overall cyclic behaviour of the Setkit coupling beams was well predicted. The underestimation of the drift capacity was due to shear sliding at the beam-wall interface which was not properly captured by VecTor2. Despite the well represented cyclic behaviour at the member level, which was largely influenced by reinforcement yielding, proper representation of the nonlinear hysteretic response of concrete is critical for predicting the localized behaviour, load capacity, and failure mode of some structures (Vecchio, 1999).

<div align="center">

Chapter 7
Conclusions and Recommendations

</div>

7. Conclusions and Recommendations

7.1   Objectives

The objective of this thesis was to investigate the behaviour of SFRC under reversed cyclic loading. An experimental study was undertaken accordingly, to examine the cyclic shear behaviour of SFRC. For this purpose, a series of ten large-scale in-plane panel specimens were tested using University of Toronto's Panel Element Tester. The parameters of study included the fibre volume fraction, fibre diameter, and loading protocol. To supplement the panel tests, the mechanical properties of the concrete used were also experimentally studied. Specifically, cylinder compression tests, uniaxial direct tension tests, and modulus of rupture tests were performed to study the compressive, tensile, and flexural behaviour, respectively.

The analytical study undertaken was intended to investigate the accuracy of currently available constitutive models in capturing the monotonic and cyclic behaviour of shear-critical SFRC members. The study was performed using a nonlinear finite element analysis program, VecTor2. The results from the panel tests were used to verify the adequacy of the program at the element level. The series of slender SFRC coupling beams recently tested at the University of Michigan was also modelled to examine VecTor2's accuracy at the macroscopic level.

7.2   Conclusions

From this research program, the following conclusions can be drawn:

1. Overall, the results of the three material tests and panel tests were consistent and corroborated one another. Trends established for the parameters studied were generally observed in all tests.
2. For end-hooked steel fibres, a high dosage (fibre volume fraction of 1.0 or 1.5%) of thin fibres (fibre aspect ratio of 79) provided the greatest structural improvements.
3. The pre-cracked response of concrete was in general not affected by fibre addition.

4. Under direct tension, increasing the number of fibres by increasing the fibre content or decreasing the fibre diameter led to improved post-cracked behaviour. The improvement was primarily in the form of higher residual stress and toughness.

5. For fibres used in this work, strain hardening was achieved only in the flexural tests; however, the tension test did exhibit hardening-type characteristics for concrete with higher fibre contents.

6. Based on the panel tests, SFRC with higher fibre contents exhibited higher maximum shear stress, better crack control characteristics, and reduced cyclic deterioration.

7. SFRC constructed of thicker fibres led to poorer performance in terms of shear resistance and crack control.

8. Under reversed cyclic loading, SFRC panels exhibited stable hysteretic response with insignificant strength degradation and no noticeable changes in ductility. With the exception for panels with a fibre content of 0.5%, all panels' monotonic backbone curve closely matched the reversed cyclic envelope curve.

9. Concrete with a fibre volume fraction of 0.5% and no transverse reinforcement cannot provide adequate shear resistance, especially under reversed cyclic loading conditions; the degree of cyclic deterioration was noticeably higher for this concrete.

10. SFRC panels containing a fibre content of 1.5% managed to withstand at least 82% of the maximum shear stress sustained by the conventionally reinforced panels with a transverse reinforcement ratio of 0.42%.

11. This strength capacity together with its tolerance for cyclic damages suggested short thin end-hooked steel fibres with a high fibre volume fraction may be used in place of low percentages of conventional transverse steel reinforcement for capacity based designed members, regardless of the loading protocol.

12. SFRC panels reached at most 58% of the maximum shear strain sustained by the conventionally reinforced panels.

13. This lack of ductility suggested the use of steel fibres for the full replacement of significant amounts of transverse reinforcement (e.g. 0.42%), especially for deformation critical members such as ductile structural elements, is not advisable.

14. Significant reduction in the transverse steel requirements with the addition of steel fibres is practical for both force controlled and deformation controlled elements.

15. Demonstrated through the use of VecTor2, the Modified Compression Field Theory and Disturbed Stress Field Model together with the Simplified Diverse Embedment Model was found to be a viable approach to model SFRC response to general loading.

16. The default behavioural model in VecTor2 provided accurate predictions for the monotonic backbone curve of SFRC and plain concrete. The force capacity was accurately represented while the deformation capacity predictions were more scattered but adequate.

17. However, plastic offset during load reversals and strength degradation as a result of the cycling of load for panel elements was not captured with the use of VecTor2.

18. The default behavioural models in VecTor2 consistently underestimated the contribution of steel fibre to concrete tensile stress.

19. VecTor2 provided reasonable predictions for the cracking characteristics of the panels, but did noticeably underestimated SFRC's mean crack spacing and overestimated normal concrete's mean crack width.

20. Changes made over the past year to VecTor2 generally led to improved predictions.

7.3 Recommendations for Future Work

As a result of this thesis, the following recommendations for future work are made:

1. A more comprehensive database of cyclically loaded SFRC panel tests should be collected to further assess the influence of fibre aspect ratio and fibre diameter on the cyclic behaviour of SFRC.

2. A reassessment of the SFRC tension models in VecTor2 should be performed to address the underestimation of contribution of steel fibre reinforcement to concrete tensile stress.

3. A model for the effects of crack remaining open and crack slip on the plastic offset in cyclically loaded concrete elements is required. The effects of fibre addition should also be accounted for in this model.

4. Investigations should be performed to address the peculiar unloading branch of SFRC elements in VecTor2.

References

ACI Committee 318. (2005). Building Code Requirements for Structural Concrete (ACI 318-05) and Commentary. *Amercain Concrete Institute, Farmington Hills, MI*, 430 p.

ACI Committee 318. (2008). Building Code Requirements for Structural Concrete (ACI 318-08) and Commentary. *Amercain Concrete Institute, Farmington Hills, MI*, 436 p.

ACI Committee 544. (1988). Design Considerations for Steel Fiber Reinforced Concrete. *ACI Structural Journal, 85*(5), September 1988, pp.563-579.

ACI Committee 544. (1993). Guide for Specifying, Proportioning, Mixing, Placing, and Finishing Steel. *ACI Materials Journal, 90*(1), January-February 1993, pp.94-101.

ACI Committee 544. (2008). State-of-the-art Report on Fiber Reinforced Concrete - ACI 544.1R-96 (Reapproved 2002). *ACI Manual of Concrete Practice*, Part 6, pp. ACI544.1R-7 - ACI544.1R-23.

Adebar, P., Mindess, S., St.-Pierre, D., & Olund, B. (1997). Shear Tests of Fiber Concrete Beams without Stirrups. *ACI Structural Journal, 94*(1), January-February 1997, pp. 68-76.

Aoude, H., Belghiti, M., Cook, W. D., & Mitchell, D. (2012). Response of Steel Fiber-Reinforced Concrete Beams with and without Stirrups. *ACI Structural Journal, 109*(3), May-June 2012, pp. 359-368.

Ashou, S. A., Hasanain, G. S., & Wafa, F. F. (1992). Shear Behavior of High-Strength Fiber Reinforced Concrete Beams. *ACI Structural Journal, 89*(2), March-April 1992, pp. 176-184.

ASTM Standard C1018-97. (1997). Standard Test Method for Flexural Toughness and First-Crack Strength of Fiber-Reinforced Concrete (Using Beam with Third-Point Loading). *ASTM International, West Conshohocken, PA*, 8 p.

ASTM Standard C1609/C1609M-12. (2012). ASTM C1609/C1609M Standard Test Methods for Flexural Performance of Fiber-Reinforced Concrete (Using Beam with Third-Point Loading). *ASTM International, West Conshohocken, PA*, 9 p.

ASTM Standard C192/C192M-02. (2002). Standard Practice for Making and Curing Concrete Test Specimens in the Laboratory. *ASTM International, West Conshohocken, PA*, 8 p.

ASTM Standard C469. (2002). Standard Test Method for Static Modulus of Elasticity and Poisson's Ratio of Concrete in Compression. *ASTM International, West Conshohocken, PA*, 5 p.

Athanasopoulou, A., & Parra-Montesinos, G. J. (2013). Experimental Study on the Seismic Behavior of High- Performance Fiber-Reinforced Concrete Low-Rise Walls. *ACI Structural Journal, 110*(5), September-October 2013, pp. 767-778.

Bekaert. (2013). *Product data sheet for dramix fibers.* Retrieved June 06, 2013, from http://www.bekaert.com/building

Bentz, E. (2010). *Augustus: Post Processor for VecTor2 (Version 5.6.5).* Copyright 1996-2010 E. Bentz.

Calvi, P. (2014). *Shear Slip of Panels.* Ph.D. Dissertation, University of Toronto, Department of Civil Engineering, [NOT YET PUBLISHED].

CAN/CSA Standard A23.3-04. (2004). Design of Concrete Structures (Third Edition). *Cement Association of Canada, Canada*, 214 p.

CAN/CSA Standard S6-06. (2006). Canadian Highway Bridge Design Code. *Canadian Standards Association*, pp. 301-379.

Carnovale, D. J. (2013). *Behaviour and Analysis of Steel and Macro-synthetic Fibre Reinforced Concrete Subjected to Reversed Cyclic Loading: A Pilot Investigation.* M.A.Sc. Dissertation, University of Toronto, Department of Civil Engineering, 323 p.

Chalioris, C. E. (2013). Steel fibrous RC beams subjected to cyclic deformations under predominant shear. *Engineering Structures, 49*, April 2013, pp. 104-118.

Chao, S. H., Naaman, A. E., & Parra-Montesinos, G. J. (2009). Bond Behavior of Reinforcing Bars in Tensile Strain-Hardening Fiber-Reinforced Cement Composites. *ACI Structural Journal, 106*(6), November-December 2009, pp. 897-906.

Choi, K., Park, H., & Wight, J. K. (2007). Shear Strength of Steel Fiber-Reinforced Concrete Beams without Web Reinforcement. *ACI Structural Journal, 104*(1), January-February 2007, pp. 12-22.

Collins, M., & Mitchell, D. (1997). Prestressed Concrete Structures. *Response Publications, Toronto and Montreal*, 766 p.

Comité Euro International du Béton (CEB/FIP). (1978). Model Code for Concrete Structures. *CEB-FIP International Recommendations, third edition, Paris, France*, 348 pp.

Daniel, L., & Loukili, A. (2002). Behavior of high-strength fiber-reinforced concrete beams under cyclic loading. *ACI Structural Journal, 99*(3), May-June 2002, pp.248-256.

Deluce, J. R. (2011). *Cracking behaviour of Steel Fibre Reinforced Concrete Containing Conventional Steel Reinforcement.* M.A.Sc. Dissertation, University of Toronto, Department of Civil Engineering, 507 p.

Deluce, J. R., & Vecchio, F. J. (2013). Cracking Behavior of Steel Fiber-Reinforced Concrete Members Containing Conventional Reinforcement. *ACI Structural Journal, 110*(3), May-June 2013, pp. 481-490.

Deluce, J. R., Lee, S. C., & Vecchio, F. J. (2014). Crack Model for Steel Fiber-Reinforced Concrete Members Containing Conventional Reinforcement. *ACI Structural Journal, 111*(1), January-February 2014, pp. 93-102.

Dinh, H. H. (2009). *Shear Behavior of Steel Fiber Reinforced Concrete Beams Without Stirrup Reinforcement.* Ph.D. Dissertation, University of Michigan, Department of Civil Engineering, 309 p.

Falkner, H., Henke, V., & Hinke, U. (1997). Steel Fibre Concrete for Deep Building Pits in Ground Water. *Bauingenieur, 72*, pp.47-52.

Fanella, D. A., & Naaman, A. E. (1985). Stress-Strain Properties of Fiber Reinforced Mortar in Compression. *ACI Journal, 82*(4), July-August 1985, pp. 475-483.

Filiatrault, A., Pineau, S., & Houde, J. (1994). Seismic Performance of Code-Designed Fiber Reinforced Concrete Joints. *ACI Structural Journal, 91*(5), September-October 1994, pp.564-571.

Filiatrault, A., Pineau, S., & Houde, J. (1995). Seismic Behavior of Steel-Fiber Reinforced Concrete Interior Beam-Column Joints. *ACI Structural Journal, 92*(5), Sept.-Oct. 1995, pp. 543-552.

Ghannoum, W. M. (1998). *Size Effect on Shear Strength of Reinforced Concrete Beams.* M.Eng. Dissertation, McGill University, Department of Civil Engineering and Applied Mechanics, p.126.

Grzhbowski, M., & Shah, S. P. (1990). Shrinkage Cracking of Fiber Reinforced Concrete. *ACI Materials Journal, 87*(2), March-April 1990, pp.138-148.

Hrynyk, T. D. (2013). *Behaviour and Modelling of Reinforced Concrete Slabs and Shells under Static and Dynamic Loads.* Ph. D. Dissertation, University of Toronto, Department of Civil Engineering, p. 455.

Jiuru, T., Chaobin, H., Kaijian, Y., & Yongcheng, Y. (1992). Seismic behavior and shear strength of framed joint using steel-fiber reinforced concrete. *Journal of Structural Engineers, 118*(2), 1992, pp. 341-358.

Johnston, C. D. (2001). *Fibre-reinforced cements and concretes.* Ottawa, Ontario, Canada: Gordon and Breach Science Publishers, 372 p.

Khaloo, A. R., & Kim, N. (1997). Influence of Concrete and Fiber Characteristics on Behavior of Steel Fiber-Reinforced Concrete under Direct Shear. *ACI Materials Journal, 94*(6), November-December 1997, pp. 592-600.

Lee, S. C., Cho, J. Y., & Vecchio, F. J. (2011). Diverse Embedment Model for Steel Fiber-Reinforced Concrete in Tension: Model Verification. *ACI Materials Journal, 108*(5), September-October 2011, pp. 526-525.

Lee, S. C., Cho, J. Y., & Vecchio, F. J. (2012). Simplified Diverse Embedment Model for SFRC Element in Tension. *ACI Materials Journal, 110*(4), July-August 2013, pp. 403-.

Lequesne, R., Setkit, M., Parra-Montesinos, G. J., & Wight, J. K. (2010). Seismic Detailing and Behavior of Coupling Beams with High-Peformance Fibre Reinforced Concrete. *ACI Special Publication, 272*, Oct. 2010, pp. 189-204.

Mansour, A., Srebric, J., & Burley, B. J. (2007). Development of straw-cement composite sustainable building material for low-cost housing in Egypt. *Journal of Applied Sciences Research, 3*(11), 2007, pp. 1571-1580.

Mansur, M., Ong, K., & Paramasivam, P. (1986). Shear Strength of Fibrous Concrete beams without Stirrups. *Journal of Structural Engineering, 112*(9), September 1986, pp. 2066-2079.

Meda, A., Minelli, F., Plizzari, G., & Riva, P. (2005). Shear Behaviour of Steel Fibre Reinforced Concrete beams. *Materials and Structures, 38*(3), April 2005, pp. 343-351.

Minelli, F. (2005). *Plain and Fiber Reinforced Concrete Beams under Shear Loading: Structural Behavior and Design Aspects.* Ph.D. Dissertation, University of Brescia, Department of Civil Engineering, 429 p.

Naaman, A. E. (1987). High Performance Fiber Reinforced Cement Composites. *International Association for Bridge and Structural Engineering (IABSE) Symposium on Concrete Structures for the Future*, Paris - Versailles, pp. 371-376.

Naaman, A. E., Liao, W. C., Chao, S. H., & Park, S. Y. (2006). *Self-Consolidating High Performance Fiber Reinforced Concrete (SCHPFRC) - Preliminary Investigation.* Research Report UMCEE 06-02, University of Michigan, December 2006, 68 p.

Ozcebe, G., & Saatcioglu, M. (1989). Hysteretic Shear Model for Reinforced Concrete Members. *Journal of Structural Engineering, 115*(1), January 1989, pp. 132-148.

Parra-Montesinos, G. J. (2006). Shear Strength of Beams with Deformed Steel Fibers. *Concrete International*, November 2006, pp. 57-66.

Popov, E. P. (1984). Bond and Anchorage of Reinforcing Bars Under Cyclic Loading. *ACI Journal, 81*(4), July-Aug. 1984, pp. 340-349.

RILEM Technical Committee 162. (2000). Test and Design Methods for Steel Fibre Reinforced Concrete: Bending Test. *Materials and Structures, 33*(1), January-February 2000, pp. 3-5.

Romualdi, J. P., & Batson, G. B. (1963). The Mechanics of Crack Arrest in Concrete. *Journal, ASCE, 89*(EM3, Paper 3558), June 1963, pp. 147-168.

Romualdi, J. P., & Mandel, J. A. (1964). Tensile Strength of Concrete Affected by Uniformly Distributed Closely Spaced Short Lengths of Wire Reinforcements. *ACI Journal, Proceedings, 61*(6), June 1964, pp. 657-671.

Saatcioglu, M. (1991). Modeling Hysteretic Force-Deformation Relationships for Reinforced Concrete Elements. *ACI Special Publication, 127*, October 1991, pp. 153-198.

Setkit, M. (2012). *Seismic Behaviour of Slender Coupling Beams Constructed With High-Performance Fibre-Reinforced Concrete.* Ph.D. Dissertation, University of Michigan, Department of Civil Engineering, 261 p.

Setkit, M. (2014). Personal communication. University of Michigan, Department of Civil Engineering.

Shah, S. P., & Rangan, B. V. (1971). Fiber Reinforced Concrete Properties. *ACI Journal, 83*(4), July-Aug. 1986, pp. 624-628.

Soroushian, P., & Lee, C. D. (1990). Distribution and Orientation of Fibers in Steel Fiber Reinforced Concrete. *ACI Materials Journal, 87*(5), September 1990, pp. 433-439.

Susetyo, J. (2009). *Fibre Reinforcement for Shrinkage Crack Control in Prestressed, Precast Segmental Bridges.* Ph.D. Dissertation, University of Toronto, Department of Civil Engineering, 532 p.

Susetyo, J., Gauvreau, P., & Vecchio, F. J. (2011). Effectiveness of Steel Fiber as Minimum Shear Reinforcement. *ACI Structural Journal, 108*(4), July-August 2011, pp. 488-496.

Susetyo, J., Gauvreau, P., & Vecchio, F. J. (2013). Steel Fiber-Reinforced Concrete Panels in Shear: Analysis and Modeling. *ACI Structural Journal, 110*(2), March-April 2013, pp. 285-296.

Swamy, R. N., & Bahia, H. M. (1985). Effectiveness of Steel Fibres as Shear Reinforcement. *Concrete International: Design and Construction, 7*(3), March 1985, pp. 35-40.

Thomas, J., & Ramaswamy, A. (2007). Mechanical Properties of Steel Fiber-Reinforced Concrete. *Journal of Materials in Civil Engineering, 19(5)*, May 2007, pp. 385-392.

Vecchio, F. (1979). *Shear Rig Design.* M. Eng. Dissertation, University of Torono, Department of Civil Engineering, 246 p.

Vecchio, F. (1990). *VecTor2 Nonlinear Finite Element Analysis.* Copyright 1990-2014 F.J. Vecchio.

Vecchio, F. (1999). Towards Cyclic Load Modeling of Reinforced Concrete. *ACI Structural Journal, 96*(2), March-April 1999, pp. 193-202.

Vecchio, F. (2000). Disturbed Stress Field Model for Reinforced Concrete: Formulation. *ASCE Journal of Structural Engineering, 126*(9), September 2000, pp. 1071-1077.

Vecchio, F., & Collins, M. (1986). The Modified Compression Field Theory for Reinforced Concrete Elements Subjected to Shear. *ACI Journal, 83*(2), March-April 1986, pp. 219-231.

Vecchio, F., & Collins, M. (1993). Compression Response of Cracked Reinforced Concrete. *ASCE Journal of Structural Engineering, 119*(12), December 1993, pp. 3590-3610.

Voo, J., & Foster, D. (2003). *Variable Engagement Model for Fibre Reinforced Concrete in Tension.* Univeristy of New South Wales, School of Civil and Environmental Engineering, 87 p.

Wight, J. K., & MacGregor, J. G. (2009). *Reinforced Concrete: Mechanics and Design.* Upper Saddle River, N.J.: Pearson Prentice Hall.

Wong, F., Vecchio, F., & Trommels, H. (2012). *VecTor2 and Formworks User's Manual.* University of Toronto, 339 p.

Zollo, R. (1997). Fibre-Reinforced Concrete: An Overview After 30 Years of Development. *Cement and Concrete Composites, 19*, 1997, pp. 107-122.

Appendix A

Material Test Results

A.1 Cylinder Test Results

A.1.1 Control Test Set
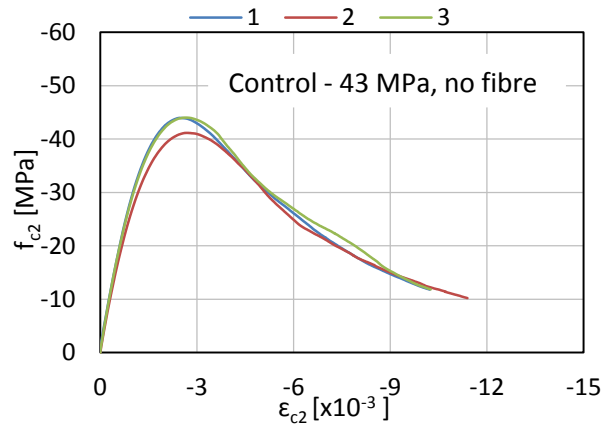
Cylinder	$f'_{c(28)}$ [MPa]	ε'_c [x10⁻³]	E_{ct} [MPa]
1	44.0	2.45	32078
2	41.2	2.72	30696
3	44.0	2.64	33338
Average	**43.0**	**2.60**	**32037**

A.1.2 F1V1 Test Set
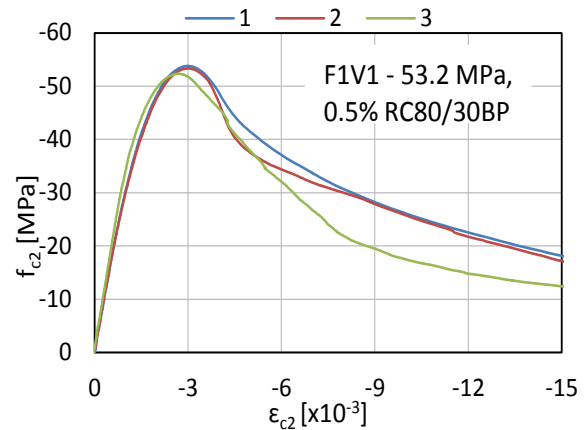
Cylinder	$f'_{c(28)}$ [MPa]	ε'_c [x10⁻³]	E_{ct} [MPa]
1	53.8	2.99	32235
2	53.3	3.01	31707
3	52.3	2.66	35591
Average	**53.2**	**2.89**	**33177**

A.1.3 F1V2 Test Set
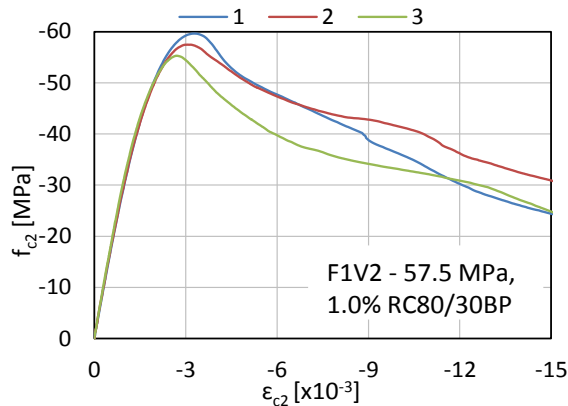
Cylinder	$f'_{c(28)}$ [MPa]	ε'_c [x10⁻³]	E_{ct} [MPa]
1	59.6	3.26	31324
2	57.5	3.05	31674
3	55.3	2.70	33501
Average	**57.5**	**3.00**	**32166**

A.1.4 F1V3 Test Set
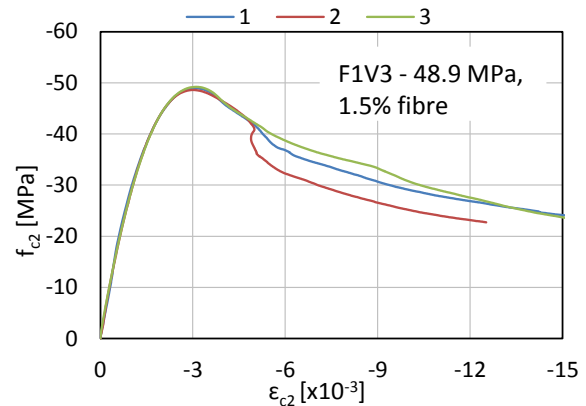
Cylinder	$f'_{c(28)}$ [MPa]	ε'_c [x10⁻³]	E_{ct} [MPa]
1	49.0	3.03	33795
2	48.6	3.06	31618
3	49.2	3.10	30722
Average	**48.9**	**3.06**	**32045**

A.1.5 F2V2 Test Set

F1V3 - 50.1 MPa, 1.0% ZP305
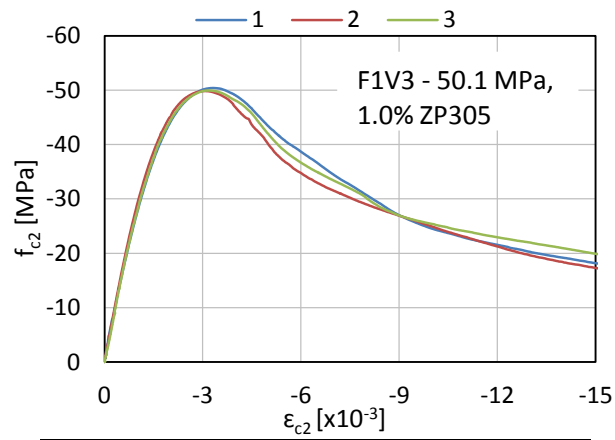
Cylinder	$f'_{c(28)}$ [MPa]	ε'_c [x10⁻³]	E_{ct} [MPa]
1	50.4	3.31	28678
2	49.8	3.03	30847
3	49.9	3.19	29891
Average	**50.1**	**3.18**	**29806**

A.2 Uniaxial Direct Tension Test Data

A.2.2 Control Test Set
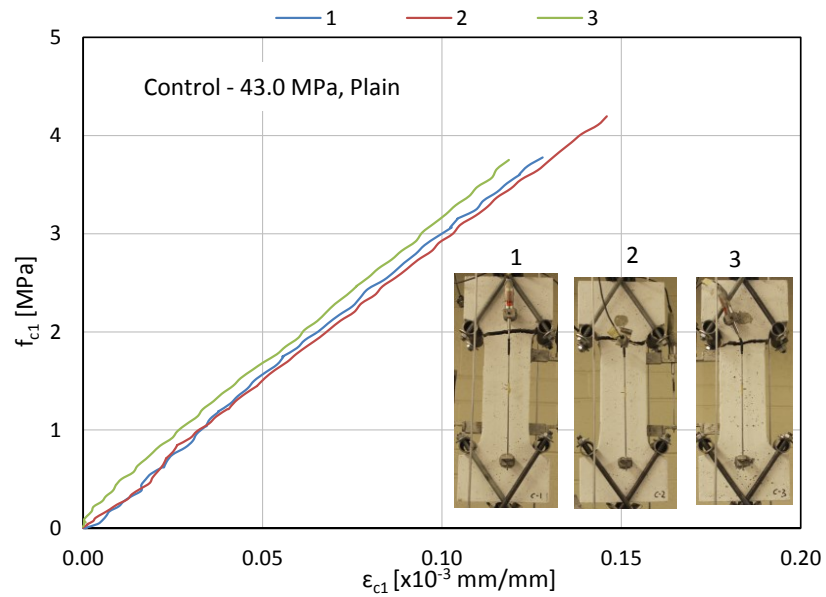
Dogbone	f'_t [MPa]	ε'_t [x10^{-3}]	E_{ct} [MPa]	f_{c1} [MPa] at a w_{cr} of			
				0.5 mm	1.5 mm	3.0 mm	6.0 mm
1	3.78	0.128	33616	-	-	-	-
2	4.20	0.146	31618	-	-	-	-
3	3.75	0.119	30877	-	-	-	-
Average	**3.91**	**0.131**	**32037**	**-**	**-**	**-**	**-**

A.2.2 F1V1 Test Set
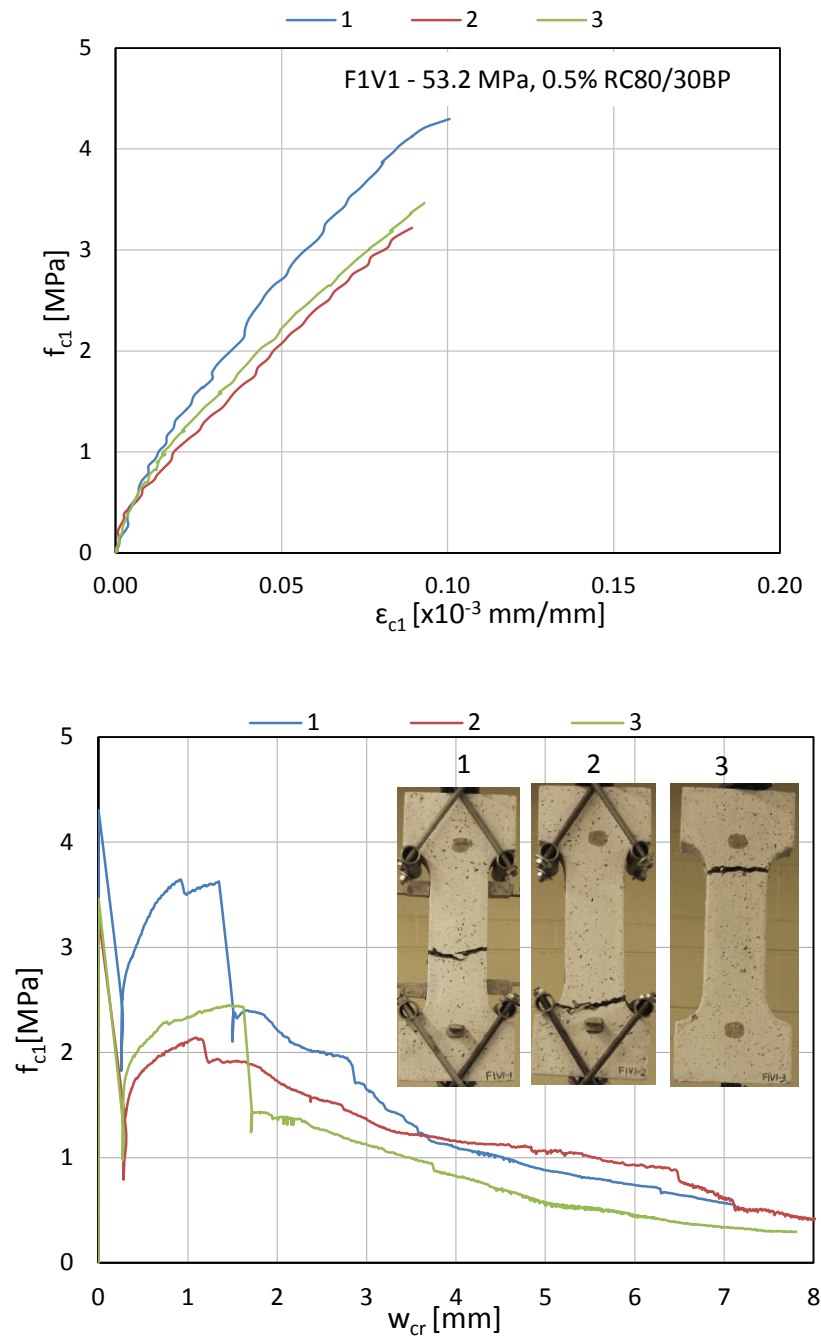
Dogbone	f'_t [MPa]	ε'_t [x10^{-3}]	E_{ct} [MPa]	f_{c1}[MPa] at a w_{cr} of			
				0.5 mm	1.5 mm	3.0 mm	6.0 mm
1	4.30	0.101	45060	3.17	2.23	1.65	0.74
2	3.22	0.089	37411	1.82	1.91	1.38	0.93
3	3.46	0.093	40948	2.06	2.44	1.13	0.45
Average	**3.66**	**0.094**	**41140**	**2.35**	**2.19**	**1.39**	**0.71**

A.2.3 F1V2 Test Set

F1V1 - 57.5 MPa, 1.0% RC80/30BP
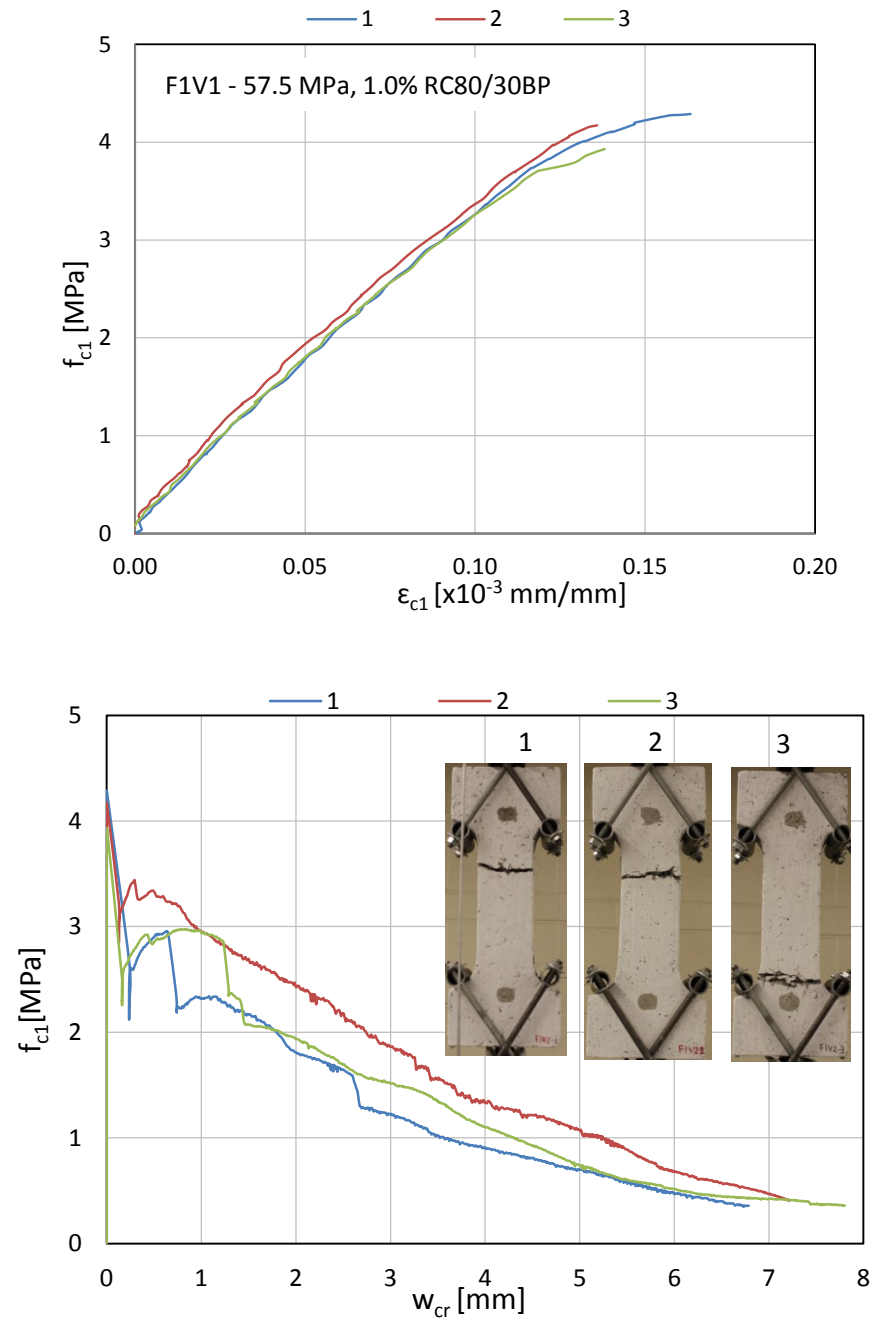
Dogbone	f'_t [MPa]	ε'_t [x10^-3]	E_{ct} [MPa]	f_{c1}[MPa] at a w_{cr} of			
				0.5 mm	1.5 mm	3.0 mm	6.0 mm
1	4.29	0.163	35727	2.90	2.17	1.22	0.49
2	4.17	0.136	34566	3.33	2.68	1.86	0.68
3	3.93	0.138	35825	2.85	2.07	1.52	0.52
Average	4.13	0.146	35373	3.03	2.31	1.54	0.56

A.2.4 F1V3 Test Set
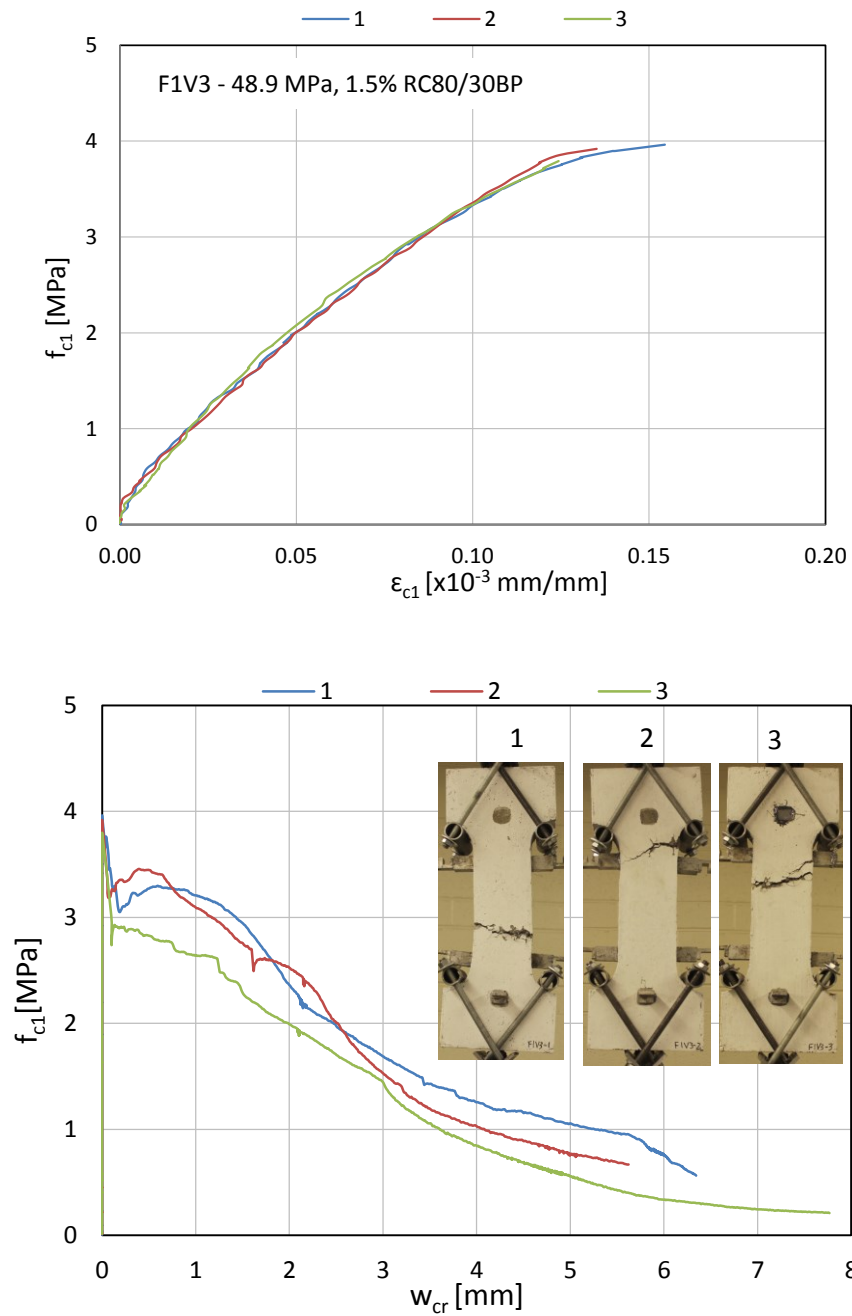
Dogbone	f'_t [MPa]	ε'_t [x10⁻³]	E_{ct} [MPa]	f_{c1}[MPa] at a w_{cr} of			
				0.5 mm	1.5 mm	3.0 mm	6.0 mm
1	3.96	0.154	34523	3.27	2.95	1.69	0.76
2	3.92	0.135	36292	3.45	2.76	1.54	0.67
3	3.79	0.124	41347	2.83	2.29	1.45	0.34
Average	**3.89**	**0.138**	**37387**	**3.18**	**2.67**	**1.56**	**0.59**

A.2.5 F2V2 Test Set

F1V3 - 50.1 MPa, 1.0% ZP305
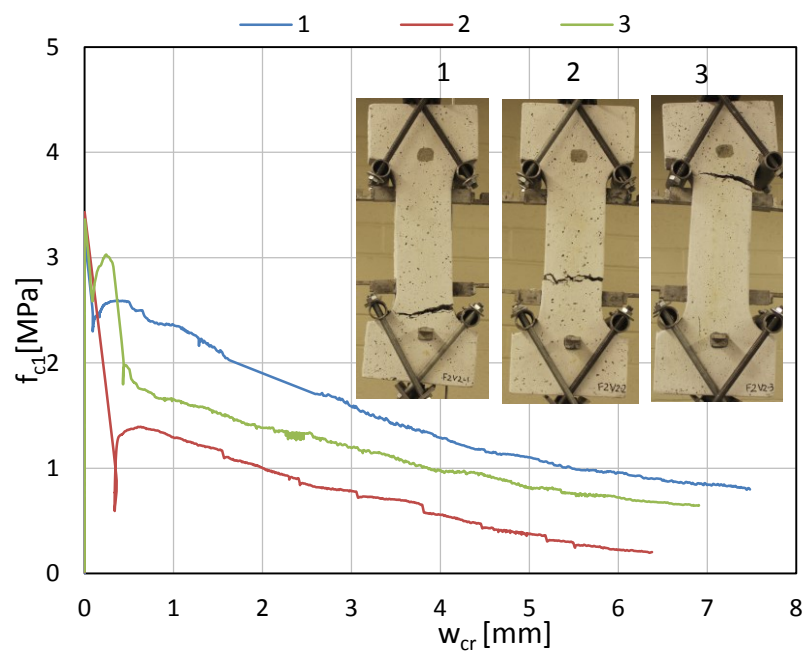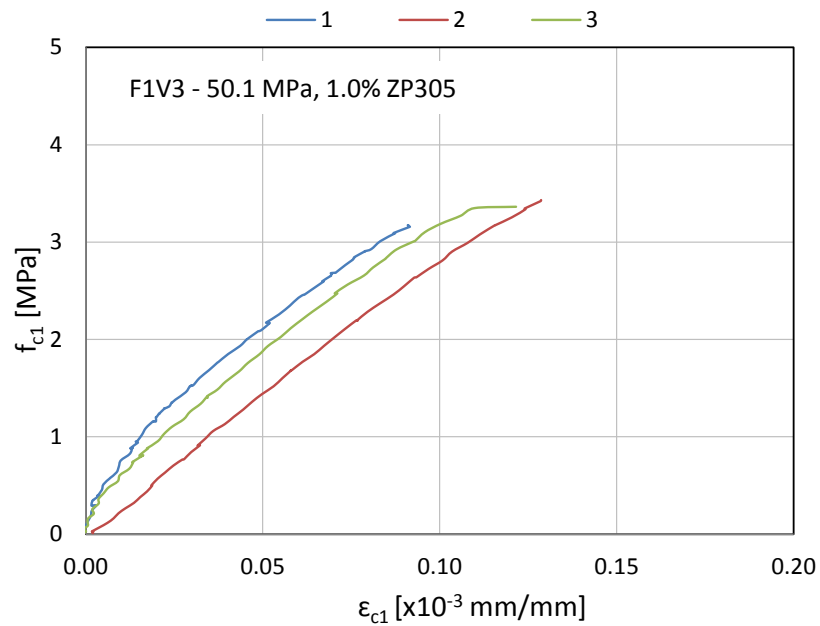
Dogbone	f'_t [MPa]	ε'_t [x10⁻³]	E_{ct} [MPa]	f_{c1} [MPa] at a w_{cr} of			
				0.5 mm	1.5 mm	3.0 mm	6.0 mm
1	3.17	0.091	40690	2.58	2.11	1.59	0.96
2	3.43	0.129	31092	1.36	1.18	0.78	0.22
3	3.36	0.122	32320	1.95	1.52	1.19	0.72
Average	**3.32**	**0.114**	**34700**	**1.96**	**1.60**	**1.19**	**0.64**

A.3 Modulus of Rupture Test Data

A.3.1 Control Test Set

MOR	f_{cr} [MPa]	δ_{cr} [mm]	f_p [MPa]	δ_p [mm]	f^D_{600} [MPa]	f^D_{150} [MPa]	T^D_{150} [J]	$R^D_{T,150}$ [%]	P [kN] at a δ_{mid} of			
									1.0 mm	2.0 mm	4.0 mm	8.0 mm
1	4.36	0.04	4.36	0.05	-	-	1.49	1.46	-	-	-	-
2	4.44	0.05	4.44	0.05	-	-	1.10	1.06	-	-	-	-
Avg.	4.40	0.05	4.40	0.05	-	-	1.30	1.26	-	-	-	-

A.3.2 F1V1 Test Set

MOR	f_{cr} [MPa]	δ_{cr} [mm]	f_p [MPa]	δ_p [mm]	f^D_{600} [MPa]	f^D_{150} [MPa]	T^D_{150} [J]	$R^D_{T,150}$ [%]	P [kN] at a δ_{mid} of			
									1.0 mm	2.0 mm	4.0 mm	8.0 mm
1	4.08	0.040	6.32	1.83	4.94	5.21	132.9	139.2	44.7	48.5	31.0	10.3
2	4.35	0.040	6.31	1.83	5.83	5.15	131.2	128.8	37.4	48.3	30.3	11.7
Avg.	4.21	0.040	6.32	1.83	5.39	5.18	132.0	134.0	41.1	48.4	30.7	11.0

A.3.3 F1V2 Test Set

F1V2 - 57.5 MPa, 1.0% RC80/30BP

MOR	f_{cr} [MPa]	δ_{cr} [mm]	f_p [MPa]	δ_p [mm]	f_{600}^D [MPa]	f_{150}^D [MPa]	T_{150}^D [J]	$R_{T,150}^D$ [%]	P [kN] at a δ_{mid} of			
									1.0 mm	2.0 mm	4.0 mm	8.0 mm
1	4.30	0.040	6.72	1.13	6.54	4.20	133.8	133.0	51.5	43.9	24.7	-
2	4.22	0.040	7.47	1.27	7.33	4.64	147.9	149.7	57.1	47.8	26.0	8.21
Avg.	4.26	0.040	7.10	1.20	6.93	4.42	140.9	141.4	54.3	45.9	25.4	8.21

A.3.4 F1V3 Test Set

F1V3 - 48.9 MPa, 1.5% RC80/30BP

MOR	f_{cr} [MPa]	δ_{cr} [mm]	f_p [MPa]	δ_p [mm]	f_{600}^D [MPa]	f_{150}^D [MPa]	T_{150}^D [J]	$R_{T,150}^D$ [%]	P [kN] at a δ_{mid} of			
									1.0 mm	2.0 mm	4.0 mm	8.0 mm
1	4.93	0.040	7.69	0.25	6.89	2.72	118.0	102.1	48.4	31.3	14.8	4.34
2	4.28	0.040	6.81	0.64	6.64	3.10	117.5	117.1	48.1	33.3	17.7	5.98
Avg.	4.61	0.040	7.25	0.45	6.77	2.91	117.7	109.6	48.3	32.3	16.3	5.16

A.3.5 F2V2 Test Set

MOR	f_{cr} [MPa]	δ_{cr} [mm]	f_p [MPa]	δ_p [mm]	f^D_{600} [MPa]	f^D_{150} [MPa]	T^D_{150} [J]	$R^D_{T,150}$ [%]	P [kN] at a δ_{mid} of			
									1.0 mm	2.0 mm	4.0 mm	8.0 mm
1	3.77	0.033	4.61	0.09	3.87	1.45	67.5	76.5	27.0	17.9	7.9	2.85
2	3.64	0.040	4.22	0.61	4.08	2.32	76.4	89.7	29.1	21.7	15.3	7.21
Avg.	3.70	0.037	4.42	0.35	3.97	1.88	71.9	83.1	28.0	19.8	11.6	5.03

A.4 Reinforcing Steel Data

A.4.1 D4 Reinforcing Steel
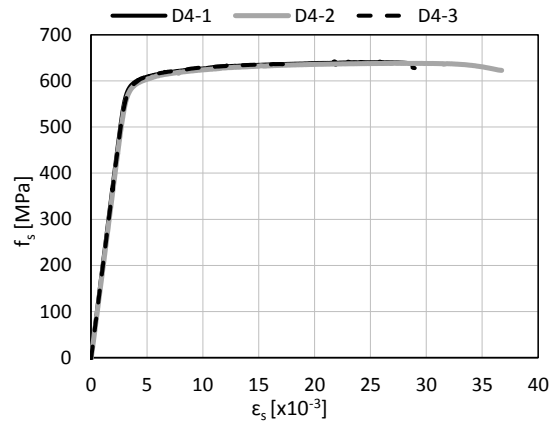
A_s=25.5 mm²
d_b=5.70 mm²

Test	E_s [GPa]	f_y* [MPa]	ε_y [x10⁻³]	f_u [MPa]	ε_u [x10⁻³]
1	193.1	484.2	2.52	642.5	21.8
2	187.7	502.1	2.71	638.5	27.2
3	190.8	485.6	2.57	636.7	16.4
Avg.	190.5	490.6	2.60	639.2	21.8

* f_y is taken as the stress at the proportionality limit

A.4.2 D8 Reinforcing Steel
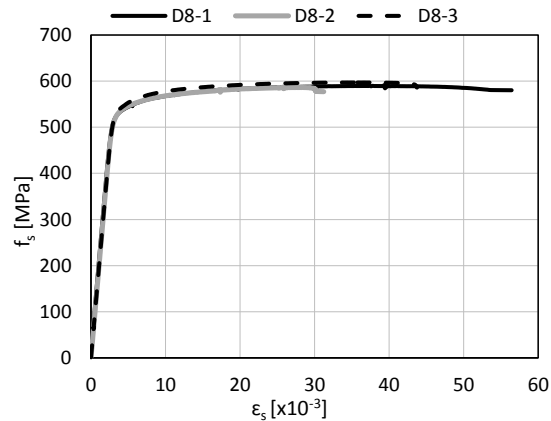
A_s=51.5 mm²
d_b=8.10 mm²

Test	E_s [GPa]	f_y* [MPa]	ε_y [x10-3]	f_u [MPa]	ε_u [x10-3]
1	184.7	455.3	2.43	591.3	39.4
2	185.4	460.0	2.51	587.3	25.8
3	184.0	458.2	2.51	597.2	35.9
Avg.	184.7	457.8	2.48	591.9	33.7

* f_y is taken as the stress at the proportionality limit

A.4.3 5/16'' High Strength Threaded Rod
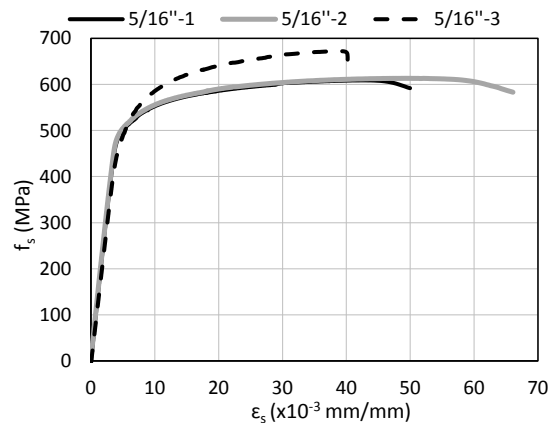
A_s=25.8 mm²
d_b=5.70 mm²

Test	E_s [GPa]	f_y* [MPa]	ε_y [x10-3]	f_u [MPa]	ε_u [x10-3]
1	131.0	342.5	2.65	608.5	40.1
2	130.5	332.0	2.51	613.3	49.4
3	119.1	324.1	2.77	672.4	38.6
Avg.	126.9	332.9	2.64	631.4	42.7

* f_y is taken as the stress at the proportionality limit

A.5 Fibre Data

A.5.1 RC80/30BP Product Data Sheet

PRODUCT DATA SHEET **BEKAERT**

Dramix® NEW

R C -80/30- B P

45⇄65⇄80 l/d | Bright | High Carbon

• **Description:** Dramix® fibres are filaments of wire, deformed and cut to lengths, for reinforcement of concrete, mortar and other composite materials. Dramix® RC-80/30-BP is a high carbon wire fibre, with hooked ends, and glued in bundles.

• **Applications:**
recommended in applications with concrete strength > C50/60

- segmental linings
- prestressed beams
- military structures
- vaults
- self levelling high strenght concrete
- high strength shotcrete

• **Geometry:**

Length (l)
30 mm

Diameter (d)
0.38 mm

80 Performance class: **80**

45⇄65⇄80 l/d Aspect ratio (= l/d): **79**

34 000 fibres/kg

Min. dosage = 10 kg/m³
(According to spacing theory McKee)

• **Tensile strength:**
- on the wire: minimum 2300 N/mm²

• **Coating:** None

• **Approvals:**

Product	Conforms to	Quality System in Belgian Plants
ATG 1857	ASTM A 820	ISO 9001 Dramix

Recommendations - mixing

1. General
√ preferably add fibres in the mixer at batching plant
√ recommended maximum dosage:

Dosage (kg/m³)	Aggregate size		
	2/8	4/16	4/32
pour	70	60	45
pump	55	45	35

√ a continuous grading is preferred
√ mix until all glued fibres are separated into individual fibres. Fibres don't increase mixing time significantly.
√ if special cements or admixtures are used, a preliminary test is recommended

2. Fibre addition

2.1. In batching plant mixer
√ never add fibres as first component in the mixer
√ fibres can be introduced together with sand and aggregates, or can be added in freshly mixed concrete
√ **only for drummixer:** unopened degradable bags can be thrown directly in the mixer

2.2. Truckmixer
√ put mixer on maximum drum speed: 12-18 rpm
√ adjust slump to a min. of 12 cm (preferably with water reducing agents or high water reducing agents)
√ add fibres with maximum speed of 40 kg/min
√ unopened degradable bags can be added provided that drum speed is min. 12 rpm
√ optional equipment: belt-hoist elevator
√ after adding the fibres, continue mixing at highest speed for 4-5 min. (± 70 rotations)

2.3. Automatic dosing
√ Fibres in bulk can be dosed at rates up to 3,5 kg/sec with a specially developed dosing equipment

Recommendations - storage

Delivered in

Protect the pallets against rain | Do not stack the pallets on top of each other | degradable bags of 20 kg on pallet 1200 kg | big bag 1100 kg

Resp. editor: Ann Lambrechts, Kortrijk   www.dramix.be - 03/2003

N.V. Bekaert S.A. - Bekaertstraat 2 - 8550 Zwevegem - Belgium
Tel. +32 (0) 56 / 76 69 86   Fax +32 (0) 56 / 76 79 47

Values are indicative only. Modifications reserved. All details describe our products in general form only. For ordering and design only use official specifications and documents. N.V. Bekaert S.A. 2003

A.5.1 ZP 305 Product Data Sheet

Dramix®

BEKAERT
better together

DATA SHEET

ZP 305

ZP 305

What is Dramix®?

Dramix® steel fibres, from industry specialist Bekaert, have set a new standard for concrete reinforcement with their unique combination of flexibility and cost-efficiency.

Dramix® is a cold drawn steel wire fibre with hooked ends for optimum anchorage.
What you get from Dramix® reinforced concrete is ductility and high load bearing capacity. On top of that, you'll find a quick and easy way to an efficient and cost effective solution.

ZP 305 offers you:

☑ **Dramix® Hi Perform**
Dramix® Hi Perform fibres are providing high performance and crack resistance. These are products of choice to create optimal ductility. Dramix® Hi Perform is used for structural, designed applications, in situ, precast or sprayed.

☑ **Dramix® Extreme**
Dramix® Extreme fibres are special engineered for extreme performant crack-control. They are made of thin wire diameters, giving a very dense wire network in each m³ concrete. The standard low dosage with Dramix® Extreme makes the products very cost-effective.

GEOMETRY AND PERFORMANCE

length (l)

30 mm

diameter (d)

0,55 mm

16.750 Fibres/kg **Minimum dosage:** 25 kg per m³ (according to **CE**)
Minimum fibre network: 12,6 km per m³ (for 25 kg/m³)

MATERIAL PROPERTIES

Tensile strength: Rm nom: 1.345 N/mm²
Tolerances: ± 7,5% Avg
Young's Modulus (Emod): ± 210.000 N/mm²

PACKAGING

60 BAGS (20kg)
1200 kg

BIG BAG
1100 kg

STORAGE

KEEP DRY

NO STACKING

APPROVALS

ISO 9001

CE

ASTM A820

- **CE LABEL:** Dramix® is certified for CE mark system 1: steel fibres for structural use.
  For detailed info: CE info sheet available on request.

- **ISO 9001 LABEL:** Dramix® is ISO 9001 certified. The same quality standards are applied in the following plants:

  - Belgium
  - Czech Republic
  - Turkey
  - Brazil
  - China
  - Indonesia

- **OTHER LABELS:** Bekaert is close to the market. Bekaert seeks conformance to every necessary, national product quality standard, in case one or more requirements are not covered in the CE or ISO 9001 certifications.

Bekaert will advise on the most suitable fibre for your application.
Ask for our recommendations on handling, dosing and mixing at:
www.bekaert.com/dosingdramix
infobuilding@bekaert.com

Modifications reserved.
All details describe our products in general form only. For detailed information, product specifications available on request.

© 2010 Bekaert

Appendix B

Panel Test Results and Analysis

B.1 CMS

Panel CMS was the monotonically loaded control panel. The panel consisted of plain non-fibrous concrete. The panel contained 3.31% reinforcement in the x-direction and 0.42% reinforcement in the y-direction. Determined from the material tests, panel CMS had a 28-day compressive strength of 43.0 MPa and a uniaxial tensile strength of 3.91 MPa; the test day compressive strength was 45.2 MPa.

B.1.1 Test Observations

The crack patterns at the various load stages for panel CMS are depicted in Figure B.1. The initial cracking occurred at a shear stress of 2.06 MPa. Multiple cracks were observed on the front and back face during initial cracking, the average initial crack width was 0.1 mm. As the load increased, new cracks were formed and the average crack width increased. After the second load stage, at a stress of 2.64 MPa, the cracks were well distributed and uniform over both faces of the panel. At the last load stage, the maximum crack width, the average crack width, and the average crack spacing were 0.50 mm, 0.20 mm, and 72.1 mm, respectively (see Figure B.2).

Yielding of transverse reinforcement occurred at a shear stress of 5.03 MPa and a shear strain of 4.30×10^{-3}. Failure occurred at a shear stress of 5.99 MPa and a shear strain of 8.58×10^{-3}. The failure was initiated by yielding of the transverse reinforcement, followed by aggregate interlock failure. Although there was significant softening in the response near the end, the failure was brittle with little warning. Before failure, the cracks were inclined approximately at an angle of 30° with respect to the x-axis. The failure crack was, however, parallel to the x-axis.
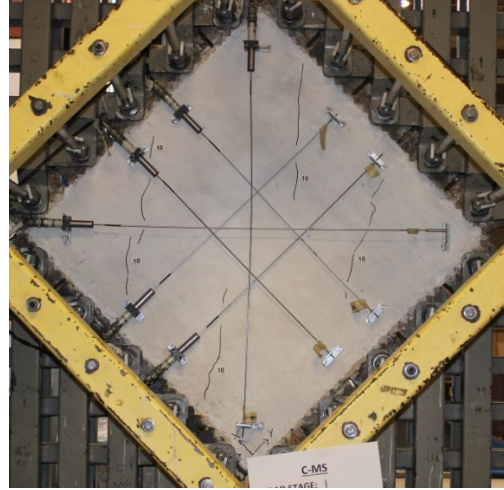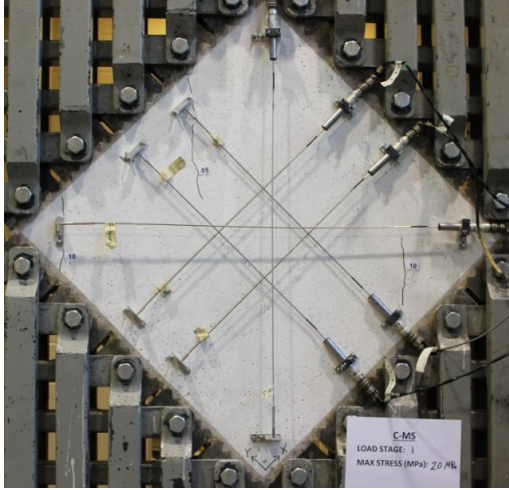
Stage 1: v_{xy}=2.06 MPa, γ_{xy}=0.12×10^{-3}; $w_{cr,max}$=0.10 mm, w_m=0.09 mm, s_m=368 mm.
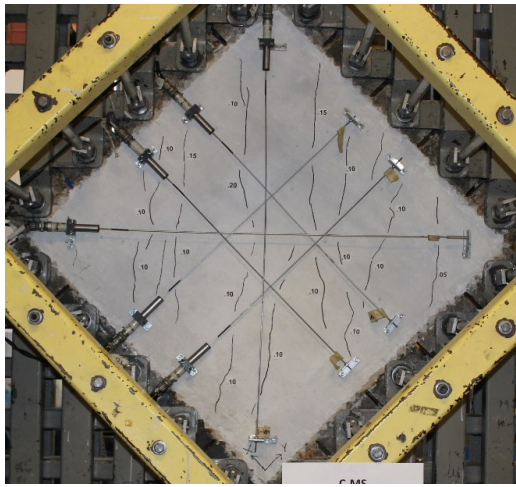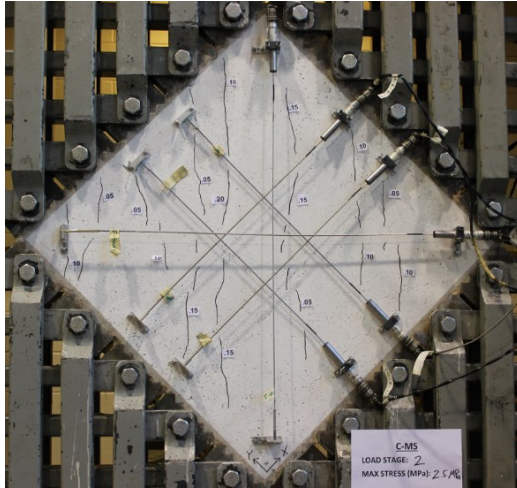
Stage 2: v_{xy}=2.64 MPa, γ_{xy}=0.91×10^{-3}; $w_{cr,max}$=0.20 mm, w_m=0.11 mm, s_m=158 mm.
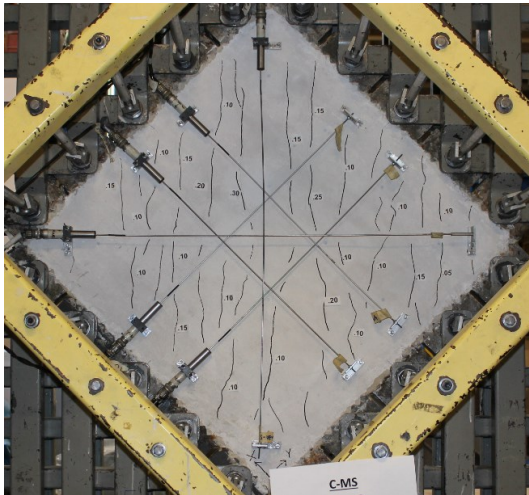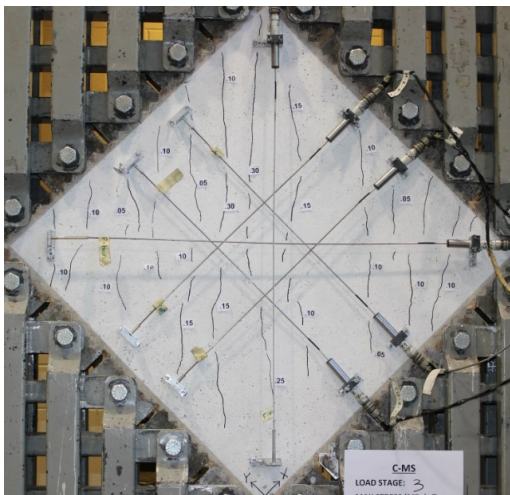
Stage 3: v_{xy}=3.10 MPa, γ_{xy}=1.68×10^{-3}; $w_{cr,max}$=0.30 mm, w_m=0.13 mm, s_m=110 mm.
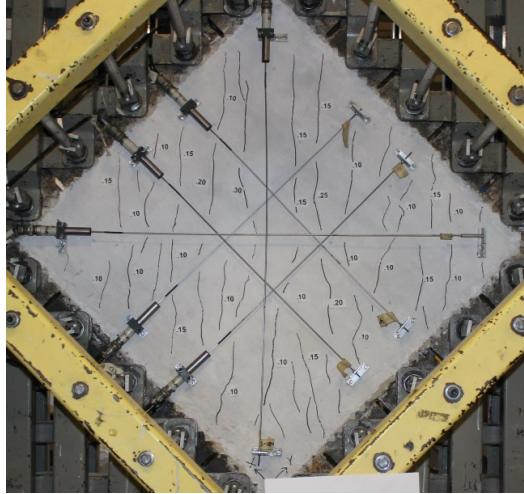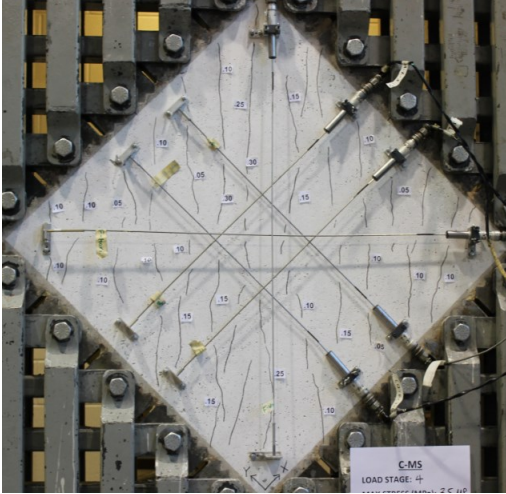
Stage 4: v_{xy}=3.65 MPa, γ_{xy}=2.36×10^{-3}; $w_{cr,max}$=0.30 mm, w_m=0.13 mm, s_m=101 mm.
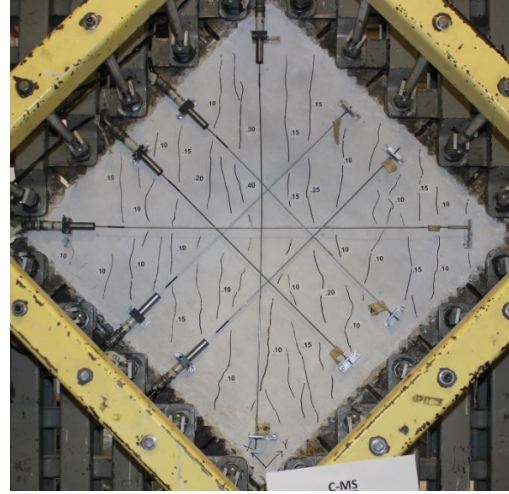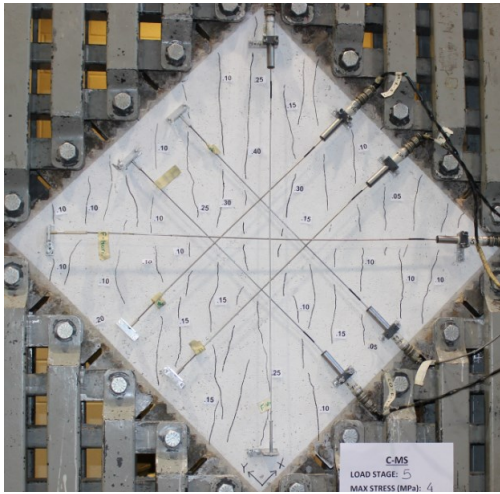
Stage 5: v_{xy}=4.17 MPa, γ_{xy}=3.0×10^{-3}; $w_{cr,max}$=0.40 mm, w_m=0.14 mm, s_m=90 mm.
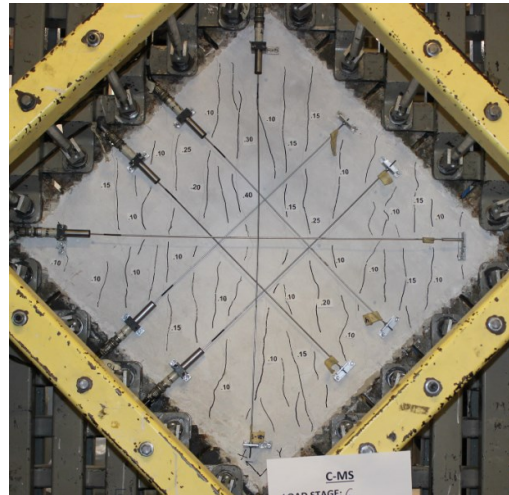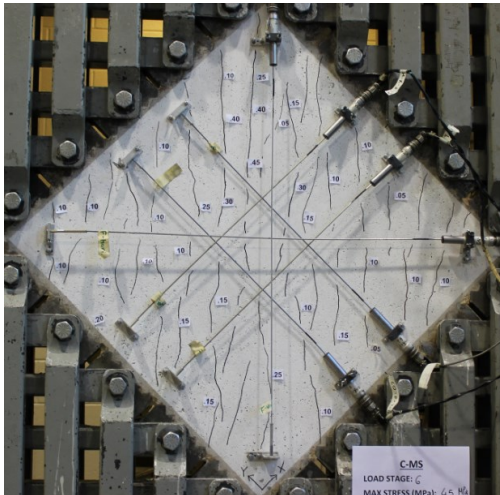
Stage 6: v_{xy}=4.68 MPa, γ_{xy}=3.81×10^{-3}; $w_{cr,max}$=0.45 mm, w_m=0.15 mm, s_m=76 mm.
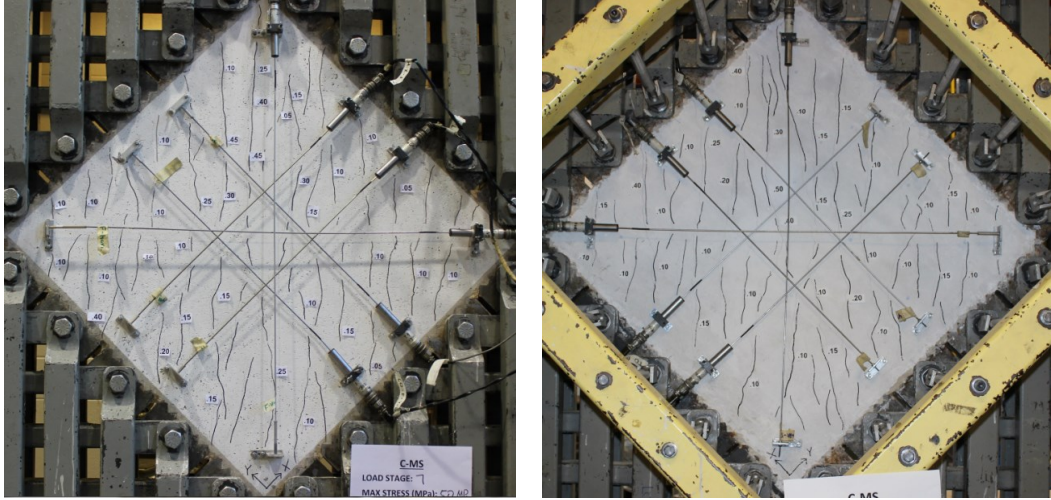
Stage 7: v_{xy}=5.21 MPa, γ_{xy}=4.74×10⁻³; $w_{cr,max}$=0.50 mm, w_m=0.20 mm, s_m=72 mm.
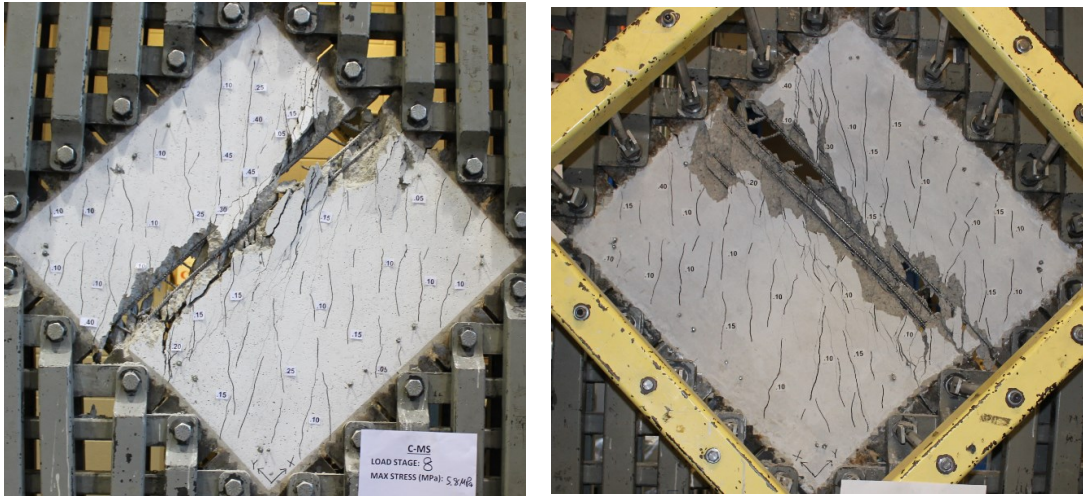
Failure: v_u=5.99 MPa, γ_u=8.58×10⁻³.

Figure B.1: Crack pattern of panel CMS
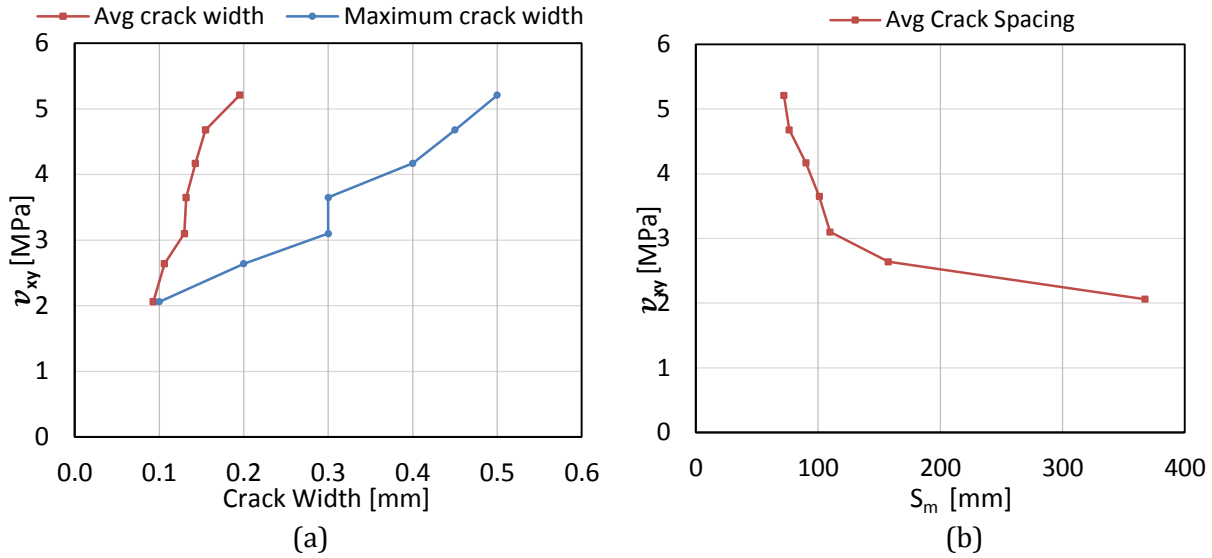
Figure B.2: Crack spacing and crack width of panel CMS

B.1.2 Data Analysis

Figure B.3 shows the response of panel CMS. As shown in the shear stress-shear strain response, the principal tensile stress-principal tensile strain response, and the principal compressive stress-strain response, the panel behaved linearly up to first-cracking, which occurred at a shear stress of 2.06 MPa with a shear strain of 0.18×10^{-3}. As the load increased, the panel displayed gradual softening with smaller crack spacing and larger crack widths. Immediately before failure, the maximum shear stress and shear strain were 5.99 MPa and 8.58×10^{-3}, respectively.

At first-cracking, the principal tensile stress and the principal tensile strain were 1.99 MPa and 0.10×10^{-3}, respectively. Afterwards, the principal tensile response gradually softened and reached a stress of 1.04 MPa with a strain of 10.7×10^{-3} at failure. Strain hardening behaviour was not observed in the principal tensile response.

Similar to the principal tensile values, the principal compressive stress and strain at first-cracking were -2.13 MPa and -0.09×10^{-3}, respectively. The compressive stress experienced by the panel was relatively small, well below its crushing strength. The overall principal compressive response was linear until failure occurred, at which the values of the principal compressive stress was -12.5 MPa with a principal compressive strain of -0.523×10^{-3}. Immediately before failure, the principal compressive strain for the front face quickly shifted toward the positive strain region, which caused the shifting in the average response.

Before first-cracking, the orientation of the principal angle was nearly identical for both stress and strain, nearing 45° as expected. Afterwards, the principal strain angle lagged behind the principal stress angle until failure was imminent. At failure, the inclination was 59.0° for the stress field and 65.2° for the strain field.

The primary reinforcement (x-direction) was not significantly stressed; the peak strain for the primary reinforcement was 1.46×10^{-3}, below its yield strain of 2.48×10^{-3}. The transverse reinforcement, however, yielded during the test which initiated the aggregate interlock failure. The peak strain for the transverse reinforcement was 8.75×10^{-3}, below its rupturing strain of 21.8×10^{-3}. In creating the transverse reinforcement stress-strain response, the nonlinear region between the initial linear portion and the highly linear plateau (between 530-610 MPa) was represented by two linear lines; that is, the entire reinforcement stress-strain response was represented by a quad-linear function for simplicity (see Figure B.3 (f)).

B.1.3 Comparison of the Front Face and Back Face Responses

The LVDT response for the front face and the back face of panel CMS is shown in Figure B.4. Overall, the out-of-plane bending was very small for this panel. The shear stress-shear strain response for both faces was nearly identical throughout the test. The initial cracks were formed on both faces at the same time. As with all other panels, the Mohr's circle for the back face shifted to the compression side, yielding higher principal compressive stresses, lower principal tensile stresses, and higher x-direction reinforcement stresses.
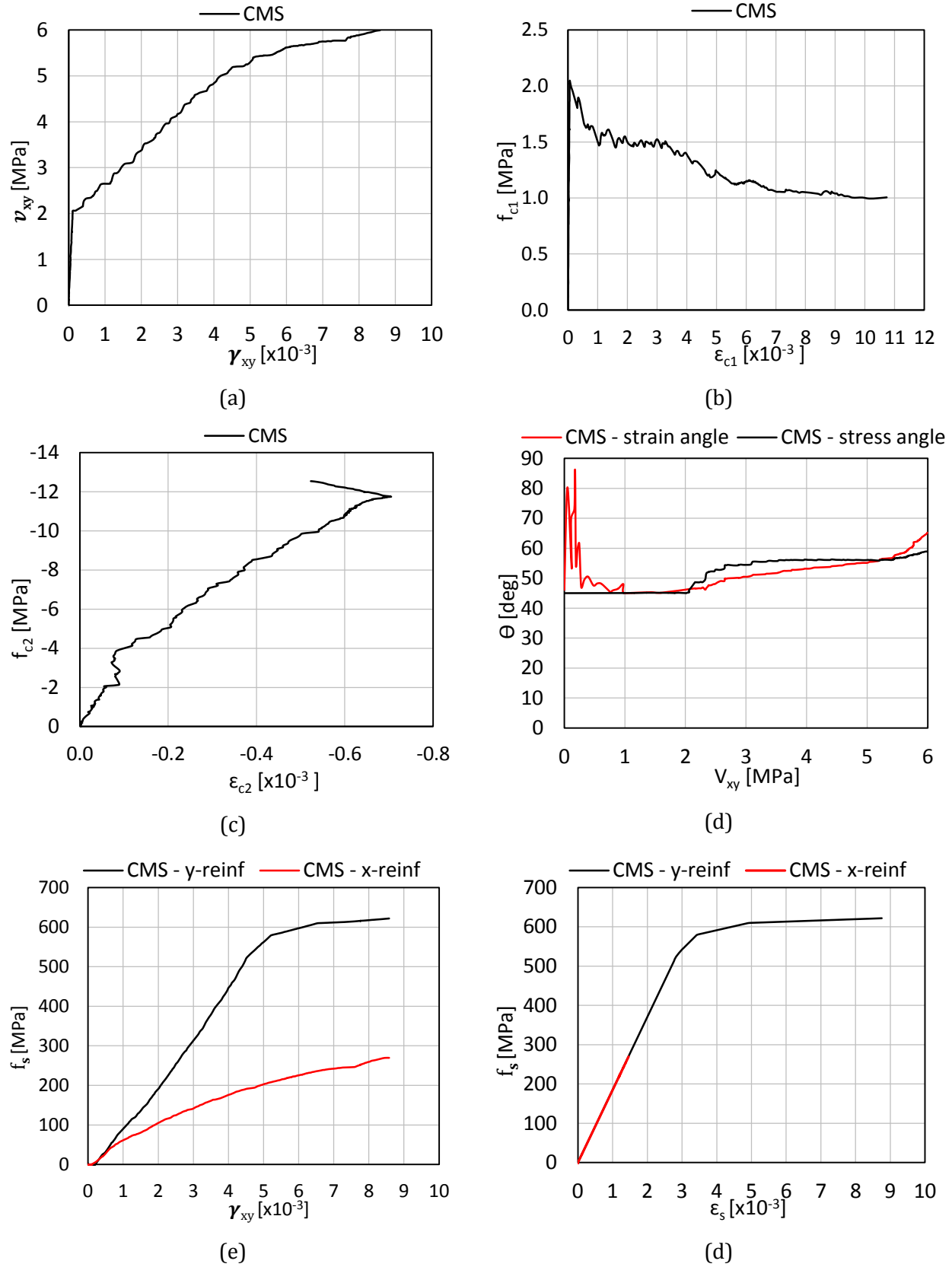
Figure B.3: Response of panel CMS

(a)

(b)

(c)

(d)
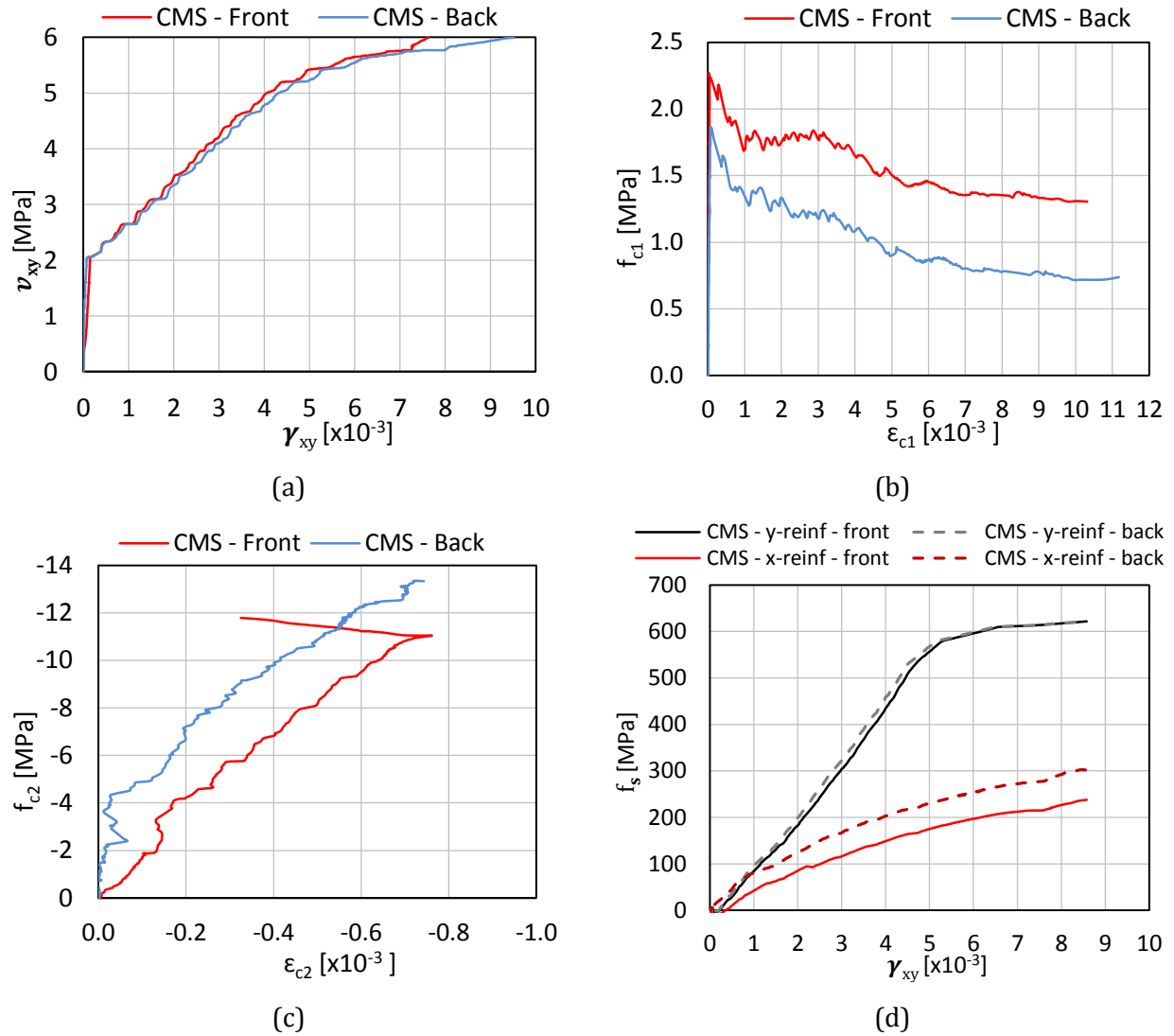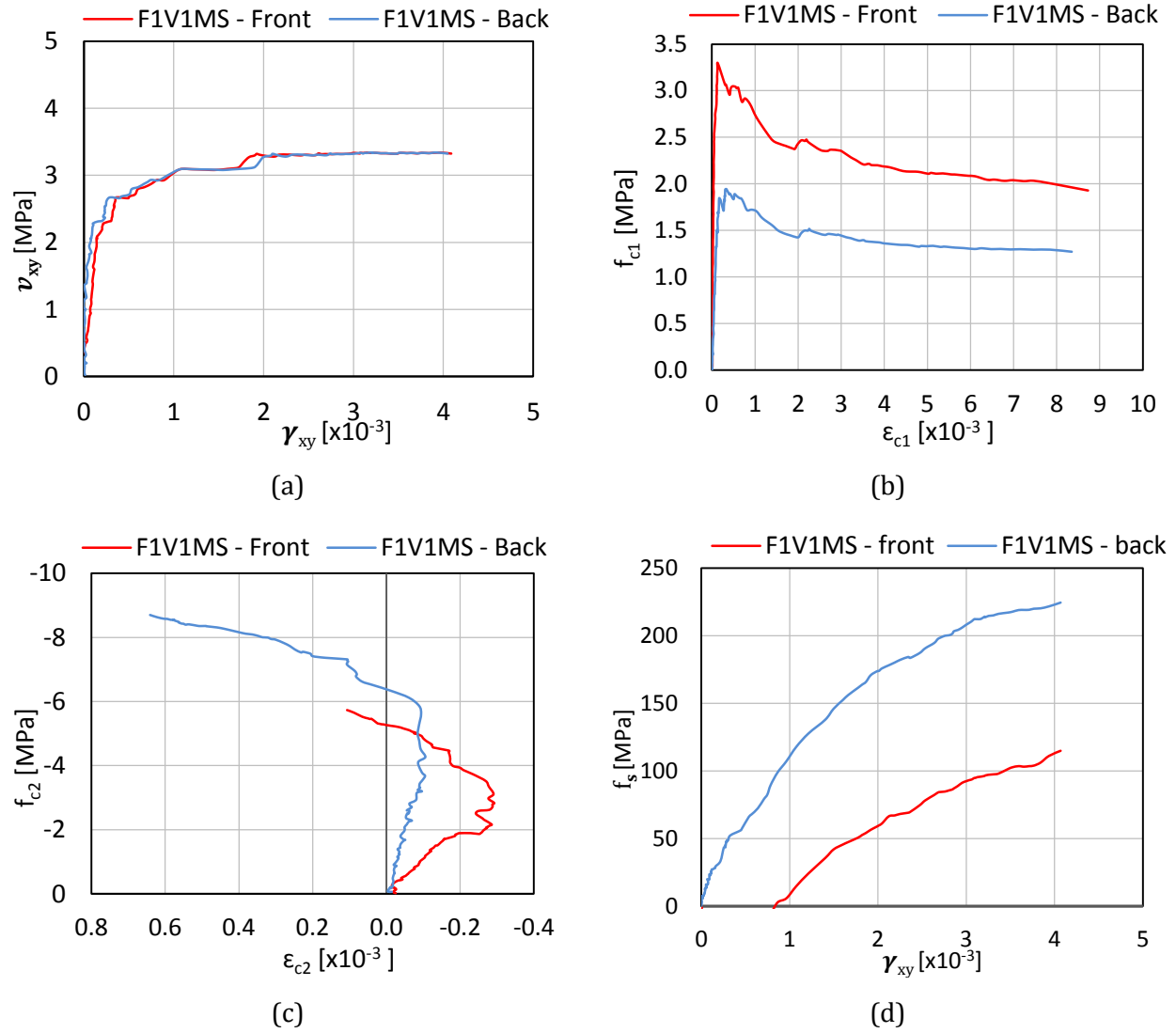
Figure B.4: Comparison of back face and front face response of panel CMS

B.2 CRC

Panel CRC was the reversed cyclically loaded control panel and was made using the same batch of concrete as CMS. Panel CRC contained 3.31% reinforcement in the primary direction and 0.42% reinforcement in the transverse direction. Determined from the material tests, this panel had a 28-day compressive strength of 43.0 MPa and a uniaxial tensile strength of 3.91 MPa; the test day compressive strength was 45.5 MPa. The double cycle peak shear stresses were 1.00 MPa, 2.10 MPa, 2.65 MPa, 3.13 MPa, 3.65 MPa, 4.20 MPa, 4.80 MPa, 5.30 MPa, and 5.60 MPa.

B.2.1 Test Observations

The crack patterns observed during the load stages are shown in Figure B.5. Through examining the test results, it was believed that the first crack occurred at a shear stress of 1.37 MPa with a shear strain of 0.16×10^{-3}. By the end of the 2nd double cycle, vertical and horizontal cracks had formed on both faces. By the 3rd double cycle, at a shear stress of 2.65 MPa, cracks in both directions became sufficiently uniform on both faces.

Yielding of the transverse reinforcement occurred during the second load stage of the 7th double cycle (stage 26), at a shear stress of -4.75 MPa and a shear strain of -4.23×10^{-3}. Failure of the specimen occurred during the excursion to the second load stage of the 9th double cycle (stage 34) at a shear stress and shear strain of -5.25 MPa and -9.87×10^{-3}, respectively. The brittle failure was initiated by the yielding of the transverse reinforcement followed by the aggregate interlock failure. The failure crack was parallel to the primary reinforcement.

As shown in Figure B.6, the crack spacing and the average crack width was identical between positive and negative shear while the maximum crack width was similar between the two directions. With increasing loads, the crack spacing decreased while the crack widths increased. The increase in the average and the maximum crack width was relatively linear until the transverse reinforcement yielded; afterwards, the crack widths increased rapidly. At the last load stage before failure, the maximum crack width, the average crack width, and the average crack spacing were 1.40 mm, 0.39 mm, and 70.0 mm, respectively.
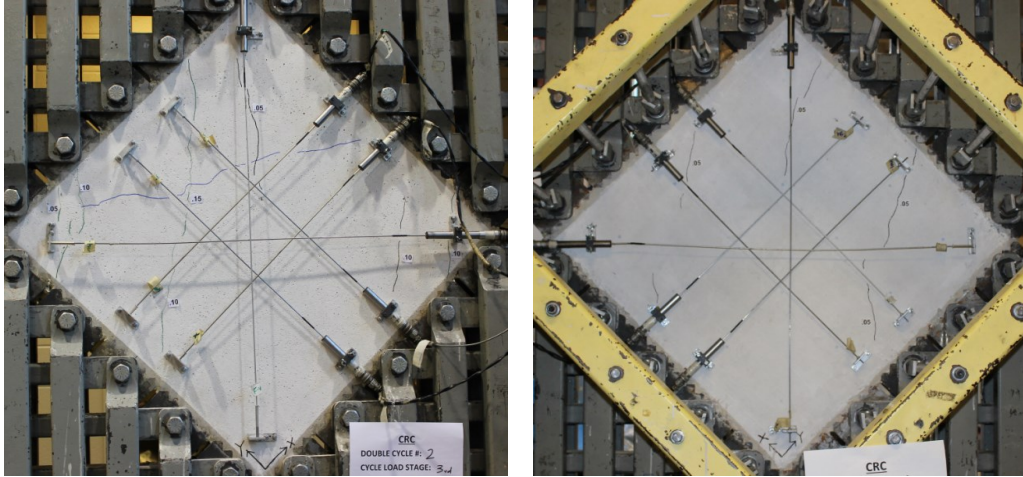
Double Cycle 2, Stage 7: v_{xy}=2.15 MPa, γ_{xy}=0.39×10⁻³; $w_{cr,max}$=0.15 mm, w_m=0.08 mm, s_m=336 mm.
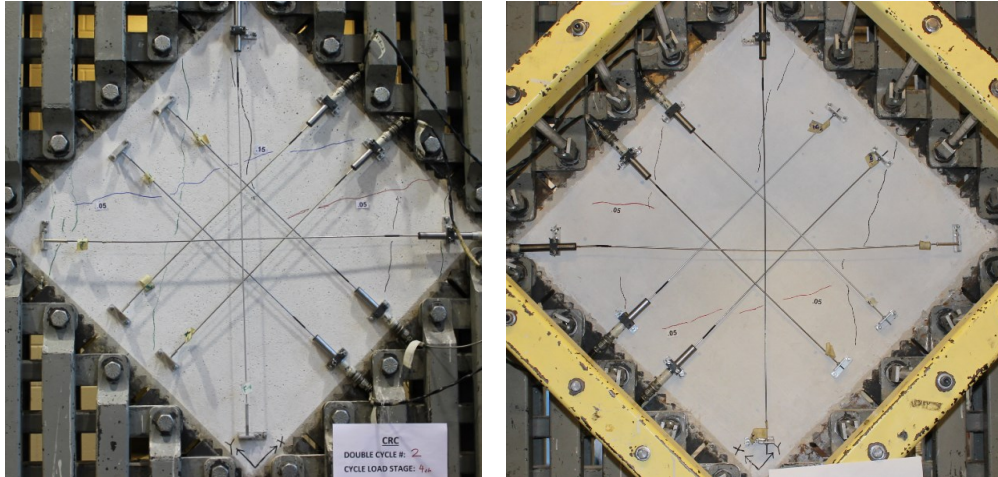
Double Cycle 2, Stage 8: v_{xy}=-2.07 MPa, γ_{xy}=-0.36×10⁻³; $w_{cr,max}$=0.15 mm, w_m=0.07 mm, s_m=525 mm.
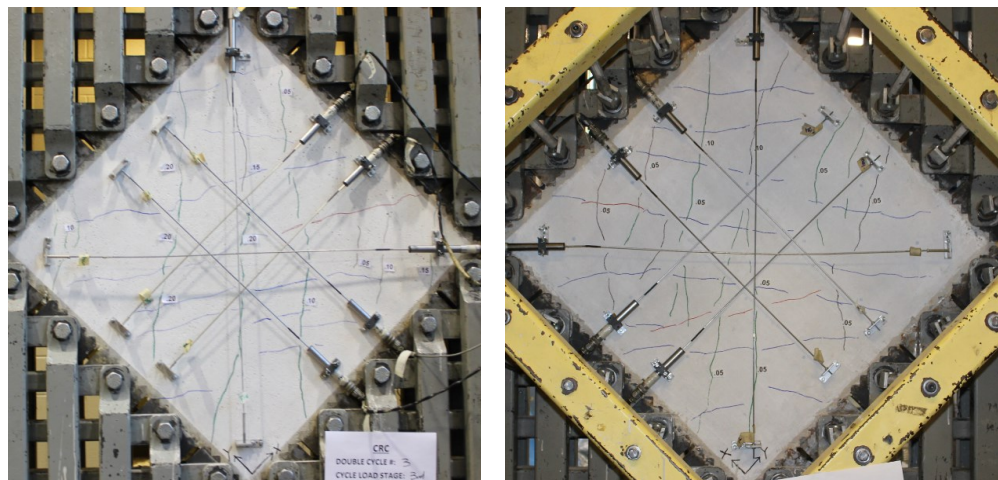
Double Cycle 3, Stage 11: v_{xy}= 2.65 MPa, γ_{xy}=1.05×10⁻³; $w_{cr,max}$= 0.20 mm, w_m= 0.10 mm, s_m=180 mm.
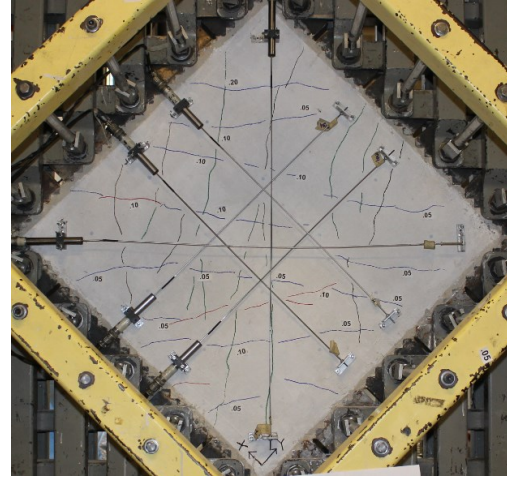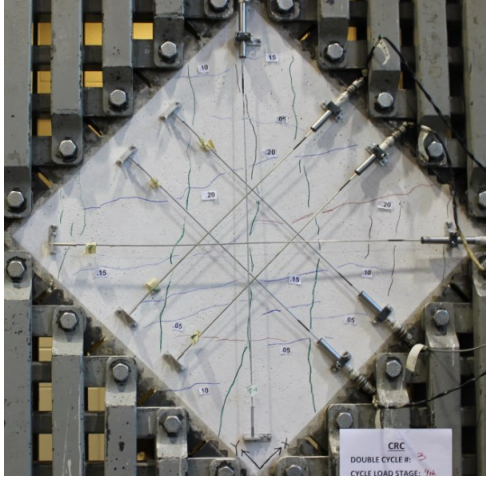
Double Cycle 3, Stage 12: v_{xy}=-2.65 MPa, γ_{xy}=-1.32×10^{-3}; $w_{cr,max}$=0.20 mm, w_m=0.10 mm, s_m=158 mm.
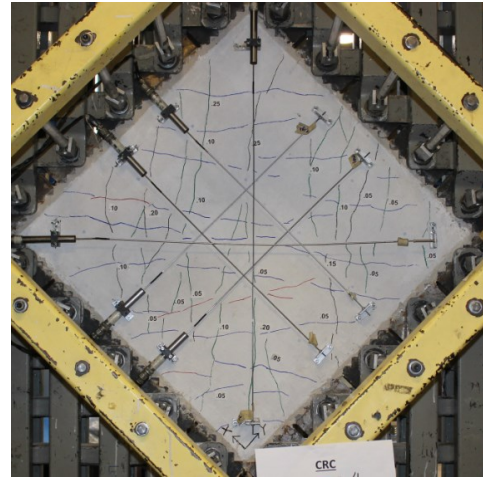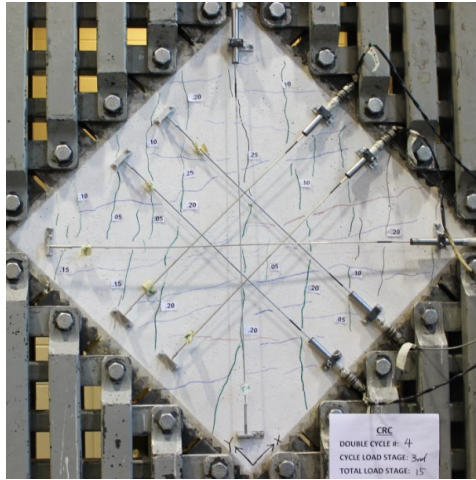
Double Cycle 4, Stage 15: v_{xy}=3.13 MPa, γ_{xy}=1.72×10^{-3}; $w_{cr,max}$=0.25 mm, w_m=0.13 mm, s_m=133 mm.
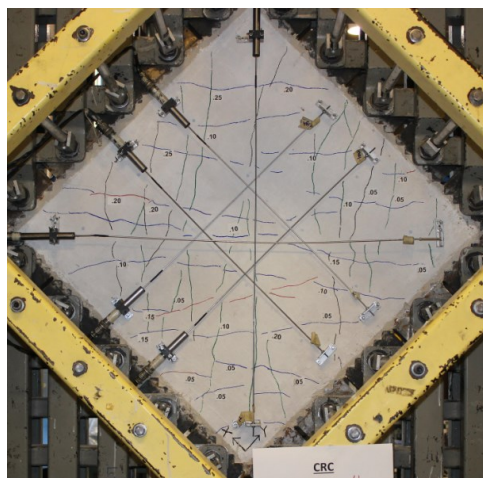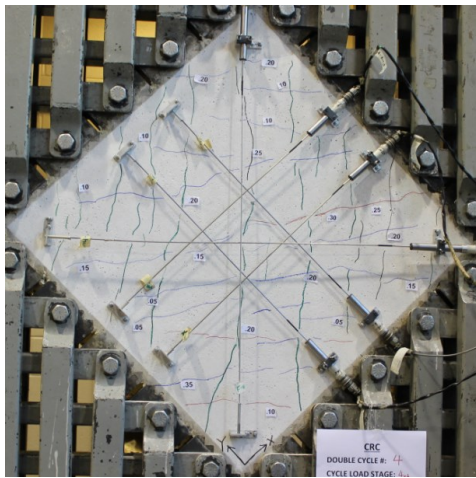
Double Cycle 4, Stage 16: v_{xy}=-3.11 MPa, γ_{xy}=-2.08×10^{-3}; $w_{cr,max}$=0.35 mm, w_m=0.14 mm, s_m=105 mm.
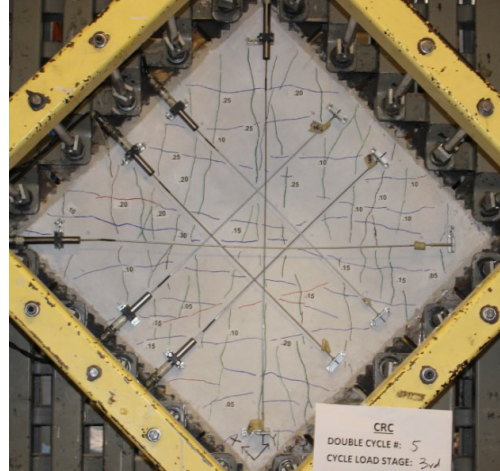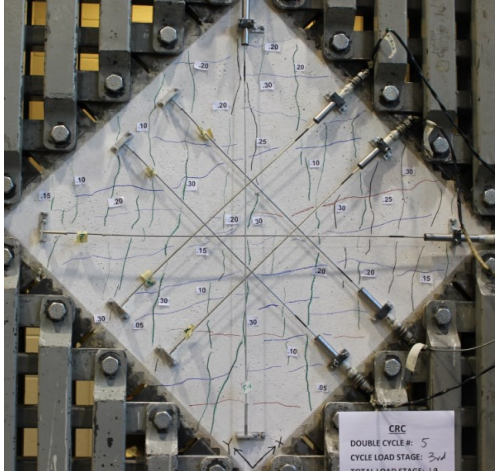
Double Cycle 5, Stage 19: v_{xy}=3.62 MPa, γ_{xy}=2.63×10^{-3}; $w_{cr,max}$=0.30 mm, w_m=0.18 mm, s_m=94 mm.
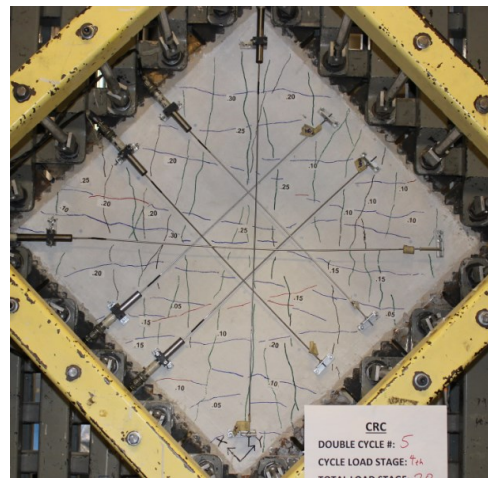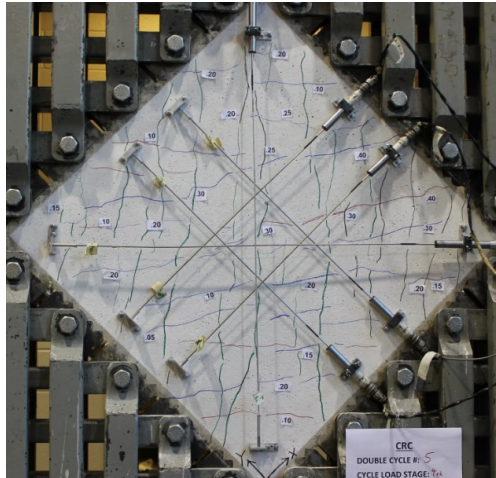
Double Cycle 5, Stage 20: v_{xy}=-3.60 MPa, γ_{xy}=-2.59×10^{-3}; $w_{cr,max}$=0.40 mm, w_m=0.18 mm, s_m=101 mm.
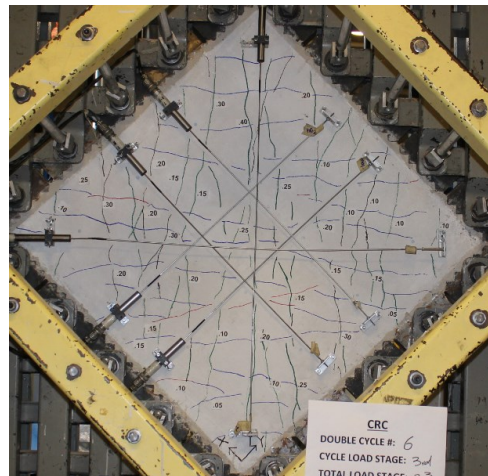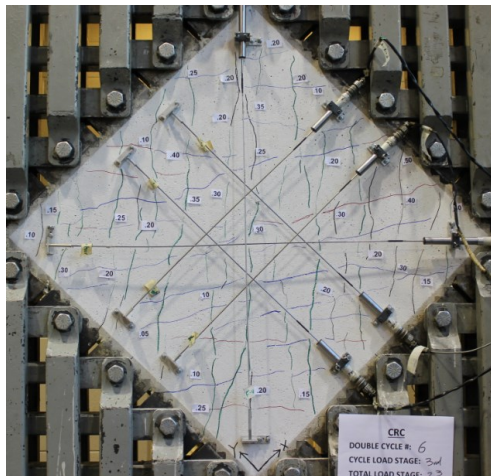
Double Cycle 6, Stage 23: v_{xy}=4.18 MPa, γ_{xy}=3.45×10^{-3}; $w_{cr,max}$=0.50 mm, w_m=0.20 mm, s_m=90 mm.
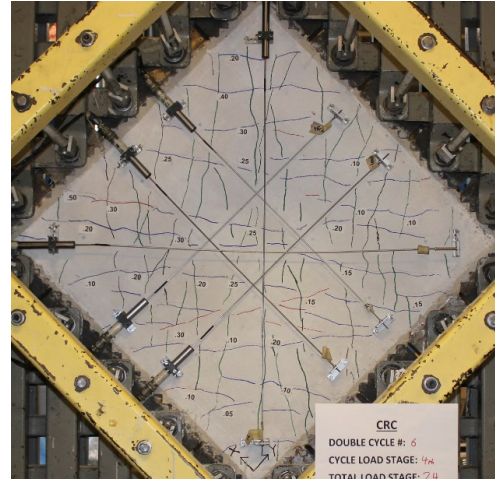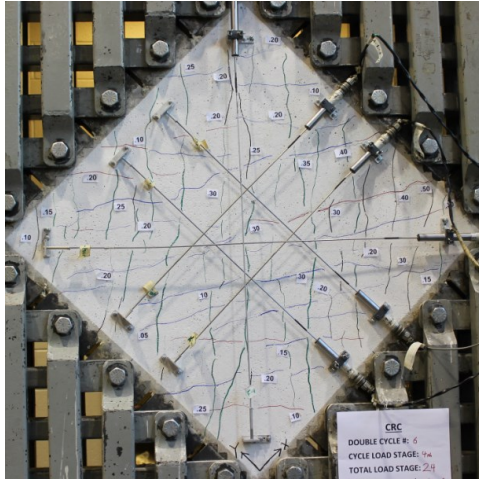
Double Cycle 6, Stage 24: v_{xy}=-4.19 MPa, γ_{xy}=-3.30×10^{-3}; $w_{cr,max}$=0.50 mm, w_m=0.22 mm, s_m=94 mm.
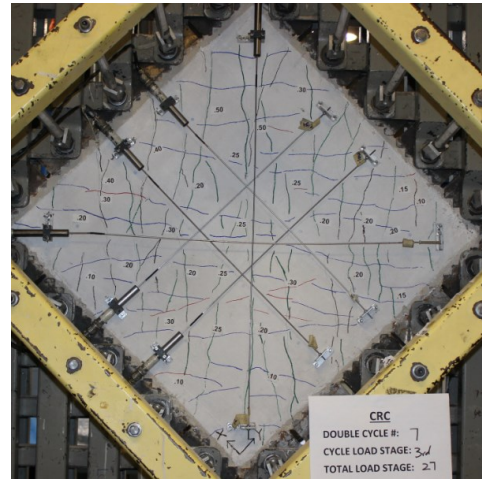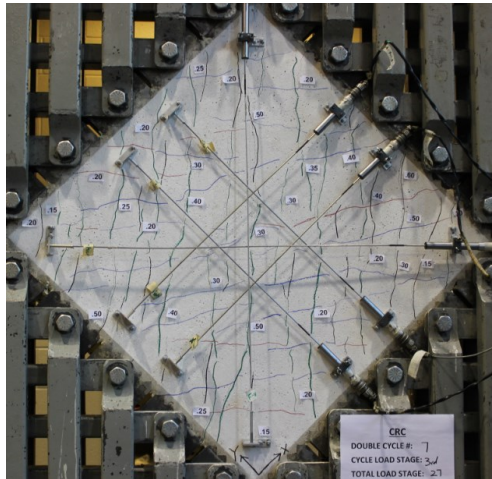
Double Cycle 7, Stage 27: v_{xy}=4.81 MPa, γ_{xy}=4.68×10^{-3}; $w_{cr,max}$=0.60 mm, w_m=0.28 mm, s_m=79 mm.
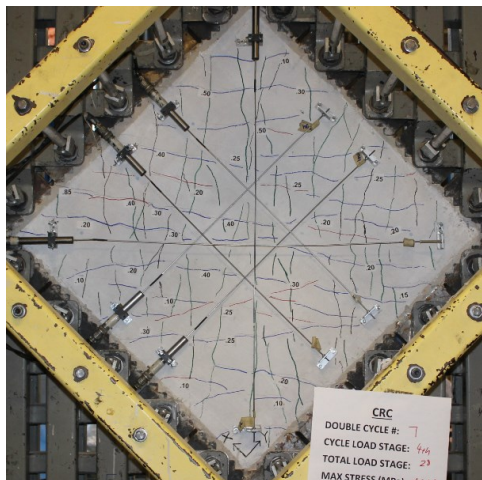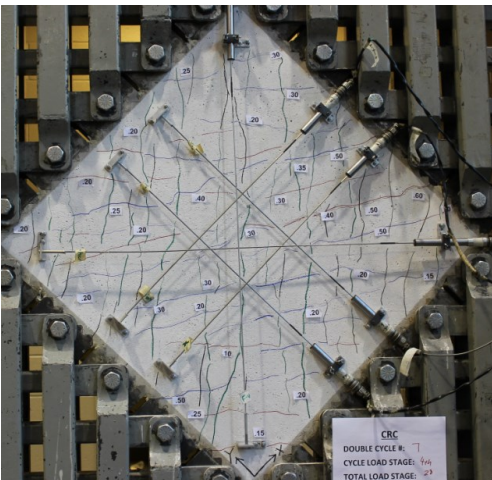
Double Cycle 7, Stage 28: v_{xy}=-4.73 MPa, γ_{xy}=-4.46×10^{-3}; $w_{cr,max}$=0.85 mm, w_m=0.29 mm, s_m=79 mm.
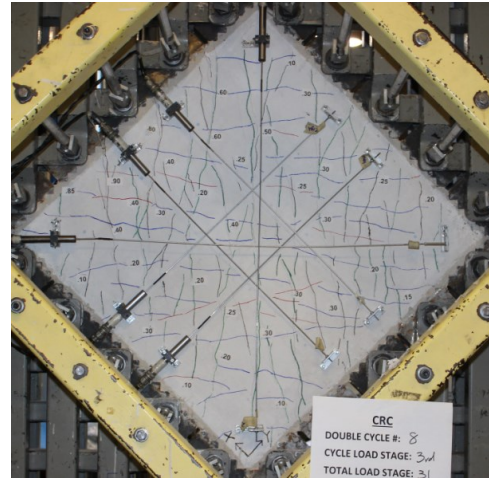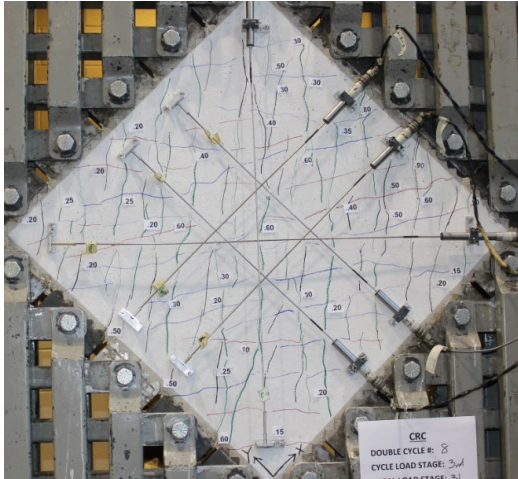
Double Cycle 8, Stage 31: v_{xy}=5.27 MPa, γ_{xy}=6.98×10^{-3}; $w_{cr,max}$=0.90 mm, w_m=0.36 mm, s_m=70 mm.
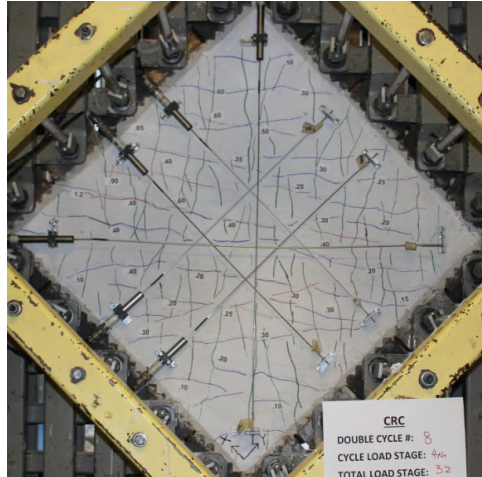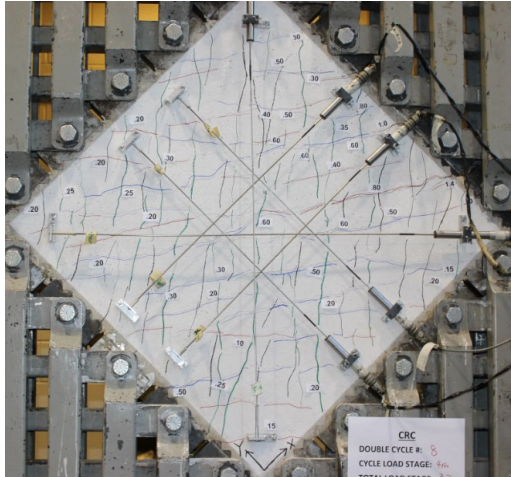
Double Cycle 8, Stage 32: v_{xy}=-5.28 MPa, γ_{xy}=-7.08×10^{-3}; $w_{cr,max}$=1.40 mm, w_m=0.39 mm, s_m=70 mm.
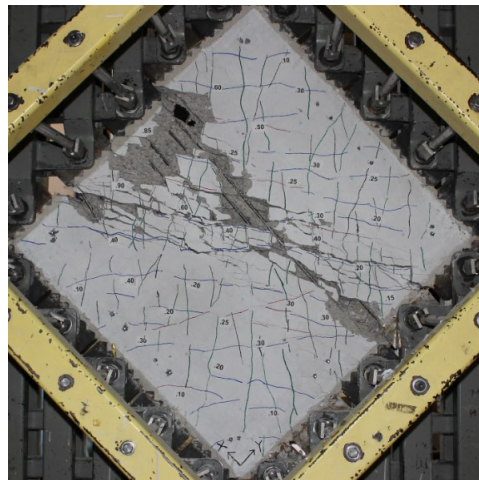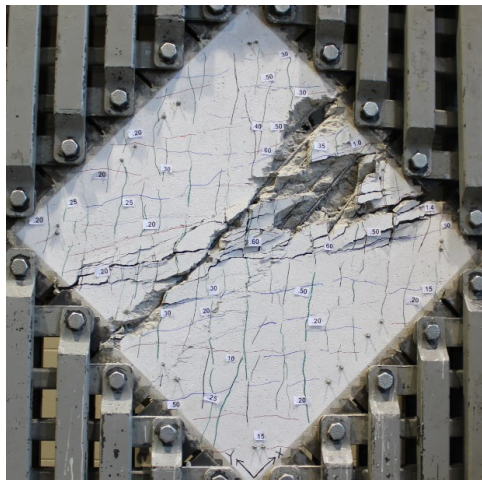
Failure: v_u=5.63 MPa, γ_u=9.77×10^{-3}.

Figure B.5: Crack pattern of panel CRC
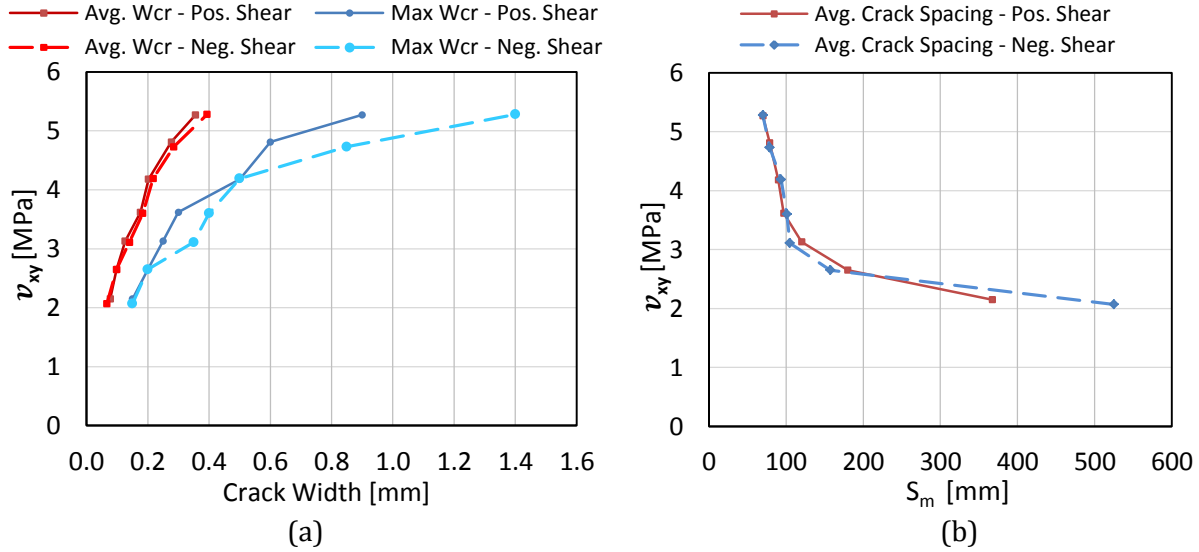
Figure B.6: Crack spacing and crack width of panel CRC

B.2.2 Data Analysis

Figure B.7 shows the various response of panel CRC. The principal responses and the shear stress-shear strain response were linear up to first-cracking, which occurred at a shear stress of 1.37 MPa with a shear strain of 0.158×10^{-3}. This relatively low cracking stress can be attributed to the initial out-of-plane bending in the positive shear direction. After yielding of the transverse reinforcement, which occurred at a shear stress of -4.75 MPa and a shear strain of -4.23×10^{-3}, the panel exhibited greater softening. Failure occurred at a shear stress and shear strain of -5.25 MPa and -9.87×10^{-3}, respectively. At the maximum load, the ultimate shear stress was 5.62 MPa with a corresponding ultimate shear strain of 9.77×10^{-3}.

As shown by the isolated cycles of the shear stress-shear strain response in Figure B.8, as the load increased, the panel showed gradual softening with progressive stiffness degradation upon reloading and unloading. The degree of pinching of the hysteretic loops, shown by the change in slope during reloading, was also more pronounced under higher loads. The degree of creep was also larger under higher loads; this is evident upon the higher peak strain from the second cycle of the double cycle.

At initial cracking, the principal tensile stress and strain were 1.38 MPa and 0.073×10^{-3}, respectively. Strain hardening behaviour was exhibited until the peak principal stress of 2.04 MPa was reached. Due to slip along the crack surfaces and cracks remaining open at low stresses, negative principal tensile stresses were exhibited. The softening of the response plateaued near 0.5

MPa. The principal tensile response was largely similar between positive shear and negative shear. The failure occurred at a principal tensile stress and strain of -0.11 MPa and 14.26×10^{-3}, respectively.

At first-cracking, the principal compressive stress and strain were -1.36 MPa and -0.085×10^{-3}, respectively. The principal compressive response was much more linear than the principal tensile response as a result of the low compressive stress experienced by the panel; the principal compressive stress at failure was -13.5 MPa with a corresponding principal compressive strain of -0.16×10^{-3}. During unloading, the principal compressive strain became tensile under low loads, suggesting crack slips and cracks remaining open. Near failure, the principal compressive response drifted toward the positive region despite the increasing loads, indicating large crack slips and greater crack openings.

Although significant noise existed in the principal orientation response, the principal stress angle was similar to the principal strain angle and trends were established. In general, the principal strain angle lagged behind the principal stress angle. Near failure, the principal stress angle was approximately 119°, while the principal strain angle was 112°.

The primary reinforcement was not significantly stressed and reached a maximums stress of 330 MPa. The transverse reinforcement, however, experienced multiple post-yielding cycles and reached a maximum reinforcement strain of 12.31×10^{-3}, below its rupturing strain. To account for the post-yielding plastic offset, the elastic-plastic response shown in Figure B.7 (e) was employed.

B.2.3 Comparison of the Front Face and Back Face Responses

Figure B.9 shows the LVDT response for the front face and the back face of panel CRC. Overall, a small amount of out-of-plain bending stress was exhibited in this panel; only the positive shear response displayed out-of-plane bending, and the response between the two faces was near convergence at a shear stress of 3.0 MPa. Consistent with the other panels, the back face of the panel was stiffer.
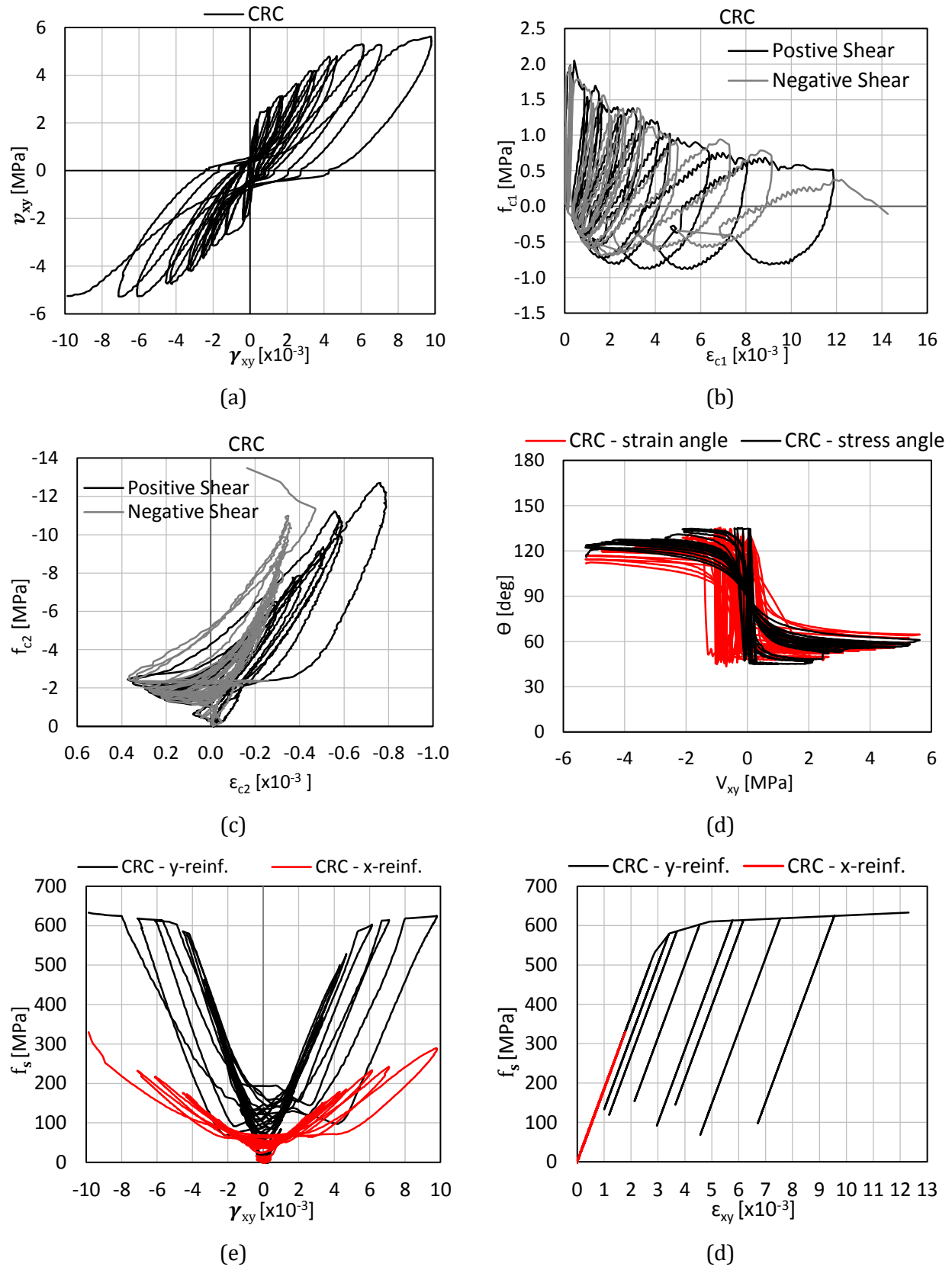
Figure B.7: Response of panel CRC

(a)

(b)

(c)

(d)

(e)

(f)
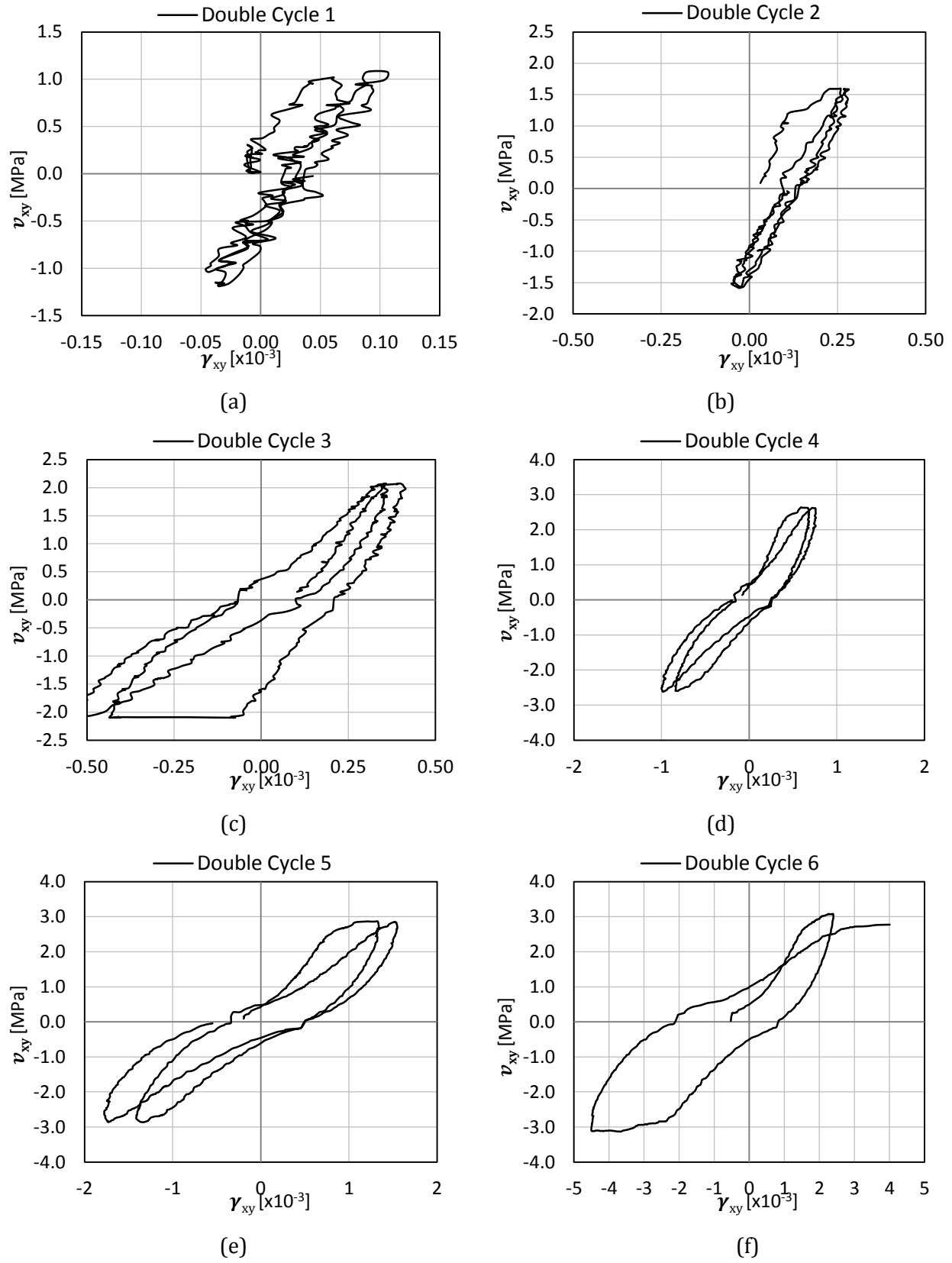
(e)

(f)

(g)
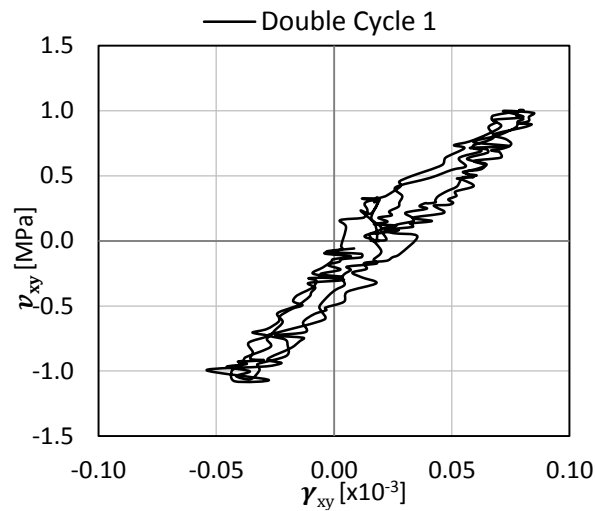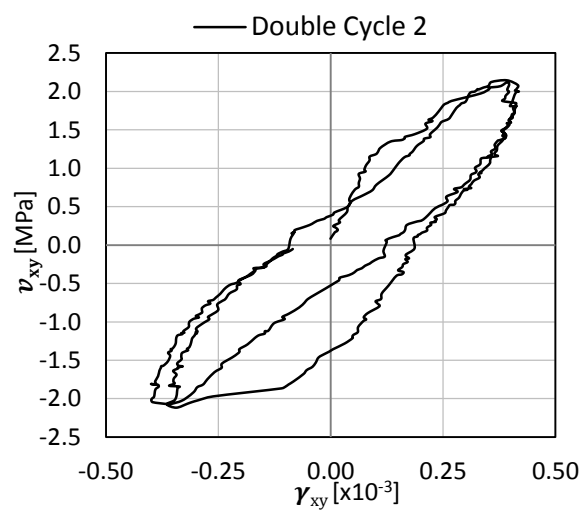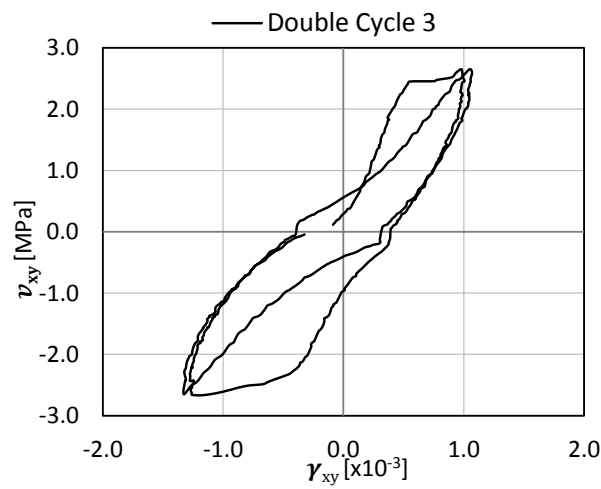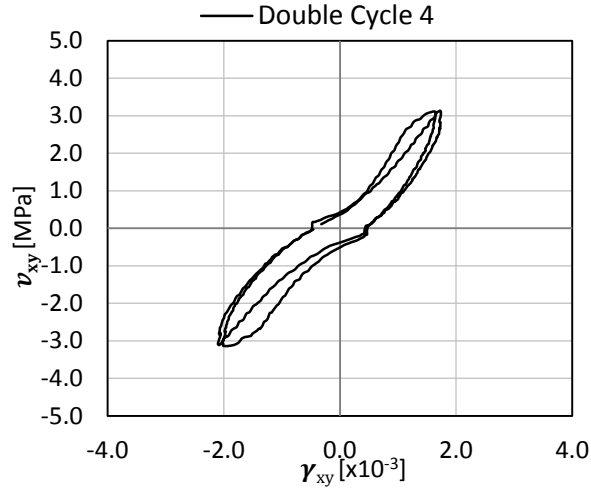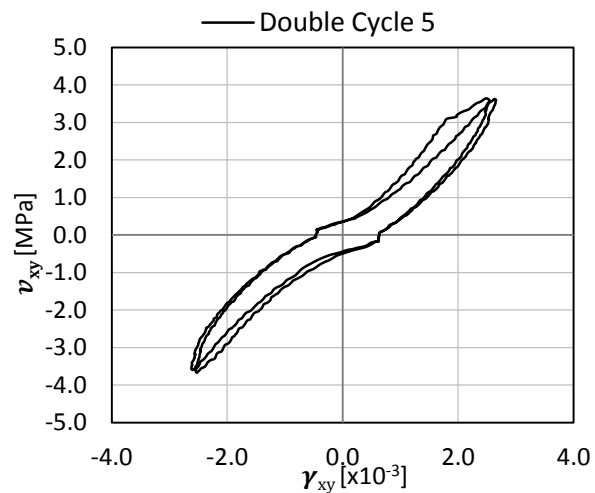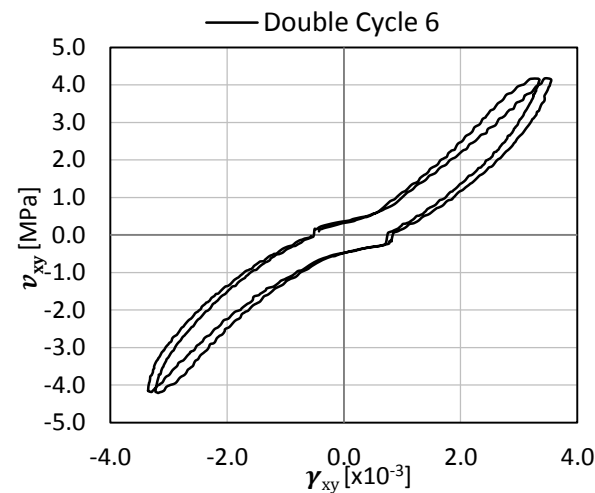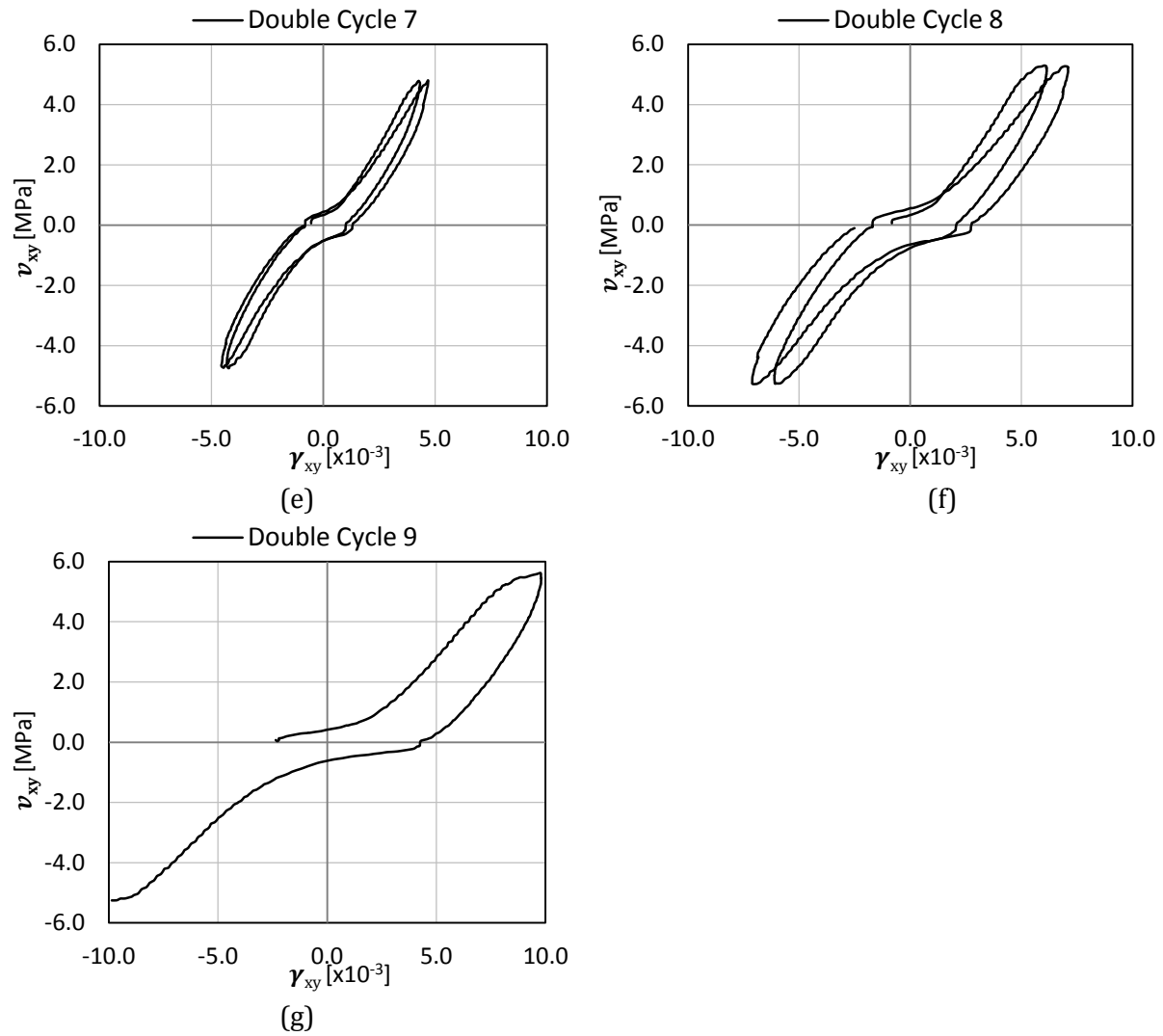
Figure B.8: Shear stress-shear strain response of CRC; isolated cycles

(a)

(b)

(c)

(d)
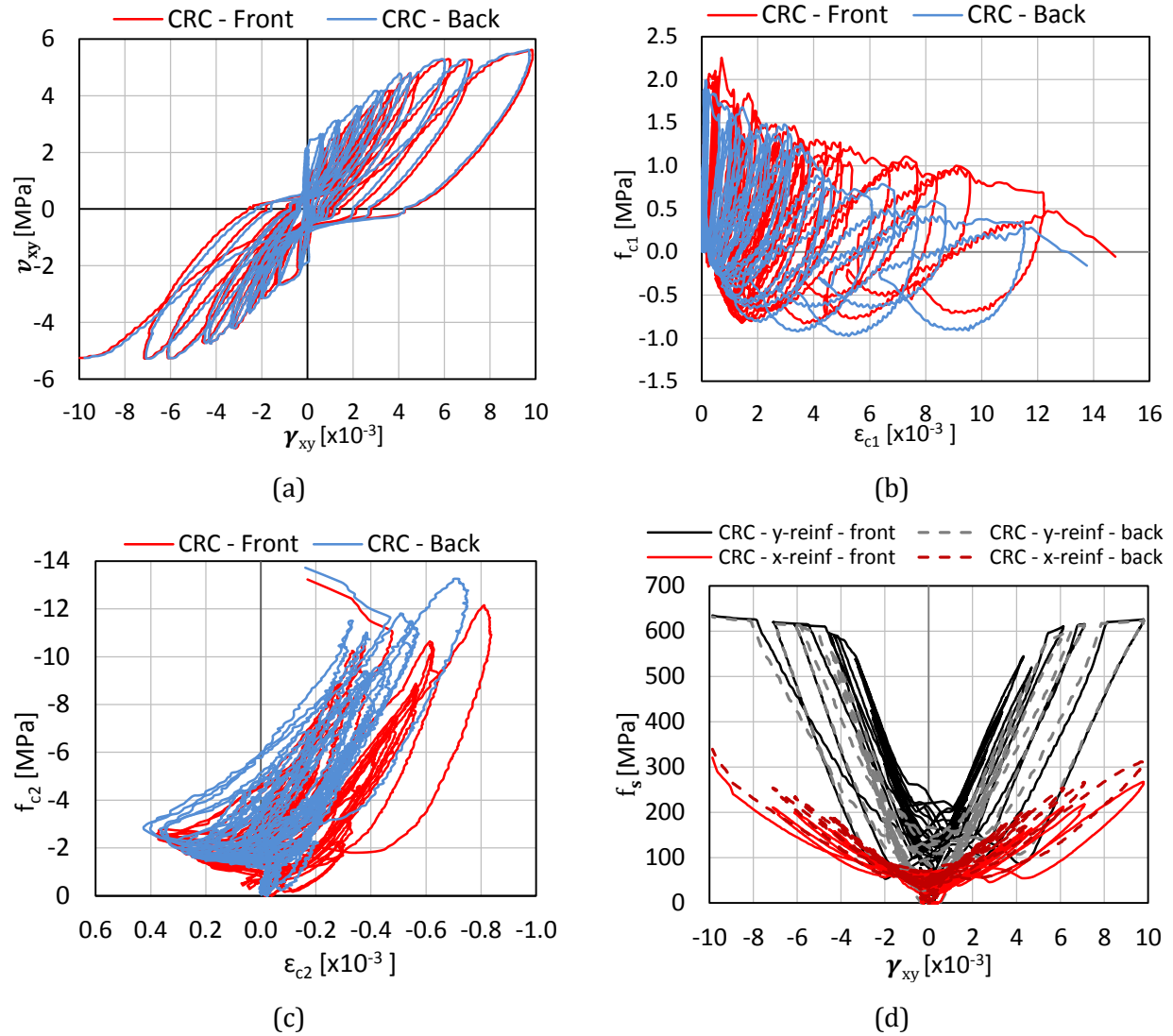
Figure B.9: Comparison of back face and front face response of panel CRC

B.3 F1V1MS

Panel F1V1MS was constructed using steel fibre reinforced concrete with 0.5% by volume of RC80/30BP fibres (l_f = 30 mm, d_f = 0.38 mm, f_{uf} = 2300 MPa). The panel was monotonically loaded. The longitudinal reinforcement ratio was 3.31% with no transverse reinforcement. This panel had a 28-day compressive strength of 53.2 MPa and a uniaxial tensile strength of 3.66 MPa; the test day compressive strength was 55.9 MPa.

B.3.1 Test Observations

Figure B.10 depicts the crack patterns of F1V1MS for each load stage. Only two load stages were taken for this panel due to the relatively weak response and the early load plateau. The first crack occurred at a shear stress of 2.18 MPa, and appeared on both the front and the back face. As the load increased, additional cracks were formed and the previously opened cracks widened. After the second load stage, at a shear stress of 3.10 MPa, the cracks were adequately uniform over both faces of the panel.

Failure occurred at a shear stress and shear strain of 2.18 MPa and 0.147×10^{-3}, respectively. The angle of the failure crack was parallel to the primary reinforcement, but the surface cracks immediately before failure were approximately 30° with respect to the x-axis. The failure was initiated by fibre pull-out followed by aggregate interlock failure. Immediately before failure, the maximum crack width, the average crack width, and the average crack spacing were 0.35 mm, 0.19 mm, and 148.8 mm, respectively.
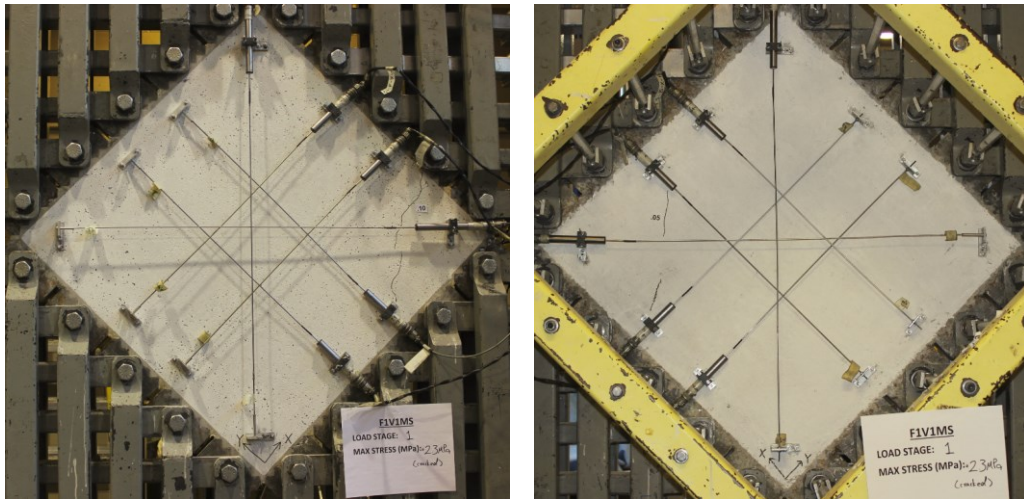
Stage 1: v_{xy}=2.31 MPa, γ_{xy}=0.22×10^{-3}; $w_{cr,max}$=0.10 mm, w_m=0.08 mm, s_m=1260 mm.
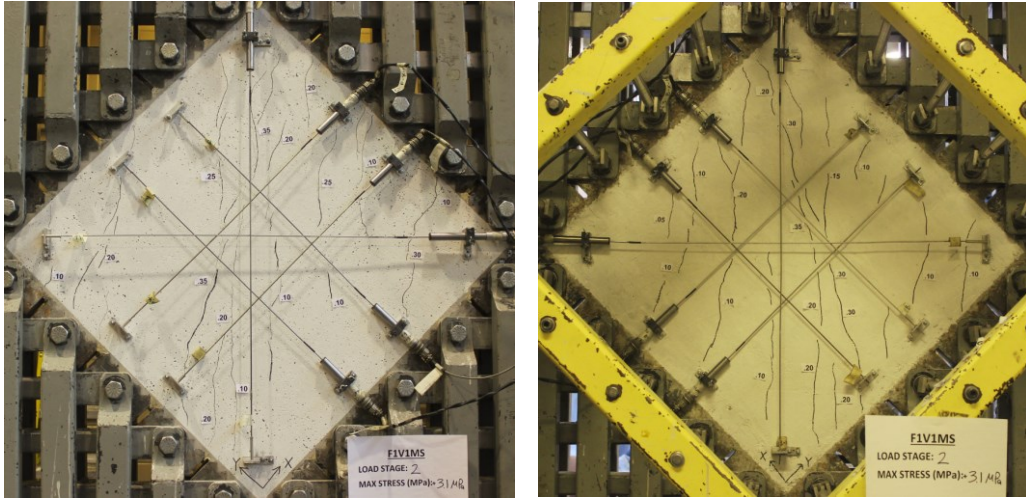
Stage 2: v_{xy}=3.10 MPa, γ_{xy}=1.66×10^{-3}; $w_{cr,max}$=0.35 mm, w_m=0.19 mm, s_m=149 mm.
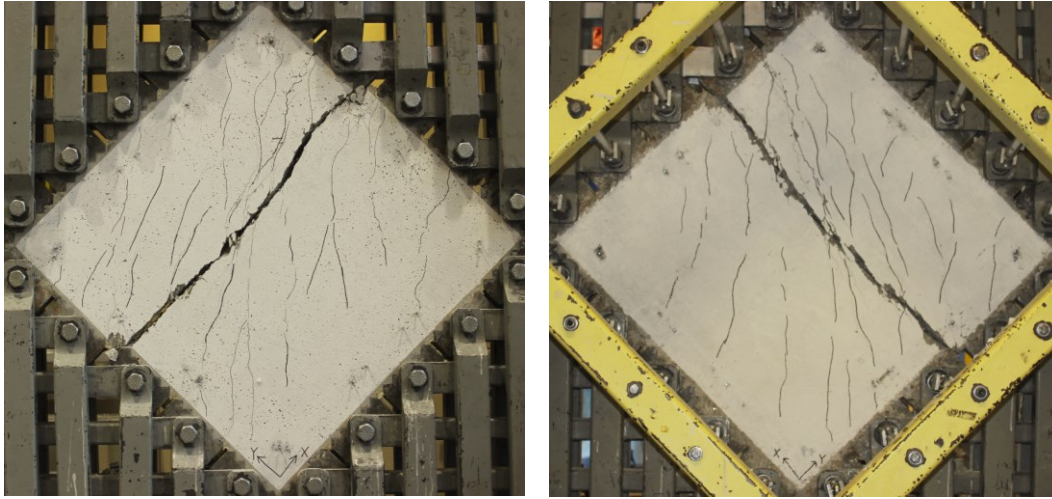
Failure: v_u=3.34 MPa, γ_u=4.07×10^{-3}.

Figure B.10: Crack pattern of panel F1V1MS

(a)

(b)
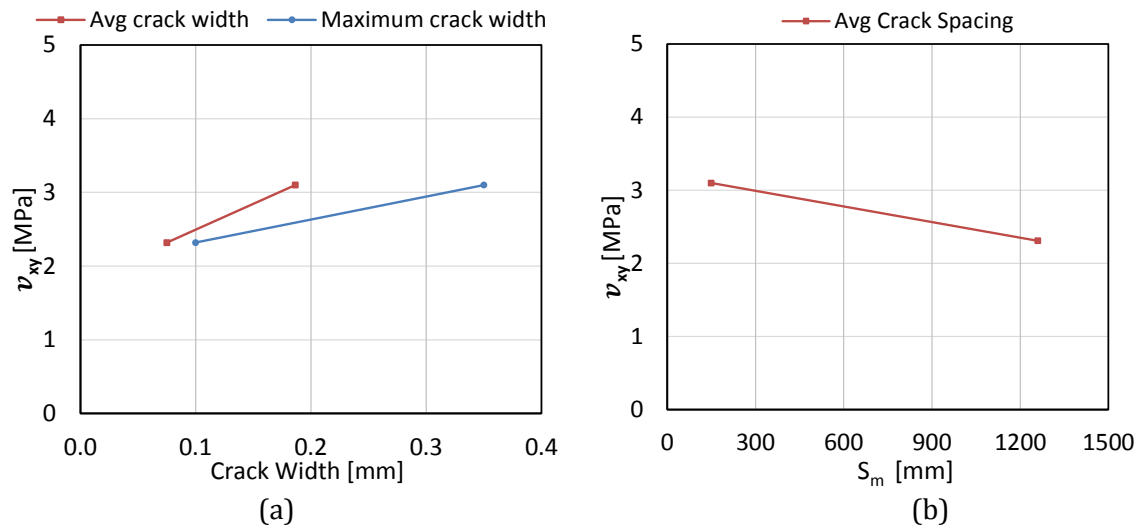
Figure B.11: Crack spacing and crack width of panel F1V1MS

B.3.2 Data Analysis

Figure B.12 shows the response of panel F1V1MS. A linear behaviour was observed in the shear stress-shear strain response of F1V1MS up to first-cracking, which occurred at shear stress of 2.18 MPa with a shear strain of 0.147×10^{-3}. During the plateau stage, as the fibres were being pulled out, the aggregate interlock mechanism could no longer transfer load across the crack and failure occurred at a shear stress and shear strain of 2.18 MPa and 0.147×10^{-3}, respectively.

The principal tensile stress and principal tensile strain at first-cracking were 2.16 MPa and 0.069×10^{-3}, respectively. Strain hardening behaviour followed thereafter until the maximum principal stress of 2.52 MPa was reached. Afterwards, the principal tensile response exhibited gradual strain softening behaviour as fibres were being pulled out. At failure, the principal tensile stress and strain were 1.54 MPa and 8.54×10^{-3}, respectively.

F1V1MS was insignificantly stressed in the principal compressive direction. At first-cracking, the principal compressive stress and strain were -2.21 MPa and -0.08×10^{-3}, respectively. As the cracks widened substantially, the principal compressive strain gradually shifted into the positive strain region. At failure, the principal compressive stress and strain were -7.16 MPa and 0.38×10^{-3}, respectively.

Before cracking, the orientation of the principal stress angle and strain angle were approximately 45°. The subsequent response indicated a general lag of the principal strain angle relative to the principal stress angle; the maximum lag was 8.7°. The primary reinforcement was not significantly stressed in this test; the peak reinforcement stress was 170 MPa.

B.3.3 Comparison of the Front Face and Back Face Responses

The LVDT response for the front face and the back face of F1V1MS is shown in Figure B.13. In short, the out-of-plane bending was insignificant for this panel. The cracking pattern was similar between both faces. At a shear stress of 2.67 MPa, the response between the two faces converged. Like all panels, the front face of the panel was less stiff and the Mohr's circle for the front face was shifted to the tension side; as a result, lower principal compressive stresses, higher principal tensile stresses, and lower x-direction reinforcement stresses were exhibited for the front face.

(a)

(b)

(c)

(d)

(e)
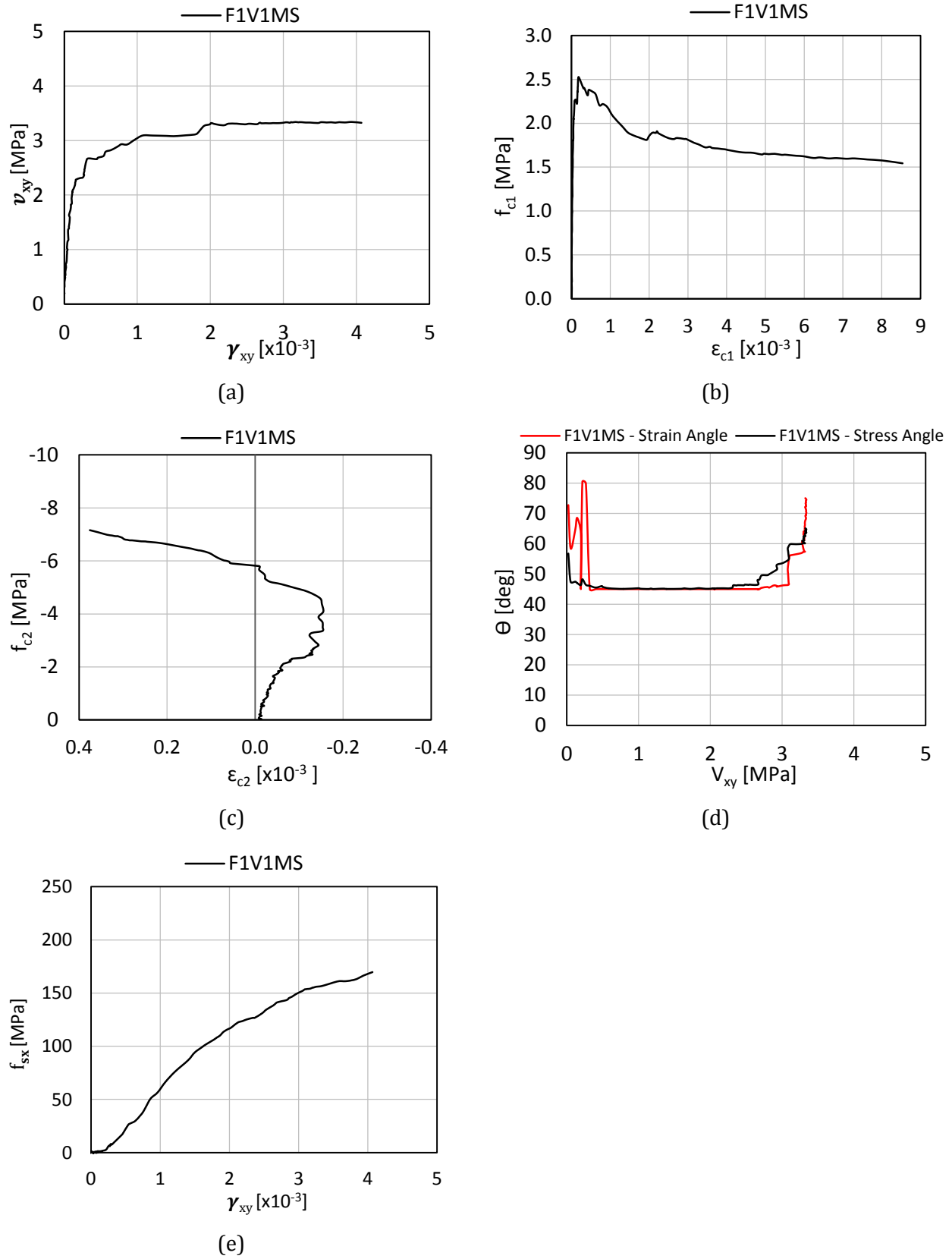
Figure B.12: Response of panel F1V1MS

Figure B.13: Comparison of back face and front face response of panel F1V1MS

B.4 F1V1RC

F1V1RC was the reversed cyclically loaded companion panel of the F1V1 pair. The panel was constructed using steel fibre reinforced concrete with 0.5% by volume of RC80/30BP fibres (l_f = 30 mm, d_f = 0.38 mm, f_{uf} = 2300 MPa). The longitudinal reinforcement ratio was 3.31% with no transverse reinforcement. This panel had a 28-day compressive strength of 53.2 MPa and a uniaxial tensile strength of 3.66 MPa; the test day compressive strength was 56.1 MPa. The double cycle peak shear stresses were 1.0 MPa, 1.6 MPa, 2.1 MPa, 2.6 MPa, 2.9 MPa, and 3.1 MPa.

B.4.1 Test Observations

Figure B.14 shows F1V1RC's crack patterns. The first crack, a vertical crack, occurred during the 2nd double cycle at a shear stress of 1.27. The first horizontal crack did not occur until the 3rd double cycle at a shear stress of -2.07 MPa. Horizontal and vertical cracks for both faces appeared during the 4th double cycle at a shear stress of 2.61 MPa. Due to out-of-plane bending, cracks in both directions for both faces were not uniformly distributed until the last load stage, at a shear stress of -3.13 MPa. Prior to this point, vertical crack were sufficiently well distributed, but the few horizontal cracks were concentrated at the lower half of the panel, below both of the x-direction LVDTs. Failure of the panel occurred at a shear stress and a shear strain of 2.77 MPa and 4.01×10^{-3}, respectively. The failure was initiated by fibre pull-out which led to an aggregate interlock failure.

As shown in Figure B.15, the crack spacing and the crack widths for positive shear lagged behind negative shear because the panel is first subjected to positive shear for all cycles; this trend was observed in all of the panels tested. With increasing stress, the crack spacing decreased linearly while the crack widths experienced a more rapid increase. During the 6th double cycle, at a shear stress of -3.13 MPa, many new horizontal cracks were developed to distribute the deformation stress evenly across the panel; as a result, the average crack width for negative shear had a rapid drop near the end. At the last load stage, the maximum crack width, the average crack width, and the average crack spacing were 1.30 mm, 0.34 mm, and 126 mm, respectively.
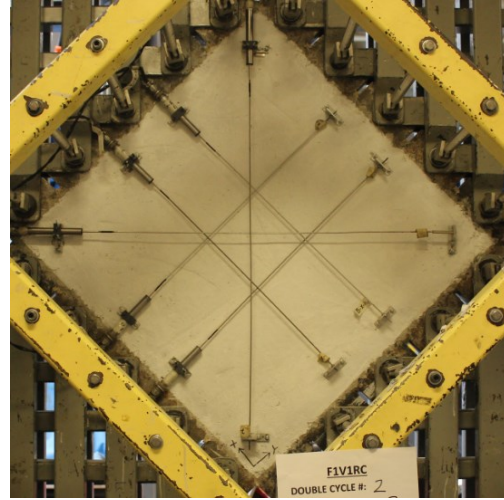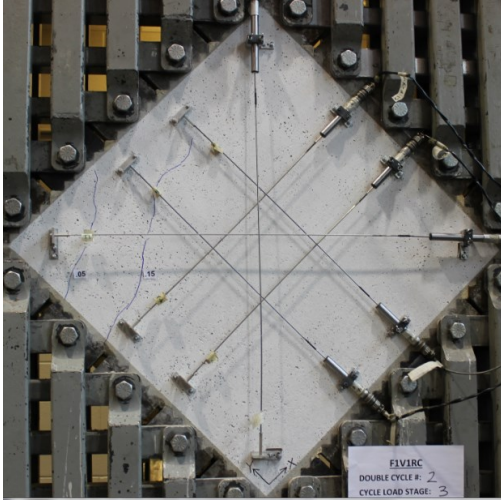
Double Cycle 2, Stage 7: v_{xy}=1.59 MPa, γ_{xy}=0.27×10^{-3}; $w_{cr,max}$=0.15 mm, w_m=0.10 mm, s_m=630 mm.
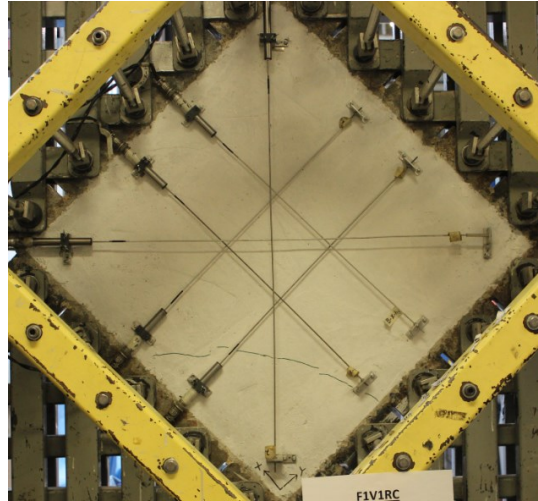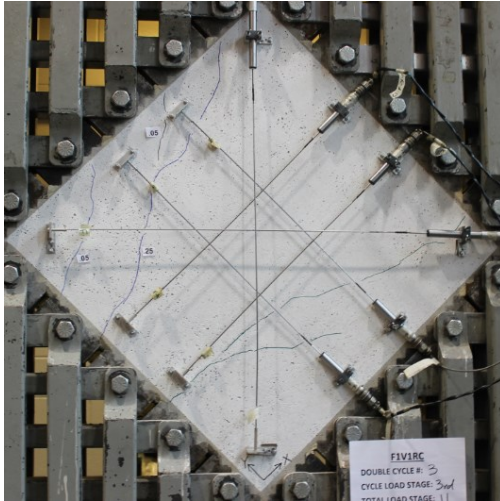
Double Cycle 3, Stage 11: v_{xy}=2.07 MPa, γ_{xy}=0.36×10^{-3}; $w_{cr,max}$=0.25 mm, w_m=0.12 mm, s_m=420 mm.
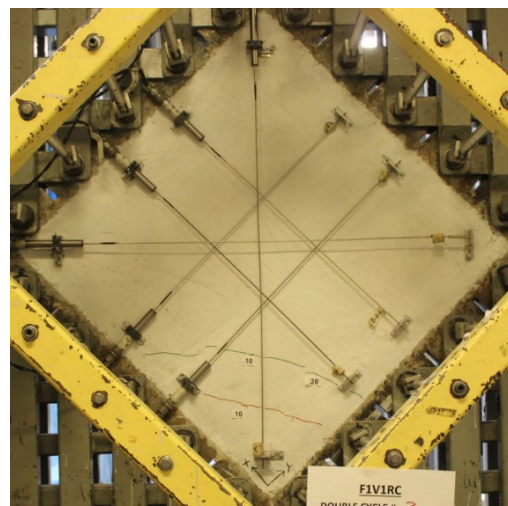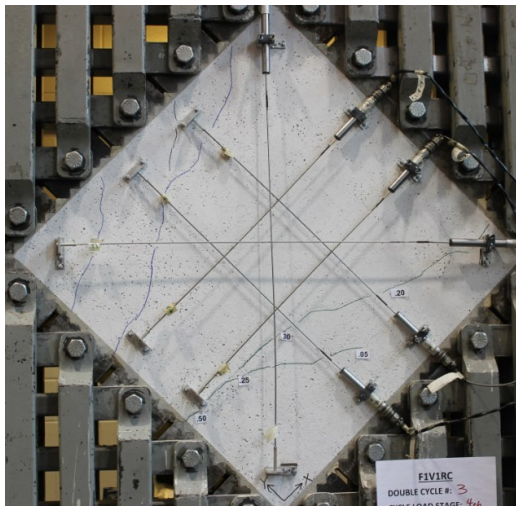
Double Cycle 3, Stage 12: v_{xy}=-2.07 MPa, γ_{xy}=-0.52×10^{-3}; $w_{cr,max}$=0.50 mm, w_m=0.21 mm, s_m=630 mm.
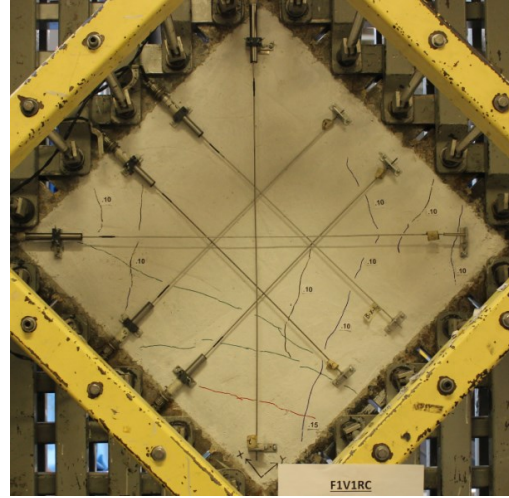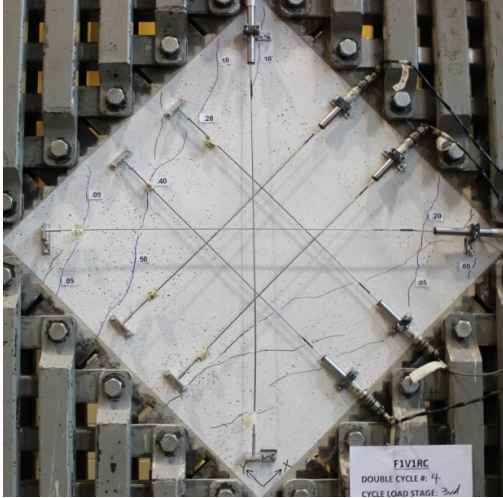
Double Cycle 4, Stage 15: v_{xy}=2.61 MPa, γ_{xy}=0.74×10⁻³; $w_{cr,max}$=0.50 mm, w_m=0.14 mm, s_m=210 mm.
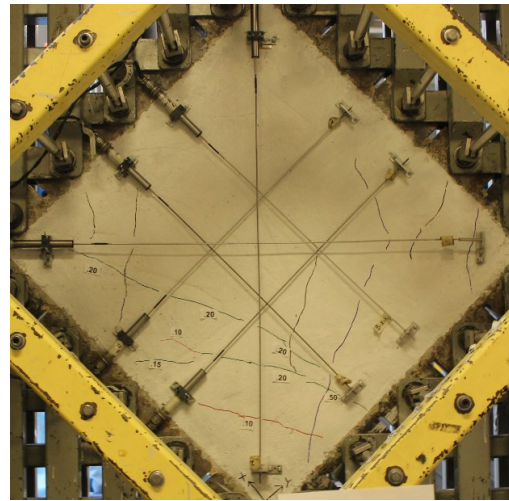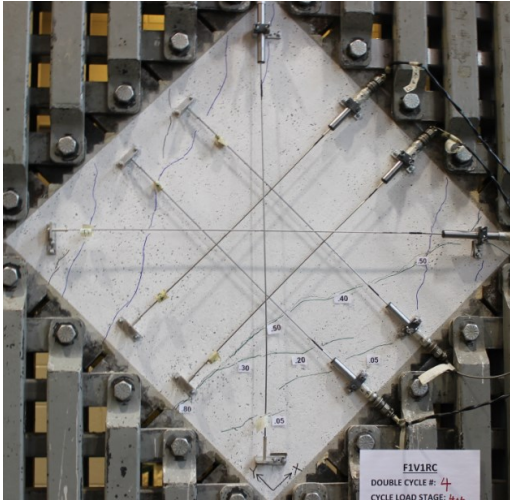
Double Cycle 4, Stage 16: v_{xy}=-2.61 MPa, γ_{xy}=-0.99×10⁻³; $w_{cr,max}$=0.80 mm, w_m=0.28 mm, s_m=367 mm.
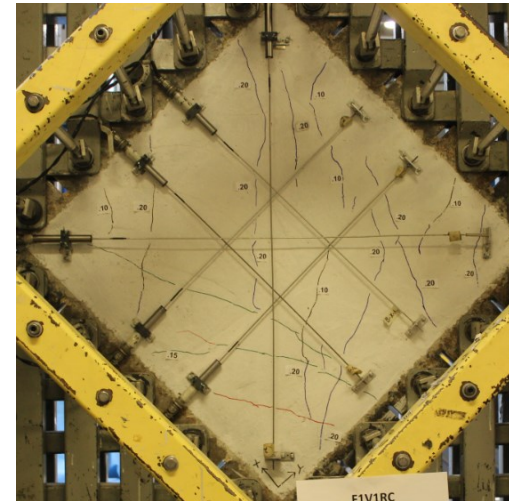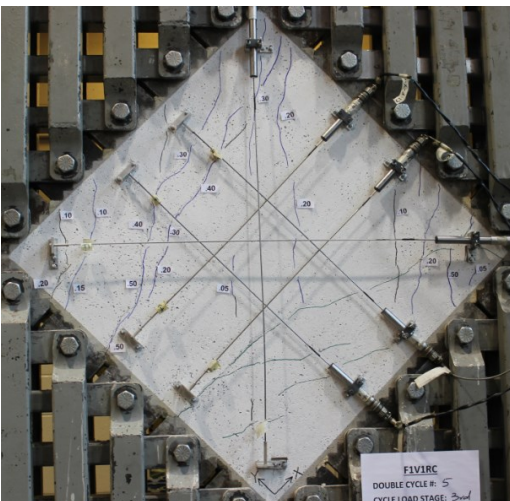
Double Cycle 5, Stage 19: v_{xy}=2.84 MPa, γ_{xy}=1.53×10⁻³; $w_{cr,max}$=0.50 mm, w_m=0.20 mm, s_m=133 mm.
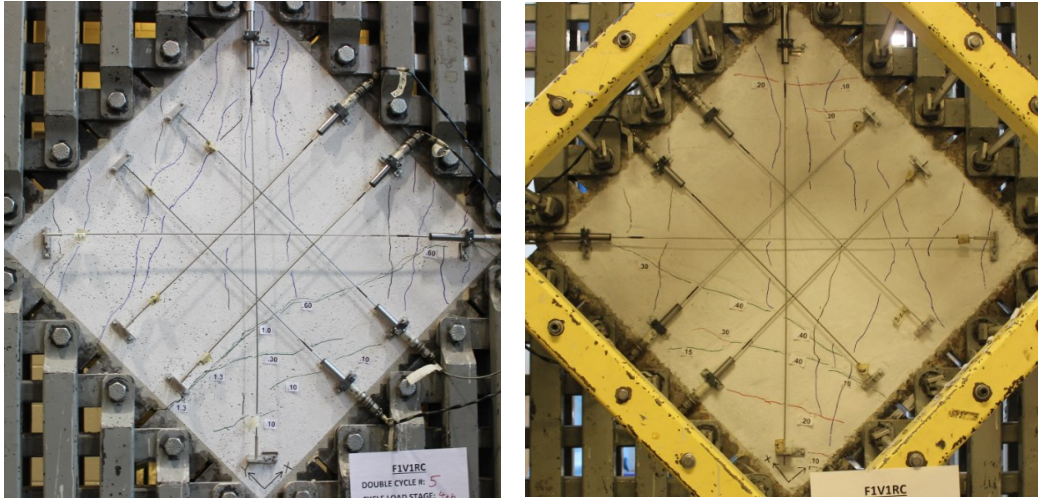
Double Cycle 5, Stage 20: v_{xy}=-2.85 MPa, γ_{xy}=-1.73×10^{-3}; $w_{cr,max}$=1.30 mm, w_m=0.42 mm, s_m=315 mm.
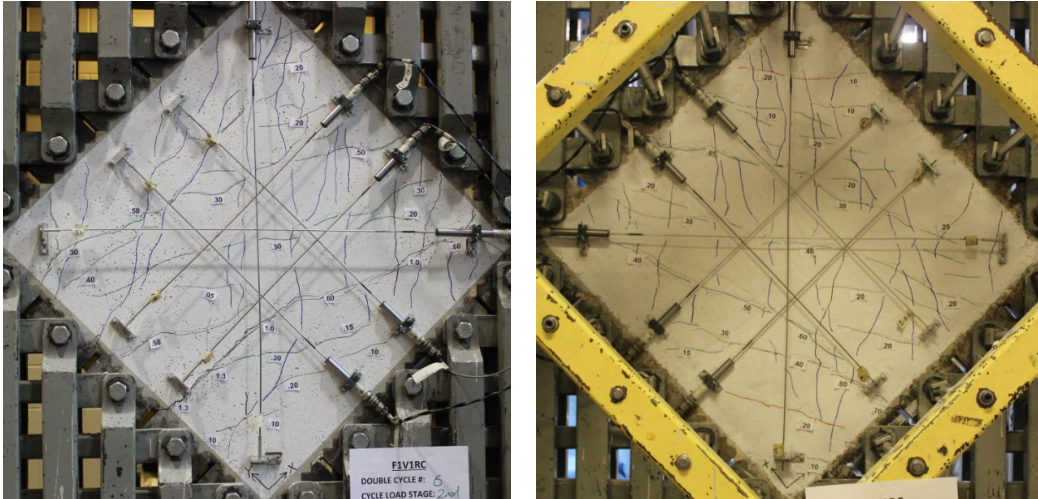
Double Cycle 6, Stage 22: v_{xy}=-3.13 MPa, γ_{xy}=-3.72×10^{-3}; $w_{cr,max}$=1.30 mm, w_m=0.34 mm, s_m=126 mm.
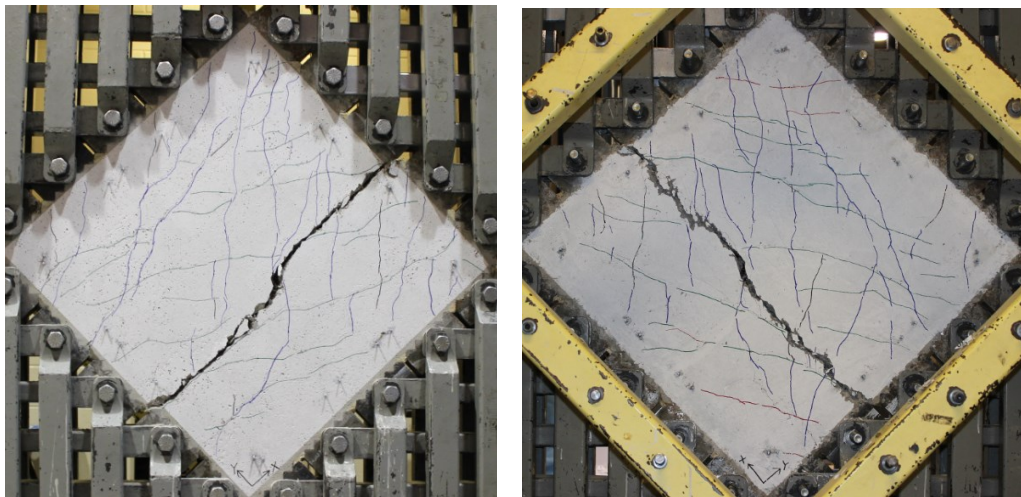
Failure: v_u=3.13 MPa, γ_u=4.51×10^{-3}.

Figure B.14: Crack pattern of panel F1V1RC
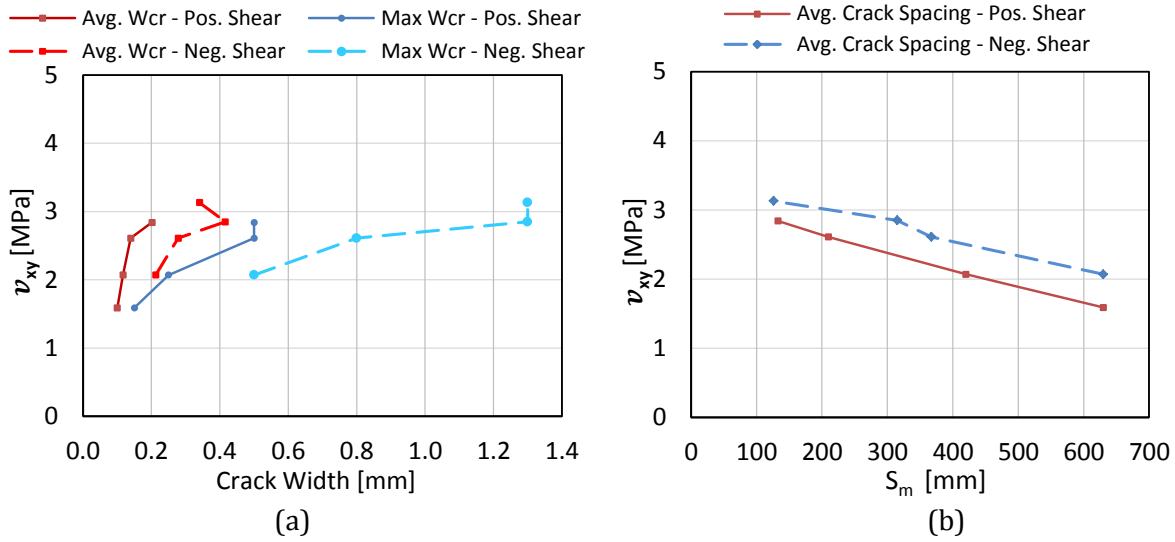
Figure B.15: Crack spacing and crack width of panel F1V1RC

B.4.2 Data Analysis

Figure B.16 shows the panel response of F1V1RC. The principal responses and shear stress-shear strain responses were linear up to first-cracking, which occurred at a shear stress of 1.27 MPa with a shear strain of $0.16×10^{-3}$. The relatively large amount of out-of-plane bending likely caused the low cracking strength. The panel exhibited significant softening on the last negative cycle then failed during the following positive cycle at a shear stress and shear strain of 2.77 MPa and $4.01×10^{-3}$, respectively. The ultimate shear stress attained was 3.13 MPa with a corresponding shear strain of $4.51×10^{-3}$.

The isolated cycles of the shear stress-shear strain response are shown in Figure B.17. Consistent with the characteristics of shear-critical reinforced concrete elements, with increasing loads, the response of F1V1RC showed progressive stiffness degradation upon reloading and unloading, increasing pinching of hysteretic loops, and an increase amount of creep. The origin of the hysteretic loops for the first two double cycles was shifted toward the positive region due to the out-of-plane bending. During the 3rd double cycle, large horizontal cracks with a maximum crack width of 0.5 mm was formed which led to a significant plateau in the 3rd double cycle's shear stress-shear strain response. This cracking helped to reduce the out-of-plane bending and the subsequent hysteretic loops were centred at the origin.

At first-cracking, the principal tensile stress and strain were 1.29 MPa and $0.104×10^{-3}$, respectively. A significant amount of strain hardening was exhibited until the maximum principal tensile stress of 2.65 MPa was reached. Afterwards, the response gradually softened until failure occurred at a

principal tensile stress and strain of 1.03 MPa and 7.61×10^{-3}, respectively. Unlike the other cyclically loaded panels, the principal stress between positive shear and negative shear did not match; the principal tensile stress was much higher for the negative direction. This is because the horizontal cracks were not uniformly distributed and were concentrated at the bottom half of the panel, below the two x-direction LVDTs. As a result, under negative shear, the x-direction LVDTs did not capture the opening of these horizontal cracks. The erroneously low x-direction LVDT measurements led to a low calculated x-direction concrete stress which caused a shift of the Mohr circle to the tension side, creating larger principal tensile stresses. In the positive shear direction, the vertical cracks were sufficiently well distributed and crossed the x-direction LVDTs; hence, appropriate principal stresses were calculated.

The principal compressive stress and strain at first-cracking were -1.25 MPa and -0.06×10^{-3}, respectively. During unloading, due to crack slips and cracks remaining open, the principal compressive strain became tensile under small loads. At failure, the principal compressive stress was -7.48 MPa with a principal compressive strain of 0.44×10^{-3}.

Under high loads, the principal stress angle lagged significantly behind the principal strain angle and the lag was especially pronounced under negative shear; the lag under negative shear was approximately 15-25° when the response had softened. This lag indicated large crack slips occurred. At failure, the principal stress angle was 70°, while the principal strain angle was 73°. The reinforcement was insignificantly stressed and reached a peak stress of 195 MPa, 43% of the yield strength.

B.4.3 Comparison of the Front Face and Back Face Responses

Figure B.18 shows the LVDT response for the front face and the back face of panel F1V1RC. As previously mentioned, F1V1RC exhibited the largest out-of-plane bending for panels tested in this work; the peak shear strain difference between the two faces was approximately 1.0×10^{-3}. Although this degree of out-of-plane bending was acceptable and less than some panel tests previously performed (Carnovale, 2013), the bending had impacted the crack locations, crack widths, crack spacing, and centre of the hysteretic loops.
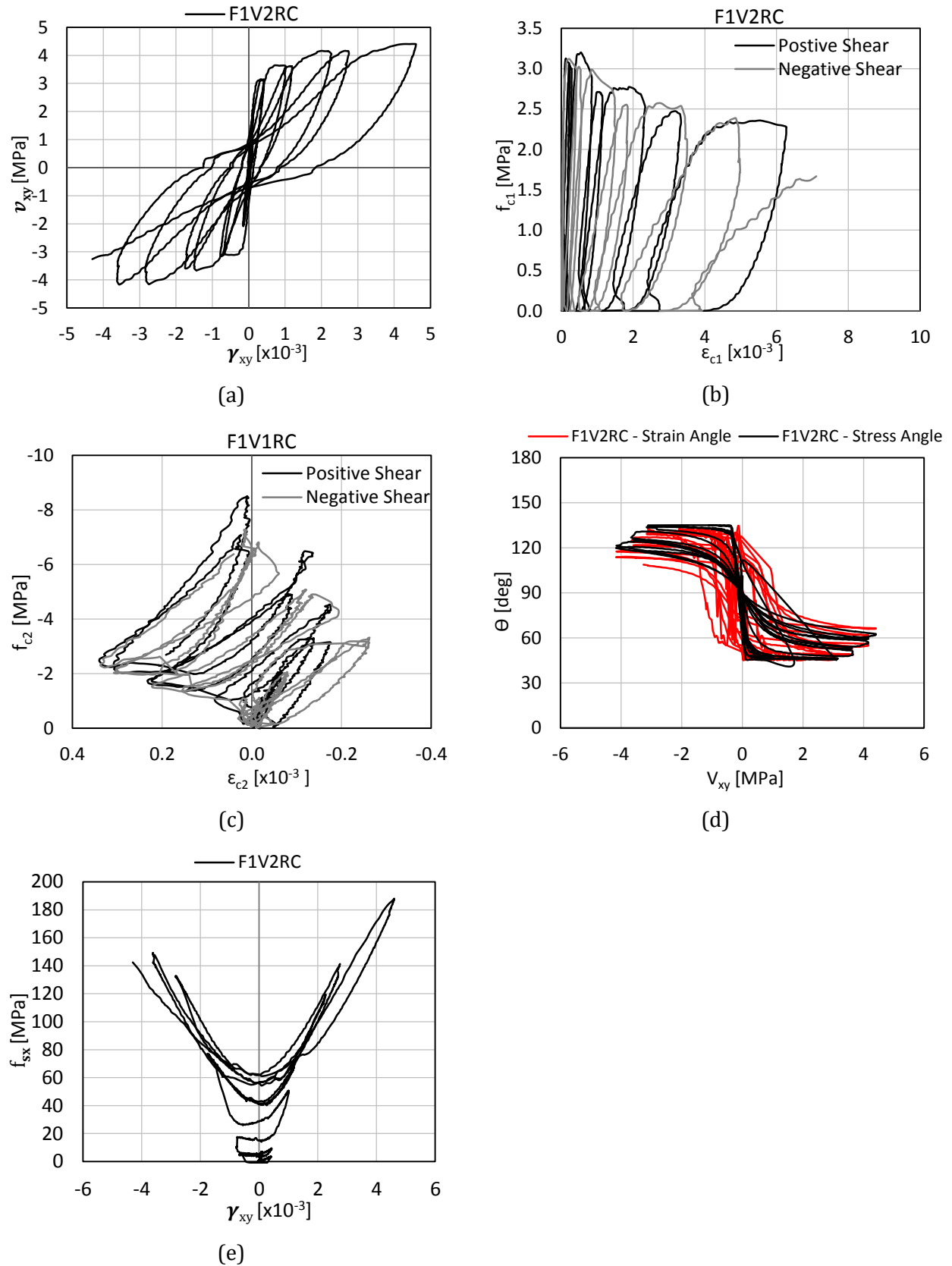
(a)

(b)

(c)

(d)

(e)
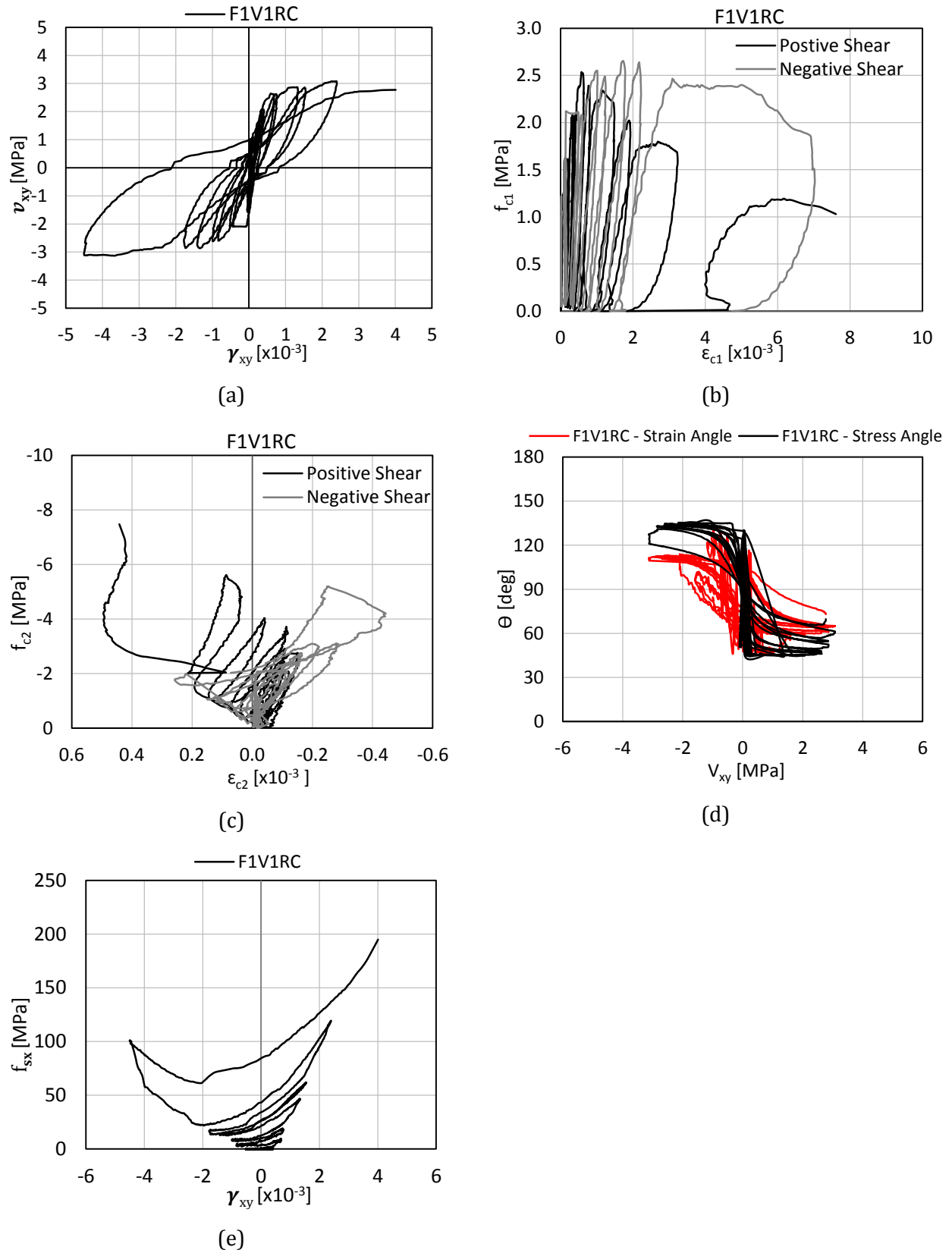
Figure B.16: Response of panel F1V1RC
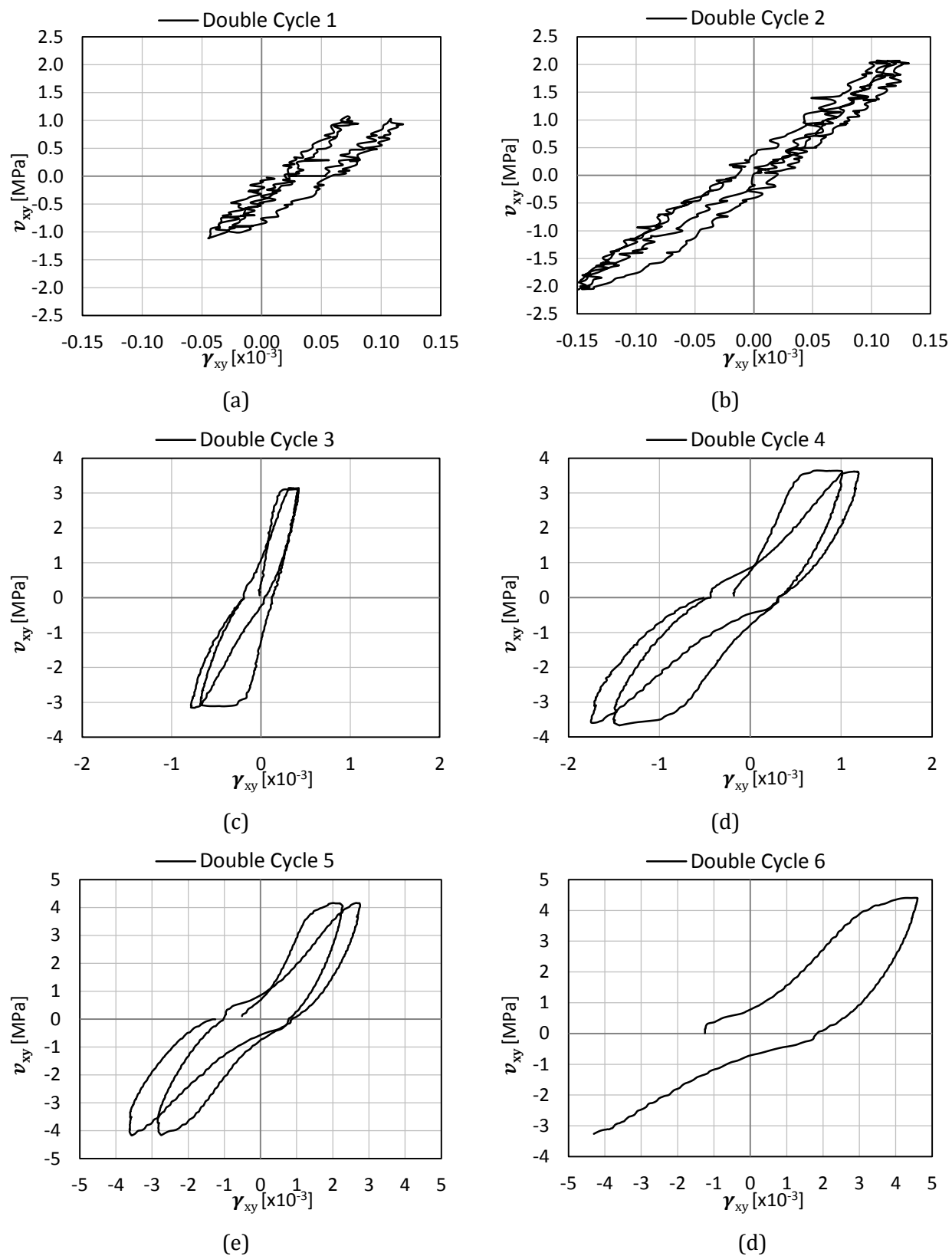
Figure B.17: Shear stress-shear strain response of F1V1RC; isolated cycles

(a)

(b)

(c)

(d)
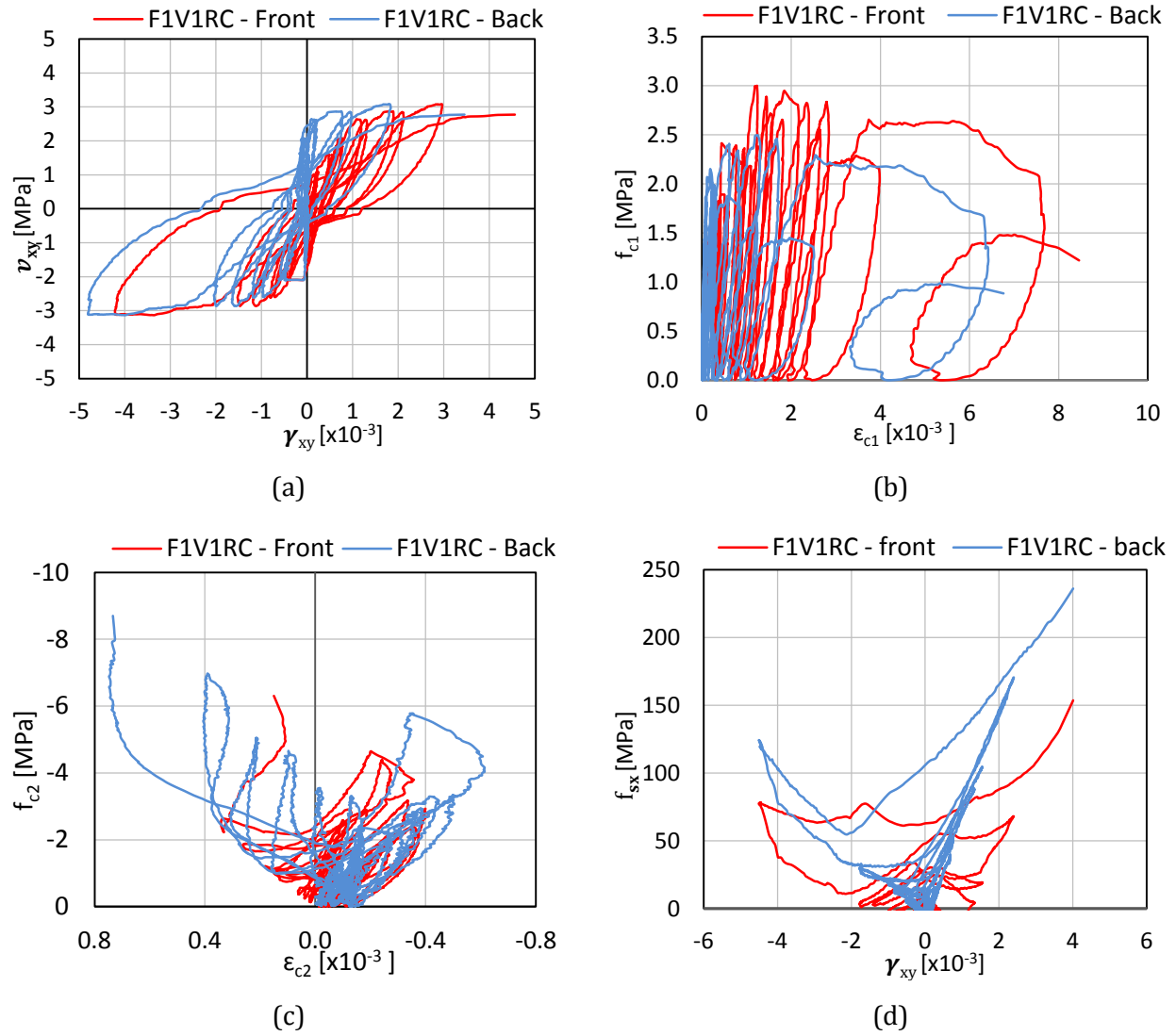
Figure B.18: Comparison of back face and front face response of panel F1V1RC

B.5 F1V2MS

Panel F1V2MS was monotonically loaded and constructed using SFRC with 1.0% by volume of RC80/30BP fibres (l_f = 30 mm, d_f = 0.38 mm, f_{uf} = 2300 MPa). The longitudinal reinforcement ratio was 3.31% and no transverse reinforcement was provided. This panel had a 28-day compressive strength of 57.5 MPa and a uniaxial tensile strength of 4.13 MPa; the test day compressive strength was 58.1 MPa.

B.5.1 Test Observations

Figure B.19 shows the crack patterns of F1V2MS for each load stage. The first crack occurred at a shear stress of 1.81 MPa and only appeared on the front face. At a shear stress of 2.57, the first crack for the back face was formed. The cracks became adequately uniform by the 4th load stage, at a shear stress of 3.62 MPa. Failure occurred at a shear stress and shear strain of 4.65 MPa and 4.96×10⁻³, respectively. The failure was caused by an aggregate interlock failure. The failure crack crossed the primary reinforcement at an angle of approximately 30° with respect to the x-axis, consistent with the angle of the surface cracks before failure.

As shown in Figure B.20, the rate of decrease for the average crack spacing was reduced with increasing stress; on the other hand, the rate of increase for the crack widths escalated under higher loads. The above trends were generally true for panels tested in this work. Cracks were closely spaced before failure. At the last load stage, the maximum crack width, the average crack width, and the average crack spacing were 0.65 mm, 0.18 mm, and 54.8 mm, respectively.
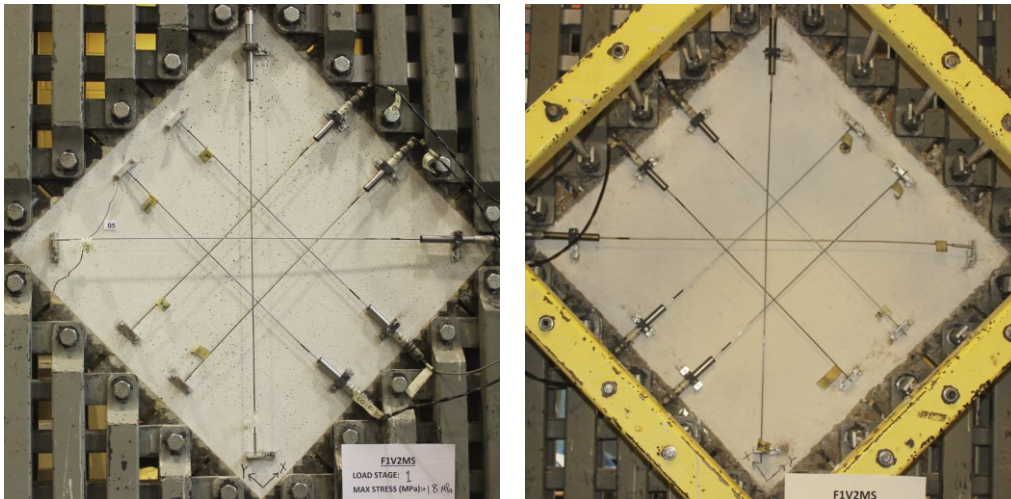
Stage 1: v_{xy}=1.81 MPa, γ_{xy}=0.138×10⁻³; $w_{cr,max}$=0.05 mm, w_m=0.05 mm, s_m=1260 mm.
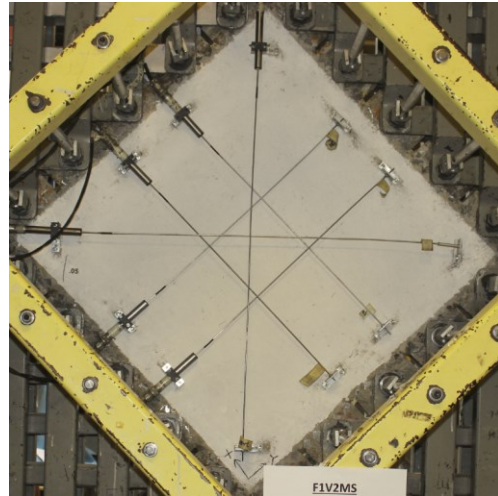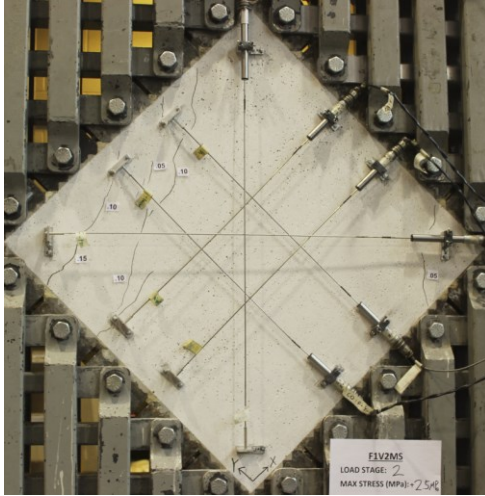
Stage 2: v_{xy}=2.57 MPa, γ_{xy}=0.35×10⁻³; $w_{cr,max}$=0.15 mm, w_m=0.09 mm, s_m=788 mm.
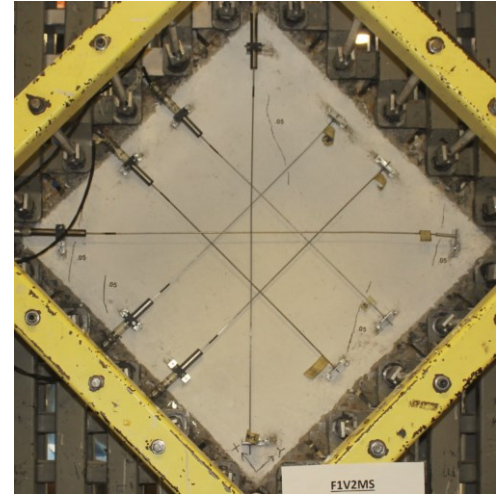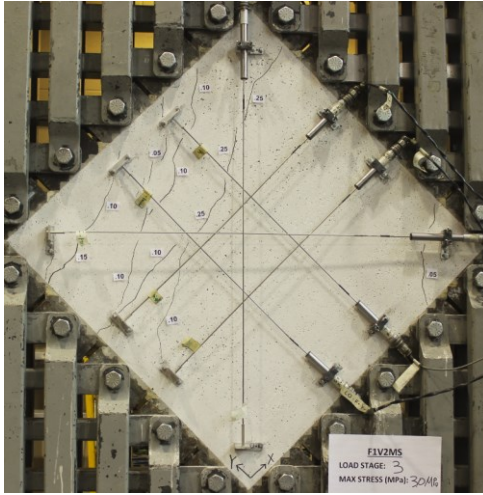
Stage 3: v_{xy}=3.08 MPa, γ_{xy}=0.6×10⁻³; $w_{cr,max}$=0.25 mm, w_m=0.1 mm, s_m=252 mm.
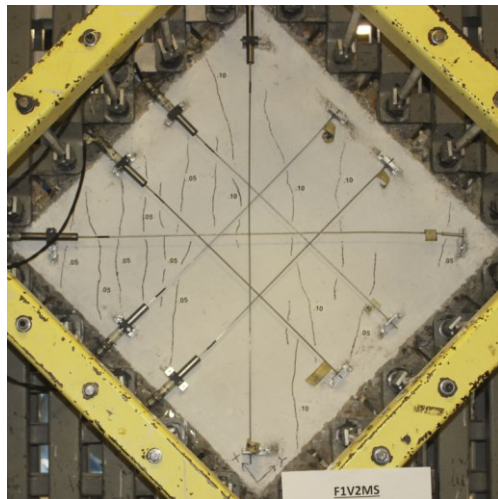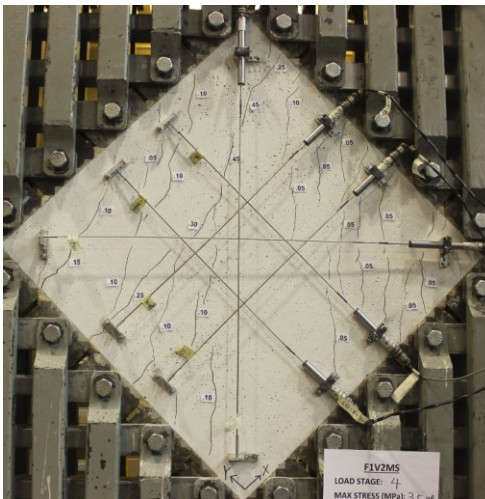
Stage 4: v_{xy}=3.62 MPa, γ_{xy}=1.46×10⁻³; $w_{cr,max}$=0.45 mm, w_m=0.11 mm, s_m=86 mm.
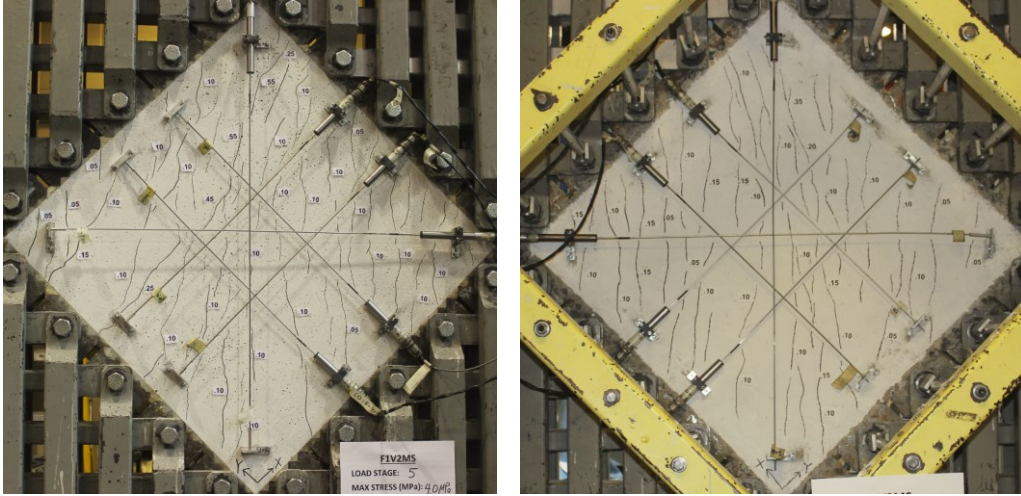
Stage 5: v_{xy}=4.14 MPa, γ_{xy}=2.58×10^{-3}; $w_{cr,max}$=0.55 mm, w_m=0.13 mm, s_m=66 mm.
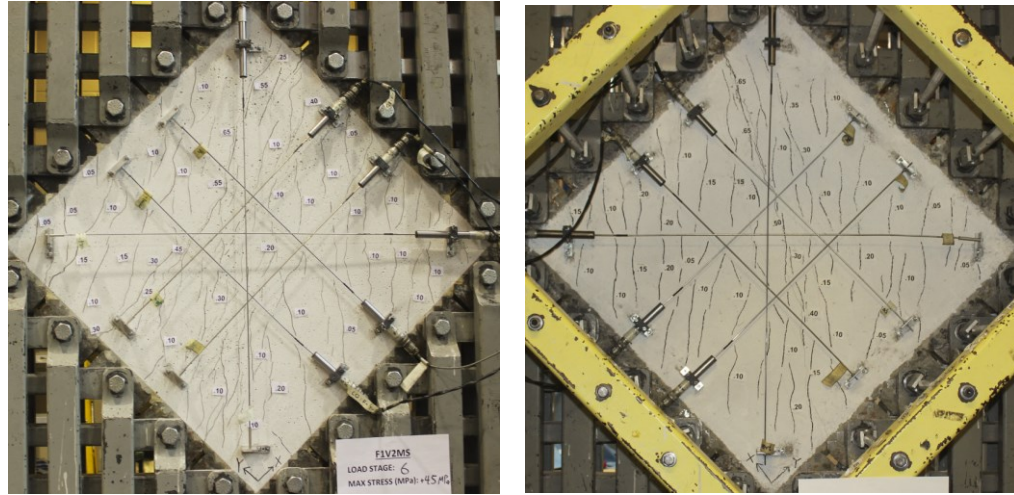
Stage 6: v_{xy}=4.61 MPa, γ_{xy}=4.21×10^{-3}; $w_{cr,max}$=0.65 mm, w_m=0.18 mm, s_m=55 mm.
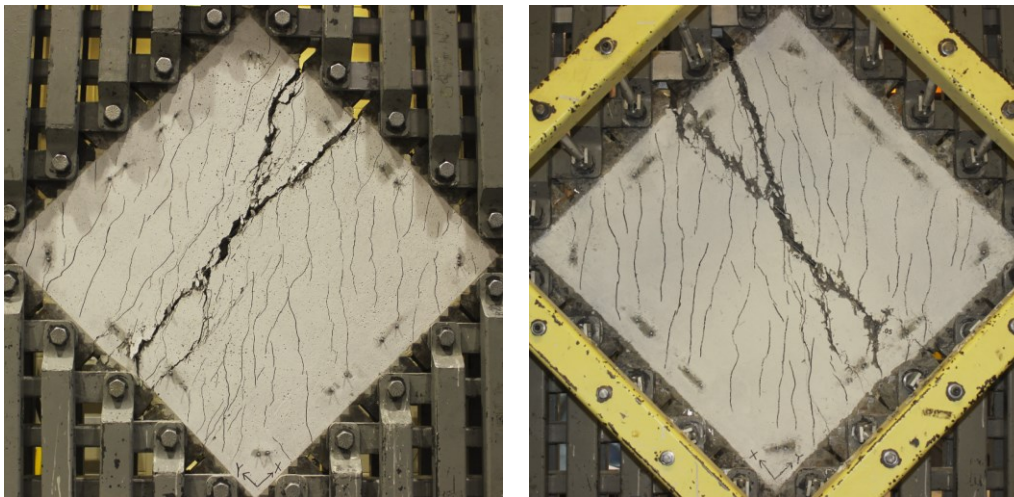
Failure: v_u=4.65 MPa, γ_u=4.96×10^{-3}.

Figure B.19: Crack pattern of panel F1V2MS
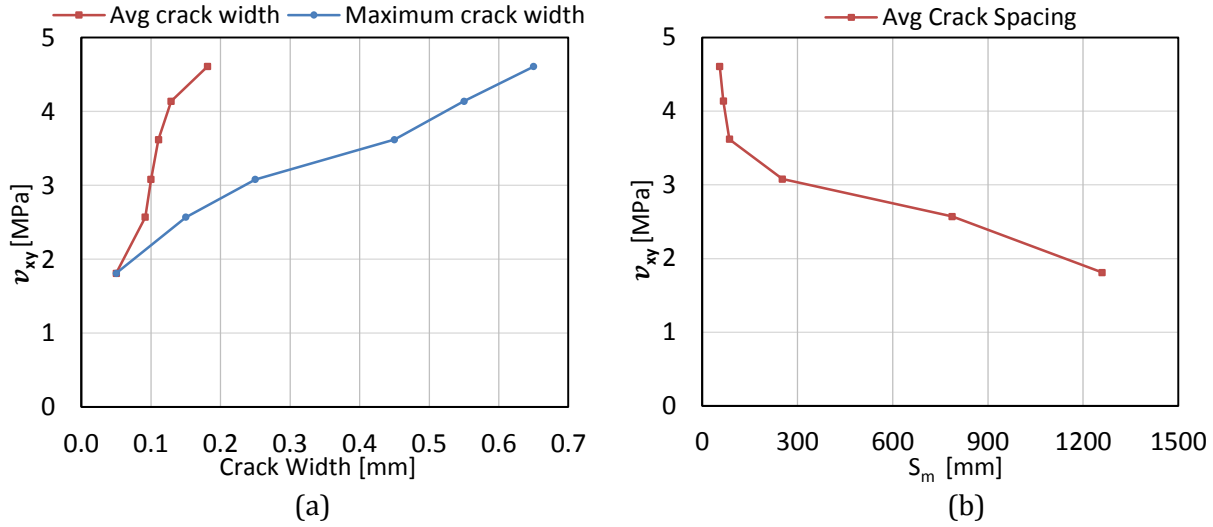
Figure B.20: Crack spacing and crack width of panel F1V2MS

B.5.2 Data Analysis

The response of panel F1V2MS is shown in Figure B.21. The first crack occurred at a shear stress of 1.81 MPa with a shear strain of 0.138×10^{-3}; the behaviour was linear up to cracking. Thereafter, the panel experienced gradual softening until failure occurred at a shear stress and shear strain of 4.65 MPa and 4.96×10^{-3}, respectively.

At first-cracking, the principal tensile stress and principal tensile strain were 1.80 MPa and 0.08×10^{-3}, respectively. Strain hardening behaviour occurred thereafter until the maximum principal stress of 3.16 MPa was reached. The subsequent response gradually softened then plateaued near a principal stress of 2.26 MPa. At failure, the principal tensile stress and strain were 2.29 MPa and 11.27×10^{-3}, respectively.

The panel was insignificantly stressed compressively. The principal compressive stress and principal compressive strain at first-cracking were -1.81 MPa and -0.06×10^{-3}, respectively. Near failure, due to the large crack openings and crack slips, the principal compressive strain gradually shifted into the positive strain region. At failure, the principal compressive stress was -9.46 MPa with a principal compressive strain of 0.56×10^{-3}.

The principal stress angle experienced a noticeable lag relative to the principal strain angle after first-cracking; the largest lag was 10.3°. Near failure, at a shear stress of 3.60 MPa, the principal strain angle converged with the principal stress angle. At failure, the principal stress angle was 63.8°, and the principal strain angle was 76.2°. The primary reinforcement was not significantly stressed; the peak reinforcement stress was 220 MPa.
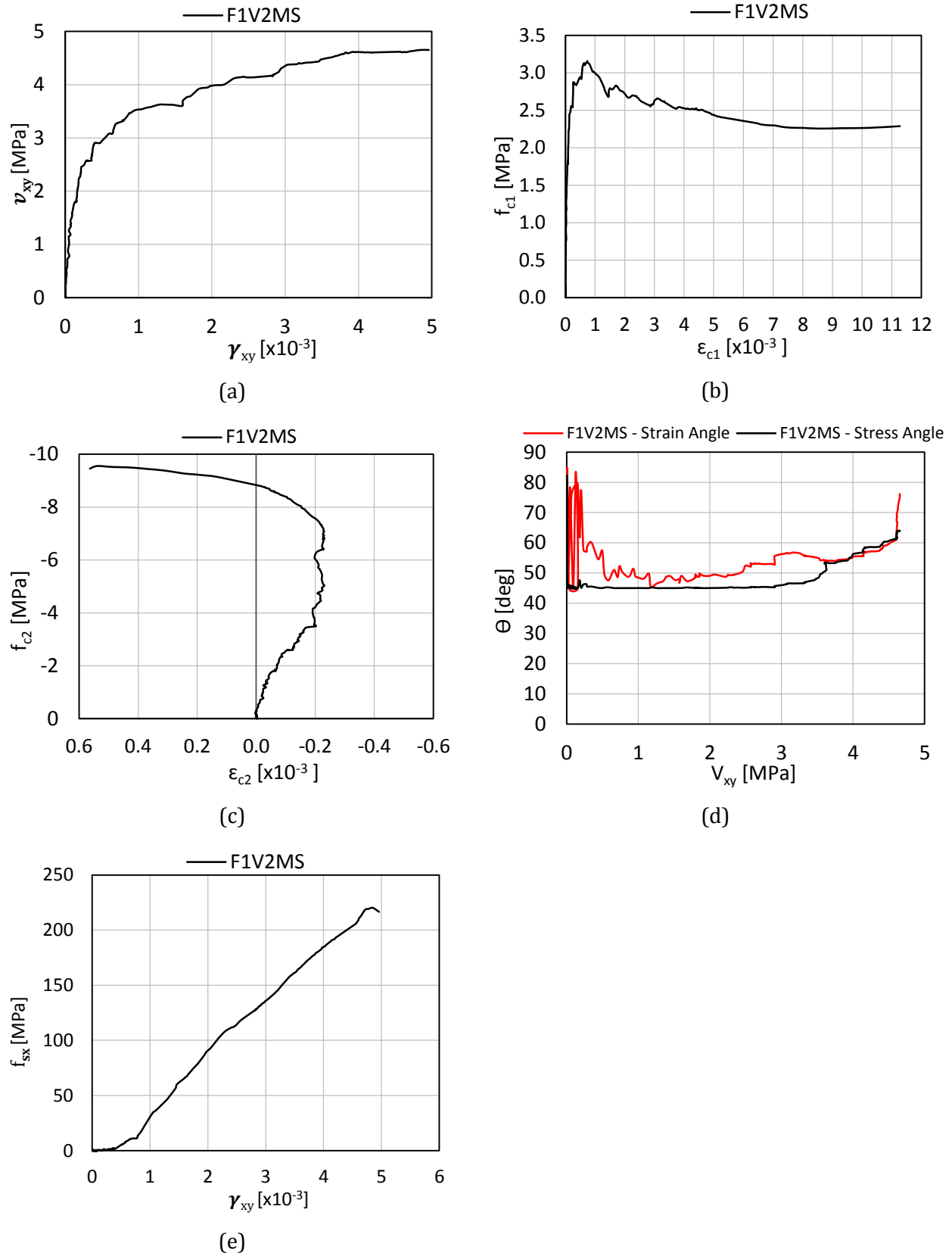
Figure B.21: Response of panel F1V2MS

(a)

(b)

(c)

(d)
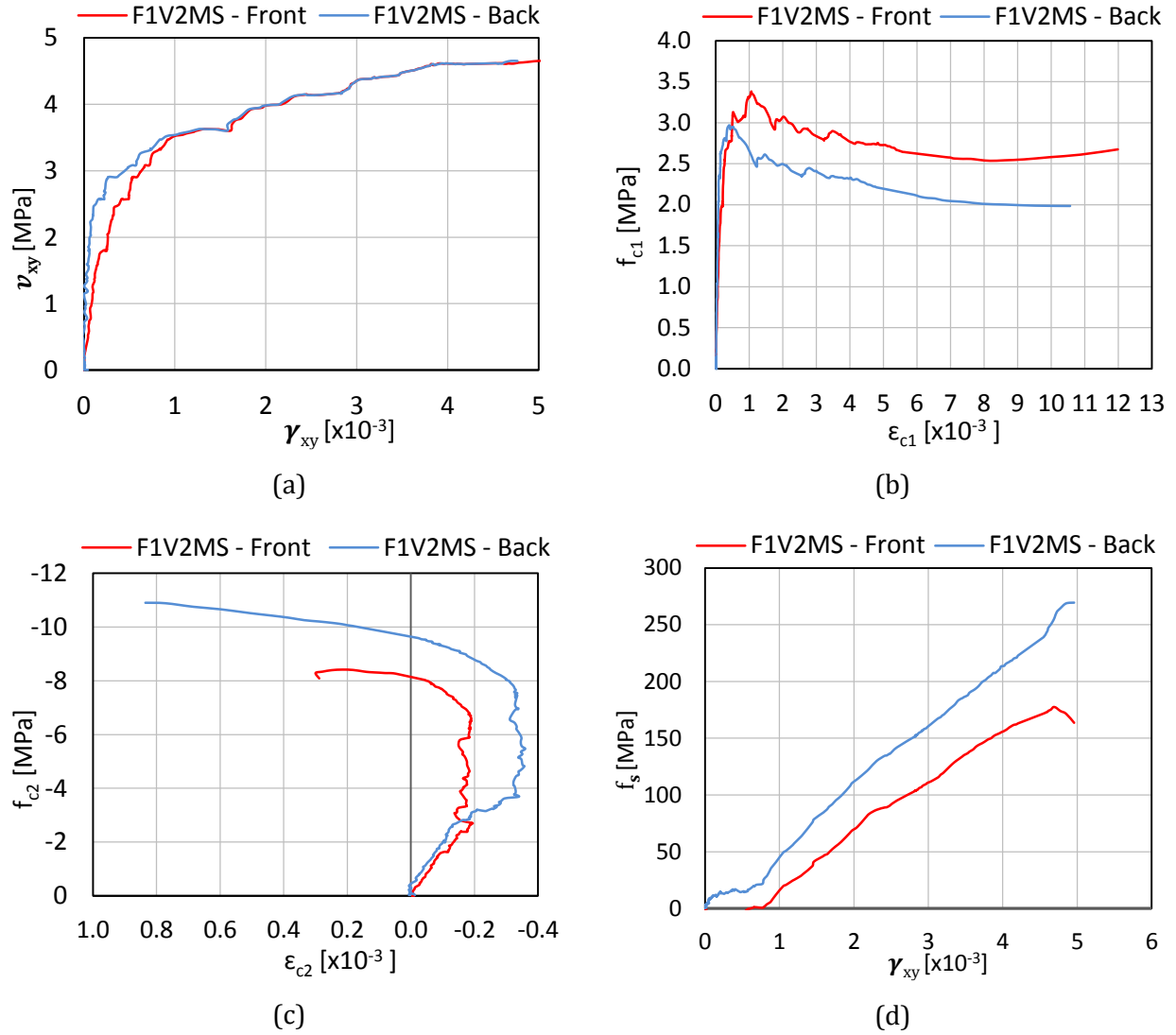
Figure B.22: Comparison of back face and front face response of panel F1V2MS

B.5.3 Comparison of the Front Face and Back Face Responses

Figure B.22 shows the LVDT response for the front face and the back face of F1V2MS. The panel exhibited a small amount of out-of-plane bending and the response at the two faces generally converged at a shear stress of 3.50 MPa. The cracking pattern for the two faces was largely identical.

B.6 F1V2RC

Panel F1V2RC was the reversed cyclically loaded companion panel of the F1V2 pair. The panel was constructed using SFRC with 1.0% by volume of RC80/30BP fibres (l_f = 30 mm, d_f = 0.38 mm, f_{uf} = 2300 MPa). The longitudinal reinforcement ratio was 3.31% and no transverse reinforcement was provided. Results from compressive cylinder and uniaxial tensile test indicated that the 28-day compressive strength was 57.5 MPa and the uniaxial tensile strength was 4.13 MPa; the test day compressive strength was 58.1 MPa. The double cycle peak shear stresses were 1.0 MPa, 2.1 MPa, 3.1 MPa, 3.6 MPa, 4.15 MPa, and 4.4 MPa.

B.6.1 Test Observations

The crack patterns of F1V2RC are shown in Figure B.23. The first crack occurred during the 3rd double cycle at a shear stress of 3.10 MPa. Multiple horizontal and vertical cracks for both faces developed subsequently during the same double cycle. Cracks in both directions and for both faces became adequately uniform by the 4th double cycle at a shear stress of 3.61 MPa. Failure of the panel occurred at a shear stress of 3.26 MPa with a shear strain of 4.3×10^{-3}. Similar to all SFRC panels, the failure was caused by the breakdown of the aggregate interlock mechanism due to fibre pull-out.

The crack spacing and crack widths of F1V2RC are shown in Figure B.24. The average crack spacing and the average crack width were similar between positive and negative shear. The increase or decrease in the crack widths and crack spacing were somewhat linear. At the last load stage, the maximum crack width, the average crack width, and the average crack spacing were 0.75 mm, 0.21 mm, and 81.4 mm, respectively.
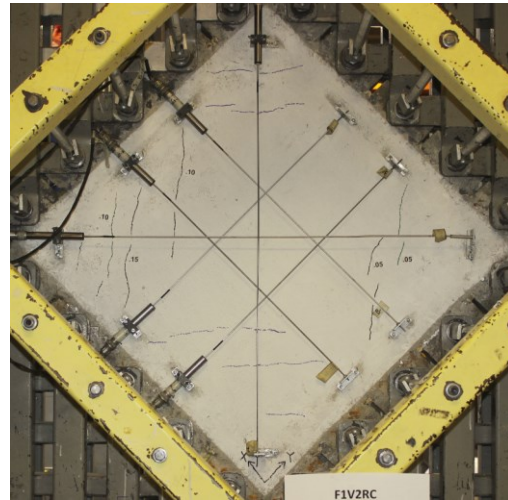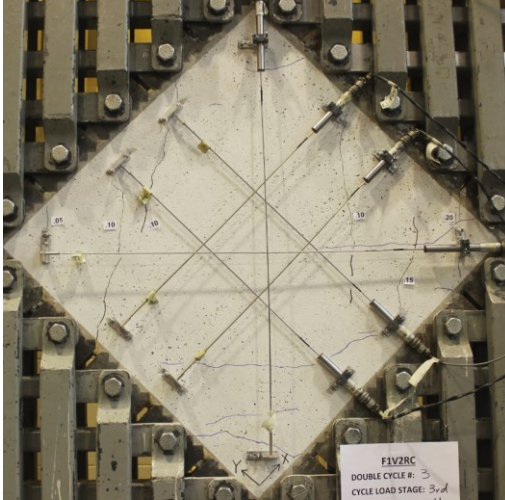
Double Cycle 3, Stage 11: v_{xy}=3.13 MPa, γ_{xy}=0.36×10⁻³; $w_{cr,max}$=0.20 mm, w_m=0.10 mm, s_m=210 mm.
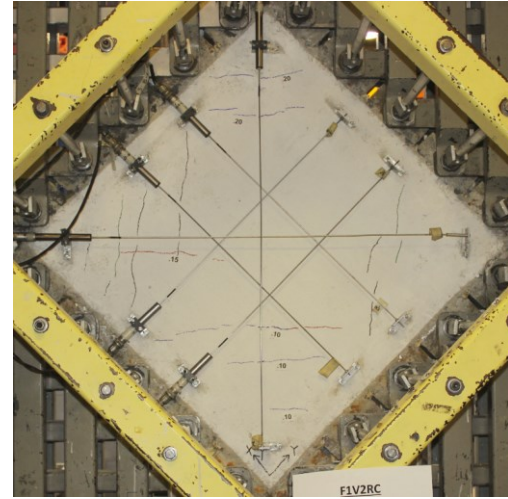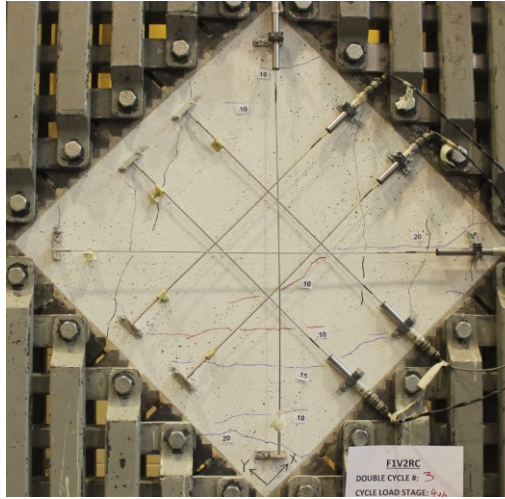
Double Cycle 3, Stage 12: v_{xy}=-3.16 MPa, γ_{xy}=-0.75×10⁻³; $w_{cr,max}$=0.20 mm, w_m=0.14 mm, s_m=195 mm.
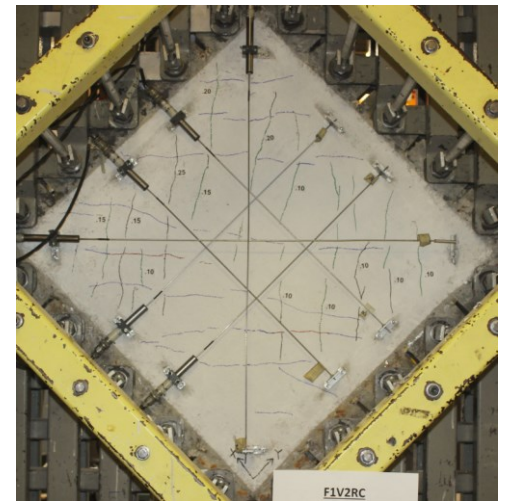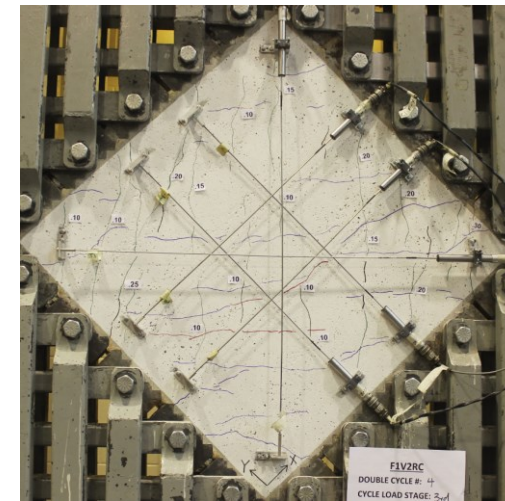
Double Cycle 4, Stage 15: v_{xy}=3.61 MPa, γ_{xy}=1.19×10⁻³; $w_{cr,max}$=0.30 mm, w_m=0.15 mm, s_m=110 mm.
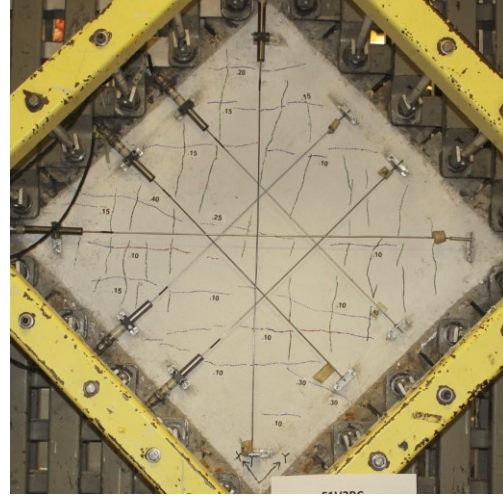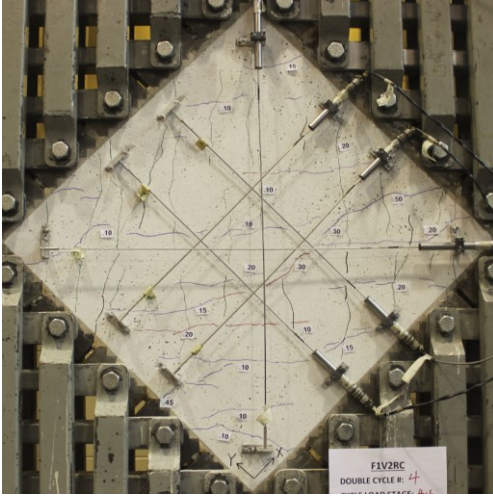
Double Cycle 4, Stage 16: v_{xy}=-3.6 MPa, γ_{xy}=-1.73×10^{-3}; $w_{cr,max}$=0.50 mm, w_m=0.18 mm, s_m=133 mm.
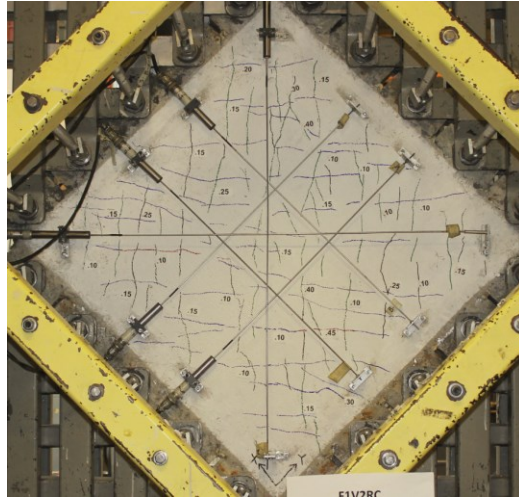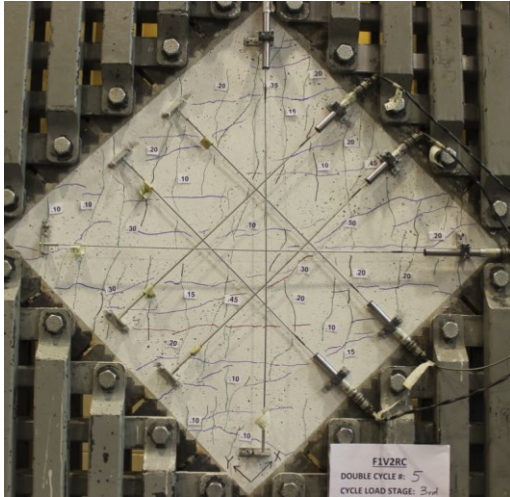
Double Cycle 5, Stage 19: v_{xy}=4.15 MPa, γ_{xy}=2.74×10^{-3}; $w_{cr,max}$=0.50 mm, w_m=0.19 mm, s_m=87 mm.
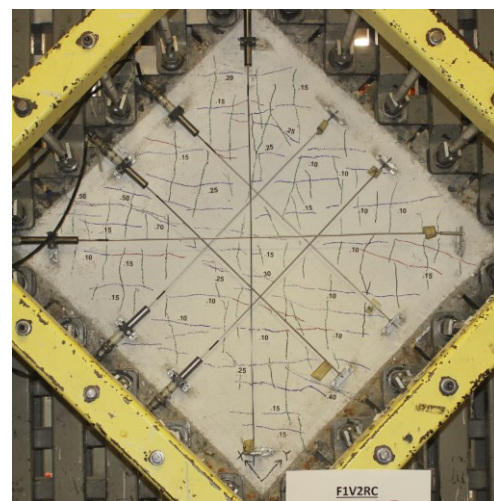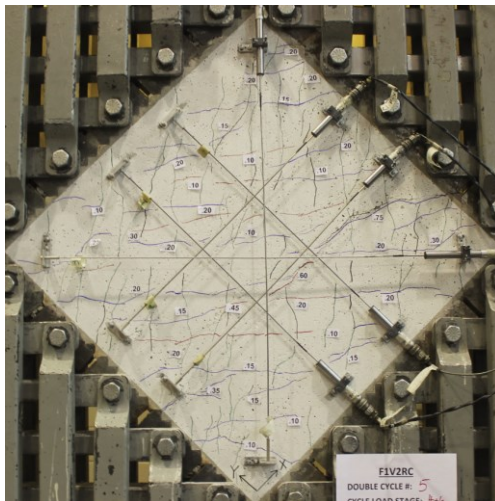
Double Cycle 5, Stage 20: v_{xy}= -4.17 MPa, γ_{xy}=-3.56×10^{-3}; $w_{cr,max}$=0.75 mm, w_m=0.21 mm, s_m=81 mm.
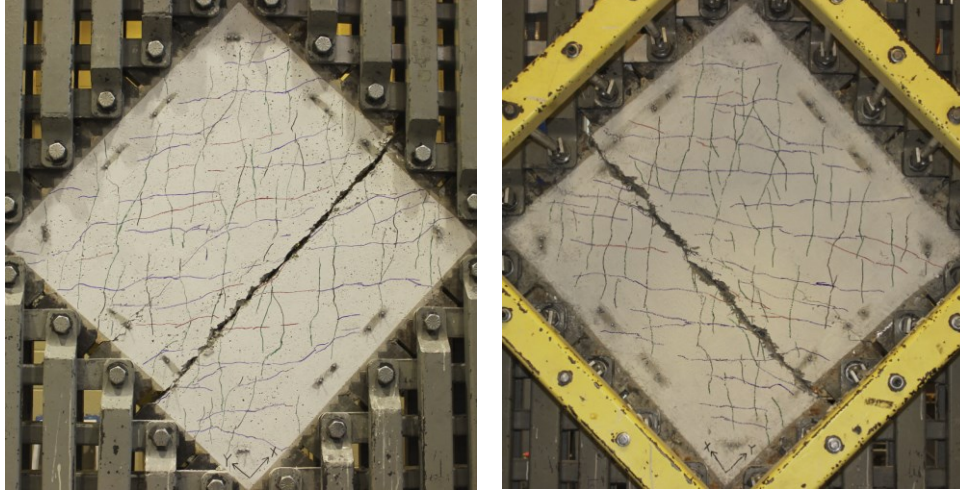
Failure: v_u=4.41 MPa, γ_u=4.60×10^{-3}.

Figure B.23: Crack pattern of panel F1V2RC

(a)   (b)
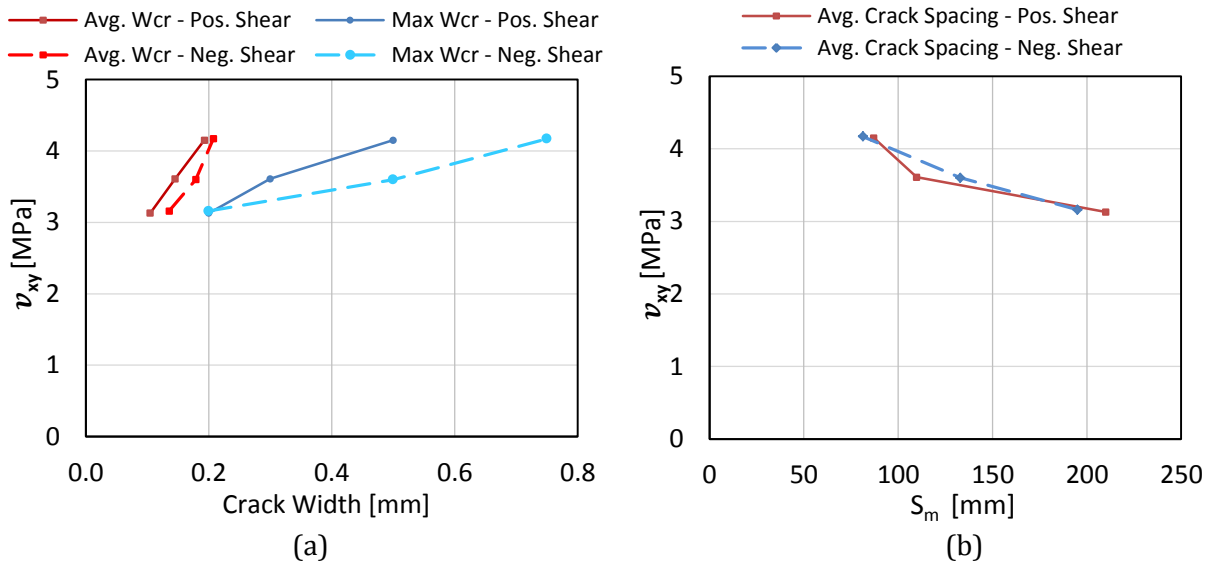
Figure B.24: Crack spacing and crack width of panel F1V2RC

B.6.2 Data Analysis

The response of F1V2RC is shown in Figure B.25. The first crack occurred at a shear stress and a shear strain of 3.10 MPa and 0.26×10^{-3}, respectively. The overall response was linear up to first-cracking, afterwards, the stiffness decreased significantly. Failure of the panel occurred at a shear stress of 3.26 MPa with a shear strain of 4.3×10^{-3}, respectively. The previously attained ultimate shear stress was 4.41 MPa with a corresponding ultimate shear strain of 4.60×10^{-3}.

As shown by the isolated shear stress-shear strain cycles in Figure B.26, under increasing loads, the panel displayed progressive stiffness degradation and greater pinching of the hysteretic loops. The

origin of the hysteretic loops was approximately at the centre. The overall isolated response was similar to the other SFRC panels.

At first-cracking, the principal tensile stress was 3.12 MPa with a principal tensile strain of 0.121×10^{-3}. Strain hardening was exhibited until the maximum principal tensile stress of 3.18 MPa was reached at a principal tensile strain of 0.48×10^{-3}. The principal tensile response gradually softened and reached a stress plateau of 2.27 MPa. At failure, the principal tensile stress and strain were 1.67 MPa and 7.1×10^{-3}, respectively.

Similar to the principal tensile values, the principal compressive stress and strain at first-cracking were -3.08 MPa and -0.14×10^{-3}, respectively. As with the other reversed cyclically loaded panels, the principal compressive strain became positive during unloading. At failure, the principal compressive stress was -6.38 MPa with a principal compressive strain of 0.04×10^{-3}. The maximum principal compressive stress reached was -8.50 MPa.

The principal strain angle was largely similar to the principal stress angle for this test. Overall, the principal strain angle lagged behind the principal stress angle, albeit to a much lesser extent compared to F1V1RC. At failure, the principal stress angle was 117°, while the principal strain angle was 109°. The reinforcement was insignificantly stressed and reached a peak stress of 188 MPa.

B.6.3 Comparison of the Front Face and Back Face Responses

The out-of-plane bending was minor for F1V2RC and was evident through comparing the shear stress-shear strain response between the front face and the back face (see Figure B.27). The out-of-plane bending appeared to only exist in the negative shear direction and began to diminish at a shear stress of -3.0 MPa. The cracking pattern for the two faces was largely identical.

(a)

(b)

(c)

(d)

(e)

Figure B.25: Response of panel F1V2RC

Figure B.26: Shear stress-shear strain response of F1V2RC; isolated cycles

(a)

(b)

(c)

(d)
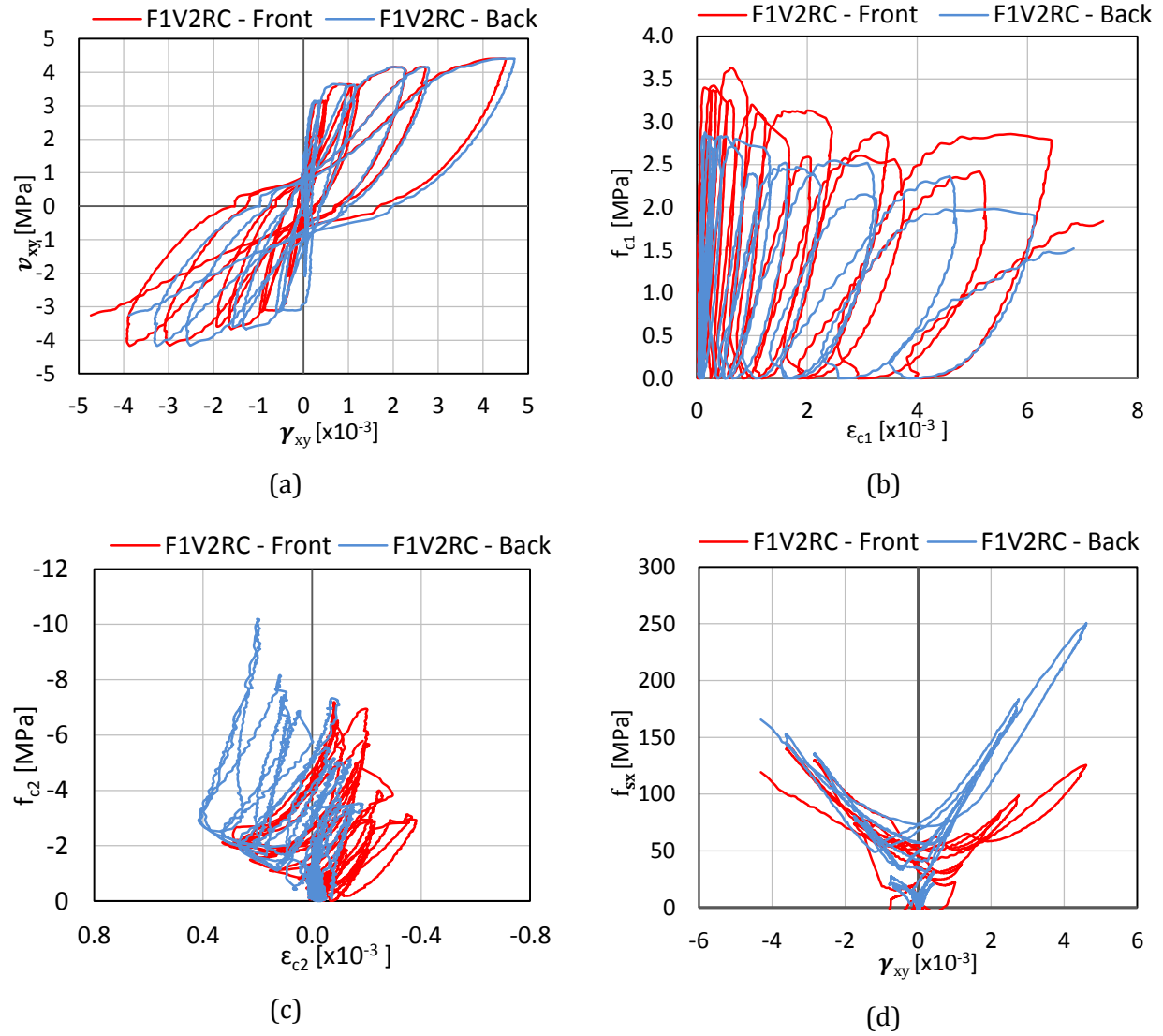
Figure B.27: Comparison of back face and front face response of panel F1V2RC

B.7 F1V3MS

Panel F1V3MS was monotonically loaded and constructed with steel fibre reinforced concrete containing 1.5% by volume of RC80/30BP fibres (l_f = 30 mm, d_f = 0.38 mm, f_{uf} = 2300 MPa). The panel had a longitudinal reinforcement ratio of 3.31% with no transverse reinforcement provided. The 28-day compressive strength was 48.9 MPa and the uniaxial tensile strength was 3.89 MPa; the test day compressive strength was 50.9 MPa.

B.7.1 Test Observations

The crack patterns of F1V3MS are shown in Figure B.28. The first crack occurred at a shear stress of 2.34 MPa, and the cracks became sufficiently uniform at a shear stress of 4.17 MPa. At failure, the maximum shear stress was 4.93 MPa. The failure was caused by the breakdown of the aggregate interlock mechanism and was very abrupt. As well, the shear stress-shear strain response for F1V3MS had a relatively high tangent stiffness at failure and did not exhibit a well-defined plateau. It is believed that the short post-cracking response was caused by the poor fibre distribution. However, the pre-peak response is believed to be not affected as the average fibre volume fraction across the panel was still 1.5% and the surface cracks developed were fairly uniform.

As shown in Figure B.29, under increasing loads, the average crack spacing decreased. The average crack width, on the other hand, was almost constant at a width of 0.6 mm up to a shear stress of 4.17 MPa; the crack widths increased rapidly thereafter. The failure crack was parallel to the primary reinforcement. At the last load stage taken prior to failure, the maximum crack width, the average crack width, and the average crack spacing were 0.50 mm, 0.12 mm, and 96.9 mm.
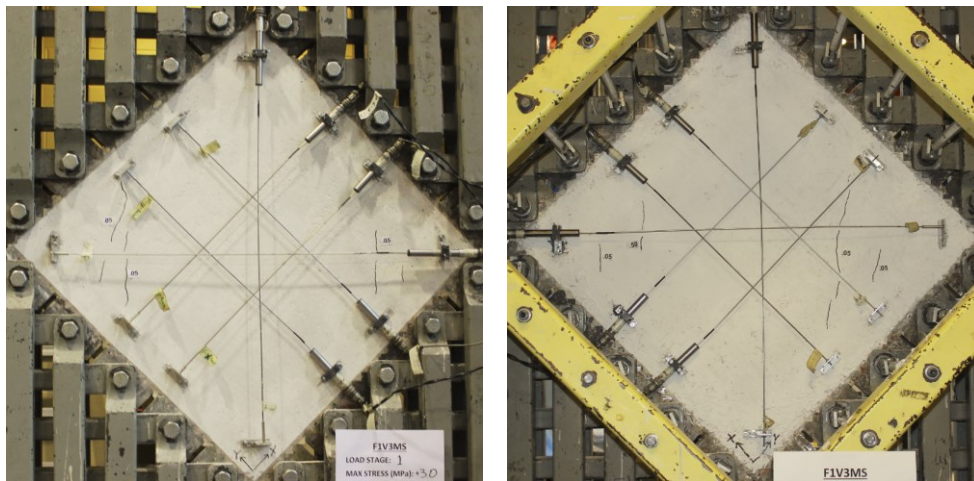
Stage 1: v_{xy}=3.12 MPa, γ_{xy}=0.44×10^{-3}; $w_{cr,max}$=0.05 mm, w_m=0.05 mm, s_m=315 mm.
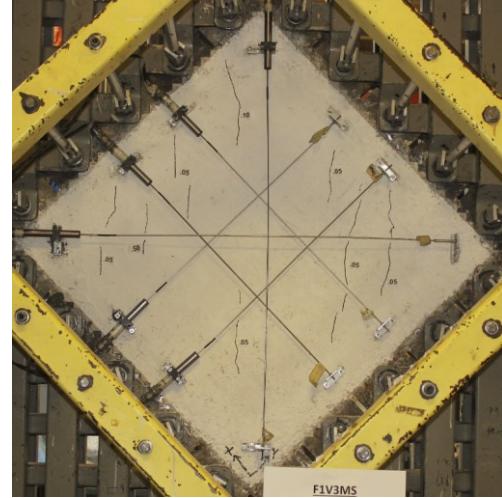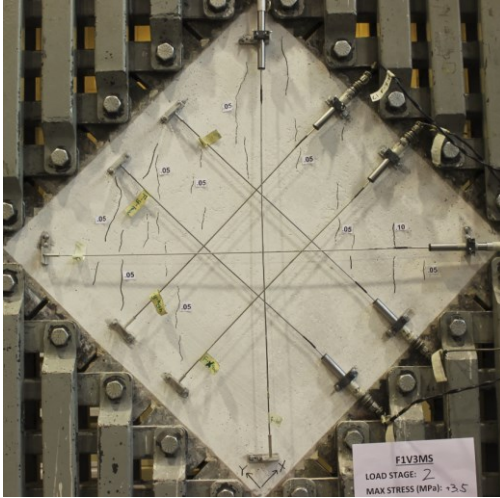
Stage 2: v_{xy}=3.70 MPa, γ_{xy}=0.91×10^{-3}; $w_{cr,max}$=0.10 mm, w_m=0.06 mm, s_m=169 mm.
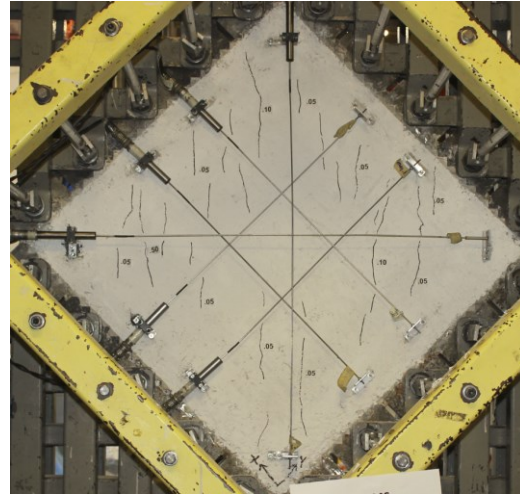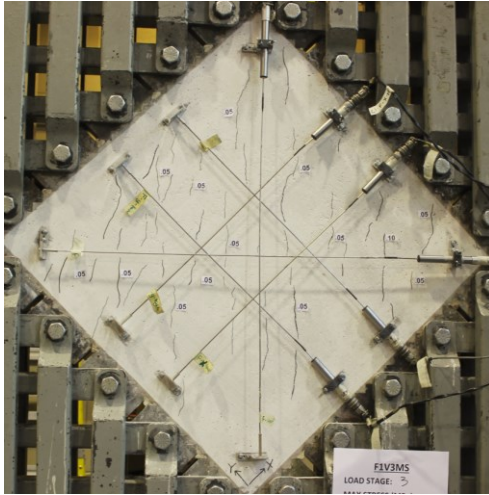
Stage 3: v_{xy}=4.17 MPa, γ_{xy}=1.62×10^{-3}; $w_{cr,max}$=0.15 mm, w_m=0.06 mm, s_m=110 mm.
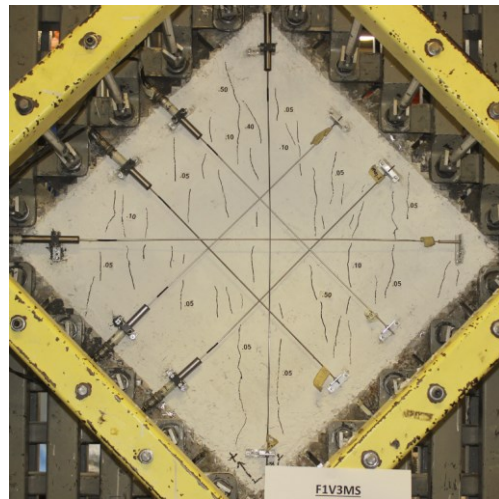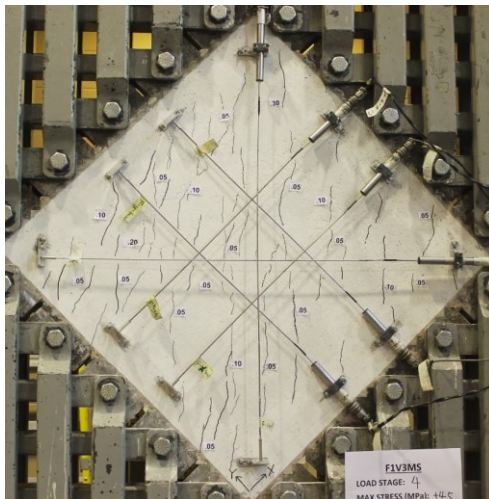
Stage 4: v_{xy}=4.61 MPa, γ_{xy}=2.70×10^{-3}; $w_{cr,max}$=0.50 mm, w_m=0.12 mm, s_m=97 mm.
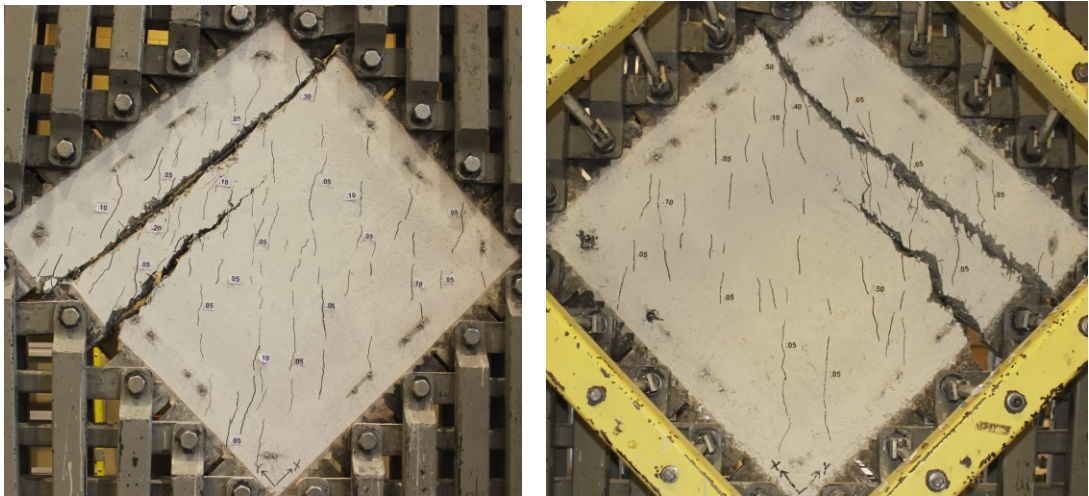
Failure: v_u=4.93 MPa, γ_u=3.40×10^{-3}.

Figure B.28: Crack pattern of panel F1V3MS

(a)   (b)
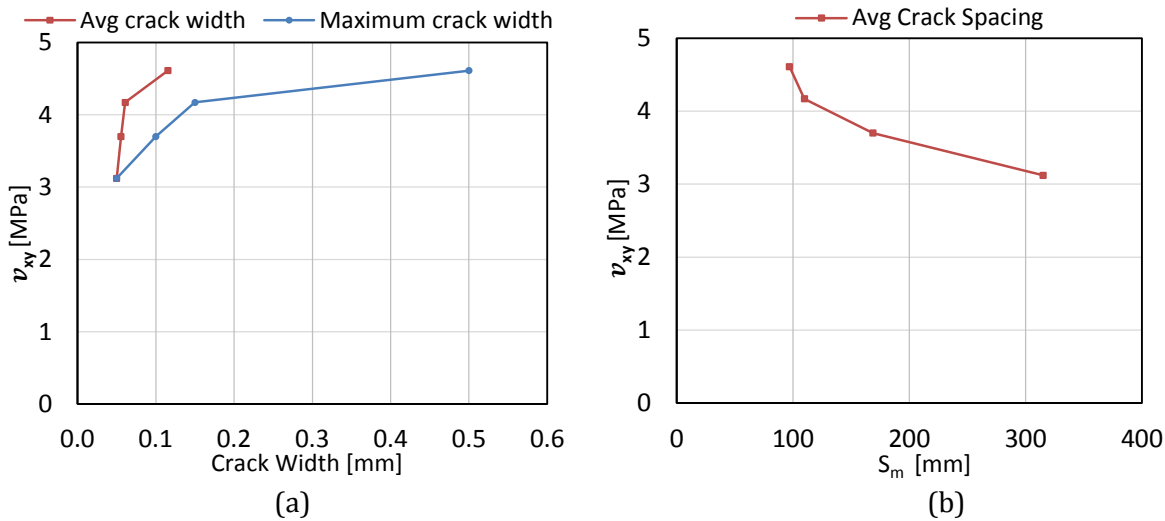
Figure B.29: Crack spacing and crack width of panel F1V3MS
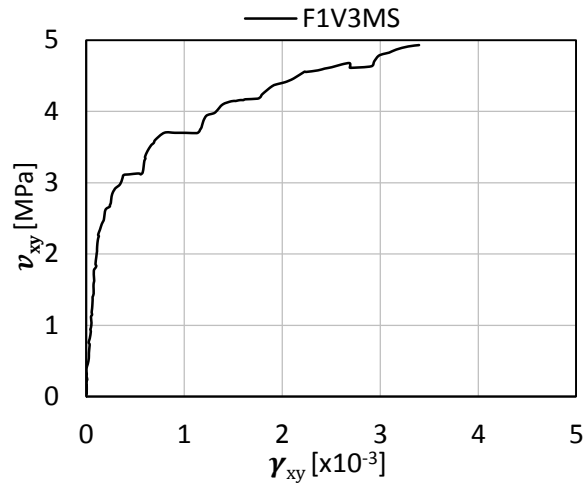
(a)
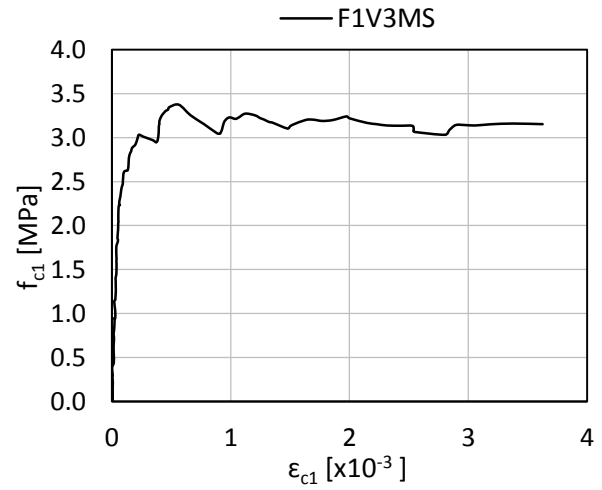
(b)
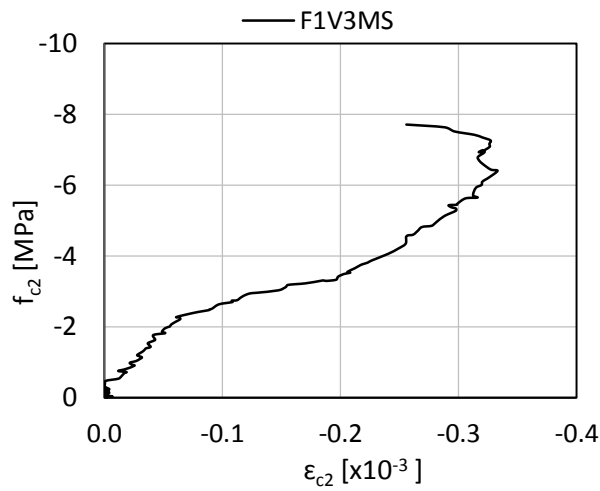
(c)
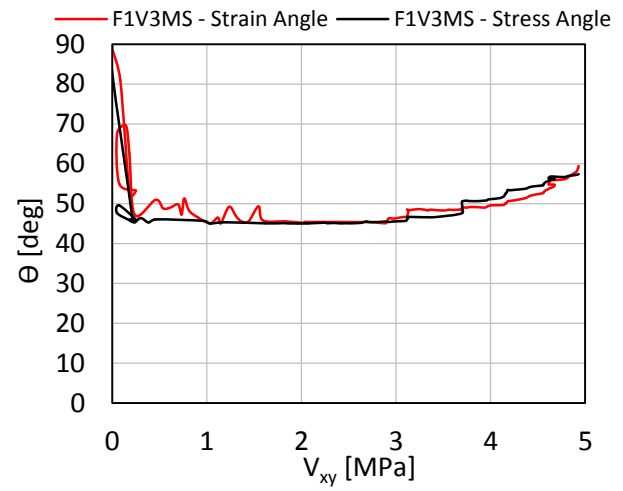
(d)
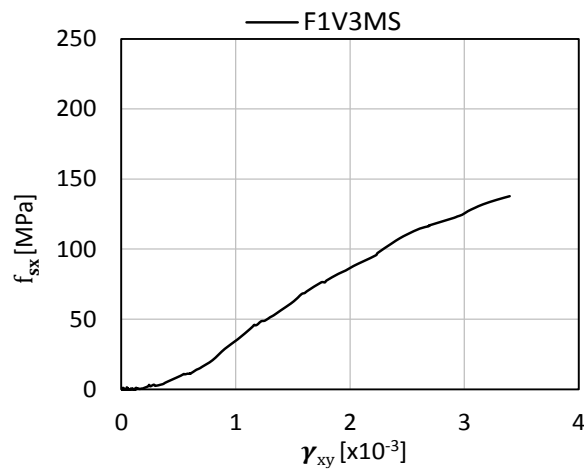
(e)

Figure B.30: Response of panel F1V3MS
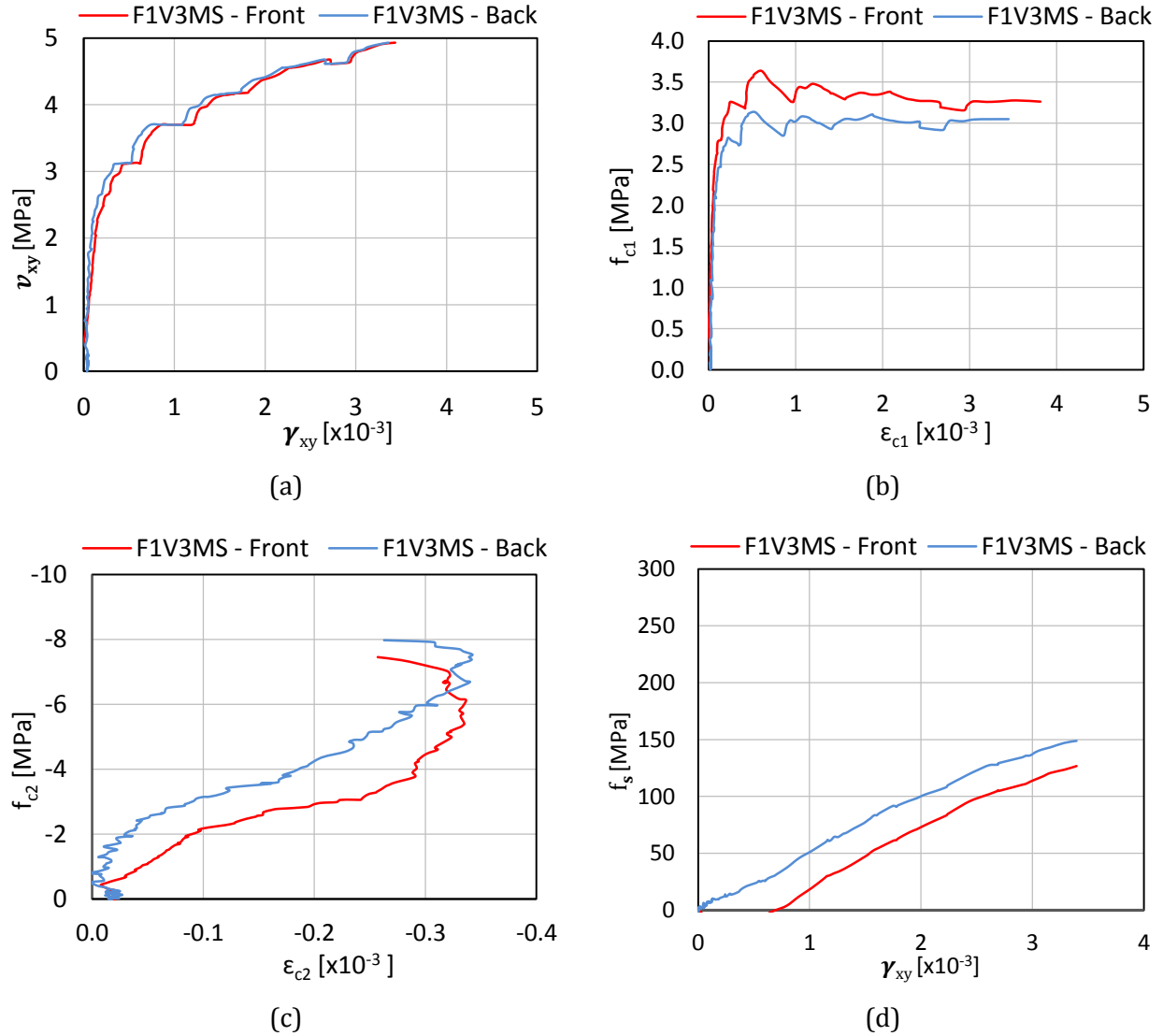
Figure B.31: Comparison of back face and front face response of panel F1V3MS

B.7.2 Data Analysis

Figure B.30 shows the response of panel F1V3MS. The behaviour was linear up to cracking, which occurred at a shear stress of 2.34 MPa with a shear strain of 0.141×10^{-3}. Gradual softening was exhibited thereafter until failure occurred at a shear stress and a shear strain of 4.93 MPa and 3.40×10^{-3}, respectively.

At first-cracking, the principal tensile stress and principal tensile strain were 2.33 MPa and 0.071×10^{-3}, respectively. Afterwards, the principal tensile response exhibited strain hardening until the maximum principal stress of 3.37 MPa was reached. Instead of displaying a gradual softened

response, a plateau was exhibited after strain hardening. At failure, the principal tensile stress and strain were 3.15 MPa and 3.63×10^{-3}, respectively.

The panel was insignificantly stressed in the principal compressive direction. At first-cracking, the principal compressive stress and principal compressive strain were -2.35 MPa and -0.07×10^{-3}, respectively. Similar to the other SFRC panels, the principal compressive strain gradually shifted into the positive strain region near failure as a result of the large crack openings and crack slips. At failure, the principal compressive stress was -7.71 MPa with a principal compressive strain of -0.28×10^{-3}.

The principal stress angle was almost identical to the principal strain angle until a shear stress of 3.70 MPa was reached. Afterwards, the principal strain angle marginally lagged behind the principal stress angle; the maximum lag was 2.84°. At failure, the principal stress angle was 57.4°, and the principal strain angle was 59.5°. The primary reinforcement was not significantly stressed; the peak reinforcement stress was 138 MPa.

B.7.3 Comparison of the Front Face and Back Face Responses

The LVDT response for the front face and back face of F1V3MS are shown in Figure B.31. The shear stress-shear strain responses for the two faces were nearly identical, indicating no significant out-of-plane bending occurred. The cracking patterns for the two faces were largely identical throughout the test.

B.8 F1V3RC

Panel F1V3RC was constructed of steel fibre reinforced concrete with 1.5% by volume of RC80/30BP fibres (l_f = 30 mm, d_f = 0.38 mm, f_{uf} = 2300 MPa). This panel had a longitudinal reinforcement ratio of 3.31% with no transverse reinforcement. The 28-day compressive strength was 48.9 MPa and the uniaxial tensile strength was 3.89 MPa; the test day compressive strength was 50.9 MPa. The double cycle peak shear stresses were 1.1 MPa, 2.1 MPa, 2.6 MPa, 3.1 MPa, 3.7 MPa, 4.2 MPa, and 4.7 MPa.

B.8.1 Test Observations

The crack patterns of F1V3RC are shown in Figure B.33. The first crack was a vertical crack on the front face of the panel and occurred during the 2nd double cycle at shear stress of 2.0 MPa. The first horizontal crack did not occur until a shear stress of 2.63 MPa was reached during the 3rd double cycle. Multiple cracks in both directions and on both faces developed during the 4th double cycle at a shear stress of 3.15 MPa. During the 6th double cycle, at a shear stress of 4.20 MPa, cracks became adequately uniform. Failure of the panel was initiated by the breakdown of the aggregate interlock mechanism and occurred at a shear stress of 4.68 MPa with a shear strain of $4.35×10^{-3}$.

Figure B.33 shows the crack spacing and crack widths of F1V3RC. After multiple cracks in both directions were formed, the crack locations, crack spacing, and crack widths were similar between the two faces. Relative to positive shear, the crack spacing and crack width for negative shear was slightly larger; this was observed in all of the panels. At the last load stage, the maximum crack width, the average crack width, and the average crack spacing were 0.70 mm, 0.25 mm, and 90.0 mm, respectively.
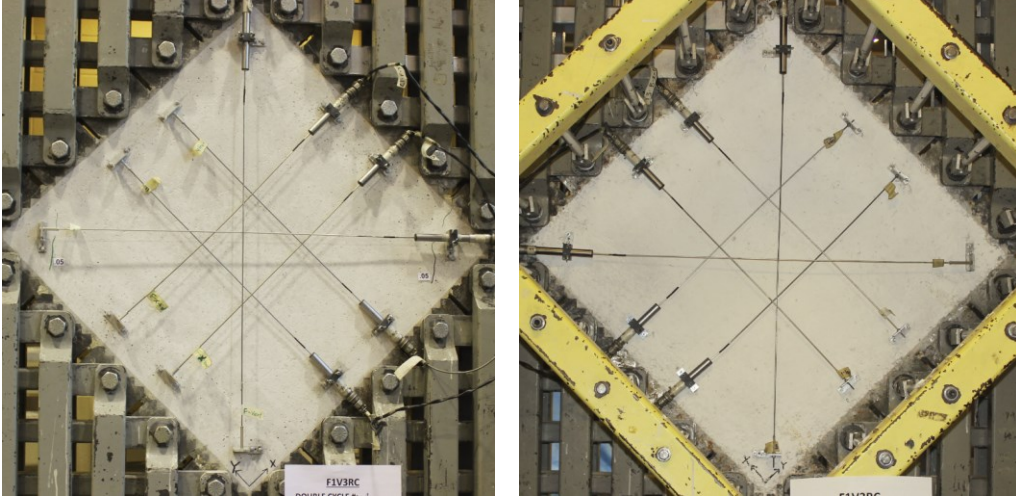
Double Cycle 2, Stage 7: v_{xy}=2.09 MPa, γ_{xy}=0.22×10^{-3}; $w_{cr,max}$=0.05 mm, w_m=0.05 mm, s_m=630 mm.
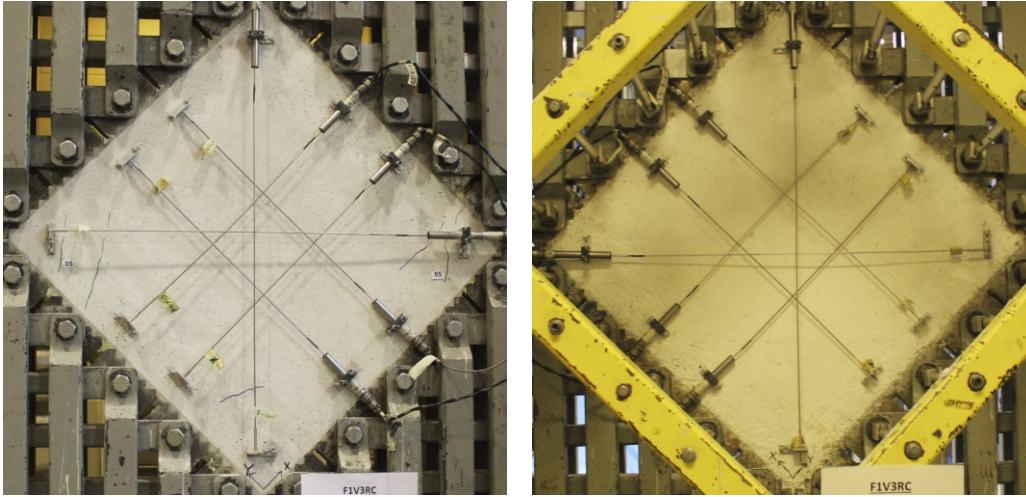
Double Cycle 3, Stage 11: v_{xy}= 2.64MPa, γ_{xy}=0.30×10^{-3}; $w_{cr,max}$= 0.05mm, w_m=0.05 mm, s_m=420 mm.
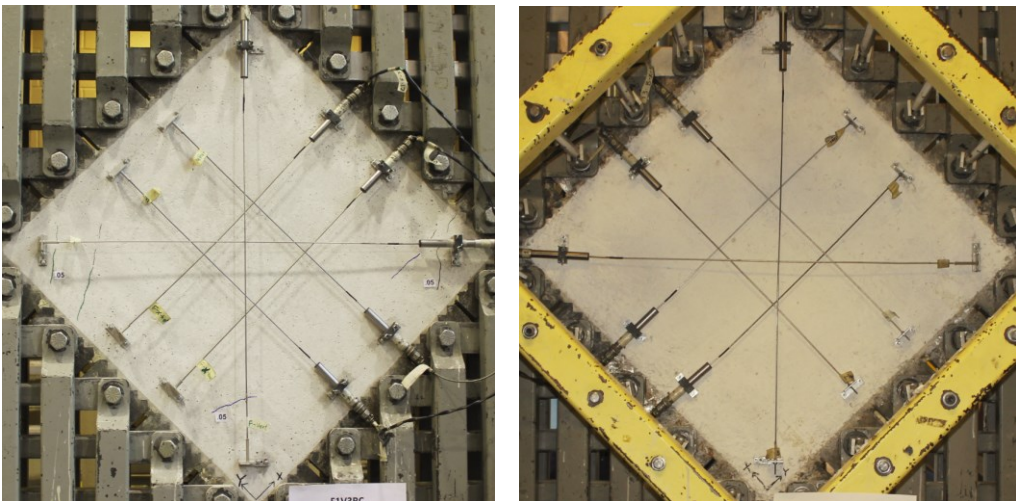
Double Cycle 3, Stage 12: v_{xy}=-2.63 MPa, γ_{xy}=-0.26×10^{-3}; $w_{cr,max}$=0.05 mm, w_m=0.05 mm, s_m=630 mm.
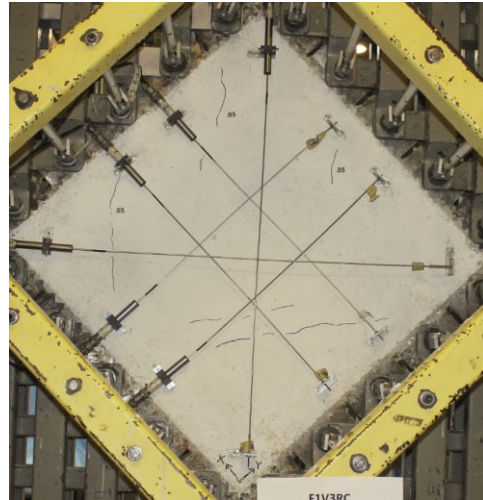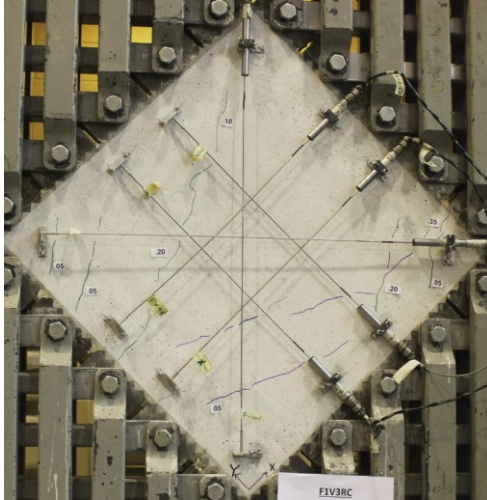
Double Cycle 4, Stage 15: v_{xy}=3.15 MPa, γ_{xy}=0.48×10⁻³; $w_{cr,max}$=0.35 mm, w_m=0.12 mm, s_m=336 mm.
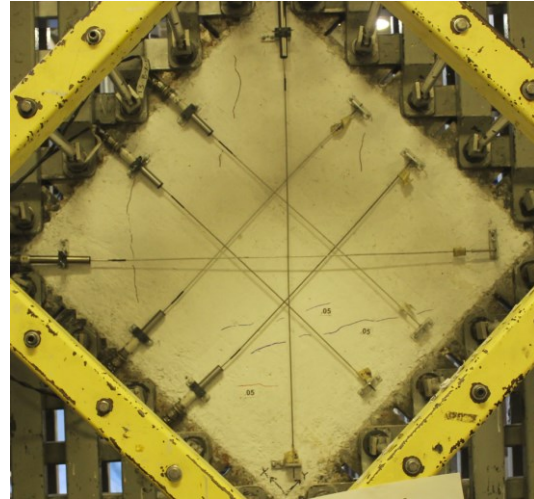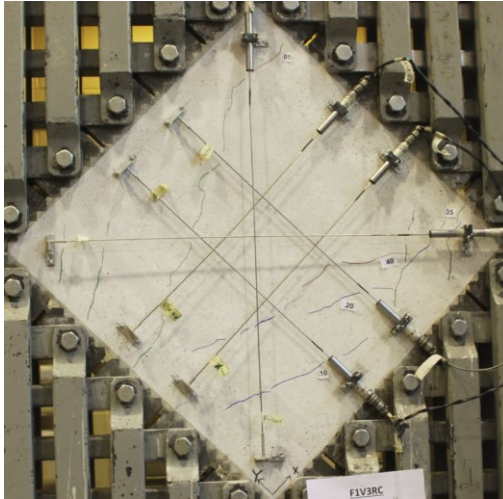
Double Cycle 4, Stage 16: v_{xy}=-3.12 MPa, γ_{xy}=-0.63×10⁻³; $w_{cr,max}$=0.40 mm, w_m=0.16 mm, s_m=368 mm.
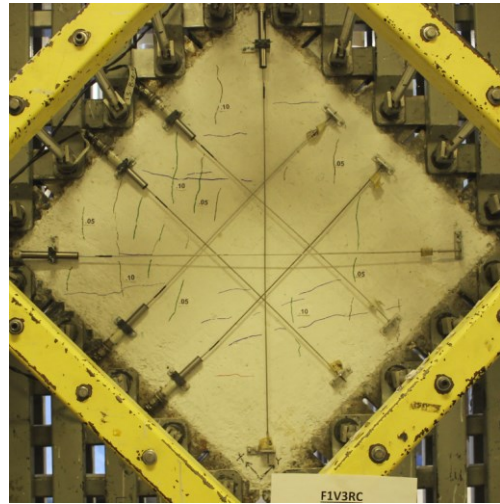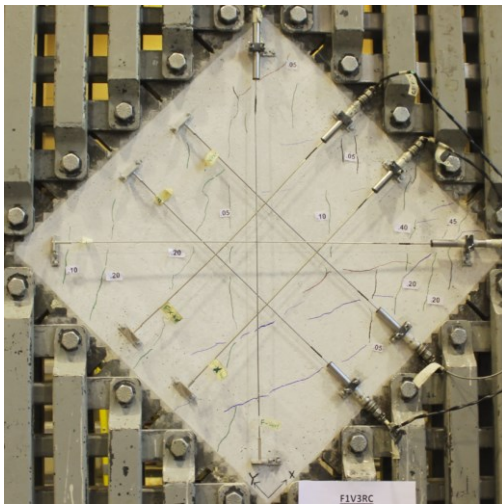
Double Cycle 5, Stage 19: v_{xy}=3.60 MPa, γ_{xy}=0.94×10⁻³; $w_{cr,max}$=0.40 mm, w_m=0.13 mm, s_m=149 mm.
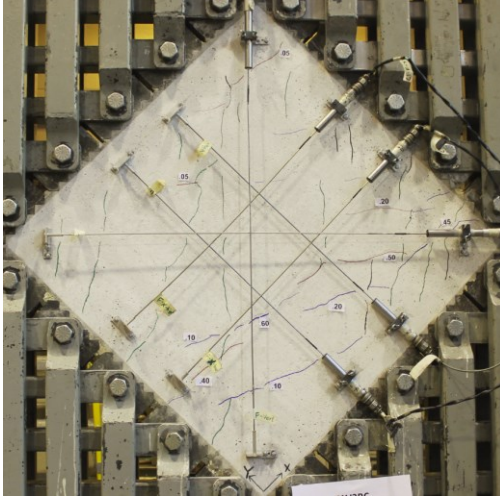
Double Cycle 5, Stage 20: v_{xy}=-3.70 MPa, γ_{xy}=-1.22×10^{-3}; $w_{cr,max}$=0.60 mm, w_m=0.17 mm, s_m=149 mm.
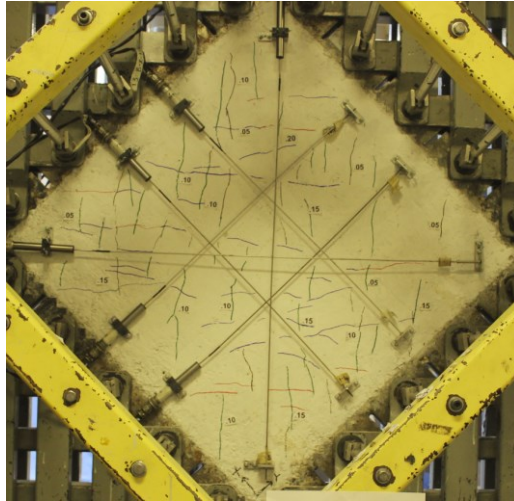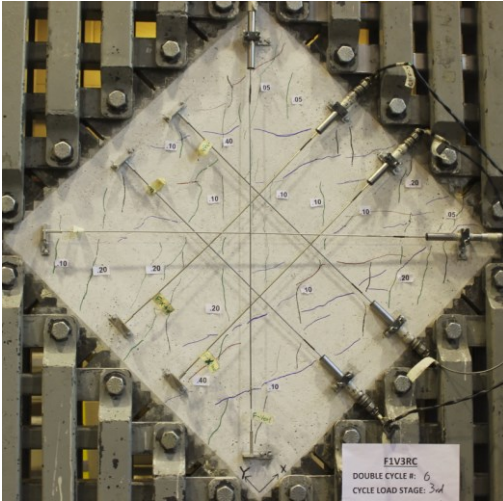
Double Cycle 6, Stage 23: v_{xy}=4.20 MPa, γ_{xy}=1.95×10^{-3}; $w_{cr,max}$=0.45 mm, w_m=0.14 mm, s_m=105 mm.
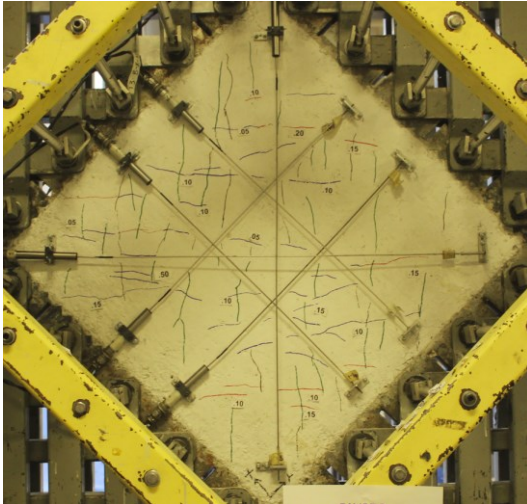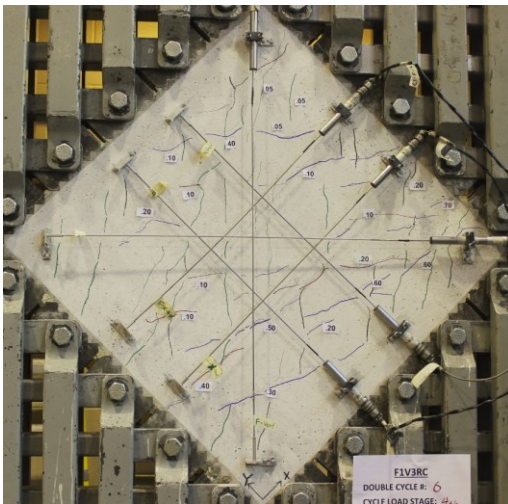
Double Cycle 6, Stage 24: v_{xy}=-4.18 MPa, γ_{xy}=-2.20×10^{-3}; $w_{cr,max}$=0.70 mm, w_m=0.20 mm, s_m=119 mm.
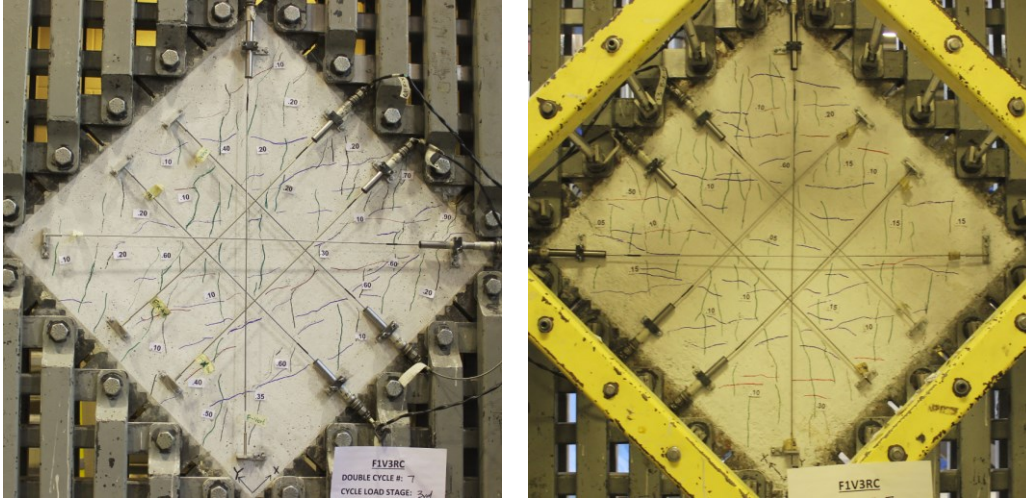
Double Cycle 7, Stage 27: v_{xy}=4.72 MPa, γ_{xy}=3.65×10^{-3}; $w_{cr,max}$=0.70 mm, w_m=0.25 mm, s_m=90 mm.
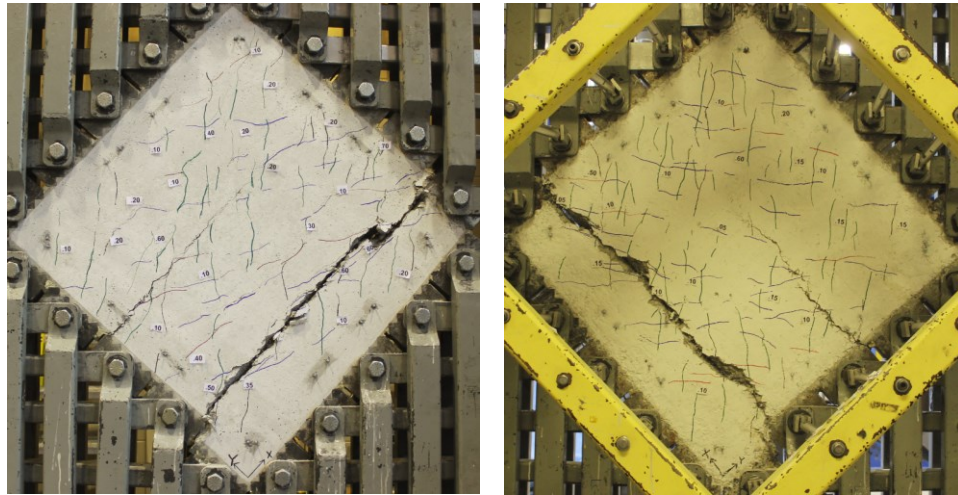
Failure: v_u=4.72 MPa, γ_u=3.72×10^{-3}.

Figure B.32: Crack pattern of panel F1V3RC

(a)   (b)
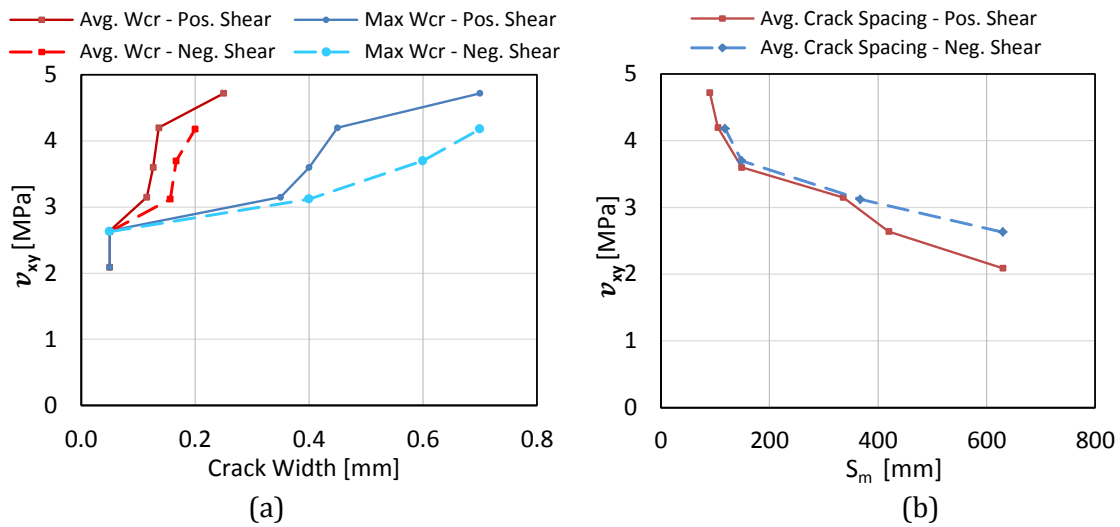
Figure B.33: Crack spacing and crack width of panel F1V3RC

B.8.2 Data Analysis

The response of F1V3RC is shown in Figure B.34. The first crack occurred at a shear stress and shear strain of 2.00 MPa and 0.19×10^{-3}, respectively. The panel experienced gradual softening thereafter and failed at a shear stress of 4.68 MPa with a shear strain of 4.35×10^{-3}. The previously attained ultimate shear stress was 4.72 MPa with a corresponding shear strain of 3.72×10^{-3}.

As shown by the isolated shear stress-shear strain cycles in Figure B.35, the initial out-of-plane bending caused the first three double cycles, up to a shear stress of 2.6 MPa, to be drifted toward the positive region. Pinching of the hysteretic loops was not visible until the 4th double cycle at a peak shear stress of 3.1 MPa. Thereafter, the degree of creep increased under increasing loads.

The principal tensile stress at first-cracking was 1.97 MPa with a principal tensile strain of 0.097×10^{-3}. Strain hardening was exhibited until a maximum principal tensile stress of 3.06 MPa was reached. Thereafter, the principal tensile response displayed a plateau. At failure, the principal tensile stress and strain were 2.59 MPa and 7.02×10^{-3}, respectively.

Similar to the principal tensile values, the principal compressive stress and strain at first-cracking were -2.03 MPa and -0.095×10^{-3}, respectively. Due to crack slips and cracks remaining open, the principal compressive strain became positive during unloading. At failure, the principal compressive stress was -8.47 MPa with a principal compressive strain of 0.18×10^{-3}; hence, the panel was insignificantly stressed in the principal compressive direction.

Like all of the reversed cyclically loaded panel tests, the principal stress angle lagged behind the principal strain angle. Although the lag was minor overall, the lag in the negative shear direction was more pronounced. At failure, the principal stress angle was 119° while the principal strain angle was 110°. The reinforcement was insignificant stressed and reached a peak stress of 177 MPa.

B.8.3 Comparison of the Front Face and Back Face Responses

Figure B.36 shows the degree of out-of-plane bending exhibited in this panel by comparing the response of the panel between the front face and back face. Overall, the panel exhibited a small degree of out-of-plane bending in both the positive and negative shear direction. The peak shear strain difference between the two faces was approximately 0.5×10^{-3}. The bending diminished toward failure.

(a)

(b)

(c)

(d)

(e)
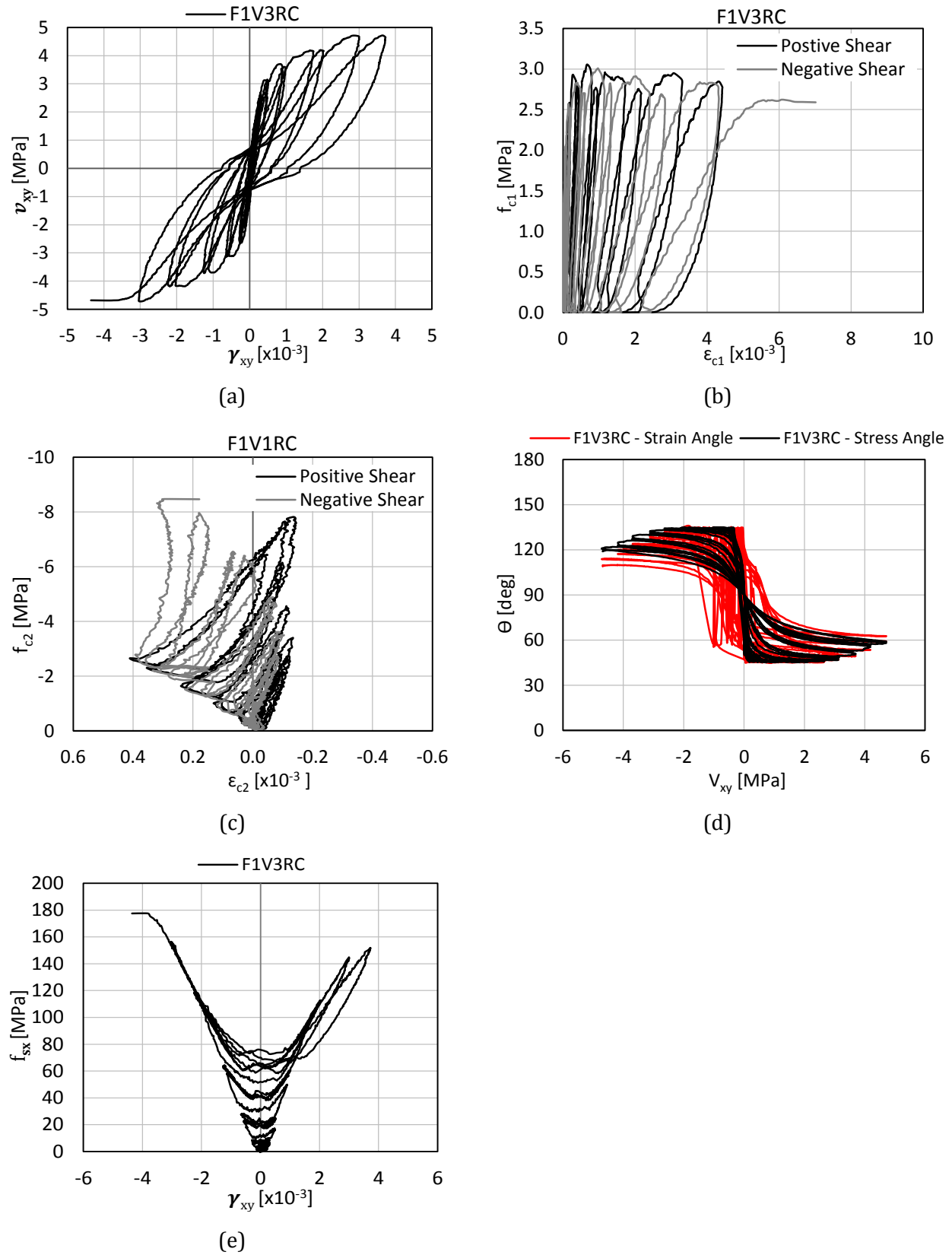
Figure B.34: Response of panel F1V3RC

(a)

(b)

(c)

(d)

(e)

(d)
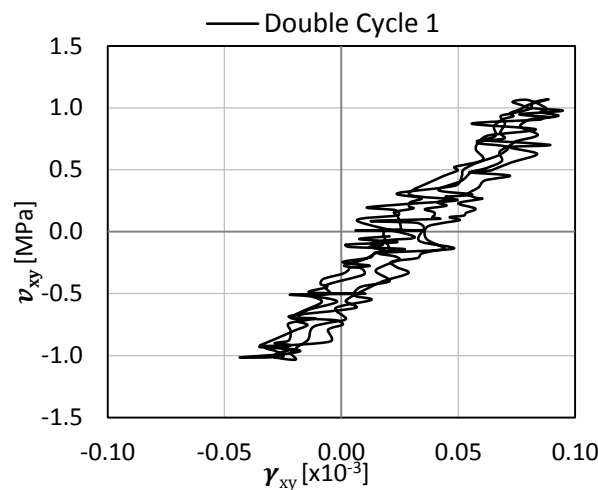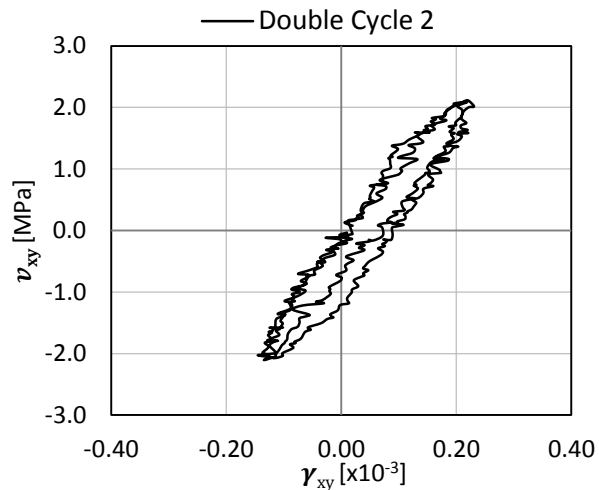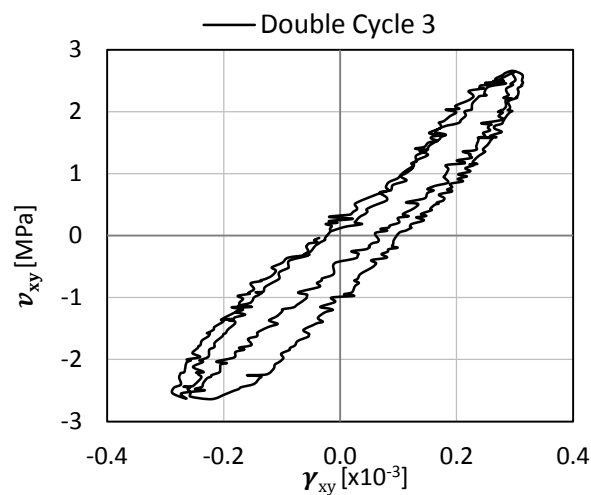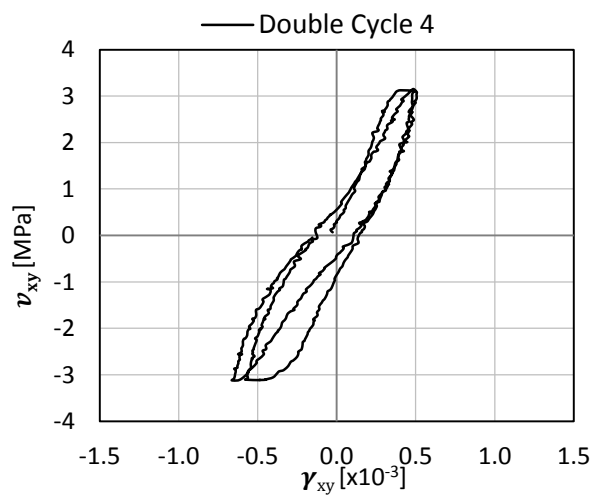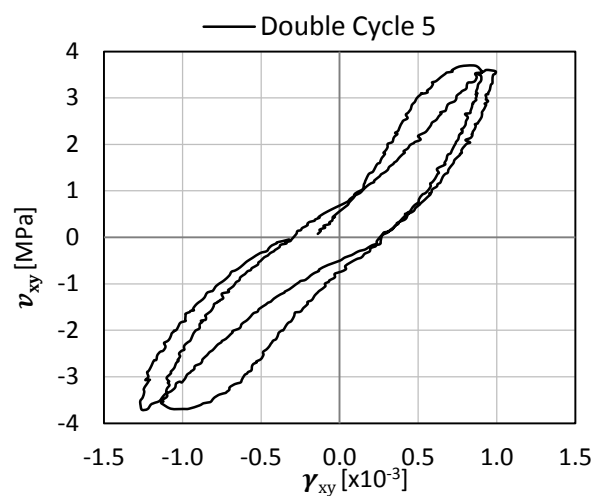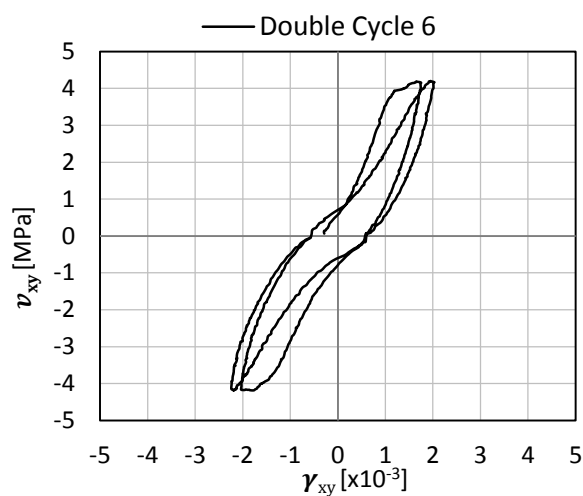
(d)
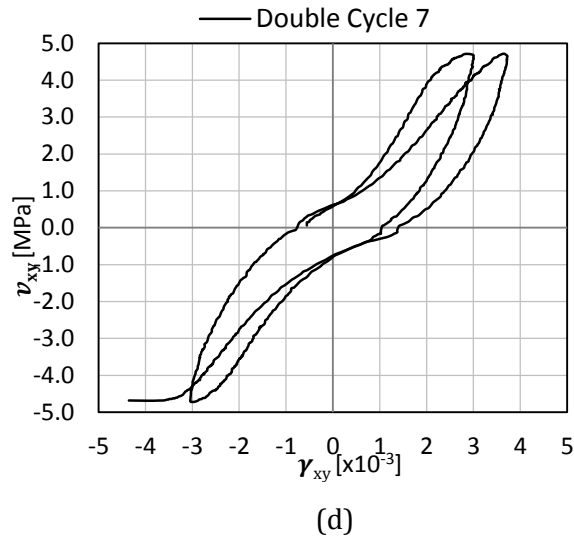
Figure B.35: Shear stress-shear strain response of F1V3RC; isolated cycles

(a)

(b)

(c)

(d)
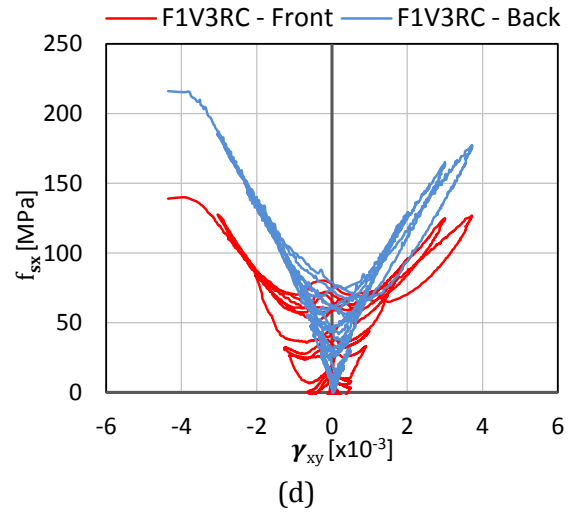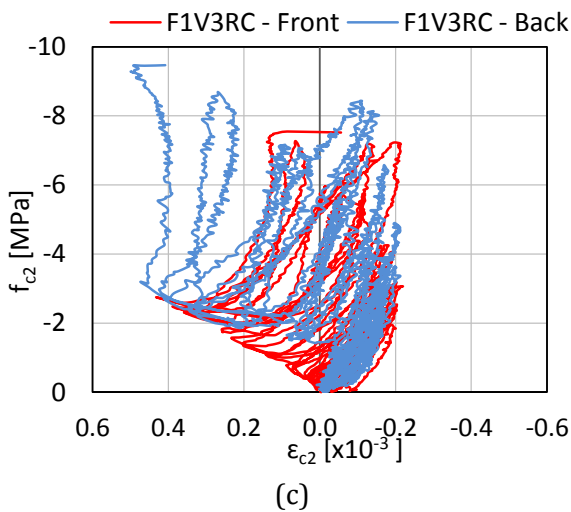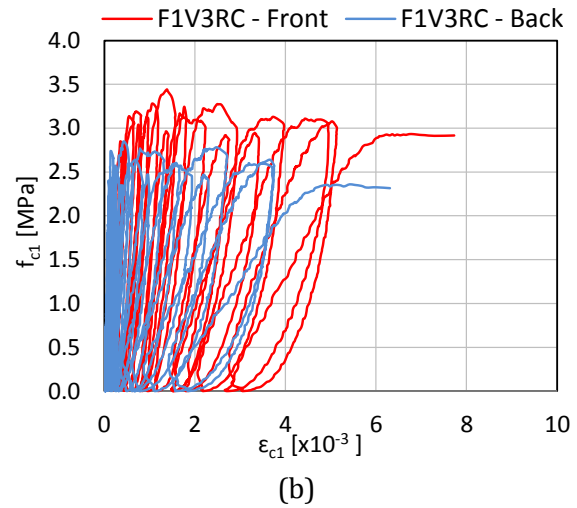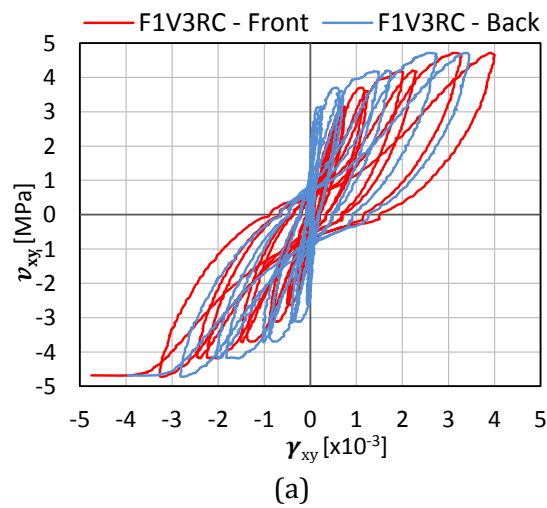
Figure B.36: Comparison of back face and front face response of panel F1V3RC

## B.9 F2V2MS

Panel F2V2MS was the monotonically loaded panel of the F2V2 pair and was constructed of steel fibre reinforced concrete containing 1.0% by volume of ZP305 fibres (l_f = 30 mm, d_f = 0.55 mm, f_{uf} = 1300 MPa). As was the case with previously discussed SFRC panels, F2V2MS contained 3.31% longitudinal reinforcement with no transverse reinforcement provided. The 28-day compressive strength was 50.1 MPa and the uniaxial tensile strength was 3.32 MPa; the test day compressive strength was 52.1 MPa.

B.9.1 Test Observations

The crack pattern of F2V2MS is shown in Figure B.37. Initial cracking occurred at a shear stress of 1.79 MPa; only one crack on the front face was formed at this load. Cracks on the back face were formed during the excursion to the second load stage, at a shear stress of 2.64 MPa. Cracks on both faces were uniformly distributed by the 4th load stage, at a shear stress of 3.66 MPa. Failure occurred at a shear stress and shear strain of 3.96 MPa and 4.16×10^{-3}, respectively. The failure was caused by the breakdown of the aggregate interlock mechanism.

The crack widths and crack spacing of F2V2MS are shown in Figure B.38. The overall trend for these crack control indicators was consistent with the other panels. At the last load stage, the maximum crack width, the average crack width, and the average crack spacing were 0.80 mm, 0.25 mm, and 74 mm, respectively.
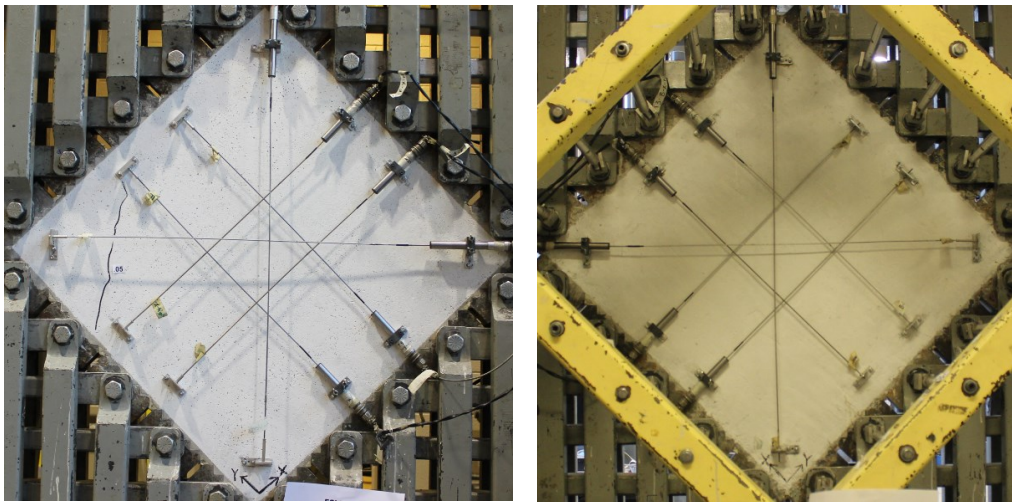
Stage 1: v_{xy}=1.79 MPa, γ_{xy}=0.211×10^{-3}; $w_{cr,max}$=0.05 mm, w_m=0.05 mm, s_m=1260 mm.
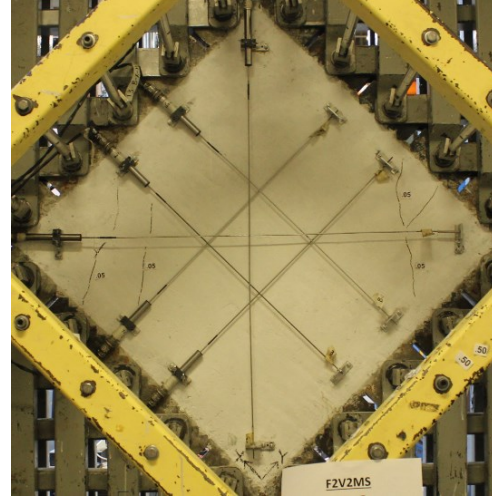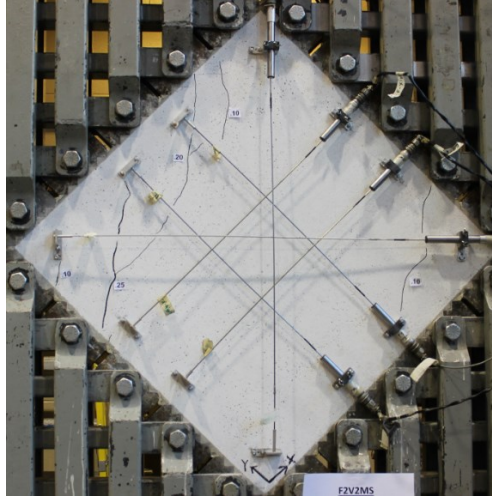
Stage 2: v_{xy}=2.64 MPa, γ_{xy}=0.57×10⁻³; $w_{cr,max}$=0.25 mm, w_m=0.11 mm, s_m=284 mm.
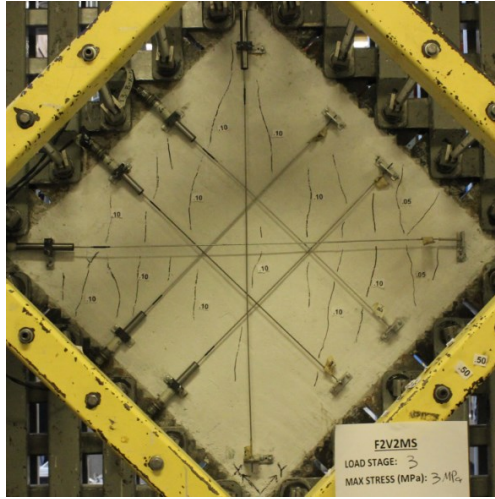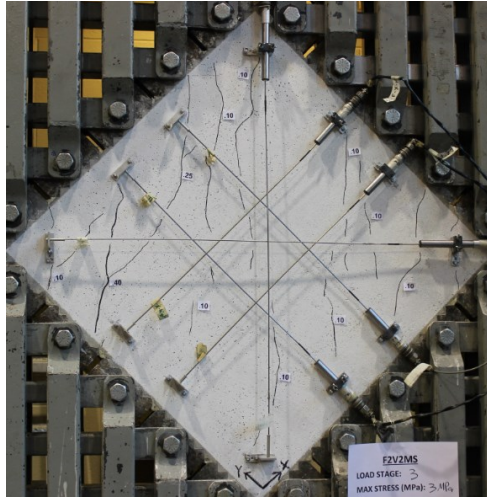
Stage 3: v_{xy}=3.09 MPa, γ_{xy}=1.19×10⁻³; $w_{cr,max}$=0.40 mm, w_m=0.11 mm, s_m=127 mm.
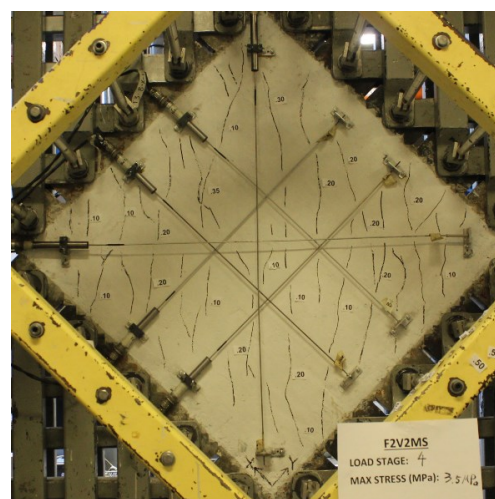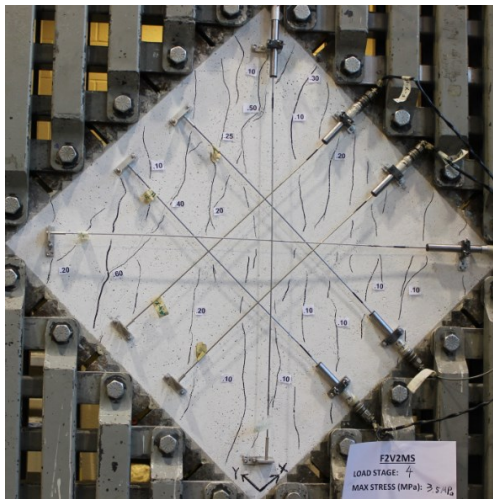
Stage 4: v_{xy}=3.66 MPa, γ_{xy}=2.46×10⁻³; $w_{cr,max}$=0.60 mm, w_m=0.19 mm, s_m=88 mm.
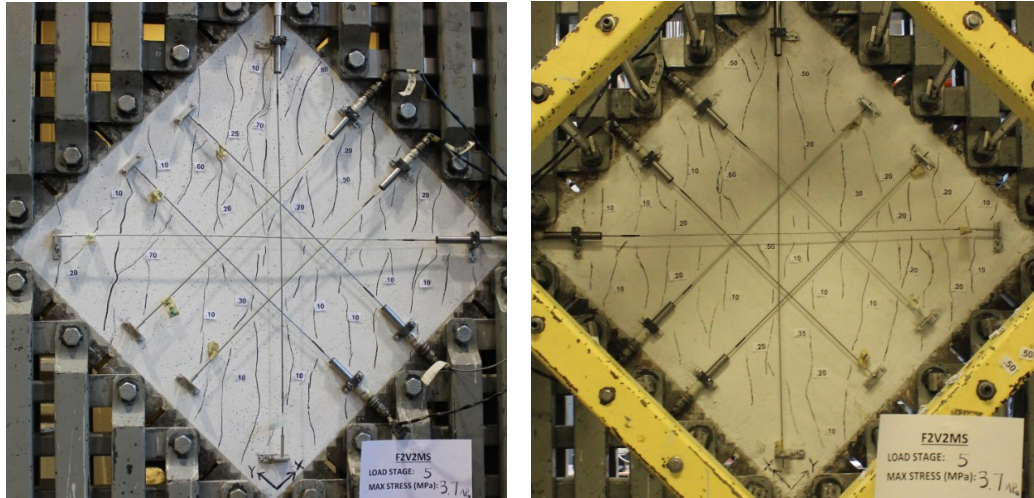
Stage 5: v_{xy}=3.80 MPa, γ_{xy}=3.08×10⁻³; $w_{cr,max}$=0.80 mm, w_m=0.25 mm, s_m=74 mm.
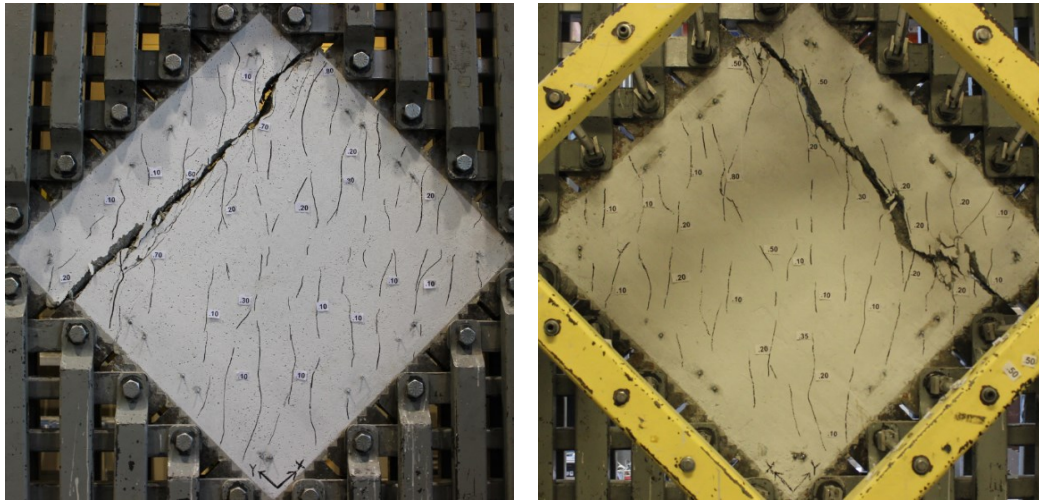
Failure: v_u=3.96 MPa, γ_u=4.16×10⁻³.

Figure B.37: Crack pattern of panel F2V2MS

(a)   (b)
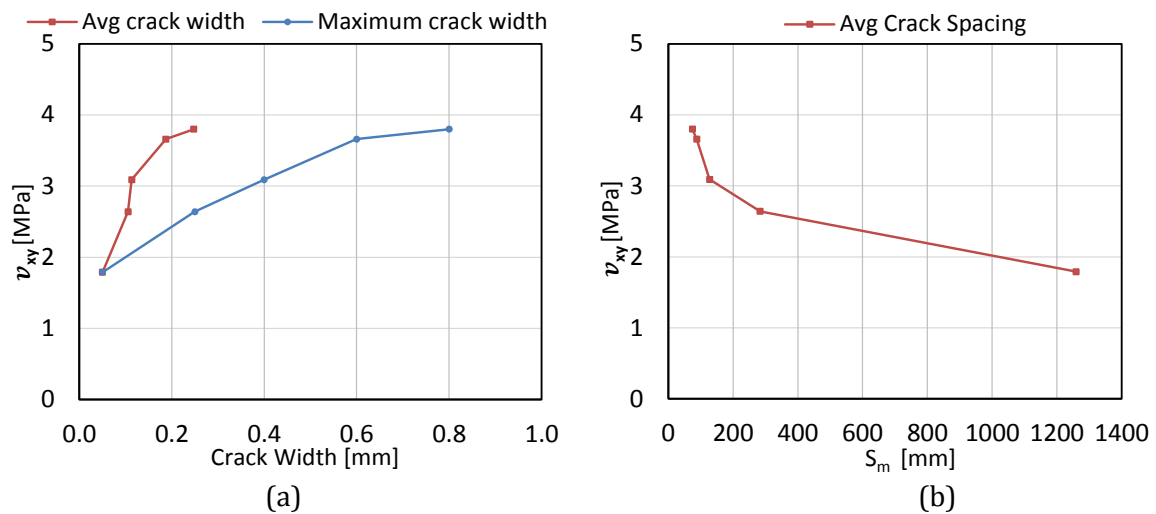
Figure B.38: Crack spacing and crack width of panel F2V2MS

B.9.2 Data Analysis

Figure B.39 depicts the shear stress-shear strain response of panel F2V2MS. The behaviour of the panel was linear up to first-cracking, which occurred at a shear stress and shear strain of 1.79 MPa with 0.211×10^{-3}, respectively. The subsequent response gradually softened until failure occurred at a shear stress of 3.96 MPa with a shear strain of 4.16×10^{-3}.

The principal tensile stress and principal tensile strain at first-cracking were 1.80 MPa and 0.109×10^{-3}, respectively. Afterwards, strain hardening behaviour was observed until the maximum principal tensile stress of 2.77 MPa was reached. Gradual softening of the principal tensile response occurred thereafter and eventually plateaued. At failure, the principal tensile stress was 2.20 MPa with a corresponding principal tensile strain of 6.02×10^{-3}.

At first-cracking, the principal compressive stress and principal compressive strain were -1.79 MPa and -0.102×10^{-3}, respectively. The principal compressive strain drifted into the positive region near failure as a result of the large crack openings and crack slips. At failure, the principal compressive stress was -7.14 MPa and the corresponding principal compressive strain was -0.02×10^{-3}.

The principal stress angle lagged behind the principal strain angle after cracking, but the two angles converged at a shear stress of 3.10 MPa. At failure, the principal stress angle was 61.0°, and the principal strain angle was 68.3°; somewhat consistent with the angle of the surface cracks before failure. The primary reinforcement reached a maximum stress of 149 MPa.

B.9.3 Comparison of the Front Face and Back Face Responses

Figure B.40 depicts the response of the front face and the back face of F2V2MS. Overall, the out-of-plane bending was insignificant for this panel; the maximum shear strain difference between the two faces was 0.39×10^{-3}. The back face of the panel was stiffer and had a higher cracking load, but the cracking patterns for the two faces were largely identical after the formation of multiple cracks.
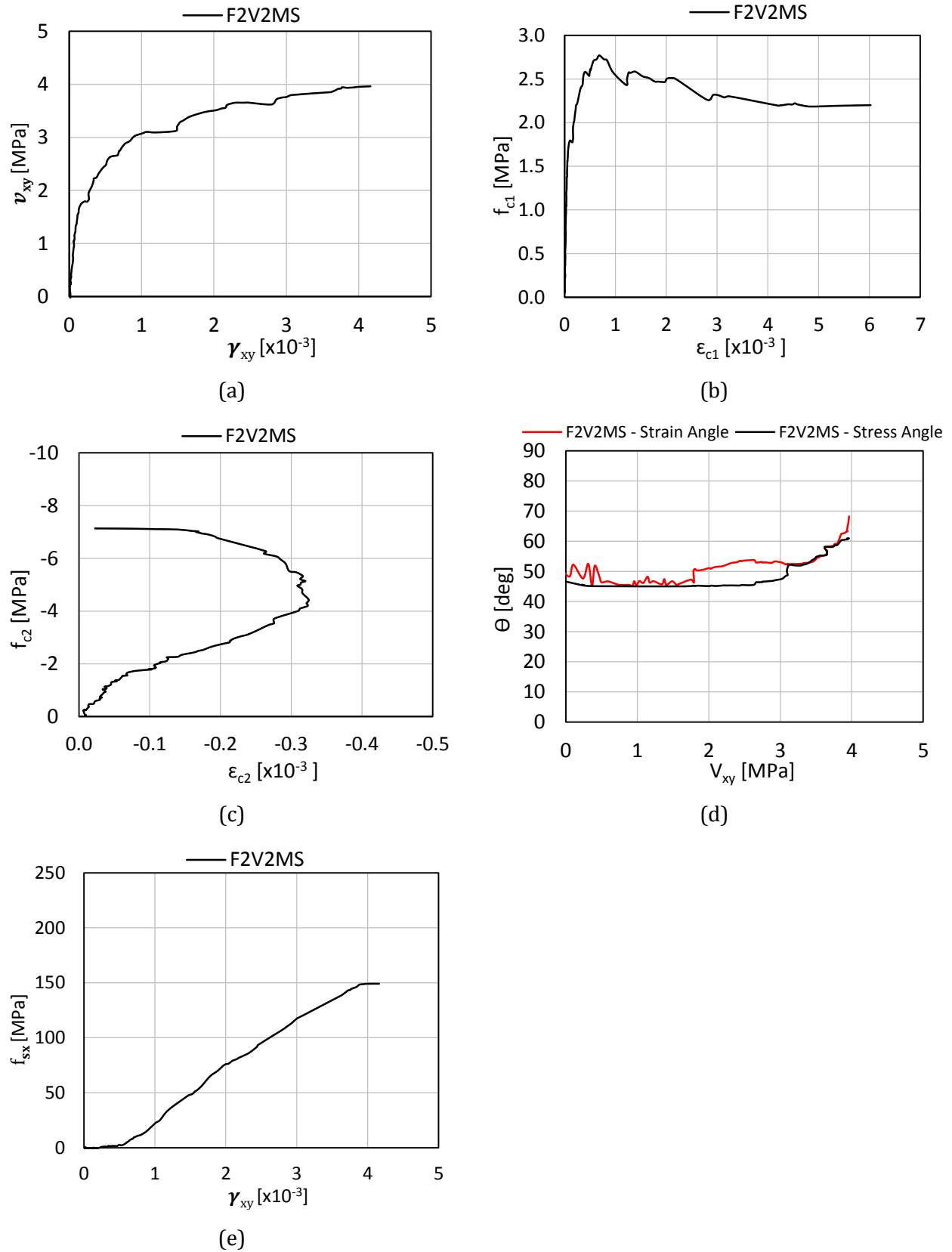
Figure B.39: Response of panel F2V2MS
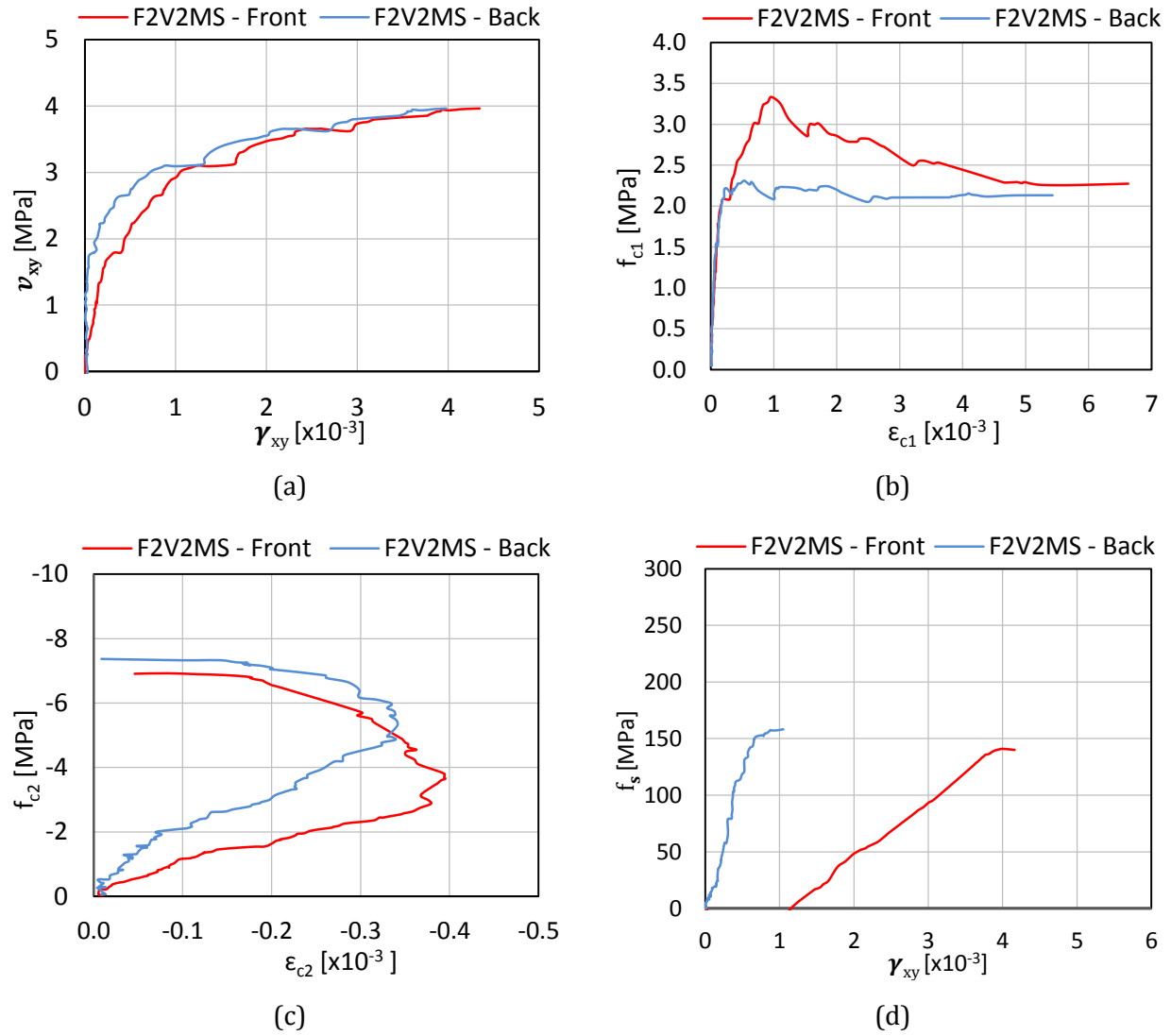
Figure B.40: Comparison of back face and front face response of panel F2V2MS

B.10 F2V2RC

Panel F2V2RC was constructed of steel fibre reinforced concrete with 1.0% by volume of ZP305 fibres (l_f = 30 mm, d_f = 0.55 mm, f_{uf} = 1300 MPa). F2V2RC contained 3.31% longitudinal reinforcement with no transverse reinforcement. The 28-day compressive strength was 50.1 MPa and the uniaxial tensile strength was 3.32 MPa; the test day compressive strength was 52.9 MPa.

B.10.1 Test Observations

Figure B.42 shows the crack patterns of F2V2RC. The first crack was a vertical crack on the front face of the panel and occurred at a shear stress of 1.82 MPa; like all panels, the width of the first crack was 0.05 mm. Vertical cracks for the back face subsequently developed during the same double cycle. Horizontal cracks, however, did not develop until the next double cycle, 3rd double cycle, at a cycle peak stress of 2.58 MPa. Cracks in both directions and on both faces became uniform during the excursion to the peak cycle shear stress of the 4th double cycle, 3.11 MPa. The panel failed after reaching a maximum shear stress of 3.47 MPa. The failure had sufficient warning as a result of the large crack width of the dominant crack. The failure was initiated by fibre pull-out followed by aggregate interlock failure and crack sliding, similar to all SFRC panels.

The crack widths and crack spacing of F2V2RC are shown in Figure B.42. Due to the initial loading direction being positive, the crack widths and crack spacing from the negative direction were slightly larger than the positive direction. At the final load stage, the maximum crack width, the average crack width, and the average crack spacing were 1.20 mm, 0.33 mm, and 115 mm, respectively.
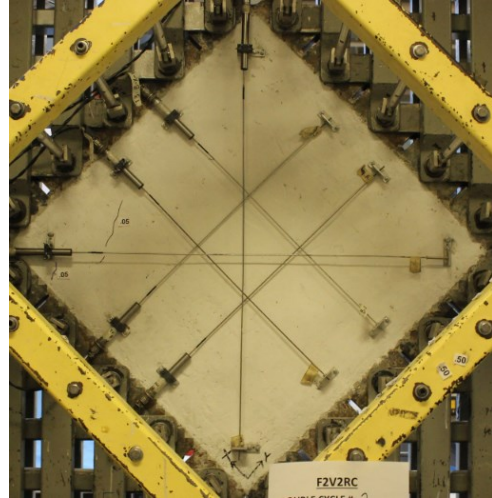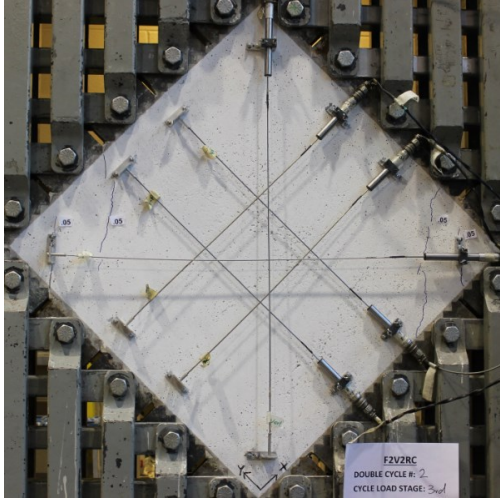
Double Cycle 2, Stage 7: v_{xy}=2.06 MPa, γ_{xy}=0.18×10⁻³; $w_{cr,max}$=0.05 mm, w_m=0.05 mm, s_m=473 mm.
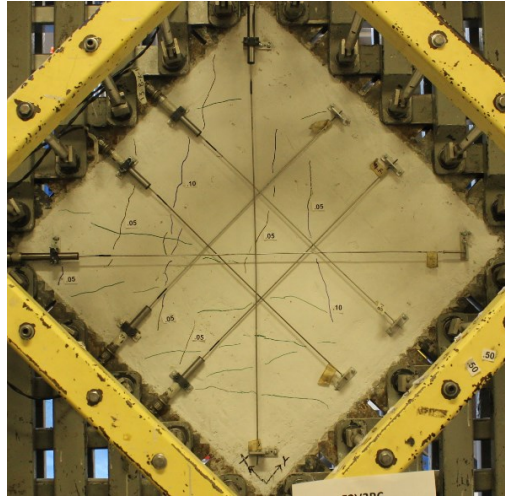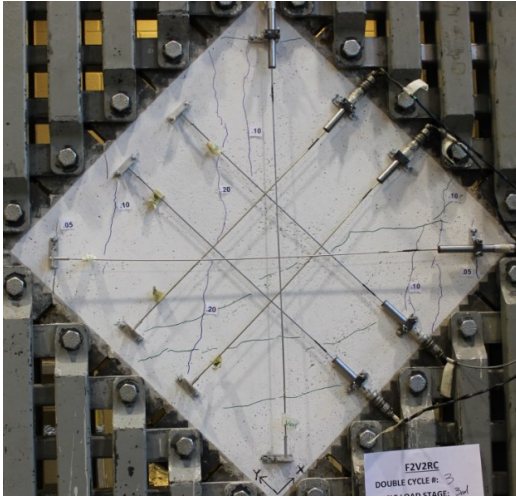
Double Cycle 3, Stage 11: v_{xy}=2.58 MPa, γ_{xy}=0.38×10⁻³; $w_{cr,max}$=0.20 mm, w_m=0.09 mm, s_m=216 mm.
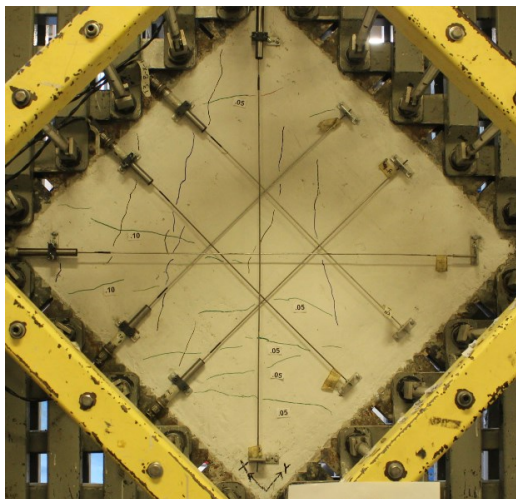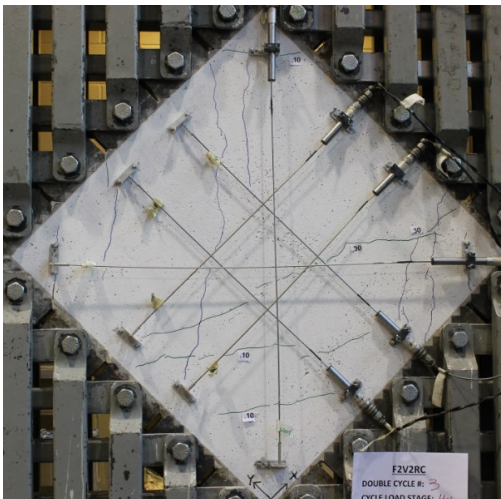
Double Cycle 3, Stage 12: v_{xy}=-2.65 MPa, γ_{xy}=-0.78×10⁻³; $w_{cr,max}$=0.30 mm, w_m=0.11 mm, s_m=248 mm.
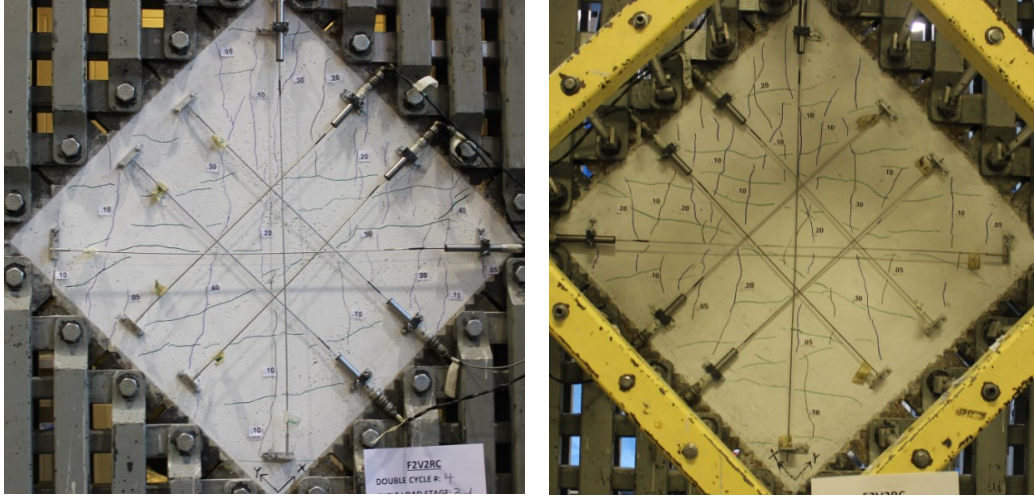
Double Cycle 4, Stage 15: v_{xy}=3.11 MPa, γ_{xy}=1.30×10⁻³; $w_{cr,max}$=0.40 mm, w_m=0.15 mm, s_m=120 mm.
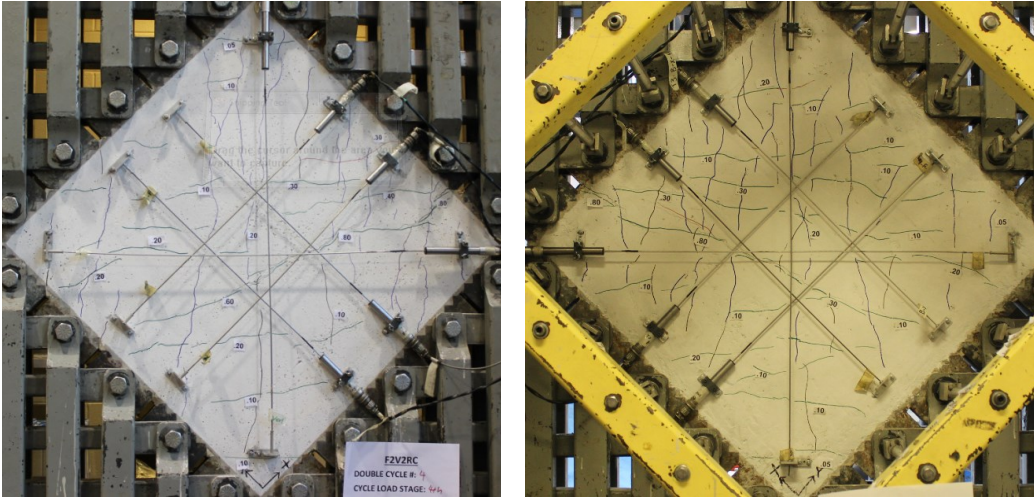
Double Cycle 4, Stage 16: v_{xy}=-3.15 MPa, γ_{xy}=-1.83×10⁻³; $w_{cr,max}$=0.80 mm, w_m=0.25 mm, s_m=120 mm.
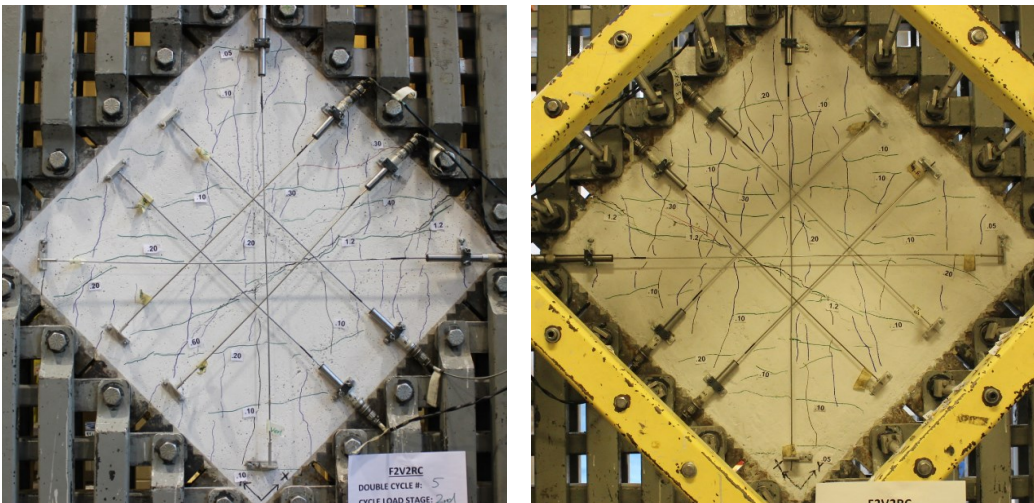
Double Cycle 5, Stage 18: v_{xy}=-3.46 MPa, γ_{xy}=-2.75×10⁻³; $w_{cr,max}$=1.20 mm, w_m=0.33 mm, s_m=115 mm.
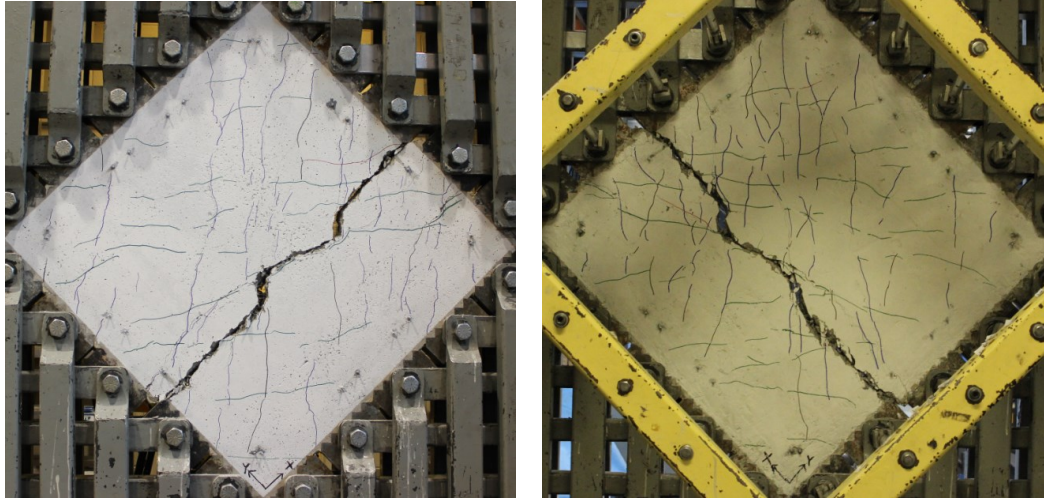
Failure: v_u=3.47 MPa, γ_u=2.75×10⁻³.

Figure B.41: Crack pattern of panel F2V2RC

(a)   (b)
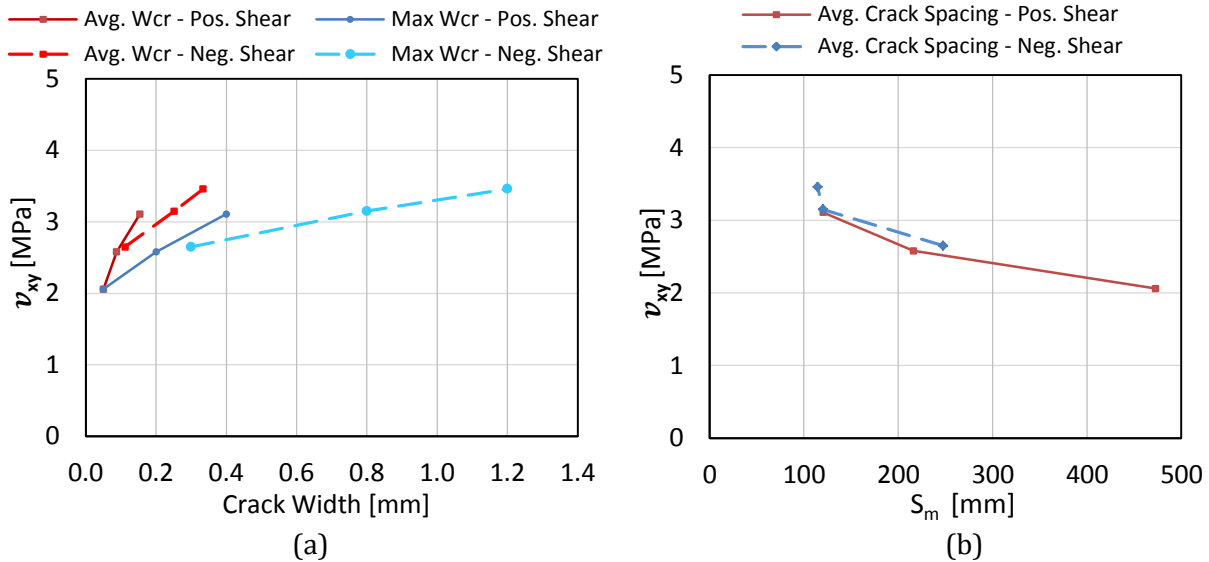
Figure B.42: Crack spacing and crack width of panel F2V2RC

B.10.2 Data Analysis

Figure B.43 shows the various panel responses. Like all panels, the overall response was linear up to first cracking, which occurred at a shear stress of 1.82 MPa with a corresponding shear strain of 0.146×10⁻³. The response gradually softened thereafter and pinching of the hysteretic loops was visible by the 3rd double cycle, under a cycle peak shear stress of 2.60 MPa. As shown in Figure B.44, each one of the isolated hysteretic loops was approximately centred at the origin. Failure of the panel took place under a shear stress of 3.30 MPa with a corresponding shear strain of 4.53×10⁻³. The previously attained ultimate shear stress was 3.47 MPa and the corresponding ultimate shear strain was 2.75×10⁻³.

At first-cracking, the principal tensile stress and strain were 1.80 MPa and 0.076×10^{-3}, respectively. Afterwards, the principal tensile stress increased to a maximum of 2.41 MPa then showed gradual softening until failure occurred. The principal tensile stress and principal tensile strain at failure were 1.59 MPa and 6.90×10^{-3}, respectively.

The principal compressive stress and principal compressive strain at first-cracking were -1.83 MPa and -0.070×10^{-3}, respectively. After the first three double cycles, beyond the peak cycle shear stress of 2.60 MPa, the principal compressive strains were positive the majority of the time, indicating large crack slips and cracks openings. At failure, the principal compressive stress was -6.83 MPa and the corresponding principal compressive strain was 0.01×10^{-3}.

Overall, the principal stress angle lagged behind the principal strain angle after initial cracking. The principal stress angle and the principal strain angle at failure were 64.2° and 69.5°, respectively. The primary reinforcement reached a peak stress of 163 MPa.

B.10.3 Comparison of the Front Face and Back Face Responses

Figure B.45 shows the comparison between the response of the front face and the back face. This panel exhibited a relatively small degree of out-of-plane bending in both the positive and the negative shear direction; the peak shear strain difference for the two faces was approximately 0.5×10^{-3}. The shear stress-shear strain response of the two faces was near convergence at a shear stress of 3.0 MPa.
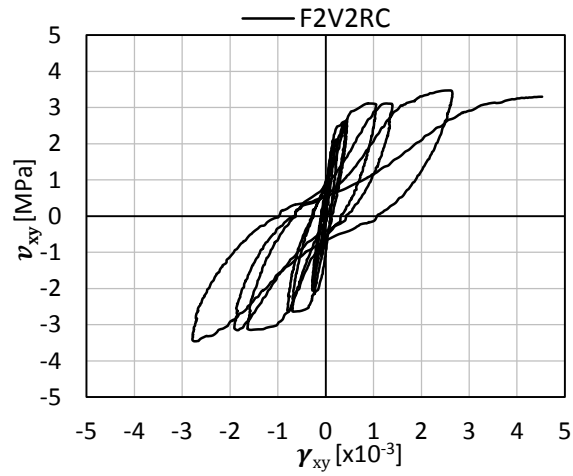
(a)
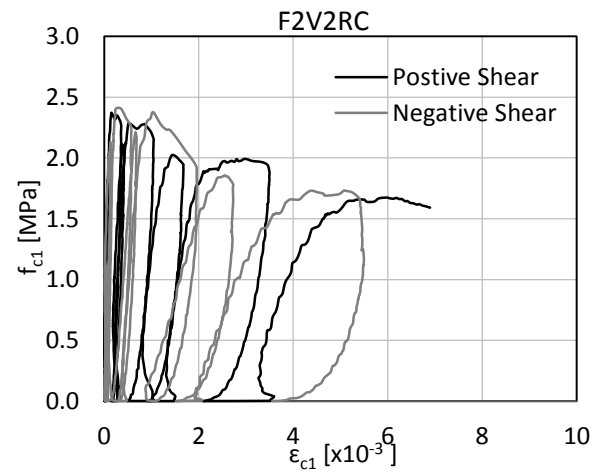
(b)
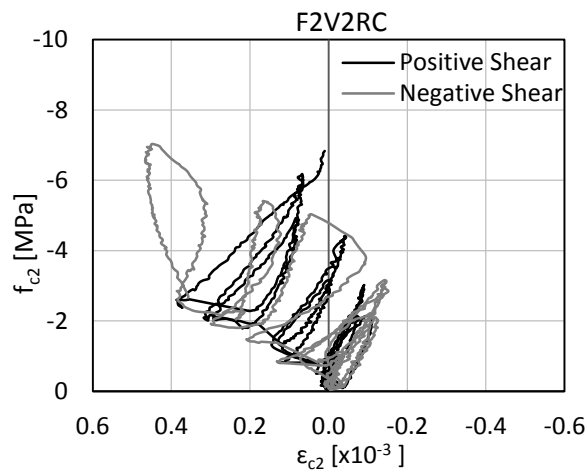
(c)
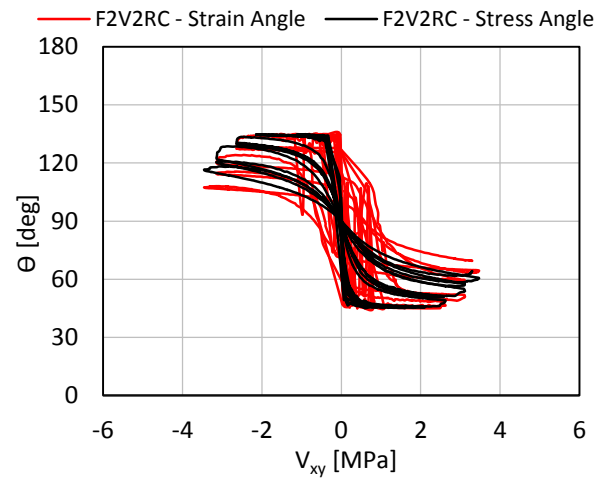
(d)
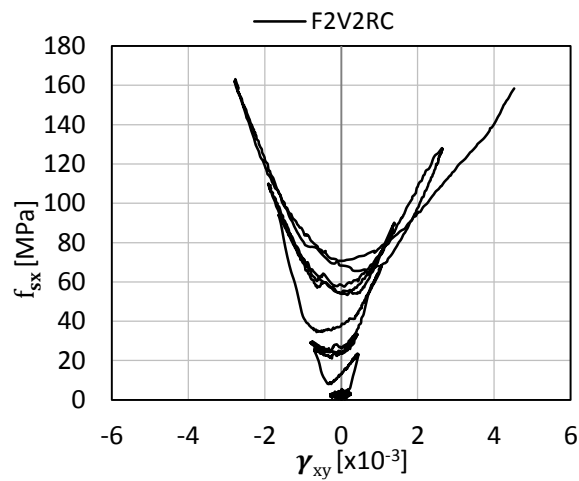
(e)

Figure B.43: Response of panel F2V2RC
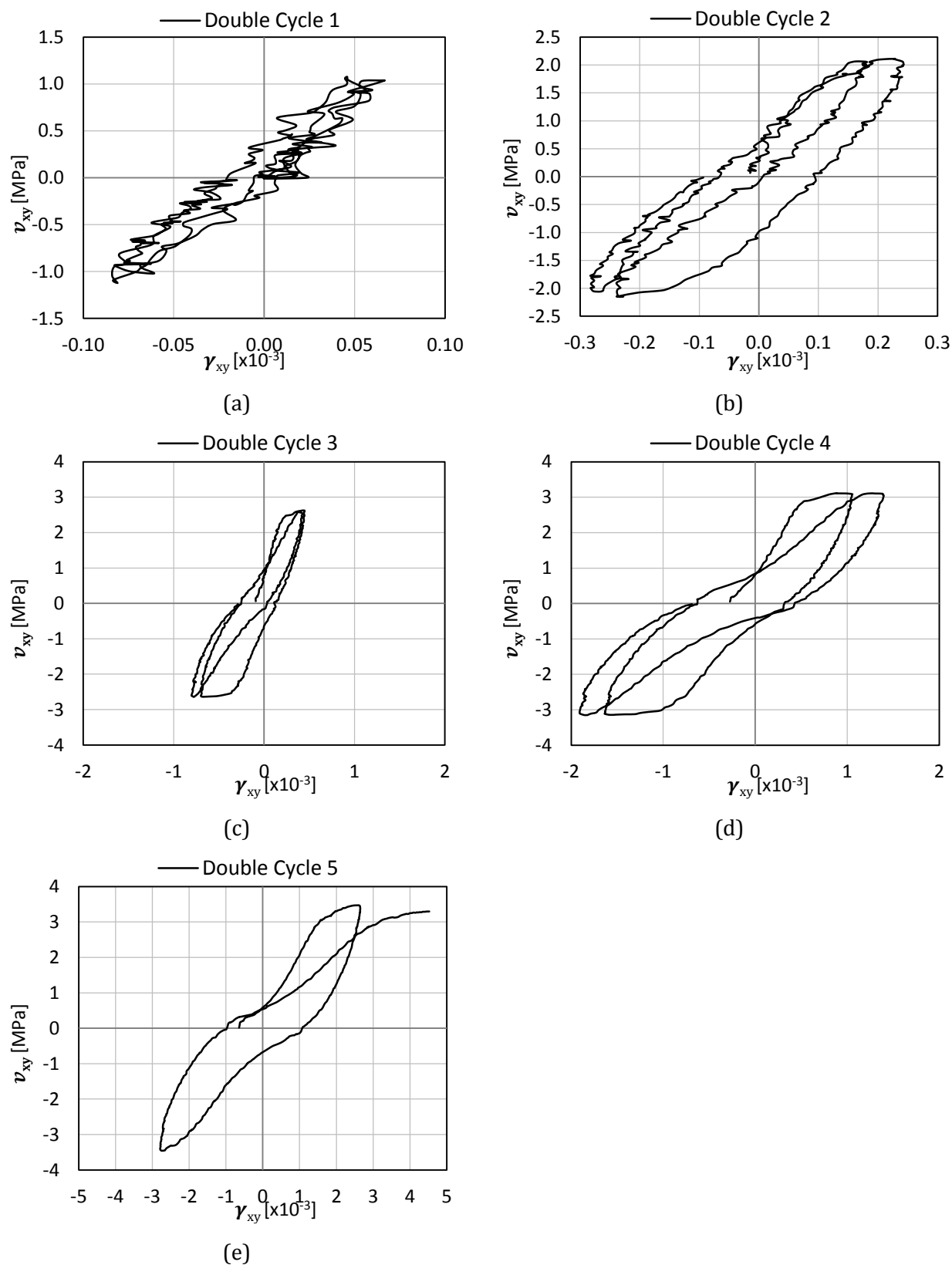
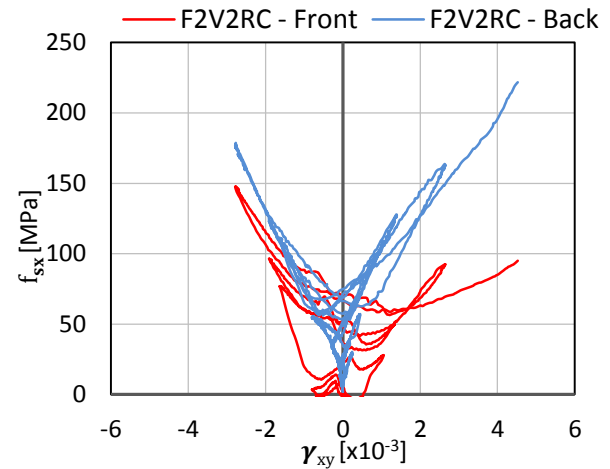Figure B.44: Shear stress-shear strain response of F2V2RC; isolated cycles
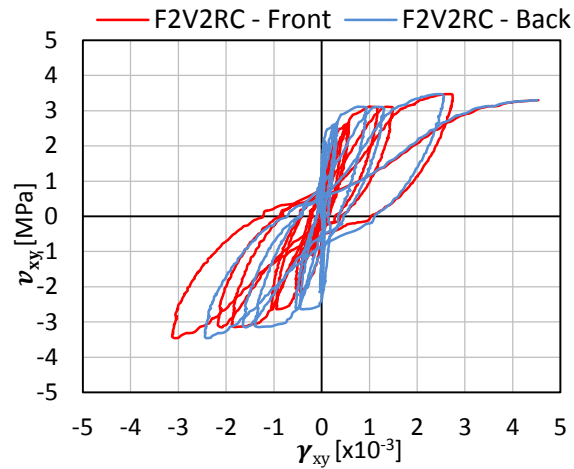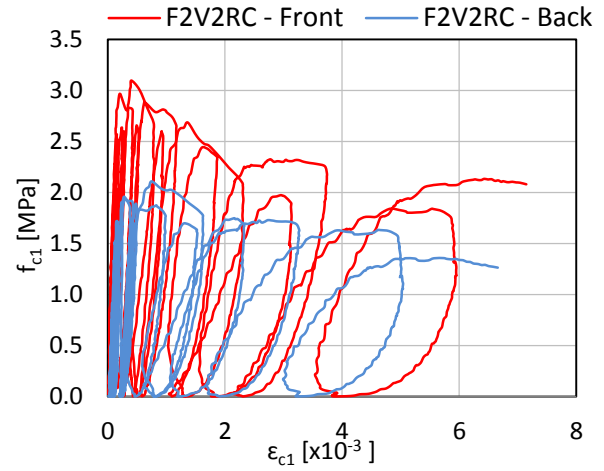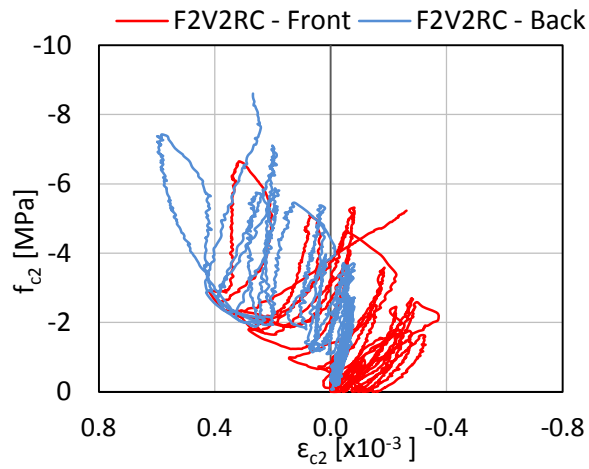
Figure B.45: Comparison of back face and front face response of panel F2V2RC

B.11 F1V2MS-P

Panel F1V2MS-P was the monotonically loaded panel for the pilot pair. The panel was designed to be identical to F1V2MS and hence, was constructed of steel fibre reinforced concrete with 1.0% by volume of RC80/30BP fibres (l_f = 30 mm, d_f = 0.38 mm, f_{uf} = 2300 MPa). The longitudinal reinforcement ratio was 3.31% and no transverse reinforcement was provided. The 28-day compressive strength was 41.2 MPa, uniaxial tensile strength was 4.00 MPa, first-cracking flexural stress was 5.29 MPa, and peak flexural strength was 6.19 MPa; the test day compressive strength was 43.2 MPa.

This pilot panel was not discussed in the body of the thesis due to the fact that it was cast using a separate batch of concrete than the one used for the cyclically loaded pilot panel, F1V2RC-P. Further, the resulting concrete compressive strength was well below that of F1V2RC-P (28% lower).

B.11.1 Test Observations

Figure B.46 shows the crack patterns of F1V2MS-P for each load stage. Initial cracking occurred at a shear stress of 1.61 MPa. Multiple cracks were formed on the front face at subsequent load stages; however, the back face did not experience first-cracking until the excursion to the 3rd load stage, for a target shear stress of 3.11 MPa. Cracks on both faces were uniformly distributed by the 3rd load stage. Failure occurred at a shear stress and shear strain of 4.52 MPa and 5.87×10^{-3}, respectively. Like all SFRC panels, the failure was caused by the breakdown of the aggregate interlock mechanism.

The crack widths and crack spacing of F1V2MS-P are shown in Figure B.47. The trends for these crack control parameters were consistent with F1V2MS and other SFRC panels. At the last load stage, the maximum crack width, the average crack width, and the average crack spacing were 0.50 mm, 0.14 mm, and 90.0 mm, respectively.
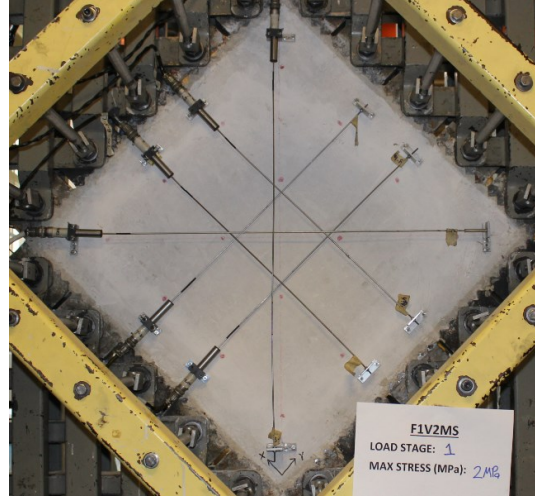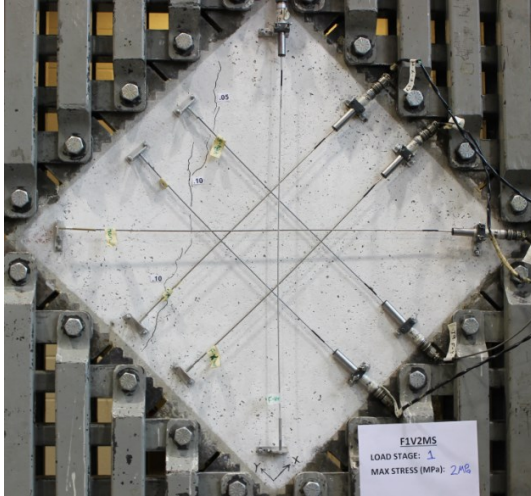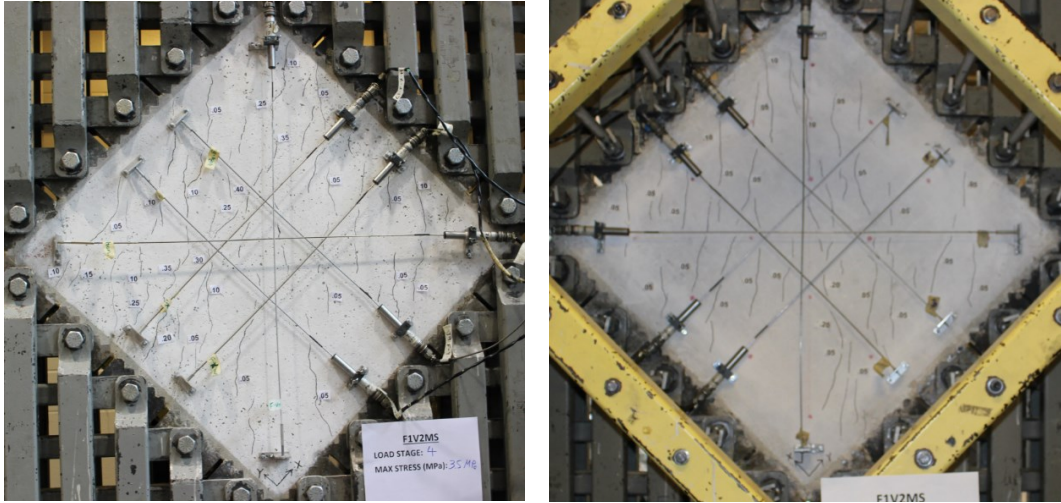
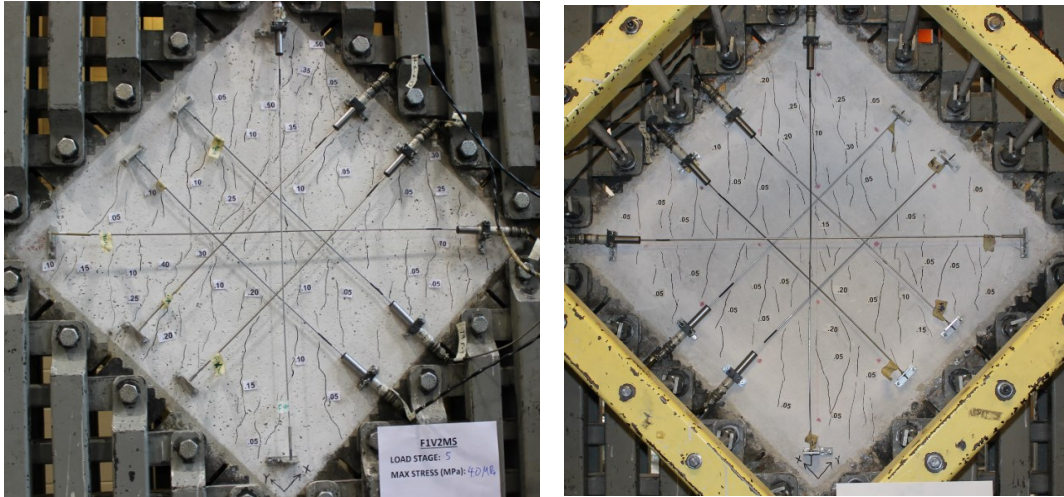Stage 1: v_{xy}=2.11 MPa, γ_{xy}=0.361×10⁻³; $w_{cr,max}$=0.1 mm, w_m=0.08 mm, s_m=1260 mm.
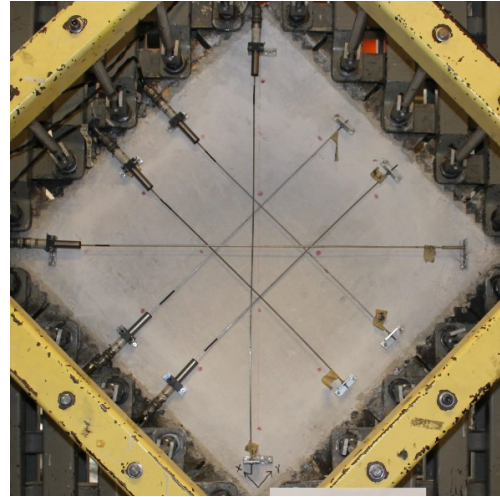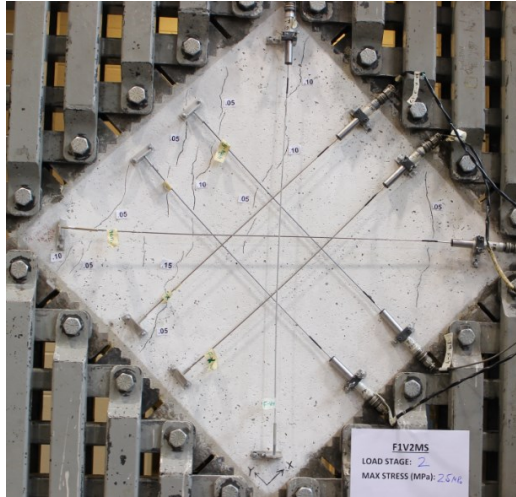
Stage 2: v_{xy}=2.65 MPa, γ_{xy}=0.66 ×10⁻³; $w_{cr,max}$=0.15 mm, w_m=0.08 mm, s_m=252 mm.
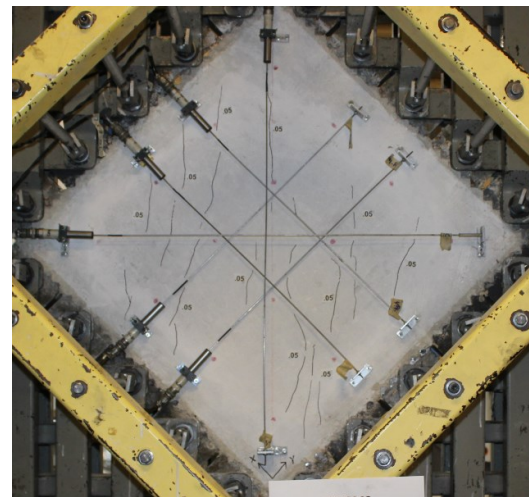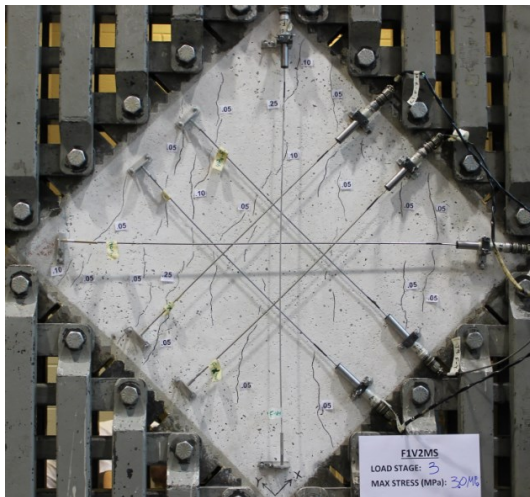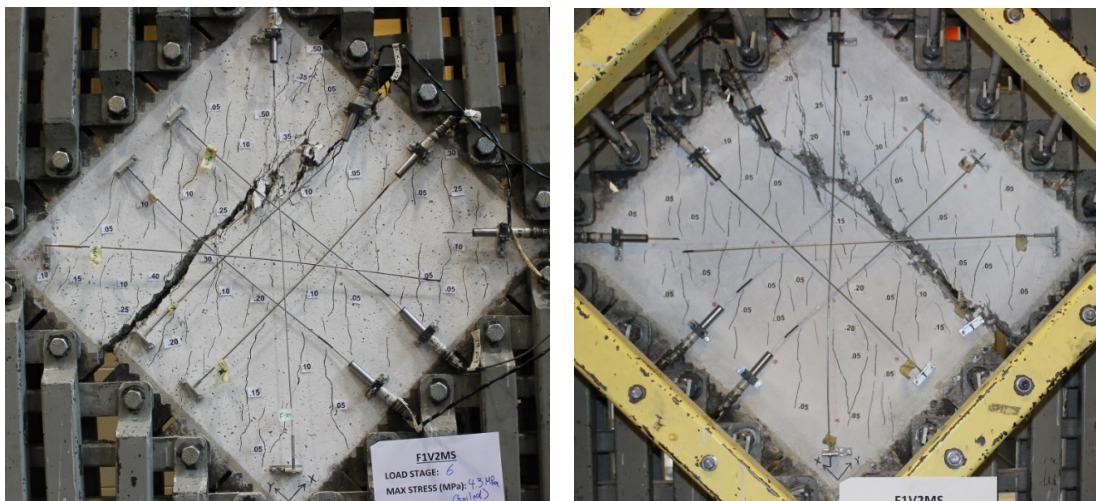

Stage 3: v_{xy}=3.11 MPa, γ_{xy}= ×10⁻³; $w_{cr,max}$=0.25 mm, w_m=0.08 mm, s_m=158 mm.

Stage 4: v_{xy}=3.69 MPa, γ_{xy}=2.24×10^{-3}; $w_{cr,max}$=0.40 mm, w_m=0.11 mm, s_m=97 mm.

Stage 5: v_{xy}=4.15 MPa, γ_{xy}=3.67×10^{-3}; $w_{cr,max}$=0.50 mm, w_m=0.14 mm, s_m=90 mm.

Failure: v_u=4.52 MPa, γ_u=5.87×10^{-3}.

Figure B.46: Crack pattern of panel F1V2MS-P
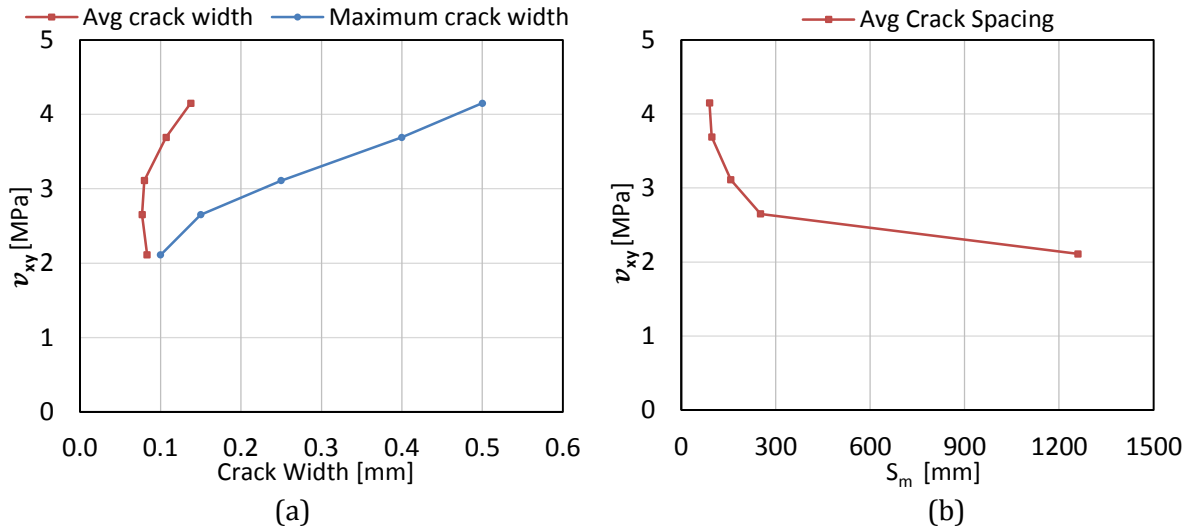
Figure B.47: Crack spacing and crack width of panel F1V2MS-P

B.11.2 Data Analysis

The response of panel F1V2MS-P is shown in Figure B.48. The overall response was linear until the formation of the first crack, which occurred at a shear stress and a shear strain of 1.61 MPa and 0.19×10^{-3}, respectively. Failure occurred at a shear stress and a shear strain of 4.52 MPa and 5.87×10^{-3}, respectively.

At first-cracking, the principal tensile stress and principal tensile strain were 1.51 MPa and 0.13×10^{-3}, respectively. Afterwards, strain hardening behaviour occurred up to a principal tensile stress of 2.21 MPa. The subsequent response exhibited a plateau. At failure, the principal tensile stress and strain were 2.33 MPa and 7.64×10^{-3}, respectively.

Similar to the other SFRC panels, F1V2MS-P was insignificantly stressed in the principal compressive direction. At first-cracking, the principal compressive stress and principal compressive strain were -1.71 MPa and -0.054×10^{-3}, respectively. Unlike the other SFRC panels, F1V2MS-P's compressive strain did not display noticeable shifts into the positive strain region, indicating small crack openings and crack slips. At failure, the principal compressive stress was -8.78 MPa with a principal compressive strain of -0.25×10^{-3}.

The principal strain angle lagged behind the principal stress angle after cracking, the largest lag was 7.2°. Near failure, the two angles began to converge. At failure, the principal stress angle was 62.7°, and the principal strain angle was 66.0°. The primary reinforcement reached a peak stress of 204 MPa.

As mentioned earlier, the primary difference between F1V2MS and F1V2MS-P was the concrete compressive strength (58.1 MPa for F1V2MS and 43.2 MPa for F1V2MS-P). As a result, a constant gap of approximately 0.40 MPa existed between the shear stress-shear strain responses of these two panels (see Figure B.49)

B.11.3 Comparison of the Front Face and Back Face Responses

Figure B.50 shows the response for the front face and the back face of F1V2MS-P. The degree of out-of-plane bending for this panel was slightly more pronounced than the other SFRC panels. The maximum shear strain difference between the two faces was 0.62×10^{-3}. Although the back face of the panel was initially stiffer, after the formation of multiple cracks on both faces, the cracking pattern and the shear stress-shear strain response were largely identical between the two faces.
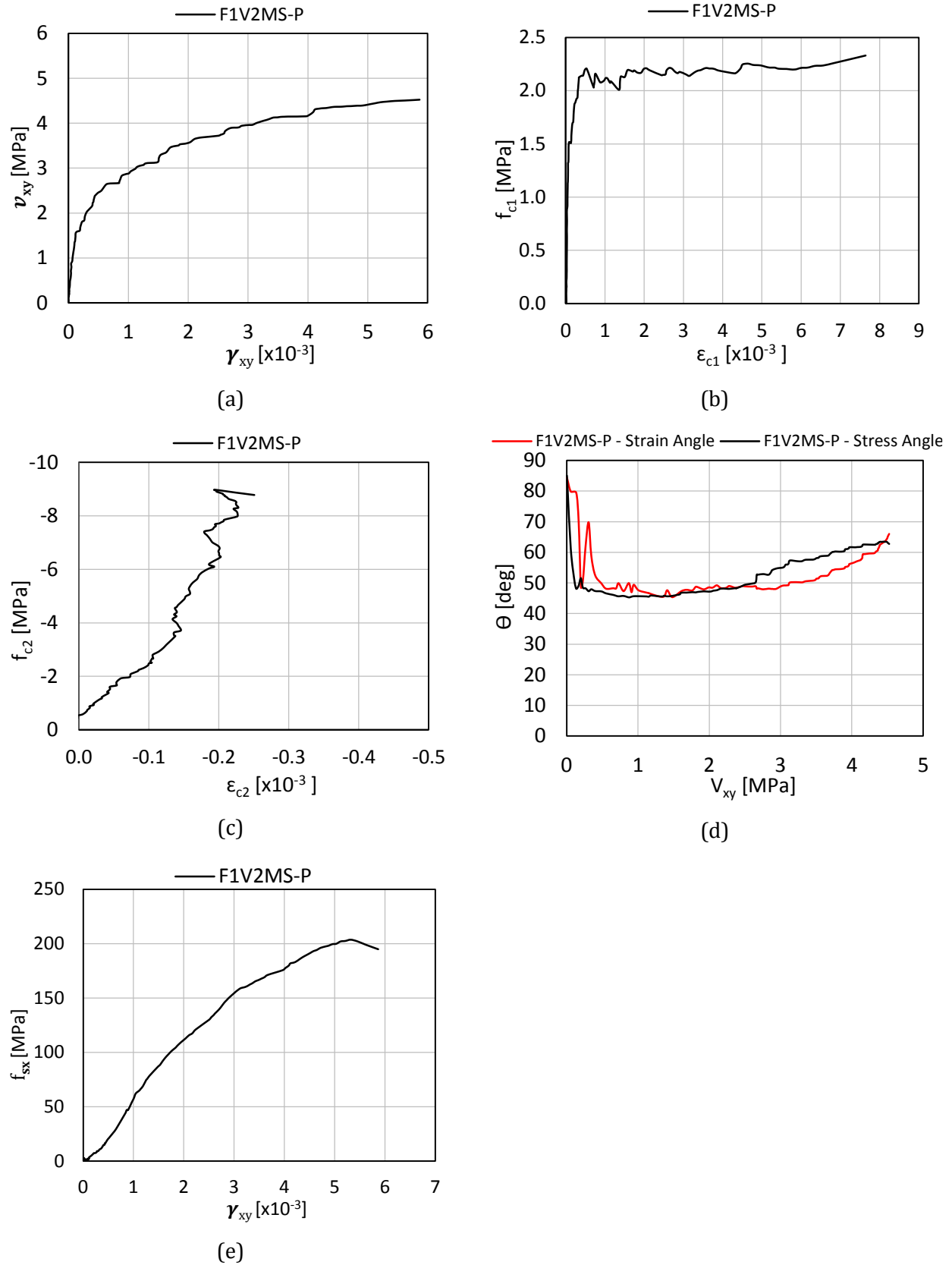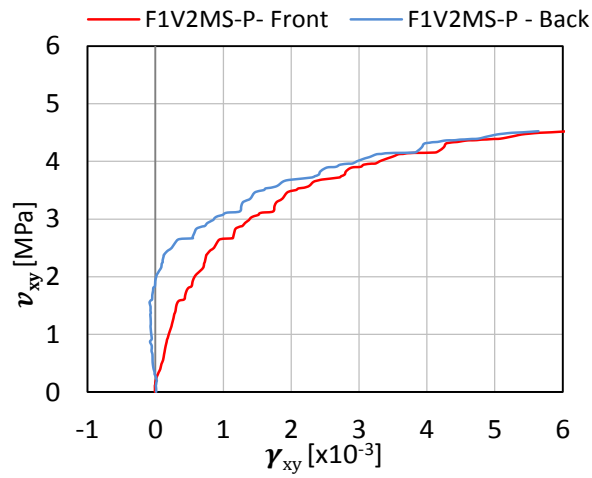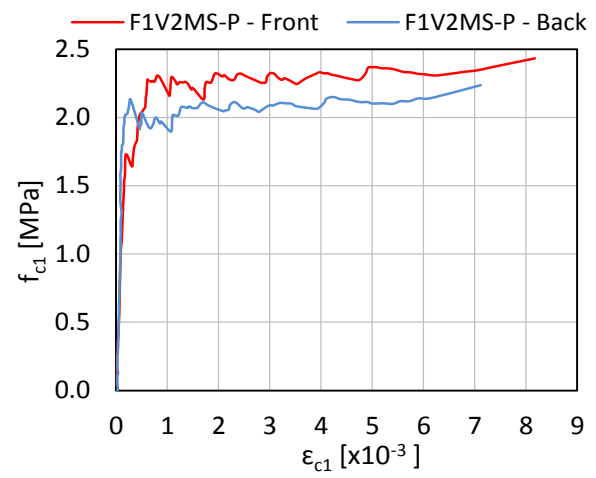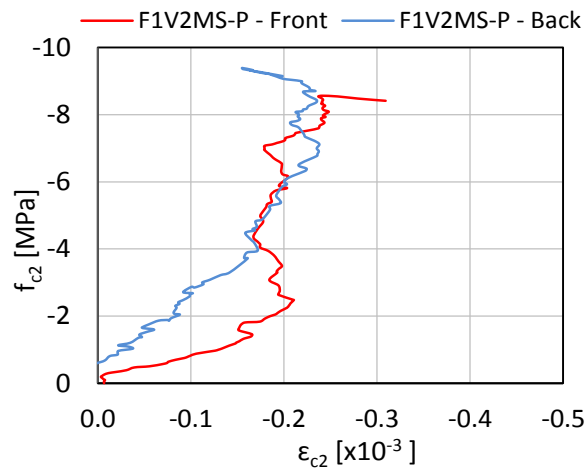
Figure B.48: Response of panel F1V2MS-P
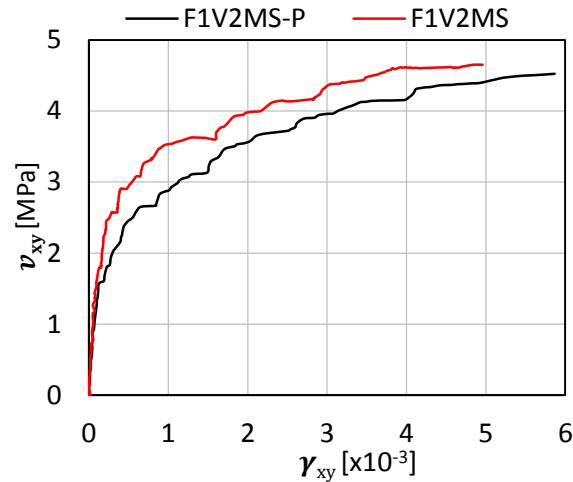
Figure B.49: Comparison against the repeated panels for F1V2MS-P
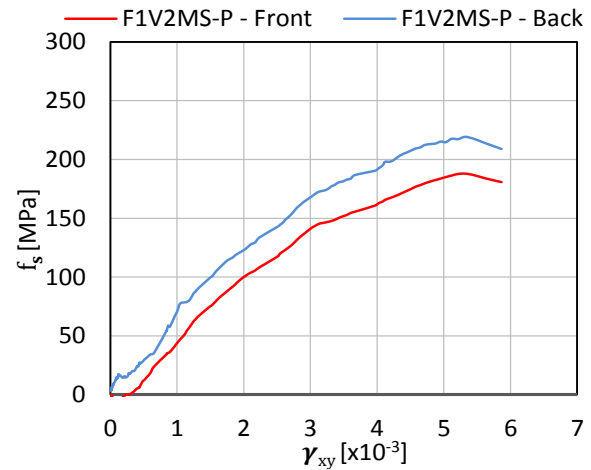

(a)

(b)

(c)

(d)

Figure B.50: Comparison of back face and front face response of panel F1V2MS-P

B.12 F1V2RC-P

Panel F1V2RC-P was the reversed cyclically loaded companion panel of the pilot pair. Identical to F1V2RC, F1V2RC-P was constructed of steel fibre reinforced concrete with 1.0% by volume of RC80/30BP fibres (l_f = 30 mm, d_f = 0.38 mm, f_{uf} = 2300 MPa). The longitudinal reinforcement ratio was 3.31%. The 28-day compressive strength was 54.4 MPa, uniaxial tensile strength was 4.57 MPa, first-cracking flexural stress was 5.97 MPa, and peak flexural strength was 9.60 MPa; the test day compressive strength was 60.2 MPa.

This panel was not examined in the body of the thesis for the following reasons. First, this panel was cast using a separate batch of concrete than the one used for the monotonically loaded pilot panel, making the comparison between the two pilot panels difficult. Second, unlike the other cyclically loaded panels, F1V2RC-P employed a very coarse loading protocol and did not result in sufficient number of loading cycles. The double cycle peak shear stresses were 1.1 MPa, 2.1 MPa, 3.2 MPa, 4.2 MPa, and 5.24 MPa.

B.12.1 Test Observations

The crack patterns of F1V2RC-P are shown in Figure B.51. The first cracked was formed at a shear stress of 3.16 MPa. Noticeable amounts of out-of-plane bending were exhibited during the early loading cycles and resulted in horizontal and vertical cracks forming on the front face only. During the excursion to the target shear stress of 4.19 MPa, uniform horizontal and vertical cracks formed on the back face. Failure of the panel occurred at a shear stress and shear strain of 4.32 MPa and 4.33×10^{-3}, respectively. The ultimate shear stress attained and the corresponding shear strain were 5.24 MPa and 4.58×10^{-3}, respectively. The panel failed due to the breakdown of the aggregate interlock mechanism.

Figure B.52 shows the crack spacing and the crack widths of F1V2RC-P. Due to the coarse loading protocol, an insufficient number of crack measurements was taken which resulted in the relatively scattered graphs for the crack width and the crack spacing. The overall trends for these crack control parameters were consistent with previously tested panels. The average crack width unexpectedly decreased under higher loads and is believed to be caused by the insufficient number of data points and the opening of a few relatively wide cracks during early load stages triggered by the out-of-plane bending. At the last load stage, the maximum crack width, the average crack width, and the average crack spacing were 0.80 mm, 0.17 mm, and 120.3 mm, respectively.
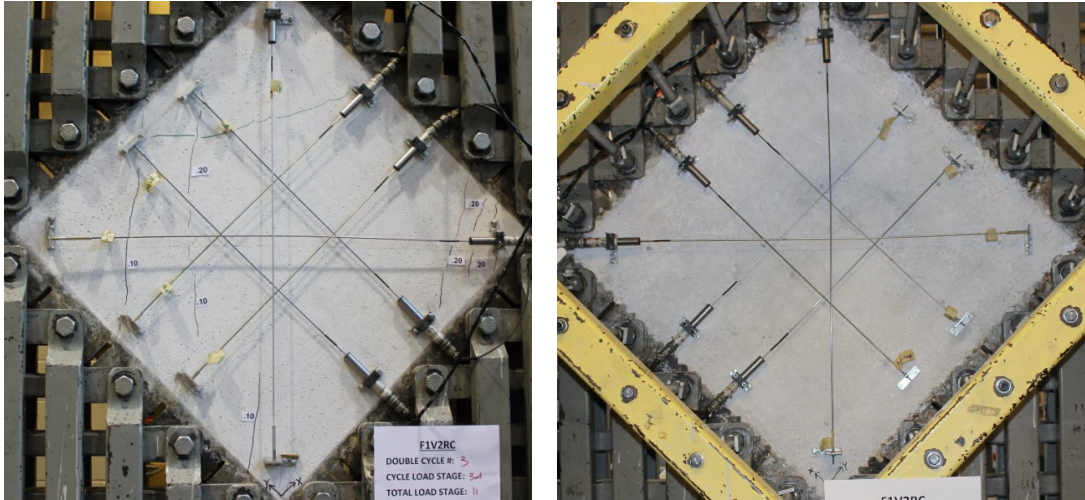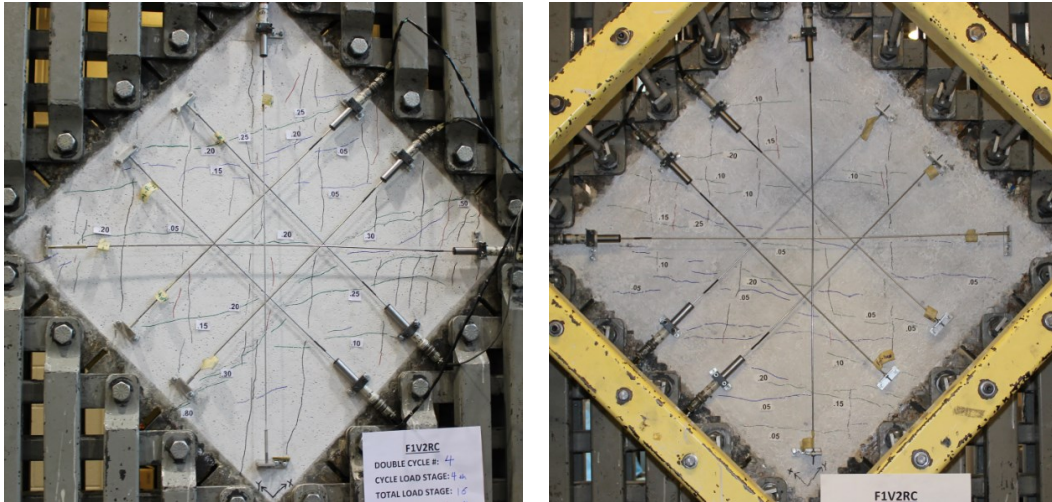
Double Cycle 3, Stage 11: v_{xy}=3.16 MPa, γ_{xy}=0.24×10^{-3}; $w_{cr,max}$=0.20 mm, w_m=0.15 mm, s_m=252 mm.
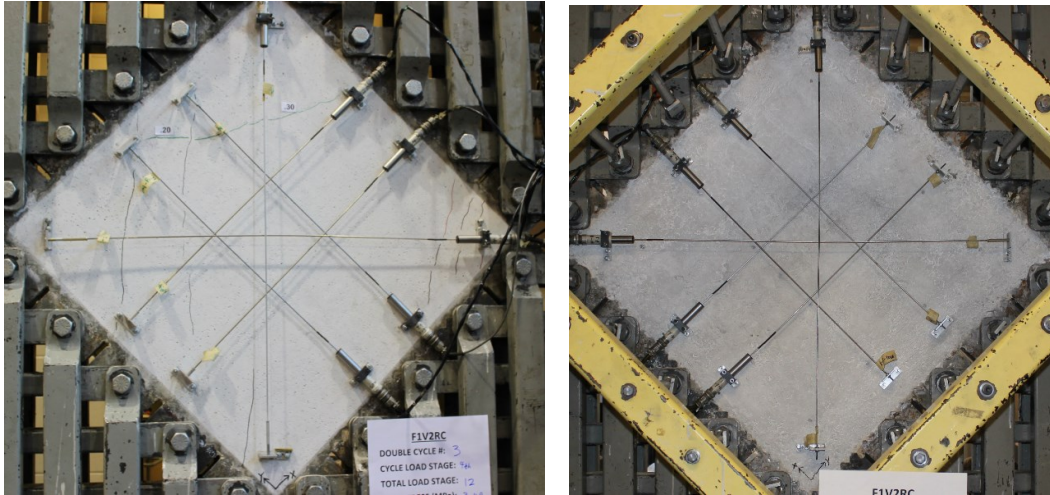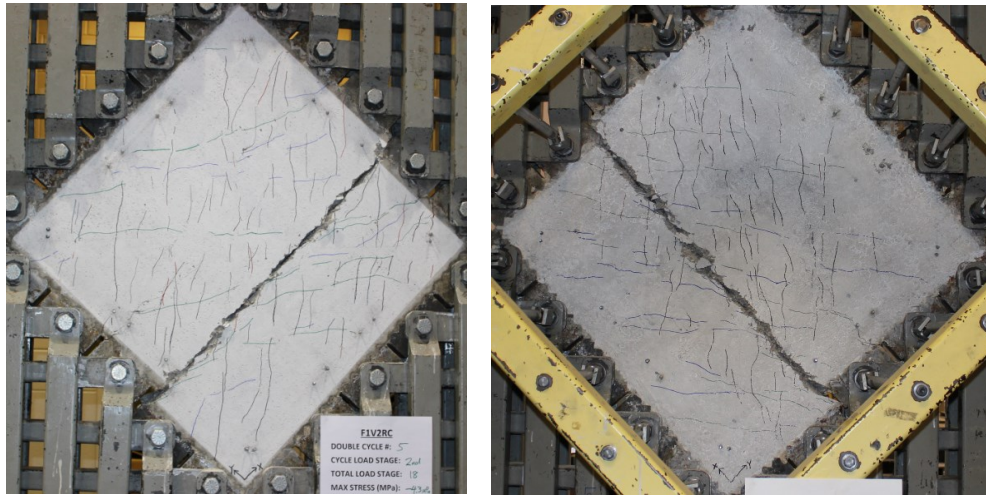

Double Cycle 3, Stage 12: v_{xy}=-3.16 MPa, γ_{xy}=-0.47×10^{-3}; $w_{cr,max}$=0.30 mm, w_m=0.25 mm, s_m=630 mm.
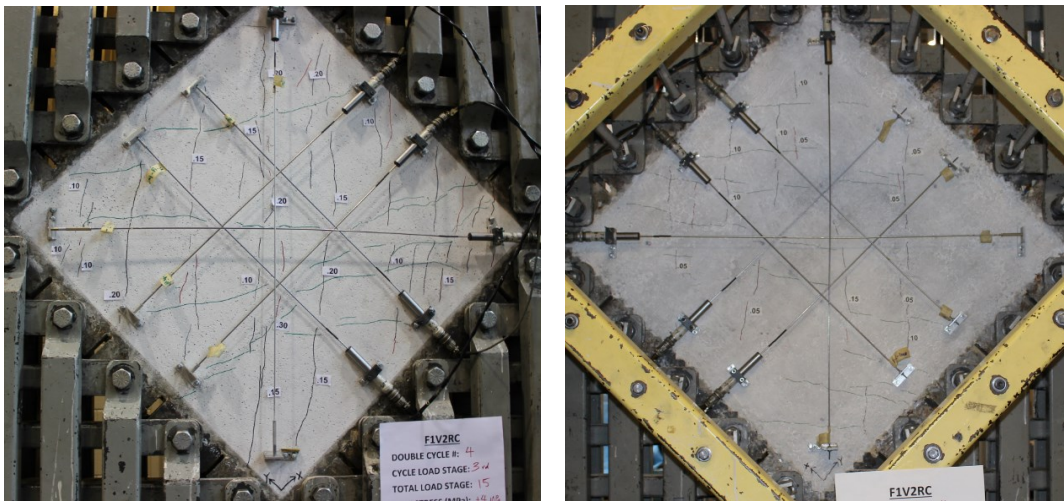
Double Cycle 4, Stage 15: v_{xy}=4.19 MPa, γ_{xy}=1.55×10^{-3}; $w_{cr,max}$=0.30 mm, w_m=0.13 mm, s_m=180 mm.

Double Cycle 4, Stage 16: v_{xy}=-4.21 MPa, γ_{xy}=-2.37×10^{-3}; $w_{cr,max}$=0.80 mm, w_m=0.17 mm, s_m=120 mm.

Failure: v_u=5.24 MPa, γ_u=4.58×10^{-3}.

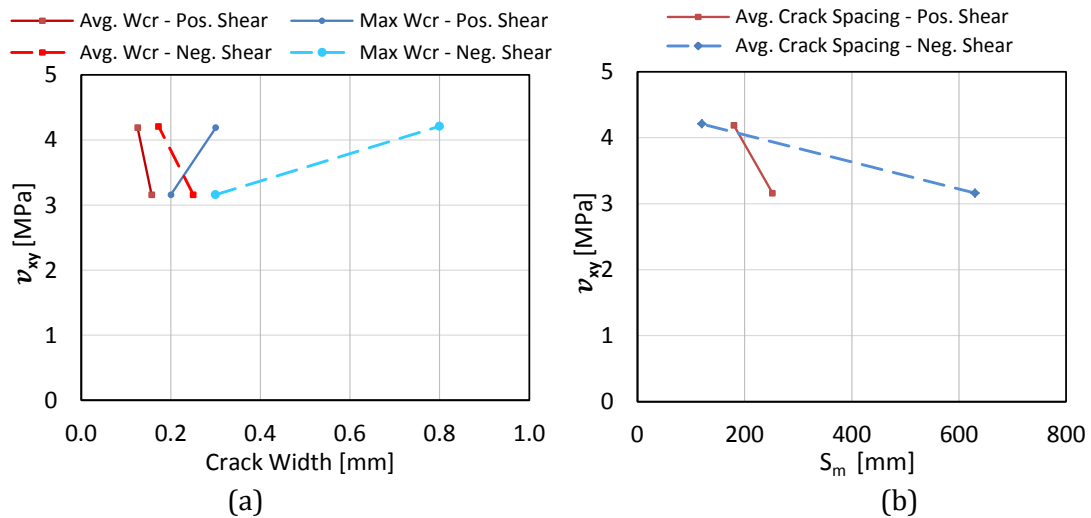Figure B.51: Crack pattern of panel F1V2RC-P

(a)

(b)

Figure B.52: Crack spacing and crack width of panel F1V2RC-P

B.12.2 Data Analysis

The response of F1V2RC-P is shown in Figure B.53. Initial cracking occurred at shear stress and shear strain of 3.16 MPa and 0.325×10^{-3}, respectively. This is consistent with the cracking stress of F1V2RC (3.10 MPa) which shared a similar compressive strength (60.2 MPa for F1V2RC-P and 58.1 MPa for F1V2RC). The response of F1V2RC-P was highly linear up to first-cracking. Failure of the panel occurred at a shear stress and shear strain of 4.32 MPa and 4.33×10^{-3}.

The isolated shear stress-shear strain cycles of F1V2RC-P are shown in Figure B.54. During the 2nd double cycle, the response softened at a shear stress of 1.51 MPa with a shear strain of 0.13×10^{-3} which led to the suspicion that a crack may have formed at this point; however, no cracks were observed during that time and the subsequent hysteretic loops of this double cycle was highly linear. Although the load increment for the 5th double cycle was consistent with the previous cycles, 1.0 MPa, the shear strain increment was very large and was approximately 3.0×10^{-3}. This loading protocol was not successful in capturing the hysteretic response and was not used in the panel tests performed thereafter.

At first-cracking, the principal tensile stress and principal tensile strain were 3.15 MPa and 0.17×10^{-3}, respectively. Afterwards, strain hardening behaviour was exhibited until the maximum principal tensile stress of 3.66 MPa was reached. The principal response gradually softened and reached a plateau of approximately 2.80 MPa. At failure, the principal tensile stress and strain were 2.98 MPa and 6.08×10^{-3}, respectively.

The principal compressive stress and strain at first-cracking were -3.16 MPa and -0.16×10^{-3}, respectively. The shifting of the principal compressive strain to the positive region was observed for this panel, consistent with the other reversed cyclically loaded panels. At failure, the principal compressive stress was -6.26 MPa with a principal compressive strain of -0.31×10^{-3}. The maximum principal compressive stress reached was -9.87 MPa.

The principal strain angle was largely similar to the principal stress angle. The principal stress angle did experience some lag relative to the principal strain angle, especially under negative shear. At failure, the principal stress angle was 125° while the principal strain angle was 111°. The reinforcement reached a peak stress of 215 MPa.

The comparison between F1V2RC-P and F1V2RC is shown in Figure B.55 (a). The response between these two identical panels was similar. The primary difference was that the pilot panel

underwent a much coarser loading protocol which resulted in fewer numbers of cycles and less strength degradation, especially for the positive shear direction. Also, these two panels were made separately which resulted in different mechanical properties despite the similar compressive strengths.

The comparison between F1V2RC-P and its companion panels, F1V2MS-P and F1V2MS, is shown in Figure B.55 (b). Note that the compressive strength for these three separately made panels was 60.2 MPa, 43.2 MPa, and 58.1 MPa for F1V2RC-P, F1V2MS-P, and F1V2MS, respectively. Relative to F1V2MS-P, the monotonic backbone curve of F1V2MS was closer to the cyclic envelope curve of F1V2RC-P due to the similar compressive strength. F1V2RC-P reached a higher shear stress than F1V2MS due to the fact that the two concrete were made separately resulting in different mechanical properties. The dogbone test results showed that the ultimate uniaxial tensile stress attained after first cracking was 3.70 MPa for F1V2RC-P, but was only 3.12 for F1V2MS and F1V2RC.

B.12.3 Comparison of the Front Face and Back Face Responses

Figure B.56 shows the LVDT response for the front face and back face of panel F1V2RC-P. This panel exhibited relatively large out-of-plane bending; the peak shear strain difference between the two faces was 1.1×10^{-3}, larger than any of the panels tested in this work. The bending caused a stiffer response and delayed cracking for the back face. The shear stress-shear strain response and the crack control characteristics between the two faces converged near failure.
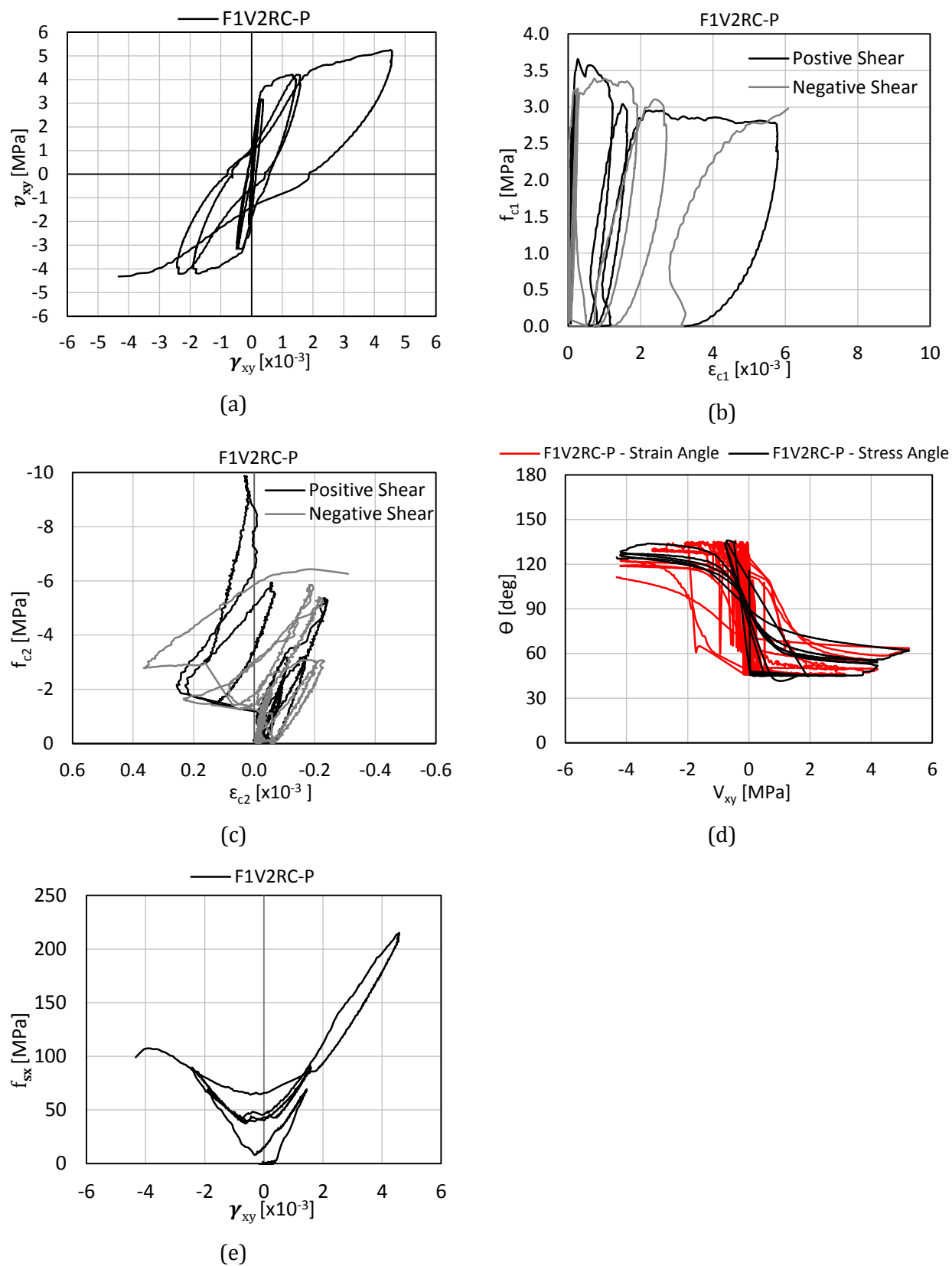
(a)

(b)

(c)

(d)

(e)

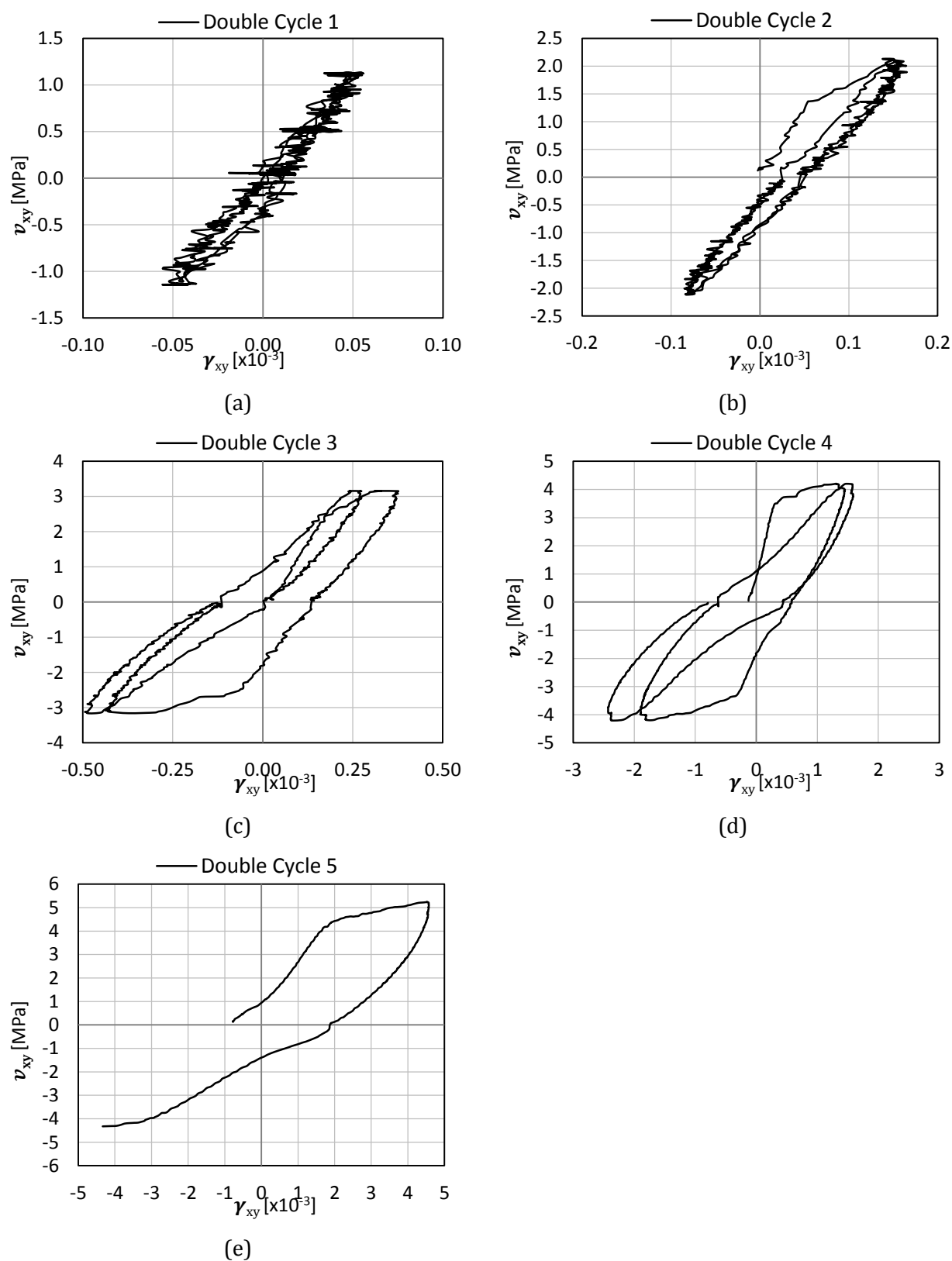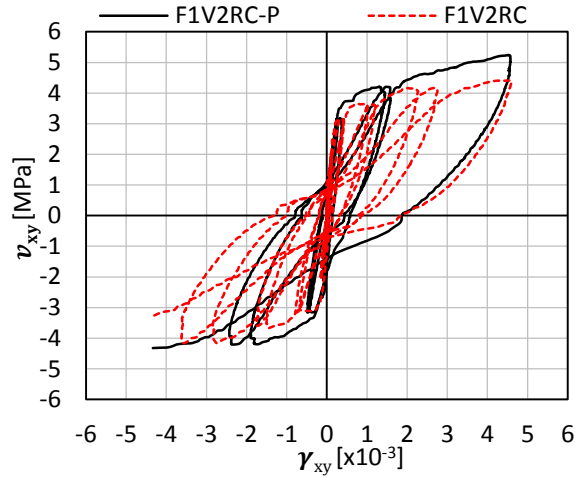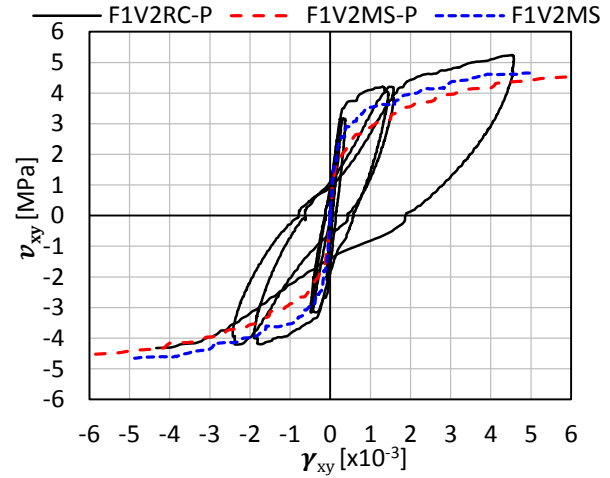Figure B.53: Response of panel F1V2RC-P

(a)

(b)

(c)

(d)

(e)

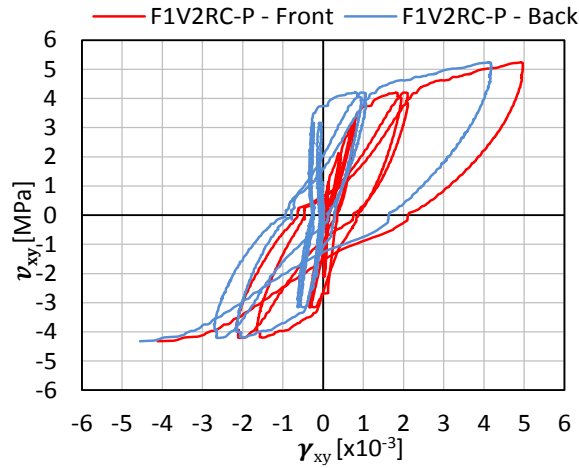Figure B.54: Shear stress-shear strain response of F1V2RC-P; isolated cycles
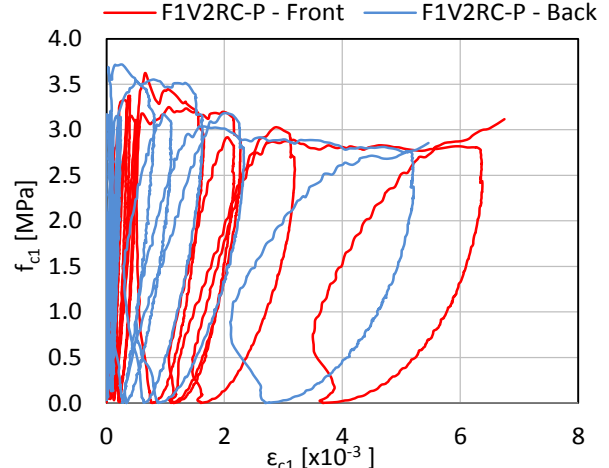
(a) Comparison with repeated panel
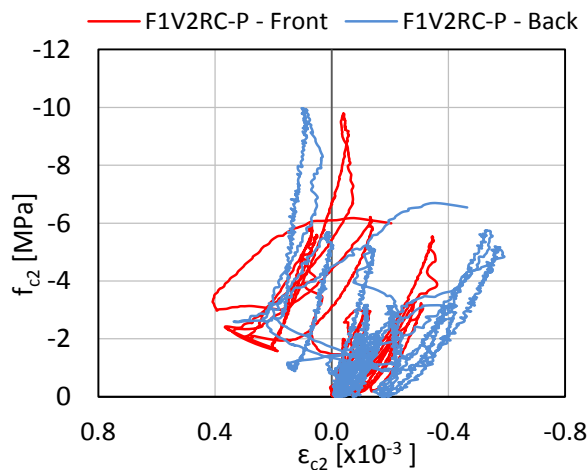
(b) Comparison with companion panels

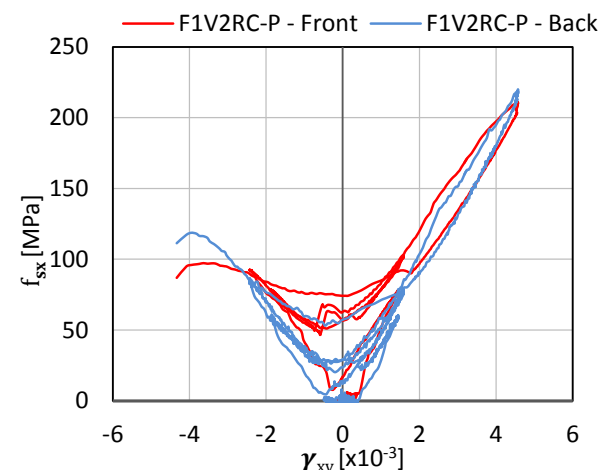Figure B.55: Comparison against the repeated panel and companion panels for F1V2RC-P

(a)

(b)

(c)

(d)

Figure B.56: Comparison of back face and front face response of panel F1V2RC-P